



---

seit 1558

Friedrich-Schiller-Universität Jena

---

Chemisch-Geowissenschaftliche Fakultät

# Characterization of polymeric systems for nanomedical applications

## Dissertation

(kumulativ)

zur Erlangung des akademischen Grades  
doctor rerum naturalium (Dr. rer. nat.)

vorgelegt dem Rat der Chemisch-Geowissenschaftlichen Fakultät der  
Friedrich-Schiller-Universität Jena

von M.Sc. Michael Wagner  
geboren am 09.04.1987 in Suhl

Gutachter:

1. Prof. Dr. Ulrich S. Schubert (Universität Jena)
2. Prof. Dr. Alfred Fahr (Universität Jena)
3. Prof. Dr. Wolfgang Parak (Universität Marburg)

Tag der öffentlichen Verteidigung: 12.12.2014

*"When you have excluded the impossible, whatever remains,  
however improbable, must be the truth."*

Sherlock Holmes



---

**Table of contents**

<b>Documentation of authorship.....</b>	<b>5</b>
<b>1. Introduction .....</b>	<b>13</b>
<b>2. Principles of field-flow fractionation and light scattering .....</b>	<b>17</b>
2.1 Theoretical background of asymmetric flow FFF .....	17
2.2 Light scattering based characterization .....	21
2.3 Advantages and critical aspects of field-flow fractionation.....	22
<b>3. Characterization of cationic polyelectrolytes .....</b>	<b>25</b>
<b>4. Polymer-based gene delivery agents .....</b>	<b>31</b>
<b>5. Self-assembly of amphiphilic block copolymers .....</b>	<b>39</b>
<b>6. Thermo-responsive polymers.....</b>	<b>51</b>
<b>7. Summary.....</b>	<b>57</b>
<b>8. Zusammenfassung .....</b>	<b>61</b>
<b>9. References.....</b>	<b>67</b>
<b>List of abbreviations.....</b>	<b>71</b>
<b>List of symbols .....</b>	<b>73</b>
<b>Curriculum vitae.....</b>	<b>75</b>
<b>Publication list .....</b>	<b>77</b>
<b>Acknowledgement / Danksagung .....</b>	<b>81</b>
<b>Declaration of authorship / Selbständigkeitserklärung .....</b>	<b>83</b>
<b>Publications P1-P10.....</b>	<b>85</b>



## Documentation of authorship

This section contains a list of the individual author contributions to the publications reprinted in this thesis.

**P1)** M. Wagner,<sup>1</sup> S. Holzschuh,<sup>2</sup> A. Träger,<sup>3</sup> A. Fahr,<sup>4</sup> U. S. Schubert,<sup>5</sup> Asymmetric flow field-flow fractionation in the field of nanomedicine, *Anal. Chem.* **2014**, *86*, 5201-5210.

Author	1	2	3	4	5
Conceptional development	X				
Preparation of the manuscript	X	X			
Liposome experiments		X			
Correction of the manuscript			X	X	X
Supervision					X
Proposed publication equivalent	0.5				

**P2)** M. Wagner,<sup>1</sup> C. Pietsch,<sup>2</sup> L. Tauhardt,<sup>3</sup> A. Schallon,<sup>4</sup> U. S. Schubert,<sup>5</sup> Characterization of cationic polymers by asymmetric flow field-flow fractionation and multi angle light scattering – a comparison with traditional techniques, *J. Chromatogr. A* **2014**, *1325*, 195-203.

Author	1	2	3	4	5
Conceptional development	X				
Characterization of all polymers	X				
Synthesis, SEC, and <sup>1</sup> H NMR of PDMAEMA, PAEMA, PtBAEMA		X			
Synthesis of L-PEI			X		
Preparation of the manuscript	X				
Correction of the manuscript				X	X
Supervision					X
Proposed publication equivalent	1.0				

**P3)** M. Wagner,<sup>1</sup> C. Pietsch,<sup>2</sup> A. Kerth,<sup>3</sup> A. Träger,<sup>4</sup> U. S. Schubert,<sup>5</sup> Physicochemical characterization of the thermo-induced self-assembly of thermo-responsive PDMAEMA-*b*-PDEGMA copolymers, *submitted*.

<b>Author</b>	<b>1</b>	<b>2</b>	<b>3</b>	<b>4</b>	<b>5</b>
Conceptional development	X	X			
AF4, DLS, zeta potential experiments	X				
Polymer synthesis		X			
Turbidimetry		X			
DSC experiments			X		
Preparation of the manuscript	X				
Correction of the manuscript				X	X
Supervision					X
Proposed publication equivalent	1.0				

**P4)** M. Hartlieb,<sup>1</sup> D. Pretzel,<sup>2</sup> M. Wagner,<sup>3</sup> S. Höppener,<sup>4</sup> P. Bellstedt,<sup>5</sup> M. Görlach,<sup>6</sup> C. Englert,<sup>7</sup> K. Kempe,<sup>8</sup> U. S. Schubert,<sup>9</sup> Core cross-linked micelles and vesicles based on the self-assembly of double hydrophilic poly(2-oxazoline) block copolymers as potential drug carrier, *submitted*.

<b>Author</b>	<b>1</b>	<b>2</b>	<b>3</b>	<b>4</b>	<b>5</b>	<b>6</b>	<b>7</b>	<b>8</b>	<b>9</b>	
Conceptional development	X									
Polymer synthesis, self-assembly	X									
AF4, DLS, zeta potential experiments			X							
Toxicity assay, FACS, cell culture, microscopy		X								
Cryo-TEM				X						
Solid state NMR measurements					X	X				
Fluorescence investigations							X			
Conceptional contribution								X		
Preparation of the manuscript	X									
Correction of the manuscript								X	X	
Supervision									X	
Proposed publication equivalent			0.25							



**P5)** M. Wagner,<sup>1</sup> A. C. Rinkenauer,<sup>2</sup> A. Schallon,<sup>3</sup> U. S. Schubert,<sup>4</sup> Opposites attract: Influence of the molar mass of branched poly(ethylene imine) on biophysical characteristics of siRNA-based polyplexes, *RSC Advances* **2013**, 3, 12774-12785.

<b>Author</b>	<b>1</b>	<b>2</b>	<b>3</b>	<b>4</b>
Conceptional development	X		X	
Titration	X			
Light scattering and ultracentrifugation studies	X			
Cytotoxicity tests, binding affinity tests, cellular uptake studies		X		
Preparation of the manuscript	X	X		
Correction of the manuscript			X	X
Supervision				X
Proposed publication equivalent	1.0			

**P6)** A. C. Rinkenauer,<sup>1</sup> A. Schallon,<sup>2</sup> U. Günther,<sup>3</sup> M. Wagner,<sup>4</sup> E. Betthausen,<sup>5</sup> U. S. Schubert,<sup>6</sup> F. H. Schacher,<sup>7</sup> A paradigm change: Efficient transfection of human leukemia cells by stimuli-responsive multicompartement micelles, *ACS Nano* **2013**, 7, 9621-9631.

<b>Author</b>	<b>1</b>	<b>2</b>	<b>3</b>	<b>4</b>	<b>5</b>	<b>6</b>	<b>7</b>
Conceptional development	X	X					X
Biological studies	X						
AF4, ultracentrifugation, DLS, zeta potential				X			
Cryo-TEM experiments			X				
Polymer synthesis					X		
Conceptional contribution				X			
Preparation of the manuscript	X	X					
Correction of the manuscript				X		X	X
Supervision						X	X
Proposed publication equivalent	0.5						

**P7)** A. T. Press,<sup>1</sup> A. Träger,<sup>2</sup> C. Pietsch,<sup>3</sup> A. Mosig,<sup>4</sup> M. Wagner,<sup>5</sup> M. G. Clemens,<sup>6</sup> N. Jbeily,<sup>7</sup> N. Koch,<sup>8</sup> M. Gottschaldt,<sup>9</sup> N. Bézière,<sup>10</sup> V. Ermolayev,<sup>11</sup> V. Ntziachristos,<sup>12</sup> J. Popp,<sup>13</sup> M. Kessels,<sup>14</sup> B. Qualmann,<sup>15</sup> U. S. Schubert,<sup>16</sup> M. Bauer,<sup>17</sup> Cell type-specific delivery of short interfering RNAs by dye-functionalized “theranostic” nanoparticles, *Nat. Commun.* **2014**, *accepted*.

<b>Author</b>	<b>1</b>	<b>2</b>	<b>3</b>	<b>4</b>	<b>5</b>	<b>6</b>	<b>7</b>	<b>8</b>	<b>9</b>
Conceptual development	X	X							
Nanoparticle preparation		X							
<i>In vivo</i> experiments	X					X	X		
Polymer synthesis & characterization			X						
<i>In vitro</i> experiments				X					
Characterization of nanoparticles					X				
RNAi & anti-HMGCR antibody assay								X	
Spinning disc microscopy								X	
Conceptual contribution				X					X
Preparation of the manuscript	X	X							X
Correction of the manuscript									X
Proposed publication equivalent					0.1				
<b>Author</b>	<b>10</b>	<b>11</b>	<b>12</b>	<b>13</b>	<b>14</b>	<b>15</b>	<b>16</b>	<b>17</b>	
MSOT experiments	X	X	X	X					
Biophotonic analyses				X					
<i>Hmgcr</i> cloning and immunodetection					X	X			
Conceptual contribution							X	X	
Preparation of the manuscript					X	X			
Correction of the manuscript				X			X	X	
Supervision							X		
Proposed publication equivalent									

**P8)** M. Wagner,<sup>1</sup> M. J. Barthel,<sup>2</sup> R. R. A. Freund,<sup>3</sup> S. Höppener,<sup>4</sup> A. Träger,<sup>5</sup> F. H. Schacher,<sup>6</sup> U. S. Schubert,<sup>7</sup> Self-assembly of poly(ethylene oxide)-*block*-poly(furfuryl glycidyl ether)-*block*-poly(allyl glycidyl ether) based triblock terpolymers: A field-flow fractionation study, *Polym. Chem.* **2014**, DOI: 10.1039/c4py00863d.

Author	1	2	3	4	5	6	7
Conceptional development	X						
AF4, DLS and Zeta potential experiments	X						
Polymer synthesis		X					
Post-polymerization functionalization			X				
Cryo-TEM experiments				X			
Conceptional contribution		X					
Preparation of the manuscript	X	X					
Correction of the manuscript					X	X	X
Supervision						X	X
Proposed publication equivalent	1.0						

**P9)** M. J. Barthel,<sup>1</sup> A. C. Rinkenauer,<sup>2</sup> M. Wagner,<sup>3</sup> U. Mansfeld,<sup>4</sup> S. Höppener,<sup>5</sup> J. A. Czaplewska,<sup>6</sup> M. Gottschaldt,<sup>7</sup> A. Träger,<sup>8</sup> F. H. Schacher,<sup>9</sup> U. S. Schubert,<sup>10</sup> Small but powerful: Co-assembly of polyether-based triblock terpolymers into sub-30 nm micelles and synergistic effects on cellular interactions, *Biomacromolecules* **2014**, *15*, 2426-2439.

Author	1	2	3	4	5	6	7	8	9	10	
Conceptional development	X	X						X	X		
Polymer synthesis & characterization	X										
Self-assembly	X										
Cell-uptake studies, toxicity tests		X									
AF4, DLS, zeta-potential studies			X								
Cryo-TEM measurements				X	X						
Synthesis of acetylated thiogalactose						X					
Preparation of the manuscript	X	X	X								
Correction of the manuscript							X	X	X	X	
Supervision									X	X	
Proposed publication equivalent			0.25								

**P10)** C. Pietsch,<sup>1</sup> U. Mansfeld,<sup>2</sup> C. Guerrero-Sanchez,<sup>3</sup> S. Höppener,<sup>4</sup> A. Vollrath,<sup>5</sup> M. Wagner,<sup>6</sup> R. Hoogenboom,<sup>7</sup> S. Saubern,<sup>8</sup> S. H. Thang,<sup>9</sup> C. R. Becer,<sup>10</sup> J. Chiefari,<sup>11</sup> U. S. Schubert,<sup>12</sup> Thermo-induced self-assembly of responsive poly(DMAEMA-*b*-DEGMA) block copolymers into multi- and unilamellar vesicles, *Macromolecules* **2012**, *45*, 9292-9302.

Author	1	2	3	4	5	6	7	8	9	10	11	12
Conceptional development	X											
Polymer synthesis and characterization	X											
LCST investigations	X											
Cryo-TEM experiments		X		X								
HT-DLS experiments					X							
Zeta potential and DLS experiments						X						
CTA synthesis									X			
Conceptional contribution										X		
Preparation of the manuscript	X								X			
Correction of the manuscript		X	X	X		X	X	X		X	X	X
Supervision												X
Proposed publication equivalent						0.25						

**Erklärung zu den Eigenanteilen des Promovenden/der Promovendin sowie der weiteren Doktoranden/Doktorandinnen als Koautoren an den Publikationen und Zweitpublikationsrechten bei einer kumulativen Dissertation**

Für alle in dieser kumulativen Dissertation verwendeten Manuskripte liegen die notwendigen Genehmigungen der Verlage („Reprint permissions“) für die Zweitpublikation vor.

Die Co-Autoren der in dieser kumulativen Dissertation verwendeten Manuskripte sind sowohl über die Nutzung, als auch über die oben angegebenen Eigenanteile informiert und stimmen dem zu.

Die Anteile der Co-Autoren an den Publikationen sind in diesem Kapitel aufgeführt (Documentation of authorship).

Ich bin mit der Abfassung der Dissertation als publikationsbasiert, d.h. kumulativ, einverstanden und bestätige die vorstehenden Angaben. Eine entsprechend begründete Befürwortung mit Angabe des wissenschaftlichen Anteils des Doktoranden/der Doktorandin an den verwendeten Publikationen werde ich parallel an den Rat der Fakultät der Chemisch-Geowissenschaftlichen Fakultät richten.

Name	Datum	Ort	Unterschrift
------	-------	-----	--------------

Name Erstbetreuer(in)	Datum	Ort	Unterschrift
-----------------------	-------	-----	--------------



## 1. Introduction

Since decades, the broad area of nanoscience and colloids attracts the attention of many researchers in the world.<sup>[1,2]</sup> In particular, the field of nanomedicines promises a variety of potential systems to treat some of the most challenging diseases of our time like cancer or autoimmune disorders.<sup>[3]</sup> Among others, this includes polymeric nanoparticles or self-assembled structures for drug delivery, viral and non-viral vectors for gene delivery as well as biotherapeutics or liposomal formulations.<sup>[4]</sup> There is an entitled hope that essential limitations of certain small molar mass drugs like low solubility, poor bioavailability and biodistribution or unspecific side effects can be overcome with these kinds of drug carriers.<sup>[5]</sup> Nanomaterials are also investigated for their usage as diagnostics and imaging tools.<sup>[6]</sup> Moreover, polymers with stimuli-responsive properties, so called “smart” materials, are in the center of research, *e.g.* for sensing applications. Nevertheless, development and routinely control of colloidal materials require detailed physicochemical characterization approaches. However, it has been mentioned by several regulatory organizations that despite of many attempts there is still a lack of robust methods for quality assessment of nanomaterial production and monitoring the properties of nanoparticles.<sup>[7]</sup> A controlled design needs a trustworthy analytical setup to examine and characterize the obtained materials and their structures in detail. Furthermore, it is mandatory to know the drugs mode of action, as multiple interactions in the human body lead to a highly complex system. From administration until clearance, manifold desirable and undesirable effects can occur, *e.g.* interactions with serum proteins in the blood, interactions with cellular membranes, initiating immune response, degradation in liver or clearance by kidney. To understand these processes, it is necessary to investigate the sample after contact with the different biological matrices. For this purpose, techniques are required, which enable a separation and characterization of individual compounds even in complex samples.

One of the first techniques available for this purpose was analytical ultracentrifugation (AUC).<sup>[8]</sup> Already developed in 1923, it represents a well-established technique in biophysics, mainly used in the field of protein science, nowadays.<sup>[9]</sup> Surprisingly, hydrodynamic studies of synthetic macromolecules are rarely found in literature.<sup>[10]</sup> By sedimentation velocity experiments, the most common type of experiment, the sedimentation coefficient ( $s_0$ ) can be determined by observation of the displacement of the sedimentation boundary over

time.<sup>[11]</sup> Subsequently, sedimentation coefficients can be related to molar masses ( $M$ ) or hydrodynamic radii ( $R_h$ ). Another tool for separation of complex samples is provided by preparative ultracentrifugation (PUC). In particular, density gradient centrifugation is one of the most efficient methods and widely applied to manifold samples like mixtures of proteins, nanoparticles or liposomes.<sup>[12,13]</sup>

A second pool of methods, routinely applied to colloids and macromolecules in solution, is based on light scattering. In principle, three techniques can be distinguished, namely dynamic light scattering (DLS), static light scattering (SLS), and electrophoretic light scattering (ELS), also known as laser Doppler velocimetry (LDV). While DLS gives information on the diffusion coefficient ( $D$ ) and, subsequently,  $R_h$ , SLS provides the weight average molar mass ( $M_w$ ), the radius of gyration ( $R_g$ , also termed root-mean-square radius, RMS), and the second virial coefficient ( $A_2$ ) of a macromolecule or colloid in solution. Both techniques are non-invasive and can be performed with very low amounts of sample, which renders them excellent for investigation of high performance materials. This is also the case for LDV, which enables the determination of the electrokinetic potential (zeta potential).<sup>[14]</sup> Nevertheless in some cases, the applied electrical field can influence delicate structures. A description of the principles and the theoretical background of DLS and SLS is given in Chapter 2.2.

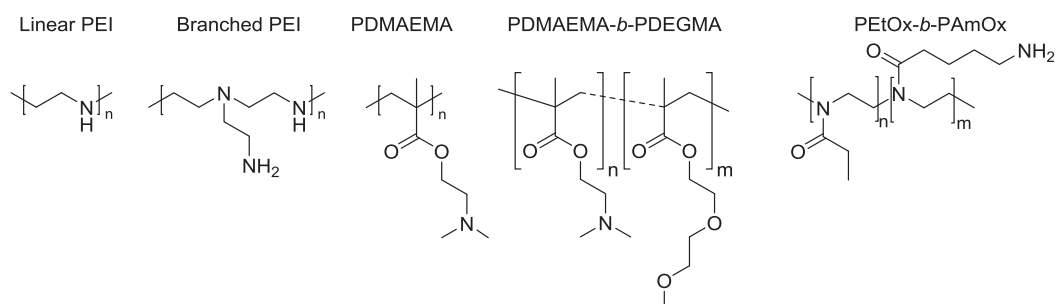
However, light scattering techniques are limited to a certain extent, if applied to suspensions with multimodal size distributions. This is due to the fact that for Rayleigh scattering (particle radius small compared to the wavelength of light,  $r < \lambda_0/20$ ) the intensity of scattered light scales with  $r^6$ . If large species (*e.g.* aggregates) are present in solution, even at very low concentration, discrimination of smaller size fractions can be the result.<sup>[15]</sup> Subsequently, the obtained size distributions or averages might be misleading and have to be interpreted with great care. These limitations were one of the key factors for the broad success of field-flow fractionation (FFF) in the last 20 years.<sup>[16]</sup>

Already presented in 1966 by J. C. Giddings, FFF comprises a class of fractionation techniques developed for the universal separation and characterization of (bio)macromolecules and colloids.<sup>[17,18]</sup> Until the 80's, many different sub-techniques were invented, *e.g.* flow FFF,<sup>[19]</sup> thermal FFF,<sup>[20]</sup> electrical FFF,<sup>[21]</sup> acoustic FFF, magnetic FFF, dielectrophoretic FFF, sedimentation FFF<sup>[22]</sup> or split flow thin cell fractionation<sup>[23]</sup> (SPLITT FFF). All sub-techniques are based on the same principle, but differ in the applied separation field. While flow FFF



relies on a liquid cross-flow, thermal FFF uses a temperature gradient between a hot and a cold wall of the channel. In electrical or magnetic FFF an electrical or magnetic field is applied, whereas in sedimentation FFF or SPLITT FFF the separation is achieved by application of a centrifugational or gravitational field, respectively. In 1984 with the first report of coupling a light scattering detector to FFF by M. Martin, FFF left its former niche existence.<sup>[24]</sup> The possibility to obtain information on size or molar mass, independent of calibration with standards or the application of the retention theory, leads to a tremendous increase of attention to these techniques.<sup>[25,26]</sup> Nowadays, asymmetric flow FFF (AF4), coupled to DLS or multi angle laser light scattering (MALLS) is the most frequently used version in the FFF family. Having a broad separation range from 1 nm to several  $\mu\text{m}$ , it is versatilely applicable for separation and analysis of all kind of (bio)macromolecules and particles.<sup>[27,28]</sup>

Therefore, the application and evaluation of AF4-MALLS-DLS for nano-sized therapeutics like drug or gene delivery systems and the corresponding polymers are in the focus of this thesis. In Chapter 2, the underlying principles and a theoretical consideration as well as a basic background of light scattering are provided. This is followed by a critical discussion of the benefits and limitations of AF4. The analysis of different polyelectrolytes, the basis of many efficient drug or gene delivery agents and stimuli-responsive polymers, is the topic of Chapter 3. As many traditional techniques show certain limitations for the characterization of cationic polymers like poly(ethylene imine) (PEI) or poly(2-(dimethylamino)ethyl methacrylate) (PDMAEMA), the potential of AF4 to support a detailed analysis is discussed (Scheme 1-1).



**Scheme 1-1. Schematic representation of the structures of different cationic polyelectrolytes.**

The obtained results are compared with AUC, proton nuclear magnetic resonance ( $^1\text{H}$  NMR), and size exclusion chromatography (SEC) investigations. The subsequent application of cationic polymers for complexation/delivery of DNA or small interfering RNA (siRNA),

including a detailed characterization, is reported in Chapter 4. A fundamental physicochemical knowledge of the complex properties, *e.g.* composition, size or charge, is mandatory for a better understanding of the gene delivery process and to increase the efficiency by design and not to depend only on intensive screening processes. In a second step, the encapsulation of siRNA/PEI based complexes into nanoparticles with a specific targeting moiety, their body distribution, and their efficiency to induce protein knockdown was studied. Moreover, a triblock terpolymer, polybutadiene-*block*-poly(methacrylic acid)-*block*-poly(2-(dimethylamino)ethyl methacrylate) (PB-*b*-PMAA-*b*-PDMAEMA), was found to enable highly efficient delivery of pDNA to suspension cells. Besides gene delivery, different co- and terpolymers based on poly(ethylene oxide)-*block*-poly(allyl glycidyl ether)-*block*-poly(*tert*-butyl glycidyl ether) (PEO-*b*-PAGE-*b*-PtBGE), poly(ethylene oxide)-*block*-poly(furfuryl glycidyl ether)-*block*-poly(allyl glycidyl ether) (PEO-*b*-PFGE-*b*-PAGE) or amine containing poly(2-oxazoline) (Scheme 1-1) were investigated concerning their self-assembly in aqueous solution and their potential for drug delivery applications (Chapter 5). To manipulate the morphologies of the triblock terpolymers, various functional groups were introduced onto the PAGE side chain *via* post-polymerization functionalization. This included the incorporation of charges by carboxy or amino groups, the adjustment of the amphiphilic character (hydrophilicity/hydrophobicity) by alkyl or fluorinated alkyl chains or the attachment of sugar moieties. Additionally, mixed micelles, formed by co-assembly of the differently functionalized polymers, were studied as well as the influence of solution conditions (*e.g.* pH value and ionic strength) on the self-assembly. Another class of drug delivery agents is based on stimuli-responsive polymers, which are able to react on environmental changes.<sup>[29,30]</sup> In particular, block copolymers, where at least one block shows a lower critical solution temperature (LCST), are attractive candidates for sensor systems and the controlled release of drugs or dyes.<sup>[31,32]</sup> The physicochemical characterization of the thermo-induced self-assembly behavior of such “smart” systems, based on poly(2-(dimethylamino)ethyl methacrylate)-*block*-poly(di(ethylene glycol) methyl ether methacrylate) (PDMAEMA-*b*-PDEGMA), is discussed in depth in Chapter 6 (Scheme 1-1).

## 2. Principles of field-flow fractionation and light scattering

Parts of this chapter have been published: P1) M. Wagner, S. Holzschuh, A. Träger, A. Fahr, U. S. Schubert, *Anal. Chem.* **2014**, *86*, 5201-5210.

DLS and SLS/MALLS, used as stand-alone techniques or coupled to flow systems are common, well-established methods for the analysis of polymers and colloids.<sup>[33]</sup> In particular, AF4 coupled to UV/RI as well as DLS and MALLS, in a multi-detector approach, represents a powerful tool to obtain manifold physicochemical information and was used throughout this thesis for various polymers, nanoparticles, and self-assembly systems. Therefore, the principles and basic theories of AF4 and light scattering are described shortly in this section. Subsequently, the benefits and limitations are highlighted as well as critically evaluated to provide a basis for the discussion of the results in Chapters 3 to 6.

### 2.1 Theoretical background of asymmetric flow FFF

In AF4, the separation takes place in an empty, narrow, ribbon-like channel of trapezoidal geometry, where a liquid cross-flow is applied perpendicular to the laminar sample flow. The channel is built up by a spacer (thickness 50 to 500  $\mu\text{m}$ ) between a porous and a nonporous plate (Figure 2-1). The porous plate is formed by a frit, covered with a membrane, which acts as accumulation wall and allows the eluent to pass, while the sample is retained. The membrane is a semipermeable ultrafiltration membrane with a defined molar mass cut-off (MWCO), typically in the range of 1 to 10  $\text{kg}\cdot\text{mol}^{-1}$ .

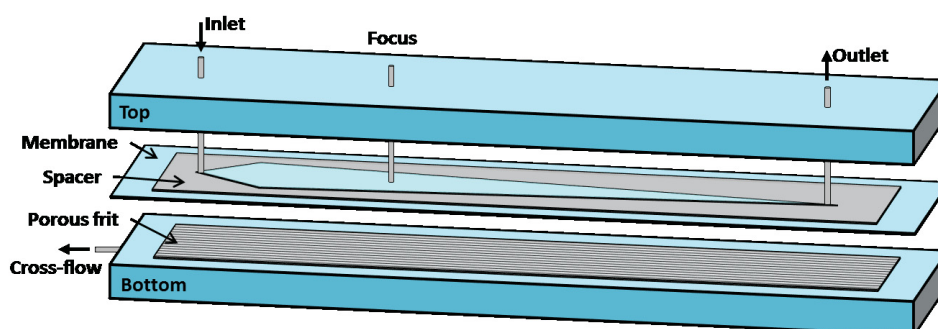


Figure 2-1. Schematic representation of an AF4 channel. The eluent is pumped from the inlet to the outlet. The membrane acts as accumulation wall and represents the porous wall. The geometry of the channel is defined by the spacer.

The eluent is pumped from the inlet, where also the sample is injected, to the outlet of the channel, where at least one detector is connected. Due to the laminar flow, a parabolic flow

profile is formed along the longitudinal axis of the channel, which leads to different flow velocities in dependence of the distance to the channel wall. The highest flow velocity is reached in the center of the channel, while it decreases to zero near the membrane. During the transport of the sample by the eluent, the cross-flow is applied perpendicular to the longitudinal axis of the channel. This results in a force, dragging the analyte to the accumulation wall (Figure 2-2). According to Fick's law, as a result of the formed concentration gradient, the diffusivity acts as a counteracting force, until an exponential steady-state-distribution of the sample is achieved.<sup>[34]</sup> Thereby, independent of the nanoparticle's size/diffusivity, the highest concentration is reached near the accumulation wall. The concentration profile of small particles with a high diffusion coefficient is extended more into the channel, than for larger ones with low diffusivity (Figure 2-2B, schematic concentration profile, left). Subsequently, smaller particles obtain a higher average distance from the wall (visualized by the particles in Figure 2-2B), occupy faster streamlines of the parabolic velocity flow profile and elute earlier.

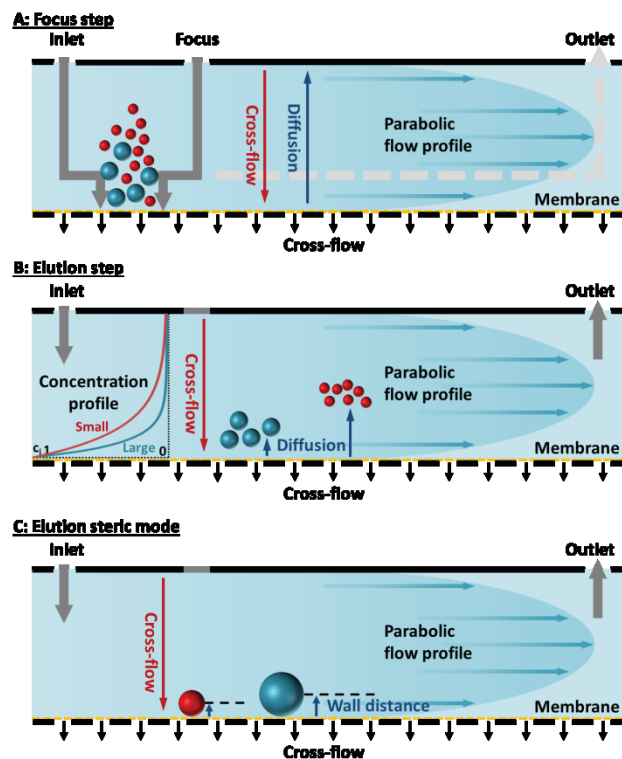


Figure 2-2. Schematic representation of the AF4 principle. The eluent is pumped from the inlet to the outlet and the cross-flow is applied perpendicular to the flow direction. The different steps are (A) the focusing process, (B) the elution process under normal mode, and (C) the elution under steric conditions.

To avoid a spreading of the sample over the entire channel length during injection, an additional focusing/relaxation process is applied to concentrate the analyte in a narrow zone

near the inlet (Figure 2-2A). This stopped-flow procedure increases the resolution, reduces band broadening, and washes out low molar mass impurities (*e.g.* salts) through the membrane.<sup>[35]</sup> For large analytes, exceeding a certain size ( $> 1 \mu\text{m}$ ), the order of retention can change from the normal (Brownian mode) to the steric mode (steric FFF), where larger particles elute first (Figure 2-2C).<sup>[36]</sup> This is based on the finite size of the colloid, its negligible low diffusion, and the strong force of the cross-flow on large particles, which are located in a thin layer very close to the accumulation wall.<sup>[37]</sup> Here, the average distance from the wall is just determined by the physical radius of the particles. As all relevant samples, discussed in this thesis, are below the size limit of around  $1 \mu\text{m}$ , the interested reader is referred to the cited literature for further details.<sup>[38,39]</sup>

The theoretical basis of FFF was developed in detail by Giddings, Wahlund and co-workers and only a brief description will be given here.<sup>[34,40]</sup> For this purpose, some simplifications and assumptions have to be made, which might not be valid under all conditions. For an extensive mathematical description, the reader is referred to the cited literature or the comprehensive “Field-Flow Fractionation Handbook”.<sup>[41]</sup> In the first part of the measurement, the focusing of the sample takes place and the distance from the inlet to the focus point,  $z_{\text{foc}}$ , as well as the focus area,  $A_{\text{foc}}$ , depend on the applied flow rates and the dimensions of the channel (eq 1, 2).<sup>[34]</sup>  $A$  is the accumulation wall area,  $\dot{V}_{\text{in}}$  the inlet flow rate,  $\dot{V}_{\text{c}}$  the cross-flow rate and  $\alpha$  the angle of the inlet triangle.

$$z_{\text{foc}} = \sqrt{\left(\frac{A}{\tan\frac{\alpha}{2}}\right)\left(\frac{\dot{V}_{\text{in}}}{\dot{V}_{\text{c}}}\right)} \quad (1)$$

$$A_{\text{foc}} = A\left(\frac{\dot{V}_{\text{in}}}{\dot{V}_{\text{c}}}\right) \quad (2)$$

For elution in chromatography, retention is usually expressed in terms of the retention ratio  $R_r$ , defined by the ratio of the void and the retention volume ( $V^0$ ,  $V_r$ ) or time ( $t^0$ ,  $t_r$ ), respectively (eq 3). In FFF, the retention ratio  $R_r$  can be obtained through eq 4.<sup>[34]</sup>

$$R_r = \frac{V^0}{V_r} = \frac{t^0}{t_r} \quad (3)$$

$$R_r = \frac{6}{w} \left[ \frac{\int_0^w e^{\left(-\frac{x}{l}\right)B(x)} x dx - \frac{1}{w} \int_0^w e^{\left(-\frac{x}{l}\right)B(x)} x^2 dx}{\int_0^w e^{\left(-\frac{x}{l}\right)B(x)} x dx} \right] \quad (4)$$

Here,  $x$  is the distance of the sample from the accumulation wall and  $w$  the channel height. For flow FFF, the parameter  $l$ , which describes the average layer thickness of the sample cloud, is given by eq 5 with the diffusion coefficient  $D$ . The term  $B(x)$  is given by eq 6.<sup>[42]</sup>

$$l = \frac{DA}{\dot{V}_c} = \frac{DV^0}{\dot{V}_c w} \quad (5)$$

$$B(x) = 1 - \frac{x^2}{w^2} + \frac{x^3}{w^3} \quad (6)$$

Assuming a constant cross-flow velocity near the accumulation wall and sample migration close to the wall ( $x/w < 0.1$ ), eq 4 can be approximated by eq 7 with the retention parameter  $\lambda$  as defined by eq 8.<sup>[34]</sup>

$$R_r = 6\lambda \left[ \coth\left(\frac{1}{2\lambda}\right) - 2\lambda \right] \quad (7)$$

$$\lambda = \frac{l}{w} = \frac{DV^0}{w^2 \dot{V}_c} \quad (8)$$

For  $R_r < 0.06$ , meaning high levels of retention, eq 7 can be further simplified within an error of 2% to  $R_r = 6\lambda$ .<sup>[34]</sup> Combination with eq 3 and 8 leads to an expression for the retention time in dependence of the diffusion coefficient and the cross-flow rate (eq 9).

$$t_r = \frac{w^2 \dot{V}_c t^0}{6DV^0} \quad (9)$$

This equation is valid for point masses, constant cross-flow rates, and the absence of self-interactions or interactions with the membrane. Using the Stokes-Einstein relationship (eq 10),  $t_r$  can be related to  $R_h$  (eq 11), where  $k_B$  is Boltzmann's constant,  $T$  the temperature and  $\eta$  the viscosity of the eluent.

$$D = \frac{k_B T}{6\pi\eta R_h} \quad (10)$$

$$t_r = \frac{\pi\eta w^2 \dot{V}_c t^0 R_h}{k_B T V^0} \quad (11)$$

To calculate  $R_h$ , the void time/volume and the channel thickness have to be known or can be calculated according to literature.<sup>[42,43]</sup> The described theoretical approach is valid for cross-flows that are constant over time. For decaying cross-flows or a combination of different steps, numerical techniques are necessary and some solutions, addressing this problem, are presented in the work of Giddings and others.<sup>[44-46]</sup> The calculation of diffusion coefficients out of retention times requires a behavior predicted by the retention theory and the

absence of non-ideal effects. Alternatively, calibration standards can be used to relate  $t_r$  to  $M$  or  $R_h$ , like for SEC. Nowadays, AF4 is mostly coupled to MALLS or DLS to obtain independent information on both, molar mass and size.

## 2.2 Light scattering based characterization

DLS as well as SLS/MALLS are widely applied as stand-alone as well as online detection techniques. MALLS is based on the angular dependent measurement of the average intensity of scattered light. Thereby, the intensity of the scattered light is related to the molar mass by the common scattering equation (eq 12),<sup>[47]</sup>

$$\frac{Kc}{R(\theta)} = \frac{1}{M_w P(\theta)} + 2A_2 c + \dots \quad (12)$$

$$R(\theta) = \frac{I(\theta) - I_s}{I_0} \cdot \frac{d^2}{V} \quad (13)$$

$$K = \frac{\left(2\pi n_0 \frac{\partial n}{\partial c}\right)^2}{\lambda_0^4 N_A} \quad (14)$$

where  $R(\theta)$  is the excess Rayleigh ratio at the scattering angle  $\theta$  (eq 13),  $M_w$  the weight average molar mass,  $c$  the concentration,  $P(\theta)$  the form factor, describing the angular dependence of the scattered light,  $A_2$  the second virial coefficient and  $K$  the contrast factor calculated according to eq 14.  $I(\theta)$  is the intensity measured at an angle  $\theta$ ,  $I_s$  the intensity of the solvent,  $I_0$  the incident intensity,  $V$  the scattering volume and  $d$  the distance from the scattering center.  $n_0$  is the refractive index of the solvent,  $\frac{\partial n}{\partial c}$  the refractive index increment,  $\lambda_0$  the laser wavelength in vacuum, and  $N_A$  Avogadro's number. In contrast to classical SLS, the second virial coefficient  $A_2$  is neglected in the majority of flow measurements with MALLS, due to the high dilution during the fractionation process. The concentration can be directly measured, if a UV or RI detector is used in series with MALLS. Furthermore, if each fraction is assumed to be monodisperse,  $M_w$  becomes similar to  $M$  and the entire molar mass distribution can be obtained from the molar mass of each slice/fraction, weighted by its concentration. For small particles ( $r < \lambda/20$ ), a simplified expression of the form factor (series expansion of  $P(\theta)$ ) can be used, which results in the well-known Zimm-equation (eq 15) with the scattering vector  $q$  (eq 16).<sup>[48]</sup>

$$\frac{Kc}{R(\theta)} = \frac{1}{M} \left(1 + \frac{R_g^2}{3} q^2\right) + 2A_2 c \quad (15)$$

$$q = \frac{4\pi n_0}{\lambda_0} \sin \frac{\theta}{2} \quad (16)$$

For larger structures, a Debye or Berry plot<sup>[49]</sup> or if the shape/conformation of the sample is known, the individual form factors, widely described in literature, should be used.<sup>[47,48,50]</sup>

For DLS, the fluctuation of the intensity of scattered light is recorded and the intensity-time-autocorrelation function  $g_2(\tau)$  is calculated according to eq 17.

$$g_2(\tau) = \frac{\langle I(t) \cdot I(t+\tau) \rangle}{\langle I(t) \rangle^2} \quad (17)$$

$I(t)$  represents the intensity at the time  $t$  or  $t+\tau$ , respectively. After transformation of  $g_2(\tau)$  into the field-time-autocorrelation function  $g_1(\tau)$  by the Siegert-relation, a fit by a mono-exponential decay function, according to eq 18 (cumulant method), gives the translational diffusion coefficient  $D$  of a monodisperse sample.<sup>[51]</sup>

$$g_1(\tau) = e^{-Dq^2\tau} \quad (18)$$

The diffusion coefficient can be related to the hydrodynamic radius by usage of the Stokes-Einstein equation (eq 10). In the case of polydisperse samples, the autocorrelation function is expressed as a sum of exponential decay functions according to eq 19.

$$g_1(\tau) = \sum_{i=0}^i A_i e^{-Dq^2\tau} \quad (19)$$

Therefore, different algorithms based on the inverse Laplace transform, like the well-known CONTIN algorithm, are available.<sup>[52]</sup> For DLS coupled to FFF, the cumulant method is often sufficient, as each single fraction is supposed to be monodisperse.

### 2.3 Advantages and critical aspects of field-flow fractionation

In contrast to classic chromatographic methods like SEC, AF4 has no stationary phase, which reduces shear induced degradation and sample adsorption, resulting in an ideal tool for delicate samples (*e.g.* preserving the biological activity of proteins).<sup>[53]</sup> Also nearly each formulation or solvent, either aqueous or organic, can be used to minimize effects on stability or structure, *e.g.* the investigation of nanoparticles in solutions under physiological conditions.<sup>[54]</sup> This is often not possible by other methods like density gradient ultracentrifugation. Additionally, a high flexibility is given as all experimental parameters can be adjusted easily. Anyhow, the most common problem of AF4 is based on interactions with the membrane. As a result of the high sample concentration near the accumulation wall, an



appropriate type of membrane and eluent has to be selected to reduce adsorption effects. A time consuming screening of different materials (*e.g.* regenerated cellulose, poly(ether sulfone) or poly(vinylidene difluoride)) with different properties (*e.g.* surface charge, smoothness or chemical stability) and various eluent compositions might be necessary to obtain a proper elution behavior. For nanoparticles, the addition of surfactants like sodium dodecyl sulfate (SDS), cetyl trimethylammonium bromide (CTAB) or different polysorbates (Tween®), which bind to the membrane surface, is often beneficial to reduce sample loss and membrane interactions.<sup>[55]</sup> Control over pH value and ionic strength of the eluent plays an important role, among others, for investigations on charged samples. Both parameters control the net-charge (accessible by zeta potential) and the resulting electrostatic interactions between the analyte itself and between the analyte and the membrane.<sup>[56,57]</sup> A more detailed discussion of these effects can be found in Chapters 3 and 5. For separation of disperse heterogeneous mixtures, one has to be aware of these interactions and adsorption on the membrane, as both can disturb an accurate quantification of the individual fractions. All mentioned non-ideal effects as well as the possibility to vary the channel height or geometry and the necessary optimization of flow rates results in an often time consuming method development. This presents a major drawback of AF4, which diminishes the advantage of a short measurement time and limits the application for routinely performed analyses.<sup>[58]</sup>

As already mentioned, AF4 provides a broad separation range from 1 nm to 100  $\mu\text{m}$ . However, this range can hardly be achieved in a single experiment. Furthermore, coupling to light scattering limits the range, where independent information on molar mass and size can be obtained to around  $10^4$  to  $10^9$   $\text{g}\cdot\text{mol}^{-1}$  or 10 to 1000 nm radius for MALLS and around 3 to 1000 nm for DLS. Nevertheless, in contrast to stand-alone light scattering techniques, a previous separation by AF4 provides a superior characterization of highly disperse samples, as discrimination effects, caused by the presence of larger fractions, are excluded. Another advantage of AF4 is that small molar mass impurities in the sample do not disturb the measurement, as they are washed out through the membrane during the focusing period. Furthermore, many detectors used for traditional liquid chromatography can also easily be coupled to AF4. Among others, this comprises inductively coupled plasma mass spectrometry (ICP-MS),<sup>[59]</sup> viscosimetry, infrared detection,<sup>[60]</sup> fluorescence spectroscopy or small angle x-ray scattering (SAXS).<sup>[61]</sup>



### 3. Characterization of cationic polyelectrolytes

Parts of this chapter have been published: P2) M. Wagner, C. Pietsch, L. Tauhardt, A. Schallon, U. S. Schubert, *J. Chromatogr. A* **2014**, *1325*, 195-203; P3) M. Wagner, C. Pietsch, A. Kerth, A. Träger, U. S. Schubert, *submitted*; P4) M. Hartlieb, D. Pretzel, M. Wagner, S. Höppener, P. Bellstedt, M. Görlach, C. Englert, K. Kempe, U. S. Schubert, *submitted*.

Polyelectrolytes represent attractive systems for drug and gene delivery applications as well as for the introduction of stimuli-responsive properties.<sup>[62]</sup> Cationic polymers like PEI or PDMAEMA are able to bind the natural anionic macromolecules DNA or RNA and form so called polyplexes, which are widely investigated as non-viral vectors for gene delivery.<sup>[63]</sup> To understand the complexation process, the resulting structures and their efficiency in biological experiments, a detailed knowledge of the physicochemical properties is mandatory. This comprises, among others, the molar mass or size distribution, the architecture as well as the conformation of the macromolecules. Different techniques are known to study these properties. Anyhow, many methods show certain limitations for cationic polyelectrolytes in the range of  $10^4 \text{ g}\cdot\text{mol}^{-1}$  ( $M_n$ ).<sup>[64,65]</sup> For example, SEC results have to be interpreted with care, due to the occurrence of strong interactions with the stationary phase and mass spectrometry is often difficult for higher molar masses due to problematic ionization.<sup>[66-68]</sup> Techniques based on colligative phenomena suffer from several difficulties, too. NMR spectroscopy or SLS are applicable, but provide just average values with limited information on the dispersity. Therefore, AF4 was studied as a potential alternative.

The major challenge concerning AF4 and cationic polymers is the presence of electrostatic sample-membrane interactions.<sup>[64]</sup> Due to a negative surface net-charge of the most common types of membranes and the cationic charge of the samples, strong electrostatic attraction occurs, which leads to massive adsorption and sample loss during fractionation. To address this problem, several possibilities were found. The simplest way is an increase of the ionic strength of the eluent to reduce the range of electrostatic interactions (Debye length) according to the Debye-Hückel theory. This is often successful for larger colloids, which exhibit just a low charge density and where low cross-flows can be applied, but fails for many polymer systems.<sup>[69]</sup> Here, hydrophobic interactions can become significant, due to the presence of hydrophobic spots on the membrane surface.<sup>[70]</sup> Another possibility relies on

the preconditioning of the membrane. Thereby, a cationic surfactant (*e.g.* CTAB) or polymer is injected and adsorbed on the membrane surface in a first experiment.<sup>[57]</sup> For subsequent measurements, a positively charged layer of surfactant or polymer on the surface provides repulsive electrostatic interactions between the samples and the accumulation wall.<sup>[71,72]</sup>

In the study of cationic polymers for gene delivery, a presaturation with PDMAEMA<sub>500</sub> (N = 500; degree of polymerization) enables a reliable characterization of PEI, poly(L-lysine) (PLL), poly(2-(amino)ethyl methacrylate) (PAEMA), poly(2-(*tert*-butylamino)ethyl methacrylate) (PtBAEMA) and PDMAEMA of different molar masses. The success of the conditioning is indicated by recovery rates below 70% for experiments on fresh membranes, followed by a recovery above 80% for the subsequent measurements. Representative results of commercial branched PEI and PDMAEMA are shown in Figure 3-1.

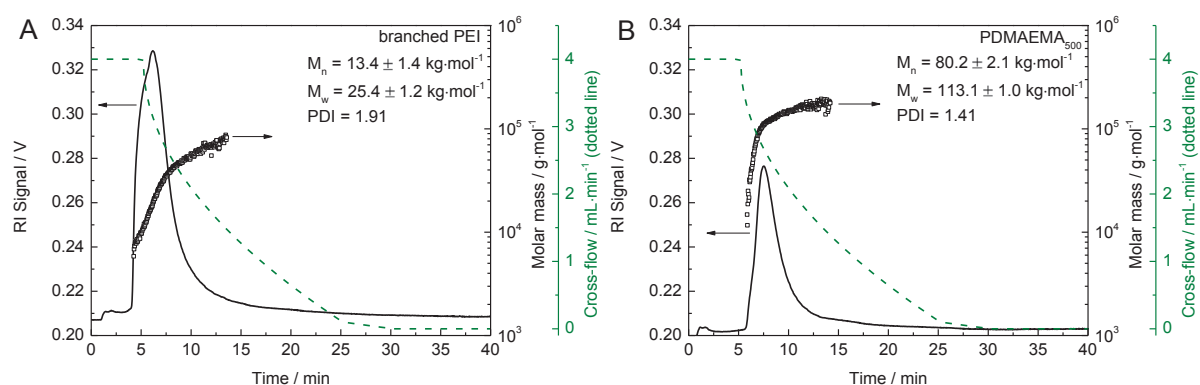


**Figure 3-1.** AF4 fractograms with cross-flow rates and molar masses of (A) branched PEI and (B) PDMAEMA<sub>500</sub>.

For PEI (and PLL) the molar masses obtained by AF4 are in good agreement with the values stated by the manufacturer ( $M_w = 25 \text{ kg}\cdot\text{mol}^{-1}$ ). For PDMAEMA, PAEMA and PtBAEMA, the results were compared with data from  $^1\text{H}$  NMR spectroscopy and AUC experiments (Table 3-1). These methods were chosen as they provide different averages, namely the number average molar mass ( $M_n$ ) by NMR as well as the sedimentation diffusion average molar mass ( $M_{sD}$ , comparable to  $M_w$ )<sup>[73]</sup> by sedimentation velocity experiments and the Svedberg equation (eq 20). Here,  $R$  is the universal gas constant,  $T$  the temperature,  $s_0$  the sedimentation coefficient,  $D$  the translational diffusion coefficient,  $\bar{v}$  the partial specific volume and  $\rho$  the solvent's density.<sup>[74]</sup>

$$M_{sD} = \frac{s_0 RT}{D(1-\bar{v}\rho)} \quad (20)$$

A comparison shows that the values obtained by AUC ( $M_{sD}$ ) and AF4-MALLS ( $M_w$ ) are in excellent agreement, while there is a significant difference to the NMR results ( $M_n$ ) for higher molar mass polymers (PDMAEMA<sub>320</sub>, PDMAEMA<sub>500</sub>). This is most probably due to limitations of NMR in this molar mass region, as the determination is based on the comparison of the integral of an end group signal and a signal of a repeating unit of the polymer backbone. With increasing degree of polymerization, the integral of the end group signal decreases, leading to a lower signal to noise ratio. Furthermore, AF4 is not affected by side reactions during the polymer synthesis, which influence the presence of the endgroup on each chain (endgroup fidelity). In comparison to AUC, less material and time is required.

Table 3-1. Molar masses and  $\bar{D}$  values of methacrylate based polymers obtained by  $^1\text{H}$  NMR, AUC, and AF4.

Sample	$M_n$ (NMR) [kg·mol <sup>-1</sup> ] <sup>[a]</sup>	$M_{sD}$ (AUC) [kg·mol <sup>-1</sup> ]	$M_n$ (AF4) [kg·mol <sup>-1</sup> ]	$M_w$ (AF4) [kg·mol <sup>-1</sup> ]	$\bar{D}$ (AF4)
PDMAEMA <sub>90</sub>	14.5 ± 0.2	16.3 ± 0.3	14.7 ± 0.7	16.8 ± 0.4	1.14
PDMAEMA <sub>230</sub>	36.3 ± 3.3	42.5 ± 0.2	36.1 ± 0.61	41.1 ± 0.72	1.14
PDMAEMA <sub>320</sub>	42.6 ± 1.9	65.8 ± 1.7	51.2 ± 1.9	67.3 ± 1.2	1.31
PDMAEMA <sub>500</sub>	72.3 ± 1.6	112.0 ± 2.6	80.2 ± 2.1	113.1 ± 1.0	1.41
PAEMA <sub>150</sub>	25.0 ± 0.2	27.2 ± 1.4	24.9 ± 1.2	29.1 ± 1.2	1.17
PtBAEMA <sub>170</sub>	31.2 ± 2.8	36.0 ± 0.6	29.9 ± 2.3	37.3 ± 1.3	1.25

<sup>[a]</sup> measured in CD<sub>2</sub>Cl<sub>2</sub> or D<sub>2</sub>O.

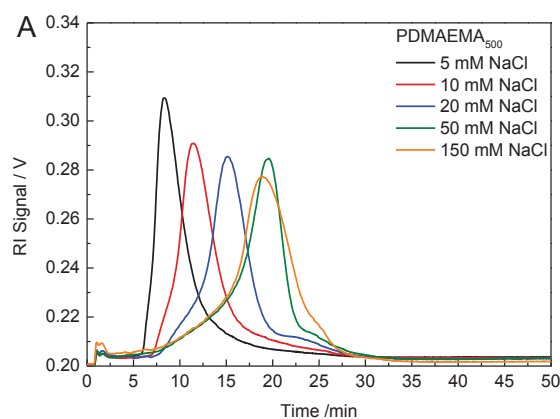


Figure 3-2. AF4 fractograms of PDMAEMA<sub>500</sub> at different concentrations of NaCl.

A retention behavior based on a presaturation by PDMAEMA is also supported by measurements at varying ionic strength. With increasing ionic strength, more precisely increasing concentration of NaCl (5 to 150 mM), an increase in retention time is observed (no increase in molar mass) (Figure 3-2). This can be explained by a reduction of the range of electrostatic interactions, associated with a reduced repulsion between the positive

(presaturated) surface and the cationic polymer. Subsequently, this shortens the characteristic distance to the accumulation wall and increases the retention time. In the same study, it could also be shown that AF4-MALLS enables conformational studies on macromolecules. Therefore, so called power-law-relationships (eq 21) can be applied, where the exponent  $\nu$  yields information on the conformation of a macromolecule.<sup>[11]</sup>

$$R_g = K_r M^\nu \quad (21)$$

In contrast to hydrodynamic methods like AUC or viscosimetry, there is no obligatory necessity to synthesize and analyze a variety of polymers with different molar masses. With AF4-MALLS,  $\nu$  can be obtained from a linear regression of a logarithmic plot of  $R_g$  versus  $M$  of each fraction of a single experiment, as shown in Figure 3-3A. For PDMAEMA, the Mark-Houwink exponent  $\nu$  decreases with increasing ionic strength from around 0.9 at 5 mM NaCl to 0.56 at 150 mM NaCl (Figure 3-3B). The value of 0.9, obtained at low ionic strength, corresponds to an elongated structure, based on the intramolecular charge repulsion and the subsequent stretching of the polymer chain. Screening of charges by addition of salt results in a decrease of  $\nu$ , associated with a more compact conformation in the range of a Gaussian chain (0.5 to 0.7).<sup>[48,75,76]</sup> In summary, AF4 coupled to light scattering provides a characterization in a short time with low amounts of material. If the polymers dispersity is not too low, detailed information like molar mass,  $\bar{M}$ , size, and conformation can be obtained in a single experiment.

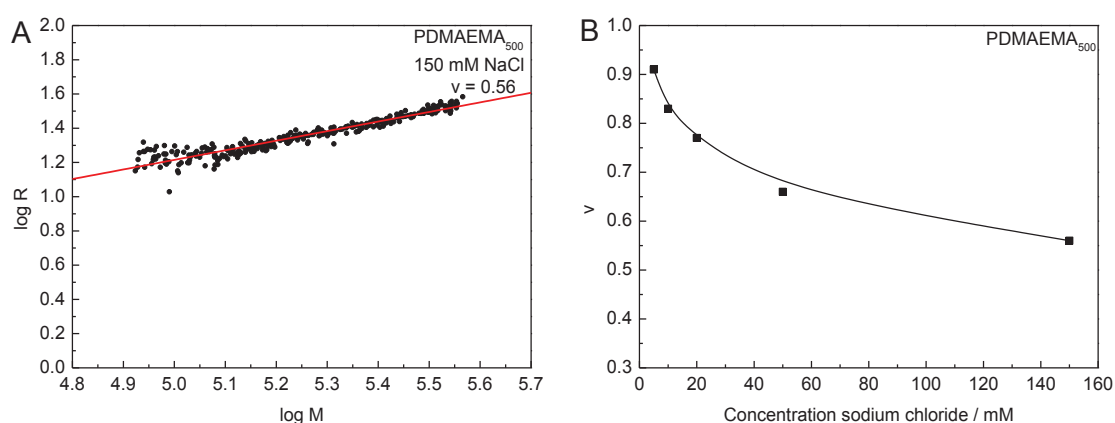


**Figure 3-3. (A) Conformation plot of PDMAEMA<sub>500</sub> in 150 mM NaCl obtained by AF4-MALLS. (B) Mark-Houwink exponents of PDMAEMA<sub>500</sub> at different concentrations of NaCl obtained by AF4.**

In another study, a different approach for characterizing cationic polymers with the AF4 was applied, which is based on the isoelectric point (IP) of the membrane material. For regenerated cellulose, the IP is in the range of pH 4.<sup>[77]</sup> Therefore, the membrane exhibits a

negative net-charge above the IP and a positive one below. Performing AF4 with an eluent of low pH value, *e.g.* acetate solution at pH 3.5, ensures the absence of electrostatic attraction between a cationic sample and the membrane. As a result, high recovery rates and a reduction of adsorption phenomena are observed, also on fresh membranes. This strategy could be successfully applied to copolymers of PDMAEMA-*b*-PDEGMA (Figure 3-4A) as well as cationic derivatives of poly(2-oxazoline) (Scheme 1-1).

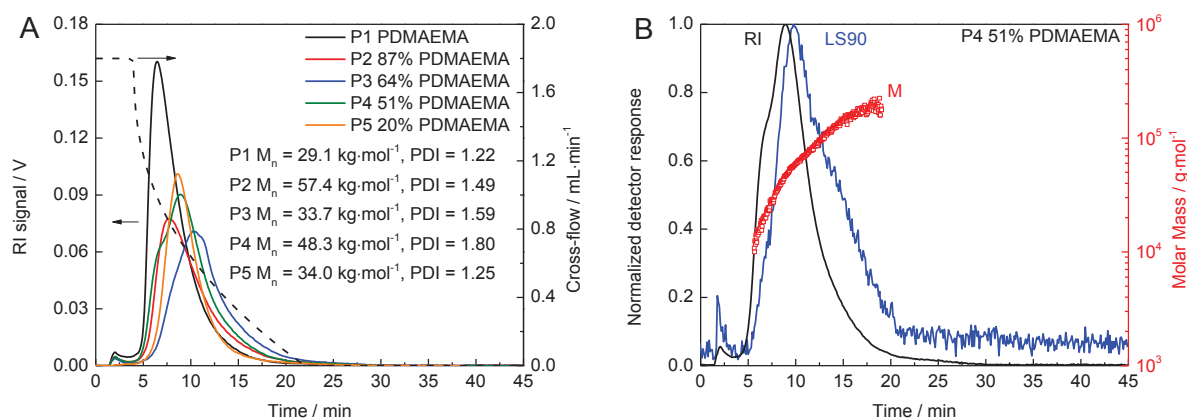


Figure 3-4. AF4 fractograms of (A) PDMAEMA-*b*-PDEGMA (different block ratios P1-P5) and (B) of P4 with indicated molar masses and LS90° trace as obtained by MALLS. The eluent is composed of 25 mM acetate and 20 mM NaCl at pH 3.5.

Table 3-2. Molar masses of cationic poly(2-oxazoline)s obtained by AF4 and <sup>1</sup>H NMR.

Composition	$M_n$ ( <sup>1</sup> H NMR) [kg·mol <sup>-1</sup> ]	$M_n$ (AF4) [g·mol <sup>-1</sup> ]	$M_n$ (AF4) [g·mol <sup>-1</sup> ]	$\bar{D}$ (AF4)
PEtOx <sub>113</sub> - <i>b</i> -PAmOx <sub>5</sub>	12.0	11.7	12.9	1.10
PEtOx <sub>92</sub> - <i>b</i> -PAmOx <sub>10</sub>	10.6	9.2	10.5	1.14
PEtOx <sub>72</sub> - <i>b</i> -PAmOx <sub>18</sub>	9.7	13.3	14.6	1.10
PEtOx <sub>82</sub> - <i>b</i> -PAmOx <sub>23</sub>	11.4	13.6	14.9	1.09
PEtOx <sub>64</sub> - <i>b</i> -PAmOx <sub>26</sub>	10.1	12.5	15.7	1.26

Figure 3-4B shows a representative light scattering trace (90°) of PDMAEMA-*b*-PDEGMA and the molar mass fractionation. For PEtOx-*b*-PAmOx, the obtained values are in good agreement with the theoretical calculations and the obtained <sup>1</sup>H NMR data (Table 3-2). Deviations are most probably due to the low molar mass and sample loss through the membrane (MWCO 10 kg·mol<sup>-1</sup>). Furthermore, the developed approach, based on the membrane's isoelectric point, is simpler and more of a general nature, than the presaturation technique. The only issue, which has to be considered, is the stability of the polymer in the eluent, composed of acetic acid / sodium acetate (20 to 50 mM) and sodium

chloride (0 to 100 mM) at pH 3.5. If this is ensured, the method seems to be universally applicable and could be established as a standard procedure in field-flow fractionation of water-soluble cationic polyelectrolytes. Besides the described polymers, this strategy could also successfully be used to characterize various other samples, *e.g.* amino acid modified dextrane or bipyridine functionalized polystyrenes for redox flow cells in energy storage research.



#### 4. Polymer-based gene delivery agents

Parts of this chapter have been published: P5) M. Wagner, A. C. Rinkenauer, A. Schallon, U. S. Schubert, *RSC Advances* **2013**, *3*, 12774-12785; P6) A. C. Rinkenauer, A. Schallon, U. Günther, M. Wagner, E. Betthausen, U. S. Schubert, F. H. Schacher, *ACS Nano* **2013**, *7*, 9621-9631; P7) A. T. Press, A. Träger, C. Pietsch, A. Mosig, M. Wagner, M. G. Clemens, N. Jbeily, N. Koch, M. Gottschaldt, N. Bézière, V. Ermolayev, V. Ntziachristos, J. Popp, M. Kessels, B. Qualmann, U. S. Schubert, M. Bauer, *Nat. Commun.* **2014**, *accepted*.

The occurrence of various diseases is based on genetic modifications and malfunctions. The potential cure of these genetic disorders by delivery of genetic material to cells is studied with remarkable effort during the last decades.<sup>[78]</sup> Thereby, two classes of delivery agents, in detail viral and non-viral vectors, can be distinguished. In particular, cationic polymers, a promising class of non-viral gene delivery agents, are in the focus of research. They show certain advantages in contrast to viral vectors, *e.g.* easy large-scale production and higher safety related to clinical issues.<sup>[79,80]</sup> Based on entropic driven interactions (release of counterions), these polymers can complex genetic material (*e.g.* DNA or RNA) to form so called polyplexes.<sup>[81]</sup> Thereby, two different strategies have to be distinguished. On the one hand, plasmid DNA, delivered to the cell nucleus, leads to the expression of certain proteins. On the other hand, delivery of siRNA into the cytoplasm results into the knockdown of harmful protein expressions. The understanding of the complexes, their mode of action and efficiency requires detailed knowledge about the physicochemical properties. The polymer has to protect the genetic material against degradation, promote the transport through the cellular membrane (and the nucleus membrane in case of pDNA) and enable the release of the genetic material. Providing all these features, the carrier should be non-toxic, too. Furthermore, the complex formation is only partially understood and several systems, which show a high efficiency in delivery of pDNA, fail for siRNA.<sup>[82,83]</sup> The “gold standard” for pDNA transfection,<sup>[63]</sup> branched PEI, and its ability to complex siRNA were investigated in this context, focusing on the influence of the polymers molar mass. While the characterization of the pure polymers is described in the previous chapter, the analysis of the complexes is discussed here.

First of all, the cytotoxicity of the studied polymers, commercial branched PEI with 0.6, 1.8, 10 and 25 kg·mol<sup>-1</sup>, was determined (Figure 4-1A). The observed cytotoxicity highly depends on the molar mass of the polymer. Whereas PEI with 0.6 kg·mol<sup>-1</sup> shows no cytotoxic effect in the investigated concentration range (up to 360 µg·mL<sup>-1</sup>), the IC<sub>50</sub> values (50% of cells are vital) decreased from 335 to 140 and 62 µg·mL<sup>-1</sup> for 1.8, 10 and 25 kg·mol<sup>-1</sup>, respectively. As further experiments were carried out below 36 µg·mL<sup>-1</sup>, corresponding to a N/P ratio of 20 (ratio of nitrogen atoms in the polymer to phosphorous atoms in the RNA), all polymers were non-toxic at those concentrations. With an ethidium bromide quenching assay, it could be shown that all polymers are able to bind to siRNA and that a N/P ratio ≥ 5 is necessary to reach full complexation (Figure 4-1B). It was also possible to induce a release of siRNA by addition of heparin, a competing natural polyanion. Except for 0.6 kg·mol<sup>-1</sup> PEI polyplexes, showing a significant higher stability, 30 U·mL<sup>-1</sup> were sufficient to release nearly 100% of siRNA.

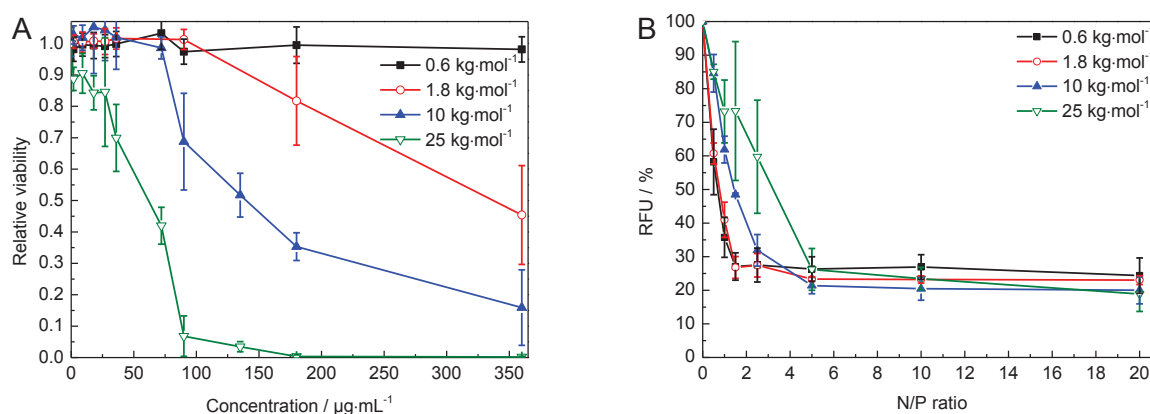


**Figure 4-1. (A) Cytotoxicity and (B) binding affinity (measured by fluorescence based on intercalation of ethidium bromide) of branched PEI of different molar masses.<sup>[84]</sup>**

As it is known that the presence of positive charges has a strong impact on the delivery process, the electrokinetic potential, also known as zeta potential, was measured at varying N/P ratios (Figure 4-2A). At low N/P ratios, a negative zeta potential, indicating an excess of negative charges, was observed, while a positive (nearly constant) zeta potential was obtained at N/P ≥ 5. These findings were in excellent agreement with the binding studies, where a N/P of 5 was necessary for full complexation. Furthermore, the zeta potential and, subsequently, the colloidal stability of the polyplexes were found to increase with molar mass.

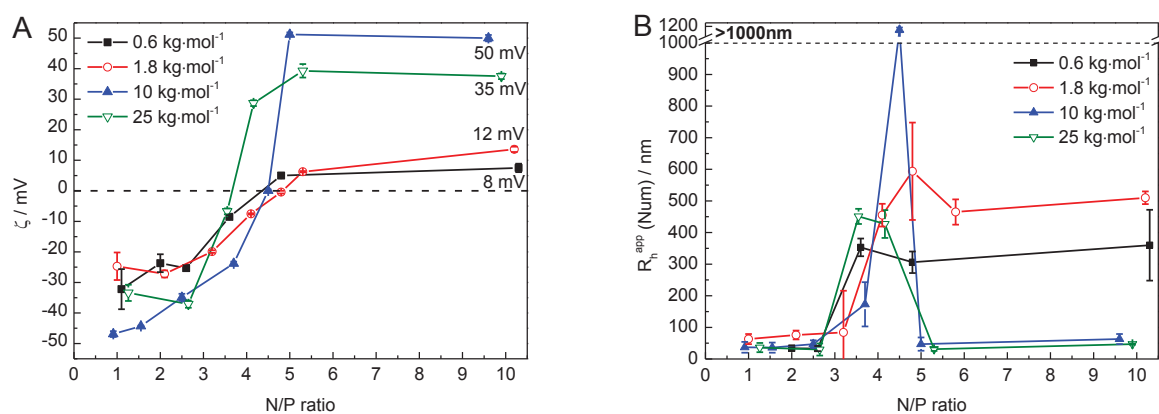


Figure 4-2. (A) Zeta potential and (B) apparent hydrodynamic radius of siRNA/PEI based polyplexes.

Dynamic light scattering was applied to access the size in terms of the hydrodynamic radius (Figure 4-2B). Radii below 100 nm were obtained at low N/P ratios of all molar masses, while a maximum ( $R_h > 300$  nm) was reached at N/P 4.5. At higher N/P ratios, the  $R_h$  of 10 and 25  $\text{kg}\cdot\text{mol}^{-1}$  PEI based polyplexes was decreased to around 50 nm, whereas low molar mass PEI showed aggregation. This correlates well with the results of the zeta potential measurements. In all cases of high absolute zeta potential values, small polyplexes were observed and aggregation occurred for potentials close to zero. The indication that the stability is dominated by repulsive electrostatic interactions could further be supported by long-term DLS measurements. All samples with high zeta potentials are stable for at least 24 h, while the others showed aggregation within a few hours.

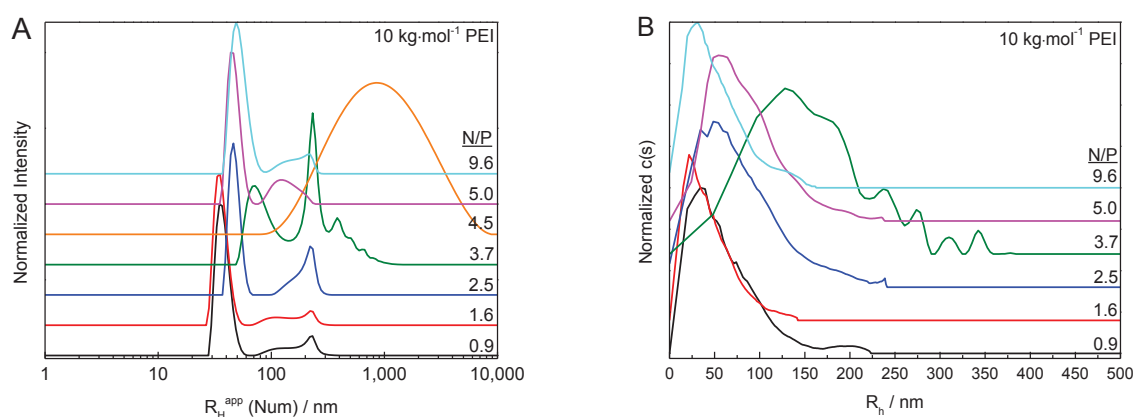


Figure 4-3. (A) DLS based number-weighted  $R_h$  distribution of polyplexes of  $10 \text{ kg}\cdot\text{mol}^{-1}$  PEI. (B)  $R_h$  distribution based on sedimentation coefficients obtained by AUC of polyplexes of  $10 \text{ kg}\cdot\text{mol}^{-1}$  PEI.

DLS size distributions revealed the presence of aggregates beside the main population for all polyplexes and the size of the aggregates varied with molar mass of PEI and the N/P ratio (Figure 4-3A). Due to the fact that large aggregates scatter much more light than the polyplexes, their fraction was most probably overestimated by DLS. Even the calculation of

number weighted distributions is based on several assumptions and interpretation has to be done carefully.

Therefore, AUC was applied as an alternative technique to obtain  $R_h$  distributions of the polyplexes. Based on the Svedberg (eq 20) and the Stokes-Einstein equation (eq 10), the sedimentation coefficient can be transformed to  $R_h$  (eq 22).<sup>[11]</sup>

$$R_H = \frac{3}{2} \left( 2s \frac{\eta v}{(1-v\rho)} \right)^{1/2} \quad (22)$$

In principle, the results obtained by DLS and AUC were in good agreement, except the absence of aggregates in the AUC data (Figure 4-3B). Moreover, no reliable data could be obtained for large polyplexes, due to their fast sedimentation. A low rotor speed of 1,000 rpm and a high radial step size had to be chosen even for polyplexes in the range of 30 to 100 nm, which resulted in a low resolution.<sup>[73]</sup> As a consequence, the amount of aggregates could not be quantified by AUC. Investigations of the cellular uptake showed that only polyplexes based on 10 and 25 kg·mol<sup>-1</sup> PEI achieved sufficient internalization. This is in agreement with the release (heparin) and light scattering experiments, indicating positively charged polyplexes for these molar masses, which are able to release the genetic material and to pass the negatively charged cell membrane. It was also possible to detect the unbound PEI, which could be quantified by PUC and UV-Vis spectroscopy. Subsequently, the real N/P ratio of the polyplexes could be calculated and was found to be around 1.3, independent of the molar mass of the utilized PEI. This highlights the important role of free PEI, in particular, as polyplexes freshly prepared at N/P 1.3 showed no cellular uptake. To sum up, DLS and LDV revealed that the polyplexes' size and stability is mainly governed by electrostatic interactions. Taking the uptake studies into account, branched PEI with a molar mass of 10 kg·mol<sup>-1</sup> was found to be the optimum in terms of balancing toxicity, uptake, binding affinity as well as polyplex size and stability.

As the polyplexes described above showed different drawbacks concerning their potential *in vivo* application,<sup>[85]</sup> the encapsulation into multifunctional, biodegradable poly(lactide-co-glycolic acid) (PLGA) nanoparticles was investigated in another study. The polymer was further coupled to a near infrared (NIR) polymethine dye-derivative *via* 1-ethyl-3-(3-dimethylaminopropyl)carbodiimide hydrochloride (EDC). Beside the dyes fluorescence, it shows a high selectivity for specific cells, giving the opportunity for active targeting. This

novel approach, combining a dye and a targeting moiety within one molecule, allows non-invasively tracking of the nanoparticles (*e.g.* body distribution or clearance) and their specific cellular uptake. Furthermore, the potential use of varying siRNA supports the establishment of a widely applicable platform tool.<sup>[86]</sup> In the present study, the utilized dye enables targeting of one kind of liver cells (hepatocytes). The polyplexes were formed by siRNA and linear PEI ( $10 \text{ kg}\cdot\text{mol}^{-1}$ ) and encapsulated *via* the double emulsion technique into dye-modified PLGA nanoparticles.<sup>[87]</sup> The particles were characterized in detail by AF4-MALLS-DLS (Figure 4-4). A monomodal distribution with low dispersity, a  $R_g$  of 70 nm and a  $R_h$  of 90 nm (both z-average) was revealed (an excellent agreement with offline DLS and SEM measurements could be observed). Furthermore, the calculation of the shape ratio according to eq 23, provides information on the particles geometry. Whereas a value of 0.775 corresponds to a hard sphere, a value of 1.0 indicates a soft (Gaussian) sphere. For various architectures, shapes and conformations values are reported elsewhere.<sup>[48,88]</sup> In principle, lower values indicate a more compact structure, while high values correspond to extended or asymmetric structures. In comparison to classic batch light scattering techniques, AF4-MALLS-DLS enables the determination of this ratio for each slice/fraction of the fractogram, which allows the characterization of differently shaped structures in a mixture within a single experiment. For the studied nanoparticles, a value of around 0.78 was obtained, which fits well to particles with a spherical geometry.

$$\rho = \frac{R_g}{R_h} \quad (23)$$

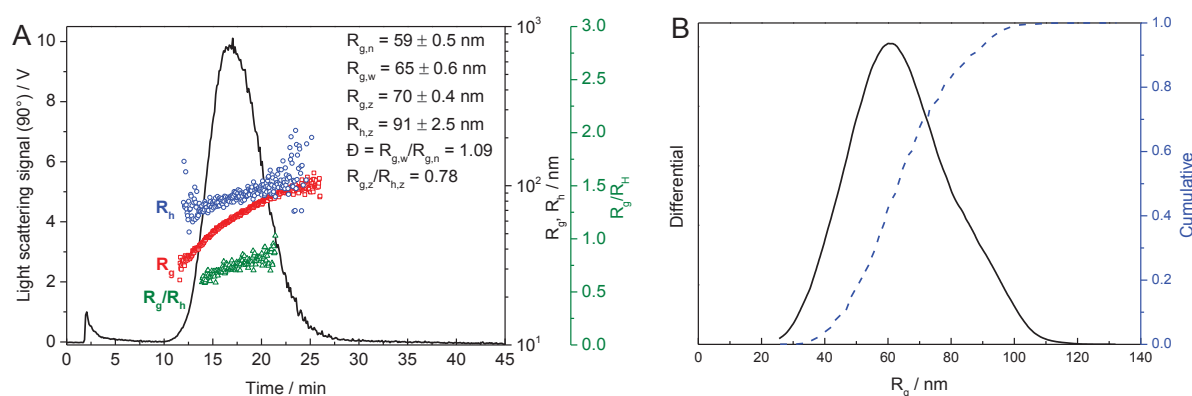


**Figure 4-4.** (A) AF4 fractogram and (B) size distribution of PLGA nanoparticles with encapsulated siRNA/PEI based polyplexes.

The amount of encapsulated siRNA was determined *via* photometric quantification of phosphorous after digestion ( $\text{H}_2\text{SO}_4/\text{H}_2\text{O}_2$ ) and an encapsulation efficiency of  $87.4 \pm 2.5\%$

was obtained. Detailed biomedical studies revealed that the particles could successfully induce knockdown of protein expression and neither show hemolysis nor aggregation of erythrocytes or cytotoxicity. A significant uptake takes place within 30 min after venous injection into mice and is exclusively associated with hepatocytes (Figure 4-5). In contrast, PLGA nanoparticles without dye are primarily taken up by endothelial and Kupffer cells (macrophages). After degradation of PLGA, the dye (only DY-635) is released into the gall bladder through the canaliculi. Taking together all results of the *in vivo* experiments, this system presents a highly promising approach for novel siRNA/drug delivery and further investigations.

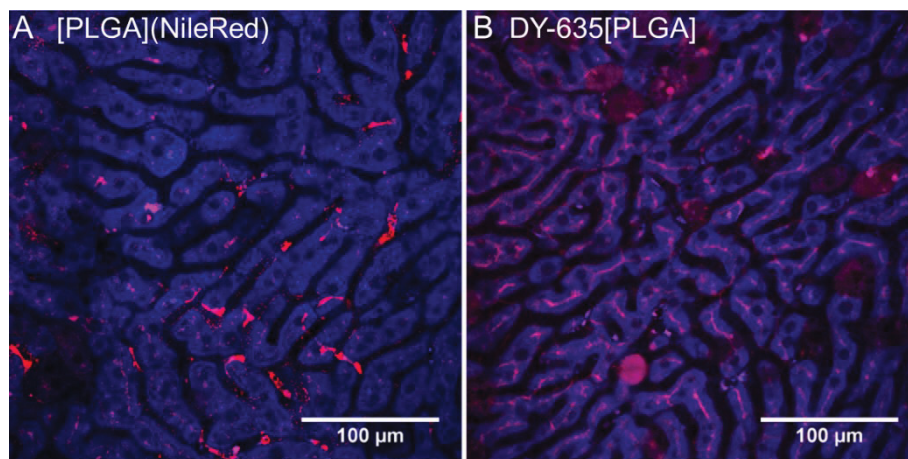


**Figure 4-5.** Intravital confocal fluorescence microscopy images of liver tissues of FVB/NRj mice 30 min after injection of nanoparticles (blue NAD(P)(H) autofluorescence - liver architecture). (A) PLGA nanoparticles (no dye functionalization on the surface, Nile red loading), mainly taken up by endothelial and Kupffer cells in the liver. (B) DY-635-PLGA nanoparticles primarily taken up by hepatocytes.

Besides homopolymers, also amphiphilic block copolymers, which are able to form micellar or vesicular nanostructures, were investigated as potential gene delivery systems. In particular, multicompartement micelles of a stimuli-responsive triblock terpolymer, PB<sub>800</sub>-*b*-PMAA<sub>200</sub>-*b*-PDMAEMA<sub>285</sub>, (BMAAD,  $M_n$  105.3 kg·mol<sup>-1</sup>) showed promising results. While the PB segments form the hydrophobic core, PDMAEMA and PMAA are present in the shell.<sup>[89]</sup> Furthermore, cationic PDMAEMA and anionic PMAA are able to build amphiphilic interpolyelectrolyte complexes, generating a pH-responsive, patchy surface with additional cationic patches of PDMAEMA (higher degree of polymerization). At neutral pH values (7.4), both blocks are charged, resulting in an intramicellar interpolyelectrolyte complex shell, a  $R_h$  of the micelle of 110 nm and a zeta potential of 17 mV. A decreased pH value (5.0) leads to a collapse of the PMAA into a shell covered by a cationic corona of the stretched PDMAEMA chains. This is accompanied with an increase in  $R_h$  to 210 nm and a zeta potential of around

30 mV. At higher pH values (10), the situation is the other way around and PDMAEMA collapses into a shell, while PMAA forms a negatively charged corona. PDMAEMA is further able to complex pDNA and the resulting polyplexes exhibit a positive net-charge and a  $R_h$  similar to the non-complexed nanostructures (120 nm). Further details were provided by AF4-MALLS, which revealed a monomodal distribution with a  $R_g$  of 97 nm for the bare micelles and 111 nm for the polyplexes (Figure 4-6). The molar mass of the bare micelles was roughly  $3.9 \cdot 10^8 \text{ g} \cdot \text{mol}^{-1}$ , resulting in an aggregation number ( $N_{\text{agg}}$ ) of around 3,700 polymer chains per micelle. The shape ratio, calculated from AF4-MALLS and offline DLS data, was around 0.93 for both, indicating a soft sphere.<sup>[48]</sup>

To evaluate the potential as gene delivery agent, transfection studies under different conditions were performed. Superior transfection efficiencies were obtained for adherent cells in serum-reduced as well as in serum containing media (74% in serum), compared to PEI (43% in serum) (Figure 4-7).

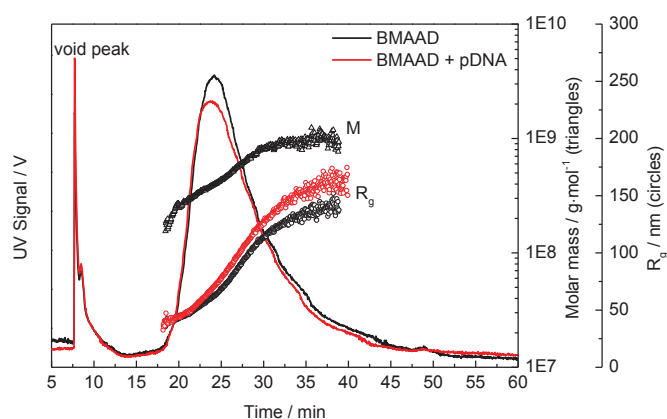


Figure 4-6. AF4 fractogram of BMAAD and the complex with pPDNA.

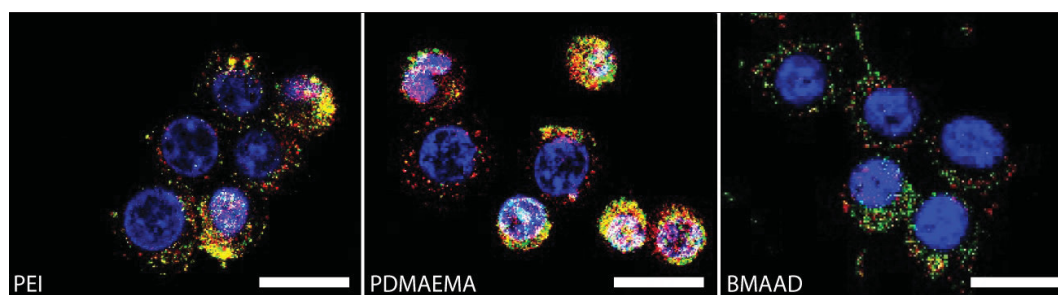
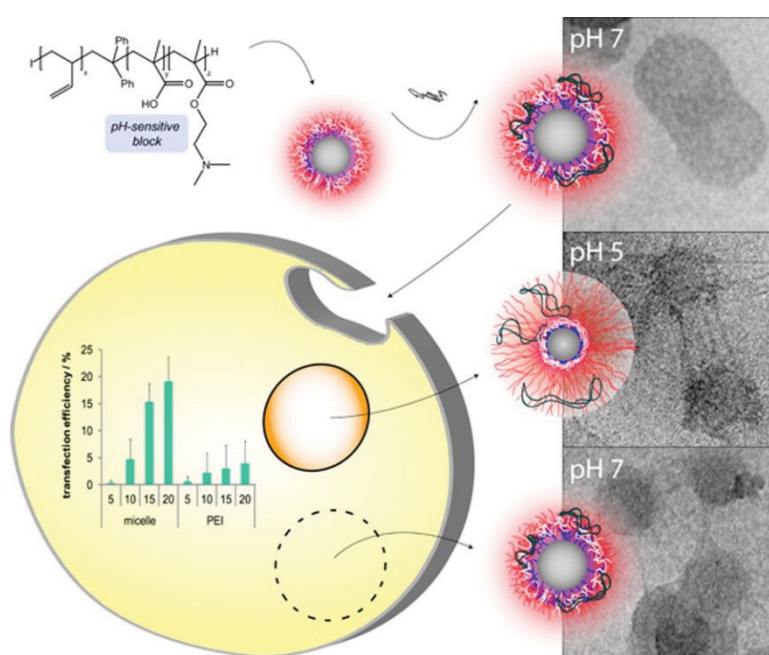


Figure 4-7. Confocal laser scanning microscopy images of HEK cells transfected with the indicated polymer based polyplexes and YOYO-1 labeled pDNA (green). Late endosomes/lysosomes were stained with LysoTracker Red (red) and cell nuclei were stained with Hoechst 33342 (blue); each scale bare represents 20 μm (co-localization of pDNA and endosomal compartment were depicted in yellow).

It was also investigated, whether even suspension cells, *e.g.* immune cells, can be transfected, as these cells are of key interest for therapy of immune defects like HIV or

cancer (leukemia).<sup>[90]</sup> Here, BMAAD based polyplexes revealed a 5-fold higher efficiency (20%) compared to PEI (Figure 4-8) for transfection of Jurkat T cells. Additionally, no cytotoxicity was detected up to  $320 \mu\text{g}\cdot\text{mL}^{-1}$  ( $\text{N/P} > 200$ ). This impressively shows that, by adopting certain design concepts from viruses, BMAAD is able to combine two usually contrary features: High transfection efficiency and low cytotoxicity.<sup>[91-93]</sup> Further details were revealed by several pH value and temperature dependent release and uptake experiments. The escape of the polyplex from the endosome is most probably based on the pH responsive behavior. At pH 7.4, the polyplexes form homogeneous, spherical structures. At pH 5, similar to the pH value inside the endosome, protonation of PDMAEMA accompanied with a stretching of the corona results in an increase in size and surface charge (Figure 4-8). This triggers the burst of the endosome and induces the endosomal escape.<sup>[94]</sup> Afterwards, in the cytoplasm (pH value is increased back to 7.4), PMAA is resolubilized and can act as a competing polyanion to induce the release of pDNA.

In summary, BMAAD micelles based on a well-defined triblock terpolymer was shown to be a superior gene carrier, exhibiting high biocompatibility. Thereby, a detailed physicochemical characterization based on AF4, cryogenic transmission electron microscopy (cryo-TEM) and dynamic, static and electrophoretic light scattering provides the basis to understand the transfection process as well as the underlying uptake and release mechanism.



**Figure 4-8.** Polyplex formation, cryo-TEM as well as transfection efficiency of human leukemia cells of BMAAD polyplexes.

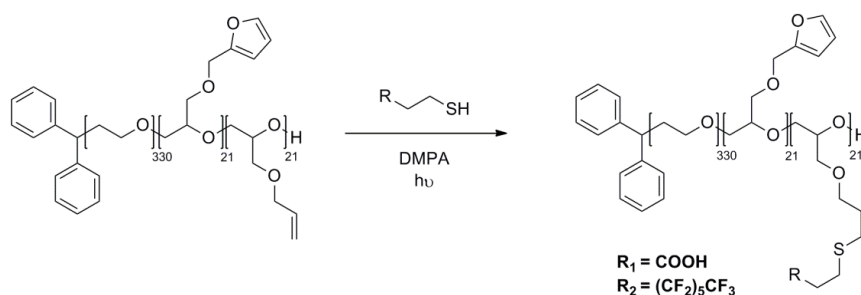


## 5. Self-assembly of amphiphilic block copolymers

Parts of this chapter have been published: P8) M. Wagner, M. J. Barthel, R. R. A. Freund, S. Höppener, A. Träger, F. H. Schacher, U. S. Schubert, *Polym. Chem.* **2014**, DOI: 10.1039/c4py00863d; P9) M. J. Barthel, A. C. Rinkenauer, M. Wagner, U. Mansfeld, S. Höppener, J. A. Czaplewska, M. Gottschaldt, A. Träger, F. H. Schacher, U. S. Schubert, *Biomacromolecules* **2014**, *15*, 2426-2439; P4) M. Hartlieb, D. Pretzel, M. Wagner, S. Höppener, P. Bellstedt, M. Görlach, C. Englert, K. Kempe, U. S. Schubert, *submitted*.

Micellar or vesicular structures based on amphiphilic block copolymers are widely investigated during the last decades and are of key interest in many research fields like material science or pharmaceuticals. In particular, their potential for drug delivery applications is studied by many scientists.<sup>[3]</sup> The encapsulation and delivery of small molecules by a nano-sized carrier represents a promising approach to address common challenges like low water solubility, degradation, enormous side effects, or a non-specific body distribution.<sup>[95]</sup> Several polymer based samples exist, which are in various stages of clinical trials.<sup>[96-98]</sup> In general, self-assembled systems consist of at least one hydrophobic block, forming the inner core and carrying the hydrophobic payload and one hydrophilic part, which builds the outer shell and ensures water solubility as well as (bio)compatibility. The latter one is often provided by poly(ethylene oxide) (PEO), which is non-toxic and exhibits the so called “stealth”-effect, reducing unspecific protein interactions.<sup>[99]</sup> As hydrophobic block, different materials like PLGA, polystyrene, or polyethers (*e.g.* PFGE, PtBGE) can be used.<sup>[100,101]</sup> On this basis, further modifications are feasible to improve the drug delivery carriers. This includes endgroup or side chain functionalization, *e.g.*, by dyes or sugar moieties for imaging or enhanced targeting applications as well as incorporation of additional polymer blocks. In particular, the introduction of a third block, resulting in an ABC triblock terpolymer structure, extends the range of accessible functionalities and morphologies.<sup>[102]</sup> Thereby, polyethers like poly(allyl glycidyl ether) (PAGE) can be functionalized *via* thiol-ene click chemistry, using the pendant double bonds in the side chain.<sup>[103]</sup> In this context, also multicompartment micelles can be realized, which enable simultaneously storage of two different guest molecules or contain several stimuli-responsive groups.<sup>[104,105]</sup>

To compare different functionalities and the influence on the obtained morphology, a toolbox based on PEO-*b*-PFGE-*b*-PAGE was synthesized by sequential living anionic ring-opening polymerization. For post-polymerization functionalization, thiol-ene click chemistry was applied to attach either 1*H*,1*H*,2*H*,2*H*-perfluorooctanethiol (PFOT, increasing hydrophobicity) or 3-mercaptopropionic acid (MPA, increasing hydrophilicity and introducing negative charges) on the PAGE block (Scheme 5-1).



**Scheme 5-1.** Schematic representation of poly(ethylene oxide)-*block*-poly(furfuryl glycidyl ether)-*block*-poly(allyl glycidyl ether) (PEO-*b*-PFGE-*b*-PAGE) and subsequent post-polymerization functionalization using thiol-ene chemistry.

DLS results after preparation of the colloidal solutions by the solvent displacement method are shown in Figure 5-1A. As the samples were not filtered, DLS revealed broad size distributions. Regarding number-weighted distributions, a major population with a  $R_h$  of 19, 23 and 7 nm could be identified for PEO-*b*-PFGE-*b*-PAGE, PEO-*b*-PFGE-*b*-PAGE<sub>PFOT</sub> and PEO-*b*-PFGE-*b*-PAGE<sub>COOH</sub>, respectively. Concerning the zeta potential,  $-12$  mV was obtained for PEO-*b*-PFGE-*b*-PAGE in pure water, while incorporation of a perfluorated alkyl chain with highly electronegative fluorine led to  $-29$  mV (Figure 5-1B). The introduction of carboxy groups led to a strong increase in  $\zeta$  to  $-45$  mV. As predicted by the Stern model, the zeta potential decreased exponentially with the ionic strength.

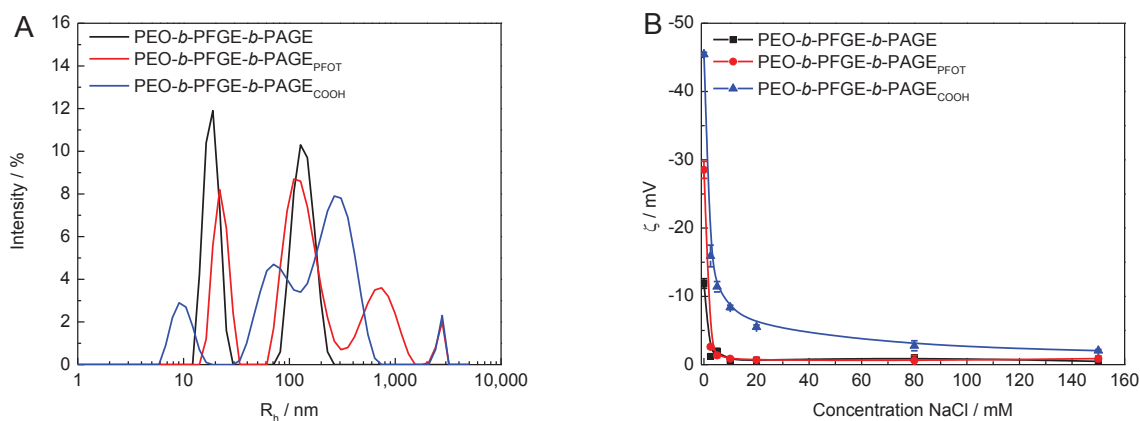


**Figure 5-1.** (A) DLS based  $R_h$  distributions and (B) zeta potential of aqueous solutions of PEO-*b*-PFGE-*b*-PAGE, PEO-*b*-PFGE-*b*-PAGE<sub>PFOT</sub> and PEO-*b*-PFGE-*b*-PAGE<sub>COOH</sub>.

To obtain further insights, investigations with AF4 coupled to MALLS and DLS were performed. As already described in Chapter 2.3, a suitable method has to be developed and separation conditions have to be optimized to ensure an appropriate analysis. This was done in detail for PEO-*b*-PFGE-*b*-PAGE, evaluating different membrane materials, eluent compositions and flow rates. The separation at different cross-flow rates is shown in Figure 5-2A. In accordance with the AF4 theory, an increase of the cross-flow pushes the sample closer to the membrane, resulting in longer elution times and an increased peak height. Consideration of the recovery rates showed that an optimum is reached at 1 mL·min<sup>-1</sup>. Besides the cross-flow, the ionic strength (*e.g.* NaCl concentration) of the eluent is important as it highly influences the electrostatic interactions between sample and membrane (Figure 5-2B). While irregular retention, due to strong and long-ranged electrostatic repulsion, occurred in pure water, 5 mM NaCl was sufficient for an appropriate fractionation. This was found to be in excellent agreement with LDV experiments, where already 5 mM NaCl reduced the zeta potential close to zero. For higher ionic strengths, an increasing amount of aggregates was observed in the AF4 fractograms, indicating other attractive membrane-sample interactions, as electrostatic contributions are screened.

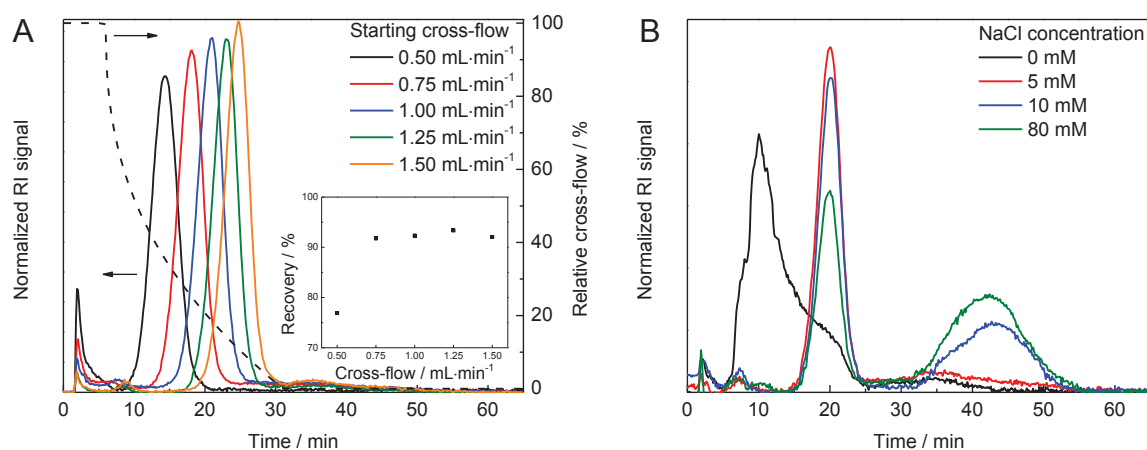


**Figure 5-2.** Variation of (A) cross-flow and (B) ionic strength (NaCl concentration) of the eluent for separation of PEO-*b*-PFGE-*b*-PAGE *via* AF4. The inlay (A) shows the recovery rate of each separation as determined by RI detection.

After the optimal conditions were identified, the different polymers were analyzed by AF4 (Table 5-1). For micelles of PEO-*b*-PFGE-*b*-PAGE, a molar mass of around 705 kg·mol<sup>-1</sup> ( $M_n$ ) was obtained, resulting in an aggregation number of 35 (Figure 5-3A). With an  $R_g$  of 14 nm and an online  $R_h$  of 21 nm, the results were in excellent agreement with the offline DLS results. Also a small amount of aggregates was observed. The calculated shape ratio ( $R_g/R_h = 0.67$ ) was slightly below the value of a hard sphere (0.775), but had to be

interpreted with care, as  $R_g$  is close to the detection limit of the MALLS detector (minimum detectable size is around 10 nm).<sup>[106]</sup> Considering this inaccuracy, the formation of compact spherical micelles could be assumed (Scheme 5-2A).<sup>[48]</sup> These results were supported by cryo-TEM (Figure 5-3B), showing spherical micelles of around 20 nm.

Table 5-1. Properties of PEO-*b*-PFGE-*b*-PAGE, PEO-*b*-PFGE-*b*-PAGE<sub>PFOT</sub> and PEO-*b*-PFGE-*b*-PAGE<sub>COOH</sub> in aqueous solution.

	PEO- <i>b</i> -PFGE- <i>b</i> -PAGE	PEO- <i>b</i> -PFGE- <i>b</i> -PAGE <sub>PFOT</sub>	PEO- <i>b</i> -PFGE- <i>b</i> -PAGE <sub>COOH</sub>
$M_n$ [kg·mol <sup>-1</sup> ]	705 ± 5.9	1,684 ± 35	82.0 ± 2.5 <sup>c</sup>
$M_w$ [kg·mol <sup>-1</sup> ]	723 ± 1.3	1,921 ± 14	101.5 ± 2.1 <sup>c</sup>
$\bar{D}_M$ ( $M_w/M_n$ )	1.03 ± 0.01	1.14 ± 0.02	1.24 ± 0.02
$N_{agg}$ <sup>a</sup>	35 ± 0.3	56 ± 1.2	3.7 ± 0.1 <sup>c</sup>
$R_g$ (peak 1) [nm]	14 ± 0.9	20 ± 2	-
$R_h$ (peak 1) [nm]	21 ± 0.3	29.5 ± 1.2	4.6 ± 0.7
$R_g/R_h$ (peak 1)	0.67 ± 0.04	0.68 ± 0.05	-
$R_{h, batch DLS}$ [nm]	18.5 ± 1	23.3 ± 3.8	7 ± 3
$R_g$ (peak 2) [nm]	-	425 ± 9 <sup>b</sup>	-
$R_h$ (peak 2) [nm]	-	146 ± 14	-
$R_g/R_h$ (peak 2)	-	2.92 ± 0.22	-
Recovery [%]	92.3 ± 1.4	85.1 ± 1.3	85.3 ± 0.3

<sup>a</sup> based on  $M_n$  and polymer molar masses obtained by <sup>1</sup>H NMR.

<sup>b</sup> based on random coil scattering factor.

<sup>c</sup> the single chain fraction was excluded for calculation.

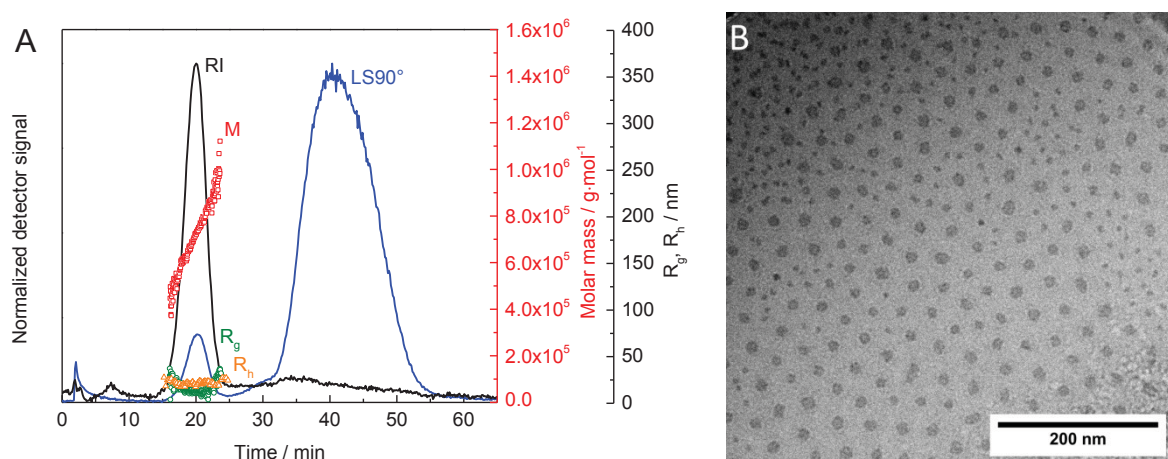
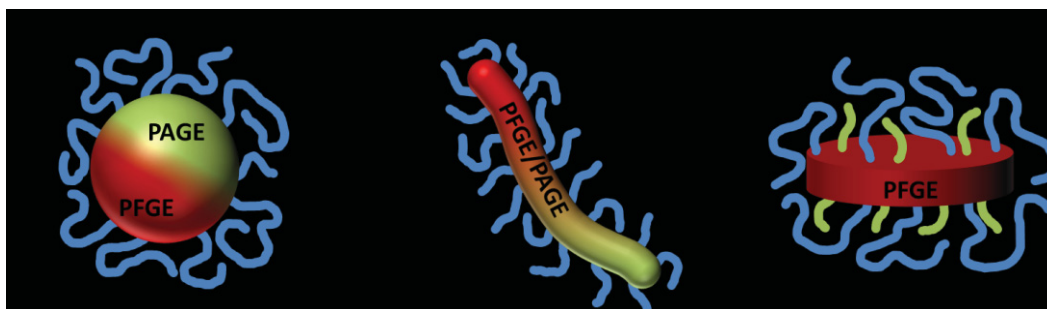


Figure 5-3. (A) AF4-MALLS-DLS fractogram and (B) cryo-TEM micrograph of PEO-*b*-PFGE-*b*-PAGE.

Furthermore, the size of the core (7 nm) and the corona (13 nm) could be determined. For PEO, the results fitted to the theoretical calculations (eq 24) based on the degree of polymerization  $N$ , the segment length  $a$  (0.36 for PEO) and the assumption of a random coil in a good solvent ( $R_g/R_h = 1.78$ ).<sup>[107]</sup>



Scheme 5-2. Schematic representation of the proposed micellar structures of (A) PEO-*b*-PFGE-*b*-PAGE, (B) PEO-*b*-PFGE-*b*-PAGE<sub>PFOT</sub> and (C) PEO-*b*-PFGE-*b*-PAGE<sub>COOH</sub>. The different colors of PFGE/PAGE (A, B) do not indicate the formation of a Janus core.

$$R_h = \frac{aN^{3/5}}{1.78} \quad (24)$$

A distinct bimodal distribution was obtained for PEO-*b*-PFGE-*b*-PAGE<sub>PFOT</sub> (Figure 5-4A). The first population with a molar mass of  $1,700 \text{ kg} \cdot \text{mol}^{-1}$  ( $M_n$ ), a  $R_g$  of 20 nm, a  $R_h$  of 30 nm and a  $\rho$  of 0.68 exhibited similar characteristics to PEO-*b*-PFGE-*b*-PAGE. The second, minor population showed a strong difference between  $R_g$  (425 nm) and  $R_h$  (146 nm), leading to a high shape ratio (2.9), indicating worm-like structures.<sup>[108]</sup> Furthermore, the broad range of  $\rho$ , ranging from 1 to 3 over the entire peak, indicates a high dispersity in terms of “length”. This could also be confirmed by cryo-TEM measurements (Figure 5-4B). The formation of such worm-like structures is based on the attachment of fluorocarbon chains, resulting in an increased overall hydrophobicity. As the width of the worm-like structures is in the same range as the spherical micelles, a similar block arrangement could be assumed, where PFGE/PAGE<sub>PFOT</sub> forms the core and PEO the corona (Scheme 5-2B). This is further supported by the presence of spherical endcaps of the worm-like structures, indicating fusion/fission processes of originally spherical micelles.

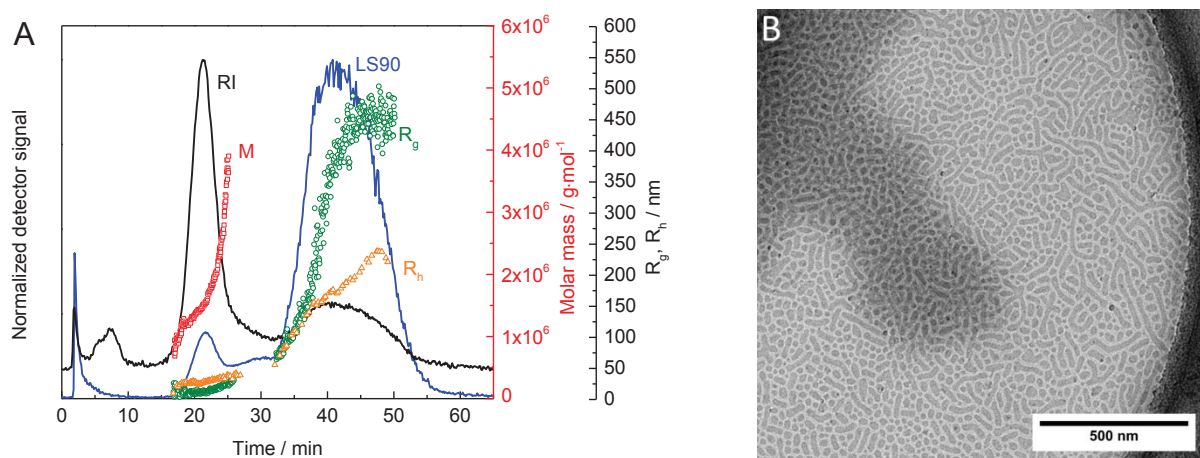
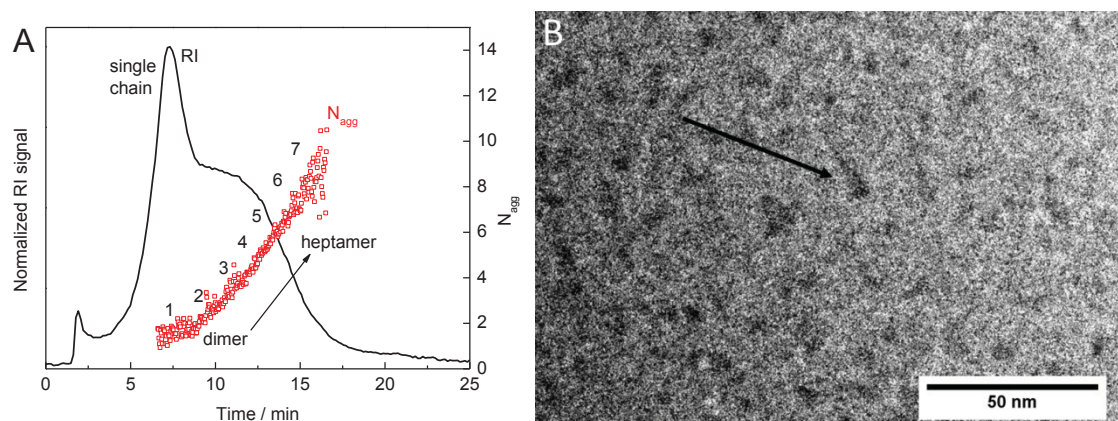


Figure 5-4. (A) AF4-MALLS-DLS fractogram and (B) cryo-TEM micrograph of PEO-*b*-PFGE-*b*-PAGE<sub>PFOT</sub>.

For PEO-*b*-PFGE-*b*-PAGE<sub>COOH</sub>, where hydrophilic carboxy groups were introduced on the PAGE side chains, one peak with a broad shoulder was observed in the AF4 fractogram (Figure 5-5A). While a  $R_h$  of around 4 nm was obtained,  $R_g$  could not be determined, as it was below the lower size limit of the MALLS detector, due to the isotropic scattering of the sample. Consideration of the polymer's molar mass showed that the peak maximum represents the single polymer chain, while the shoulder corresponds to structures, which were composed of 2 to 7 polymer chains. Careful evaluation of the cryo-TEM micrographs revealed small objects and lines, indicating a disc-like shape (Figure 5-5B). These structures might be explained by a parallel ordering of the polymer chains, where PFGE forms the core and PEO and PAGE<sub>COOH</sub> are present in the corona (Scheme 5-2C). Thereby, the longer PEO chains are able to surround also the edges of the core. Nevertheless, as the observed contrast is weak and the structures reached the limit of the applied techniques, the interpretation has to be considered with care.



**Figure 5-5. (A)** AF4-MALLS-DLS fractogram of PEO-*b*-PFGE-*b*-PAGE<sub>COOH</sub> showing the aggregation number of the different species. **(B)** cryo-TEM micrograph of PEO-*b*-PFGE-*b*-PAGE<sub>COOH</sub>.

As carboxy groups can be used to implement stimuli-responsive properties, sensitive to changes in pH value or ionic strength, PEO-*b*-PFGE-*b*-PAGE<sub>COOH</sub> was further investigated at varying solvent compositions. Addition of NaCl (0 to 150 mM) or a decrease of the pH value (ranging from 4 to 10) led to a shift to higher elution times, which correlated well with zeta potential measurements, described above. As no change in molar mass or size was observed, the shift was solely attributed to the screening of the electrostatic repulsion, taking place between the sample and the membrane as well as the protonation of functional groups. Only the relative amount of the different species changed. Based on the reduced repulsion between the individual carboxy groups in the polymer, assemblies with a higher aggregation

number were favored with increasing ionic strength or a more acidic pH value. An alternative option to influence the morphology of PEO-*b*-PFGE-*b*-PAGE<sub>COOH</sub> is the crosslinking by the addition of metal ions. This can further be affected by the degree of protonation of the carboxy groups (pH value). Therefore, different amounts of FeCl<sub>3</sub> were added to the colloidal solution at different pH values and the samples were analyzed by AF4-MALLS-DLS (Table 5-2). From pH 4 to 7.3, an increase of R<sub>h</sub> from 12 nm to 60 nm was observed with 12.5 equivalents (compared to the total number of carboxy groups) of FeCl<sub>3</sub>. At higher pH values, no reliable results were obtained as Fe(OH)<sub>3</sub> started to precipitate in the AF4 channel. Under constant a pH value, an increase of the amount of FeCl<sub>3</sub> was accompanied with an increase in size, too. From 1/3 eq. to 12.5 eq. at pH 5.6, R<sub>h</sub> increased from 5 to 30 nm (Figure 5-6). In all cases, shape ratios between 0.78 and 0.85 were obtained, indicating spherical particles. With deprotonation (higher pH value) of the polymer or increasing iron(III) content, more polymer chains can be crosslinked and, subsequently, larger nanostructures were obtained. These first results provide the basis for further investigations and a better understanding how to control the morphologies of such triblock terpolymers. Furthermore, AF4 coupled to MALLS and DLS was shown to be an excellent tool to obtain detailed physicochemical characteristics on self-assembled structures in solution. Additionally, combination with cryo-TEM was proven to be a superior setup.

**Table 5-2. AF4-MALLS-DLS results of PEO-PFGE-PAGE<sub>COOH</sub> with varying amounts of FeCl<sub>3</sub> and at different pH values.**

pH	Fe <sup>3+</sup> eq.	R <sub>g</sub> [nm]	R <sub>h</sub> [nm]	R <sub>g</sub> /R <sub>h</sub>
4.0	12.5	10.2	12.2	0.84
5.6	12.5	25.1	30.0	0.84
5.6	5	16.4	21	0.78
5.6	1	12.8	15	0.85
5.6	1/3	-	4.9	-
7.3	12.5	50.9	61.3	0.83

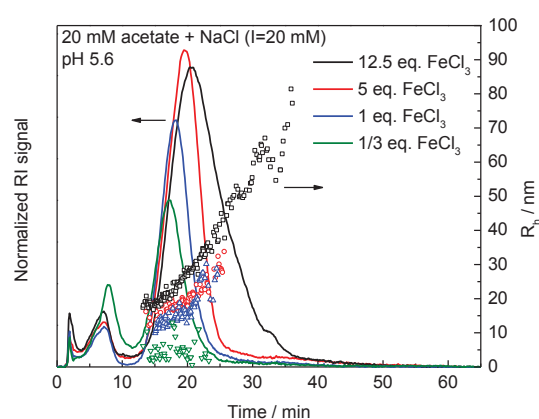


**Figure 5-6. AF4 fractograms of PEO-*b*-PFGE-*b*-PAGE<sub>COOH</sub> at pH 5.6 with different equivalents of FeCl<sub>3</sub>.**

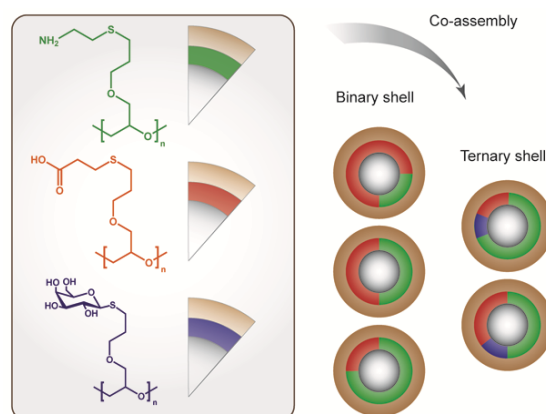
The self-assembly based on a similar platform of an ABC triblock terpolymer, PEO<sub>42</sub>-*b*-PAGE<sub>15</sub>-*b*-PtBGE<sub>12</sub> (EAT), was investigated in another study. Here, the PAGE segment was functionalized with amino (ENT) and carboxy groups (ECT), providing either positive or negative charges, as well as thiogalactose (EGT) as a model ligand for selective cellular

uptake.<sup>[109]</sup> In aqueous solution, all polymers underwent self-assembly to core-shell-corona micelles with hydrodynamic radii below 15 nm, as obtained by DLS and cryo-TEM investigations (Table 5-3). Thereby, PtBGE forms the hydrophobic core, PAGE the shell and PEO the hydrophilic corona. Additionally, a hydrophobic dye (Nile red), showing red fluorescence, was encapsulated into the core as a model drug and tracer.<sup>[110]</sup> To precisely control the functionality inside the shell (*e.g.* in terms of charge) and to influence the cellular uptake or the cytotoxicity, binary and ternary mixed micelles were created by a co-assembly process of the different triblock terpolymers (Scheme 5-3).<sup>[111]</sup> For the samples nomenclature, the superscripts represent the mixing ratio regarding the functional groups of the polymers. For all mixed systems, spherical micelles with radii below 15 nm were obtained, too. The successful formation of mixed micelles, in contrast to a mixture of two separate structures, was confirmed by LDV, DLS, and gel electrophoresis experiments.

Table 5-3. DLS and AF4 data for PEO<sub>42</sub>-*b*-PAGE<sub>15</sub>-*b*-PtBGE<sub>12</sub> based micelles and co-micelles.

Sample	$M_n \cdot 10^{-5}$ [g·mol <sup>-1</sup> ]	$N_{agg}$	$R_g$ [nm]	$R_h$ (AF4) [nm]	$R_g/R_h$	$R_h$ (batch) [nm] <sup>a</sup>
EAT	11.5 ± 0.08	225 ± 2	10.1 ± 0.6	13.0 ± 0.4	0.78 ± 0.02	11.8 ± 0.1
ENT	18.6 ± 0.3	323 ± 56	15.8 ± 1.1	17.4 ± 1.8	0.92 ± 0.15	9.5 ± 0.3
ECT	10.5 ± 0.01	156 ± 1	12.2 ± 0.8	14.4 ± 0.1	0.84 ± 0.05	13.5 ± 0.3
EGT	2.22 ± 0.07	31 ± 1	5.4 ± 0.6	5.3 ± 0.3	1.02 ± 0.14	7.1 ± 0.3
(ENT/ECT) <sup>3.5:1</sup>	12.0 ± 0.37	204 ± 6	12.3 ± 0.4	15.2 ± 0.5	0.81 ± 0.04	-
(ENT/ECT) <sup>1.2:1</sup>	7.32 ± 0.13	121 ± 2	8.9 ± 0.8	10.6 ± 1.5	0.84 ± 0.05	10.5 ± 0.2
(ENT/ECT) <sup>1:2.6</sup>	6.19 ± 0.04	99 ± 1	9.0 ± 1.6	10.4 ± 0.5	0.88 ± 0.20	10.5 ± 0.1
(ENT/ECT/EGT) <sup>3.5:1:0.5</sup>	11.3 ± 0.71	190 ± 12	13.6 ± 1.2	15.9 ± 0.1	0.86 ± 0.08	12.3 ± 0.5
(ENT/ECT/EGT) <sup>3.4:1:2.3</sup>	9.65 ± 0.48	155 ± 8	13.5 ± 1.2	15.1 ± 0.1	0.90 ± 0.08	11.5 ± 0.5

<sup>a</sup> batch DLS in 20 mM NaCl (similar to AF4).



Scheme 5-3. Co-assembly of functionalized triblock terpolymers into binary and ternary core-shell-corona micelles with a mixed shell. The fractions of the modified PAGE shell represent the mixing ratio during co-assembly.



Also for these polymers, AF4-MALLS-DLS was able to reveal further details on the self-assembly process (Table 5-3). The size as well as the spherical geometry, indicated by shape ratio between 0.775 (hard sphere) and 1.0 (soft sphere), were found to be in good accordance with cryo-TEM and offline DLS results.<sup>[48]</sup> Representative fractograms of (ENT/ECT)<sup>3.5:1</sup> and (ENT/ECT/EGT)<sup>3.5:1:0.5</sup> are shown in Figure 5-7. From the absolute molar mass, obtained *via* MALLS, also the individual composition of the mixed micelles was accessible, assuming that the composition ratios in the micelles are similar to the mixing ratios of the polymers during co-assembly.

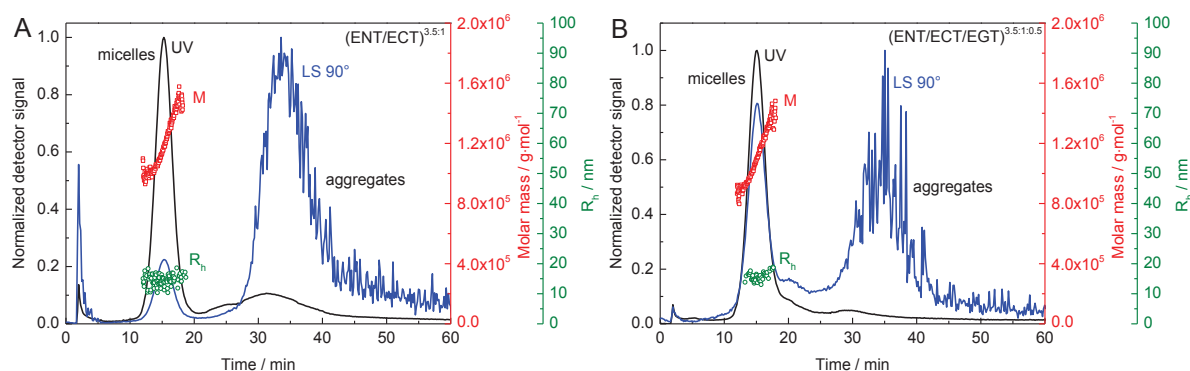
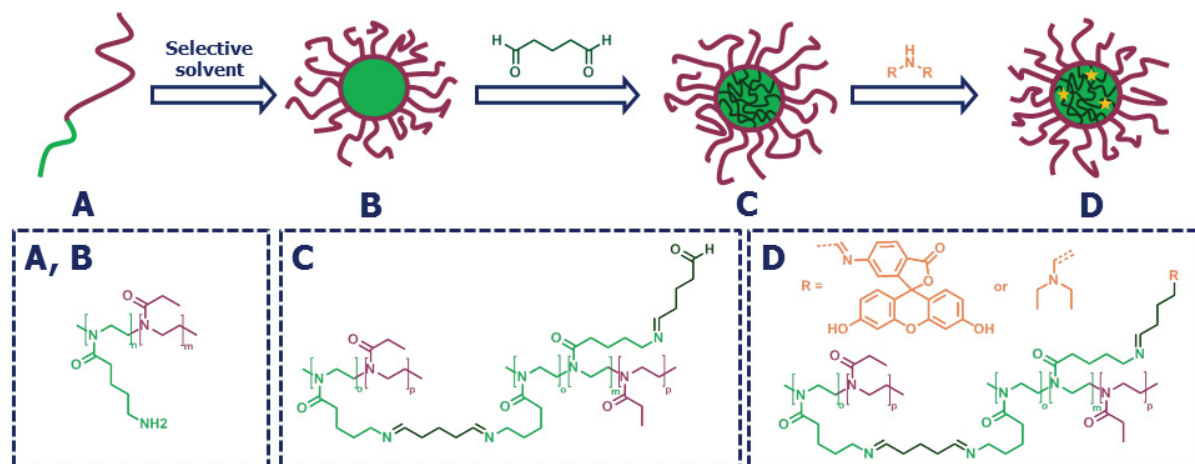


**Figure 5-7.** AF4 fractogram of triblock terpolymer micelles from (ENT/ECT)<sup>3.5:1</sup> (A) and (ENT/ECT/EGT)<sup>3.5:1:0.5</sup> (B) in 20 mM NaCl solution.

To investigate the polymer's potential for drug delivery, cytotoxicity and cellular internalization were studied. All micelles with a negative zeta potential (low amino content), EAT, ECT, EGT, (ENT/ECT)<sup>1.2:1</sup> and (ENT/ECT)<sup>1.2:6</sup>, showed no cytotoxic effect up to a concentration of 0.5 mg·mL<sup>-1</sup>. In contrast, micelles with a positive zeta potential (high amino content), ENT and (ENT/ECT)<sup>3.5:1</sup>, exhibited an IC<sub>50</sub> of 300 and 350 µg·mL<sup>-1</sup>, respectively. This trend is in excellent agreement with literature data, as it is known that cationic charges could lead to strong interactions with the negatively charged cell membrane.<sup>[13,112]</sup> Surprisingly, the ternary micelles, both with positive zeta potentials and the same charge ratio as (ENT/ECT)<sup>3.5:1</sup>, did not show any cytotoxicity at all measured concentrations. Obviously, the presence of a sugar moiety, provided by EGT, is accompanied with some kind of a shielding effect. Concerning the cellular uptake of the primary micelles, ENT and ECT revealed the highest unspecific cellular uptake of around 14% (at 10 µg·mL<sup>-1</sup>) under serum conditions in human embryonic kidney (HEK) cells, while EAT and EGT showed nearly no internalization. In contrast, co-micelles of (ENT/ECT)<sup>3.5:1</sup> demonstrated an increased uptake of around 75% under serum conditions, whereas (ENT/ECT)<sup>1.2:1</sup> and (ENT/ECT)<sup>1.2:6</sup> showed a

decreased internalization of around 8%. For the ternary micelles, the uptake decreased with increasing amount of EGT, which is in good agreement with the low uptake of primary EGT micelles. For  $(\text{ENT}/\text{ECT}/\text{EGT})^{3.5:1:0.5}$  around 35% were yielded, but, in contrast to  $(\text{ENT}/\text{ECT})^{3.5:1}$ , these structured were not cytotoxic. Utilizing these synergistic effects seems to be a promising strategy for a further development of systems with efficient internalization, low cytotoxicity and reduced non-specific serum interactions. In particular, polyether based triblock terpolymers, differently functionalized, were identified as a promising toolbox for drug delivery and could be characterized in detail.

Another highly interesting class of drug deliver agents is represented by block copolymers of PEtOx-*b*-PAmOx (Scheme 1-1). In the present study, the copolymer showed self-assembly in organic solvents (both block are soluble in water) and the structure's size could be controlled by the polarity of the solvent. After crosslinking and transfer to water, these structures were studied as potential drug delivery vehicles (Scheme 5-4). As the crosslinking process has to be quenched with a low molar mass amine, a corresponding drug or dye can directly be introduced into the system through covalent but labile imine bonds.



Scheme 5-4. Schematic representation of the self-assembly of PEtOx-*b*-PAmOx followed by crosslinking and quenching/loading.

During the preparation, either micelles ( $R_h < 20$  nm in chloroform) or vesicles (40 to 70 nm in 2-propanol) were formed, depending on the solvent. While  $R_h$  could easily be determined by DLS or AF4 in organic as well as aqueous solutions after crosslinking, the morphology, namely vesicular or micellar systems, has to be confirmed by a second independent technique. One technique alone was not able to prove the structure, even if the size gave a

strong indication. The first hint was given by AF4, where shape ratios below 0.8 were obtained, indicating a micellar geometry for structures formed in chloroform (below 20 nm). In contrast, ratios of around 1.0 were obtained for particles in 2-propanol, hinting towards the presence of soft (hollow) spheres or vesicles, respectively (40 to 70 nm). This was supported by cryo-TEM of the organic solutions, where the observed structures exhibited similarities with the burst shell of a vesicle. This clearly shows that only a combination of different techniques provides a reliable knowledge about the physicochemical characteristics in many cases. Even if AF4-MALLS-DLS provides superior information on the molar mass, size and dispersity of each individual fraction of the sample, the particles geometry should be proven by an independent method like electron microscopy or AUC. Besides, micelles as well as vesicles showed no cytotoxic effect up to  $2.5 \text{ mg}\cdot\text{mL}^{-1}$  and were efficiently internalized into L929 mouse fibroblast cells (Figure 5-8). Thereby, both structures were localized in the lysosome, while an accumulation on the cellular membrane or a localization in the nucleus could be excluded (6-amino fluorescein as model drug).

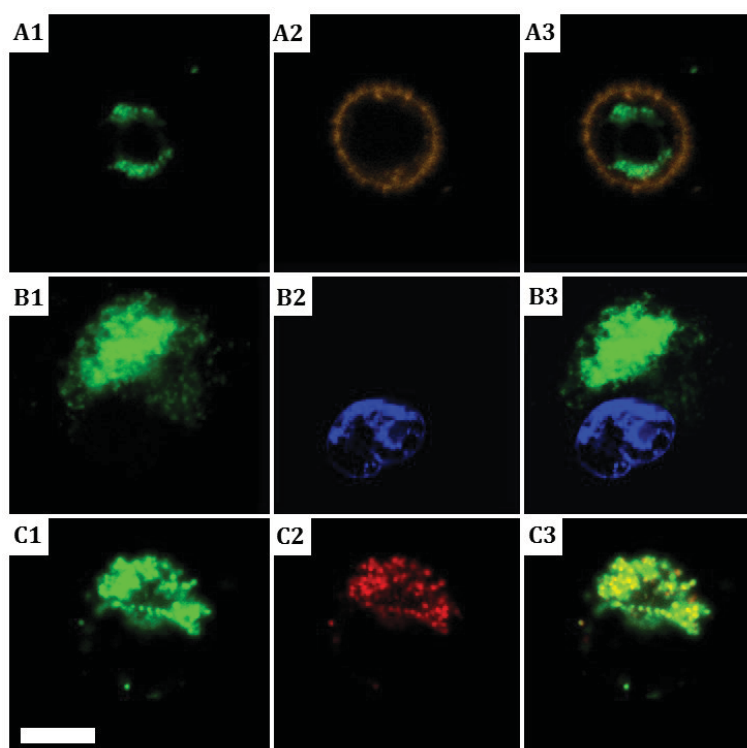


Figure 5-8. Representative confocal laser scanning microscopy images of detached L929 cells after 24 h incubation with vesicles at a concentration of  $0.1 \text{ mg}\cdot\text{mL}^{-1}$ . Cell membranes (A2), cell nuclei (B2), or late endosomes/lysosomes (C2) were specifically stained and correlated with the fluorescence signal of the vesicles (A1, B1, and C1). Overlay of both channels (A3, B3 and C3) proves intracellular (A3) but extra-nuclear (B3) localization of the vesicles and their apparent co-localization with lysosomal structures (C3). Identical results were obtained for micelles. The scale bar represents  $10 \mu\text{m}$ .



## 6. Thermo-responsive polymers

Parts of this chapter have been published: P3) M. Wagner, C. Pietsch, A. Kerth, A. Träger, U. S. Schubert, *submitted*; P10) C. Pietsch, U. Mansfeld, C. Guerrero-Sanchez, S. Höppener, A. Vollrath, M. Wagner, R. Hoogenboom, S. Saubern, S. H. Thang, C. R. Becer, J. Chiefari, U. S. Schubert, *Macromolecules* **2012**, *45*, 9292-9302.

Polymers, in particular amphiphilic block copolymers, which exhibit thermo-responsive properties, represent highly attractive systems for “smart” materials.<sup>[29,30]</sup> The thermo-induced self-assembly to micellar or vesicular structures, based on the lower critical solution temperature (LCST) of at least one block, provides an attractive strategy for sensing or drug delivery applications.<sup>[113,114]</sup> For example, the encapsulation and releases of dyes or drugs can be stimulated by a change in temperature.<sup>[31,115]</sup> The corresponding phase transition is mainly driven by the unfavorable entropy of mixing. In water, it is based on the formation of hydrogen bonds between the water molecules and the polymer chains. Heating above the cloud point temperature ( $T_{CP}$ ) leads to the breaking of the hydrogen bonds, accompanied by an increase of hydrophobic interactions between the polymer chains.<sup>[116]</sup> In case of PDMAEMA-*b*-PDEGMA, both corresponding homopolymers show a LCST behavior. While the  $T_{CP}$  of PDEGMA is around 27 °C, the  $T_{CP}$  of PDMAEMA is highly depending on the molar mass as well as the solution conditions like the pH value or the ionic strength and values between 20 and 80 °C are reported.<sup>[117-119]</sup> This results in a material, which is sensitive against two or more different stimuli at the same time and, therefore, the influence of solution parameters on the LCST behavior and the self-assembly is of high interest.<sup>[120]</sup> In this study, a series of thermo-responsive diblock copolymers of PDMAEMA-*b*-PDEGMA was synthesized by reversible addition-fragmentation chain transfer (RAFT) polymerization. The molar mass distribution of these polymers was determined by AF4-MALLS, as already described in Chapter 3 (Figure 3-4). The final ratio between both blocks was obtained *via* <sup>1</sup>H NMR spectroscopy, using the areas of PDMAEMA ((CH<sub>3</sub>)<sub>2</sub>N- at 2.26 ppm) and PDEGMA (CH<sub>2</sub>-O- at 3.54 to 3.66 ppm) signals. First information on the phase behavior of the polymers were revealed by turbidimetry (Table 6-1). In pure water, a  $T_{CP}$  of 52.7 °C and 28.4 °C (50% transmission) was obtained for PDMAEMA and PDEGMA at 2.5 mg·mL<sup>-1</sup>, respectively.<sup>[117]</sup> With increasing content of PDMAEMA, a roughly linear increase of the  $T_{CP}$  was observed for

the copolymers. Furthermore, concentration dependent measurements showed an increase of the transition temperature with dilution. For PDMAEMA<sub>64</sub>-*b*-PDEGMA<sub>36</sub> (subscripts represent molar block ratios), no clear cloud point could be determined, which is most probably due to the formation of small micellar structures.<sup>[121]</sup> In contrast, two steps and, subsequently, two  $T_{CP}$  values were identified for PDMAEMA<sub>51</sub>-*b*-PDEGMA<sub>49</sub>: A first  $T_{CP1}$  at around 34 °C and a second one ( $T_{CP2}$ ) at around 46 °C, indicating a double thermo-responsive behavior.

**Table 6-1. Cloud point temperatures ( $T_{CP}$ ) obtained by turbidimetry and DSC measurements at 2.5 mg·mL<sup>-1</sup>.**

DMAEMA:DEGMA	100:0	87:13	64:36	51:49	20:80	0:100
$T_{CP}$ [°C]	52.7	47.0	- <sup>a</sup>	34.4; 46.1	30.3	28.1
$T_{DSC}$ [°C]	54.1	48.8	33.8	34.9	31.3	29.8

<sup>a</sup> no clear cloud point.

To obtain deeper insights into the formed nanostructures, DLS measurements were performed (Figure 6-1A). All polymers showed a  $R_h$  smaller 5 nm below  $T_{CP}$ , corresponding to the hydrated polymer chain. Above  $T_{CP}$ , PDMAEMA and PDEGMA revealed the typical coil-to-globule transition, accompanied by precipitation in case of PDEGMA. A similar behavior was observed for block copolymers where one of both blocks, either PDMAEMA or PDEGMA, is dominant. If both blocks have similar dimensions, self-assembly occurred at 30 to 35 °C with a  $R_h$  of around 20 to 35 nm, respectively. To obtain detailed information on the size distribution and shape, AF4-MALLS-DLS was applied (Figure 6-1B).<sup>[122,123]</sup> To enable fractionation under similar conditions for all polymers, an eluent containing 100 mM NaCl was used. For PDMAEMA and PDMAEMA<sub>87</sub>-*b*-PDEGMA<sub>13</sub>, a single peak was obtained at all temperatures (15 to 65 °C), which corresponds to the hydrated polymer chain as indicated by MALLS detection (compare Figure 3-4). The missing of any nanostructures at higher temperatures was attributed to the concentration dependence of the cloud point and the low concentration in the AF4 channel. At the present channel concentration of around 0.04 mg·mL<sup>-1</sup> (at the peak maximum) the cloud point is shifted to values above 65 °C. An analogous effect was observed for PDMAEMA<sub>20</sub>-*b*-PDEGMA<sub>80</sub>, where AF4 at 45 °C revealed nanostructures with a  $R_h$  of 24 nm, in contrast to DLS, showing large aggregates. Subsequent dilution of the DLS samples to a concentration similar to AF4 gave comparable hydrodynamic radii. This strong concentration dependence indicates a first limitation for analysis of thermo-responsive polymers by AF4. For PDEGMA, the formation of large aggregates was

observed above 35 °C, which blocked the detector tubings in the system. This indicates an enormous increase in size, which correlates with DLS results.

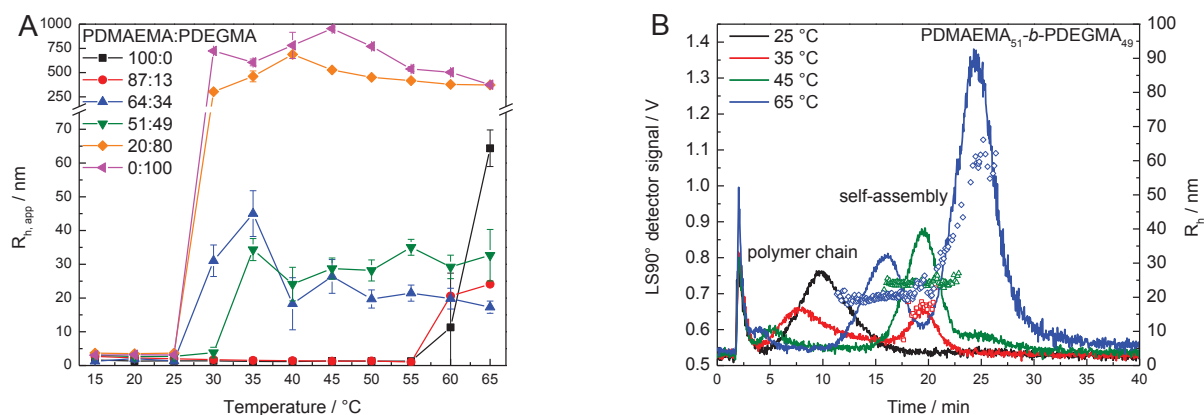


**Figure 6-1. (A) Apparent hydrodynamic radius of PDMAEMA-*b*-PDEGMA as obtained by offline DLS measurements. (B) AF4 fractogram of PDMAEMA<sub>51</sub>-*b*-PDEGMA<sub>49</sub> with hydrodynamic radii obtained by online DLS investigations.**

The AF4 results of PDMAEMA<sub>51</sub>-*b*-PDEGMA<sub>49</sub> (Figure 6-1B), indicating vesicular structures ( $R_h$  20 nm,  $R_g/R_h$  1.0), were in good agreement with DLS results. The vesicular geometry could also be confirmed by cryo-TEM measurements. At 65 °C larger aggregates are formed, which originated from increased interactions with the membrane.<sup>[70]</sup> Nevertheless, due to the high sensitivity of MALLS for large aggregates, their concentration can be regarded as being rather low. Similar to the DLS results, no second transition ( $T_{CP2}$ ) could be identified by AF4. Fractionation of PDMAEMA<sub>64</sub>-*b*-PDEGMA<sub>36</sub> showed a similar trend. Here, hydrodynamic radii of around 25 nm were obtained above 30 °C, but smaller  $R_g$  values (around 20 nm) resulted in an average shape ratio of 0.8, indicating spherical micelles. Furthermore, the comparison of AF4 and DLS of all samples showed that the use of number-weighted offline DLS data is in most cases appropriate to describe the investigated structures.

To reveal further details on the observed nanostructures, LDV was applied (Figure 6-2A). Heating of PDMAEMA and PDEGMA above their  $T_{CP}$  resulted in an increase of the absolute value of the zeta potential. This observation was attributed to the dehydration of the polymer chain and an orientation of the more hydrophilic (and charge bearing) side chains towards the aqueous environment of the formed globules. A similar trend with lower absolute values of the zeta potential was observed for PDMAEMA<sub>87</sub>-*b*-PDEGMA<sub>13</sub>, having only a short PDEGMA block. All other block copolymers showed two distinct changes upon heating, namely a significant increase of the zeta potential at around 30 to 35 °C and a decrease at around 55 to 60 °C. The first change was related to the phase transition,

accompanied by self-assembly. Upon heating, the PDEGMA block collapses and forms the hydrophobic part, while the PDMAEMA block is located at the surface, leading to higher zeta potentials. This is also supported by temperature dependent  $^1\text{H}$  NMR measurements (Figure 6-2B).

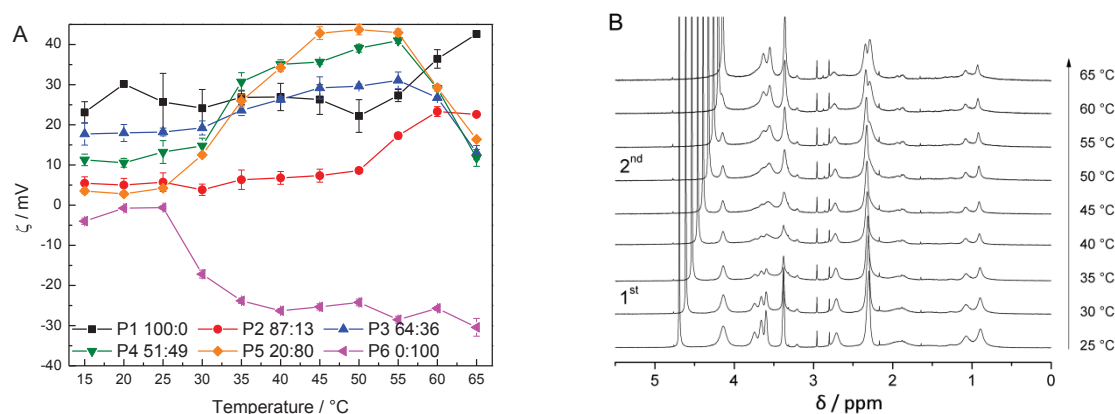


**Figure 6-2.** (A) Zeta potential of PDMAEMA-*b*-PDEGMA in pure water. (B) Temperature dependent  $^1\text{H}$  NMR spectra of PDMAEMA<sub>51</sub>-*b*-PDEGMA<sub>49</sub> in D<sub>2</sub>O (5 mg·mL<sup>-1</sup>).

By increasing the temperature from 25 to 40  $^{\circ}\text{C}$ , the PDEGMA signals at 3.3 to 3.9 ppm (ethylene glycol and  $-\text{OCH}_3$  groups) decreased significantly, denoting the collapse of the PDEGMA segments. The PDMAEMA block is still visible at 45  $^{\circ}\text{C}$  ( $\text{CH}_3\text{-N-}$  at 2.3 ppm) and it is supposed that it forms the hydrophilic part. Further heating until 65  $^{\circ}\text{C}$  leads to a decrease and shift of some signals for PDMAEMA ( $\text{CH}_3\text{-N-}$  at 2.2 ppm) and an increase of some PDEGMA signals (ethylene glycol groups at 3.6, 3.7 ppm,  $-\text{OCH}_3$  groups at 3.3 ppm), indicating a different microenvironment of (at least parts of) the PDMAEMA and PDEGMA segments and a rearrangement of the nanostructures. Considering the decrease in zeta potential, a collapse of the PDMAEMA block, linked with a migration of the PDEGMA segments back to the surface of the structures to stabilize them in aqueous solution, seems to be reliable. This migration leads to a partial hydration of the PDEGMA chains and the reappearance of the signals in the NMR spectra (3.6 to 3.7 ppm). Interestingly, this is not related with a change in size. To address the question, how far these structural changes are related to a thermodynamically defined phase transition, differential scanning calorimetry (DSC) was applied (Figure 6-3). It was found that the obtained transition temperatures were in good agreement with the DLS results and turbidimetry based values and that only the first cloud point corresponds to an actual phase transition. To our current knowledge, the second change is solely associated with a reordering of the internal structure of the aggregates.



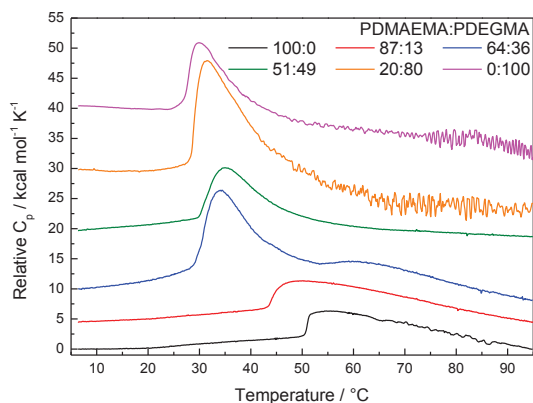


Figure 6-3. DSC results of PDMAEMA-*b*-PDEGMA in pure water at 2.5 mg·mL<sup>-1</sup>.

As PDMAEMA is also sensitive against changes in pH value or ionic strength, PDMAEMA<sub>51</sub>-*b*-PDEGMA<sub>49</sub> was chosen for further investigations concerning the solvent composition. First, the polymer was dissolved in aqueous solutions containing 0, 5, 100 or 500 mM NaCl, respectively. DLS measurements showed that the  $T_{CP}$  is shifted from 35 °C at 0 and 5 mM NaCl to 30 °C at 100 mM and to 25 °C at 500 mM NaCl (Figure 6-4A). This is based on the screening of charges, reducing the solubility of the PDMAEMA segments. Thereby, the impact on the hydrodynamic radii was rather small. In all cases, radii of 20 to 30 nm were obtained, except for 500 mM NaCl at 60 °C, where precipitation occurred. Concerning AF4, analysis was not possible in pure water, due to strong electrostatic interactions between the PDMAEMA segments and the membrane (compare Chapter 3). AF4 experiments at 5 mM and 100 mM NaCl were rather similar ( $R_h$  around 25 nm,  $\rho$  around 1.0), except for  $T > 65$  °C, where strong interactions with the membrane prevented successful analysis, too. For 100 mM NaCl, AF4 and offline DLS were in excellent agreement, except for 30 °C, where AF4 showed the free polymer chain, while DLS indicates already the presence of colloidal structures. This difference was related to the lower sample concentration during AF4 separation, linked with a higher  $T_{CP}$  as described above. At 500 mM NaCl below 60 °C, AF4 results with a  $R_h$  of around 27 nm were in good agreement with DLS. Above 60 °C, AF4 showed no increase in size as observed by offline measurements ( $R_h$  around 600 nm). Subsequent DLS measurements of diluted solutions (0.04 mg·mL<sup>-1</sup>,  $R_h$  30 nm) revealed that the observed aggregation is also a concentration dependent effect.

For pH dependent studies, different buffer system (25 mM) were used (Figure 6-4B). No transition was detected at pH 4 over the investigated temperature range. This is attributed to the high degree of protonation of the PDMAEMA segments, keeping the polymer soluble

( $pK_a$  around 6).<sup>[124]</sup> For pH 5.6 to 8.2, the  $T_{CP}$  decreased from 40 to 30 °C with a  $R_h$  in the range of 20 to 30 nm. These results could also be confirmed by AF4. At pH 10, heating above  $T_{CP}$  (around 30 °C) led to precipitation, due to the low solubility of the PDMAEMA block at basic pH values (deprotonation). In this case, also no AF4 data could be obtained over the entire temperature range as the polymer becomes more hydrophobic with deprotonation, which results in enhanced membrane adsorption.<sup>[70]</sup> The formation of large aggregates at pH 10 above the  $T_{CP}$  also led to a blockage of the backpressure tubing.

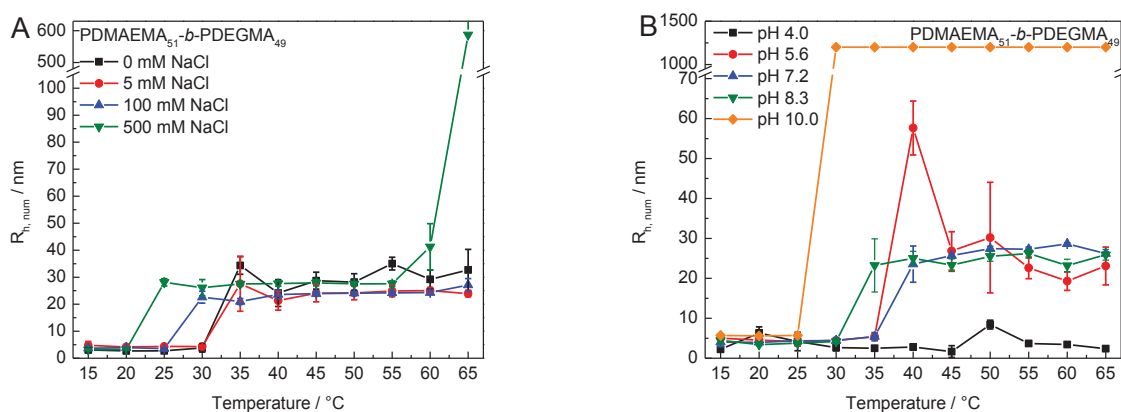


Figure 6-4. (A) DLS results of PDMAEMA<sub>51</sub>-b-PDEGMA<sub>49</sub> at varying NaCl concentration and pH. Larger aggregates are indicated as > 1,000 nm.

These results critically illustrate two restricting factors: First, the eluent of AF4 has to be considered for interpretation and comparison with other methods, as PDMAEMA-*b*-PDEGMA, its cloud point, and its self-assembly behavior, is highly sensitive against changes in solution composition. Modification of the eluent might lead to fractionation problems, due to electrostatic interactions or (irreversible) adsorption on the membrane. Second, the difference in concentration between AF4 and offline techniques should be as low as possible. Moreover, the strong dependency of the cloud point on the polymer concentration limits the applicability for drug delivery and a thermo-induced release application. On the other hand, one can take advantage out of this effect. For example, a substance can be encapsulated at higher polymer concentration at 37 °C ( $T_{CP}$  below 37 °C) and later on be released upon dilution ( $T_{CP}$  above 37 °C). Nevertheless, AF4 was confirmed to be a powerful tool to obtain detailed insights into the size and shape of the colloidal structures. In particular for DLS, where different algorithms and differently weighted datasets render the interpretation of multimodal distributions difficult, coupling to AF4 represents a highly promising alternative. Furthermore, these results showed that the  $T_{CP}$  of PDMAEMA-*b*-PDEGMA can easily be adjusted in a broad range by variation of the solution conditions.

## 7. Summary

Colloidal systems, based on polymeric nanoparticles or self-assembled systems, gained significant attention during the last decades. In particular, their use as therapeutics or diagnostic agents is in the focus of research. A variety of materials and techniques is available for preparation of the targeted nanostructures as well as for the encapsulation of active compounds. To understand the obtained morphologies and their mode of action, a robust in-depth characterization is required, accessing the physicochemical properties. Furthermore, the compliance with quality standards and a high level of safety for *in vivo* studies have to be ensured for pharmaceutical applications. As presented in this thesis, asymmetric flow field-flow fractionation (AF4) investigations in combination with light scattering experiments shows the potential to fulfill these requirements. Thereby, the advantages of dynamic and static light scattering (DLS/SLS), namely non-invasive measurements with high sensitivity even at low sample concentration, are combined with a highly flexible and gentle separation technique, providing an analysis of nearly all nano-sized soft matter (Figure 7-1).

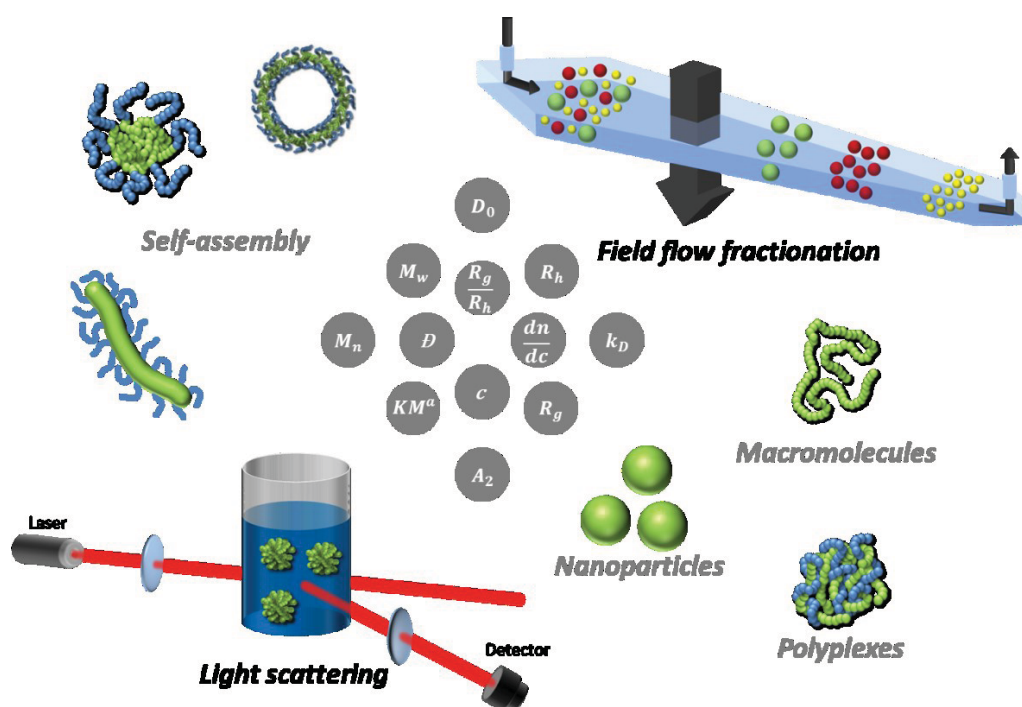


Figure 7-1. Overview of techniques, samples and characteristic properties discussed in this thesis.

It was demonstrated that AF4 coupled to a multi angle laser light scattering (MALLS) detector enables a detailed characterization of cationic polyelectrolytes, a class of polymers where many other techniques showed substantial limitations. Methods for poly(ethylene

imine) (PEI), poly(2-(dimethylamino)ethyl methacrylate) (PDMAEMA) or poly(L-lysine) (PLL), which are the most prominent materials for gene delivery, could be developed, providing the molar mass and size distribution within short time and requiring only low amounts of sample. Therefore, different approaches were evaluated. This comprises a screening of electrostatic interactions by an increase of the ionic strength, a presaturation with a cationic surfactant or polymer to provide repulsive interactions and a decrease of the eluents pH value below the isoelectric point of the membrane material. The latter one was found to be generally applicable to various kinds of cationic polymers. The application of power-law relationships or calculation of the shape ratio gave detailed information on the conformation of the macromolecules. Here, coupling of AF4 and light scattering provides the advantage to separate and identify differently shaped species of a sample by a single experiment. The obtained results could be confirmed by  $^1\text{H}$  NMR spectroscopy and analytical ultracentrifugation (AUC) measurements, two powerful techniques, which are well established for the analysis of polymers.

In a next step, branched PEI was used for the formation of polyplexes with small interfering ribonucleic acid (siRNA) and the influence of the molar mass on the polyplex properties was investigated. Here, an excellent correlation between the net-charge and size or stability of the polyplexes was found, indicating dominant electrostatic interactions. For DLS multimodal size distributions were observed, which have to be interpreted with care. Therefore, AUC was evaluated as an alternative. The obtained results were found to be in good accordance for particles below 150 nm ( $R_h$ ). Limitations were observed for larger samples with a high sedimentation velocity, resulting in a low resolution. Anyhow, the possibility to detect low concentrations of unbound PEI beside the polyplexes renders ultracentrifugation a very powerful tool. Polyplexes composed of linear PEI and siRNA were also encapsulated using the double emulsion technique into dye-labeled poly(lactide-co-glycolic acid) (PLGA) nanoparticles, which show a high selectivity for liver cells, enabling targeted delivery. By a combination of AF4, DLS, laser Doppler velocimetry (LDV), scanning electron microscopy (SEM) and UV-Vis spectroscopy, the nanoparticles and the loading could be characterized in detail. With AF4 it was possible to confirm that the spherical particles were nearly monodisperse in terms of size and shape. Subsequent *in vitro* as well as *in vivo* studies revealed that these “theranostic” systems are successfully applicable as a kind of platform tool. This promising approach also hints towards the future trends of what is possible in

“personalized” nanomedicine. Beside homopolymers and nanoparticles, also a terpolymer, which undergoes self-assembly to multicompartment micelles, was shown to be a promising gene delivery agent for transfection of adherent as well as human leukemia cells. The ability of polybutadiene-*block*-poly(methacrylic acid)-*block*-poly(2-(dimethylamino)ethyl methacrylate) (PB-*b*-PMAA-*b*-PDMAEMA) block copolymers to form intracellular interpolyelectrolyte complexes in dependence of the pH value was found to be the origin of an efficient delivery and release of plasmid deoxyribonucleic acid (pDNA). Thereby, the poly(methacrylic acid) (PMAA) block is able to act as a competing polyanion, weakening the binding between PDMAEMA and the genetic material. The results also reveal the pathway how to combine high transfection efficiency with high biocompatibility to obtain a powerful advanced gene carrier *via* the synthesis and self-assembly of well-defined block copolymers.

The self-assembly of another triblock terpolymer, poly(ethylene oxide)-*block*-poly(allyl glycidyl ether)-*block*-poly(*tert*-butyl glycidyl ether) (PEO-*b*-PAGE-*b*-PtBGE), was investigated for its potential for drug delivery applications with Nile red as a model compound. The obtained morphologies and the influence of different functionalizations were studied by a combination of AF4, DLS, LDV and cryogenic transmission electron microscopy (cryo-TEM) as well as different biological assays and cell uptake experiments. Furthermore, the differently functionalized copolymers can be used as a platform to adjust the physico- and biochemical properties by the formation of binary and ternary mixed micelles. Using this approach, a high internalization rate can be combined with low cytotoxicity and the introduction of targeting moieties. The functionalization of a similar systems, poly(ethylene oxide)-*block*-poly(furfuryl glycidyl ether)-*block*-poly(allyl glycidyl ether) (PEO-*b*-PFGE-*b*-PAGE), was studied concerning the alteration of the hydrophilic/hydrophobic balance by incorporation of carboxy groups or fluorocarbon chains *via* thiol-ene click chemistry. Here, AF4 provides a reliable and detailed characterization regarding size and molar mass distribution of the present species. Indications about shape, in this case spherical, worm-like or disc-like structures, had to be confirmed by a second technique like cryo-TEM, as the  $R_g$  value was close to the lower detection limit of the MALLS detector. Furthermore, a detailed strategy for the AF4 method development was provided and it could be shown for several samples that AF4 represents an ideal technique to investigate the influence of solution conditions like pH value or ionic strength. Thereby, the unique feature of AF4 is the gentle separation of even sensitive colloidal structures from residual polymer, aggregates or other compounds, which were not

detectable or are problematic for analysis by other techniques. Also block copolymers of amine containing poly(2-oxazoline)s, synthesized by cationic ring opening polymerization were found to be effective drug delivery vehicles. As self-assembly processes take place in organic solvents, the particle size and morphology was shown to be adjustable by the polarity of the solvent. For the transfer to water, the system was crosslinked and a drug/dye was introduced, covalently but labile bound to the supernumerous aldehyde groups of the crosslinker. AF4 and cryo-TEM were found to be an ideal combination to obtain reliable information about size and shape of the drug carriers, in this case either spherical micelles or vesicles.

Besides, the thermo-induced, lower critical solution temperature (LCST) based, self-assembly process of smart materials into micellar or vesicular structures could be achieved with poly(2-(dimethylamino)ethyl methacrylate)-*block*-poly(di(ethylene glycol) methyl ether methacrylate) (PDMAEMA-*b*-PDEGMA) copolymers, synthesized *via* reversible addition-fragmentation chain transfer polymerization (RAFT). The phase behavior was studied in detail by a combination of different methods and up to two structural transitions were observed, where the first one was related to the corresponding phase transition. The second one was attributed to an internal rearrangement of the nanostructures without an impact on the size. It was also shown that the cloud point can be controlled by adjustment of the pH value and the ionic strength, due to the charge-bearing PDMAEMA block. Moreover, AF4 could be successfully established at temperatures up to 65 °C. Observed limitations of AF4 and differences to offline measurements were critically discussed and could be traced back to either membrane interactions or the concentration dependence of the cloud point.

In summary, this thesis presents the characterization of manifold colloidal systems. Thereby, the establishment of AF4 and the corresponding method development was in the focus. The results were compared with well-known techniques like DLS, AUC, <sup>1</sup>H NMR or cryo-TEM and provide the basis to understand the interactions of nano-sized materials with biological systems. Even if some limitations were observed, AF4 provided substantial benefits and will help to push the characterization of polymers and colloids in general forward. The presented results will help to overcome current challenges and to establish AF4 as routinely applicable tool. Furthermore, they will contribute to an advanced understanding of self-assembly processes and the development of efficient drug and gene carrier systems.

## 8. Zusammenfassung

Kolloidale Systeme, basierend auf polymeren Nanopartikeln oder selbstassemblierenden Strukturen, gewannen in den letzten Jahrzehnten signifikant an Interesse. Insbesondere die Verwendung für therapeutische oder diagnostische Zwecke steht im Mittelpunkt der aktuellen Forschung. Für die Herstellung der gewünschten Nanomaterialien sowie für die Verkapselung von Wirkstoffen stehen eine Vielzahl an Polymeren und Techniken zur Verfügung. Um die resultierenden Strukturen und deren Wirkungsweise zu verstehen, ist eine umfassende Charakterisierung bezüglich ihrer physikochemischen Eigenschaften unabdingbar. Des Weiteren muss die Einhaltung verschiedener Qualitätsstandards für eine pharmazeutische Anwendung sichergestellt sein. Wie in dieser Arbeit dargestellt werden konnte, zeigt die asymmetrische Fluss Feld-Fluss Fraktionierung (AF4), gekoppelt mit verschiedenen Lichtstreckentechniken, das Potenzial die oben genannten Bedingungen zu erfüllen. Dabei werden die Vorteile der Lichtstreuung – nicht-invasive Messungen bei hoher Empfindlichkeit und niedriger Probenkonzentration – mit einer flexiblen und sanften Trennmethode verbunden, welche die Charakterisierung nahezu jedweder Polymere und Nanomaterialien in Lösung erlaubt (Figure 8-1).

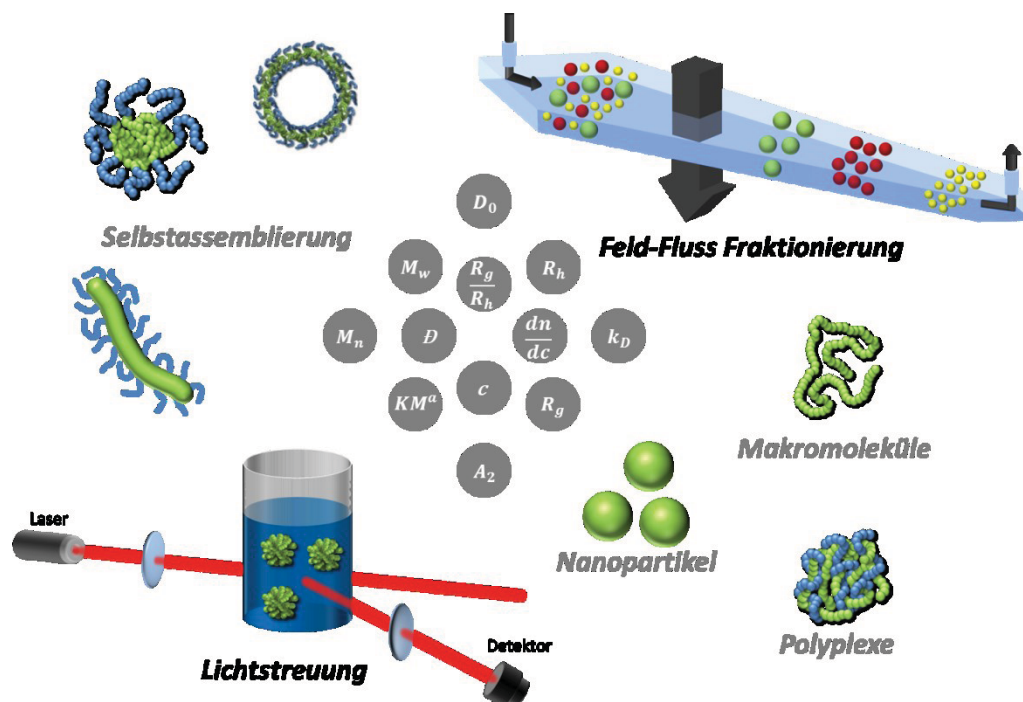


Figure 8-1. Übersicht über die Techniken, Materialien und physikochemischen Eigenschaften, die im Rahmen dieser Arbeit diskutiert wurden.

Es konnte gezeigt werden, dass AF4 eine detaillierte Charakterisierung kationischer Polymere ermöglicht, welche mit klassischen Methoden nur eingeschränkt untersucht werden können. Für die bekanntesten Materialien wie Poly(ethylenimin) (PEI), Poly(2-(dimethylamino)ethylmethacrylat) (PDMAEMA) oder Poly(L-lysin) (PLL) konnten Methoden entwickelt werden, die die Bestimmung der Molmassen- und Größenverteilung innerhalb kurzer Zeit und mit geringen Probenvolumina ermöglichen. Um die zumeist auftretenden attraktiven, elektrostatischen Wechselwirkungen zwischen der Membran und der Probe zu reduzieren, wurden verschiedene Ansätze, wie eine Erhöhung der Ionenstärke, eine Sättigung der Membran mit einem kationischen Detergenz oder Polymer sowie die Erniedrigung des pH-Wertes des Eluenten unter den isoelektrischen Punkt der Membran, untersucht. Dabei stellte sich die letzte Variante als vielversprechend und für eine Vielzahl kationischer Polymere als allgemein anwendbar heraus. Über das Verhältnis  $R_g/R_h$  sowie den Anstieg aus der doppelt logarithmischen Auftragung von  $R_g$  gegen  $M$  können zusätzliche Informationen bezüglich der Konformation bzw. Partikelgeometrie gewonnen werden. Weiterhin ermöglicht dies die Trennung und Identifizierung unterschiedlicher Geometrien/Konformationen in einer Probe innerhalb eines einzelnen Experimentes. Die über AF4 erzielten Ergebnisse konnten mittels  $^1\text{H}$  NMR Spektroskopie sowie analytischer Ultrazentrifugation (AUC) bestätigt werden.

Der Einfluss der molaren Masse von PEI auf die Komplexierung von „small interfering ribonucleic acid“ (siRNA) und die Eigenschaften der resultierenden Polyplexe wurde ebenfalls untersucht. Es wurde eine starke Korrelation zwischen der Nettoladung und der Größe sowie der Stabilität der Polyplexe gefunden, was auf die Dominanz elektrostatischer Wechselwirkungen hinweist. Zur Unterstützung der Interpretation, der durch dynamische Lichtstreuung (DLS) erhaltenen multimodalen Größenverteilungen, wurde AUC als alternative Methode genutzt. Während die Ergebnisse für kleinere Polyplexe (unter 150 nm) gut übereinstimmen, ließen sich größere Aggregate nicht mittels AUC bestimmen. Dies konnte auf die hohe Sedimentationsgeschwindigkeit und die damit verbundene geringe Messdauer sowie die niedrige Auflösung zurückgeführt werden. Im Gegensatz zu DLS war jedoch die Bestimmung der Menge an freiem Polymer mittels AUC möglich. Des Weiteren wurden Polyplexe aus linearem PEI und siRNA mittels Doppel-Emulsionsverfahren in Poly(lactid-co-glycolid) (PLGA) Nanopartikel verkapselt, welche über einen speziellen Farbstoff mit einer hohen Selektivität für bestimmte Leberzellen verfügen und damit eine



aktiven, zielgerichteten Transport ermöglichen. Mittels AF4, DLS, Laser Doppler Velocimetrie (LDV), Rasterelektronenmikroskopie (SEM) und UV-Vis Spektroskopie konnten diese Partikel sowie deren Beladung im Detail charakterisiert werden. Anschließende *in vitro* und *in vivo* Studien zeigten, dass derartige therapeutisch-diagnostische Systeme äußerst erfolgreich angewendet werden können. Die einfache Variation der jeweiligen siRNA oder des Farbstoffes ermöglicht es, eine Vielzahl potenzieller Krankheiten zu adressieren und zeigt einen eindeutigen Trend bezüglich der Möglichkeiten einer „personalisierten“ Medizin. Neben Nanopartikeln und Homopolymeren stellen kompartimentierte Mizellen des Triblock Terpolymers Polybutadien-*block*-Poly(methacrylsäure)-*block*-Poly(2-(dimethylamino)ethylmethacrylat) (PB-*b*-PMAA-*b*-PDMAEMA) eine weitere Art vielversprechender Gentransporter dar, welchen neben adhären Zellen auch die Transfektion humaner Leukämiezellen (Suspensionszellen) ermöglichen. Es konnte gezeigt werden, dass die Ursache für die hohe Effizienz in der pH-Wert abhängigen Bildung intramizellarer Interpolyelektrolytkomplexe liegt. PMAA diene dabei als konkurrierendes Polyanion, um die Bindung zwischen PDMAEMA und Plasmid-Desoxyribonukleinsäure (pDNA) zu schwächen und deren Freisetzung zu ermöglichen. Des Weiteren zeigt dieses System, wie es über die Synthese und Selbstassemblierung definierter Blockcopolymerer möglich ist, eine hohe Transfektionseffizienz mit hoher Biokompatibilität zu vereinen.

Ebenfalls untersucht wurde die Selbstassemblierung von Poly(ethylenoxid)-*block*-Poly(allylglycidylether)-*block*-Poly(*tert*-butylglycidylether) (PEO-*b*-PAGE-*b*-PtBGE) mit Nilrot als Modellfarbstoff. Dabei stand insbesondere der Einfluss verschiedener Funktionalisierungen des PAGE Segments auf die resultierenden Strukturen, die Zytotoxizität und die Zellaufnahme im Mittelpunkt. Weiterhin dienten die unterschiedlich funktionalisierten Polymere als Plattform für zahlreiche binäre und ternäre „Mischmizellen“, welche mittels einer Kombination aus AF4, DLS, LDV, Gelelektrophorese und Cryo-Transmissionselektronenmikroskopie (cryo-TEM) detailliert charakterisiert werden konnten. Mithilfe dieses Ansatzes ließen sich die physiko- und biochemischen Eigenschaften der Mizellen derart modifizieren, dass eine hohe Zellaufnahme bei gleichzeitig niedriger Toxizität erreicht wird. Weiterhin besteht die Möglichkeit der Einführung von funktionellen Gruppen und Seitenketten zur gezielten Adressierung bestimmter Zellen. Bei einem ähnlichen System, Poly(ethylenoxid)-*block*-Poly(furfurylglycidylether)-*block*-Poly(allylglycidylether) (PEO-*b*-PFGE-*b*-PAGE), wurde die Funktionalisierung des PAGE-Blocks mittels Thiol-En Chemie zur

Variation des hydrophilen/hydrophoben Charakters durch Einführung von Carboxy-Gruppen oder fluorierten Alkylketten verwendet. Mittels AF4 wurden verlässliche Werte für die Größen- und Molmassenverteilungen aller Polymere erhalten. Da der  $R_g$  der Nanostrukturen, im vorliegenden Fall sphärische, diskusförmige oder wurmartige Mizellen, am unteren Limit des Lichtstreuungs-Detektors liegt, wurden die Anhaltspunkte bezüglich der Partikelgeometrie (basierend auf dem Verhältnis  $R_g/R_h$ ) mittels cryo-TEM überprüft und bestätigt. Dass AF4 gekoppelt mit Lichtstreuung und im Verbund mit cryo-TEM eine ideale Kombination zur physikochemischen Charakterisierung darstellt, konnte auch für Blockcopolymere aminhaltiger Poly(2-oxazolin)e gezeigt werden. Nach erfolgreicher Synthese über kationische Ringöffnungspolymerisation ließ sich die Selbstassemblierung dieser doppelt hydrophilen Polymere durch die Wahl des jeweiligen organischen Lösungsmittels kontrollieren. Für den Einsatz als Wirkstofftransporter in wässrigen Systemen wurden die Strukturen mittels Glutaraldehyd quervernetzt, was gleichzeitig die kovalente aber labile Bindung eines Wirk- oder Farbstoffes wie 6-Aminofluorescein an die überschüssigen Aldehydgruppen ermöglichte. Des Weiteren wurde gezeigt, dass die so erhaltenen Mizellen und Vesikel effektiv von L929 Zellen aufgenommen werden.

Die temperaturinduzierte Selbstassemblierung zu Mizellen bzw. Vesikeln, welche auf dem Vorhandensein einer unteren kritischen Lösungstemperatur basiert (LCST), wurde ebenfalls im Rahmen dieser Arbeit untersucht. Blockcopolymere von Poly(2-(dimethylamino)ethylmethacrylat)-*block*-Poly(di(ethylenglycol)methylethermethacrylat) (PDMAEMA-*b*-PDEGMA), synthetisiert mittels reversibler Additions-Fragmentierungs-Kettenübertragungs-Polymerisation (RAFT), konnten dazu genutzt werden „intelligente“ Systeme zu erzeugen, welche auf äußere Stimuli wie Temperatur oder pH-Wert Änderungen reagieren. Detaillierte Studien mittels AF4, Lichtstreuung, NMR-Spektroskopie und dynamischer Differenzkalorimetrie (DSC) zeigten, dass zwei Übergänge stattfinden, wobei nur der Erste dem eigentlichen Phasenübergang entspricht. Der zweite Übergang, sofern vorhanden, stellt dagegen nur eine Neuordnung der inneren Struktur dar, welche keinen Einfluss auf die Partikelgröße insgesamt hat. Weiterhin konnte gezeigt werden, dass sich aufgrund des PDMAEMA-Blocks die Übergangstemperatur präzise mittels pH-Wert und Ionenstärke einstellen lässt. Ein Schwerpunkt lag in der Etablierung der AF4 bei Temperaturen bis 65 °C. Die beobachteten Abweichungen zu klassischen Methoden konnten dabei entweder auf

Wechselwirkungen mit der Membran oder die Konzentrationsabhängigkeit der Trübungstemperatur ( $T_{CP}$ ) zurückgeführt werden.

Insgesamt wurde in dieser Dissertation die Charakterisierung verschiedenster Polymere und kolloidaler Systeme präsentiert. Die Etablierung der AF4 und die dazugehörige Methodenentwicklung standen dabei im Zentrum. Die Ergebnisse wurden mit Daten klassischer Methoden wie DLS, AUC,  $^1H$  NMR oder cryo-TEM verglichen und kritisch diskutiert. Diese stellen die Grundlage dar, um einerseits das Verhalten und die Wirkungsweise in biologischen Systemen und andererseits das Prinzip der Selbstassemblierung an sich besser zu verstehen. Die Anwendung der AF4 brachte in allen Fällen, trotz einiger Einschränkungen, entscheidende Vorteile in der Charakterisierung von Makromolekülen und Kolloiden. Die hier gezeigten Ergebnisse leisten einen substantiellen Beitrag zur Etablierung der AF4 als moderne Standardmethode der Polymeranalytik und tragen zu einem besseren Verständnis von Selbstassemblierungsprozessen und der Entwicklung effizienter Wirkstoff-Transporter bei.



## 9. References

- [1] R. Duncan, R. Gaspar, *Mol. Pharm.* **2011**, *8*, 2101-2141.
- [2] S. Parveen, R. Misra, S. K. Sahoo, *Nanomed. Nanotechnol. Biol. Med.* **2012**, *8*, 147-166.
- [3] S. D. Steichen, M. Caldorera-Moore, N. A. Peppas, *Eur. J. Pharm. Sci.* **2013**, *48*, 416-427.
- [4] K. Riehemann, S. W. Schneider, T. A. Luger, B. Godin, M. Ferrari, H. Fuchs, *Angew. Chem. Int. Ed.* **2009**, *48*, 872-897.
- [5] W. H. De Jong, P. J. A. Borm, *Int. J. Nanomedicine* **2008**, *3*, 133-149.
- [6] A. Vollrath, S. Schubert, U. S. Schubert, *J. Mater. Chem. B* **2013**, *1*, 1994-2007.
- [7] S. K. R. Williams, J. R. Runyon, A. A. Ashames, *Anal. Chem.* **2011**, *83*, 634-642.
- [8] T. Svedberg, J. B. Nichols, *J. Am. Chem. Soc.* **1923**, *45*, 2910-2917.
- [9] J. Lebowitz, M. S. Lewis, P. Schuck, *Protein Sci.* **2002**, *11*, 2067-2079.
- [10] G. M. Pavlov, I. Perevyazko, U. S. Schubert, *Macromol. Chem. Phys.* **2010**, *211*, 1298-1310.
- [11] G. M. Pavlov, I. Y. Perevyazko, O. V. Okatova, U. S. Schubert, *Methods* **2011**, *54*, 124-135.
- [12] O. Akbulut, C. R. Mace, R. V. Martinez, A. A. Kumar, Z. H. Nie, M. R. Patton, G. M. Whitesides, *Nano Lett.* **2012**, *12*, 4060-4064.
- [13] A. Vollrath, D. Pretzel, C. Pietsch, I. Perevyazko, S. Schubert, G. M. Pavlov, U. S. Schubert, *Macromol. Rapid Commun.* **2012**, *33*, 1791-1797.
- [14] A. V. Delgado, F. Gonzalez-Caballero, R. J. Hunter, L. K. Koopal, J. Lyklema, *J. Colloid Interface Sci.* **2007**, *309*, 194-224.
- [15] R. Finsky, N. Dejaeger, *Part. Part. Syst. Charact.* **1991**, *8*, 187-193.
- [16] T. Kowalkowski, B. Buszewski, C. Cantado, F. Dondi, *Crit. Rev. Anal. Chem.* **2006**, *36*, 129-135.
- [17] J. C. Giddings, *J. Sep. Sci.* **1966**, *1*, 123-125.
- [18] J. C. Giddings, *J. Chromatogr.* **1976**, *125*, 3-16.
- [19] J. Gigault, B. Grassl, I. Le Hecho, G. Lespes, *Microchim. Acta* **2011**, *175*, 265-271.
- [20] G. H. Thompson, M. N. Myers, J. C. Giddings, *Anal. Chem.* **1969**, *41*, 1219-1222.
- [21] K. D. Caldwell, J. C. Giddings, M. N. Myers, L. F. Kesner, *Science* **1972**, *176*, 296-298.
- [22] J. C. Giddings, F. J. F. Yang, M. N. Myers, *Anal. Chem.* **1974**, *46*, 1917-1924.
- [23] J. C. Giddings, *Sep. Sci. Technol.* **1985**, *20*, 749-768.
- [24] M. Martin, J. Hes, *Sep. Sci. Technol.* **1984**, *19*, 685-707.
- [25] D. Roessner, W. M. Kulicke, *J. Chromatogr. A* **1994**, *687*, 249-258.
- [26] W. Fraunhofer, G. Winter, *Eur. J. Pharm. Biopharm.* **2004**, *58*, 369-383.
- [27] J. C. Giddings, M. N. Myers, K. D. Caldwell, S. R. Fisher, *Methods Biochem. Anal.* **1980**, *26*, 79-136.
- [28] F. von der Kammer, S. Legros, E. H. Larsen, K. Loeschner, T. Hofmann, *Trends Analyt. Chem.* **2011**, *30*, 425-436.
- [29] C. Pietsch, R. Hoogenboom, U. S. Schubert, *Angew. Chem. Int. Ed.* **2009**, *48*, 5653-5656.
- [30] I. Dimitrov, B. Trzebicka, A. H. E. Müller, A. Dworak, C. B. Tsvetanov, *Prog. Polym. Sci.* **2007**, *32*, 1275-1343.
- [31] D. Schmaljohann, *Adv. Drug Delivery Rev.* **2006**, *58*, 1655-1670.
- [32] S. H. Qin, Y. Geng, D. E. Discher, S. Yang, *Adv. Mater.* **2006**, *18*, 2905-2909.

- [33] Y. Jiang, M. E. Miller, P. Li, M. E. Hansen, *Am. Lab.* **2000**, *32*, 98-99.
- [34] K. G. Wahlund, J. C. Giddings, *Anal. Chem.* **1987**, *59*, 1332-1339.
- [35] J. C. Giddings, M. A. Benincasa, M. K. Liu, P. Li, *J. Liq. Chromatogr.* **1992**, *15*, 1729-1747.
- [36] L. Dulog, T. Schauer, *Prog. Org. Coat.* **1996**, *28*, 25-31.
- [37] J. C. Giddings, *Analyst* **1993**, *118*, 1487-1494.
- [38] J. C. Giddings, M. N. Myers, K. D. Caldwell, J. W. Pav, *J. Chromatogr.* **1979**, *185*, 261-271.
- [39] K. G. Wahlund, A. Zattoni, *Anal. Chem.* **2002**, *74*, 5621-5628.
- [40] J. C. Giddings, *J. Chem. Educ.* **1973**, *50*, 667-669.
- [41] M. E. Schimpf, K. D. Caldwell, J. C. Giddings, *Field-Flow Fractionation Handbook*, Wiley, New York, **2000**.
- [42] A. Litzén, *Anal. Chem.* **1993**, *65*, 461-470.
- [43] A. Hakansson, E. Magnusson, B. Bergenstahl, L. Nilsson, *J. Chromatogr. A* **2012**, *1253*, 120-126.
- [44] P. S. Williams, J. C. Giddings, *Anal. Chem.* **1987**, *59*, 2038-2044.
- [45] P. S. Williams, M. C. Giddings, J. C. Giddings, *Anal. Chem.* **2001**, *73*, 4202-4211.
- [46] J. J. Kirkland, C. H. Dilks, S. W. Rementer, W. W. Yau, *J. Chromatogr.* **1992**, *593*, 339-355.
- [47] B. Chu, T. B. Liu, *J. Nanopart. Res.* **2000**, *2*, 29-41.
- [48] W. Burchard, *Adv. Polym. Sci.* **1999**, *143*, 113-194.
- [49] M. Andersson, B. Wittgren, K. G. Wahlund, *Anal. Chem.* **2003**, *75*, 4279-4291.
- [50] W. Burchard, *Macromolecules* **1977**, *10*, 919-927.
- [51] R. Pecora, *J. Nanopart. Res.* **2000**, *2*, 123-131.
- [52] S. W. Provencher, *Comput. Phys. Commun.* **1982**, *27*, 229-242.
- [53] D. C. Rambaldi, A. Zattoni, P. Reschiglian, R. Colombo, E. De Lorenzi, *Anal. Bioanal. Chem.* **2009**, *394*, 2145-2149.
- [54] D. C. Rambaldi, P. Reschiglian, A. Zattoni, *Anal. Bioanal. Chem.* **2011**, *399*, 1439-1447.
- [55] S. G. Stevenson, K. R. Preston, *J. Liq. Chromatogr. Relat. Technol.* **1997**, *20*, 2835-2842.
- [56] M. A. Benincasa, C. Delle Fratte, *J. Chromatogr. A* **2004**, *1046*, 175-184.
- [57] A. Ulrich, S. Losert, N. Bendixen, A. Al-Kattan, H. Hagedorfer, B. Nowack, C. Adlhart, J. Ebert, M. Lattuada, K. Hungerbuhler, *J. Anal. At. Spectrom.* **2012**, *27*, 1120-1130.
- [58] B. Wittgren, K. G. Wahlund, *J. Chromatogr. A* **1997**, *791*, 135-149.
- [59] S. Dubascoux, I. Le Hecho, M. Hasseloev, F. Von der Kammer, M. P. Gautier, G. Lespes, *J. Anal. At. Spectrom.* **2010**, *25*, 613-623.
- [60] E. P. C. Mes, H. de Jonge, T. Klein, R. R. Welz, D. T. Gillespie, *J. Chromatogr. A* **2007**, *1154*, 319-330.
- [61] A. F. Thünemann, P. Knappe, R. Bienert, S. Weidner, *Anal. Methods* **2009**, *1*, 177-182.
- [62] E. S. Gil, S. M. Hudson, *Prog. Polym. Sci.* **2004**, *29*, 1173-1222.
- [63] O. Boussif, F. Lezoualch, M. A. Zanta, M. D. Mergny, D. Scherman, B. Demeneix, J. P. Behr, *Proc. Natl. Acad. Sci.* **1995**, *92*, 7297-7301.
- [64] M. A. Benincasa, J. C. Giddings, *J. Microcolumn Sep.* **1997**, *9*, 479-495.
- [65] C. Augsten, K. Mäder, *Int. J. Pharm.* **2008**, *351*, 23-30.
- [66] M. Sahnoun, M.-T. Charreyre, L. Veron, T. Delair, F. D'Agosto, *J. Polym. Sci., Part A: Polym. Chem.* **2005**, *43*, 3551-3565.
- [67] L. Tauhardt, K. Kempe, K. Knop, E. Altuntas, M. Jäger, S. Schubert, D. Fischer, U. S. Schubert, *Macromol. Chem. Phys.* **2011**, *212*, 1918-1924.

- [68] X.-l. Jiang, Y.-f. Chu, J. Liu, G.-y. Zhang, R.-x. Zhuo, *Chin. J. Polym. Sci.* **2011**, *29*, 421-426.
- [69] R. N. Qureshi, W. T. Kok, *Anal. Bioanal. Chem.* **2011**, *399*, 1401-1411.
- [70] S. Hupfeld, D. Ausbacher, M. Brandl, *J. Sep. Sci.* **2009**, *32*, 3555-3561.
- [71] M. A. Benincasa, J. C. Giddings, *Anal. Chem.* **1992**, *64*, 790-798.
- [72] G. Yohannes, M. Jussila, K. Hartonen, M.-L. Riekkola, *J. Chromatogr. A* **2011**, *1218*, 4104-4116.
- [73] K. L. Planken, H. Cölfen, *Nanoscale* **2010**, *2*, 1849-1869.
- [74] T. Pauck, H. Cölfen, *Anal. Chem.* **1998**, *70*, 3886-3891.
- [75] H. Thielking, W. M. Kulicke, *Anal. Chem.* **1996**, *68*, 1169-1173.
- [76] E. Alasonati, M. A. Benincasa, V. I. Slaveykova, *J. Sep. Sci.* **2007**, *30*, 2332-2340.
- [77] M. Pontie, *J. Membr. Sci.* **1999**, *154*, 213-220.
- [78] J. B. Lee, J. Hong, D. K. Bonner, Z. Poon, P. T. Hammond, *Nat. Mater.* **2012**, *11*, 316-322.
- [79] J. P. Behr, *Acc. Chem. Res.* **2012**, *45*, 980-984.
- [80] C. M. Varga, N. C. Tedford, M. Thomas, A. M. Klibanov, L. G. Griffith, D. A. Lauffenburger, *Gene Ther.* **2005**, *12*, 1023-1032.
- [81] J. Ziebarth, Y. M. Wang, *Biophys. J.* **2009**, *97*, 1971-1983.
- [82] S. Sundaram, L. K. Lee, C. M. Roth, *Nucleic Acids Res.* **2007**, *35*, 4396-4408.
- [83] M.-E. Bonnet, P. Erbacher, A.-L. Bolcato-Bellemin, *Pharm. Res.* **2008**, *25*, 2972-2982.
- [84] M. J. Waring, *J. Mol. Biol.* **1965**, *13*, 269-282.
- [85] M. Neu, D. Fischer, T. Kissel, *J. Gene Med.* **2005**, *7*, 992-1009.
- [86] B. J. Hong, A. J. Chipre, S. T. Nguyen, *J. Am. Chem. Soc.* **2013**, *135*, 17655-17658.
- [87] J. P. Rao, K. E. Geckeler, *Prog. Polym. Sci.* **2011**, *36*, 887-913.
- [88] L. Nilsson, *Food Hydrocolloids* **2013**, *30*, 1-11.
- [89] E. Betthausen, M. Drechsler, M. Fortsch, F. H. Schacher, A. H. E. Müller, *Soft Matter* **2011**, *7*, 8880-8891.
- [90] H. Keller, C. Yunxu, G. Marit, M. Pla, J. Reiffers, J. Theze, P. Froussard, *Gene Ther.* **1999**, *6*, 931-938.
- [91] C. V. Synatschke, A. Schallon, V. Jerome, R. Freitag, A. H. E. Müller, *Biomacromolecules* **2011**, *12*, 4247-4255.
- [92] D. S. Dimitrov, *Nat. Rev. Microbiol.* **2004**, *2*, 109-122.
- [93] A. M. Paredes, D. Ferreira, M. Horton, A. Saad, H. Tsuruta, R. Johnston, W. Klimstra, K. Ryman, R. Hernandez, W. Chiu, D. T. Brown, *Virology* **2004**, *324*, 373-386.
- [94] Y. Lee, K. Miyata, M. Oba, T. Ishii, S. Fukushima, M. Han, H. Koyama, N. Nishiyama, K. Kataoka, *Angew. Chem. Int. Ed.* **2008**, *47*, 5163-5166.
- [95] H. Ding, X. J. Wang, S. Zhang, X. L. Liu, *J. Nanopart. Res.* **2012**, *14*, 1254.
- [96] T. Y. Kim, D. W. Kim, J. Y. Chung, S. G. Shin, S. C. Kim, D. S. Heo, N. K. Kim, Y. J. Bang, *Clin. Cancer. Res.* **2004**, *10*, 3708-3716.
- [97] Y. Matsumura, T. Hamaguchi, T. Ura, K. Muro, Y. Yamada, Y. Shimada, K. Shirao, T. Okusaka, H. Ueno, M. Ikeda, N. Watanabe, *Br. J. Cancer* **2004**, *91*, 1775-1781.
- [98] J. Hrkach, D. Von Hoff, M. M. Ali, E. Andrianova, J. Auer, T. Campbell, D. De Witt, M. Figa, M. Figueiredo, A. Horhota, S. Low, K. McDonnell, E. Peeke, B. Retnarajan, A. Sabnis, E. Schnipper, J. J. Song, Y. H. Song, J. Summa, D. Tompsett, G. Troiano, T. V. Hoven, J. Wright, P. LoRusso, P. W. Kantoff, N. H. Bander, C. Sweeney, O. C. Farokhzad, R. Langer, S. Zale, *Sci. Transl. Med.* **2012**, *4*, 128ra139.
- [99] K. Knop, R. Hoogenboom, D. Fischer, U. S. Schubert, *Angew. Chem. Int. Ed.* **2010**, *49*, 6288-6308.

- [100] S. L. Lin, W. J. Zhu, X. H. He, Y. H. Xing, L. Y. Liang, T. Chen, J. P. Lin, *J. Phys. Chem. B* **2013**, *117*, 2586-2593.
- [101] M. Libera, B. Trzebicka, A. Kowalczyk, W. Walach, A. Dworak, *Polymer* **2011**, *52*, 250-257.
- [102] C. Auschra, R. Stadler, *Macromolecules* **1993**, *26*, 2171-2174.
- [103] M. J. Robb, L. A. Connal, B. F. Lee, N. A. Lynd, C. J. Hawker, *Polym. Chem.* **2012**, *3*, 1618-1628.
- [104] T. P. Lodge, A. Rasdal, Z. B. Li, M. A. Hillmyer, *J. Am. Chem. Soc.* **2005**, *127*, 17608-17609.
- [105] K. Van Butsele, S. Cajot, S. Van Vlierberghe, P. Dubruel, C. Passirani, J. P. Benoit, R. Jerome, C. Jerome, *Adv. Funct. Mater.* **2009**, *19*, 1416-1425.
- [106] A. Zattoni, D. C. Rambaldi, P. Reschiglian, M. Melucci, S. Krol, A. M. C. Garcia, A. Sanz-Medel, D. Roessner, C. Johann, *J. Chromatogr. A* **2009**, *1216*, 9106-9112.
- [107] A. Besheer, J. Vogel, D. Glanz, J. Kressler, T. Groth, K. Mäder, *Mol. Pharm.* **2009**, *6*, 407-415.
- [108] J. R. Silveira, G. J. Raymond, A. G. Hughson, R. E. Race, V. L. Sim, S. F. Hayes, B. Caughey, *Nature* **2005**, *437*, 257-261.
- [109] R. Yang, F. H. Meng, S. B. Ma, F. S. Huang, H. Y. Liu, Z. Y. Zhong, *Biomacromolecules* **2011**, *12*, 3047-3055.
- [110] P. Greenspan, E. P. Mayer, S. D. Fowler, *J. Cell. Biol.* **1985**, *100*, 965-973.
- [111] A. B. E. Attia, Z. Y. Ong, J. L. Hedrick, P. P. Lee, P. L. R. Ee, P. T. Hammond, Y. Y. Yang, *Curr. Opin. Colloid Interface Sci.* **2011**, *16*, 182-194.
- [112] J. Nguyen, X. Xie, M. Neu, R. Dumitrescu, R. Reul, J. Sitterberg, U. Bakowsky, R. Schermuly, L. Fink, T. Schmehl, T. Gessler, W. Seeger, T. Kissel, *J. Gene. Med.* **2008**, *10*, 1236-1246.
- [113] J. Hu, G. Zhang, Z. Ge, S. Liu, *Prog. Polym. Sci.* **2014**, *39*, 1096-1143.
- [114] Y. Li, B. S. Lokitz, C. L. McCormick, *Angew. Chem. Int. Ed.* **2006**, *45*, 5792-5795.
- [115] O. Onaca, R. Enea, D. W. Hughes, W. Meier, *Macromol. Biosci.* **2009**, *9*, 129-139.
- [116] L. Yang, T. Liu, K. Song, S. Wu, X. Fan, *J. Appl. Polym. Sci.* **2013**, *127*, 4280-4287.
- [117] S. Han, M. Hagiwara, T. Ishizone, *Macromolecules* **2003**, *36*, 8312-8319.
- [118] F. A. Plamper, A. Schmalz, M. Ballauff, A. H. E. Müller, *J. Am. Chem. Soc.* **2007**, *129*, 14538-14539.
- [119] Q. Zhang, J.-D. Hong, R. Hoogenboom, *Polym. Chem.* **2013**, *4*, 4322-4325.
- [120] F. L. Baines, S. P. Armes, N. C. Billingham, Z. Tuzar, *Macromolecules* **1996**, *29*, 8151-8159.
- [121] V. S. Joseph, S. Kim, Q. Zhang, R. Hoogenboom, J.-D. Hong, *Polymer* **2013**, *54*, 4894-4901.
- [122] M. Gaumet, A. Vargas, R. Gurny, F. Delie, *Eur. J. Pharm. Biopharm.* **2008**, *69*, 1-9.
- [123] R. Finsy, N. Dejaeger, R. Sneyers, E. Gelade, *Part. Part. Syst. Charact.* **1992**, *9*, 125-137.
- [124] F. A. Plamper, M. Ruppel, A. Schmalz, O. Borisov, M. Ballauff, A. H. E. Müller, *Macromolecules* **2007**, *40*, 8361-8366.



## List of abbreviations

AF4	Asymmetric flow field-flow fractionation
AUC	Analytical ultracentrifugation
BMAAD	Polybutadiene- <i>block</i> -poly(methacrylic acid)- <i>block</i> -poly(2-(dimethylamino)ethyl methacrylate)
CMC	Critical micelle concentration
CTAB	Cetyl trimethylammonium bromide
DLS	Dynamic light scattering
DMPA	2,2-Dimethoxy-2-phenylacetophenone
DNA	Deoxyribonucleic acid
DSC	Differential scanning calorimetry
Cryo-TEM	Cryogenic transmission electron microscopy
EAT	PEO <sub>42</sub> - <i>b</i> -PAGE <sub>15</sub> - <i>b</i> -PtBGE <sub>12</sub>
ECT	PEO <sub>42</sub> - <i>b</i> -PAGE <sub>15,COOH</sub> - <i>b</i> -PtBGE <sub>12</sub>
EDC	1-Ethyl-3-(3-dimethylaminopropyl)carbodiimide
EGT	PEO <sub>42</sub> - <i>b</i> -(PAGE <sub>10,Gal</sub> -CO-PAGE <sub>5</sub> )- <i>b</i> -PtBGE <sub>12</sub>
ELS	Electrophoretic light scattering (see also LDV)
ENT	PEO <sub>42</sub> - <i>b</i> -(PAGE <sub>8,NH2</sub> -CO-PAGE <sub>7</sub> )- <i>b</i> -PtBGE <sub>12</sub>
FFF	Field-flow fractionation
<sup>1</sup> H NMR	Proton nuclear magnetic resonance
ICP-MS	Inductively coupled plasma mass spectrometry
IP	Isoelectric point
LCST	Lower critical solution temperature
LDV	Laser Doppler velocimetry
MALLS	Multi angle laser light scattering
MPA	3-Mercaptopropionic acid
MWCO	Molar weight cut-off
NIR	Near infrared
NMR	Nuclear magnetic resonance spectroscopy
N/P	Nitrogen over phosphate ratio
PAEMA	Poly(2-(amino)ethyl methacrylate)

## List of abbreviations

---

PAGE	Poly(allyl glycidyl ether)
PAmOx	Deprotected poly(2-(4-(( <i>tert</i> -butoxycarbonyl)amino)butyl)-2-oxazoline)
PB	Polybutadiene
PDEGMA	Poly(di(ethylene glycol) methyl ether methacrylate)
PDI	Polydispersity index
PDMAEMA	Poly(2-(dimethylamino)ethyl methacrylate)
PEI	Poly(ethylene imine)
PEO	Poly(ethylene oxide)
PEtOx	Poly(2-ethyl-2-oxazoline)
PFGE	Poly(furfuryl glycidyl ether)
PFOT	1 <i>H</i> ,1 <i>H</i> ,2 <i>H</i> ,2 <i>H</i> -perfluorooctanethiol
PLGA	Poly(lactide- <i>co</i> -glycolic acid)
PLL	Poly(L-lysine)
PMAA	Poly(methacrylic acid)
PtBAEMA	Poly(2-( <i>tert</i> -butylamino)ethyl methacrylate)
PtBGE	Poly( <i>tert</i> -butyl glycidyl ether)
PUC	Preparative ultracentrifugation
RAFT	Reversible addition-fragmentation chain transfer (polymerization)
RFU	Relative fluorescence unit
RI	Refractive index
RMS	Root-mean-square radius
RNA	Ribonucleic acid
SAXS	Small angle x-ray scattering
SDS	Sodium dodecyl sulfate
SEC	Size exclusion chromatography
siRNA	Small interfering ribonucleic acid
SLS	Static light scattering
SPLITT FFF	Split flow thin cell fractionation
UV	Ultraviolet

## List of symbols

$\alpha$	Angle of the inlet triangle	$n_0$	Refractive index of the solvent
$a$	Segment length	$N$	Degree of polymerization
$A$	Accumulation wall area	$N_A$	Avogadro's number
$A_2$	Second virial coefficient	$N_{agg}$	Aggregation number
$A_{foc}$	Focus zone area	$P(\theta)$	Form factor
$A_i$	Constant factor	$\rho_0$	Solvent density
$c$	Concentration	$q$	Scattering vector
$d$	Distance from the scattering center	$r$	Particle radius
$D$	Diffusion coefficient	$R$	Universal gas constant
$\mathcal{D}$	Dispersity ( $M_w/M_n$ )	$R_r$	Retention ratio
$\frac{\partial n}{\partial c}$	Refractive index increment	$R(\theta)$	Excess Rayleigh ratio
$\eta$	Viscosity	$R_g$	Radius of gyration
$g_1(\tau)$	Field-time-autocorrelation function	$R_h$	Hydrodynamic radius
$g_2(\tau)$	Intensity-time-autocorrelation function	$s_0$	Sedimentation coefficient
$\theta$	Scattering angle	$t$	Time
$\Delta H$	Enthalpy changes	$T$	Temperature
$I(t)$	Intensity at time $t$	$t^0$	Void time
$I(\theta)$	Intensity at scattering angle $\theta$	$t_r$	Retention time
$I_{0/s}$	Incident/solvent intensity	$\tau$	Correlation time
$IC_{50}$	50% inhibitory concentration	$\nu$	Mark-Houwink exponent
$K$	Contrast factor	$V$	Scattering volume
$K_r$	Constant Mark-Houwink factor	$V^0$	Void volume
$k_B$	Boltzmann's constant	$V_r$	Retention volume
$l$	Layer thickness of the sample cloud	$\dot{V}_c$	Cross-flow rate
$\lambda$	Retention parameter	$\dot{V}_{in}$	Inlet flow rate
$\lambda_0$	Laser wavelength in vacuum	$w$	Channel height
$M$	Molar Mass	$x$	Accumulation wall distance
$M_w$	Mass average molar mass	$z_{foc}$	Focus zone to inlet distance
$\bar{v}$	Partial specific volume	$\zeta$	Zeta potential



---

**Curriculum vitae**
**Michael Wagner****Education**

- |   |                          |
|---|--------------------------|
| <p><b>PhD student</b>, Friedrich Schiller University Jena<br/>         Laboratory of Organic and Macromolecular Chemistry (IOMC)<br/> <i>“Characterization of polymeric systems for nanomedical applications”</i><br/>         Supervisor: Prof. Dr. Ulrich S. Schubert</p> | <p>Since 11/2011</p>     |
| <p><b>Master Thesis</b>, Boehringer Ingelheim Pharma GmbH &amp; Co. KG<br/> <i>“Characterization of colloidal protein stability by dynamic and electrophoretic light scattering”</i><br/>         Supervisor: Prof. Dr. Alfred Blume,<br/>         Dr. Patrick Garidel</p>  | <p>02/2011 – 10/2011</p> |
| <p><b>Chemistry, M. Sc.</b>, Martin Luther University Halle-Wittenberg<br/>         Specialization: Physical Chemistry</p>  | <p>10/2009 – 10/2011</p> |
| <p><b>Chemistry, B. Sc.</b>, Martin Luther University Halle-Wittenberg<br/>         Bachelor Thesis: <i>“Investigations of monolayers of poly(ethylene glycol)-phospholipids”</i></p>   | <p>10/2006 – 09/2009</p> |
| <p><b>University entrance qualification:</b> Abitur (A-Level)<br/>         Kooperative Gesamtschule am Schwemmbach, Erfurt</p>  | <p>1997 – 2005</p>       |

Jena, 18.12.2014

---

 Michael Wagner



---

## Publication list

### *Peer-reviewed publications*

1. M. Wagner, M. J. Barthel, R. R. A. Freund, S. Höppener, A. Träger, F. H. Schacher, U. S. Schubert, Self-assembly of poly(ethylene oxide)-*block*-poly(furfuryl glycidyl ether)-*block*-poly(allyl glycidyl ether) based triblock terpolymers: A field-flow fractionation study, *Polym. Chem.* **2014**, DOI: 10.1039/c4py00863d.
2. A. T. Press, A. Träger, C. Pietsch, A. Mosig, M. Wagner, M. G. Clemens, N. Jbeily, N. Koch, M. Gottschaldt, N. Bézière, V. Ermolayev, V. Ntziachristos, J. Popp, M. Kessels, B. Qualmann, U. S. Schubert, M. Bauer, Cell type-specific delivery of short interfering RNAs by dye-functionalized “theranostic” nanoparticles, , *Nat. Commun.* **2014**, *accepted*.
3. M. Wagner, S. Holzschuh, A. Träger, A. Fahr, U. S. Schubert, Asymmetric flow field-flow fractionation in the field of nanomedicine, *Anal. Chem.* **2014**, *86*, 5201-5210.
4. M. J. Barthel, A. C. Rinkenauer, M. Wagner, U. Mansfeld, S. Höppener, J. A. Czaplewska, M. Gottschaldt, A. Träger, F. H. Schacher, U. S. Schubert, Small but powerful: Co-assembly of polyether-based triblock terpolymers into sub-30 nm micelles and synergistic effects on cellular interactions, *Biomacromolecules* **2014**, *15*, 2426-2439.
5. C. von der Ehe, C. Weber, M. Wagner, J. Czaplewska, M. Gottschaldt, U. S. Schubert, Synthesis of thermoresponsive glycopolymers combining RAFT polymerization and a thiol-ene reaction and subsequent immobilization onto solid supports, *Macromol. Chem. Phys.* **2014**, *215*, 1306-1318.
6. P. Garidel, A. Blume, M. Wagner, Prediction of colloidal stability of high concentration protein formulations, *Pharm. Dev. Technol.* **2014**, DOI: 10.3109/10837450.2013.871032.

7. M. Wagner, C. Pietsch, L. Tauhardt, A. Schallon, U. S. Schubert, Characterization of cationic polymers by asymmetric flow field-flow fractionation and multi angle light scattering – a comparison with traditional techniques, *J. Chromatogr. A* **2014**, *1325*, 195-203.
8. A. C. Rinkenauer, A. Schallon, U. Günther, M. Wagner, E. Betthausen, U. S. Schubert, F. H. Schacher, A paradigm change: Efficient transfection of human leukemia cells by stimuli-responsive multicompartment micelles, *ACS Nano* **2013**, *7*, 9621-9631.
9. K. Knop, D. Pretzel, A. Urbanek, T. Rudolph, D. H. Scharf, A. Schallon, M. Wagner, S. Schubert, M. Kiehntopf, A. A. Brakhage, F. H. Schacher, U. S. Schubert, Star-shaped drug carriers for doxorubicin with POEGMA and POEtOxMA brush-like shells: A structural, physical, and biological comparison, *Biomacromolecules* **2013**, *14*, 2536-2548.
10. M. Wagner, K. Reiche, A. Blume, P. Garidel, Viscosity measurements of antibody solutions by photon correlation spectroscopy: An indirect approach – limitations and applicability for high-concentration liquid protein solutions, *Pharm. Dev. Technol.* **2013**, *18*, 963-970.
11. C. Weber, M. Wagner, D. Baykal, S. Höppener, R. M. Paulus, G. Festag, E. Altuntas, F. H. Schacher, U. S. Schubert, Easy access to amphiphilic heterografted poly(2-oxazoline) comb copolymers, *Macromolecules* **2013**, *46*, 5107–5116.
12. M. Wagner, A. C. Rinkenauer, A. Schallon, U. S. Schubert, Opposites attract: Influence of the molar mass of branched poly(ethylene imine) on biophysical characteristics of siRNA-based polyplexes, *RSC Advances* **2013**, *3*, 12774-12785.
13. C. Pietsch, U. Mansfeld, C. Guerrero-Sanchez, S. Höppener, A. Vollrath, M. Wagner, R. Hoogenboom, S. Saubern, S. H. Thang, C. R. Becer, J. Chiefari, U. S. Schubert, Thermo-induced self-assembly of responsive poly(DMAEMA-*b*-DEGMA) block copolymers into multi- and unilamellar vesicles, *Macromolecules* **2012**, *45*, 9292-9302.



14. M. Wagner, K. Reiche, A. Blume, P. Garidel, The electrokinetic potential of therapeutic proteins and its modulation: Impact on protein stability, *Colloids Surf., A* **2012**, 415, 421-430.

*Submitted Publications*

M. Wagner, C. Pietsch, A. Kerth, A. Träger, U. S. Schubert, Physicochemical characterization of the thermo-induced self-assembly of thermo-responsive PDMAEMA-*b*-PDEGMA copolymers, *submitted*.

M. Hartlieb, D. Pretzel, M. Wagner, S. Höppener, P. Bellstedt, M. Görlach, C. Englert, K. Kempe, U. S. Schubert, Core cross-linked micelles and vesicles based on the self-assembly of double hydrophilic poly(2-oxazoline) block copolymers as potential drug carrier, *submitted*.

*Oral contributions*

M. Wagner, A. Träger, U. S. Schubert, High-throughput characterization of nanoparticles: "HT DLS", **DECHEMA Workshop: High-throughput and combinatorial experimentation in polymer science**, Jena, Germany, October **2013**.

M. Wagner, A. C. Rinkenauer, A. Schallon, U. S. Schubert, Size matters: Influence of the molar mass of branched poly(ethylene imine) on siRNA based polyplexes for efficient gene silencing, **20th International AUC Conference**, San Antonio, Texas, USA, March **2012**.

*Poster presentations*

M. Wagner, C. Pietsch, L. Tauhardt, A. Schallon, U. S. Schubert, Characterization of cationic polymers for gene delivery by AF4 and analytical ultracentrifugation, **SCM-6**, Dresden, Germany, February **2013**.

M. Wagner, A. C. Rinkenauer, A. Schallon, U. S. Schubert, Study of siRNA based polyplexes using branched poly(ethylene imine) in a wide range of molar masses, **NanoConSens Annual Meeting**, Jena, Germany, September **2012**.

M. Wagner, A. C. Rinkenauer, A. Schallon, U. S. Schubert, Structural characterization of polyplexes based on siRNA and branched poly(ethylene imine) for efficient siRNA delivery, **20th International AUC Conference**, San Antonio, Texas, USA, March **2012**.

## **Acknowledgement / Danksagung**

An dieser Stelle möchte ich mich bei allen bedanken, die mich bei der Anfertigung dieser Arbeit unterstützt haben. An erster Stelle richtet sich mein Dank an meinen wissenschaftlichen Betreuer Prof. Dr. Ulrich S. Schubert für die Möglichkeit in einer so breit aufgestellten Arbeitsgruppe auf einem wissenschaftlich hochinteressanten Thema zu promovieren. Meine besondere Wertschätzung gilt dabei dem mir überlassen Freiraum für eigene Ideen und das Vertrauen in deren zielgerichtete Umsetzung. Besonderer Dank gehört auch Jun.-Prof. Dr. Felix H. Schacher für die zahlreichen fachlichen Diskussionen sowie für seine konstruktive Kritik und viele wertvolle Anregungen.

Des Weiteren bedanke ich mich bei allen Mitarbeitern der Arbeitsgruppe und der Kooperationspartner, die zum Gelingen dieser Arbeit beigetragen haben, für die wunderbare Arbeitsatmosphäre sowie für die unschätzbare Hilfe bei allen Problemen des Laboralltags. Insbesondere Dr. Christian Pietsch, Dr. Markus Barthel, Dr. Christine Weber, Matthias Hartlieb und Lutz Tauhardt danke ich für die fortwährende Versorgung mit neuen Polymeren mit (immer wieder) herausfordernden Eigenschaften und unbekanntem Verhalten. Dr. Stephanie Höppener danke ich für die vielen TEM-Messungen und die Hilfe bei der Interpretation selbiger. Mein Dank gilt auch Carolin Fritzsche für sämtliche Zytotoxizitäts- und Hämolyse Experimente. Ebenfalls danken möchte ich Dr. Stephanie Schubert und Dr. Antje Vollrath für die gute Zusammenarbeit und die Unterstützung durch zahlreiche Diskussionen.

Ich möchte an dieser Stelle auch drei Personen hervorheben, die mich während der letzten drei Jahre fast täglich im Wissenschaftsdschungel begleitet haben: Dr. Anja Träger, Alexandra Rinkenauer und Sarah Crotty. Eure Ideen und Denkanstöße haben maßgeblich zu dieser Arbeit beigetragen. Unsere unzähligen Gespräche, Diskussionen und Freizeitabende bleiben unvergesslich. Ich freue mich mit euch gleich drei außergewöhnliche Freundschaften gewonnen zu haben.

Mein größter Dank gilt meiner gesamten Familie und Jessica für den Rückhalt und die Unterstützung in allen Lebenslagen.



## **Declaration of authorship / Selbständigkeitserklärung**

Ich erkläre, dass ich die vorliegende Arbeit selbständig und unter Verwendung der angegebenen Hilfsmittel, persönlichen Mitteilungen und Quellen angefertigt habe.

I certify that the work presented here is, to the best of my knowledge and belief, original and the result of my own investigations, except as acknowledged, and has not been submitted, either in part or whole, for a degree at this or any other university.

Jena, 18.12.2014

---

Michael Wagner



**Publications P1-P10**

- P1 Reprinted with permission from *Anal. Chem.* **2014**, *86*, 5201-5210. Copyright 2014 American Chemical Society.
- P2 *J. Chromatogr. A* **2014**, *1325*, 195-203. Reprinted with permission. Copyright 2013 Elsevier.
- P3 Manuscript submitted to *Macromolecules*.
- P4 Manuscript submitted to *Biomacromolecules*.
- P5 *RSC Advances* **2013**, *3*, 12774-12785. Reproduced by permission of The Royal Society of Chemistry.
- P6 Reprinted with permission from *ACS Nano* **2013**, *7*, 9621-9631. Copyright 2013 American Chemical Society.
- P7 Manuscript accepted for publication in *Nat. Commun.*
- P8 *Polym. Chem.* **2014**, DOI: 10.1039/c4py00863d. Reproduced by permission of The Royal Society of Chemistry.
- P9 Reprinted with permission from *Biomacromolecules* **2014**, *15*, 2426-2439. Copyright 2014 American Chemical Society.
- P10 Reprinted with permission from *Macromolecules* **2012**, *45*, 9292-9302. Copyright 2012 American Chemical Society.





## Publication P1

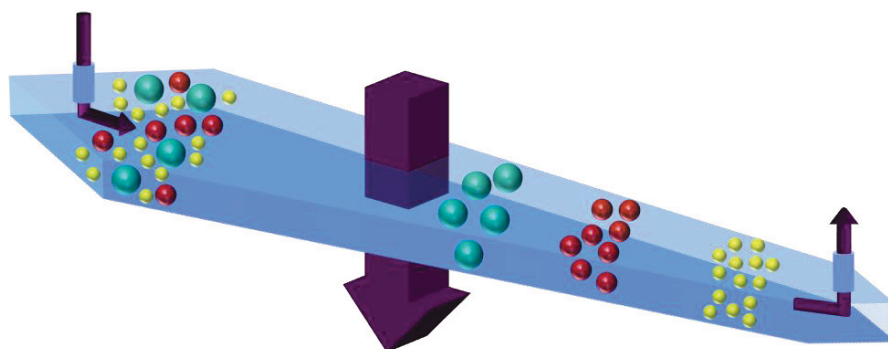
---

### Asymmetric flow field-flow fractionation in the field of nanomedicine

M. Wagner, S. Holzschuh, A. Träger, A. Fahr, U. S. Schubert

*Anal. Chem.* **2014**, *86*, 5201-5210.

---





# Asymmetric Flow Field-Flow Fractionation in the Field of Nanomedicine

Michael Wagner,<sup>†,‡</sup> Stephan Holzschuh,<sup>§</sup> Anja Traeger,<sup>†,‡</sup> Alfred Fahr,<sup>‡,§</sup> and Ulrich. S. Schubert<sup>\*,†,‡</sup>

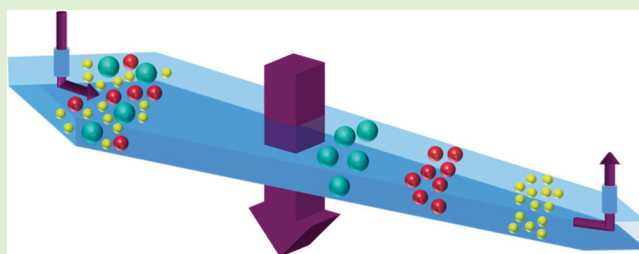
<sup>†</sup>Laboratory of Organic and Macromolecular Chemistry (IOMC), Friedrich Schiller University Jena, Humboldtstrasse 10, 07743 Jena, Germany

<sup>‡</sup>Jena Center for Soft Matter (JCSM), Friedrich Schiller University Jena, Philosophenweg 7, 07743 Jena, Germany

<sup>§</sup>Department of Pharmaceutical Technology, Friedrich Schiller University Jena, Lessingstrasse 8, 07743 Jena, Germany

## S Supporting Information

**ABSTRACT:** Asymmetric flow field-flow fractionation (AF4) is a widely used and versatile technique in the family of field-flow fractionations, indicated by a rapidly increasing number of publications. It represents a gentle separation and characterization method, where nonspecific interactions are reduced to a minimum, allows a broad separation range from several nano- up to micrometers and enables a superior characterization of homo- and heterogenic systems. In particular, coupling to multiangle light scattering provides detailed access to sample properties. Information about molar mass, polydispersity, size, shape/conformation, or density can be obtained nearly independent of the used material. In this Perspective, the application and progress of AF4 for (bio)macromolecules and colloids, relevant for “nano” medical and pharmaceutical issues, will be presented. The characterization of different nanosized drug or gene delivery systems, e.g., polymers, nanoparticles, micelles, dendrimers, liposomes, polyplexes, and virus-like-particles (VLP), as well as therapeutic relevant proteins, antibodies, and nanoparticles for diagnostic usage will be discussed. Thereby, the variety of obtained information, the advantages and pitfalls of this emerging technique will be highlighted. Additionally, the influence of different fractionation parameters in the separation process is discussed in detail. Moreover, a comprehensive overview is given, concerning the investigated samples, fractionation parameters as membrane types and buffers used as well as the chosen detectors and the corresponding references. The perspective ends up with an outlook to the future.



Nowadays, the understanding and development of nanomedicines like biopharmaceuticals or nanoparticles for drug and gene delivery requires the improvement of analytical characterization methods.<sup>1–3</sup> Moreover, the effects of drugs in the human body are complex, and it is essential to understand the fate of a drug as well as its mode of action. To investigate these effects, methods are required for separating and analyzing single components from complex biological samples. The increasing importance for separation techniques of suspended analytes (particular or macromolecular form) in all fields of life sciences was one of the key factors for the success of field-flow fractionation (FFF) in the last years. Invented by J. C. Giddings in 1966, field-flow fractionation comprises a class of fractionation techniques, based on a flat channel, where a separation field, perpendicular to the direction of the sample flow is applied.<sup>4</sup>

In asymmetric flow FFF (AF4), the separation is achieved by a liquid cross-flow which takes place in a narrow, ribbon-like channel of trapezoidal geometry, which is built up by a spacer, between a porous and a nonporous plate (Figure 1). The porous plate is covered by a membrane, which acts as accumulation wall and allows the eluent to pass the membrane, while the particles/macromolecules are retained. The first AF4

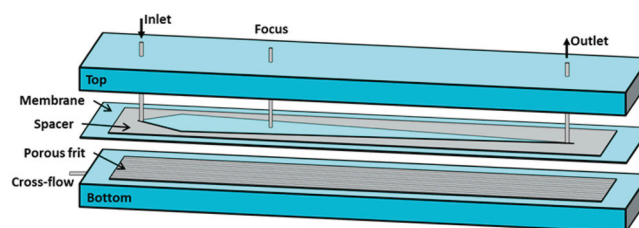


**Figure 1.** Schematic representation of an AF4 channel. The eluent is pumped from the inlet to the outlet. The membrane acts as accumulation wall and represents the porous wall. The geometry of the channel is defined by the spacer.

system was presented in 1987 by Giddings and Wahlund.<sup>5</sup> Since 20 years, it is the most used and versatile technique in the family of FFF and has nearly replaced the symmetric version, indicated by the rapidly increasing number of publications.<sup>5,6</sup>

During the transport of the analyte by the eluent, the application of the cross-flow results in a force, dragging the

Received: February 19, 2014

Accepted: May 6, 2014

Published: May 6, 2014

particles/macromolecules to the surface of the membrane (Figure 2). Because of the formed concentration gradient, the

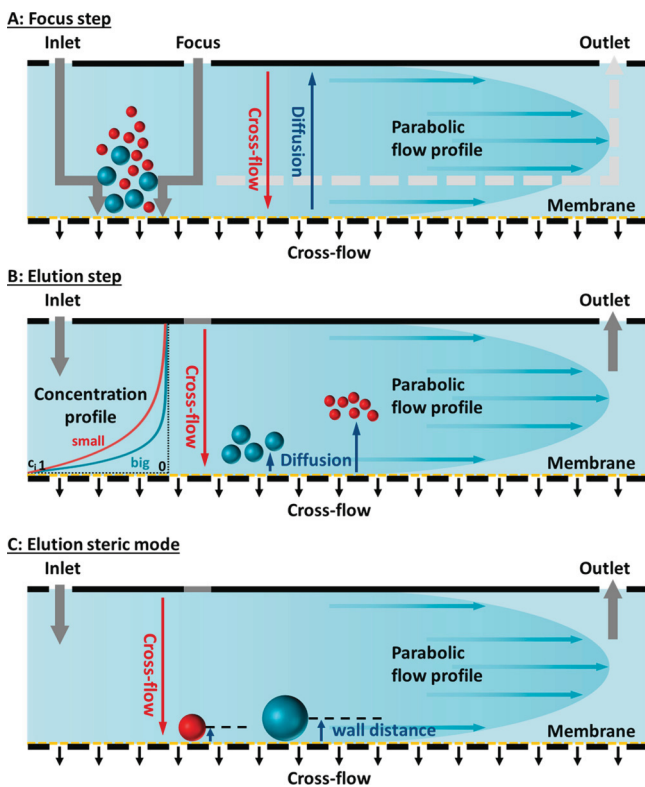


**Figure 2.** Schematic representation of the AF4 principle. The eluent is pumped from the inlet to the outlet, and the cross-flow is applied perpendicular to the flow direction. The different steps are (A) the focusing process (stopped flow) and (B) the elution process under normal mode; part C shows elution under steric conditions.

diffusivity acts as a counteracting force, until an exponential steady-state-distribution of the analyte with the highest concentration at the wall is reached (Fick's law).<sup>5</sup> According to the individual diffusion coefficient of each particle, the concentration profile is extended more or less into the channel and different streamlines of the parabolic velocity flow profile were occupied (Figure 2B, schematic concentration profiles, left). With decreasing size/increasing diffusion coefficient of the particles or macromolecules, the concentration profile is more extended into the channel resulting in a higher average (characteristic) distance from the wall (visualized by the particles in Figure 2B) and faster elution. It has to be kept in mind, that even for small particles, the highest concentration is reached near the wall and that Figure 2 is an exaggerated schematic visualization. Furthermore, in the beginning of a measurement, an additional focusing/relaxation procedure is normally applied to concentrate the analyte in a narrow zone and avoid spreading over the whole channel length during injection (Figure 2A). If the size of the analyte exceeds a certain limit (usually  $>1 \mu\text{m}$ ), the retention behavior changes from the normal, also termed Brownian mode, to the steric mode (steric FFF). In steric FFF, the sample is located in a thin layer very close to the wall and the order of retention changes in a way that larger particles/macromolecules elute first (Figure 2C). As most types of therapeutics as discussed in this Perspective are below this size limit, the reader is referred to literature for further details.<sup>7,8</sup> The theoretical basis of FFF was developed in

detail by Giddings, Wahlund, and co-workers.<sup>5,9–11</sup> For an extensive theoretical description and detailed insights, the reader is referred to cited literature or the comprehensive "Field-Flow Fractionation Handbook".<sup>12</sup>

As many modern medicines and diagnostics are based on colloidal/macromolecular matter like proteins/antibodies, viruses, liposomes, quantum dots (QD), nanoparticles, as well as other polymeric drug and gene delivery systems, AF4 enables a certain progress in the understanding of such systems. Nowadays, AF4 coupled to different detectors allows the acquisition of key parameters, e.g., molar mass, size, density, diffusivity, surface, aggregation, conformation, or shape.<sup>13</sup> In the past, a RI or UV detector was attached to FFF and the hydrodynamic radius as well as the molar mass was obtained by a calibration with standards or applying FFF theory. As nonideal effects, like membrane interactions or self-interaction of the sample, lead to deviations from the theoretical approach,<sup>14</sup> FFF was limited to a few applications. In 1984, M. Martin reported the first coupling of an online light scattering detector.<sup>15</sup> As it was now possible to obtain independent information about size and molar mass, greater attention was paid to these techniques.<sup>16</sup> Nowadays, a multiangle laser light scattering (MALLS) or dynamic light scattering (DLS) detector is commonly used for the analysis during the fractionation process.<sup>17,18</sup> In contrast to traditional batch DLS or SLS, the prior fractionation by AF4 allows the investigation of complex heterogeneous and polydisperse mixtures. As the intensity of scattered light scales with  $r^6$ , smaller analytes are mostly discriminated in batch light scattering, if larger populations as aggregates are present in solution. This often results in misleading distributions or averages and prohibits quantification of single populations. This can be circumvented by the prior fractionation by AF4. The biggest drawback of light scattering based detectors is their limited application for small particles/macromolecules. For MALLS, a radius of gyration of at least 10 nm is necessary due to the uniform scattering of small particles. In general, a MALLS detector ranges from around  $10^4$  to  $10^9 \text{ g mol}^{-1}$  or from around 10 to 1000 nm radius, depending on the refractive index increment ( $\partial n/\partial c$ ) and the number of angles where the intensity of the scattered light is measured. Because of the fact that the intensity of scattered light scales with  $r^6$ , high concentration of small particles/macromolecules have to be injected, which can lead to separation problems or particle–membrane interactions. If the characterization is not adequate by the detection techniques mentioned above, other methods can easily be coupled online or offline to AF4 as far as the sample concentration is sufficiently high. This includes inductively coupled plasma mass spectrometry (ICPMS),<sup>19,20</sup> laser-induced breakdown detection (LIBD),<sup>21</sup> viscosimetry, infrared detection,<sup>22</sup> nephelometric turbidity,<sup>23</sup> fluorescence spectroscopy, X-ray fluorescence analysis (XFA),<sup>24</sup> nuclear magnetic resonance spectroscopy (NMR), small-angle X-ray scattering (SAXS),<sup>25,26</sup> electron microscopy, light microscopy, as well as different variations of mass spectrometry.<sup>27</sup>

Beside the simple hyphenation to other methods, further advantages are the automation, the low measurement time, the easy collection of fractions, and primarily the absence of a package material or a stationary phase.<sup>28</sup> In classic chromatography techniques, such as, e.g., size exclusion chromatography (SEC), strong forces can act between the stationary phase and the sample, which can result in considerable (shear) degradation, irreversible adsorption, coelution, or denaturation

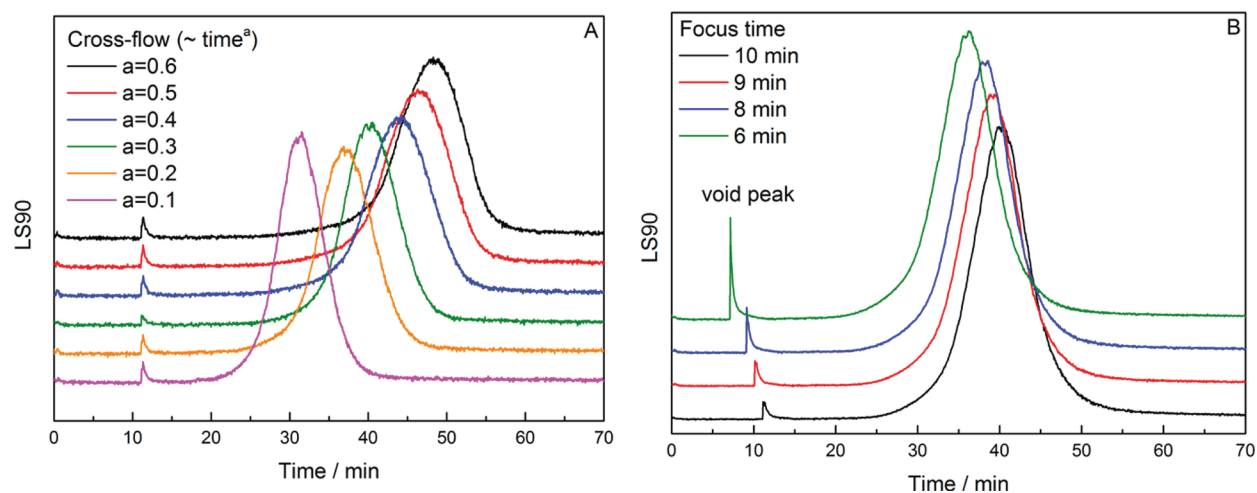


**Figure 3.** Influence of AF4 parameters on the retention of liposomes. Fractogram of mTHPC containing POPC liposomes at (A) different cross-flow rates (power function gradient with different exponents  $a$ ) and (B) different focusing time (the difference in elution time corresponds to the different focusing times). Detector flow 1.2 mL/min, focus flow 3 mL/min for all samples, 500  $\mu\text{m}$  spacer. The initial cross-flow was set to 2 mL/min and reduced with a power function gradient within 60 min to zero. Afterward cross-flow was kept constant at 0 mL/min to ensure complete elution ( $a = 0.3$  for part B). For varying cross-flow exponents, the focusing time was set to 10 min.

of the investigated analyte.<sup>29</sup> In contrast, in an empty channel the applied flow is less tortuous, resulting in lower shear forces and a very gentle separation method, applicable to very delicate samples of biological origin like proteins or nucleic acids.<sup>30</sup> In addition, the capability of AF4 enhances with increasing molar mass without the limitation of an exclusion limit as for SEC.<sup>31</sup> A wide range of solvents or buffers can be applied, fractionation can be performed at different temperatures, and even complex, broadly dispersed multicomponent samples can be analyzed without extensive sample preparation. The possibility to alter the flow rates quickly and precisely, and thereby to control the retention behavior, enables the individual tuning for optimal separation and resolution of each sample. Unfortunately, this exceptional flexibility of AF4 is also one of the most important drawbacks as eluent, flow conditions, and single parameters have to be optimized for each sample. Up until now, this lessens the advantage in time and prevents AF4 from being applied routinely as a standard method. As it can be very difficult to find a suitable set of parameters for fractionation, a list of pharmaceutical relevant samples analyzed in the literature is presented in Tables 1–4 (Supporting Information), listing the used membrane, eluent, and detection method (as described in the respective publication) with short comments and the corresponding references.

### ■ ON THE ROAD TO THE RIGHT CONDITIONS

One advantage of AF4 is the use of an empty channel without a stationary phase, which minimizes shear induced degradation and reduces interactions with the sample in contrast to SEC. Nevertheless, there are interactions, mainly with the membrane. As the sample is mostly located at the membrane surface during separation, adsorption can become a massive problem in AF4. Therefore, the choice of an appropriate membrane material and eluent is crucial and often time-consuming. Various membrane materials are available, e.g., regenerated cellulose (RC), cellulose triacetate (CTA), poly(ether sulfone) (PES), polypropylene (PP), polyamide (PA), polycarbonate (PC), or polyvinylidene difluoride (PVDF), differing in their thickness, surface, surface charge, smoothness, and mechanical as well as chemical stability. The eluent and the sample have to be

compatible with the membrane to reduce adsorption effects. If interactions with the membrane cannot be avoided or lead to massive adsorption and sample loss, the addition of a surfactant like Triton X-100, sodium dodecyl sulfate (SDS), cetyltrimethylammonium bromide (CTAB), or different polysorbates (Tween) could be beneficial.<sup>32</sup> This effect is mainly based on membrane conditioning by binding of the surfactant on the membrane surface. If irreversible adsorption of a sample occurs, instead of the use of surfactants, a presaturation of the membrane can be achieved by injection of a small amount of sample on a fresh membrane. This conditioning leads to the formation of a monolayer of adsorbed sample on the membrane and a higher mostly constant recovery for further experiments with the same sample.<sup>28,33</sup> Buffers to adjust the pH value or addition of salts to increase the ionic strength also influence the retention behavior and affect possible interactions, in particular when charged samples are investigated.<sup>34,35</sup> This is due to electrostatic interactions between the analyte itself and between the analyte and the membrane.<sup>36–38</sup> The chosen buffer and the resulting pH influence the net-charge of the sample material and the membrane by (de)protonation of basic or acidic groups. Hence, the attractive or repulsive electrostatic interactions are affected and elution times correlate well with the zeta potential of the sample.<sup>37,39</sup> If membrane and sample are oppositely charged, attractive electrostatic interactions will occur, leading to late elution, immense adsorption effects, or aggregation. For a similarly charged membrane strong electrostatic repulsion occurs, which results in the movement of the analyte in a larger characteristic distance to the accumulation wall. Thus, faster streamlines are occupied by the sample, leading to a fast elution. The same repulsive electrostatic forces are present between the charged particles/macromolecules itself, inducing a high exclusion volume and a stretching of similar charged chains. Both influences the retention time and increases the effect of band broadening. An increase of the ionic strength by adding salts shields electrostatic forces and can help to reduce these effects.<sup>40,41</sup> In contrast, if the ionic strength is high and electrostatic repulsion negligible, aggregation of the sample can occur due to dominating van-der-Waals forces. Furthermore, interactions between hydrophobic spots on the

membrane and hydrophobic domains of the sample (e.g., hydrophobic side chains or backbone) can occur. In particular, proteins are known to adsorb on surfaces when a pH near the isoelectric point (pI) of the protein is used, where no significant electrostatic force is present.<sup>42</sup> All these adsorption effects disturb accurate quantification of analytes and render AF4 a more qualitative technique. Furthermore, salts as well as neutral excipients can have specific effects on the interactions taking place in the channel, e.g., complexation of cations by poly(ethylene glycol) (PEG) samples.<sup>43,44</sup>

Besides, four flow rates have to be optimized for a standard AF4: the inlet flow rate, the focus flow rate, the cross-flow rate, and the detector/outlet flow rate. Most attention has to be paid on the choice of cross-flow and its scheduling, as it influences the distance between the sample and accumulation wall.<sup>36</sup> The general influence is represented in Figure 3A for *m*-tetrahydroxyphenylchlorin (mTHPC, temoporfin) containing 1-palmitoyl-2-oleoyl-*sn*-glycero-3-phosphocholine (POPC) liposomes, showing that an increase of the cross-flow increases the retention time and enhances the fractionation. Anyhow, very high cross-flow rates could induce a sample loss by adsorption during the fractionation process, leading to lower mass recoveries.<sup>45</sup> In addition, the dilution of the sample, taking place due to the better fractionation, might be a problem as it decreases the signal-to-noise ratio during detection. In contrast, a very low cross-flow rate will result in a larger void peak and inadequate fractionation. An increase of cross-flow also leads to a higher concentration of the sample within the focus zone. This will increase the sample–sample interactions, which can result in aggregation or, in the case of polymers, entanglements of chains.<sup>46</sup> Beside the cross-flow, the focus flow (more precisely the ratio of inlet and focus flow) is highly important, as it is responsible for the formation of the focus zone and the steady-state distribution of the particles/macromolecules within. With increasing focus flow/decreasing inlet flow, the focus zone is located closer to the sample inlet. For adequate focusing, a certain focusing time is necessary.<sup>5</sup> If the focusing time is too short, the sample is not relaxed and the steady-state distribution is not achieved. This can lead to peak broadening, inadequate fractionation, and an increase of the void peak. In contrast, a high focusing time increases the local concentration of the sample and its self-interactions as well as the interactions with the membrane. Additionally, for aggregation sensitive systems like antibodies or their conjugates, difficulties arise as they tend to show aggregation/self-association or deaggregation in dependence of the cross-flow and focus conditions.<sup>47</sup> In Figure 3B, the influence of the focusing time on the fractionation of mTHPC containing POPC liposomes is shown (compare ref 36 for DPPC/DPPG liposomes). It can be seen that with increasing focusing time, the void peak is reduced. Considering all nonideal aspects, the influence of the flow conditions has to be investigated and adapted individually for each sample to ensure a proper separation.<sup>45</sup>

## ■ NANOMEDICINES IN THE CHANNEL

**Synthetic Systems: Nanoparticles.** Different types of nanoparticles (NP) are under investigation for manifold pharmaceutical applications.<sup>1,3,48,49</sup> Novel polymeric nanoparticles or nanogels<sup>50</sup> were used for drug or gene delivery, i.e., incorporation of hydrophobic drugs. This encapsulation often improves the bioavailability, stability, and solubility of the drug. Furthermore, magnetic metal nanoparticles, quantum

dots, or the incorporation of dyes, contrast agents, or magnetic materials into polymer or silica particles provides access to nanosized diagnostic and imaging tools.<sup>51–53</sup> For application of nanoparticles in a biological environment, precise knowledge regarding particle size, size distribution (polydispersity), particle density, surface, and particle shape is important as these key factors influence, among other things, biodistribution and the accumulation in tissues or the cellular uptake.<sup>54,55</sup> Moreover, the particle size influences properties like the optical, electrical, or magnetic behavior of the nanoparticle itself (e.g., surface plasmon resonance).<sup>56</sup> AF4 offers the possibility to yield accurate size distributions at high resolution, without the problem of discriminating smaller particles as in batch DLS. If nanoparticles are present in a heterogeneous system containing, e.g., aggregates or other colloidal substances, AF4 enables the possibility to separate and characterize the individual components in a single experiment. In comparison with classical membrane separation techniques or preparative ultracentrifugation, this is advantageous in terms of time and resolution. As an illustrative example, Winter and co-workers investigated gelatin nanoparticles as a drug delivery agent loaded with an antibody fragment and a granulocyte colony stimulating factor (G-CSF) as model protein drugs.<sup>57</sup> The preliminary characterization of the gelatin raw material confirms the advantage of AF4 to be a gentle separation technique.<sup>58</sup> In contrast to SEC, where raw gelatin with a molar mass of around  $10^2 \text{ kg mol}^{-1}$  was partially degraded due to high shear forces or elute close to the exclusion limit, it could be well characterized in a nondestructive way by AF4. After intensive optimization of the fractionation parameters, the AF4 study of the gelatin NPs reveals accurate information on size (150–300 nm) and polydispersity, whereas batch DLS suggested just a monodisperse sample.<sup>57</sup> Furthermore, AF4 enables the accurate determination of the loading (encapsulation) efficiency of drug carriers. If the drug itself is a macromolecule, e.g., a protein, it can be separated from the nanoparticles. The area under the curve (AUC) of the detector signal (RI/UV) of the unloaded protein enables the calculation of its concentration. In this context, AF4 is also usable to examine storage and time stability of nanoparticles, as changes in concentration, drug release, and size due to degradation or aggregation will be visible in the fractogram. Prerequisites for this method are baseline separation from the void peak, quantitative elution of the sample, and the absence of any adsorption phenomena. A similar issue belongs to the determination of the degree of surface modification, e.g., by grafting of polymers on nanoparticles or colloids. For example, the degree of PEGylation of nanostructures can be easily determined by direct fractionation of the reaction mixture (e.g., separating the residual PEG from the PEGylated nanoparticles) and subsequent integration of the UV/RI signal.<sup>59</sup> In the case of low molar mass drugs/dyes, the efficiency of drug loading cannot be determined directly as the unbound drug will not be retained by the membrane and the UV/RI signal of the encapsulated drug cannot be used. This is due to the dependence of the extinction coefficient on the molecular environment, which is, for example, different for the aqueous environment outside and the hydrophobic surrounding inside the nanoparticles.<sup>60,61</sup> Up until now, two possibilities are known to address this problem. On the one hand, the maximal loading capacity can be accessed by AF4 analysis of a series of nanoparticles with varying amounts of a drug. Assuming that all drug is incorporated, the maximum number of drug molecules per nanoparticle can be calculated.<sup>61</sup> On the

other hand, an additional UV detector can be coupled to the waste-line of the cross-flow outlet to quantify the amount of residual unbound drug, permeating through the membrane during the focusing period.<sup>62</sup> Unfortunately, the establishment of such a method requires an intensive optimization procedure, to ensure that no free dye is adsorbed or retained on the membrane.<sup>63</sup> However, in our opinion AF4 represents a potential alternative to study also the encapsulation of low molar mass drugs into drug delivery systems.

**Polymeric Self-Assemblies and Macromolecules.** Similar to nanoparticles, defined polymer architectures or self-assembled structures of amphiphilic polymers can be used to encapsulate and deliver drugs or dyes. Manifold systems investigated by AF4 are known in literature, e.g., polymeric stars with varying number of arms and arm length,<sup>64</sup> dendrimers, micelles,<sup>65</sup> vesicles, or other morphologies formed by self-assembly of co- or terpolymers.<sup>66–68</sup> Temperature responsive polymers, showing a lower critical solution temperature (LCST), were also investigated for drug delivery applications.<sup>69</sup> An illustrative and comprehensive example was given recently by Lederer et al., who investigated maltose decorated lysine-dendronized maleimide copolymers of different generations.<sup>62</sup> The glycosylation by maltose increases the biocompatibility and allows active targeting of cells. A strong dependency of size and shape on pH, generation number, and concentration was found for the dendronized maleimide polymer due to the protonable amine groups. AF4 together with molecular dynamic simulations, AFM, and cryo-TEM could show that at low generation numbers coil-like structures were obtained, while worm-like structures were observed at higher generations. Information on the conformations/shape could either be obtained by AF4 and calculation of the shape ratio  $\rho$  (the ratio of the radius of gyration  $R_g$  and the hydrodynamic radius of the particle  $R_H$ ) or application of scaling laws (eq 1) to the MALLS/DLS data of the fractionation.<sup>70–72</sup> If the radius of gyration  $R_g$  (or  $R_H$ ) is plotted against the molar mass  $M$  in a double logarithmic plot, the slope of the curve,  $\nu$ , provides information about the conformation/shape of the macromolecule ( $K$  is a constant).

$$R_g = KM^\nu \quad (1)$$

An example is shown for generation zero of the maleimide copolymer in Figure 4. At pH 7 a slope of 0.67 is obtained, corresponding to a coil-like conformation, whereas a value of 0.25 at pH 11 correlates with dense and globular structures.<sup>70</sup> At pH 3.5, two conformations seem to be present, a low molar mass rod-like ( $\nu = 0.98$ ) fraction and a dense, still anisotropic, high molar mass fraction ( $\nu = 0.45$ ) (a sphere would have a value of 0.33). This shows impressively how AF4 enables a full characterization according to size, shape/conformation, and molar mass, also for dendrimers of high molar mass, where other methods like SEC or MS suffer from problems.

The delivery of genetic material, e.g., plasmid DNA (pDNA) or small interfering RNA (siRNA) represents a promising strategy for the treatment of genetic diseases by expression of transferred proteins or inhibition of protein synthesis.<sup>73,74</sup> Therefore, gene carriers, which are able to deliver nucleic acids into eukaryotic cells, are in the focus of scientists since decades.<sup>75,76</sup> Common nonviral systems for this approach are complexes based on cationic polymers (polyplexes) or lipids (lipoplexes).<sup>77–79</sup> As crucial characteristics as cytotoxicity, cellular uptake, or transfection efficiency strongly depend on physicochemical parameters like polymer molar mass and

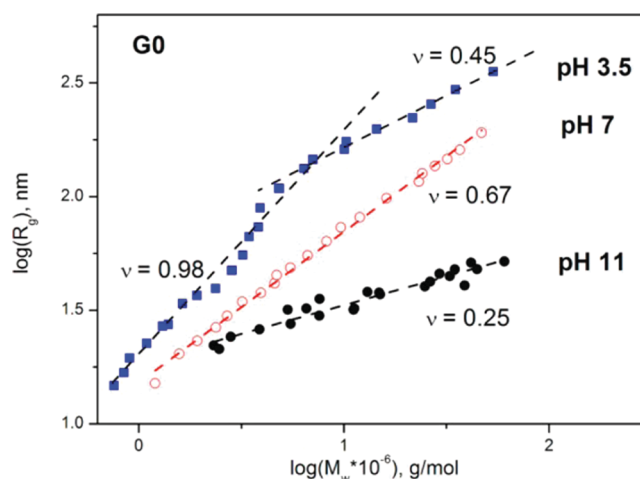


**Figure 4.** Scaling-law relationships obtained by AF4 of a maleimide copolymer at different pH. Reprinted from ref 70. Copyright 2012 American Chemical Society.

architecture, a detailed characterization of the used polyelectrolytes and the formed polyplexes is mandatory. In particular, the determination of the molar mass of cationic polymers is still challenging. For example, SEC is problematic due to strong interactions of the polyelectrolyte with the stationary phase and the lack of suitable standards.<sup>80</sup> Other methods like light scattering or nuclear magnetic resonance (NMR) spectroscopy just provide average values and no information about polydispersity. Here, AF4-MALLS can overcome some of these challenges enabling the determination of accurate size and molar mass distributions of the used polymers and formed polyplexes.<sup>81</sup> A detailed study on polyplexes prepared from pDNA and rhodamine B labeled chitosan was performed by Ma et al.<sup>82–84</sup> The most important challenge for successful AF4 separation and analysis of gene carriers is the establishment of an eluent composition and membrane material suitable for such heterogeneous mixtures, containing a cationic polymer, anionic DNA/RNA, and complexes of different net-charge (depending on the mixing ratio). Therefore, the membrane has to be compatible with different charges and varying degrees of hydrophobicity of all components to ensure proper retention and negligible sample adsorption. In the present case, this problem was solved by an amphiphilic RC membrane and an acetate buffer (pH 4). Fractograms of the polyplexes and pure chitosan are shown in Figure 5.<sup>83</sup> The first peak is associated with the free chitosan, while the second peak is related to the formed polyplexes. Here, AF4-MALLS-DLS has the outstanding advantage to characterize the polyplexes in terms of size and shape and to separate and quantify the free polymer in a single experiment. In contrast, traditional methods as ultracentrifugation are more time-consuming. Anyhow, results from both methods are in excellent agreement.<sup>83</sup> In particular for polyplexes, the accurate determination of the amount of free polymer is inevitable, as far as it influences the cytotoxicity and the transfection efficiency and reveals information about the composition and the virtual N/P ratio (nitrogen to phosphorus) realized within the polyplexes.<sup>85</sup>

In the work of Ma et al., all polyplexes prepared with a N/P ratio of 3–15 (at mixing) resulted in a virtual N/P ratio of 1.3–1.6. As mentioned above, information about shape of the polyplexes can be obtained by calculation of  $R_g/R_H$ . Dependent of the molar mass, structure, and concentration of the single

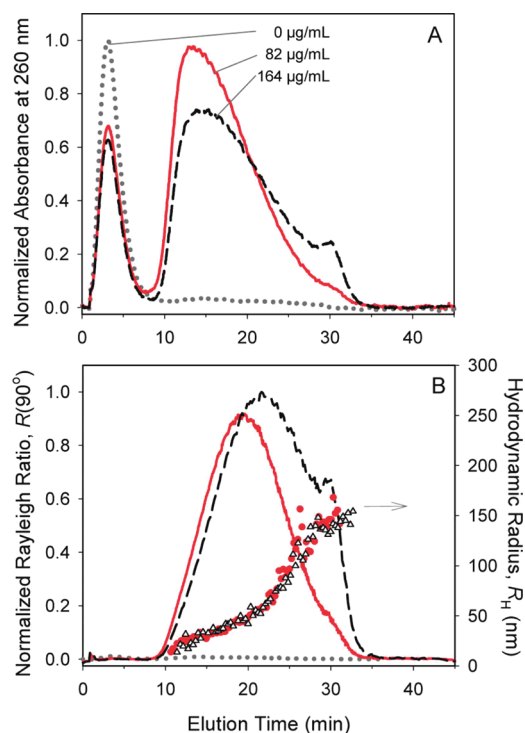


**Figure 5.** AF4 fractogram of chitosan/DNA polyplexes at different DNA concentrations (gray, 0  $\mu\text{g mL}^{-1}$ ; red, 82  $\mu\text{g mL}^{-1}$ ; black, 164  $\mu\text{g mL}^{-1}$ ; N/P, 5). (A) Absorbance at 260 nm, (B) Rayleigh ratio at  $90^\circ$  (lines) and hydrodynamic radius (symbols). Reprinted from ref 83. Copyright 2010 American Chemical Society.

components, values between 1.0 and 1.5 were obtained for the polyplexes, indicating a conformation ranging from a soft “Gaussian” sphere up to that of a polymeric star. In agreement with previous studies, the authors suggested that the polyplexes form spherical clusters with unbound chitosan loops or tails on the surface.<sup>83</sup> The merit of AF4-MALLS-DLS in this case is that information about shape/conformation can be assigned to each fraction of the whole sample in a fast and reliable manner, which allows the identification of differently shaped species in a solution or population. To prove AF4 results, a fraction collector can easily be coupled to the system and the fractions can be analyzed by other techniques, e.g., scanning electron microscopy (SEM) (Figure 6).<sup>84</sup>

**Liposomes.** Biological systems related to nanomedicine involve biotherapeutics, proteins, viruses, virus-like-particles

(VLP), and liposomes. Liposomes are phospholipid vesicles, which can contain hydrophilic substances encapsulated into the inner aqueous core and/or lipophilic drugs incorporated into the phospholipid bilayer, both, separate, or simultaneously.<sup>86</sup> The first liposomal and nanoscaled drug delivery system that received regulatory approval by the FDA in 1995 was Doxil containing the anthracycline antibiotic doxorubicin for the treatment of Kaposi’s sarcoma.<sup>87</sup> Today, various liposomal drug delivery systems are already FDA-approved for clinical use.<sup>88</sup> Size and size distribution are thereby the two key factors during the development of liposomal formulations. While smaller liposomes can decrease complement recognition and improve bioavailability, larger liposomes can increase the drug payload.<sup>89,90</sup> One possibility to access these drug distributions and drug recovery in liposomes is the use of radioactive double labeling and fractionation by AF4 combined with subsequent analysis via liquid scintillation counting (LSC).<sup>36</sup> In a study of Kuntsche et al., the recovery rate of the lipid component is usually over 90%, while the recovery rate of the incorporated drug is highly dependent on its octanol–water partition coefficient ( $\log P$ ). For the lipophilic photosensitizer mTHPC, a recovery rate of at least 82% was measured. However, the recovery rates for other drugs like testosterone (11%) and corticosterone (2%) were much lower, pointing out a possible drawback of AF4.<sup>36</sup> Traces of all drugs were detected in the membrane, and testosterone as well as corticosterone were found in the cross-flow outlet too. It can be supposed that there is some kind of “washing out phenomena” due to the high dilution and membrane interactions during AF4 analysis. For EPC (egg phosphatidylcholine) liposomes, Hupfeld et al. assumed that sample loss and delay in elution were caused by adsorption phenomena. Probably, there are “reactive spots” on the membrane with an increased interaction between liposomes and the membrane as visualized by membrane photographs after injection of rhodamine labeled phosphatidylethanolamine liposomes.<sup>91</sup> During a sequence of injections, adsorption becomes less prominent and the AUC is increasing until a constant elution behavior is obtained. Obviously, a certain amount of liposomes is necessary to saturate those spots whose quantity fluctuates between different membranes.<sup>91</sup> Interestingly, Kuntsche et al. could not observe this effect for DPPC/DPPG liposomes.<sup>36</sup> Moreover, by studying the drug to lipid ratio by AF4, it was recently shown that the incorporation of membrane additives into fluid state liposomes composed of POPC and POPG can lead to a change of bending stiffness of the lipid bilayer.<sup>92</sup> As smaller liposomes show in principal a

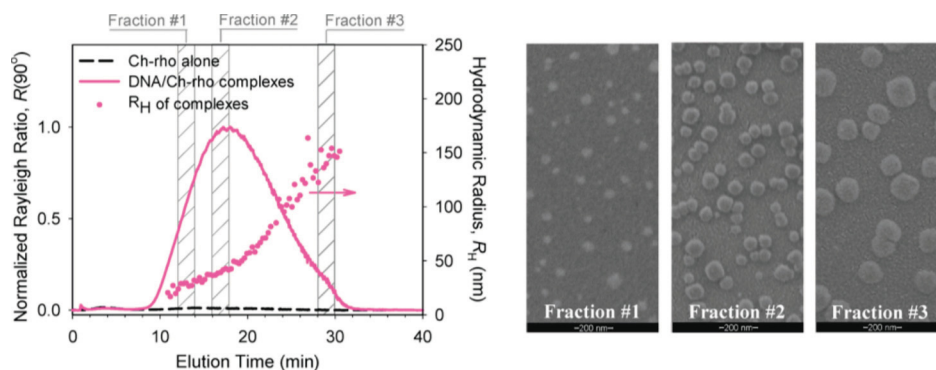


**Figure 6.** (Left) AF4 fractogram of chitosan/DNA polyplexes. (Right) ESEM images of collected fractions at indicated time intervals. It can be seen that AF4 and ESEM results are in excellent agreement. Reprinted from ref 84. Copyright 2010 American Chemical Society.



higher curvature than larger ones, this will result in a selective partitioning of bilayer additives with respect to the liposome's size. A comparison of AF4-MALLS with LSC of the individual fractions showed that cholesterol is enriched in larger (less strongly curved) liposomes as it rigidifies the host membrane. Contrary, mTHPC softens the membrane leading to an increased accumulation in smaller liposomes.<sup>92</sup>

**Proteins and Viruses.** Another application of AF4 is in protein separation, particularly for biotherapeutics. These formulations comprises a worldwide annual volume over \$110 billion, including blockbusters such as adalimumab (Humira, AbbVie, \$3.5 billion in 2011), infliximab (Remicade, Centocor, \$3.5 billion in 2011), and etanercept (Enbrel, Amgen, \$3.4 billion in 2011).<sup>93</sup> AF4 represents a well-suitable method for the challenging task of fast and reliable characterization for formulation development and to ensure drug safety of biotherapeutics.<sup>94–96</sup> After careful optimization of the eluent composition, AF4 enables an accurate quantification of monomer content and associates/aggregates in protein formulations as it allows a separation/characterization over the entire size range of a few nanometer to several micrometers.<sup>97</sup> For example, Veurink et al. investigated the aggregation breaking effect of different anti-inflammatory corticosteroids, (e.g., dexamethasone phosphate) on the angiogenesis inhibitors bevacizumab (Avastin, Roche) and ranibizumab (Lucentis, Novartis).<sup>95,96</sup> By using AF4, it was possible to show that the addition of corticosteroids reduces dimer and trimer content and, therefore, stabilize the antibody remarkably. Furthermore, AF4 can provide a closer look into the aggregation behavior concerning aggregates shape. Utilizing the shape ratio obtained by AF4-MALLS-DLS, the shape of different aggregates can be related to their biological effect. An impressive example was given by Silveira et al., who investigated the relationship between infectivity, converting activity, and the size and shape of protease resistant prion protein (PrP<sup>res</sup>)-containing aggregates.<sup>98</sup> It could be shown that highest specific infectivity and highest specific converting activity was attributed to nonfibrillar particles of about 17–27 nm, correlating to a molar mass of 300–600 kDa and a fairly compact, spherical or ellipsoid form ( $R_g/R_H = 0.9$ ). Larger aggregates (50–230 nm) showed substantially lower activities and  $R_g/R_H$  increases up to 2.35 indicating the formation of highly extended structures like fibrils, whereas smaller oligomers with  $\leq 5$  monomers revealed no visible infectivity and almost no converting activity.<sup>99</sup> These findings could provide new insights for the treatment of PrP related diseases. As AF4 works without a stationary phase, mechanical or shear stress on proteins (typical for SEC measurements) is minimal and the biological activity of such delicate samples can be preserved.<sup>100</sup> Moreover, an eluent similar to the native medium or formulation buffer can be used to preserve the native state of the protein, which is usually not possible using methods like density gradient ultracentrifugation, a standard technique for this purpose.<sup>101,102</sup> Besides, SEC often requires high ionic strengths in order to avoid interactions with the stationary phase, which influences the protein conformation, too.

AF4 is also capable to separate complex samples like human serum and its components.<sup>27,103,104</sup> In this field, also manifold progress concerning technical developments can be observed. For example, Yohannes et al. used a miniaturized AF4 with a total volume of 0.25 mL to study lipoprotein aggregation and fusion and they were able to separate the different lipoprotein classes, including the HDL-subclasses HDL<sub>2</sub> as well as

HDL<sub>3</sub>.<sup>105</sup> For lipoprotein particle detection in serum samples of patients with coronary artery disease (CAD), Lee et al. established a guard channel washing process, which enabled the depletion of smaller proteins leading to a reduced membrane contamination.<sup>106</sup> An online coupling of AF4 and a dual enzymatic reaction system to detect cholesterol and triglyceride was presented by Qureshi et al. and Rambaldi et al.<sup>103,107</sup> After a miniaturized AF4 serum separation, the channel-flow was split into two lines and enzymatic reagents to determine cholesterol and triglyceride levels were pumped into the respective line, which acted as an enzymatic reactor. Validation of the system revealed results comparable with standard enzymatic reactions and the literature.<sup>108</sup> Furthermore, the coupling of chip-type AF4 and electrospray ionization tandem mass spectrometry (ESI-MS-MS), recently shown by Kim et al., provides additional information and enables a high-speed screening of specific lipids contained in blood serum and lipoproteins (top-down lipidomic analysis).<sup>27,109</sup> Finally, a two-dimensional separation method using an online multilane channel system for isoelectric focusing (IEF) and AF4 was developed by Kim et al. in order to analyze human urinary proteomes.<sup>110,111</sup> The experimental setup is shown in Figure 7. First, proteins were

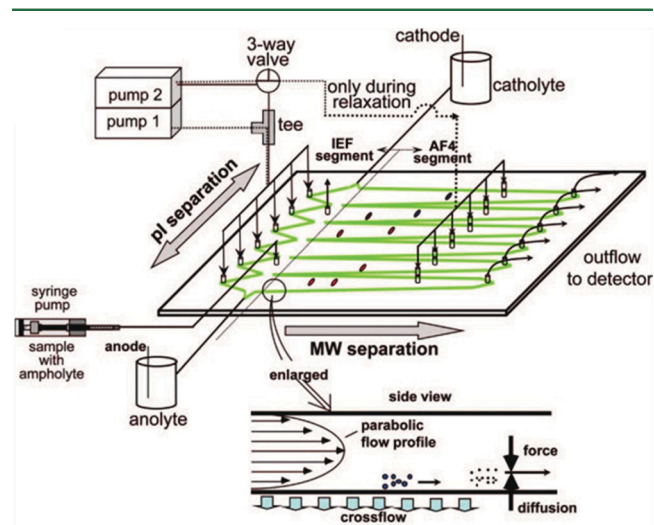


**Figure 7.** Schematics of a multilane AF4 channel for IEF-AF4. First the proteins are separated by IEF. Afterward, protein bands are transferred to each of the six channel lanes for separation by AF4. Reprinted from ref 111. Copyright 2009 American Chemical Society.

separated according to their isoelectric point by mixing the sample with ampholyte solution and injection into the IEF segment. When IEF separation was completed, the bands were transferred to the AF4 channels through six outlets. After validation of the system by separating a mixture of various protein standards with known size and *pI*, human urinary proteomes were separated, fractions were collected and further analyzed by ESI-MS/MS after tryptic digestion. The authors could identify 245 urinary proteins, thereof 110 unknown.<sup>110</sup> Last but not least, McEvoy et al. developed a method for virus counting utilizing AF4.<sup>112</sup> A sample of known concentration of influenza virus was separated and the particle sizes as well as the aggregation states were determined. It was demonstrated that a method to count spherical particles can be applied to quantify the total amount of disaggregated virus species. Calculations revealed a total number of  $2.79 \times 10^{10}$  virus particles per

experiment, which corresponds to a deviation of only 1.9% compared with the theoretical value of  $2.9 \times 10^{10}$ .

## CONCLUSION AND OUTLOOK

As presented, AF4 is still further emerging and shows great potential for pharmaceutical laboratories as it represents a highly flexible and powerful analytical technique applicable to nearly all fields in life sciences, in particular nanomedicine. For drug and gene delivery, the power of AF4 is the gentle separation of polymeric nanoparticles or self-assembled systems from residual polymer, aggregates or drug/dye without disturbing the self-assembled structure and simultaneously characterization. Several advantages and applications were discussed. The missing of a stationary phase reduces interactions and adsorption effects and enables analysis of highly sensitive samples like biotherapeutics or polyplexes under biological relevant conditions. Moreover, the separation channel is simple in physical terms and experimental parameters can be adjusted easily. Furthermore, the possibility to use nearly any aqueous or organic solvent, a broad separation range from 1 nm to 100  $\mu\text{m}$ , and the easy coupling to analytical techniques like MALLS or ICPMS renders AF4 a powerful method for separation and characterization of fragile and complex mixtures.<sup>2,113</sup> Comparison with batch techniques like DLS, SLS, and others shows that an analysis including a fractionation in the starting phase of a project provides a better understanding of the investigated system, avoiding misinterpretation due to average values or the presence of aggregates. Nevertheless, some drawbacks and challenges do exist. Up until now, AF4 is more laborious, expensive to use, and not routinely available in analytical laboratories. Additionally, almost every study needs also alternative particle characterization techniques (e.g., electron microscopy) in parallel to obtain full insight into the investigated system. Besides, even if the general range of AF4 scales from 1 nm to several  $\mu\text{m}$ , the separation of particles in one sample with larger differences in size will lead to peak broadening and a loss of resolution and might be impossible (more than a factor of 50 in size) in a single experiment. The optimization procedure of all parameters, necessary for each sample, limits the advantage of a short measurement time and is in conflict with the establishment of AF4 as a routinely applied standard method like SEC. An awareness of possible sample loss due to adsorption on the membrane is highly recommended. Furthermore, the interaction with the membrane often affects the retention behavior, which might lead to peak broadening or tailing, perturbation of the separation of compounds, or complete retaining of single particles/macromolecules. Particle–membrane interactions are also a major problem for accurate quantification of single fractions. In particular, for mixtures of compounds, where charge and hydrophobicity differ, extensive screening of different membranes and eluent compositions is often required. This presents a grand challenge for manufacturers as there is a need for improved membranes, especially designed for FFF applications, providing a flat and smooth surface with uniform pore sizes and surface charge. Further developments will also include new channel designs like hollow-fiber flow field-flow fractionation (HFF) or miniaturization of AF4 channels for saving solvent, time, and sample material.<sup>114,115</sup> Moreover, modifications like “frit-inlet”,<sup>116</sup> where a part of the top wall is substituted by a permeable frit thereby avoiding a focus procedure or “frit-outlet”,<sup>117</sup> where a frit at the end of the channel removes the upper part of the outlet stream, leading to higher detector

concentration (enrichment factors of around 3–6) become more and more established in the last years. From our point of view, there is also a trend in studying highly heterogeneous systems, e.g., nanoparticles, polyplexes, or liposomes and their interaction with human blood serum or cell culture media relevant for biotechnology related issues. This can reveal information about the formation of protein corona, a topic which is paid increasing attention and AF4 can help to understand how drug/gene delivery systems behave in a natural environment like the human body. However, the interest in AF4 is still growing and AF4 will help to understand and analyze systems, where other methods are inadequate. Once the method is established, AF4 is a multifunctional technique for separation and characterization of nearly all nanosized soft and hard matter in a short time. In particular, in the field of nanomedicine, AF4 helps to analyze small changes in size distribution or drug loading efficiency, which are important aspects of quality control and essential for regulatory affairs and medical approval.

## ASSOCIATED CONTENT

### Supporting Information

Four tables of pharmaceutical relevant systems analyzed by AF4. This material is available free of charge via the Internet at <http://pubs.acs.org>.

## AUTHOR INFORMATION

### Corresponding Author

\*E-mail: [ulrich.schubert@uni-jena.de](mailto:ulrich.schubert@uni-jena.de).

### Notes

The authors declare no competing financial interest.

## ACKNOWLEDGMENTS

This work was supported by the Carl-Zeiss Foundation (Strukturantrag JCSM).

## REFERENCES

- (1) Qureshi, R. N.; Kok, W. T. *Anal. Bioanal. Chem.* **2011**, *399*, 1401–1411.
- (2) Levin, S. *Biomed. Chromatogr.* **1991**, *5*, 133–137.
- (3) Fraunhofer, W.; Winter, G. *Eur. J. Pharm. Biopharm.* **2004**, *58*, 369–383.
- (4) Grushka, E.; Caldwell, K. D.; Myers, M. N.; Giddings, J. C. *Sep. Purif. Methods* **1973**, *2*, 127–151.
- (5) Wahlund, K. G.; Giddings, J. C. *Anal. Chem.* **1987**, *59*, 1332–1339.
- (6) Myers, M. N. *J. Microcolumn Sep.* **1997**, *9*, 151–162.
- (7) Giddings, J. C.; Myers, M. N.; Caldwell, K. D.; Pav, J. W. *J. Chromatogr.* **1979**, *185*, 261–271.
- (8) Wahlund, K. G.; Zattoni, A. *Anal. Chem.* **2002**, *74*, S621–S628.
- (9) Giddings, J. C. *J. Chem. Phys.* **1968**, *49*, 81–85.
- (10) Giddings, J. C.; Yang, F. J.; Myers, M. N. *Anal. Chem.* **1976**, *48*, 1126–1132.
- (11) Giddings, J. C. *Pure Appl. Chem.* **1979**, *51*, 1459–1471.
- (12) Schimpf, M. E.; Caldwell, K. D.; Giddings, J. C. *Field-Flow Fractionation Handbook*; Wiley: New York, 2000.
- (13) Giddings, J. C. *Science* **1993**, *260*, 1456–1465.
- (14) Qing, D.; Schimpf, M. E. *Anal. Chem.* **2002**, *74*, 2478–2485.
- (15) Martin, M. *Chromatographia* **1982**, *15*, 426–432.
- (16) Roessner, D.; Kulicke, W. M. *J. Chromatogr., A* **1994**, *687*, 249–258.
- (17) Jiang, Y.; Miller, M. E.; Li, P.; Hansen, M. E. *Am. Lab.* **2000**, *32*, 98–99.
- (18) Krahn, W.; Luckas, M.; Lucas, K. *Part. Part. Syst. Char.* **1988**, *5*, 72–76.

- (19) Beckett, R. *At. Spectrosc.* **1991**, *12*, 228–232.
- (20) Dubascoux, S.; Le Hecho, I.; Hasseloev, M.; Von der Kammer, F.; Gautier, M. P.; Lespes, G. *J. Anal. At. Spectrom.* **2010**, *25*, 613–623.
- (21) Thang, N. M.; Knopp, R.; Geckeis, H.; Kim, J. I.; Beck, H. P. *Anal. Chem.* **2000**, *72*, 1–5.
- (22) Mes, E. P. C.; de Jonge, H.; Klein, T.; Welz, R. R.; Gillespie, D. *J. Chromatogr., A* **2007**, *1154*, 319–330.
- (23) von der Kammer, F.; Baborowski, M.; Friese, K. *J. Chromatogr., A* **2005**, *1100*, 81–89.
- (24) Exner, A.; Theisen, M.; Panne, U.; Niessner, R. *Fresenius J. Anal. Chem.* **2000**, *366*, 254–259.
- (25) Thünemann, A. F.; Knappe, P.; Bienert, R.; Weidner, S. *Anal. Methods* **2009**, *1*, 177–182.
- (26) Knappe, P.; Boehmert, L.; Bienert, R.; Karmutzki, S.; Niemann, B.; Lampen, A.; Thünemann, A. F. *J. Chromatogr., A* **2011**, *1218*, 4160–4166.
- (27) Kim, K. H.; Lee, J. Y.; Lim, S.; Moon, M. H. *J. Chromatogr., A* **2013**, *1280*, 92–97.
- (28) Yohannes, G.; Jussila, M.; Hartonen, K.; Riekkola, M.-L. *J. Chromatogr., A* **2011**, *1218*, 4104–4116.
- (29) Otte, T.; Pasch, H.; Macko, T.; Brull, R.; Stadler, F. J.; Kaschta, J.; Becker, F.; Buback, M. *J. Chromatogr., A* **2011**, *1218*, 4257–4267.
- (30) Williams, S. K. R.; Lee, D. *J. Sep. Sci.* **2006**, *29*, 1720–1732.
- (31) Giddings, J. C. *J. Chromatogr.* **1989**, *470*, 327–335.
- (32) Stevenson, S. G.; Preston, K. R. *J. Liq. Chromatogr. Relat. Technol.* **1997**, *20*, 2835–2842.
- (33) Benincasa, M. A.; Giddings, J. C. *Anal. Chem.* **1992**, *64*, 790–798.
- (34) Benincasa, M. A.; Delle Fratte, C. *J. Chromatogr., A* **2004**, *1046*, 175–184.
- (35) Ulrich, A.; Losert, S.; Bendixen, N.; Al-Kattan, A.; Hagendorfer, H.; Nowack, B.; Adhart, C.; Ebert, J.; Lattuada, M.; Hungerbühler, K. *J. Anal. At. Spectrom.* **2012**, *27*, 1120–1130.
- (36) Kuntsche, J.; Decker, C.; Fahr, A. *J. Sep. Sci.* **2012**, *35*, 1993–2001.
- (37) Hupfeld, S.; Ausbacher, D.; Brandl, M. *J. Sep. Sci.* **2009**, *32*, 1465–1470.
- (38) Hupfeld, S.; Moen, H. H.; Ausbacher, D.; Haas, H.; Brandl, M. *Chem. Phys. Lipids* **2010**, *163*, 141–147.
- (39) Alpermann, T.; Rüdell, K.; Rütger, R.; Steiniger, F.; Nietzsche, S.; Filiz, V.; Förster, S.; Fahr, A.; Weigand, W. *Orig. Life Evol. Biosph.* **2011**, *41*, 103–119.
- (40) Moon, M. H.; Park, I.; Kim, Y. H. *J. Chromatogr., A* **1998**, *813*, 91–100.
- (41) Alasonati, E.; Benincasa, M. A.; Slaveykova, V. I. *J. Sep. Sci.* **2007**, *30*, 2332–2340.
- (42) Wagner, M.; Reiche, K.; Blume, A.; Garidel, P. *Colloids Surf., A* **2012**, *415*, 421–430.
- (43) Lang, T.; Eslahian, K. A.; Maskos, M. *Macromol. Chem. Phys.* **2012**, *213*, 2353–2361.
- (44) Benincasa, M. A.; Caldwell, K. D. *J. Chromatogr., A* **2001**, *925*, 159–169.
- (45) Wittgren, B.; Wahlund, K. G. *J. Chromatogr., A* **1997**, *791*, 135–149.
- (46) Adolphi, U.; Kulicke, W. M. *Polymer* **1997**, *38*, 1513–1519.
- (47) Demeule, B.; Palais, C.; Machaidze, G.; Gurny, R.; Arvinte, T. *mAbs* **2009**, *1*, 142–150.
- (48) Katz, E.; Willner, I. *Angew. Chem., Int. Ed.* **2004**, *43*, 6042–6108.
- (49) Fedotov, P. S.; Vanifatova, N. G.; Shkinev, V. M.; Spivakov, B. Y. *Anal. Bioanal. Chem.* **2011**, *400*, 1787–1804.
- (50) Shimoda, A.; Sawada, S.; Kano, A.; Maruyama, A.; Moquin, A.; Winnik, F. M.; Akiyoshi, K. *Colloids Surf., B* **2012**, *99*, 38–44.
- (51) Belete, A.; Mäder, K. *Drug Dev. Ind. Pharm.* **2013**, *39*, 186–196.
- (52) Melucci, M.; Zambianchi, M.; Barbarella, G.; Manet, I.; Montalti, M.; Bonacchi, S.; Rampazzo, E.; Rambaldi, D. C.; Zattoni, A.; Reschiglian, P. *J. Mater. Chem.* **2010**, *20*, 9903–9909.
- (53) Vollrath, A.; Schubert, S.; Schubert, U. S. *J. Mater. Chem. B* **2013**, *1*, 1994–2007.
- (54) Al-Hajaj, N. A.; Moquin, A.; Neibert, K. D.; Soliman, G. M.; Winnik, F. M.; Maysinger, D. *ACS Nano* **2011**, *5*, 4909–4918.
- (55) Cabral, H.; Matsumoto, Y.; Mizuno, K.; Chen, Q.; Murakami, M.; Kimura, M.; Terada, Y.; Kano, M. R.; Miyazono, K.; Uesaka, M.; Nishiyama, N.; Kataoka, K. *Nat. Nanotechnol.* **2011**, *6*, 815–823.
- (56) Reschiglian, P.; Rambaldi, D. C.; Zattoni, A. *Anal. Bioanal. Chem.* **2011**, *399*, 197–203.
- (57) Fraunhofer, W.; Winter, G.; Coester, C. *Anal. Chem.* **2004**, *76*, 1909–1920.
- (58) Schultes, S.; Mathis, K.; Zillies, J.; Zwiorek, K.; Coester, C.; Winter, G. *LC GC Eur.* **2009**, *22*, 390–403.
- (59) Zillies, J. C.; Zwiorek, K.; Winter, G.; Coester, C. *Anal. Chem.* **2007**, *79*, 4574–4580.
- (60) Knop, K.; Mingotaud, A.-F.; El-Akra, N.; Violleau, F.; Souchard, J.-P. *Photochem. Photobiol. Sci.* **2009**, *8*, 396–404.
- (61) Ehrhart, J.; Mingotaud, A.-F.; Violleau, F. *J. Chromatogr., A* **2011**, *1218*, 4249–4256.
- (62) Lederer, A.; Boye, S. *LC GC Eur.* **2011**, *24*, 620–628.
- (63) Boye, S.; Polikarpov, N.; Appelhans, D.; Lederer, A. *J. Chromatogr., A* **2010**, *1217*, 4841–4849.
- (64) Schacher, F. H.; Elbert, J.; Patra, S. K.; Yusoff, S. F. M.; Winnik, M. A.; Manners, I. *Chem.—Eur. J.* **2012**, *18*, 517–525.
- (65) Loos, K.; Boker, A.; Zettl, H.; Zhang, A. F.; Krausch, G.; Müller, A. H. E. *Macromolecules* **2005**, *38*, 873–879.
- (66) Wittgren, B.; Wahlund, K. G.; Derand, H.; Wesslen, B. *Macromolecules* **1996**, *29*, 268–276.
- (67) Petrov, P. D.; Drechsler, M.; Müller, A. H. E. *J. Phys. Chem. B* **2009**, *113*, 4218–4225.
- (68) Knop, K.; Pretzel, D.; Urbanek, A.; Rudolph, T.; Scharf, D. H.; Schallon, A.; Wagner, M.; Schubert, S.; Kiehntopf, M.; Brakhage, A. A.; Schacher, F. H.; Schubert, U. S. *Biomacromolecules* **2013**, *14*, 2536–2548.
- (69) Yohannes, G.; Shan, J.; Jussila, M.; Nuopponen, M.; Tenhu, H.; Riekkola, M.-L. *J. Sep. Sci.* **2005**, *28*, 435–442.
- (70) Boye, S.; Appelhans, D.; Boyko, V.; Zschoche, S.; Komber, H.; Friedel, P.; Formanek, P.; Janke, A.; Voit, B. I.; Lederer, A. *Biomacromolecules* **2012**, *13*, 4222–4235.
- (71) Burchard, W. *Adv. Polym. Sci.* **1999**, *143*, 113–194.
- (72) Nilsson, L. *Food Hydrocolloids* **2013**, *30*, 1–11.
- (73) Fire, A.; Xu, S. Q.; Montgomery, M. K.; Kostas, S. A.; Driver, S. E.; Mello, C. C. *Nature* **1998**, *391*, 806–811.
- (74) Lee, J. B.; Hong, J.; Bonner, D. K.; Poon, Z.; Hammond, P. T. *Nat. Mater.* **2012**, *11*, 316–322.
- (75) Behr, J. P. *Acc. Chem. Res.* **2012**, *45*, 980–984.
- (76) Boussif, O.; Lezoualch, F.; Zanta, M. A.; Mergny, M. D.; Scherman, D.; Demeneix, B.; Behr, J. P. *Proc. Natl. Acad. Sci. U.S.A.* **1995**, *92*, 7297–7301.
- (77) Wagner, M.; Rinkenauer, A. C.; Schallon, A.; Schubert, U. S. *RSC Adv.* **2013**, *3*, 12774–12785.
- (78) Synatschke, C. V.; Schallon, A.; Jerome, V.; Freitag, R.; Müller, A. H. E. *Biomacromolecules* **2011**, *12*, 4247–4255.
- (79) Lee, H.; Williams, S. K.; Allison, S. D.; Anchordoquy, T. J. *Anal. Chem.* **2001**, *73*, 837–43.
- (80) Guillauneuf, Y.; Castignolles, P. *J. Polym. Sci., Part A: Polym. Chem.* **2008**, *46*, 897–911.
- (81) Wagner, M.; Pietsch, C.; Tauhardt, L.; Schallon, A.; Schubert, U. S. *J. Chromatogr., A* **2013**, *1325*, 195–203.
- (82) Ma, P. L.; Buschmann, M.; Winnik, F. M. In *Abstracts of Papers: 240th Annual American Chemical Society Meeting*, Boston, MA, August 22–26, 2010; Publication No. 477.
- (83) Ma, P. L.; Buschmann, M. D.; Winnik, F. M. *Anal. Chem.* **2010**, *82*, 9636–9643.
- (84) Ma, P. L.; Buschmann, M. D.; Winnik, F. M. *Biomacromolecules* **2010**, *11*, 549–554.
- (85) Akinc, A.; Thomas, M.; Klivanov, A. M.; Langer, R. J. *Gene Med.* **2005**, *7*, 657–663.
- (86) Buse, J.; El-Aneed, A. *Nanomedicine* **2010**, *5*, 1237–1260.
- (87) Barenholz, Y. *J. Controlled Release* **2012**, *160*, 117–34.
- (88) Chang, H. I.; Yeh, M. K. *Int. J. Nanomed.* **2012**, *7*, 49–60.

- (89) Hupfeld, S.; Holsaeter, A. M.; Skar, M.; Frantzen, C. B.; Brandl, M. *J. Nanosci. Nanotechnol.* **2006**, *6*, 3025–3031.
- (90) Yohannes, G.; Pystynen, K. H.; Riekkola, M.-L.; Wiedmer, S. K. *Anal. Chim. Acta* **2006**, *560*, 50–56.
- (91) Hupfeld, S.; Ausbacher, D.; Brandl, M. *J. Sep. Sci.* **2009**, *32*, 3555–3561.
- (92) Decker, C.; Fahr, A.; Kuntsche, J.; May, S. *Chem. Phys. Lipids* **2012**, *165*, 520–529.
- (93) Bartholow, M. *Pharm. Times* July, 10, **2012**.
- (94) Smith, M. H.; South, A. B.; Gaulding, J. C.; Lyon, L. A. *Anal. Chem.* **2010**, *82*, 523–530.
- (95) Veurink, M.; Stella, C.; Tabatabay, C.; Pournaras, C. J.; Gurny, R. *Eur. J. Pharm. Biopharm.* **2011**, *78*, 271–277.
- (96) Veurink, M.; Westermaier, Y.; Gurny, R.; Scapozza, L. *Pharm. Res.* **2013**, *30*, 1176–1187.
- (97) Weber, C.; Wagner, M.; Baykal, D.; Höppener, S.; Paulus, R. M.; Festag, G.; Altuntas, E.; Schacher, F. H.; Schubert, U. S. *Macromolecules* **2013**, *46*, 5107–5116.
- (98) Silveira, J. R.; Raymond, G. J.; Hughson, A. G.; Race, R. E.; Sim, V. L.; Hayes, S. F.; Caughey, B. *Nature* **2005**, *437*, 257–261.
- (99) Silveira, J. R.; Hughson, A. G.; Caughey, B. *Method Enzymol* **2006**, *412*, 21–33.
- (100) Rambaldi, D. C.; Zattoni, A.; Reschiglian, P.; Colombo, R.; De Lorenzi, E. *Anal. Bioanal. Chem.* **2009**, *394*, 2145–2149.
- (101) Rambaldi, D. C.; Reschiglian, P.; Zattoni, A. *Anal. Bioanal. Chem.* **2011**, *399*, 1439–1447.
- (102) Witos, J.; Cilpa, G.; Yohannes, G.; Oorni, K.; Kovanen, P. T.; Jauhiainen, M.; Riekkola, M.-L. *J. Sep. Sci.* **2010**, *33*, 2528–2535.
- (103) Qureshi, R. N.; Kok, W. T.; Schoenmakers, P. J. *Anal. Chim. Acta* **2009**, *654*, 85–91.
- (104) Qureshi, R. N.; Kaal, E.; Janssen, H.-G.; Schoenmakers, P. J.; Kok, W. T. *Anal. Chim. Acta* **2011**, *706*, 361–366.
- (105) Yohannes, G.; Sneck, M.; Varjo, S. J.; Jussila, M.; Wiedmer, S. K.; Kovanen, P. T.; Oorni, K.; Riekkola, M.-L. *Anal. Biochem.* **2006**, *354*, 255–265.
- (106) Lee, J. Y.; Choi, D.; Johan, C.; Moon, M. H. *J. Chromatogr., A* **2011**, *1218*, 4144–4148.
- (107) Rambaldi, D. C.; Reschiglian, P.; Zattoni, A.; Johann, C. *Anal. Chim. Acta* **2009**, *654*, 64–70.
- (108) Li, P.; Hansen, M.; Giddings, J. C. *J. Liq. Chromatogr. Relat. Technol.* **1997**, *20*, 2777–2802.
- (109) Kim, K. H.; Moon, M. H. *Anal. Chem.* **2011**, *83*, 8652–8658.
- (110) Kim, K. H.; Moon, M. H. *J. Proteome Res.* **2009**, *8*, 4272–4278.
- (111) Kim, K. H.; Moon, M. H. *Anal. Chem.* **2009**, *81*, 1715–1721.
- (112) McEvoy, M.; Razinkov, V.; Wei, Z. P.; Casas-Finet, J. R.; Tous, G. I.; Schenerman, M. A. *Biotechnol. Prog.* **2011**, *27*, 547–554.
- (113) Messaud, F. A.; Sanderson, R. D.; Runyon, J. R.; Otte, T.; Pasch, H.; Williams, S. K. R. *Prog. Polym. Sci.* **2009**, *34*, 351–368.
- (114) Johann, C.; Elsenberg, S.; Roesch, U.; Rambaldi, D. C.; Zattoni, A.; Reschiglian, P. *J. Chromatogr., A* **2011**, *1218*, 4126–4131.
- (115) Oh, S.; Kang, D.; Ahn, S.-M.; Simpson, R. J.; Lee, B.-H.; Moon, M. H. *J. Sep. Sci.* **2007**, *30*, 1082–1087.
- (116) Giddings, J. C. *Anal. Chem.* **1990**, *62*, 2306–2312.
- (117) Li, P.; Hansen, M.; Giddings, J. C. *J. Microcolumn Sep.* **1998**, *10*, 7–18.

## Supporting Information

### Asymmetric flow field-flow fractionation in the field of nanomedicine

Michael Wagner,<sup>1,2</sup> Stephan Holzschuh,<sup>3</sup> Anja Traeger,<sup>1,2</sup> Alfred Fahr<sup>2,3</sup>,  
Ulrich. S. Schubert<sup>1,2\*</sup>

*1 - Laboratory of Organic and Macromolecular Chemistry (IOMC), Friedrich Schiller University  
Jena, Humboldtstrasse 10, 07743 Jena, Germany*

*2 - Jena Center for Soft Matter (JCSM), Friedrich Schiller University Jena, Philosophenweg 7,  
07743 Jena, Germany*

*3 - Department of Pharmaceutical Technology, Friedrich Schiller University Jena, Lessingstrasse 8,  
07743 Jena, Germany*

*ulrich.schubert@uni-jena.de; www.schubert-group.com*

#### Abstract

Asymmetric flow field-flow fractionation (AF4) is a widely used and versatile technique in the family of field-flow fractionations, indicated by a rapidly increasing number of publications. It represents a gentle separation and characterization method, where non-specific interactions are reduced to a minimum, allows a broad separation range from several nano- up to micrometers and enables a superior characterization of homo- and heterogenic systems. In particular, coupling to multi angle light scattering provides detailed access to sample properties. Information about molar mass, polydispersity, size, shape/conformation or density can be obtained nearly independent of the used material. In this perspective, the application and progress of AF4 for (bio)macromolecules and colloids, relevant for “nano” medical and pharmaceutical issues, will be presented. The characterization of different nano-sized drug or gene delivery systems, *e.g.* polymers, nanoparticles, micelles, dendrimers, liposomes, polyplexes, and virus-like-particles (VLP), as well as therapeutic relevant proteins, antibodies, and nanoparticles for diagnostic usage will be discussed. Thereby, the variety of obtained information, the advantages and pitfalls of this emerging technique will be highlighted. Additionally, the influence of different fractionation parameters in the separation process is discussed in detail. Moreover, a comprehensive overview is given, concerning the investigated samples, fractionation parameters as membrane types and buffers used as well as the chosen detectors and the corresponding references. The perspective ends up with an outlook to the future.

## Register of pharmaceutical relevant systems analyzed by AF4

Table 1: Nanoparticles (NP).

Analyte	Membrane (MWCO) <sup>a</sup>	Eluent	Detection	Comment	Ref.
ABT-102 (amorphous solid dispersion)	RC (10)	not specified	UV, RI, MALLS		1
C <sub>60</sub> Fullerene	PES (10)	pure water	DLS	Stability in aqueous solutions	2-4
C <sub>60</sub> , C <sub>70</sub> Fullerene	RC (10)	0.4% NaCl	UV, MALLS	<i>In vitro</i> toxicity assessment and separation of BSA from fullerenes	5
Carbon nanotubes (single wall)	RC, CTA, PES	NH <sub>4</sub> NO <sub>3</sub> at various pH and ionic strength	MALLS	Length determination	6
CdSe (CdZnS) core-shell QD	RC (10), PES (10)	pure water	UV (300 nm), Fluorescence MALLS, DLS,	Uptake and elimination in human cells	7
CdSe/ZnS QD (PEG coated), latex NP	RC (1)	0.1 mM NaN <sub>3</sub> , 0.01% FL-70	UV (254 nm), Fluorescence	Toxicity in aquatic environment	8
Cellulose nanocrystals	RC (10)	0.02% NaN <sub>3</sub>	RI, MALLS, DLS		9
Gelatin NP	RC (1, 5, 10), PES (1)	5 mM Na <sub>2</sub> HPO <sub>4</sub> , 14 mM NaCl, pH 7.4; 2 mM Na <sub>2</sub> HPO <sub>4</sub> , 14 mM NaCl, pH 6.0	UV (220, 260, 280 nm), RI, MALLS	Drug loading of nucleic acids and proteins	10
Gelatin NP (PEG coated)	RC (5)	50 mM phosphate buffer, pH 7.0; 50 mM NaCl	UV (260 nm), RI	Quantification of PEG coating	11
Gelatin NP, gelatin, chitosan	RC (5, 10)	gelatin: PBS, pH 6.0; chitosan: 0.5 M acetate buffer, pH 4.0	UV, RI, MALLS		12
Gold nanorods	PES (10)	various ratios of NH <sub>4</sub> NO <sub>3</sub> , CTAB (0.5 mM ionic strength)	UV, MALLS, DLS	Influence of eluent composition	13
Gold nanorods	RC (5)	0.02% NaN <sub>3</sub> ; 0.03% CTAB	UV	Fractionation and investigation of surface plasmon resonance	14
Gold NP	RC (10), PVDF (30)	pure water	UV, MALLS, DLS	Influence of eluent composition	15
Gold NP	RC (10)	0.02% NaN <sub>3</sub>	UV, MALLS, DLS	Adsorption of BSA	16
Gold NP	RC (10)	pure water	UV (525 nm)	Offline characterization by DLS after fraction collection	17
Gold NP	CTA (10), PES (1), PVDF (30), PA	pure water	UV, MALLS, DLS, ICP-MS	Comparison with batch techniques and method development	18
Gold NP	PES (10)	0.01% NaN <sub>3</sub> , 0.025% FL-70	ICP-MS	Separation of gold NP mixtures and comparison with hydrodynamic chromatography (HDC)	19
Gold NP	CTA (1)	pure water	UV, RI, MALLS	Fluorescent gold clusters	20
Gold NP	PES (10)	0.05% SDS, 3% methanol	MALLS, DLS, ICP-MS	Characterization of NPs in rat liver	21
Gold NP	not specified	not specified	UV, MALLS	Gold NP clusters	22
Gold NP (polymer coated), silica NP (oligothiophene doped), CdSe/ZnS QD (polymer coated)	RC (10, 30)	gold: 10 mM NaCl; silica: 50:50 ethanol/water; 5 mM Tris, pH 8.7; QD: 5 mM borate buffer, pH 9.1, 5 mM NaNO <sub>3</sub> , 0.02% NaN <sub>3</sub>	UV, RI, MALLS		23

Gold NP, silver NP, TiO <sub>2</sub> NP	CTA (10), PES (100), PVDF (30)	pure water	UV, MALLS, DLS, ICP-MS	Influence of eluent composition and membrane	24
Iron oxide NP	RC (10)	0.1% Na <sub>3</sub> PO <sub>4</sub>	UV, SAXS		25
Iron oxide NP	RC	10 mM phosphate buffer, pH 7.4, 5% mannitol	UV (254 nm), MALLS	Stabilization by lipid-based amphiphiles	26
Iron oxide NP	RC (10)	not specified	UV (300 nm), SAXS		27
Iron oxide NP	RC	not specified	UV, MALLS, DLS		28
Iron oxide NP	RC (5)	0.02% NaN <sub>3</sub>	MALLS	Fractionation in a semi-preparative channel	29
Iron oxide NP (Resovist®)	RC (10)	0.2% NovaChem Surfactant 100	UV (300 nm), SAXS		30
Latex core-shell NP	RC (30)	2 mM Tris buffer, 0.03% Brij 35	UV (254 nm), MALLS	Influence of pH, ionic strength, and functionalization on swelling behavior	31
Latex core-shell NP	RC (30)	phosphate buffer at various concentration and pH	UV (254 nm)		32
Latex NP	RC (5)	0.02% NaN <sub>3</sub> , 0.1% FL-70	UV (254 nm)	Steric FFF	33
Latex NP	RC (30)	0.02% NaN <sub>3</sub> , 0.1% FL-70	UV (254 nm)		34
Latex NP	not specified	0.02% NaN <sub>3</sub> , 0.05% SDS	RI, MALLS		35
Latex NP	RC (5)	1 mM NaClO <sub>4</sub> , 0.01% Tween® 20	MALLS, LIBD	Laser-induced breakdown detection	36
Latex NP	RC	different salts at varying concentration	UV (254 nm)	Specific ion effects	37
Latex NP	RC (10)	0.1% SDS	UV, TALLS (two angle LS)	Aggregation study	38
Latex NP	RC (10)	0.02% NaN <sub>3</sub> , 0.005% SDS	RI, MALLS		39
Latex NP, bovine serum albumin (BSA), dextran, pectin	not specified	0.1 M NaNO <sub>3</sub> , 0.02% NaN <sub>3</sub>	RI, MALLS		40
Lecithin/Pluronic® core-shell NP, latex NP	CTA (10)	0.02% NaN <sub>3</sub>	UV (254 nm)		41
Lipid NP (siRNA loaded)	RC (10)	PBS, 0.02% NaN <sub>3</sub>	RI, MALLS	Comparison of SEC and AF4	42
Lopinavir/Ritonavir® containing NP	RC (10)	10 mM NaNO <sub>3</sub>	UV (237 nm), RI, MALLS	NP formation upon dispersion of melt extrudate formulations	43
Magnetite NP (dextran, mitoxantrone coated), TmPO <sub>4</sub> NP, diclofenac antiserum, albumin, γ-globulin, PSS, sewage plant samples	RC (1, 10), PES (0.3, 2)	1 mM NaCl; PBS, pH 7.4; 30 mM Tris buffer; 0.1% SDS; 0.001% Tween® 20	UV, ICP-MS	Slot-outlet technique used	44
PEG-PLA core-shell NP	RC (10)	0.02% NaN <sub>3</sub> , 0.05% SDS	UV (254 nm)	Encapsulation of retinoic acid	45
PEG-PLA NP	PES (5)	pure water; 10% fetal bovine serum (FBS); 50% FBS	MALLS	Tumor accumulation of NPs ( <i>in vivo</i> )	46
PEG-PLA NP	PES (5)	0.02% NaN <sub>3</sub>	MALLS	<i>In vivo</i> study of NP	47
PLA NP	RC	0.02% NaN <sub>3</sub> , 0.1% FL-70	UV (254 nm)	Encapsulation of prodrug 5'-octanoyl-CPA	48
PLGA NP	RC (10)	0.1% SDS	UV, MALLS	Comparison of size distributions by DLS, SAXS, AF4, TEM	49

Poly( <i>n</i> -butyl acrylate)-poly( <i>n</i> -butyl methacrylate) (PBA-PBMA) core-shell NP	not specified	0.018% NaCl; 0.003% Tween® 20	MALLS	Detailed characterization of core-shell structure	50
Poly( <i>N</i> -iso-propylacrylamide) nanogel, poly( <i>N</i> -iso-propylmethacrylamide) nanogel	not specified	not specified	UV, MALLS	Core/shell nanogels for drug delivery	51
Poly( <i>N</i> -iso-propylacrylamide)/poly( <i>N</i> -iso-propylmethacrylamide) core/shell nanogels	not specified	formate buffer, pH 3.3 (15 mM ionic strength)	UV, MALLS	Degradable shells on thermoresponsible nanogels	52
Poly( <i>N</i> -iso-propylmethacrylamide) nanogels	not specified	not specified	RI, MALLS	Peptide-functionalized nanogels for targeted siRNA delivery	53
Poly( <i>N</i> -iso-propylmethacrylamide) nanogels	RC (10)	0.02% NaN <sub>3</sub>	RI, MALLS	Degradation of nanogels	54
Poly(organosiloxane) core-shell NP (incorporated iron oxide NP)	PES (4)	5 mM NaCl, 0.01% Tween® 20	UV (254 nm)	Encapsulation of magnetic iron oxide NP into core-shell systems	55
Poly(organosiloxane) core-shell NP, latex NP	RC (10)	toluene	not specified	Determination of Hamaker constants	56
Poly(organosiloxane) NP	RC (10)	0.02% NaN <sub>3</sub> , 0.01% Tween® 20	UV (254 nm)	Influence of synthesis parameters on size	57, 58
Pullulan-PEG nanogel	RC (10)	PBS, pH 7.4	UV, MALLS, DLS	Crosslinked nanogel for sustained drug release	59
Silica NP	RC (10)	0.02% NaN <sub>3</sub>	RI, MALLS, DLS	Characterization of amine-functionalized silica NP	60
Silica NP (oligothiophenes doped)	RC (10)	0.025% SDS in 50:50 ethanol/water	Fluorescence, MALLS	Color tuning of diagnostic NPs	61
Silica NP (PEG coated)	not specified	0.04% SDS; 0.02% NaN <sub>3</sub> ; 0.01% NaCl	MALLS	Stability of PEG coated silica NPs	62
Silver NP	RC (10), PES (10), PVDF (30)	carbonate buffer, pH 7.4	UV, MALLS, DLS, ICP-MS	Influence of membrane, eluent and flow conditions	63
Silver NP	PVDF (30)	pure water	UV, MALLS, DLS, ICP-MS	Comparison with batch techniques	64
Silver NP	RC (1), PES (1)	0.01% SDS, pH 8	UV (254 nm), ICP-MS		65
Silver NP	PES (0.3)	5 mM NaNO <sub>3</sub>	UV (254, 400 nm), ICP-MS	Interaction of silver NPs with natural organic matter	66
Silver NP	PES (10)	not specified	UV, DLS	Transformation of silver NPs	67
Silver NP	PES (10)	not specified	UV, MALLS, DLS, ICP-MS	Interaction of silver NPs with natural organic matter	68
Silver NP	RC (10)	pure water	UV (420 nm), ICP-MS		69
Silver NP	RC (10)	0.01% NaN <sub>3</sub> , 0.025% FL-70	ICP-MS		70
Silver NP	RC (10)	0.02% NaN <sub>3</sub> , 0.05% SDS	UV, MALLS, ICP-MS	Toxicity of silver NPs in aquatic environment	71
ZnS NP (Mn doped)	RC (5)	pure water	UV (280 nm)		72

<sup>a</sup> Molar mass cut-off (MWCO) in kg·mol<sup>-1</sup>.

**Table 2: Polymers and complexes or conjugates formed thereof.**

Analyte	Membrane (MWCO) <sup>a</sup>	Eluent	Detection	Comment	Ref.
Amylose- <i>b</i> -poly(styrene)	RC (5)	THF	UV, RI, MALLS		73
Chitosan	RC (10)	0.1 M acetate buffer, pH 4.2, 0.02% NaN <sub>3</sub>	RI, MALLS	Comparison of AF4 and traditional methods	74,75
Chitosan/DNA polyplexes	RC (10) (amphiphilic)	50 mM acetate buffer, pH 4.0 (ionic strength 20 mM by NaCl)	UV (260, 556 nm), MALLS, DLS	Analysis of polyplexes and determination of free chitosan	76-78
Dextran, PEG,	RC	pure water; 0.5 M NaCl	RI	Power-law relationships to calculate M out of D	79



PSS (poly(styrene sulfonate)), pullulan					
Dextran, pullulan	RC (10)	100 mM NaNO <sub>3</sub>	RI, MALLS	AF4 at different temperatures	80
Dextran, pullulan	RC (10)	pure water; 0.1 M NaCl, 0.02% NaN <sub>3</sub>	RI, MALLS	Resolution and separation range of AF4	81
Ethylhydroxyethyl cellulose	RC (10)	10 mM NaCl, 0.002% NaN <sub>3</sub>	RI, MALLS	Study on conformation	82,83
Gelatin/PSS complexes	not specified	10 mM acetate buffer, pH 5.6, 0.1% Tween® 20	UV	Gelatin/polyelectrolyte complexes	84
Maltose modified hyperbranched PEI	RC (5, 10), PES (5, 10)	0.02% NaN <sub>3</sub>	UV (550 nm, at cross-flow outlet), RI, MALLS	Accumulation wall as ultrafiltration device for small drug molecules	85,86
Maltose-decorated lysine-dendronized maleimide copolymers	RC (10)	0.02% NaN <sub>3</sub> ; acetate buffer; NaNO <sub>3</sub>	UV (550 nm), RI, MALLS	pH dependency of shape and aggregation	86,87
PEG	RC	varying concentrations of Na <sub>2</sub> SO <sub>4</sub> , K <sub>2</sub> SO <sub>4</sub>	RI	Influence of salt and ionic strength	88
PEG, PSS	PES (10)	various buffers at different ionic strength and pH	UV, ESI-MS		89
PEG- <i>b</i> -PBA	not specified (5)	pure water	RI, UV, MALLS	Formation of vesicles and micelles by amphiphilic block copolymers	90
PEG- <i>b</i> -PCL	RC (10)	0.02% NaN <sub>3</sub>	UV (214, 412 nm), RI, MALLS, DLS	Encapsulation of pheophorbide(a)	91,92
PEG- <i>b</i> -PVP, PEG- <i>b</i> -PLA, PEG- <i>b</i> -PLGA, PEG- <i>b</i> -PCL	PES (5)	50 mM NaCl, 0.05% NaN <sub>3</sub>	RI, MALLS	Interactions of micelles with human plasma	93
Poly(acrylamide), PSS, PVP	PES (8), PP	15 mM HNO <sub>3</sub> ; Tris-HNO <sub>3</sub> buffer; varying concentration of KCl, Na <sub>2</sub> SO <sub>4</sub>	UV (200, 254 nm)		94
Poly(acrylic acid)	RC (5)	50 mM NaCl; 50 mM NaOH; 50 mM glycine	RI, SAXS		95
Poly(amidoamine) dendrimers	RC (10)	0.1 M phosphate buffer at different pH	RI	Interaction of PAMAM with BSA	96
Poly(glycomethacrylate) star (25 arms) based on silsesquioxane NP	not specified (5)	25 mM NaNO <sub>3</sub> , 0.02% NaN <sub>3</sub>	UV, RI, MALLS	Synthesis and characterization	97
Poly(methacryloxyethyl trimethylammonium chloride)/poly(ethylene glycol)- <i>b</i> -poly(sodium methacrylate) complexes	CTA (10)	NaCl (20, 80, 160 mM)	UV (214 nm)	Charge stoichiometry of polyelectrolyte complexes	98
Poly(methyl glyoxylate- <i>co</i> -potassium glyoxylate)	RC (10)	0.1 M LiNO <sub>3</sub> , 0.02% NaN <sub>3</sub>	RI, MALLS		99
Poly( <i>N</i> - <i>iso</i> -propylacrylamide)	RC (10)	pure water	UV (212, 254 nm), RI	Investigation of LCST behavior	100
Poly(styrene- <i>co</i> -(methyl methacrylate)- <i>co</i> -(maleic anhydride) (PEG grafted onto)	RC (10)	varying concentrations of Na <sub>2</sub> SO <sub>4</sub> , KCl, Na <sub>3</sub> PO <sub>4</sub>	UV	Influence of salt on charged, amphiphilic copolymers	101,102
Polyspartate/poly(trimethylammonium propyl methacrylamide chloride) complexes	RC (10)	NaCl; CaCl <sub>2</sub> at different ionic strength	RI, MALLS; DLS	Water-soluble polyelectrolyte complexes	103
PSS	RC (10)	0.1 M NaNO <sub>3</sub> , 0.02% NaN <sub>3</sub>	RI, MALLS		104
PSS	RC (10)	0.1 M NaNO <sub>3</sub> , 0.02% NaN <sub>3</sub>	RI, MALLS	Resolution and separation range of AF4	104
PSS, PVP, latex beads,	RC (10)	0.02% NaN <sub>3</sub> , 0.01% Tween® 20	UV (260 nm)	Water-soluble polymers	105

aldolase, BSA, ferritin, thyroglobulin					
Pullulan	RC (10)	0.1 M NaNO <sub>3</sub> , 0.02% NaN <sub>3</sub>	RI, MALLS		106
PVP	RC (10), PES (10)	pure water	RI, MALLS	Frit inlet, frit outlet	107
PVP	RC (5)	0.1 M NaCl, 0.02% NaN <sub>3</sub>	RI, DLS, SAXS		108
Starch-PEI/DNA polyplexes	RC (5)	PBS, pH 7.4	RI, MALLS	Degradation of hydroxethyl starch-PEI conjugates	109
α-Carrageenan	RC (10)	0.1 M NaCl; 0.1 M KCl, 0.1 M NaI	RI, MALLS	Solution behavior of α-carrageenan	110
κ-Carrageenan	RC (10)	0.1 M NaCl; 0.1 M NaI	RI, MALLS	Conformation under different salt conditions	111
κ-carrageenan xanthan	RC (10)	0.1 M NaCl; 0.1 M NaI	RI, MALLS		112

<sup>a</sup> Molar mass cut-off (MWCO) in kg·mol<sup>-1</sup>.

**Table 3: Liposomes.**

Analyte	Membrane (MWCO) <sup>a</sup>	Eluent	Detection	Comment	Ref.
DMPC/cholesterol/DCP liposomes (encapsulated sulforhodamine B)	not specified	not specified	MALLS	Entrapment efficiency	113
DMPC/cholesterol/DCP liposomes	RC (10)	PBS	MALLS, DLS	Size distribution of liposomes prepared by microfluidics	114
DMPC/DMPG/cholesterol liposomes (encapsulated hemoglobin)	not specified	PBS, pH 7.3	RI, MALLS	Dependency of preparation parameters on hemoglobin encapsulation efficiency	115 116
DMPC/DMPG/cholesterol/DSPE-PEG 2000/α-tocopherol/k <sup>+</sup> ionophore liposomes (encapsulated actin and hemoglobin, LEAChb)	not specified	F-buffer (50 mM KCl, 2 mM MgCl <sub>2</sub> , 1 mM ATP), pH 8.0	RI, MALLS	Shape, size distribution and encapsulation efficiency of liposomes of LEAChb	117
DMPG liposomes	CTA (10)	5 mM phosphate buffer at various pH and ionic strength (by NaCl)	UV (254, 410 nm)	Interactions with cytochrome c	118
DOPE/DSPC/DSPC-PEG 2000/cholesterol liposomes (encapsulated doxorubicin, Caelyx®)	RC (10)	10 mM NaNO <sub>3</sub>	UV, RI, MALLS	Size distribution and morphology prior and after ultrasound exposure	119
DOTAP/DOPE/DNA complexes, Lipofectamine®/DNA complexes	RC (30), PC (30 nm), PP (0.055- 0.125 μm)	0.089 M Tris- borate buffer, pH 8.6, 0.02% NaN <sub>3</sub>	UV (260 nm), RI, MALLS	Study of cationic lipid/DNA complexes for gene delivery	120
DPPC/DPPG liposomes (encapsulated temporin, corticosterone, testosterone)	RC (5, 10)	NaCl (0, 25, 50, 100 mM) + 0.02% NaN <sub>3</sub>	RI, MALLS	Influence of fractionation parameters, offline recovery of drug and lipids	121
DSPC/DSPA liposomes	RC (10)	pure water, 0.05% SDS, 0.02% NaN <sub>3</sub>	UV (254 nm)	Dependency of sonication time and temperature during preparation on size	122
DSPC/DSPE-PEG 500/cholesterol lipid disks	not specified	not specified	UV (214 nm), MALLS		123
EPC liposomes	not specified	10 mM NaNO <sub>3</sub>	RI, MALLS	Comparison of different techniques	124
EPC liposomes	not specified	200 mM NaCl	MALLS	Number weighted vesicle size distributions	125
EPC liposomes (encapsulated monomeric actin (G-actin))	not specified (10)	G-Buffer (5 mM Tris-HCl, pH 8.0, 0.2 mM CaCl <sub>2</sub> , 0.2 mM ATP); F-buffer (50 mM KCl, 2 mM MgCl <sub>2</sub> ,	MALLS	Effect of actin concentration and ionic strength of buffer on structure of actin- containing liposomes	126

			1 mM ATP)			
EPC/DOPE liposomes (rhodamine B labeled)	RC (10)	10 mM NaNO <sub>3</sub> , 150 mM sucrose	UV (280, 571 nm), RI, MALLS	Influence of ionic strength and osmotic pressure on separation	127	
EPC/POPC/PA/PI/PS/PG/cholesterol liposomes	RC (10)	8.5 mM phosphate buffer, pH 7.4	UV (254 nm)	Stability of liposomal formulations under different conditions	128	
EPC/Sudan Red G liposomes; EPC/DOPE liposomes (rhodamine B labeled)	RC (10)	10 mM NaNO <sub>3</sub>	UV (280, 501, 571 nm) RI, MALLS	Influence of concentration and membrane adsorption phenomena	129	
Lecithin liposomes (encapsulated THP-C11)	RC (5)	0.02% NaN <sub>3</sub>	MALLS		130	
Lipobeads (DPPC/cholesterol/DCP/DiD as outer shell, NIPA/MBA/DEAP as core)	RC (10)	PBS (5 mM, 10 mM)	MALLS	Lipobeads prepared by microfluidics	131	
PC/PG/cholesterol liposomes	RC (10)	PBS; Tris-HCl (various concentrations)	UV (254 nm), DLS	Influence of ionic strength and pH on separation	132	
POPC/DMPC (PEGylated) liposomes, POPC/DSPC (PEGylated) liposomes	RC (10)	20 mM HEPES, pH 7.4	UV (254 nm)	Comparison to conventional methods	133	
POPC/POPG liposomes, DPPC/DPPG liposomes (encapsulated temoporfin or cholesterol)	RC (5, 10)	0.02% NaN <sub>3</sub>	RI, MALLS	Correlation between selective drug partitioning and size	134	
Proteoliposomes, synaptic vesicles	RC (10)	20 mM HEPES, pH 7.4, 150 mM KCl, 0.02% NaN <sub>3</sub>	DLS (offline)	Purification	135	
SPC liposomes, EPC liposomes	RC (10)	NaNO <sub>3</sub> (5, 10, 20, 50 mM)	UV (280 nm), RI, MALLS	Influence of fractionation parameters	136	

<sup>a</sup> Molar mass cut-off (MWCO) in kg·mol<sup>-1</sup>.

**Table 4: Proteins, viruses and virus-like-particles**

Analyte	Membrane (MWCO) <sup>a</sup>	Eluent	Detection	Comment	Ref.
Acid phosphatase (APase)	RC	100 mM NaH <sub>2</sub> PO <sub>4</sub> , pH 4.3, pH 7.0	UV (227 nm)		137
Albumin, ferritin, hemoglobin, human and rat plasma, ovalbumin, γ-globulin	RC	20 mM PBS, 0.3% SDS, pH 7.2	UV	Fractionation of plasma, SDS induced structural formation of proteins	138
Alcohol dehydrogenase, apoferritin, BSA, carbonic anhydrase, cytochrome C	RC composite (10)	10 mM NH <sub>4</sub> HCO <sub>3</sub>	UV (280 nm)	Two-dimensional separation by isoelectric focusing-AF4	139
Alcohol dehydrogenase, BSA, carbonic anhydrase, exosomes (from human mesenchymal stem cell line, B10), latex NP	RC composite (10)	0.1 M PBS, pH 7.4	UV (280 nm)	Miniaturized AF4	140
Aldolase, BSA, ferritin, β-lactoglobulin	RC (10)	10 mM phosphate buffer, pH 7.4	UV (280 nm)	Optimization of parameters	141
Algae (unicellular, different species), HSA (Fraction V), plasmids, sodium hyaluronate	RC (10, 30)	Tris-HNO <sub>3</sub> , pH 7.4, 0.02% NaN <sub>3</sub> , 1 mM EDTA	UV (260, 280, 420 nm), Fluorescence	Optimization of separation conditions	142
Amyloid Aβ <sub>1-42</sub> peptide	PES (10)	1 mM phosphate buffer, pH 7.4, 0.02% SDS	UV (220 nm), MALLS	Time-dependent aggregation	143
Antibodies (IgG1)	RC (10)	0.1 M PBS, pH 6.5	UV (280 nm)	Separation of antibody-aggregates in comparison to SEC	144
Antibodies (IgG1)	RC (10)	various buffers	UV (280 nm),	Aggregation study	145

Antibodies (IgG1)	RC (10)	100 mM phosphate buffer, pH 7.2, 100 mM Na <sub>2</sub> SO <sub>4</sub>	MALLS UV (280 nm), Fluorescence, MALLS	Heat induced aggregation of IgG1	146
Antibodies (IgG1, IgG2), HAS	RC (10)	4 mM phosphate buffer at various pH, 135 mM NaCl	UV (215, 280 nm), RI, MALLS	Strength and stoichiometry of IgG binding to receptors	147
Antibodies (monoclonal)	RC (10)	10 mM sodium citrate, 100 mM NaCl, pH 5.5	UV (280 nm), RI, MALLS	Comparison of various methods for detection of protein aggregation	54
Antibody (IgG1), etanercept;	RC (10)	100 mM phosphate buffer, pH 7.2, 100 mM Na <sub>2</sub> SO <sub>4</sub>	UV (280 nm), MALLS	Characterization and quantification of submicron protein aggregates	148
Apo ferritin, BSA, carbonic anhydrase, thyroglobulin	RC (10)	BSA: 50 mM NaCl; others: PBS	RI, MALLS	Combination of AF4 and HF5	149
Apo ferritin, BSA, ferritin, fibrinogen, xanthan gum	RC (10)	fibrinogen: 0.5 M KCl, 1 mM MgCl, 0.1 mM EDTA; xanthan: phosphate buffer, pH 6.5 (ionic strength 0.3 M); others: pure water	UV	Comparison of AF4 and analytical ultracentrifugation	150
Apo ferritin, $\gamma$ -globulin, ovalbumin, thyroglobulin, transferrin	RC (30)	0.1 M Tris-HCl, pH 7.8	UV (280 nm)	Frit-Inlet AF4	151
Bacteriophages Q $\beta$ , MS2, f2, $\phi$ X174, ferritin	RC	20 mM PBS, pH 7.1	UV		152
BSA	not specified (10)	not specified	UV, RI, MALLS,		153
BSA	RC (10)	8.5 mM phosphate buffer, pH 7.4, 150 mM NaCl	UV (280 nm), MALLS	Heat-induced BSA aggregation	154
BSA, ferritin, ovalbumin, pullulan, $\beta$ -lactoglobulin	not specified (10)	0.05 M Tris, 0.1 H <sub>3</sub> PO <sub>4</sub> , pH 7.5, 0.02% NaN <sub>3</sub>	RI	Calibration with proteins and pullulan	155
Carbonic anhydrase, ferritin, transferrin	RC (5, 10, 20); PES (10)	10 mM NH <sub>4</sub> HCO <sub>3</sub> , 0.02% NaN <sub>3</sub>	UV (280 nm), ESI-MS	Chip-type channel design; protein identification	156
Cow pea mosaic virus (CPMV), satellite tobacco necrosis virus (STNV)	RC (10), PLGC (10)	Tris-HNO <sub>3</sub> , pH 7.5, 0.02% NaN <sub>3</sub>	UV	Influence of channel geometry	157
Cow pea mosaic virus (CPMV), human serum albumin (HAS) fraction V	RC (10)	different buffers at varying concentration	UV (280 nm)	Influence of carrier, temperature, sample load	158
Cytochrome c, ferritin, HSA (fraction V), plasmids, satellite tobacco necrosis virus (STNV), semliki forest virus (SFV), thyroglobulin	PLGC (10)	Tris-HNO <sub>3</sub> , pH 7.4, 0.02% NaN <sub>3</sub> , 1 mM EDTA	UV (260, 280 nm)	Optimization of separation conditions	159
Exosomes (from HB1.F3 human neural stem cells)	RC composite (10)	0.1 M PBS, pH 7.4	UV (280 nm)	Offline MS of protein fractions (proteasome analysis)	160
Fibroblast growth factor complex (FGF21/FGFR/ $\beta$ -Klotho)	not specified	4 mM phosphate buffer, various pH, 135 mM NaCl	UV (215, 280 nm), RI, MALLS		161
Glucagon	not specified (1, 10)	0.01 M HCl	UV (278 nm), MALLS	Glucagon aggregation as model for fibril formation	162
Granulocyte colony stimulating factor	RC (10)	50 mM NaNO <sub>3</sub> ,	UV (280 nm),		163

(PEGylated, PEG-G-CSF)			0.02% NaN <sub>3</sub>	RI, MALLS	
Green fluorescent protein inclusion bodies (GFPIBs)	RC (10)		0.04% FL-70	RI, MALLS	164
HDL, phospholipid transfer protein (PLTP), DPPC liposomes	RC (10)		10 mM phosphate buffer, 150 mM NaCl, 1 mM EDTA, 0.02% NaN <sub>3</sub> , pH 7.4	UV (254, 280 nm)	Separation after incubation 165
Hemoglobin (glycosylated)	not specified		not specified	RI, MALLS	166
Human plasma	RC (20)		10 mM NH <sub>4</sub> HCO <sub>3</sub>	ESI-MS-MS	Top-down lipidomic analysis of human lipoproteins 167
Human plasma	RC (30)		Tris-HCl, pH 7.8	UV (280, 610 nm)	Role of lipoproteins for coronary artery disease 168
Human plasma	RC (10)		various buffers	UV (280 nm)	Miniaturized AF4 169
Human plasma	RC (10)		PBS, pH 7.4	UV (280 nm, 500 nm), MALLS	Dual online enzymatic determination of lipoprotein-cholesterol and lipoprotein-triglycerides 170
Human plasma	RC (10)		20 mM phosphate buffer, pH 7.4, 0.02% NaN <sub>3</sub>	UV (500 nm)	Dual online enzymatic determination of lipoprotein-cholesterol and lipoprotein-triglycerides 171
Human plasma	RC (10)		10 mM NH <sub>4</sub> HCO <sub>3</sub> , pH 8.2	UV (280 nm, 600 nm), Fluorescence	Application of a prior guard channel to deplete small plasma proteins 172
Human plasma	RC (10)		PBS, pH 7.4	UV (500 nm)	Determination of lipoprotein-cholesterol and lipoprotein-triglycerides by coupling AF4 and GC-MS 173
Human plasma	RC (30)		15 mM phosphate buffer, pH 7.2	UV (280, 600 nm), RI, MALLS	Size and shape characterization 174
Human plasma	not specified		PBS, pH 7.4	UV (280 nm)	Symmetric FFF 175
Human plasma, N-benzoyl-staurosporine	RC (3, 10)		36 mM PBS, pH 7.4, 100 mM NaCl, 0.001% NaN <sub>3</sub> , 0.005% Tween® 80	UV (210 nm)	Drug transfer to plasma proteins: separation, adsorption and recovery 176
Human urine	RC composite (20)		10 mM NH <sub>4</sub> HCO <sub>3</sub>	UV (280 nm)	Two-dimensional separation by isoelectric focusing-AF4 177
Influenza virus	RC (10)		0.1 M PBS, pH 7.4	MALLS	Setup optimization 178
Influenza virus (B/Yamanashi/166/98), adenovirus	RC (10); CTA (10)		not specified	MALLS	Aggregation of viruses 179
LDL	RC (10)		various PBS and acetate buffers	UV (280 nm)	Effect of oxidation on size distribution 180
Lipoproteins	RC (10)		9 mM phosphate buffer, pH 7.4, 140 mM NaCl	UV	Effect of sugars on lipoprotein structure 181
Lung cancer serum	RC (10)		1 mM CaCl <sub>2</sub> , 1 mM MgCl <sub>2</sub> , 1 mM MnCl <sub>2</sub> , 50 mM TBS	UV (280 nm)	Lectin-based size sorting strategy to enrich glycopeptides 182
Pic gastric mucin	RC (10)		10 mM NaCl	RI, MALLS	Effect of pH on association behavior 183
PolyHb (glutaraldehyde cross-linked hemoglobin)	not specified		50 mM Tris, pH 7.2	RI, MALLS	Molar mass distribution 184-186
Prostatic cancer cell lysate (DU145 HRPC and PrEC cells), α-casein	RC composite (20)		10 mM NH <sub>4</sub> HCO <sub>3</sub>	UV (280 nm)	Coupling of AF4 and isoelectric focusing 187
Prostatic cancer cell lysate (DU145 HRPC cells)	RC composite (10)		0.1 M PBS, pH 7.6	UV (254 nm)	Purification of cell lysates in supramicrometer range 188
Proteose peptone component 3 (milk	not specified		5 mM Tris-HCl,	UV (205 nm),	Molar mass and size of 189

protein, PP3)	(10)	pH 7.5, 150 mM NaCl	RI, MALLS	tetrameric aggregates	
PrP <sup>res</sup> (protease-resistant PrP protein)	PES (10)	20 mM Tris, pH 7.0, 0.1% sodium n-undecyl sulphate (SUS)	RI, MALLS, DLS	Correlation of PrP aggregate size with infectivity and converting activity	190,191
<i>Pseudomonas putida</i> (P. putida, bacteria)	RC, PES	0.1 mM NaN <sub>3</sub>	UV (254 nm)	Investigation of biofouling of membranes	192
Qb VLP	RC, CTA, PES	20 mM phosphate buffer, pH 7.0, 150 mM NaCl	UV (260 nm), MALLS	Influence of various fractionation parameters	193,194
Ranibizumab (IgG fragment), bevacizumab (IgG)	not specified	various buffers	UV (280 nm), MALLS	Aggregation of mAbs	195
Trastuzumab (IgG1) antibody	PES (10)	0.9% NaCl; 5% dextrose	UV (280 nm), MALLS	Aggregation study	196
VLPs	RC (10)	20 mM phosphate buffer, pH 7.0, 150 mM NaCl	UV (260 nm), MALLS		197
VP1 VLP (derived from human polyoma JC-Virus)	RC (10)	20 mM Tris-HCl, pH 7.5, NaCl at various concentrations	UV, Fluorescence, RI, MALLS, DLS	Characterization of VLPs	198
VP1 VLP (derived from murine polyoma virus)	RC (10)	various buffers	UV (280 nm), RI, MALLS		199
VP1 VLP (derived from murine polyoma virus)	not specified	lysis-buffer	UV	Modeling impact of aggregates on chromatographic performance	200
VP1 VLP (derived from murine polyoma virus)	not specified	10 mM Tris, 50 mM NaCl, 0.01 mM CaCl <sub>2</sub> , pH 8.0	UV, MALLS	Quantification of VP1-VLP	201
VP1 VLP (derived from murine polyoma virus)	RC (10)	lysis-buffer	UV (280 nm), RI, MALLS		202
VP2 VLP (derived from murine polyoma virus)	not specified (10)	lysis-buffer	UV (280 nm), MALLS	Effect of encapsulation on the structure of VLPs	203

<sup>a</sup> Molar mass cut-off (MWCO) in kg·mol<sup>-1</sup>.

## References

- (1) Frank, K. J.; Westedt, U.; Rosenblatt, K. M.; Hölig, P.; Rosenberg, J.; Mägerlein, M.; Fricker, G.; Brandl, M. *Int. J. Nanomedicine* **2012**, *7*, 5757-5768.
- (2) Isaacson, C.; Zhang, W.; Powell, T.; Ma, X.; Bouchard, D. *Environ. Sci. Technol.* **2011**, *45*, 5170-5177.
- (3) Isaacson, C. W.; Bouchard, D. C. *Environ. Sci. Technol.* **2010**, *44*, 8971-8976.
- (4) Isaacson, C. W.; Bouchard, D. *J. Chromatogr. A* **2010**, *1217*, 1506-1512.
- (5) Kato, H.; Shinohara, N.; Nakamura, A.; Horie, M.; Fujita, K.; Takahashi, K.; Iwahashi, H.; Endoh, S.; Kinugasa, S. *Mol. BioSyst.* **2010**, *6*, 1238-1246.
- (6) Gigault, J.; Le Hecho, I.; Dubascoux, S.; Potin-Gautier, M.; Lespes, G. *J. Chromatogr. A* **2010**, *1217*, 7891-7897.
- (7) Al-Hajaj, N. A.; Moquin, A.; Neibert, K. D.; Soliman, G. M.; Winnik, F. M.; Maysinger, D. *ACS Nano* **2011**, *5*, 4909-4918.
- (8) Lee, S.; Kim, K.; Shon, H. K.; Kim, S. D.; Cho, J. *J. Nanopart. Res.* **2011**, *13*, 3051-3061.
- (9) Guan, X.; Cueto, R.; Russo, P.; Qi, Y.; Wu, Q. *Biomacromolecules* **2012**, *13*, 2671-9.
- (10) Fraunhofer, W.; Winter, G.; Coester, C. *Anal. Chem.* **2004**, *76*, 1909-1920.
- (11) Zillies, J. C.; Zwiorek, K.; Winter, G.; Coester, C. *Anal. Chem.* **2007**, *79*, 4574-4580.
- (12) Schultes, S.; Mathis, K.; Zillies, J.; Zwiorek, K.; Coester, C.; Winter, G. *Lc Gc Europe* **2009**, *22*, 390-403.
- (13) Gigault, J.; Cho, T. J.; MacCuspie, R. I.; Hackley, V. A. *Anal. Bioanal. Chem.* **2013**, *405*, 1191-1202.
- (14) Runyon, J. R.; Goering, A.; Yong, K. T.; Williams, S. K. *Anal. Chem.* **2013**, *85*, 940-8.
- (15) Cho, T. J.; Hackley, V. A. *Anal. Bioanal. Chem.* **2010**, *398*, 2003-2018.

- (16) Tsai, D.-H.; DelRio, F. W.; Keene, A. M.; Tyner, K. M.; MacCuspie, R. I.; Cho, T. J.; Zachariah, M. R.; Hackley, V. A. *Langmuir* **2011**, *27*, 2464-2477.
- (17) Calzolari, L.; Gilliland, D.; Garcia, C. P.; Rossi, F. J. *Chromatogr. A* **2011**, *1218*, 4234-4239.
- (18) Hagendorfer, H.; Kaegi, R.; Traber, J.; Mertens, S. F. L.; Scherrers, R.; Ludwig, C.; Ulrich, A. *Anal. Chim. Acta* **2011**, *706*, 367-378.
- (19) Gray, E. P.; Bruton, T. A.; Higgins, C. P.; Halden, R. U.; Westerhoff, P.; Ranville, J. F. *J. Anal. At. Spectrom.* **2012**, *27*, 1532-1539.
- (20) Lemke, K.; Prietzel, C.; Koetz, J. *J. Colloid Interface Sci.* **2013**, *394*, 141-146.
- (21) Schmidt, B.; Loeschner, K.; Hadrup, N.; Mortensen, A.; Sloth, J. J.; Koch, C. B.; Larsen, E. H. *Anal. Chem.* **2011**, *83*, 2461-2468.
- (22) Tsai, D.-H.; Cho, T. J.; DelRio, F. W.; Taurozzi, J.; Zachariah, M. R.; Hackley, V. A. *J. Am. Chem. Soc.* **2011**, *133*, 8884-8887.
- (23) Zatonni, A.; Rambaldi, D. C.; Reschiglian, P.; Melucci, M.; Krol, S.; Garcia, A. M. C.; Sanz-Medel, A.; Roessner, D.; Johann, C. *J. Chromatogr. A* **2009**, *1216*, 9106-9112.
- (24) Ulrich, A.; Losert, S.; Bendixen, N.; Al-Kattan, A.; Hagendorfer, H.; Nowack, B.; Adlhart, C.; Ebert, J.; Lattuada, M.; Hungerbuhler, K. *J. Anal. At. Spectrom.* **2012**, *27*, 1120-1130.
- (25) Knappe, P.; Boehmert, L.; Bienert, R.; Karmutzki, S.; Niemann, B.; Lampen, A.; Thünemann, A. F. *J. Chromatogr. A* **2011**, *1218*, 4160-4166.
- (26) Belete, A.; Mäder, K. *Drug Dev. Ind. Pharm.* **2013**, *39*, 186-196.
- (27) Thünemann, A. F.; Kegel, J.; Polte, J.; Emmerling, F. *Anal. Chem.* **2008**, *80*, 5905-5911.
- (28) Lohrke, J.; Briel, A.; Mäder, K. *Nanomed.* **2008**, *3*, 437-452.
- (29) Dutz, S.; Kuntsche, J.; Eberbeck, D.; Müller, R.; Zeisberger, M. *Nanotechnology* **2012**, *23*.
- (30) Thünemann, A. F.; Rolf, S.; Knappe, P.; Weidner, S. *Anal. Chem.* **2009**, *81*, 296-301.
- (31) Frankema, W.; van Bruijnsvoort, M.; Tijssen, R.; Kok, W. T. *J. Chromatogr. A* **2002**, *943*, 251-261.
- (32) Ratanathanawongs, S. K.; Shiundu, P. M.; Giddings, J. C. *Colloids Surf., A* **1995**, *105*, 243-250.
- (33) Giddings, J. C.; Chen, X. R.; Wahlund, K. G.; Myers, M. N. *Anal. Chem.* **1987**, *59*, 1957-1962.
- (34) Botana, A. M.; Ratanathanawongs, S. K.; Giddings, J. C. *J. Microcolumn Sep.* **1995**, *7*, 395-402.
- (35) Roessner, D.; Kulicke, W. M. *J. Chromatogr. A* **1994**, *687*, 249-258.
- (36) Thang, N. M.; Knopp, R.; Geckeis, H.; Kim, J. I.; Beck, H. P. *Anal. Chem.* **2000**, *72*, 1-5.
- (37) Lang, T.; Eslahian, K. A.; Maskos, M. *Macromol. Chem. Phys.* **2012**, *213*, 2353-2361.
- (38) Lattuada, M.; Olivo, C.; Gauer, C.; Storti, G.; Morbidelli, M. *Langmuir* **2010**, *26*, 7062-7071.
- (39) Thielking, H.; Roessner, D.; Kulicke, W. M. *Anal. Chem.* **1995**, *67*, 3229-3233.
- (40) Thielking, H.; Kulicke, W. M. *J. Microcolumn Sep.* **1998**, *10*, 51-56.
- (41) Kang, D. Y.; Kim, M. J.; Kim, S. T.; Oh, K. S.; Yuk, S. H.; Lee, S. *Anal. Bioanal. Chem.* **2008**, *390*, 2183-2188.
- (42) Zhang, J.; Haas, R. M.; Leone, A. M. *Anal. Chem.* **2012**, *84*, 6088-6096.
- (43) Kanzer, J.; Hupfeld, S.; Vasskog, T.; Tho, I.; Hoelig, P.; Mägerlein, M.; Fricker, G.; Brandl, M. *J. Pharm. Biomed. Anal.* **2010**, *53*, 359-365.
- (44) Prestel, H.; Niessner, R.; Panne, U. *Anal. Chem.* **2006**, *78*, 6664-6669.
- (45) Moon, M. H.; Kim, K.; Byun, Y.; Pyo, D. *J. Liq. Chromatogr. Relat. Technol.* **1999**, *22*, 2729-2740.
- (46) Schädlich, A.; Caysa, H.; Mueller, T.; Tenambergen, F.; Rose, C.; Göpferich, A.; Kuntsche, J.; Mäder, K. *ACS Nano* **2011**, *5*, 8710-8720.
- (47) Schädlich, A.; Rose, C.; Kuntsche, J.; Caysa, H.; Mueller, T.; Göpferich, A.; Mäder, K. *Pharm. Res.* **2011**, *28*, 1995-2007.
- (48) Robinson, H. C.; Horner, A. A.; Hook, M.; Ogren, S.; Lindahl, U. *J. Biol. Chem.* **1978**, *253*, 6687-93.
- (49) Augsten, C.; Kiselev, M. A.; Gehrke, R.; Hause, G.; Mäder, K. *J. Pharm. Biomed. Anal.* **2008**, *47*, 95-102.
- (50) Suresh, K. I.; Bartsch, E. *J. Appl. Polym. Sci.* **2013**, *127*, 208-216.
- (51) Blackburn, W. H.; Lyon, L. A. *Colloid Polym. Sci.* **2008**, *286*, 563-569.
- (52) Gaulding, J. C.; South, A. B.; Lyon, L. A. *Colloid Polym. Sci.* **2013**, *291*, 99-107.
- (53) Blackburn, W. H.; Dickerson, E. B.; Smith, M. H.; McDonald, J. F.; Lyon, L. A. *Bioconjugate Chem.* **2009**, *20*, 960-968.

- (54) Smith, M. H.; South, A. B.; Gaulding, J. C.; Lyon, L. A. *Anal. Chem.* **2010**, *82*, 523-530.
- (55) Utech, S.; Scherer, C.; Krohne, K.; Carrella, L.; Rentschler, E.; Gasi, T.; Ksenofontov, V.; Felser, C.; Maskos, M. *J. Magn. Magn. Mater.* **2010**, *322*, 3519-3526.
- (56) Noskov, S.; Scherer, C.; Maskos, M. *J. Chromatogr. A* **2013**, *1274*, 151-8.
- (57) Jungmann, N.; Schmidt, M.; Maskos, M. *Macromolecules* **2001**, *34*, 8347-8353.
- (58) Jungmann, N.; Schmidt, M.; Maskos, M.; Weis, J.; Ebenhoch, J. *Macromolecules* **2002**, *35*, 6851-6857.
- (59) Shimoda, A.; Sawada, S.; Kano, A.; Maruyama, A.; Moquin, A.; Winnik, F. M.; Akiyoshi, K. *Colloids Surf., B* **2012**, *99*, 38-44.
- (60) Soto-Cantu, E.; Cueto, R.; Koch, J.; Russo, P. S. *Langmuir* **2012**, *28*, 5562-5569.
- (61) Melucci, M.; Zambianchi, M.; Barbarella, G.; Manet, I.; Montalti, M.; Bonacchi, S.; Rampazzo, E.; Rambaldi, D. C.; Zattoni, A.; Reschiglian, P. *J. Mater. Chem.* **2010**, *20*, 9903-9909.
- (62) Xu, H.; Yan, F.; Monson, E. E.; Kopelman, R. *J. Biomed. Mater. Res., Part A* **2003**, *66A*, 870-879.
- (63) Loeschner, K.; Navratilova, J.; Legros, S.; Wagner, S.; Grombe, R.; Snell, J.; von der Kammer, F.; Larsen, E. H. *J. Chromatogr. A* **2013**, *1272*, 116-125.
- (64) Hagendorfer, H.; Kaegi, R.; Parlinska, M.; Sinnet, B.; Ludwig, C.; Ulrich, A. *Anal. Chem.* **2012**, *84*, 2678-2685.
- (65) Bolea, E.; Jimenez-Lamana, J.; Laborda, F.; Castillo, J. R. *Anal. Bioanal. Chem.* **2011**, *401*, 2723-2732.
- (66) Delay, M.; Dolt, T.; Woellhaf, A.; Sembritzki, R.; Frimmel, F. H. *J. Chromatogr. A* **2011**, *1218*, 4206-4212.
- (67) Pettibone, J. M.; Gigault, J.; Hackley, V. A. *ACS Nano* **2013**, *7*, 2491-2499.
- (68) Gigault, J.; Hackley, V. A. *Anal. Chim. Acta* **2013**, *763*, 57-66.
- (69) Hoque, M. E.; Khosravi, K.; Newman, K.; Metcalfe, C. D. *J. Chromatogr. A* **2012**, *1233*, 109-115.
- (70) Mitrano, D. M.; Barber, A.; Bednar, A.; Westerhoff, P.; Higgins, C. P.; Ranville, J. F. *J. Anal. At. Spectrom.* **2012**, *27*, 1131-1142.
- (71) Unrine, J. M.; Colman, B. P.; Bone, A. J.; Gondikas, A. P.; Matson, C. W. *Environ. Sci. Technol.* **2012**, *46*, 6915-6924.
- (72) Dieckmann, Y.; Cölfen, H.; Hofmann, H.; Petri-Fink, A. *Anal. Chem.* **2009**, *81*, 3889-3895.
- (73) Loos, K.; Boker, A.; Zettl, H.; Zhang, A. F.; Krausch, G.; Müller, A. H. E. *Macromolecules* **2005**, *38*, 873-879.
- (74) Augsten, C.; Mäder, K. *Int. J. Pharm.* **2008**, *351*, 23-30.
- (75) Mao, S.; Augsten, C.; Mäder, K.; Kissel, T. *J. Pharm. Biomed. Anal.* **2007**, *45*, 736-741.
- (76) Ma, P. L.; Buschmann, M.; Winnik, F. M. *Abstr. Pap. Am. Chem. Soc.* **2010**, *240*.
- (77) Ma, P. L.; Buschmann, M. D.; Winnik, F. M. *Anal. Chem.* **2010**, *82*, 9636-9643.
- (78) Ma, P. L.; Buschmann, M. D.; Winnik, F. M. *Biomacromolecules* **2010**, *11*, 549-554.
- (79) Kirkland, J. J.; Dilks, C. H.; Rementer, S. W. *Anal. Chem.* **1992**, *64*, 1295-1303.
- (80) Viebke, C.; Williams, P. A. *Anal. Chem.* **2000**, *72*, 3896-3901.
- (81) Wittgren, B.; Wahlund, K. G. *J. Chromatogr. A* **1997**, *760*, 205-218.
- (82) Andersson, M.; Wittgren, B.; Wahlund, K. G. *Anal. Chem.* **2001**, *73*, 4852-4861.
- (83) Andersson, M.; Wittgren, B.; Schagerlof, H.; Momcilovic, D.; Wahlund, K. G. *Biomacromolecules* **2004**, *5*, 97-105.
- (84) Tan, J. S.; Harrison, C. A.; Li, J. T.; Caldwell, K. D. *J. Polym. Sci., Part B: Polym. Phys.* **1998**, *36*, 537-542.
- (85) Boye, S.; Polikarpov, N.; Appelhans, D.; Lederer, A. *J. Chromatogr. A* **2010**, *1217*, 4841-4849.
- (86) Lederer, A.; Boye, S. *Lc Gc Europe* **2011**, *24*, 620-628.
- (87) Boye, S.; Appelhans, D.; Boyko, V.; Zschoche, S.; Komber, H.; Friedel, P.; Formanek, P.; Janke, A.; Voit, B. I.; Lederer, A. *Biomacromolecules* **2012**, *13*, 4222-4235.
- (88) Benincasa, M. A.; Caldwell, K. D. *J. Chromatogr. A* **2001**, *925*, 159-169.
- (89) Hasselov, M.; Hulthe, G.; Lyven, B.; Stenhagen, G. *J. Liq. Chromatogr. Relat. Technol.* **1997**, *20*, 2843-2856.
- (90) Petrov, P. D.; Drechsler, M.; Müller, A. H. E. *J. Phys. Chem. B* **2009**, *113*, 4218-4225.



- (91) Knop, K.; Mingotaud, A.-F.; El-Akra, N.; Violleau, F.; Souchard, J.-P. *Photochem. Photobiol. Sci.* **2009**, *8*, 396-404.
- (92) Ehrhart, J.; Mingotaud, A.-F.; Violleau, F. *J. Chromatogr. A* **2011**, *1218*, 4249-4256.
- (93) Miller, T.; Rachel, R.; Besheer, A.; Uezguen, S.; Weigandt, M.; Göpferich, A. *Pharm. Res.* **2012**, *29*, 448-459.
- (94) Benincasa, M. A.; Giddings, J. C. *J. Microcolumn Sep.* **1997**, *9*, 479-495.
- (95) Knappe, P.; Bienert, R.; Weidner, S.; Thünemann, A. F. *Macromol. Chem. Phys.* **2010**, *211*, 2148-2153.
- (96) Lee, S.; Kwen, H. D.; Lee, S. K.; Nehete, S. V. *Anal. Bioanal. Chem.* **2010**, *396*, 1581-1588.
- (97) Muthukrishnan, S.; Plamper, F.; Mori, H.; Müller, A. H. E. *Macromolecules* **2005**, *38*, 10631-10642.
- (98) Yohannes, G.; Holappa, S.; Wiedmer, S. K.; Andersson, T.; Tenhu, H.; Riekkola, M.-L. *Anal. Chim. Acta* **2005**, *542*, 222-229.
- (99) Glinel, K.; Vaugelade, C.; Muller, G.; Bunel, C. *Int. J. Polym. Anal. Charact.* **2000**, *6*, 89-107.
- (100) Yohannes, G.; Shan, J.; Jussila, M.; Nuopponen, M.; Tenhu, H.; Riekkola, M.-L. *J. Sep. Sci.* **2005**, *28*, 435-442.
- (101) Wittgren, B.; Wahlund, K. G.; Derand, H.; Wesslen, B. *Macromolecules* **1996**, *29*, 268-276.
- (102) Wittgren, B.; Wahlund, K. G.; Derand, H.; Wesslen, B. *Langmuir* **1996**, *12*, 5999-6005.
- (103) Le Cerf, D.; Simon, S.; Argillier, J.-F.; Picton, L. *Anal. Chim. Acta* **2007**, *604*, 2-8.
- (104) Thielking, H.; Kulicke, W. M. *Anal. Chem.* **1996**, *68*, 1169-1173.
- (105) Tank, C.; Antonietti, M. *Macromol. Chem. Phys.* **1996**, *197*, 2943-2959.
- (106) Adolph, U.; Kulicke, W. M. *Polymer* **1997**, *38*, 1513-1519.
- (107) Jiang, Y.; Miller, M. E.; Li, P.; Hansen, M. E. *Am. Lab.* **2000**, *32*, 98-99.
- (108) Knappe, P.; Bienert, R.; Weidner, S.; Thünemann, A. F. *Polymer* **2010**, *51*, 1723-1727.
- (109) Noga, M.; Edinger, D.; Klager, R.; Wegner, S. V.; Spatz, J. P.; Wagner, E.; Winter, G.; Besheer, A. *Biomaterials* **2013**, *34*, 2530-8.
- (110) Bourgoin, A.; Zabackis, E.; Poli, J. B. *Food Hydrocolloids* **2008**, *22*, 1607-1611.
- (111) Wittgren, B.; Borgstrom, J.; Piculell, L.; Wahlund, K. G. *Biopolymers* **1998**, *45*, 85-96.
- (112) Viebke, C.; Williams, P. A. *Food Hydrocolloids* **2000**, *14*, 265-270.
- (113) Reiner, J. E.; Jahn, A.; Stavis, S. M.; Culbertson, M. J.; Vreeland, W. N.; Burden, D. L.; Geist, J.; Gaitan, M. *Anal. Chem.* **2010**, *82*, 180-188.
- (114) Jahn, A.; Vreeland, W. N.; DeVoe, D. L.; Locascio, L. E.; Gaitan, M. *Langmuir* **2007**, *23*, 6289-6293.
- (115) Arifin, D. R.; Palmer, A. F. *Biotechnol. Prog.* **2003**, *19*, 1798-1811.
- (116) Arifin, D. R.; Palmer, A. F. *Artif. Cells Blood Substit. Biotechnol.* **2005**, *33*, 113-136.
- (117) Li, S. L.; Nickels, J.; Palmer, A. F. *Biomaterials* **2005**, *26*, 3759-3769.
- (118) Yohannes, G.; Wiedmer, S. K.; Tuominen, E. K. J.; Kinnunen, P. K. J.; Riekkola, M.-L. *Anal. Bioanal. Chem.* **2004**, *380*, 757-766.
- (119) Evjen, T. J.; Hupfeld, S.; Barnert, S.; Fossheim, S.; Schubert, R.; Brandl, M. *J. Pharm. Biomed. Anal.* **2013**, *78-79*, 118-22.
- (120) Lee, H.; Williams, S. K.; Allison, S. D.; Anchordoquy, T. J. *Anal. Chem.* **2001**, *73*, 837-43.
- (121) Kuntsche, J.; Decker, C.; Fahr, A. *J. Sep. Sci.* **2012**, *35*, 1993-2001.
- (122) Moon, M. H.; Giddings, J. C. *J. Pharm. Biomed. Anal.* **1993**, *11*, 911-920.
- (123) Vainikka, K.; Reijmar, K.; Yohannes, G.; Samuelsson, J.; Edwards, K.; Jussila, M.; Riekkola, M.-L. *Anal. Biochem.* **2011**, *414*, 117-124.
- (124) Hupfeld, S.; Holsaeter, A. M.; Skar, M.; Frantzen, C. B.; Brandl, M. *J. Nanosci. Nanotechnol.* **2006**, *6*, 3025-3031.
- (125) Korgel, B. A.; van Zanten, J. H.; Monbouquette, H. G. *Biophys. J.* **1998**, *74*, 3264-3272.
- (126) Li, S.; Palmer, A. F. *Langmuir* **2004**, *20*, 4629-4639.
- (127) Hupfeld, S.; Moen, H. H.; Ausbacher, D.; Haas, H.; Brandl, M. *Chem. Phys. Lipids* **2010**, *163*, 141-147.

- (128) Yohannes, G.; Pystynen, K. H.; Riekkola, M.-L.; Wiedmer, S. K. *Anal. Chim. Acta* **2006**, *560*, 50-56.
- (129) Hupfeld, S.; Ausbacher, D.; Brandl, M. *J. Sep. Sci.* **2009**, *32*, 3555-3561.
- (130) Kaluderovic, G. N.; Dietrich, A.; Kommera, H.; Kuntsche, J.; Mäder, K.; Mueller, T.; Paschke, R. *Eur. J. Med. Chem.* **2012**, *54*, 567-572.
- (131) Hong, J. S.; Stavis, S. M.; Lacerda, S. H. D.; Locascio, L. E.; Raghavan, S. R.; Gaitan, M. *Langmuir* **2010**, *26*, 11581-11588.
- (132) Moon, M. H.; Park, I.; Kim, Y. H. *J. Chromatogr. A* **1998**, *813*, 91-100.
- (133) Linden, M. V.; Meinander, K.; Hellel, A.; Yohannes, G.; Riekkola, M.-L.; Butcher, S. J.; Viitala, T.; Wiedmer, S. K. *Electrophoresis* **2008**, *29*, 852-862.
- (134) Decker, C.; Fahr, A.; Kuntsche, J.; May, S. *Chem. Phys. Lipids* **2012**, *165*, 520-529.
- (135) Castorph, S.; Henriques, S. S.; Holt, M.; Riedel, D.; Jahn, R.; Salditt, T. *Eur. Phys. J. E* **2011**, *34*.
- (136) Hupfeld, S.; Ausbacher, D.; Brandl, M. *J. Sep. Sci.* **2009**, *32*, 1465-1470.
- (137) Litzén, A.; Garn, M. B.; Widmer, H. M. *J. Biotechnol.* **1994**, *37*, 291-295.
- (138) Giddings, J. C.; Yang, F. J.; Myers, M. N. *Anal. Biochem.* **1977**, *81*, 395-407.
- (139) Kim, K. H.; Moon, M. H. *Anal. Chem.* **2009**, *81*, 1715-1721.
- (140) Oh, S.; Kang, D.; Ahn, S.-M.; Simpson, R. J.; Lee, B.-H.; Moon, M. H. *J. Sep. Sci.* **2007**, *30*, 1082-1087.
- (141) Qureshi, R. N.; Kok, W. T. *Lc Gc Europe* **2010**, *23*, 18-25.
- (142) Wahlund, K. G.; Litzén, A. *J. Chromatogr.* **1989**, *461*, 73-87.
- (143) Rambaldi, D. C.; Zattoni, A.; Reschiglian, P.; Colombo, R.; De Lorenzi, E. *Anal. Bioanal. Chem.* **2009**, *394*, 2145-2149.
- (144) Litzén, A.; Walter, J. K.; Krischollek, H.; Wahlund, K. G. *Anal. Biochem.* **1993**, *212*, 469-480.
- (145) Weber, C.; Wagner, M.; Baykal, D.; Höppener, S.; Paulus, R. M.; Festag, G.; Altuntas, E.; Schacher, F. H.; Schubert, U. S. *Macromolecules* **2013**, *46*, 5107-5116.
- (146) Wagner, M.; Reiche, K.; Blume, A.; Garidel, P. *Pharm. Dev. Technol.* **2013**, *18*, 963-970.
- (147) Pollastrini, J.; Dillon, T. M.; Bondarenko, P.; Chou, R. Y. T. *Anal. Biochem.* **2011**, *414*, 88-98.
- (148) Hawe, A.; Romeijn, S.; Filipe, V.; Jiskoot, W. *J. Pharm. Sci.* **2012**, *101*, 4129-4139.
- (149) Johann, C.; Elsenberg, S.; Roesch, U.; Rambaldi, D. C.; Zattoni, A.; Reschiglian, P. *J. Chromatogr. A* **2011**, *1218*, 4126-4131.
- (150) Pauck, T.; Cölfen, H. *Anal. Chem.* **1998**, *70*, 3886-3891.
- (151) Moon, M. H.; Kwon, H.; Park, I. *J. Liq. Chromatogr. Relat. Technol.* **1997**, *20*, 2803-2814.
- (152) Giddings, J. C.; Yang, F. J.; Myers, M. N. *J. Virol.* **1977**, *21*, 131-138.
- (153) Johann, C.; Ramage, P.; Hemmig, R. *Lc Gc Europe* **2005**, *18*, 535-538.
- (154) Yohannes, G.; Wiedmer, S. K.; Elomaa, M.; Jussila, M.; Aseyev, V.; Riekkola, M.-L. *Anal. Chim. Acta* **2010**, *675*, 191-198.
- (155) Ji, E.; Choi, S.-H.; Yoon, K. R.; Chun, J.-H.; Lee, S. *Bull. Korean Chem. Soc.* **2006**, *27*, 1433-1438.
- (156) Kim, K. H.; Moon, M. H. *Anal. Chem.* **2011**, *83*, 8652-8658.
- (157) Litzén, A.; Wahlund, K. G. *Anal. Chem.* **1991**, *63*, 1001-1007.
- (158) Litzén, A.; Wahlund, K. G. *J. Chromatogr.* **1991**, *548*, 393-406.
- (159) Litzén, A.; Wahlund, K. G. *J. Chromatogr.* **1989**, *476*, 413-421.
- (160) Kang, D.; Oh, S.; Ahn, S.-M.; Lee, B.-H.; Moon, M. H. *J. Proteome Res.* **2008**, *7*, 3475-3480.
- (161) Yie, J.; Wang, W.; Deng, L.; Tam, L.-T.; Stevens, J.; Chen, M. M.; Li, Y.; Xu, J.; Lindberg, R.; Hecht, R.; Veniant, M.; Chen, C.; Wang, M. *Chem. Biol. Drug Des.* **2012**, *79*, 398-410.
- (162) Hoppe, C. C.; Nguyen, L. T.; Kirsch, L. E.; Wiencek, J. M. *J. Biol. Eng.* **2008**, *2*, 10.
- (163) Rebolj, K.; Pahovnik, D.; Zagar, E. *Anal. Chem.* **2012**, *84*, 7374-83.
- (164) Luo, J.; Leeman, M.; Ballagi, A.; Elfving, A.; Su, Z. G.; Janson, J. C.; Wahlund, K. G. *J. Chromatogr. A* **2006**, *1120*, 158-164.
- (165) Setälä, N. L.; Holopainen, J. M.; Metso, J.; Wiedmer, S. K.; Yohannes, G.; Kinnunen, P. K. J.; Ehnholm, C.; Jauhiainen, M. *Biochemistry* **2007**, *46*, 1312-1319.
- (166) Zhang, Y.; Bhatt, V. S.; Sun, G.; Wang, P. G.; Palmer, A. F. *Bioconjugate Chem.* **2008**, *19*, 2221-2230.

- (167) Kim, K. H.; Lee, J. Y.; Lim, S.; Moon, M. H. *J. Chromatogr. A* **2013**, *1280*, 92-7.
- (168) Park, I.; Paeng, K. J.; Yoon, Y.; Song, J. H.; Moon, M. H. *J. Chromatogr. B* **2002**, *780*, 415-422.
- (169) Yohannes, G.; Sneck, M.; Varjo, S. J.; Jussila, M.; Wiedmer, S. K.; Kovanen, P. T.; Oorni, K.; Riekkola, M.-L. *Anal. Biochem.* **2006**, *354*, 255-265.
- (170) Qureshi, R. N.; Kok, W. T.; Schoenmakers, P. J. *Anal. Chim. Acta* **2009**, *654*, 85-91.
- (171) Rambaldi, D. C.; Reschiglian, P.; Zattoni, A.; Johann, C. *Anal. Chim. Acta* **2009**, *654*, 64-70.
- (172) Lee, J. Y.; Choi, D.; Johan, C.; Moon, M. H. *J. Chromatogr. A* **2011**, *1218*, 4144-4148.
- (173) Qureshi, R. N.; Kaal, E.; Janssen, H.-G.; Schoenmakers, P. J.; Kok, W. T. *Anal. Chim. Acta* **2011**, *706*, 361-366.
- (174) Rambaldi, D. C.; Zattoni, A.; Casolari, S.; Reschiglian, P.; Roessner, D.; Johann, C. *Clin. Chem.* **2007**, *53*, 2026-2029.
- (175) Li, P.; Hansen, M.; Giddings, J. C. *J. Liq. Chromatogr. Relat. Technol.* **1997**, *20*, 2777-2802.
- (176) Madorin, M.; van Hoogevest, P.; Hilfiker, R.; Langwost, B.; Kresbach, G. M.; Ehrat, M.; Leuenberger, H. *Pharm. Res.* **1997**, *14*, 1706-1712.
- (177) Kim, K. H.; Moon, M. H. *J. Proteome Res.* **2009**, *8*, 4272-4278.
- (178) Wei, Z.; McEvoy, M.; Razinkov, V.; Polozova, A.; Li, E.; Casas-Finet, J.; Tous, G. I.; Balu, P.; Pan, A. A.; Mehta, H.; Schenerman, M. A. *J. Virol. Methods* **2007**, *144*, 122-132.
- (179) McEvoy, M.; Razinkov, V.; Wei, Z. P.; Casas-Finet, J. R.; Tous, G. I.; Schenerman, M. A. *Biotechnol. Prog.* **2011**, *27*, 547-554.
- (180) Kuldvee, R.; D'Ulivo, L.; Yohannes, G.; Lindenburg, P. W.; Laine, M.; Oorni, K.; Kovanen, P.; Riekkola, M.-L. *Anal. Chem.* **2006**, *78*, 2665-2671.
- (181) Witos, J.; Cilpa, G.; Yohannes, G.; Oorni, K.; Kovanen, P. T.; Jauhiainen, M.; Riekkola, M.-L. *J. Sep. Sci.* **2010**, *33*, 2528-2535.
- (182) Kim, J. Y.; Kim, S.-K.; Kang, D.; Moon, M. H. *Anal. Chem.* **2012**, *84*, 5343-5350.
- (183) Maleki, A.; Lafitte, G.; Kjoniksen, A.-L.; Thuresson, K.; Nystrom, B. *Carbohydr. Res.* **2008**, *343*, 328-340.
- (184) Eike, J. H.; Palmer, A. F. *Biotechnol. Prog.* **2004**, *20*, 1225-1232.
- (185) Eike, J. H.; Palmer, A. F. *Biotechnol. Prog.* **2004**, *20*, 946-952.
- (186) Eike, J. H.; Palmer, A. F. *Biotechnol. Prog.* **2004**, *20*, 953-962.
- (187) Kim, K. H.; Kim, J. Y.; Kim, M. O.; Moon, M. H. *J. Proteomics* **2012**, *75*, 2297-2305.
- (188) Kang, D.; Yoo, J. S.; Kim, M. O.; Moon, M. H. *J. Proteome Res.* **2009**, *8*, 982-991.
- (189) Pedersen, L. R. L.; Nielsen, S. B.; Hansted, J. G.; Petersen, T. E.; Otzen, D. E.; Sorensen, E. S. *FEBS J.* **2012**, *279*, 336-347.
- (190) Silveira, J. R.; Raymond, G. J.; Hughson, A. G.; Race, R. E.; Sim, V. L.; Hayes, S. F.; Caughey, B. *Nature* **2005**, *437*, 257-261.
- (191) Silveira, J. R.; Hughson, A. G.; Caughey, B. *Method Enzymol* **2006**, *412*, 21-33.
- (192) Lim, S. B.; Lee, S. Y.; Choi, S.; Moon, J.; Hong, S. K. *Desalination* **2010**, *264*, 236-242.
- (193) Panyam, J.; Dali, M. M.; Sahoo, S. K.; Ma, W.; Chakravarthi, S. S.; Amidon, G. L.; Levy, R. J.; Labhasetwar, V. *J. Control. Release* **2003**, *92*, 173-187.
- (194) Lang, R.; Winter, G.; Vogt, L.; Zürcher, A.; Dorigo, B.; Schimmele, B. *Drug Dev. Ind. Pharm.* **2009**, *35*, 83-97.
- (195) Veurink, M.; Stella, C.; Tabatabay, C.; Pournaras, C. J.; Gurny, R. *Eur. J. Pharm. Biopharm.* **2011**, *78*, 271-277.
- (196) Demeule, B.; Palais, C.; Machaidze, G.; Gurny, R.; Arvinte, T. *mAbs* **2009**, *1*, 142-150.
- (197) Lang, R.; Vogt, L.; Zürcher, A.; Winter, G. *Am. Lab.* **2010**, *42*, 13-15.
- (198) Citkowitz, A.; Petry, H.; Harkins, R. N.; Ast, O.; Cashion, L.; Goldmarm, C.; Bringmarm, P.; Plummer, K.; Larsen, B. R. *Anal. Biochem.* **2008**, *376*, 163-172.
- (199) Miklautz, H.; Riemann, J.; Vidic, H. J. *J. Liq. Chromatogr.* **1986**, *9*, 2073-93.
- (200) Lipin, D. I.; Raj, A.; Lua, L. H. L.; Middelberg, A. P. J. *J. Chromatogr. A* **2009**, *1216*, 5696-5708.
- (201) Pease, L. F., III; Lipin, D. I.; Tsai, D.-H.; Zachariah, M. R.; Lua, L. H. L.; Tarlov, M. J.; Middelberg, A. P. J. *Biotechnol. Bioeng.* **2009**, *102*, 845-855.
- (202) Lipin, D. I.; Lua, L. H. L.; Middelberg, A. P. J. *J. Chromatogr. A* **2008**, *1190*, 204-214.

(203) Lipin, D. I.; Chuan, Y. P.; Lua, L. H. L.; Middelberg, A. P. J. *Arch. Virol.* **2008**, *153*, 2027-2039.

## Publication P2

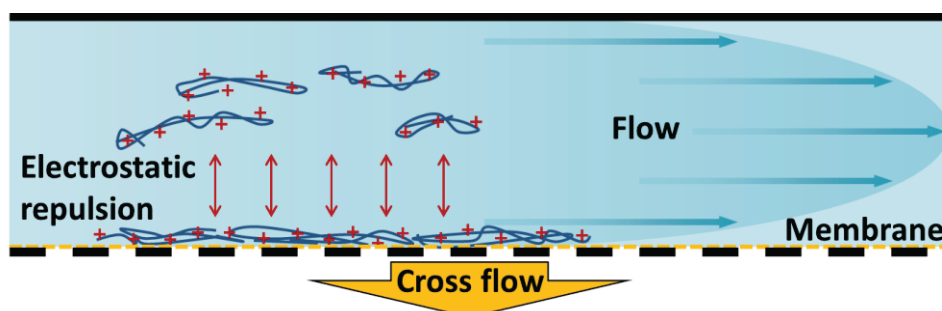
---

Characterization of cationic polymers by asymmetric flow field-flow fractionation and multi angle light scattering – a comparison with traditional techniques

M. Wagner, C. Pietsch, L. Tauhardt, A. Schallon, U. S. Schubert

*J. Chromatogr. A* **2013**, *1325*, 195-203.

---







# Characterization of cationic polymers by asymmetric flow field-flow fractionation and multi-angle light scattering—A comparison with traditional techniques



Michael Wagner<sup>a,b</sup>, Christian Pietsch<sup>a,b</sup>, Lutz Tauhardt<sup>a,b</sup>, Anja Schallon<sup>a,b</sup>,  
Ulrich S. Schubert<sup>a,b,\*</sup>

<sup>a</sup> Laboratory of Organic and Macromolecular Chemistry (IOMC), Friedrich Schiller University Jena, Humboldtstraße 10, 07743 Jena, Germany

<sup>b</sup> Jena Center for Soft Matter (JCSM), Friedrich Schiller University Jena, Philosophenweg 7, 07743 Jena, Germany

## ARTICLE INFO

### Article history:

Received 18 April 2013

Received in revised form

10 September 2013

Accepted 26 November 2013

Available online 7 December 2013

### Keywords:

Cationic polymers

Field flow fractionation

Gene delivery

PEI

PDMAEMA

PPL

## ABSTRACT

In the field of nanomedicine, cationic polymers are the subject of intensive research and represent promising carriers for genetic material. The detailed characterization of these carriers is essential since the efficiency of gene delivery strongly depends on the properties of the used polymer. Common characterization methods such as size exclusion chromatography (SEC) or mass spectrometry (MS) suffer from problems, e.g. missing standards, or even failed for cationic polymers. As an alternative, asymmetrical flow field-flow fractionation (AF4) was investigated. Additionally, analytical ultracentrifugation (AUC) and <sup>1</sup>H NMR spectroscopy, as well-established techniques, were applied to evaluate the results obtained by AF4. In this study, different polymers of molar masses between 10 and 120 kg mol<sup>-1</sup> with varying amine functionalities in the side chain or in the polymer backbone were investigated. To this end, some of the most successful gene delivery agents, namely linear poly(ethylene imine) (LPEI) (only secondary amines in the backbone), branched poly(ethylene imine) (B-PEI) (secondary and tertiary amino groups in the backbone, primary amine end groups), and poly(L-lysine) (amide backbone and primary amine side chains), were characterized. Moreover, poly(2-(dimethylamino)ethyl methacrylate) (PDMAEMA), poly(2-(amino)ethyl methacrylate) (PAEMA), and poly(2-(*tert*-butylamino)ethyl methacrylate) (PtBAEMA) as polymers with primary, secondary, and tertiary amines in the side chain, have been investigated. Reliable results were obtained for all investigated polymers by AF4. In addition, important factors for all methods were evaluated, e.g. the influence of different elution buffers and AF4 membranes. Besides this, the correct determination of the partial specific volume and the suppression of the polyelectrolyte effect are the most critical issues for AUC investigations.

© 2013 Elsevier B.V. All rights reserved.

## 1. Introduction

Polyelectrolytes, in particular cationic polymers, are a highly promising class of compounds in biological, pharmaceutical, and medical research. They represent promising carriers for genetic material like DNA or RNA into cells [1–3]. The efficiency of gene delivery strongly depends on different parameters, such as the molar mass and architecture of the used polymer, since they influence the cytotoxicity, the cellular uptake, and transfection efficiency, or in the case of siRNA the protein knockdown. To investigate these structure–property relationships, a detailed

molecular characterization of the polymers with respect to their physico-chemical properties is essential. In particular, key parameters such as molar mass, radius, architecture, intermolecular interactions, and conformation strongly influence the resulting macroscopic properties. For the determination of the molar mass, a large range of techniques are available in modern analytical and bioanalytical chemistry. Unfortunately, common methods like size exclusion chromatography (SEC) or mass spectrometry (MS) suffer problems or failed for polyelectrolytes, in particular for cationic ones [4,5]. While results from MS (MALDI–TOF MS or ESI–TOF MS) are difficult to achieve and the interpretation becomes more complex due to the probable multiply charged species in the polymer chain [6], SEC results should be regarded carefully, due to strong interactions of the polyelectrolytes with the column material and the lack of suitable standards for most of the cationic polymers [7]. Here, the development of modern stationary phases and the coupling of a multi-angle light scattering (MALS)

\* Corresponding author at: Laboratory of Organic and Macromolecular Chemistry (IOMC), Friedrich Schiller University Jena, Humboldtstraße 10, 07743 Jena, Germany. Tel.: +49 3641948201.

E-mail addresses: [ulrich.schubert@uni-jena.de](mailto:ulrich.schubert@uni-jena.de), [u.s.schubert@tue.nl](mailto:u.s.schubert@tue.nl) (U.S. Schubert).

detector to SEC can circumvent some of these limitations [8]. Other methods like viscosimetry or techniques based on colligative phenomena are applicable, but suffer the drawback that the constants in the Kuhn–Mark–Houwink–Sakurada equation are not available for most of these polymers, moreover, the determination of the degree of protonation of the polymer in water and the degree of dissociation are problematic. As a consequence, in solution the amount of species having counterions is not known. Further, important methods for characterization are NMR spectroscopy, static light scattering (SLS), and analytical ultracentrifugation (AUC). However, just average values and no or limited information about the polydispersity index (PDI) of the sample can be obtained. Having knowledge of the PDI is important from a synthetic and applicational point of view, particularly when structure–property relationships are investigated.

Due to intrinsic limitations described for the other analytical methods, asymmetric flow field-flow fractionation (AF4) coupled to a UV/RI and a MALS detector was investigated in this study as an alternative characterization method for cationic polyelectrolytes. AF4 was firstly introduced in 1966 by J. Calvin Giddings. It is an emerging technique and nowadays widely applied for colloids, e.g. nanoparticles or proteins [9]. Although preferred for the analysis of high molar mass samples, only rarely studies were performed using synthetic macromolecules, in particular polyelectrolytes of lower molar mass [10–13]. With AF4, the polymers are separated in a trapezoidal channel without any porous packing material according to their diffusion coefficient [14]. The separation of the sample is achieved by application of a cross-flow perpendicular to the direction of the sample flow through a semipermeable membrane with a defined molar mass cut-off (MWCO). A detailed description and theoretical consideration for the calculation of the diffusion coefficient based on the retention time was given by Wahlund and Giddings [15]. In comparison to classic chromatography techniques such as HPLC or SEC, AF4 contains no stationary phase, which reduces disturbing interactions and adsorption effects in the most cases. Moreover, the flow is less tortuous for the sample, due to the decreased shear forces in an empty channel. This is advantageous for sensitive biological samples [16]. Nowadays, in most cases, a MALS detector is used for the analysis after the fractionation process [17]. The calculation of molar mass or radius of gyration is based on the same principle as classic static light scattering. A common way to treat the data uses the well-known Zimm-plot. In contrast to classical SLS, the second virial coefficient  $A_2$  can be neglected due to the high dilution during the fractionation process.

In contrast to AF4, analytical ultracentrifugation (AUC) and  $^1\text{H}$  NMR spectroscopy are well-established techniques, which are used for many years for the characterization of biological and synthetic macromolecules [18–20]. It should be noted that both methods yield different molar mass averages. While  $^1\text{H}$  NMR spectroscopy gives the number average molar mass ( $M_n$ ), in AUC the sedimentation diffusion average molar mass ( $M_{SD}$ ) is obtained from sedimentation velocity experiments and the Svedberg equation (1). These methods can be used for the comparison of the results and to show the potentials and possible limitations of AF4 with regard to the characterization of (cationic) polymers.

In this study, cationic polymers of different molar masses with varying amine functionalities in the side chain or the polymer backbone (Fig. 1) were investigated for the first time by AF4. As the most successful gene delivery agents, a tailor-made linear, and commercially available linear and branched poly(ethylene imine)s (L-PEI, B-PEI) were characterized [21]. Moreover, poly(2-(dimethylamino)ethyl methacrylate) (PDMAEMA), poly(2-(amino)ethyl methacrylate) (PAEMA), and poly(2-(*tert*-butylamino)ethyl methacrylate) (*t*BAEMA) as polymers with primary, secondary, and tertiary amines in the side chain were studied. Additionally, two samples of different molar masses of commercially available poly(L-lysine) (PLL), a prominent polyamino acid in gene delivery research [22], are analyzed by AF4. As AF4-MALS is typically not applied to low molar mass ( $M < 100 \text{ kg mol}^{-1}$ ) polymers, this study focuses on the evaluation of AF4 as a potential alternative for characterization of these cationic polyelectrolytes. Therefore, the results obtained from the synthesized methacrylate based cationic polymers are compared to well-established methods like  $^1\text{H}$  NMR spectroscopy, SEC and AUC. Beside the determination of the molar masses and the polydispersity index values, different types of membranes and eluents were evaluated to identify optimal conditions for the analysis. This should also reveal potential interactions with the membrane and show how far it affects the retention behavior and the obtained results. PDMAEMA was studied in more detail by AF4 to gain deeper insight into the conformation as well as the influence of ionic strength and pH value on the retention behavior. This study shows that AF4 allows fast and reliable characterization of cationic polymers. Moreover, the limitations concerning molar mass limits and membrane interactions for different classes of cationic polymers are discussed in detail.

## 2. Experimental

### 2.1. Materials

Poly(L-lysine) (PLL) and branched poly(ethylene imine) (B-PEI<sub>com</sub>) were purchased from Sigma Aldrich (Steinhausen, Germany). Linear poly(ethylene imine) (L-PEI<sub>com</sub>) was purchased from Polysciences (Eppelheim, Germany). Methyl tosylate and 2-ethyl-2-oxazoline (EtOx) were purchased from Acros Organics (Geel, Belgium), distilled to dryness over barium oxide (BaO), and stored under argon. A second linear poly(ethylene imine) (L-PEI<sub>600</sub>) was synthesized by acidic hydrolysis of poly(2-ethyl-2-oxazoline) (PEtOx) in a microwave synthesizer (Biotage) as described recently (see supporting info SI-I) [6].

2-(Dimethylamino)ethyl methacrylate (DMAEMA), 2-aminoethyl methacrylate hydrochloride (AEMA) and 2-(*tert*-butylamino)ethyl methacrylate (*t*BAEMA) were purchased from Sigma–Aldrich and purified by stirring in the presence of inhibitor-remover for hydroquinone or hydroquinone monomethyl ether (Aldrich) for 30 min prior to use. The initiators 4,4'-azobis(4-cyanopentanoic acid) (ACVA), 1,1'-azobis(cyclohexane carbonitrile) and 4-cyano-4-(phenylcarbonothioylthio)pentanoic acid as well as 4-cyano-4-[(dodecylsulfanylthiocarbonyl) sulfanyl] pentanoic acid RAFT agents were purchased from

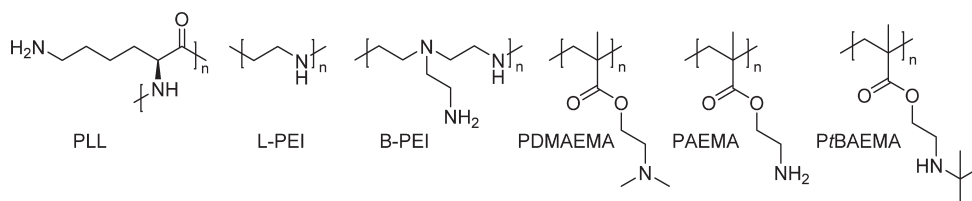


Fig. 1. Schematic representation of the structure of the polymers used in this study.



Sigma–Aldrich. Poly(2-(dimethylamino)ethyl methacrylate) (PDMAEMA), poly(2-(amino)ethyl methacrylate) (PAEMA), and poly(2-(*tert*-butylamino)ethyl methacrylate) (PtBAEMA) were synthesized using the RAFT polymerization technique (see supporting info SI-II) [23,24]. All solvents, salts and other chemicals used in this study were of analytical grade or better.

## 2.2. Analytical ultracentrifugation (AUC)

AUC was performed using a Beckman XL-I analytical ultracentrifuge (ProteomeLab XLI Protein Characterization System). Experiments were carried out in double-sector epon or aluminum centerpieces, depending on the solvent, with optical path length of 12 mm in a four holes rotor setup. Each cell was filled with 0.44 mL of solvent and 0.42 mL of sample. A rotor speed of 40,000 rpm was used for all samples. The system was equilibrated for 40 min at 25 °C in the centrifuge. Sedimentation data were recorded by absorbance optics. Data analysis was done by the Sedfit software [25]. For  $c(s)$  analysis of sedimentation data, the partial specific volume of the polymers was determined *via* AUC using the “density variation method” as described by Mächtle [26]. For calculating the molar mass the Svedberg equation (1) was used:

$$M_{sD} = \frac{s_0 RT}{D_0(1 - \bar{v}\rho)} \quad (1)$$

Here,  $R$  is the universal gas constant,  $T$  is the temperature,  $s_0$  is the sedimentation coefficient,  $D_0$  is the translational diffusion coefficient,  $\bar{v}$  is the partial specific volume and  $\rho$  is the density of the solvent. Solvent density and viscosity measurements were performed on a DMA 02 density meter (Anton Paar, Graz, Austria) and an AMVn falling sphere viscometer (Anton Paar).  $s_0$  was obtained by measurement of at least three concentrations and extrapolation to zero concentration using the Gralen relations [27].

## 2.3. Dynamic light scattering

Dynamic light scattering (DLS) was performed using an ALV-CGS-3 system (ALV, Langen, Germany) equipped with a He–Ne laser operating at a wavelength of  $\lambda = 633$  nm. The counts were detected at angles  $\theta$  of 30°, 60°, 90°, 120°, and 150°. All measurements were carried out at 25 °C after an equilibration time of 120 s. All polymers were measured at three different concentrations. For analyzing the autocorrelation function, the CONTIN algorithm [28] was applied. The diffusion coefficient was obtained by linear extrapolation of the apparent diffusion coefficient to zero concentration and  $\theta = 0^\circ$ . Hydrodynamic radii were calculated according to the Stokes–Einstein equation (2):

$$R_H = \frac{kT}{6\pi\eta D_0} \quad (2)$$

Here,  $R_H$  is the hydrodynamic radius,  $k$  is the Boltzmann constant,  $T$  is the absolute temperature,  $\eta$  is the viscosity of the sample, and  $D_0$  is the translational diffusion coefficient.

## 2.4. Asymmetric flow field-flow fractionation (AF4)

Asymmetric flow field-flow fractionation (AF4) was performed on an AF2000 MT System (Postnova Analytics, Landsberg, Germany) coupled to an UV (PN3211, 260 nm), RI (PN3150) and MALS (PN3070, 633 nm) detector. The eluent is delivered by three different pumps (tip, focus, cross-flow) and the sample is injected by an autosampler (PN5300) into the channel. The channel has a trapezoidal geometry and an overall area of 31.6 cm<sup>2</sup>. The nominal height of the spacer was 500  $\mu$ m and a regenerated cellulose membrane (Z-MEM-AQU-670, PostNova Analytics) with a MWCO of 10 kg mol<sup>-1</sup> was used as accumulation wall, if not stated otherwise.

All experiments were carried out at 25 °C. For each measurement 20  $\mu$ L of the sample were injected with an injection flow rate of 0.2 mL min<sup>-1</sup> for 7 min. For PLL and L/B-PEI the detector flow rate was set to 0.6 mL min<sup>-1</sup> and 0.8 mL min<sup>-1</sup> for PDMAEMA, PAEMA and PtBAEMA. The cross-flow rate was set to 5 mL min<sup>-1</sup> for PLL, 4.5 mL min<sup>-1</sup> for L-PEI and 4 mL min<sup>-1</sup> for B-PEI<sub>com</sub> as well as the methacrylate based polymers. After the focusing step, the cross-flow rate was kept constant for 5 min and then reduced under an exponential gradient (0.5) within 20 min to 0.1 mL min<sup>-1</sup>. Afterwards, the cross-flow rate was reduced under a linear gradient to zero within 5 min and then kept constant for 20 min to ensure complete elution. For calculation of the molar mass and the radius of gyration from the MALS signal, the Zimm plot, according to Eq. (3), was used [29]. All measurements were repeated five times

$$\frac{Kc}{R(\theta)} = \frac{1}{M} \left( 1 + \frac{2}{3!} \langle R_g^2 \rangle \left[ \frac{4\pi n_0}{\lambda} \sin \frac{\theta}{2} \right]^2 \right) \quad (3)$$

$$K = \frac{(2\pi n_0 (dn/dc))^2}{\lambda^4 N_A} \quad (4)$$

Here,  $K$  is a constant factor according to Eq. (4),  $c$  is the concentration,  $R$  is the excess Rayleigh ratio,  $M$  is the molar mass,  $R_g$  is the radius of gyration,  $\lambda$  is the laser wavelength,  $\theta$  is the scattering angle,  $n_0$  is the refractive index of the solvent,  $N_A$  is the Avogadro's number and  $dn/dc$  is the refractive index increment.

## 2.5. Refractive index increment

The refractive index increment of the samples was measured by manual injection of a known concentration directly into the AF4 channel without any focusing or cross-flow. Integration of the RI signal and comparison with the injected mass gives the  $dn/dc$  value. All measurements were repeated five times. To increase the accuracy, all polymers were dissolved in the eluent of the corresponding AF4 run.

## 2.6. <sup>1</sup>H NMR spectroscopy

Proton nuclear magnetic resonance (<sup>1</sup>H NMR) spectra were recorded on a Bruker AC 300 (300 MHz) spectrometer at 298 K. The chemical shifts are reported in parts per million (ppm,  $\delta$  scale) relative to the signals from the NMR solvents. The standard deviations were calculated using the individual –CH<sub>2</sub>– signals of the polymer.

## 2.7. Size-exclusion chromatography

Size-exclusion chromatography (SEC) of the PEtOx precursor, PDMAEMA and PAEMA was performed on a system using an Agilent1200 series system, a G1310A pump, G1329A autosampler, a G1362A refractive index detector and both a PSS Gram 30 and a PSS Gram 1000 column in series, whereby *N,N*-dimethylacetamide (DMAc) with 50 mM lithium chloride was used as an eluent at 1 mL min<sup>-1</sup> flow rate and the column oven was set to 40 °C. The system was calibrated against polystyrene ( $M_n$  from 374 g mol<sup>-1</sup> to 1,040,000 g mol<sup>-1</sup>) standards. Additional SEC experiments of PtBAEMA were performed on a JASCO system equipped with a PU-980 pump, a RI-930 refractive index detector and a PSS SUPREMA-MAX guard/300 Å column using water with 0.1% trichloroacetic acid (pH 2.3) and 0.05 M NaCl as eluent and the column oven was set to 30 °C. A calibration with low PDI pullulan standards was used.

### 3. Results and discussion

In principle, AF4 coupled to a UV/RI-MALS detector allows a detailed characterization of biological and synthetic macromolecules or nanoparticles by combination of a gentle separation with the broad molar mass and size range of SLS. Nevertheless, AF4-MALS was, to the best of our knowledge, never applied on these kinds of polymers. Therefore, the results have to be compared to already well-established methods. On the one hand, data from the supplier were used for the commercially available polymers (PLL, B-PEI<sub>com</sub>, L-PEI<sub>com</sub>) that are often obtained by classic light scattering, SEC, or viscosity. On the other hand, polymers synthesized in our lab (polymethacrylates, L-PEI<sub>600</sub>) were characterized using AUC, SEC, and end group analysis by <sup>1</sup>H NMR.

#### 3.1. AF4 – choice of eluent and membrane

For AF4, several types of membranes with different MWCOs and different eluents can be used to influence the retention of the sample. Besides the limitations of the MALS detector, the MWCO of the membrane predefines the lowest molar mass, which can be studied. All samples with a molar mass below the MWCO will, in theory, pass through the membrane and, hence, cannot be analyzed. Another important parameter, with regard to the used solvent and the potential interactions between the sample and the membrane surface, is the chemical nature of the membrane. The available membranes have different surface charges as well as varying degrees of hydrophilicity and hydrophobicity. In the case of aqueous eluents, the interactions with the sample can be affected by adjusting the pH, addition of surfactants or increasing the ionic strength, e.g. for screening of charges. Also the adsorption of ions or the addition of chaotropic or kosmotropic agents, which influence the hydration of the sample, can alter the interactions and the resulting retention behavior [30]. Since the investigated polymers show a high positive charge density and in the case of the methacrylate based polymers a hydrophobic backbone, several eluent compositions and three different membranes were evaluated, namely: a regenerated cellulose (RC), a cellulose triacetate (CTA), and a polyvinylidene difluoride (PVDF) membrane. As eluents water with different amounts of sodium chloride, sodium azide, sodium hydroxide, and solutions containing urea as chaotropic agent were investigated. Additionally, an acetate as well as an ammonia buffer at different pH values and ionic strength were studied. On PVDF and CTA based membranes, strong sample interactions were observed, leading to peak deformation and broadening (SI-III). This behavior was independent of the ionic strength, which was varied from 0 to 150 mM NaCl. In particular, CTA membranes with a MWCO < 10 kg mol<sup>-1</sup> and PVDF membranes (MWCO 30 kg mol<sup>-1</sup>) showed large deviations between different batches. These findings can probably be attributed to a non-uniform pore size distribution. The best results were obtained using a RC membrane with a MWCO of 10 kg mol<sup>-1</sup> and water containing 0.02% NaN<sub>3</sub>, to avoid bacterial growth, as eluent. The isoelectric point of this membrane is around 3.4, so that it is negatively charged at pH > 3.4 and positively charged at pH < 3.4 [31]. At neutral pH, this causes attractive

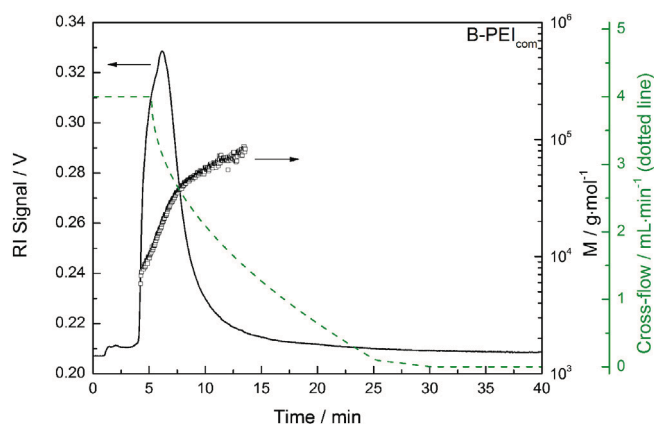


Fig. 2. AF4 fractogram with the corresponding cross-flow rate and molar masses of B-PEI<sub>com</sub>.

electrostatic interactions between the negative surface of the membrane and the positive charges in the polymer, and consequently leads to the adsorption of polymer chains onto the surface of a fresh RC membrane after the first injection. During further injections repulsive forces occur between the now positively charged membrane surface and the sample, leading to reduced interactions and fast retention [32]. Taking this into account, the polyelectrolyte saturated RC membrane was used to determine the molar mass of all polymers investigated in this study.

#### 3.2. Poly(ethylene imine) (PEI)

PEI is a well-known cationic polymer and used in several applications, e.g. for waste water treatment [33], as flocculant in paper industry [34], and it is of high interest in the field of gene delivery [35]. PEI is widely applied for the delivery of plasmid DNA as well as mRNA or siRNA [36–38]. Different architectures and molar masses are available, but typically, linear or hyperbranched structures with molar masses of around 25 kg mol<sup>-1</sup> were used [39,40]. Here, two commercially available PEIs, a linear (L-PEI<sub>com</sub>) and a branched (B-PEI<sub>com</sub>), with a given molar mass ( $M_w$ ) of around 25 kg mol<sup>-1</sup> as well as a tailor-made linear PEI (L-PEI<sub>600</sub>) with a theoretical molar mass ( $M_n$ ) of around 26 kg mol<sup>-1</sup> were characterized. The results obtained by AF4-MALS and the Zimm-plot are shown in Table 1. A representative AF4 fractogram of B-PEI<sub>com</sub> is shown in Fig. 2 (for L-PEIs see SI-IV). In the case of B-PEI<sub>com</sub> a complete separation between the void peak and the main peak was observed, whereas for both L-PEIs no full baseline separation was possible. This was also the case at higher cross-flows (data not shown). The measured values agree well to the data provided by the manufacturers and the PDI values are in the known range for hyperbranched and linear PEIs [6]. For B-PEI<sub>com</sub> the  $M_n$  obtained by AF4 (13.4 kg mol<sup>-1</sup>) is higher compared to the value given by the manufacturer (10 kg mol<sup>-1</sup>). This deviation is probably due to the MWCO of the RC membrane (10 kg mol<sup>-1</sup>), which can lead to a loss of low molar mass species through the membrane. For the L-PEI<sub>600</sub> the  $M_n$  (24.3 kg mol<sup>-1</sup>) obtained by AF4-MALS differs only slightly

Table 1  
Molar masses given by the manufacturers and values obtained by AF4 for PEI.

Sample	Molar mass/kg mol <sup>-1</sup>	$M_n$ (AF4)/kg mol <sup>-1</sup>	$M_w$ (AF4)/kg mol <sup>-1</sup>	PDI (AF4)
B-PEI <sub>com</sub>	10.0 ( $M_n$ ) <sup>a</sup> , 25.0 ( $M_w$ ) <sup>b</sup>	13.4 ± 1.4	25.4 ± 1.2	1.91
L-PEI <sub>com</sub>	25.0 ( $M_w$ ) <sup>b</sup>	19.9 ± 1.5	26.1 ± 1.3	1.31
L-PEI <sub>600</sub>	26.0 (theoretical $M_n$ ) <sup>c</sup>	24.3 ± 2.7	32.0 ± 2.7	1.32

<sup>a</sup> Obtained by SEC as specified by the manufacturer.

<sup>b</sup> Obtained by light scattering as specified by the manufacturer.

<sup>c</sup> Calculated from the M/I ratio used for the synthesis of the PETox precursor.

**Table 2**  
Molar masses given by the manufacturers and values obtained by AF4 of PLL.

Sample	Molar mass/kg mol <sup>-1</sup>	M <sub>n</sub> (AF4)/kg mol <sup>-1</sup>	M <sub>w</sub> (AF4)/kg mol <sup>-1</sup>	PDI (AF4)
PLL-1	15–30 (M <sub>n</sub> ) <sup>a</sup>	16.8 ± 0.7	20.9 ± 0.8	1.25
PLL-2	30–70 (M <sub>n</sub> ) <sup>a</sup>	23.4 ± 1.86	30.8 ± 2.9	1.32

<sup>a</sup> Obtained by viscosity as specified by the manufacturer.

from the theoretical M<sub>n</sub> (26 kg mol<sup>-1</sup>), which is calculated from the monomer to initiator ratio (M/I) used for the synthesis of the poly(2-ethyl-2-oxazoline) (PEtOx) precursor. This slight difference probably derives from difficulties in adjusting the M/I ratio. For high molar masses only a very small amount of initiator is required in comparison to the monomer, which results in an increased weighing error. Taking the refractive index increment into account, the studied PEIs reached the lower detection limit of the MALS detector (low signal to noise ratio) for calculation of molar masses from the Zimm plot. In particular, linear PEIs with lower molar masses (<10 kg mol<sup>-1</sup>) did not show a reliable light scattering signal, which can be distinguished from the baseline (data not shown). A molar mass of 15–20 kg mol<sup>-1</sup> was found to be the acceptable minimum for L-PEI. For these low molar mass polymers the radius of gyration could not be obtained. Here, the minimum is around 8–10 nm [41].

### 3.3. Poly(L-lysine) (PLL)

Another class of polymers with high importance for industrial and research applications is the polyamino acid poly(L-lysine) (PLL). It is widely used for the preparation of surfaces for cell attachment, as preservative in food products, and also as polyplex forming carrier in the field of gene delivery [3,42–44]. In this study, PLLs of two different molar masses were investigated. The results obtained by AF4-MALS are shown in Table 2. Fractograms of PLL-1 and PLL-2 are shown in Fig. 3 and SI-V, respectively. While the values obtained for PLL-1 are in accordance with the data provided by the supplier (15–30 kg mol<sup>-1</sup>, measured by viscosity), the molar masses by AF4 for PLL-2 are lower (M<sub>n</sub> 23.4 kg mol<sup>-1</sup>), compared to the given specification (30–70 kg mol<sup>-1</sup>, measured by viscosity). Two explanations are conceivable. First, the data obtained by viscosity are limited to the accurate determination of the constants in the Kuhn–Mark–Houwink–Sakurada equation (5) and, second, some kind of polymer degradation could occur. It should also be noted that the lower detection limit of the light scattering signal for accurate measurement of the molar mass is reached for PLL-1, resulting in a low signal to noise ratio. However, the data show that

AF4 is still applicable for the analysis of this kind of biodegradable polymers even if they have a low molar mass.

### 3.4. Methacrylate based polymers

The third class of polymers, investigated in this study, is based on polymethacrylates. Within this class, polymers with primary, secondary and tertiary amino groups in the side chain were investigated, namely PAEMA, PtBAEMA, and PDMAEMA (Fig. 1). In particular, PDMAEMA is well-known for gene delivery applications [45,46] and was, therefore, further investigated at four different molar masses. All methacrylate based polymers were successfully characterized by AF4. A representative fractogram of PDMAEMA<sub>500</sub> is shown in Fig. 4 (for PAEMA, PtBAEMA and the other PDMAEMAs see SI-VI). Reliable molar masses and, even more importantly, PDI values were obtained (Table 3). For comparison with traditional chromatography methods, analysis was additionally performed on a common SEC-RI system with DMAc/LiCl as eluent and polystyrene as calibration standard. It was found that the obtained molar mass (SI-II) differs significantly from the results obtained by AF4. This finding is ascribed to the lack of a suitable standard and the use of a MALS detector similar as for AF4 would circumvent this problem. However, this does not solve the problem of polymer-column interactions which can occur for this kind of polymers, as shown for PtBAEMA<sub>170</sub> in SI-VII. Since interactions were present at both, AF4 and SEC, the general statement that AF4 shows less interactions than SEC cannot be abided for these cationic polyelectrolytes. To verify the AF4 data, <sup>1</sup>H NMR and AUC were applied (Table 3). As a standard method to determine M<sub>n</sub>, end group analysis by <sup>1</sup>H NMR was performed by comparison of the integral, in this case the aromatic RAFT end group and the integrals from the repeating units in the polymer. Unfortunately, this method is limited to relatively low molar masses, as the integral volumes of the end group decreases with increasing degree of polymerization. A typical <sup>1</sup>H NMR spectrum for PDMAEMA<sub>320</sub> synthesized via RAFT is shown in SI-VIII. In addition to <sup>1</sup>H NMR spectroscopy, AUC was applied. It is a powerful technique for characterization of macromolecules and

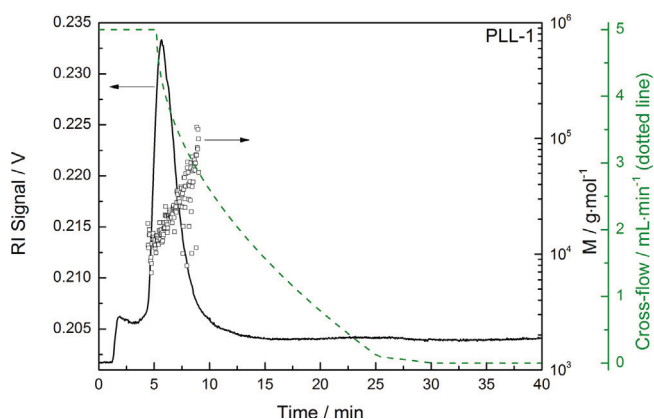


**Fig. 3.** AF4 fractogram with the corresponding cross-flow rate and molar masses of PLL-1.

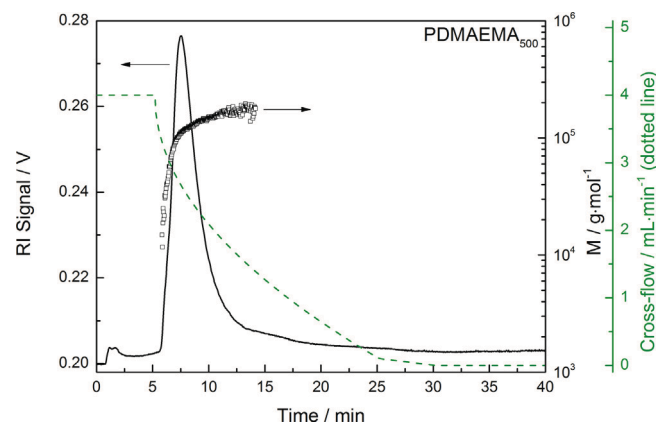


**Fig. 4.** AF4 fractogram with the corresponding cross-flow rate and molar masses of PDMAEMA<sub>500</sub>.

**Table 3**  
Molar masses and PDI values of the methacrylate based cationic polymers obtained by  $^1\text{H}$  NMR spectroscopy, AUC, and AF4.

Sample	$M_n$ (NMR)/ $\text{kg mol}^{-1}$ <sup>a</sup>	$M_{SD}$ (AUC)/ $\text{kg mol}^{-1}$	$M_n$ (AF4)/ $\text{kg mol}^{-1}$	$M_w$ (AF4)/ $\text{kg mol}^{-1}$	PDI (AF4)
PDMAEMA <sub>90</sub>	14.5 ± 0.2	16.3 ± 0.3	14.7 ± 0.7	16.8 ± 0.4	1.14
PDMAEMA <sub>230</sub>	36.3 ± 3.3	42.5 ± 0.2	36.1 ± 0.61	41.1 ± 0.72	1.14
PDMAEMA <sub>320</sub>	42.6 ± 1.9	65.8 ± 1.7	51.2 ± 1.9	67.3 ± 1.2	1.31
PDMAEMA <sub>500</sub>	72.3 ± 1.6	112.0 ± 2.6	80.2 ± 2.1	113.1 ± 1.0	1.41
PAEMA <sub>150</sub>	25.0 ± 0.2	27.2 ± 1.4	24.9 ± 1.2	29.1 ± 1.2	1.17
PtBAEMA <sub>170</sub>	31.2 ± 2.8	36.0 ± 0.6	29.9 ± 2.3	37.3 ± 1.3	1.25

<sup>a</sup> Measured in  $\text{CD}_2\text{Cl}_2$  or  $\text{D}_2\text{O}$ .

nanomedicines, such as nanoparticles or polyplexes [47]. The molar mass ( $M_{SD}$ ), obtained by sedimentation velocity experiments and the Svedberg equation (1), is a weight-average molar mass comparable to  $M_w$  [48]. Here, the translational diffusion coefficient, which is measured by DLS, is required for calculations. For an accurate determination of the molar mass by AUC the suppression of the polyelectrolyte effect is of the utmost importance [48]. Therefore, an aqueous solution of 150 mM NaCl and 1 mM NaOH was used to guaranty that the polymers are in the unionized state [49]. For PtBAEMA<sub>170</sub>, which is not soluble under these conditions, methanol containing 1 mM NaOH was used as solvent. The suppression of the polyelectrolyte effect can be proven by the measurement of the reduced viscosity as shown exemplarily for PDMAEMA<sub>500</sub> in SI-IX. A linear positive slope at low concentrations indicates the absence of any polyelectrolyte specific behavior. An overview of the molar mass obtained by AUC can be found in Table 3. For PAEMA<sub>150</sub>, PtBAEMA<sub>170</sub>, PDMAEMA<sub>90</sub>, and PDMAEMA<sub>230</sub> the molar masses obtained by AF4-MALS are in good accordance with the molar masses from  $^1\text{H}$  NMR spectroscopy, AUC, and the theoretical molar masses. For the two polymers with higher molar mass (PDMAEMA<sub>320/500</sub>), the results from AF4 correlate well to those by AUC, whereas larger deviations to the molar masses obtained by  $^1\text{H}$  NMR were observed. These differences are probably caused by limitations of  $^1\text{H}$  NMR spectroscopy for high molar mass polymers, as the signal integral of the used RAFT agents decreases with increasing molar mass (M/I), resulting in a lower signal to noise ratio. This results in the calculation of lower molar masses. In case of the synthesis of high molar mass polymers by RAFT, also the probability of side reactions, e.g. chain termination reaction, increases, affecting the end group fidelity (not each chain has the specific RAFT end group). Here, AF4-MALS is more reliable since the accuracy in light scattering increases with increasing size and molar mass. An advantage of AF4 over AUC is the reduced measurement time. Moreover, less material is required for the measurements and information about the polydispersity can easily be obtained.

Since the molar masses of the investigated PDMAEMA polymers ranges from around 15 to 80  $\text{kg mol}^{-1}$ , larger differences between the retention times of the different polymers were expected, as their diffusion coefficients differ remarkably. However, this was not the case. All polymers show similar retention times or just slight changes (Fig. 4 and SI-VI). This indicates that the elution is highly influenced by other forces, than cross-flow and diffusion, leading to a certain equilibrium height in the channel. Probably the repulsive electrostatic forces between the positive charges on the surface and the sample in solution govern the retention. This leads to a larger equilibrium height of the polymer and results in a faster elution due to the higher flow velocity in the center of the channel. This assumption is supported by the observation that a change of the cross-flow rate (up to  $6\text{ mL min}^{-1}$ ) only slightly influenced the retention time (data not shown). To gain further information on the interactions and the conformation of PDMAEMA, the high molar mass PDMAEMA<sub>500</sub> was investigated in more detail.

### 3.5. Influence of sample concentration and ionic strength

As already mentioned, the choice of eluent and its composition essentially influences the retention behavior in AF4. In particular, for charged samples, like polyelectrolytes, the ionic strength of the solvent plays an important role for the interactions in the separation channel. An increase of ionic strength results in a reduction of the range of attractive or repulsive electrostatic forces (Debye length) and can, therefore, be used to adjust the interactions between the polymer or colloid itself and the interactions between the polymer and the membrane surface. To investigate this effect on the retention behavior, PDMAEMA<sub>500</sub> was studied at different concentrations of NaCl (5–150 mM) by AF4 (Fig. 5). The applied separation method was the same as for molar mass determination of all methacrylate based polymers. It was found that the retention time is shifted to higher values with increasing concentration of NaCl or ionic strength, respectively. The recovery rate increased slightly from around 80% at 5 mM to 84% at 150 mM NaCl. Additionally, a peak broadening with a shoulder in the beginning and at the end was observed. At salt concentrations higher than 50 mM NaCl, the retention time and the peak shape does not change significantly, except small alterations of the shoulder at the end. This can probably be attributed to the switch-off of the cross-flow at 25 min and was a general observation for different polymers and methods. The molar masses obtained at different concentrations of NaCl are identical and show no deviations therefore, excluding the possibility of the degradation or alteration of the sample. The shift in the retention time is a further indication of the dominating effect of electrostatic interactions at low ionic strength. As mentioned above (3.1), the fresh membrane surface is saturated with cationic PDMAEMA<sub>500</sub> after the first run, as indicated by a lower recovery rate of 70% in contrast to around 80% for subsequent runs. The repulsive long-ranged electrostatic interactions between

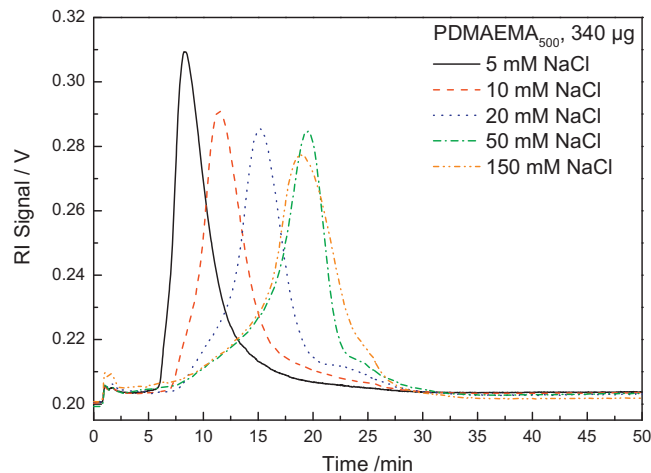


**Fig. 5.** AF4 fractograms (RI) of PDMAEMA<sub>500</sub> at different concentrations of NaCl present in the eluent.

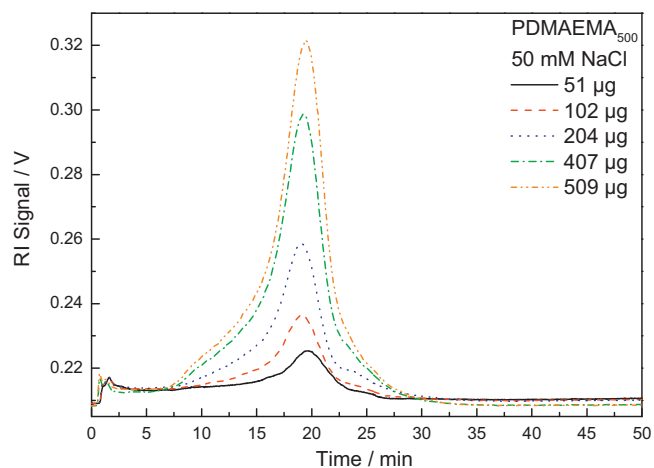


Fig. 6. AF4 fractograms (RI) of PDMAEMA<sub>500</sub> and different amounts of injected polymer mass.

the positive formulated surface and the cationic polymer lead to a movement of the sample in a certain distance to the membrane, resulting in a faster elution, caused by a higher flow velocity in the center of the channel compared to the accumulation wall. With increasing ionic strength, the long-ranged electrostatic forces are more shielded and the sample could move closer to the membrane [50], facilitating other short-ranged interactions such as Van-der-Waals or hydrophobic interactions. In particular, the hydrophobic backbone of PDMAEMA chains on the membrane surface and in the sample, lead to attractive interactions and can explain the late elution at high ionic strength and the peak broadening/tailing.

The amount of the polymer sample was altered to evaluate in detail the possible limitations of the determination of the molar masses by AF4. It is known that the volume injected into the channel can influence the retention time and the peak shape, if overloading occurs [4]. In general, the overloading depends on the focusing of the sample zone. If the concentration of the sample in the zone becomes too high some molecules are excluded, which leads to the broadening of peaks. Also intermolecular interactions will increase and can start to affect the elution. In general, the overloading starts to take place at a certain critical concentration which decreases with increasing molar mass. Also for low molar mass samples, where a relative high amount of sample is necessary for a reliable light scattering signal, this effect has to be taken into account. In general, it could be observed that polyelectrolytes elute earlier with increasing sample load, whereas neutral polymers in aqueous solution show an increase of retention time [4,51]. Additionally, a peak distortion and zone broadening is widely described in literature [14,52]. For polyelectrolytes, overloading is mainly influenced by electrostatic repulsion, both, inter/intra-molecular and between sample and membrane. With increasing charge the critical concentration is reduced and the sample is repelled from the accumulation wall. Overloading is also influenced by the ionic strength. An increase of the ionic strength suppresses electrostatic forces and, therefore, reduces the excluded volume of the chains, the chain expansion, and the electrostatic repulsion from the membrane. To see if any effect of the peak distortion was caused by sample overloading [52], the AF4 experiment with PDMAEMA<sub>500</sub> in 50 mM NaCl was repeated with different amounts of injected polymer mass. As shown in Fig. 6, a slightly higher retention time was found for the lowest amount of PDMAEMA<sub>500</sub>, which is typically observed for charged polymers and in accordance with other studies mentioned above. It also indicates that polyelectrolyte effects are still present. This is in agreement with measurements of reduced viscosity (SI-IX), showing the presence of such effects

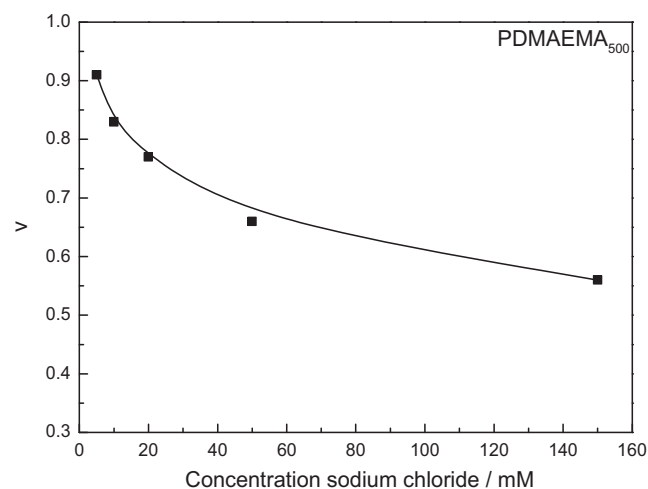


Fig. 7. Mark-Houwink exponent of PDMAEMA<sub>500</sub> at different concentrations of NaCl obtained by AF4.

even at 150 mM NaCl. However, the peak shape does not depend on the injected amount of sample for the investigated range. The recovery rate for all amounts of sample is constant at 83%, a value, which is also typically observed for polyelectrolytes [53]. Molar masses obtained from the light scattering signal are similar for all amounts of injected masses. Taking all results into account, overloading seems to be slightly present, but does not affect the characterization of the polymers.

### 3.6. Conformational investigations using AF4

It was expected that not only the interactions between different polymer chains (intermolecular) and between the polymer and the membrane, but also the intramolecular interactions vary with the ionic strength and, therefore, influence the conformation of the macromolecule [53]. The conformation of a macromolecule can be described by the exponent of the Kuhn–Mark–Houwink–Sakurada equation or the so called power-law-relationships (5), where the molar mass ( $M$ ) is combined, e.g. with the radius of gyration ( $R_g$ ), the sedimentation coefficient ( $s_0$ ), the diffusion coefficient ( $D_0$ ) or the intrinsic viscosity ( $\eta$ ).

$$X = KM^\nu \quad (5)$$

$$\log X = \log K + \nu * \log M \quad (6)$$

Here,  $X = R_g, s_0, D_0$  or  $[\eta]$ . In AF4-MALS, the exponent ( $\nu$ ) is calculated as the slope in a log–log plot of the radius against the molar mass of each slice, as illustrated in SI-X for PDMAEMA<sub>500</sub> in 150 mM NaCl. A slope of 0.56 was found, which fits well to the typical range for a linear chain (0.5–0.7). The dependency of the slope ( $\nu$ ), or the conformation of the polymer chain is related to the ionic strength as shown in Fig. 7. At low ionic strength (5 mM) a value of around 0.91 is obtained, which decreases to 0.56 at 150 mM NaCl. Moreover, it can be observed that even above a NaCl concentration of 50 mM the conformation still changes. In contrast, the ionic strength dependent fractograms (Fig. 5) showed a constant retention time and peak shape above 50 mM NaCl. This indicates that no relevant (detectable) changes in hydrodynamic radius ( $R_H$ ) or interactions with the membrane occurred. This observation clearly illustrates the differences between inter/intra-molecular interactions of the polymer chains and interactions with the membrane. While an exponent  $\nu$  of 1 describes a rod like structure and a value of 0.33 a sphere, a value of 0.9 was typically observed for elongated structures [54,55]. It is assumed that this is caused by the

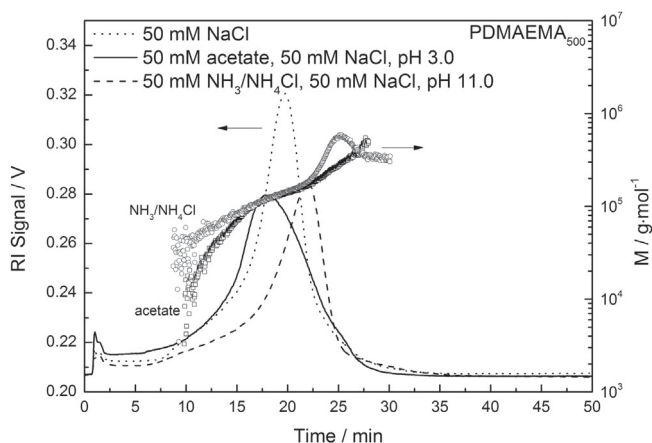


**Fig. 8.** AF4 fractograms of PDMAEMA<sub>500</sub> in different buffers: 50 mM acetate, 50 mM NaCl, pH 3.0, 50 mM NH<sub>3</sub>/NH<sub>4</sub>Cl, 50 mM NaCl, pH 11.0 and 50 mM NaCl.

electrostatic repulsion of the positive charges present in the side chain. With increasing ionic strength, the charges are screened and the range of the electrostatic forces is diminished. This reduces the repulsion between the side chains and leads to a conformation similar to a Gaussian chain, as indicated by an exponent of around 0.56.

The power-law-relationships were also applied to the data of the sedimentation and diffusion coefficients for all PDMAEMAs (SI–XI). Here, a value of 0.39 for the sedimentation and value of  $-0.62$  for the diffusion coefficient was obtained. Both exponents are in the limits for a Gaussian chain (0.35–0.5 for  $s$  and  $-0.5$  to  $-0.7$  for  $D$ ). Since the sedimentation velocity is more sensitive to the polyelectrolyte effect (molar mass obtained by Eq. (3)), the polymers should be in the unionized state [48]. For this reason, the sedimentation velocity and dynamic light scattering experiments were conducted in 150 mM NaCl + 1 mM NaOH. The polyelectrolyte effect is even present at neutral pH and 150 mM NaCl, as shown by measurements of the reduced viscosity (SI–IX). Fortunately, this does not seem to affect the determination of the molar mass by AF4-MALS. Moreover, a separation before the light scattering measurement has a time-related advantage, in particular for the characterization of polymers using AF4. Providing that the sample polydispersity is not too low, information about the conformation of the macromolecule can be obtained from a single experiment. In contrast, traditional techniques (e.g. sedimentation, diffusion or viscosity) to study the conformation require synthesis and analysis of a variety of polymers of different molar masses.

### 3.7. Influence of the pH value

For charged colloids, e.g. proteins, with positive and negative charges or polyelectrolytes with just one type of charge, the pH value of the solvent dramatically influences the structure of the sample. The pH primarily affects the protonation of the functional groups and, therefore, the appearance of charges, in a synthetic or biological macromolecule. For the characterization of PDMAEMA<sub>500</sub> by AF4 two other pH regions, an acidic and a basic, were investigated. First, a pH value of 3.0 was chosen (50 mM acetic acid/sodium acetate and 50 mM NaCl). As the isoelectric point (IEP) of a fresh RC membrane is around 3.4, the cellulose is expected to be positively charged at pH 3 [31]. The second region of interest was pH 11, where PDMAEMA is nearly unionized (50 mM ammonia/ammonium chloride buffer and 50 mM NaCl). The results obtained at pH 3.0 show a molar mass distribution similar to previous results (Fig. 8). In addition, a small shift in the retention time

and a peak deformation was observed. By comparing both fractograms (neutral pH and pH 3) at 50 mM NaCl, it is obvious that the retention behavior seems not to be influenced by the pH value. Probably the repulsive electrostatic forces at this ionic strength are shielded and short-ranged interactions, caused by the hydrophobic backbone or van-der-Waals interactions, dominate the retention, even at pH 3.

The situation is more complex at pH 11, where PDMAEMA is in the unionized state. The retention time is slightly shifted to higher values but the progression of molar mass shows an irregular behavior at 26 min (Fig. 8). This might be caused by massive interactions of the hydrophobic backbone with the membrane or the tubes of the AF4 system, since the molecule is uncharged at pH 11 and no repulsive electrostatic interactions are present. An aminolysis of the ester groups in the PDMAEMA polymer seems to be unlikely for the applied NH<sub>3</sub> concentration (50 mM) and temperature. From a practical point of view, the observed effect of decreasing molar mass just appears at the end of the peak where the concentration is rather low and does not influence the molar mass distribution noticeably. Nevertheless, further experiments are necessary to elucidate the origin of this effect and to exclude that it is caused by irregular changes of the membrane surface by the buffer used in the experiment.

## 4. Conclusion

In this study, the characterization of cationic polymers, which are of great interest for gene delivery and numerous industrial applications, by asymmetric flow field-flow fractionation (AF4) was presented for the first time. It could be shown that AF4 coupled to multi-angle light scattering enables a fast and reliable determination of molar masses and PDI values of polymers such as poly(ethylene imine), poly(L-lysine) and poly(2-(dimethylamino)ethyl methacrylate) and its derivatives. For the validation of the results, <sup>1</sup>H NMR spectroscopy and AUC were applied. It was found that the lower molar mass limit, which yields a reliable light scattering signal, was around 15 kg mol<sup>-1</sup>, depending on the refractive index increment. For polymers with a lower molar mass <sup>1</sup>H NMR spectroscopy or AUC is recommended. With increasing molar mass the accuracy of AF4-MALS increases and becomes more adequate, due to the fact that information about polydispersity, different mass averages and conformation can be obtained from a single measurement.

Furthermore, different membranes and eluents were evaluated for AF4 and the influence of ionic strength, injected mass of the analyte, and pH value was investigated. It could be shown that the retention behavior at low ionic strength is probably dominated by repulsive electrostatic forces between the polymer, adsorbed on the membrane surface, and the sample. In contrast, hydrophobic or other short-ranged interactions are important at higher ionic strength. Both diminish the advantage of AF4 to show less interaction with the sample than column based techniques. Up to now, no ideal membrane material was found for these cationic polyelectrolytes. Additionally, the conformation of PDMAEMA was studied by power-law-relationships in dependence of the ionic strength. It was found that the exponent,  $\nu$ , decreases from 0.91 at 5 mM NaCl to 0.56 at 150 mM NaCl, which probably describes the conformational change from a stretched chain to a linear Gaussian chain. The recovery rate of around 80% was in the typical range for cationic polymers. In summary, we could successfully present that AF4 is a well-suitable method for the characterization of cationic polymers, with respect to their molar masses, PDI values, and conformational information within short time and requiring only low amounts of samples. This enables a more detailed investigation of cationic

polymers used for further applications, e.g. for the formation of polyplexes in gene delivery.

## Acknowledgements

This project was funded by the Carl-Zeiss Foundation (Strukturrantrag JCSM). Furthermore, the authors would like to thank Nicole Fritz for technical assistance at the AF4, and Kristian Kempe for the synthesis of the poly(2-ethyl-2-oxazoline) precursor.

## Appendix A. Supplementary data

Supplementary data associated with this article can be found, in the online version, at <http://dx.doi.org/10.1016/j.chroma.2013.11.049>.

## References

- [1] O. Boussif, F. Lezoualch, M.A. Zanta, M.D. Mergny, D. Scherman, B. Demeneix, J.P. Behr, *Proc. Natl. Acad. Sci. U.S.A.* 92 (1995) 7297.
- [2] A. Fire, S.Q. Xu, M.K. Montgomery, S.A. Kostas, S.E. Driver, C.C. Mello, *Nature* 391 (1998) 806.
- [3] A. Akinc, M. Thomas, A.M. Klibanov, R. Langer, *J. Gene Med.* 7 (2005) 657.
- [4] M.A. Benincasa, J.C. Giddings, *J. Microcolumn Sep.* 9 (1997) 479.
- [5] C. Augsten, K. Mäder, *Int. J. Pharm.* 351 (2008) 23.
- [6] L. Tauhardt, K. Kempe, K. Knop, E. Altuntas, M. Jäger, S. Schubert, D. Fischer, *U.S. Schubert, Macromol. Chem. Phys.* 212 (2011) 1918.
- [7] Y. Guillauneuf, P. Castignolles, *J. Polym. Sci. Part A: Polym. Chem.* 46 (2008) 897.
- [8] X.-L. Jiang, Y.-F. Chu, J. Liu, G.-Y. Zhang, R.-X. Zhuo, *Chin. J. Polym. Sci.* 29 (2011) 421.
- [9] J.C. Giddings, *J. Sep. Sci.* 1 (1966) 123.
- [10] W. Fraunhofer, G. Winter, *Eur. J. Pharm. Biopharm.* 58 (2004) 369.
- [11] G. Yohannes, M. Jussila, K. Hartonen, M.-L. Riekkola, *J. Chromatogr. A* 1218 (2011) 4104.
- [12] F.A. Messaud, R.D. Sanderson, J.R. Runyon, T. Otte, H. Pasch, S.K.R. Williams, *Prog. Polym. Sci.* 34 (2009) 351.
- [13] A.C. Makan, T. Otte, H. Pasch, *Macromolecules* 45 (2012) 5247.
- [14] A. Litzén, K.G. Wahlund, *J. Chromatogr.* 548 (1991) 393.
- [15] K.G. Wahlund, J.C. Giddings, *Anal. Chem.* 59 (1987) 1332.
- [16] H. Cölfen, M. Antonietti, *Adv. Polym. Sci.* 150 (2000) 67.
- [17] L. Nilsson, M. Leeman, K.G. Wahlund, B. Bergenstahl, *Biomacromolecules* 7 (2006) 2671.
- [18] P. Schuck, M.A. Perugini, N.R. Gonzales, G.J. Howlett, D. Schubert, *Biophys. J.* 82 (2002) 1096.
- [19] B. Schulze, C. Friebe, S. Höppener, G.M. Pavlov, A. Winter, M.D. Hager, U.S. Schubert, *Macromol. Rapid Commun.* 33 (2012) 597.
- [20] G.M. Pavlov, A.M. Breul, M.D. Hager, U.S. Schubert, *Macromol. Chem. Phys.* 213 (2012) 904.
- [21] J.P. Behr, *Acc. Chem. Res.* 45 (2012) 980.
- [22] R.J. Christie, N. Nishiyama, K. Kataoka, *Endocrinology* 151 (2009) 466.
- [23] J. Chiefari, Y.K. Chong, F. Ercole, J. Krstina, J. Jeffery, T.P.T. Le, R.T.A. Mayadunne, G.F. Meijs, C.L. Moad, G. Moad, E. Rizzardo, S.H. Thang, *Macromolecules* 31 (1998) 5559.
- [24] C. Pietsch, U. Mansfeld, C. Guerrero-Sanchez, S. Höppener, A. Vollrath, M. Wagner, R. Hoogenboom, S. Saubern, S.H. Thang, C.R. Becer, J. Chiefari, U.S. Schubert, *Macromolecules* 45 (2012) 9292.
- [25] P. Schuck, *Biophys. J.* 78 (2000) 1606.
- [26] W. Mächtle, *Macromol. Chem. Phys.* 185 (1984) 1025.
- [27] T. Pauck, H. Cölfen, *Anal. Chem.* 70 (1998) 3886.
- [28] S.W. Provencher, *Comput. Phys. Commun.* 27 (1982) 229.
- [29] M. Andersson, B. Wittgren, K.G. Wahlund, *Anal. Chem.* 75 (2003) 4279.
- [30] T. Lang, K.A. Eslahian, M. Maskos, *Macromol. Chem. Phys.* 213 (2012) 2353.
- [31] S. Lee, H.D. Kwen, S.K. Lee, S.V. Nehete, *Anal. Bioanal. Chem.* 396 (2010) 1581.
- [32] A. Ulrich, S. Losert, N. Bendixen, A. Al-Kattan, H. Hagendorfer, B. Nowack, C. Adlhart, J. Ebert, M. Lattuada, K. Hungerbühler, *J. Anal. At. Spectrom.* 27 (2012) 1120.
- [33] K. Matsumoto, A. Suganuma, D. Kunui, *Powder Technol.* 25 (1980) 1.
- [34] A. von Harpe, H. Petersen, Y.X. Li, T. Kissel, *J. Control. Release* 69 (2000) 309.
- [35] E. Wagner, *Acc. Chem. Res.* 45 (2012) 1005.
- [36] A. Kwok, S.L. Hart, *Nanomed. Nanotechnol. Biol. Med.* 7 (2011) 210.
- [37] O.M. Merkel, D. Librizzi, A. Pfestroff, T. Schurraat, K. Buyens, N.N. Sanders, S.C. De Smedt, M. Béhé, T. Kissel, *J. Control. Release* 138 (2009) 148.
- [38] C. Scholz, E. Wagner, *J. Control. Release* 161 (2012) 554.
- [39] M.-E. Bonnet, P. Erbacher, A.-L. Bolcato-Bellemin, *Pharm. Res.* 25 (2008) 2972.
- [40] S.M. Zou, P. Erbacher, J.S. Remy, J.P. Behr, *J. Gene Med.* 2 (2000) 128.
- [41] A. Zattoni, D.C. Rambaldi, P. Reschiglian, M. Melucci, S. Krol, A.M.C. Garcia, A. Sanz-Medel, D. Roessner, C. Johann, *J. Chromatogr. A* 1216 (2009) 9106.
- [42] D.T. Curriel, S. Agarwal, E. Wagner, M. Cotten, *Proc. Natl. Acad. Sci. U.S.A.* 88 (1991) 8850.
- [43] C. Plank, K. Mechtler, F.C. Szoka, E. Wagner Jr., *Hum. Gene Ther.* 7 (1996) 1437.
- [44] M. Sanjoh, S. Hiki, Y. Lee, M. Oba, K. Miyata, T. Ishii, K. Kataoka, *Macromol. Rapid Commun.* 31 (2010) 1181.
- [45] C.V. Synatschke, A. Schallon, V. Jerome, R. Freitag, A.H.E. Müller, *Biomacromolecules* 12 (2011) 4247.
- [46] P. van de Wetering, J.Y. Cherng, H. Talsma, D.J.A. Crommelin, W.E. Hennink, *J. Control. Release* 53 (1998) 145.
- [47] I.Y. Perevyazko, M. Bauer, G.M. Pavlov, S. Höppener, S. Schubert, D. Fischer, *U.S. Schubert, Langmuir* 28 (2012) 16167.
- [48] K.L. Planken, H. Cölfen, *Nanoscale* 2 (2010) 1849.
- [49] L.N. Andreeva, S.V. Bushin, M.A. Bezrukova, T.N. Nekrasova, R.T. Imanbaev, V.D. Pautov, O.V. Nazarova, Y.I. Zolotova, E.F. Panarin, *Russ. J. Appl. Chem.* 85 (2012) 417.
- [50] S. Lee, P.O. Nilsson, G.S. Nilsson, K.G. Wahlund, *J. Chromatogr. A* 1011 (2003) 111.
- [51] M.A. Benincasa, C. Delle Fratte, *J. Chromatogr. A* 1046 (2004) 175.
- [52] A. Litzén, K.G. Wahlund, *Anal. Chem.* 63 (1991) 1001.
- [53] E. Alasonati, M.A. Benincasa, V.I. Slaveykova, *J. Sep. Sci.* 30 (2007) 2332.
- [54] W. Burchard, *Adv. Polym. Sci.* 143 (1999) 113.
- [55] H. Thielking, W.M. Kulicke, *Anal. Chem.* 68 (1996) 1169.

## Supporting information

### Characterization of Cationic Polymers by Asymmetric Flow Field-Flow Fractionation and multi angle light scattering – A Comparison with Traditional Techniques

Michael Wagner,<sup>1,2</sup> Christian Pietsch,<sup>1,2</sup> Lutz Tauhardt,<sup>1,2</sup> Anja Schallon,<sup>1,2</sup> Ulrich. S. Schubert<sup>1,2\*</sup>

<sup>1</sup> *Laboratory of Organic and Macromolecular Chemistry (IOMC), Friedrich Schiller University Jena, Humboldtstraße 10, 07743 Jena, Germany*

<sup>2</sup> *Jena Center for Soft Matter (JCSM), Friedrich Schiller University Jena, Philosophenweg 7, 07743 Jena, Germany*

*ulrich.schubert@uni-jena.de; www.schubert-group.com*

#### SI-I: Synthesis L-PEI<sub>600</sub>

A solution of dry acetonitrile (Acros Organics, Geel Belgium), 2-ethyl-2-oxazoline (monomer), and methyl tosylate (initiator) was prepared with a total monomer concentration of 4 M and a total monomer-to-initiator ratio of 600 as recently published.[1] The mixture was heated in a microwave synthesizer at 140 °C for a pre-determined time. A sample was taken and full monomer conversion was confirmed by <sup>1</sup>H NMR spectroscopy. Subsequently, the solvent was removed. The resulting PEtOx ( $M_n = 40.6 \text{ kg}\cdot\text{mol}^{-1}$ , PDI = 1.79, 3.8 g) was dissolved in 6 M aqueous hydrochloric acid (15 mL) and heated at 130 °C for 1 h in the microwave synthesizer. After removing the acid under reduced pressure, the residue was dissolved in water and 3 M aqueous NaOH was added until precipitation occurred. The precipitate was filtered off, recrystallized from water, filtered, dissolved in methanol, and precipitated into ice-cold diethyl ether. Subsequently, the L-PEI<sub>600</sub> was dried for 3 day at 40 °C. The degree of hydrolysis was 99% as determined by <sup>1</sup>H NMR spectroscopy.

<sup>1</sup>H NMR (300 MHz, CD<sub>3</sub>OD):  $\delta = 3.65$  (t, CH<sub>2</sub>-OH), 2.73 (br., N-CH<sub>2</sub>), 2.39 (s, CH<sub>3</sub>-N).

#### SI-II: Synthesis PDMAEMA, PAEMA and PtBAEMA via RAFT

In a typical polymerization experiment, 1.258 g of DMAEMA ( $8.0 \times 10^{-3}$  mol), 2.8 mg of 4,4'-azobis(4-cyanopentanoic acid), ACVA, initiator ( $1.0 \times 10^{-5}$  mol), 11.18 mg of 4-cyano-4-(phenylcarbonothioylthio) pentanoic acid (used as a CTA) RAFT agent ( $4.0 \times 10^{-5}$  mol) and ethanol/water (in total 50/50 vol%) were mixed together in a 10 mL glass vial as follows DMAEMA



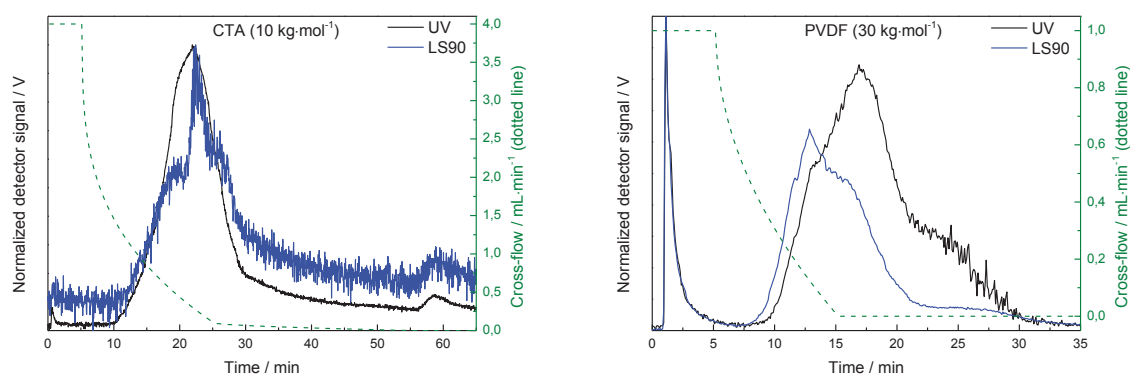
monomer, followed by individual stock solutions of initiator and RAFT agent dissolved in ethanol and filled with water up to a ratio of 50/50 vol%. The ratio between [CTA] and [AIBN] was 1:0.25. Before closing the vial, the reaction solutions were degassed by sparging argon for at least 30 min prior to use. Subsequently, the reaction was performed in an oil bath at 70 °C for 12 h keeping a total monomer concentration of 2.0 M or 3.0 M. After the polymerization, acetone was added to the final mixtures, and the polymers were subsequently precipitated into cold diethyl ether. The utilized reaction conditions, monomer concentration and [M]/[CTA] ratios are summarized in Table 1. In the case of PDMAEMA-90 the 1,1'-azobis(cyclohexane carbonitrile) initiator and as RAFT agent the 4-cyano-4-[(dodecylsulfanylthiocarbonyl) sulfanyl]pentanoic acid were used.

**Table 1: Overview of the selected reaction conditions and SEC data of methacrylate based polymers.**

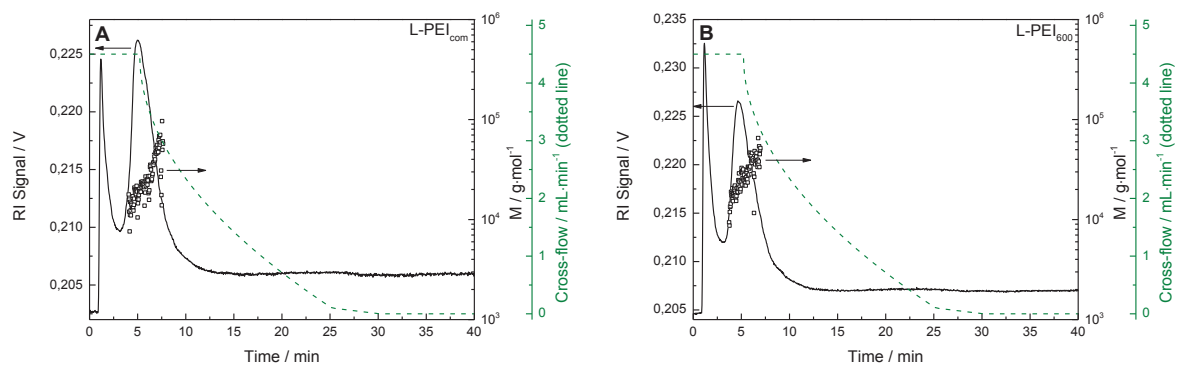
Sample	amine	[M]/[CTA]	<i>c</i> / M	$M_n$ (SEC) / kg·mol <sup>-1</sup>	PDI (SEC)
PDMAEMA <sub>90</sub>	<i>tert.</i>	100/1	3.0	15.2 <sup>[a]</sup>	1.21
PDMAEMA <sub>230</sub>	<i>tert.</i>	200/1	2.0	25.7 <sup>[a]</sup>	1.34
PDMAEMA <sub>320</sub>	<i>tert.</i>	600/1	3.0	47.2 <sup>[a]</sup>	1.35
PDMAEMA <sub>500</sub>	<i>tert.</i>	1200/1	3.0	66.9 <sup>[a]</sup>	1.37
PAEMA <sub>150</sub>	<i>prim.</i>	200/1	2.0	77.8 <sup>[b]</sup>	1.15
PtBAEMA <sub>170</sub>	<i>sec.</i>	200/1	2.0	37.8 <sup>[a]</sup>	1.25

<sup>[a]</sup> Calculated from SEC (DMAc) using PS calibration. <sup>[b]</sup> Calculated from aqueous SEC (CF<sub>3</sub>COOH/NaCl/pH 2.3) using Pullulan calibration.

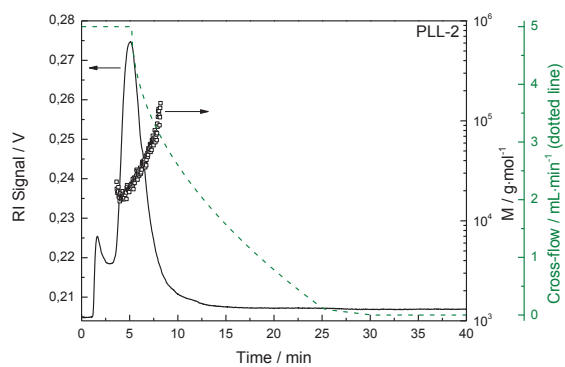
### SI-III: AF4 fractogram of PDMAEMA<sub>500</sub> on a 10 kg·mol<sup>-1</sup> CTA and 30 kg·mol<sup>-1</sup> PVDF membrane and 150 mM NaCl as eluent.



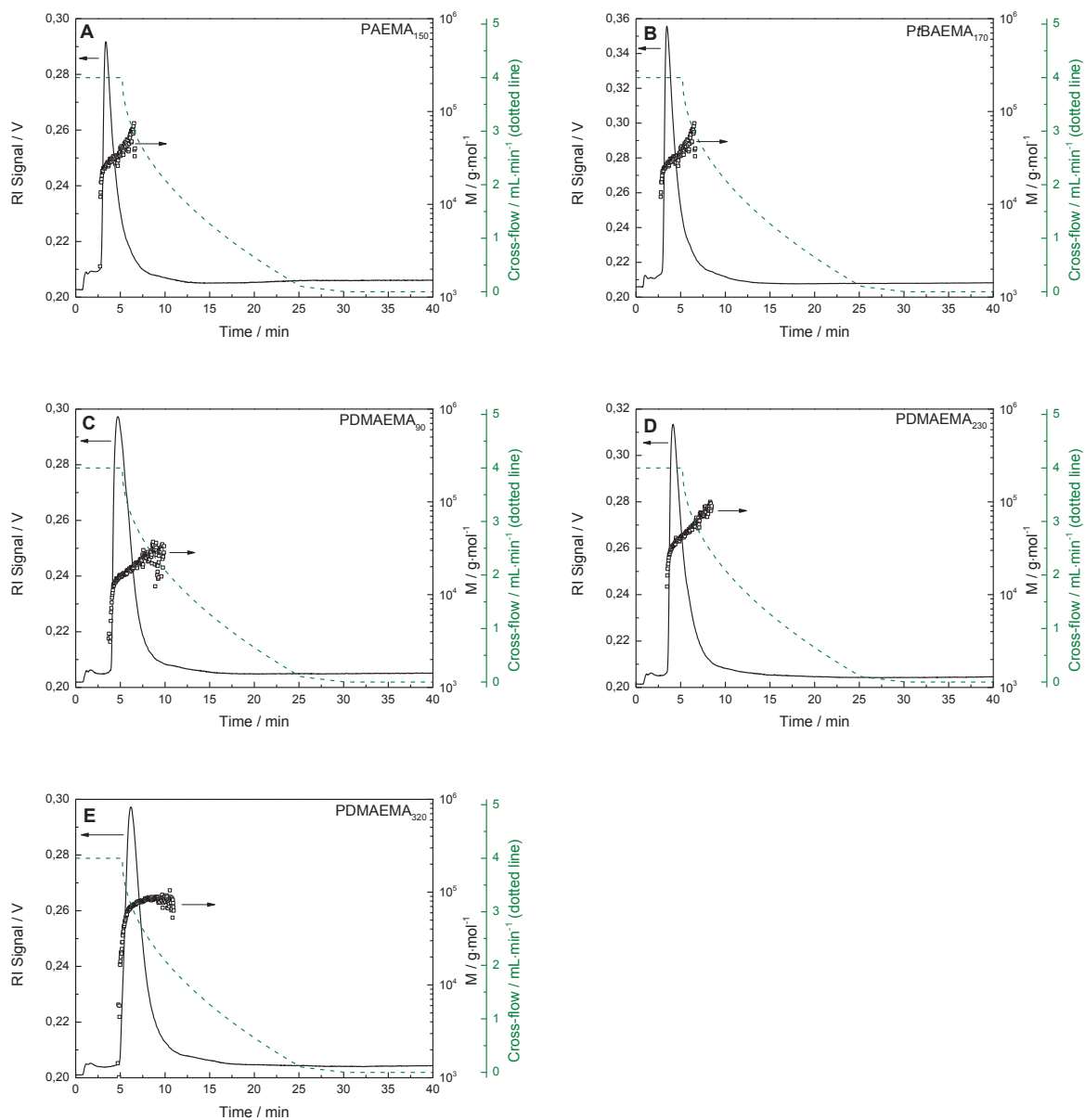
**SI-IV: AF4 fractograms with the corresponding cross-flow rates and molar masses of (A) L-PEI<sub>com</sub>, and (B) L-PEI<sub>600</sub>.**



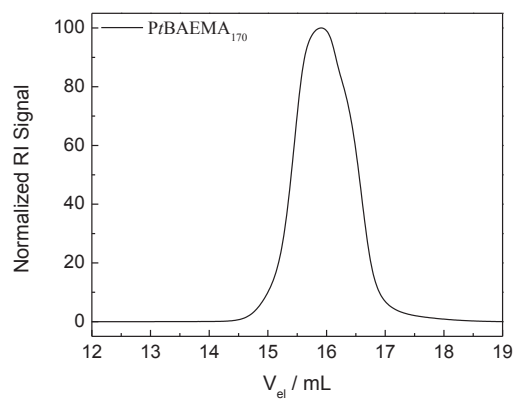
**SI-V: AF4 fractograms with the corresponding cross-flow rates and molar masses of PLL-2.**



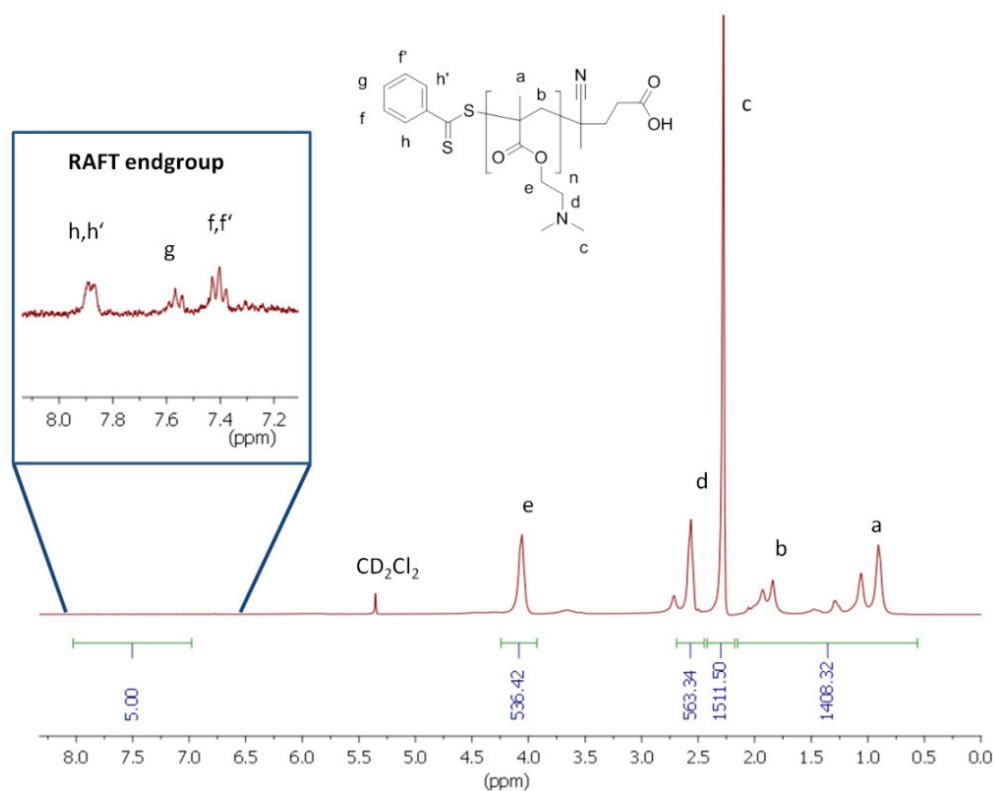
**SI-VI: AF4 fractograms with the corresponding cross-flow rates and molar masses of (A) PAEMA<sub>150</sub>, (B) PtBAEMA<sub>170</sub>, (C) PDMAEMA<sub>90</sub>, (D) PDMAEMA<sub>230</sub>, and (E) PDMAEMA<sub>320</sub>.**



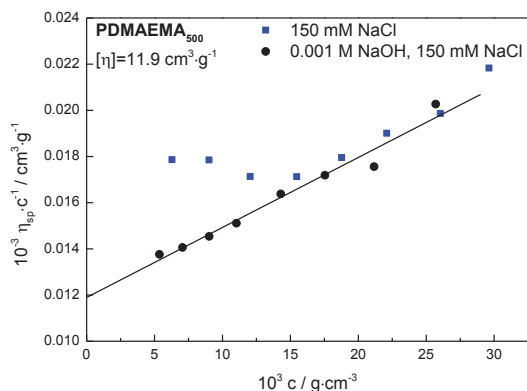
**SI-VII: SEC results of PzBAEMA<sub>170</sub> with DMAC/LiCl as eluent and polystyrene as calibration standard.**



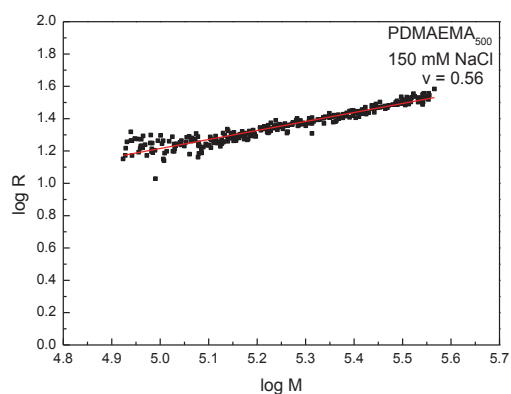
**SI-VIII: <sup>1</sup>H NMR of PDMAEMA<sub>320</sub> in CD<sub>2</sub>Cl<sub>2</sub>**



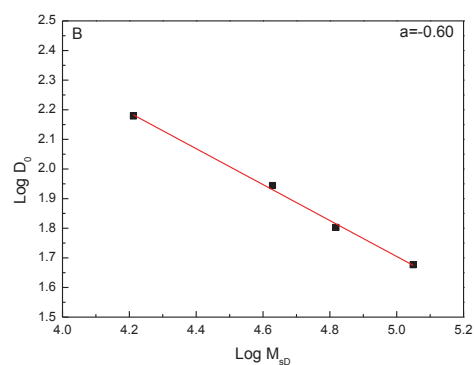
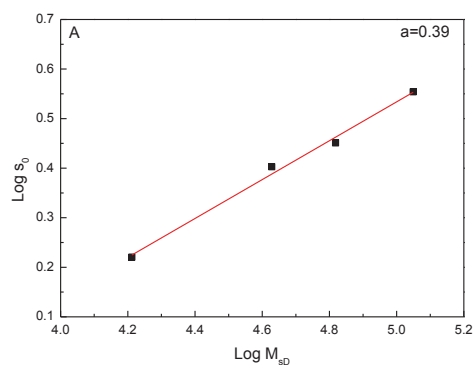
**SI-IX: Measurement of reduced viscosity for PDMAEMA<sub>500</sub>**



**SI-X: Conformation plot of PDMAEMA<sub>500</sub> in 150 mM NaCl obtained by AF4-MALS.**



**SI-XI: Log-log plots of (A)  $s_0$  and (B)  $D_0$  against the different molar masses of PDMAEMA in 150 mM NaCl + 1 mM NaOH.**



## References

- [1] L. Tauhardt, K. Kempe, K. Knop, E. Altuntas, M. Jäger, S. Schubert, D. Fischer, U.S. Schubert, *Macromol. Chem. Phys.* 212 (2011) 1918.

## Publication P3

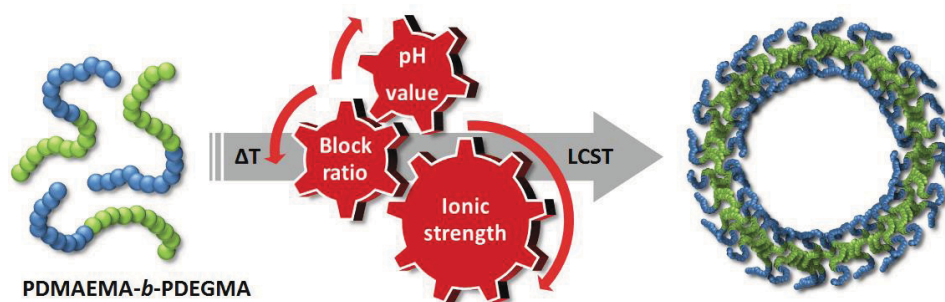
---

Physicochemical characterization of the thermo-induced self-assembly of thermo-responsive PDMAEMA-*b*-PDEGMA copolymers

M. Wagner, C. Pietsch, A. Kerth, A. Träger, U. S. Schubert

*Manuscript submitted.*

---







# Physicochemical characterization of the thermo-induced self-assembly of thermo-responsive PDMAEMA-*b*-PDEGMA copolymers

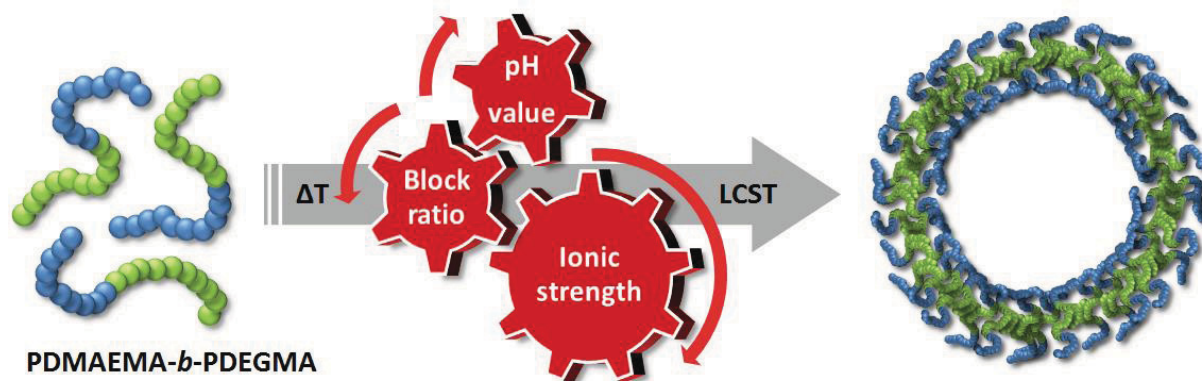
Michael Wagner,<sup>1,2</sup> Christian Pietsch,<sup>1,2</sup> Andreas Kerth,<sup>3</sup> Anja Traeger,<sup>1,2</sup> Ulrich. S. Schubert<sup>1,2\*</sup>

1 - Laboratory of Organic and Macromolecular Chemistry (IOMC), Friedrich Schiller University Jena, Humboldtstrasse 10, 07743 Jena, Germany

2 - Jena Center for Soft Matter (JCSM), Friedrich Schiller University Jena, Philosophenweg 7, 07743 Jena, Germany

3 - Institute of Chemistry - Physical Chemistry, Martin Luther University Halle-Wittenberg, von-Danckelmann-Platz 4, 06120 Halle, Germany

Corresponding author: [ulrich.schubert@uni-jena.de](mailto:ulrich.schubert@uni-jena.de)



## Abstract

Diblock copolymers of poly[2-(dimethylamino)ethyl methacrylate]-*block*-poly[di(ethylene glycol) methyl ether methacrylate], PDMAEMA-*b*-PDEGMA, were synthesized by reversible addition-fragmentation chain transfer (RAFT) polymerization. The block ratio was varied to study the influence on the lower critical solution temperature (LCST) and the corresponding phase transition in water. Besides turbidimetry, differential scanning calorimetry (DSC), dynamic light scattering (DLS) and laser Doppler velocimetry (LDV), asymmetric flow field-flow fractionation (AF4) coupled to DLS and multi angle laser light scattering (MALLS) was established as an alternative route to characterize these systems in terms of molar mass of the polymer chain and size of the colloids after the phase transition. It was found that AF4-MALLS allowed accurate determination of molar masses in the studied range. Nevertheless, some limitations were observed, which are critically discussed. The cloud point and phase transition of all materials, as revealed by turbidimetry, could be confirmed by DSC. For block copolymers with block ratios in the range of 50:50, a thermo-induced self-assembly into micellar and vesicular structures with hydrodynamic radii ( $R_h$ ) of around 25 nm was observed upon heating. At higher temperatures, a reordering of the self-assembled structures could be detected. The thermo-responsive behavior was further investigated in dependence of pH value and ionic strength. Variation of the pH value mainly influences the solubility of the PDMAEMA segment, where a decrease of the pH value increases the transition temperature. A change of ionic strength influences the copolymers in a way that the LCST is reduced with increasing ionic strength due to the screening of electrostatic interactions.

## Keywords

Block copolymers, LCST, field-flow fractionation, self-assembly, light scattering, differential scanning calorimetry

## Introduction

Smart materials like thermo-responsive polymers received increasing attention over the last years.<sup>[1-5]</sup> In particular, polymers have attracted significant regard which exhibit a lower critical solution temperature (LCST).<sup>[6,7]</sup> Amphiphilic block copolymers, where at least one block shows an LCST, can undergo thermo-induced self-assembly processes and the formation of micellar and vesicular structures in aqueous solution is widely described.<sup>[8-12]</sup> Such materials represent attractive systems for sensing or biomedical applications like in drug delivery processes as an external stimulus (*e.g.* temperature) can be used for encapsulation and release of dyes or active substances.<sup>[13-17]</sup>

The phase transition at the LCST is mainly driven by the unfavorable entropy of mixing. In water, this is based on the formation of hydrogen bonds between water molecules and the polymer chain.<sup>[18]</sup> Heating above the cloud point temperature ( $T_{CP}$ ) leads to the breaking of the hydrogen bonds and to an increase of hydrophobic interactions between the polymer chains.<sup>[19]</sup> Recently, we reported on the LCST behavior of a series of diblock copolymers, poly[2-(dimethylamino)ethyl methacrylate]-*block*-poly[di(ethylene glycol) methyl ether methacrylate] (PDMAEMA-*b*-PDEGMA), with different block ratios synthesized by reversible addition-fragmentation chain transfer (RAFT) polymerization (Figure 1).<sup>[20]</sup> Both blocks, PDEGMA as well as PDMAEMA, exhibit a LCST behavior, where PDEGMA has a  $T_{CP}$  at around 27 °C. For PDMAEMA, the  $T_{CP}$  highly depends on the used molar mass as well as the pH value and ionic strength of the solution as both influence the degree of protonation of the amine groups and the resulting electrostatic interactions.<sup>[21-26]</sup> In deionized water,  $T_{CP}$  values between 45 and 55 °C were observed, depending on the polymer concentration.<sup>[27]</sup> This leads to a double hydrophilic block copolymer below  $T_{CP}$  and amphiphilic materials above, where the LCST can easily be adjusted by several solution conditions. Subsequently, the block copolymer can self-assemble into different micellar or vesicular structures. In particular, if both blocks have similar dimensions, we could observe two  $T_{CP}$  values, where the first transition, related to the PDEGMA block, was linked to the formation of multilamellar vesicles, which transformed into unilamellar vesicles after the second  $T_{CP}$ .<sup>[20]</sup> The question was now, to which extent these structural changes are related to a thermodynamically defined phase transition. Furthermore, the solution properties of PDMAEMA-*b*-PDEGMA are affected by changes in pH value as well as ionic strength and their influence on the LCST behavior and the self-assembly is of high interest.<sup>[28-30]</sup> This would result in a material which is sensitive against two or more different stimuli at the same time, as demonstrated for other systems like poly(*N*-isopropyl acrylamide)-*block*-poly(acrylic acid) in the past.<sup>[31,32]</sup>

For the characterization of thermo-induced self-assembly processes and the resulting aggregate morphologies, dynamic and static light scattering (DLS/SLS) are commonly used, as they are non-invasive and can be performed easily with low sample concentration and volume. Nevertheless,

some limitations exist. While SLS provides just average values, DLS data has to be interpreted with care, if highly disperse or multimodal systems are involved. To circumvent these problems and to obtain a deeper insight into the self-organization of the thermo-responsive polymers, asymmetric flow field-flow fractionation (AF4) can be applied. Firstly described by J. Calvin Giddings in 1966, field flow fractionation (FFF) is nowadays a powerful technique for separation and characterization of (bio)macromolecules and colloids.<sup>[33-38]</sup> The theoretical details are discussed in detail elsewhere.<sup>[39-43]</sup> Due to the absence of a stationary phase, AF4 provides a gentle fractionation with a laminar flow, which is well-suitable for sensitive and delicate samples. The most eminent challenge of AF4 is related to interactions with the semipermeable membrane, which acts as accumulation wall. In particular for cationic samples, adsorption often heavily influences the measurement and renders AF4 a more qualitative tool.<sup>[44]</sup> To the best of our knowledge, AF4 is rarely used for the analysis of polymers showing LCST behavior.<sup>[45]</sup> Nowadays, a multi angle laser light scattering (MALLS) or a DLS detector is hyphenated to AF4 to obtain independent information about molar mass, radius of gyration ( $R_g$ ), hydrodynamic radius ( $R_h$ ), dispersity ( $\mathcal{D}$ ), or shape.<sup>[46-50]</sup>

In this study, we describe a series of diblock copolymers based on PDMAEMA-*b*-PDEGMA with different block ratios, synthesized *via* reversible addition–fragmentation chain transfer (RAFT) radical polymerization. The LCST and the thermo-induced self-assembly were studied by turbidimetry and DLS investigations. Differential scanning calorimetry (DSC) was used to obtain further information on the observed cloud point temperatures, in particular the second  $T_{CP}$  for polymers with comparable block ratios. Laser Doppler velocimetry (LDV), a tool to measure the electrokinetic potential, was applied to provide additional insights into the self-organization of the polymers. Furthermore, AF4 coupled to MALLS and DLS was evaluated as a tool to study the observed transitions and to obtain reliable molar masses of the polymers. Thereby, potential advantages and limitations were critically discussed. The diblock copolymer, which showed two cloud point temperatures, was investigated in detail, concerning the influence of pH value and ionic strength on the self-assembly and the LCST.

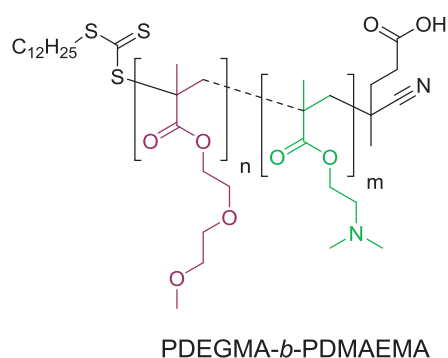


**Figure 1: Schematic representation of the investigated polymer structures.**

## Experimental

### Materials

Di(ethylene glycol) methyl ether methacrylate (DEGMA) and 2-(dimethylamino)ethyl methacrylate (DMAEMA) were purchased from Sigma-Aldrich and purified by stirring in the presence of inhibitor-remover for hydroquinone or hydroquinone monomethyl ether (Aldrich) for 30 minutes prior to use. Block copolymers of PDMAEMA-*b*-PDEGMA were synthesized as described previously.<sup>[20]</sup> The corresponding molar masses and dispersity indices ( $\mathcal{D}$ ) of the block copolymers are described therein. The block ratios are listed in Table 1. Sodium chloride, sodium acetate trihydrate, disodium hydrogen phosphate dihydrate, sodium dihydrogen phosphate and ammonium chloride were purchased from Carl Roth. Acetic acid (100%) and ammonia solution (25%) were purchased from VWR. All chemicals were of analytical grade or better and used as received.

The pH value of buffer solutions was adjusted by mixing the different salts or free acids/bases, respectively. The ionic strength of all buffers and NaCl solutions was calculated considering the dissociation constants of the individual ion species. For pH dependent investigations with different buffer salts, a total buffer concentration of 25 mM was used. All further experiments were performed with a polymer concentration of 2.5 mg·mL<sup>-1</sup>.

### Turbidimetry

Cloud point measurements for the identification of the LCST behavior were performed by heating the polymer (2.5 mg mL<sup>-1</sup>) in deionized water or the corresponding pH buffer from 2 to 105 °C with a heating rate of 1.0 °C min<sup>-1</sup>, followed by cooling to 0 °C at a cooling rate of 1.0 °C min<sup>-1</sup> after keeping it 10 minutes at 105 °C. This cycle was repeated three times. During these controlled cycles the transmission of the solutions was monitored in a Crystal16™ from Avantium Technologies. The cloud points are reported as the 50% transmittance temperature of the second heating run.

### Differential scanning calorimetry (DSC)

DSC experiments were performed with a Microcal VP-DSC (MicroCal Inc., Northampton, USA). In all experiments a heating and cooling rate of 1.0 °C min<sup>-1</sup>, a time resolution of 4 s and a temperature range from 5 to 95 °C was used. All samples were kept at the respective starting temperature for 30 minutes. Aqueous polymer solutions were prepared at 2.5 mg·mL<sup>-1</sup> and the reference cell was filled with deionized water. Three heating and cooling scans were performed for each sample to prove reproducibility. All presented curves show the second heating scan, where the baseline was corrected by subtracting the water-water baseline. Finally, the scan was normalized with respect to the concentration.

## Dynamic light scattering

Batch dynamic light scattering was performed on a Zetasizer Nano ZS (Malvern Instruments, Herrenberg, Germany). All measurements were performed in folded capillary cells (DTS1071, Malvern Instruments, Herrenberg, Germany). Each sample was heated from 15 to 65 °C in steps of 5 K. At each temperature, after an equilibration time of 30 min, 5 measurements with 3 runs of 30 s were carried out ( $\lambda = 633$  nm). The counts were detected at an angle of 173°. For each sample, two heating and cooling cycles were analyzed. Apparent hydrodynamic radii,  $R_h$ , were number-weighted and calculated according to the Stokes–Einstein equation. PDI values were obtained by cumulant analysis

## Laser Doppler velocimetry (LDV)

Laser Doppler velocimetry was used to measure the electrokinetic potential, also known as zeta potential. The measurements were performed on a Zetasizer Nano ZS in folded capillary cells (DTS1071). Each sample was heated from 15 to 65 °C in steps of 5 K. At each temperature, after an equilibration time of 30 min, 5 measurements with 20 runs were carried out using the slow-field and fast-field reversal mode with 100 V. For each sample, two heating and cooling cycles were analyzed. The zeta potential ( $\zeta$ ) was calculated from the electrophoretic mobility ( $\mu$ ) according to the Henry Equation.<sup>[51]</sup> For each sample and temperature, the Henry coefficient,  $f(ka)$ , was calculated separately according to Ohshima, considering samples size.<sup>[52]</sup>

## Asymmetric flow field-flow fractionation (AF4)

Asymmetric flow field-flow fractionation (AF4) was performed on an AF2000 MT System (Postnova Analytics, Landsberg, Germany) coupled to an UV (PN3211, 260 nm), RI (PN3150), MALLS (PN3070, 633 nm) and DLS (ZetaSizer Nano ZS, 633 nm) detector. The eluent is delivered by two different pumps (tip and focus-flow) and the sample is injected by an autosampler (PN5300) into the channel. The channel has a trapezoidal geometry and an overall area of 31.6 cm<sup>2</sup>. The nominal height of the spacer was 500  $\mu$ m and a regenerated cellulose membrane with a molar mass cut-off of 10,000 g·mol<sup>-1</sup> was used as accumulation wall. For molar mass determination of all polymers, the temperature was set to 25 °C and an acetate buffer (25 mM) with pH 3.5 and 20 mM NaCl was used as eluent. The detector flow rate was set to 0.5 mL·min<sup>-1</sup> and 20  $\mu$ L (10 mg·mL<sup>-1</sup>) were injected with an injection flow rate of 0.2 mL·min<sup>-1</sup> for 7 min. The cross-flow was set to 1.8 mL·min<sup>-1</sup>. After the focusing period and a transition time of 1 min, the cross-flow was kept constant for 3 min and then decreased under a power function gradient (0.4) to 0 within 18 min. Afterwards the cross-flow was kept constant at zero for at least 25 min to ensure complete elution. The refractive index increment ( $dn/dc$ ) was measured by manual injection of a known concentration directly into the channel

without any focusing or cross-flow. The  $dn/dc$  was calculated as the average of at least three injections from the area under the RI curve ( $AUC_{RI}$ ). For fractionation at higher temperatures, the tubings of the inlet and focus flow, where elongated to 3 m and placed in the channel oven to ensure an appropriate temperature equilibrium of the eluent and the sample during fractionation in the channel. The detector flow rate was set to  $0.5 \text{ mL}\cdot\text{min}^{-1}$  and  $20 \text{ }\mu\text{L}$  ( $10 \text{ mg}\cdot\text{mL}^{-1}$ ) were injected with an injection flow rate of  $0.2 \text{ mL}\cdot\text{min}^{-1}$  for 7 min. The cross-flow was set to  $1.5 \text{ mL}\cdot\text{min}^{-1}$ . After the focusing period and a transition time of 1 min the cross-flow was decreased under a power function gradient (0.5) to 0 within 20 min. Afterwards, the cross-flow was kept constant for 20 min. For calculation of the molar mass and the radius of gyration by MALLS, a Zimm plot was used. All measurements were repeated three times.

## Results & discussion

The diblock copolymers (PDMAEMA-*b*-PDEGMA) were synthesized *via* sequential monomer addition using reversible addition–fragmentation chain transfer (RAFT) polymerization. The controlled variation of the block length (ratio DMAEMA to DEGMA) in the copolymer was performed in 20 mol% steps. The amphiphilic block copolymers were characterized by size-exclusion chromatography (SEC) showing a molar mass ( $M_n$ ) range from 20 000 to 36 000  $\text{g}\cdot\text{mol}^{-1}$  with a molar mass distribution  $\mathcal{D} < 1.35$ . The final composition (mol% fractions) of the diblock copolymers is listed in Table 1.<sup>[20]</sup>

### Molar mass by AF4-MALLS

As the LCST depends, among others, on the molar mass of the polymer, an accurate characterization of the PDMAEMA-*b*-PDEGMA block copolymers is mandatory. In particular for cationic polymers with molar masses ( $M_n$ ) in the range of  $10^4 \text{ g}\cdot\text{mol}^{-1}$ , it is known that many methods classically available for polymers experience problems.<sup>[37]</sup> While suitable SEC columns are rarely found, Kuhn-Mark-Houwink constants for viscosimetry are often unknown and techniques like nuclear magnetic resonance spectroscopy (NMR) or mass spectrometry (MS) are at their limits in this molar mass region. Therefore, AF4 coupled to RI and MALLS was applied as a potential alternative. As already described in a previous study, the most important restriction of AF4 analysis of cationic samples is adsorption onto the membrane, which acts as accumulation wall.<sup>[44]</sup> This membrane is usually composed of regenerated cellulose or poly(ether sulfone) and bears a negative potential, which leads to attractive electrostatic interactions with cationic materials. Different possibilities exist to circumvent this effect. An increase of ionic strength by addition of sodium chloride helps to reduce the range of electrostatic interaction.<sup>[53,54]</sup> But accompanied with that, hydrophobic interactions can become significant, as it is reported that the membrane surface also features hydrophobic spots.<sup>[55]</sup> If a high ionic strength eluent does not allow appropriate fractionation, as observed for several cationic polymers like

poly(ethylene imine) or PDMAEMA, a pre-saturation of the membrane by cationic surfactants or the analyte itself often is beneficial.<sup>[44]</sup> Here, the membrane is covered by a monolayer of the sample in a first experiment, which leads to repulsive electrostatic interactions between the sample and the modified membrane and to higher recovery rates during subsequent experiments.<sup>[56,57]</sup> This approach, a pre-saturation with PDMAEMA, was mainly used in this study to conduct experiments with different eluents under similar membrane conditions. Another possibility relies on the isoelectric point of regenerated cellulose membranes, which is in the range of pH 4.<sup>[58]</sup> If an eluent with a pH value below 4 is used, the membrane carries a slightly positive charge, which results in high recovery rates and reduction of adsorption phenomena already for fresh membranes. This can be seen in the fractograms of the block copolymers, shown in Figure 2A. Here, an eluent composed of 25 mM acetate and 20 mM sodium chloride with a pH value of 3.5 was used. In all cases, monomodal distributions with recovery rates above 80% were obtained. A representative light scattering trace (90°) as well as the corresponding molar masses can be exemplarily seen in Figure 2B for PDMAEMA<sub>51</sub>-*b*-PDEGMA<sub>49</sub> (subscripts represent molar block ratio)). Number and weight average molar masses as well as the resulting dispersity indices are summarized in Table 1. In all cases, reliable molar masses were obtained except for PDEGMA, which showed unexpectedly high values. We assume that this is related to the RI detector, operating at least 7 to 8 °C above room temperature (22 °C), which is slightly above the LCST of PDEGMA. This is supported by a strong light scattering signal at the void peak, indicating the elution of large aggregates and <sup>1</sup>H NMR measurements, where comparison of the integral of the aromatic RAFT endgroup and the repeating units of the polymer yielded a molar mass ( $M_n$ ) of around 16,800 g·mol<sup>-1</sup>. Therefore, for all experiments described below, only the MALLS and DLS detector, which could be accurately heated in the investigated temperature range (15 to 65 °C), were coupled to AF4. The described effect did not seem to influence the molar mass determination of PDMAEMA and the copolymers, as their cloud points are above 30 °C. Furthermore, the low pH value of the eluent increases the solubility of the PDMAEMA block and subsequently the  $T_{CP}$ , keeping the polymer chains soluble (see below). The significant difference to the previously published SEC results was attributed to the missing suitable standards (no MALLS detection) and interactions with the column material, which render SEC difficult to interpret in the present case.<sup>[20]</sup> Nevertheless, the trend between AF4 and SEC (in *N,N*-dimethylacetamide, DMAc) is comparable. Except for PDEGMA with a relatively low molar mass, the calculation from <sup>1</sup>H NMR spectroscopy also reached its limit due to the low signal to noise ratio for the endgroup signals. Taking together all characterization data for the samples investigated here, the molar mass obtained by AF4 seemed to be the most reliable.



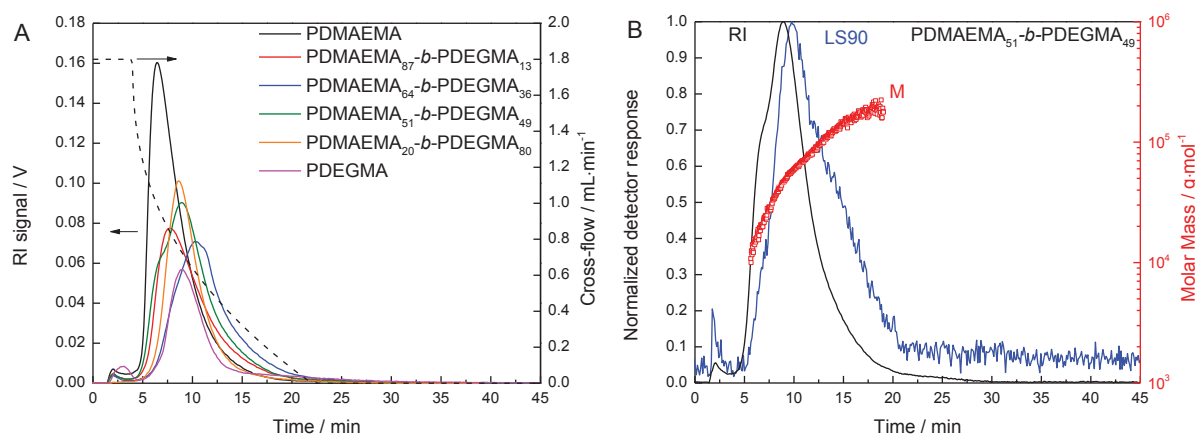


**Figure 2:** AF4 fractograms of (A) PDMAEMA-*b*-PDEGMA of different block ratios and (B) of PDMAEMA<sub>51</sub>-*b*-PDEGMA<sub>49</sub> with indicated molar masses and LS90° trace as obtained by MALLS. The eluent is composed of 25 mM acetate and 20 mM NaCl at pH 3.5.

**Table 1:** Molar masses of PDMAEMA-*b*-PDEGMA as obtained by AF4-MALLS.

PDMAEMA/PDEGMA block ratio (mol%) <sup>a</sup>	dn/dc [mL·g <sup>-1</sup> ]	M <sub>n</sub> [g·mol <sup>-1</sup> ]	M <sub>w</sub> [g·mol <sup>-1</sup> ]	Đ
100:0	0.193	29,000 ± 1,100	35,300 ± 700	1.22 ± 0.02
87:13	0.181	34,400 ± 1,900	51,100 ± 400	1.49 ± 0.08
64:36	0.161	57,400 ± 1,300	91,100 ± 300	1.59 ± 0.03
51:49	0.156	33,700 ± 4,500	59,800 ± 1,100	1.80 ± 0.22
20:80	0.150	48,300 ± 1,900	60,500 ± 1,3900	1.25 ± 0.08
0:100	0.083	106,900 ± 5,800 <sup>b</sup>	115,100 ± 5,600	1.09 ± 0.02

<sup>a</sup> obtained by <sup>1</sup>H NMR as described in Ref.<sup>[20]</sup>

<sup>b</sup> <sup>1</sup>H NMR measurements yielded a molar mass (M<sub>n</sub>) of around 16,800 g·mol<sup>-1</sup>.

## Influence of the block copolymer composition on the LCST

After synthesis and molar mass characterization, the cloud point temperatures were determined by turbidimetry measurements. The second of three heating and cooling cycles is displayed in Figure 3A. Except for PDMAEMA<sub>64</sub>-*b*-PDEGMA<sub>36</sub> and PDMAEMA<sub>51</sub>-*b*-PDEGMA<sub>49</sub>, one distinct transition, indicated by a decrease from 100% to nearly 0% transmission, was observed. For PDMAEMA, a cloud point temperature, T<sub>CP</sub>, of 52.7 °C (50% transmission) was obtained, which decreased with increasing content of PDEGMA in the block copolymers, until a T<sub>CP</sub> of 28.1 °C was reached for pure PDEGMA (Table 2). No clear transition or T<sub>CP</sub> could be observed for PDMAEMA<sub>64</sub>-*b*-PDEGMA<sub>36</sub>, which is most probably due to the formation of small micellar structures.<sup>[20,59]</sup> Two T<sub>CP</sub> could be observed for PDMAEMA<sub>51</sub>-*b*-PDEGMA<sub>49</sub>, where PDMAEMA and PDEGMA are equally present, a lower T<sub>CP1</sub> at around 34 °C and a second T<sub>CP2</sub> at around 46 °C. It was assumed in former studies that T<sub>CP1</sub> corresponds to the LCST of the PDEGMA block, while T<sub>CP2</sub> describes the transition of the PDMAEMA block.<sup>[20,27,59]</sup> To obtain deeper insights into the formed structures, DLS and LDV were performed. First of all, for comparison of the turbidimetry and DLS measurements, the average count rate as a

measure for the intensity of the scattered light is shown in Figure 3B. For the block copolymers with at least 50% PDEGMA, the change in count rate is in good agreement with the observed  $T_{CP}$  values. For the block copolymers, where PDMAEMA is the majority block (> 60%), the transition points obtained by count rate measurements are slightly shifted in contrast to turbidimetry experiments. This is most probably a kinetic effect due to different heating rates and the absence of stirring during count rate/DLS measurements, while a stirrer was used for turbidimetry experiments.<sup>[59]</sup>

**Table 2: Cloud point temperatures ( $T_{CP}$ ) obtained by turbidimetry and DSC measurements for PDMAEMA-*b*-PDEGMA with different block ratios.**

DMAEMA:DEGMA	100:0	87:13	64:36	51:49	20:80	0:100
$T_{CP}$ [°C]	52.7	47.0	-	34.4; 46.1	30.3	28.1
$T_{DSC}$ [°C]	54.1	48.8	33.8	34.9	31.3	29.8

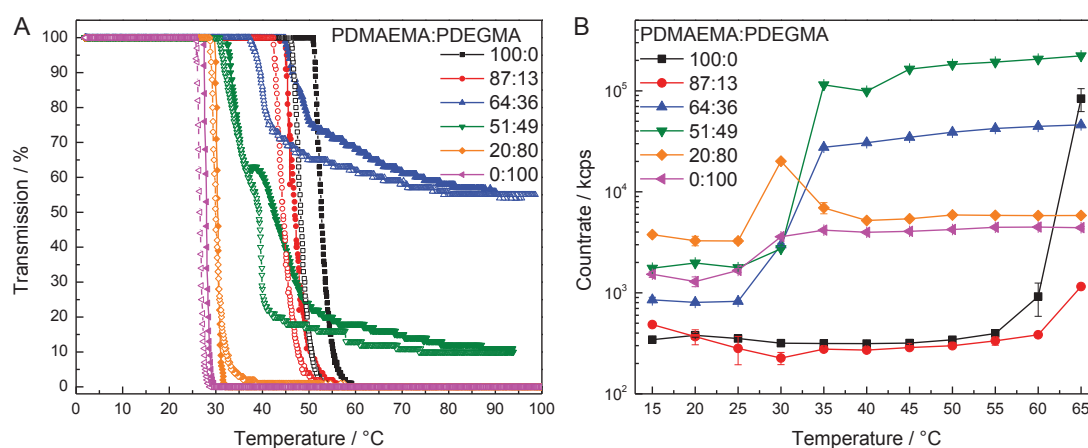


**Figure 3: (A) Turbidimetry measurements (solid line – heating; dotted line – cooling) and (B) count rate measurements of PDMAEMA-*b*-PDEGMA with different block ratios.**

The DLS results for all polymers are displayed in Figure 6A. Hysteresis between heating and cooling cycles was only observed for PDEGMA, which precipitates on the cuvette bottom above  $T_{CP}$  and is slowly redissolved upon cooling without stirring. Below  $T_{CP}$ , all polymers show  $R_h$  values of around 1 to 4 nm, corresponding to the hydrated single polymer chain. Above  $T_{CP}$ , PDMAEMA forms aggregates of around 10 nm at 60 °C, which further increase to around 65 nm until 65 °C. PDMAEMA<sub>87</sub>-*b*-PDEGMA<sub>13</sub> with a low PDEGMA content<sub>7</sub> showed the same trend with radii of around 20 to 25 nm above  $T_{CP}$ . For PDMAEMA<sub>64</sub>-*b*-PDEGMA<sub>36</sub> and PDMAEMA<sub>51</sub>-*b*-PDEGMA<sub>49</sub> the radius increased to 45 and 35 nm at 35 °C, respectively, presumably due the thermo-induced self-assembly into vesicular structures.<sup>[20]</sup> Further heating led to a slight decrease to around 20 nm for PDMAEMA<sub>64</sub>-*b*-PDEGMA<sub>36</sub> and 30 nm for PDMAEMA<sub>51</sub>-*b*-PDEGMA<sub>49</sub>, which is then roughly constant until 65 °C. An influence of the proposed second transition ( $T_{CP2}$ ) on  $R_h$  was not observed. Furthermore, a maximum in size could be observed for PDMAEMA<sub>64</sub>-*b*-PDEGMA<sub>36</sub> at 35 °C. Currently,

the origin of this effect is rather unclear, but we assume that it might be related to the formation of some kind of metastable aggregates.<sup>[60]</sup> The (first)  $T_{CP}$  is also accessible by the PDI values obtained by cumulant analysis of the DLS data of all copolymers and PDMAEMA (data not shown). Here, the PDI decreases by crossing  $T_{CP}$  from around 0.6 to 0.8 to values below 0.3. Again, a second transition was not observed for PDMAEMA<sub>51</sub>-*b*-PDEGMA<sub>49</sub>. For PDMAEMA<sub>20</sub>-*b*-PDEGMA<sub>80</sub> and PDEGMA, large aggregates ( $R_h > 300$  nm, PDI > 0.6) were formed above the transition temperature. Thereby, aggregates of PDEGMA started to precipitate over time and therefore the transition is not detectable by the PDI values of the cumulant analysis.

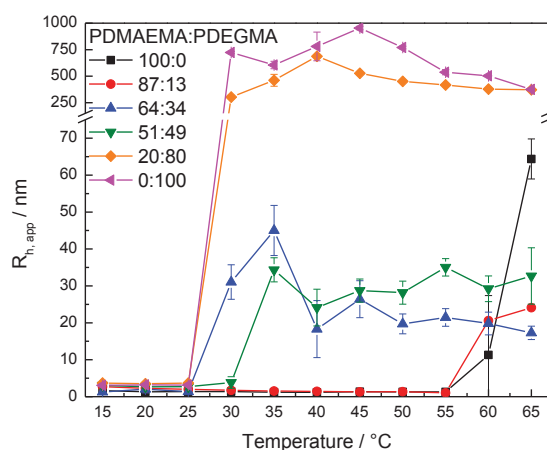


**Figure 4: (A) Apparent hydrodynamic radius of PDMAEMA-*b*-PDEGMA as obtained by DLS in deionized water.**

To elucidate whether the use of number-weighted DLS data gave appropriate results and to obtain detailed information on both, size distribution and shape, AF4 coupled to MALLS and DLS was evaluated as potential characterization method for thermo-responsive block copolymers. To enable fractionation under similar conditions for all polymers, an eluent containing 100 mM sodium chloride was found to be suitable and recovery rates > 80% were obtained with a membrane made of regenerated cellulose and a cut-off of 10,000 g·mol<sup>-1</sup>. Except for PDMAEMA<sub>51</sub>-*b*-PDEGMA<sub>49</sub>, which was fractionated at 15 to 65 °C in steps of 5 K, all polymers were analyzed at 20, 45 and 65 °C. A single peak is obtained for PDMAEMA and PDMAEMA<sub>87</sub>-*b*-PDEGMA<sub>13</sub> (high PDMAEMA content) at all temperatures, which corresponds to the hydrated chain as indicated by MALLS detection (compare Figure 2). The absence of any aggregates even at 65 °C, which is in conflict with turbidimetry and DLS experiments, was attributed to the concentration dependence of the cloud point and the low concentration in the channel. As  $T_{CP}$  is increasing with decreasing concentration,<sup>[20]</sup> it is shifted to values above 65 °C at the concentration in the channel (roughly 0.04 mg·mL<sup>-1</sup> in the peak maximum). The fractionation of PDMAEMA<sub>51</sub>-*b*-PDEGMA<sub>49</sub> (Figure 5A) revealed the presence of block copolymer unimers until 30 °C as indicated by the signal at 9.2 min. A second signal appears at 19.5 min at 35 °C, which corresponds to vesicles and a  $R_h$  of around 20 nm is obtained by online DLS. Further heating

led to a small increase of  $R_h$  (representative fractograms in Figure 5B) and a reduction of elution time for all peaks. We attribute this to an increase of the respective diffusion coefficient, according to the Stokes-Einstein equation and AF4 theory.<sup>[40]</sup> Furthermore, the amount of hydrated polymer chains is reduced with increasing temperature. It can be seen that above 55 °C larger aggregates are formed, which originated from increased interactions between the vesicles and the membrane.<sup>[55]</sup> Nevertheless, due to the high sensitivity of MALLS for large aggregates, their concentration can be regarded as being rather low. A comparison of offline and online DLS as well as the radius of gyration ( $R_g$ , Table 3) showed that, in principle, slightly lower radii are obtained by AF4-MALLS-DLS. This is most probably due to the usage of NaCl in the eluent, which reduces electrostatic interactions, in particular the repulsion between PDMAEMA segments and, therefore, reduces the particle's size. For the free, hydrated chain no size could be determined as it is below the detection limit of the online measurement.<sup>[37]</sup> Calculation of the shape ratio,  $R_g/R_h$ , gave values of around 1 for all temperatures above 30 °C, which supports the formation of vesicular rather than micellar structures.<sup>[61]</sup> Similar to offline DLS measurements, no second transition could be identified in terms of size or shape. Fractionation of PDMAEMA<sub>64</sub>-*b*-PDEGMA<sub>36</sub> shows a similar trend. Here, hydrodynamic radii of around 25 nm were obtained above 30°C, but smaller  $R_g$  values (around 20 nm) resulted in an average shape ratio < 0.8, indicating the presence of micellar structures. During fractionation of PDMAEMA<sub>20</sub>-*b*-PDEGMA<sub>80</sub> and PDEGMA at 20 °C also block copolymer unimers could be detected. At 45 °C, a  $R_h$  of around 24 nm is obtained for PDMAEMA<sub>20</sub>-*b*-PDEGMA<sub>80</sub>, which is in contrast to offline DLS results, showing larger aggregates. At the moment, we assume that this is an effect related to the concentration and the ionic strength of the solution. Offline DLS at conditions similar to AF4 (100 mM NaCl, 0.04 mg·mL<sup>-1</sup> copolymer) provided hydrodynamic radii comparable to AF4 results. No fractionation could successfully be performed for PDEGMA above 35°C. This was due to the formation of large aggregates, blocking the detector tubings in the system, which is therefore in good agreement with offline DLS. These results clearly showed that AF4 is able to provide a detailed characterization of thermo-responsive systems. Moreover, the comparison of AF4 and offline DLS of all samples revealed that the use of number-weighted offline DLS data is in most cases appropriate to describe the investigated structures.

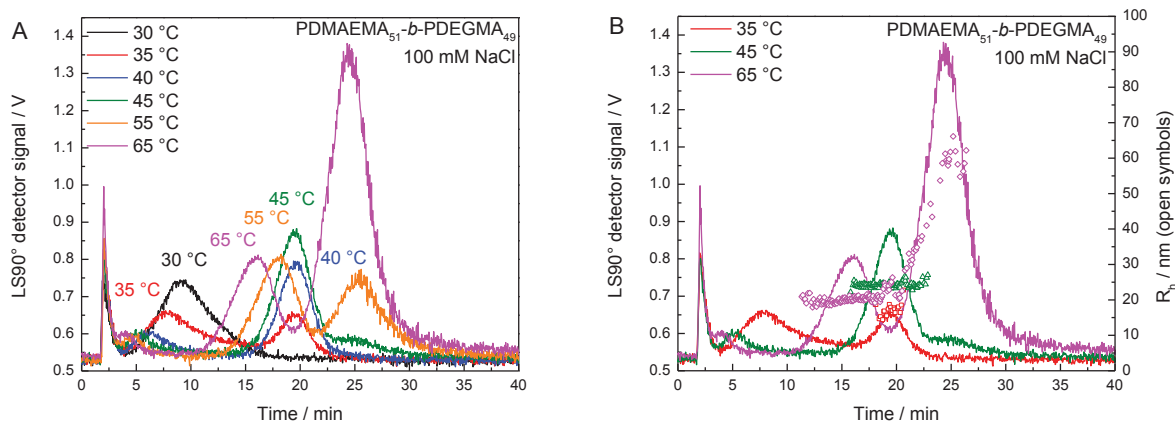


**Figure 5:** AF4-MALLS-DLS fractograms (light scattering trace at 90°) of PDMAEMA<sub>51</sub>-*b*-PDEGMA<sub>49</sub> at (A) different temperatures and (B) at representative temperatures with indicated hydrodynamic radii obtained by online DLS.

**Table 3:** Comparison of offline DLS and data obtained by AF4-MALLS-DLS of PDMAEMA<sub>51</sub>-*b*-PDEGMA<sub>49</sub>.

T [°C]	R <sub>h</sub> [nm] offline	R <sub>h</sub> [nm] online	R <sub>g</sub> [nm] online	R <sub>g</sub> /R <sub>h</sub> online
20	2.7	-	-	-
25	2.7	-	-	-
30	3.8	-	-	-
35	34.4	17.3	16.2	0.94
40	24.1	23.2	22.7	0.98
45	28.7	24.7	26.7	1.08
50	28.2	22.3	23.1	1.04
55	35.0	24.0	22.8	0.95
60	29.2	20.3	22.0	1.08
65	32.7	20.2	20.1	1.00

To gain further insights into the thermo-induced self-assembly of PDMAEMA-*b*-PDEGMA and the postulated second transition, Laser Doppler velocimetry (LDV) was applied. For measuring the zeta potential of colloids LDV represents a powerful tool to study the influence of electrostatic contributions on the self-assembly, in particular, if polyelectrolytes are investigated. Homopolymers of PDMAEMA and PDEGMA revealed a significant increase in zeta potential, either positive (PDMAEMA) or negative (PDEGMA), above their  $T_{CP}$  (Figure 6B). This is due to the dehydration of the polymer chain and an orientation of the more hydrophilic side chains towards the aqueous environment of the formed particles. While the positive charge of the side chains of PDMAEMA is provided by the protonated tertiary amines, the negative zeta potential of PDEGMA most probably resulted from the ethylene glycol side chains as also observed in former studies of poly(ethylene glycol) based polymers.<sup>[62]</sup> PDMAEMA<sub>87</sub>-*b*-PDEGMA<sub>13</sub> showed a similar trend as PDMAEMA which is most probably due to the very high PDMAEMA content. Only the absolute values of the zeta potential are lower. For all other block copolymers, the zeta potential revealed two distinct changes upon heating. A first significant increase can be observed at around 30 to 35 °C and a decrease at around 55 to 60 °C. The first change in zeta potential is related to the transition, leading to the

formation of block copolymer aggregates, where cationic PDMAEMA is located at the surface and formed the hydrophilic part, while PDEGMA becomes the hydrophobic block. During the second transition, it was assumed that PDMAEMA collapses. Interestingly, this behavior is not accompanied by a change in hydrodynamic radius or radius of gyration. We currently assume that a reordering takes place during the collapse of PDMAEMA, where more polar PDEGMA groups migrate back to the surface of the collapsed structure, leading to a reduced zeta potential. This is supported by temperature dependent cryo-TEM and  $^1\text{H}$  NMR measurements in former studies.<sup>[20]</sup> In particular, the  $^1\text{H}$  NMR results, which showed first a decrease and then a reappearance of the signals for PDEGMA upon heating from 20 to 65 °C, promote this interpretation. Previous cryo-TEM experiments indicated the formation of unilamellar vesicles out of multilamellar ones.<sup>[20]</sup> Interestingly, the transitions of the zeta potential are only reflected by turbidimetry experiments of PDMAEMA<sub>51</sub>-*b*-PDEGMA<sub>49</sub>. Up to now, we have no distinct explanation for this behavior but it might be based on the differences in the molar mass of the materials. Anyhow, to address the question, if the reordering above 55 °C corresponds to a second phase transition, DSC was applied to all polymers (Figure 6B). Thereby, a polymer concentration of 2.5 mg·mL<sup>-1</sup>, similar to all other experiments, was used. For all polymers, only one exothermic phase transition was detected and the transition temperatures (peak maximum) were in good agreement with values for  $T_{\text{CP1}}$ , based on turbidimetry and DLS (Table 2). The noisy signals for PDEGMA and PDMAEMA<sub>20</sub>-*b*-PDEGMA<sub>80</sub> are most probably due to the precipitation of the polymer upon heating above  $T_{\text{CP}}$ . The obtained results clearly showed that the second transition, observed by zeta potential measurements,  $^1\text{H}$  NMR and turbidimetry, is not related to an actual phase transition. Considering all experimental data, the second transition is to our current knowledge best described as a reordering of the internal structure of the formed aggregates that is based on the collapse of PDMAEMA and a migration of PDEGMA segments back to the surface of the structures to stabilize them in aqueous solution.

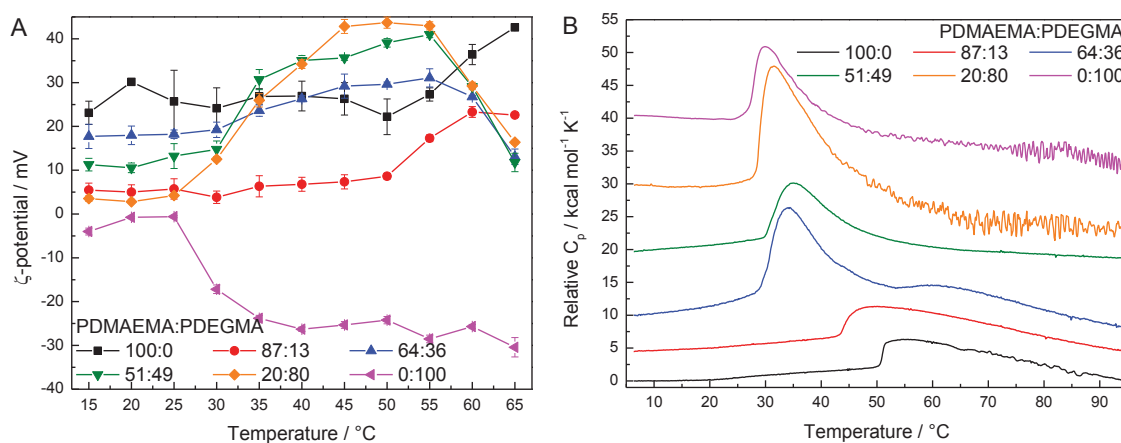


Figure 6: (A) Zeta potential and (B) DSC results of PDMAEMA-*b*-PDEGMA in deionized water at 2.5 mg·mL<sup>-1</sup>.

## Influence of ionic strength on the LCST and the self-assembly behavior

To obtain further insights into the thermo-induced self-assembly behavior of the block copolymers, PDMAEMA<sub>51</sub>-*b*-PDEGMA<sub>49</sub> was chosen for further investigations concerning the influence of ionic strength and the pH value. As the formation of vesicles was supposed to depend on the electrostatic interactions between PDEGMA (negative zeta potential) and PDMAEMA (positive zeta potential),<sup>[20]</sup> the influence of the range of electrostatic interactions, *i.e.* the influence of ionic strength was investigated first. For this purpose, the polymer was dissolved in aqueous solutions containing 0, 5, 100 and 500 mM NaCl, respectively. Subsequently, DLS was performed and the count rate as well as the apparent number weighted hydrodynamic radii are shown in Figure 7. Count rate measurements showed that the addition of low amounts of NaCl has no significant effect on the LCST (35 °C). Increasing the ionic strength to 100 mM led to a shift to lower temperatures of around 30 and 25 °C at 500 mM NaCl. This is primarily due to the screening of charges that reduces the solubility of the PDMAEMA segments. Moreover, a decrease in count rate was observed at 500 mM NaCl above 60 °C, due to precipitation and sedimentation of the block copolymer. Under such high values of ionic strength, the electrostatic repulsion, which often ensures colloidal stability, is strongly diminished, resulting in aggregation. In this case, also a strong hysteresis could be observed, which is due to a rather slow redissolution upon cooling after precipitation. Even if the ionic strength influences the transition temperature, the impact on the hydrodynamic radii of the vesicular structures is rather small. In all cases, constant radii between 20 and 30 nm were obtained above the  $T_{CP}$  and also the (second) reordering did not show any impact on size, except for 500 mM NaCl, where larger aggregates are formed. A support of these findings by zeta potential measurements was not possible, as the high ionic strength leads to zeta potentials close to zero and high currents in the cell during the measurement.

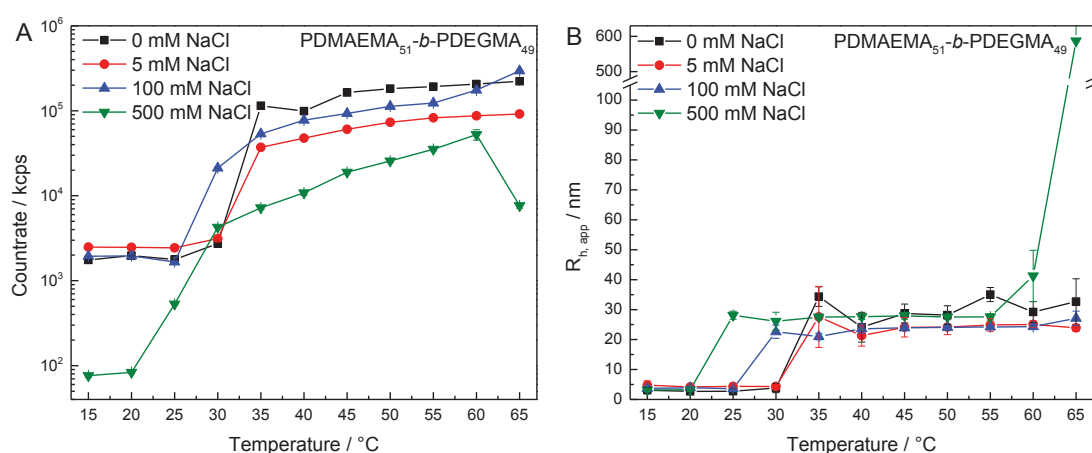


Figure 7: (A) Count rate and (B) DLS measurements of the apparent hydrodynamic radius (NNLS algorithm) of PDMAEMA<sub>51</sub>-*b*-PDEGMA<sub>49</sub> at varying temperature and ionic strength (NaCl concentration).

The influence of the ionic strength on the self-assembly behavior of PDMAEMA<sub>51</sub>-*b*-PDEGMA<sub>49</sub> was also investigated by AF4-MALLS-DLS. Here, the sample was dissolved in water, containing the corresponding amount of NaCl, which was also used as eluent for fractionation. In pure water, no fractionation was possible, due to strong interactions between the polymer and the membrane, indicated by a very low recovery (< 40%) and irregular elution at all temperatures.<sup>[44]</sup> At 5 mM NaCl, fractionation at temperatures below 60 °C could be realized. Below 35 °C, a fractogram similar to Figure 2B was obtained. The elution time of the peak was slightly reduced and could be identified by MALLS as block copolymer unimer. AF4 measurements between 35 and 65 °C showed an elution profile similar to previous experiments with a slight shift to lower elution times, too. The obtained (online)  $R_h$  and  $R_g$  values also scale in the range of 20 to 25 nm with shape ratios,  $R_g/R_h$ , of around 1, indicating the presence of vesicular structures. For 100 mM NaCl (Figure 5), AF4 and offline DLS were in excellent agreement except for 30 °C, where AF4 detected block copolymer unimers, while offline DLS already indicates the presence of colloidal structures. This difference close to the  $T_{CP}$  is again attributed to the lower sample concentration during AF4 separation, which is connected to a higher transition temperature. A reduced recovery of around 60 to 70% was obtained at all temperatures with 500 mM NaCl, most probably due to the high ionic strength and the resulting screening of electrostatic forces within the sample and between sample and membrane. Nevertheless, elution profiles similar to experiments in 100 mM NaCl were obtained, with a slight shift to higher elution times. Online DLS detection gave radii of around 27 nm, which is in excellent agreement with offline measurements below 60 °C. Above 60 °C, AF4 showed no increase in size or aggregation as observed by offline DLS ( $R_h$  around 600 nm). To prove whether this is an artefact of the AF4 measurements or a concentration dependent effect, we diluted the sample for offline DLS measurements to around 0.04 mg·mL<sup>-1</sup>, which is similar to the concentration in the AF4 channel during elution (peak maximum). Obtained (offline) hydrodynamic radii of around 30±4 nm, with PDI values below 0.15 showed that this aggregation is a concentration dependent effect. It further critically illustrates the necessity to consider the AF4 eluent as well as the difference in concentration in the channel, when results are interpreted and compared with offline experiments. Moreover, the strong dependency of the cloud point on the polymer concentration limits its applicability for drug delivery applications and thermo-induced release. On the other hand, this effect might be used for encapsulation of substances at higher polymer concentrations (*e.g.*  $T_{CP}$  below 37 °C), which are released during dilution (*e.g.*  $T_{CP}$  above 37 °C).

### **Influence of the pH value on the LCST and the self-assembly behavior**

Due to the fact that the solubility and the LCST of PDMAEMA can easily be adjusted by the pH value, we also investigated PDMAEMA<sub>51</sub>-*b*-PDEGMA<sub>49</sub> at varying pH values. Therefore, we used different



buffer system with a total concentration of 25 mM: Acetate buffer at pH 4 and 5.6, phosphate buffer at pH 7.2 and ammonia buffer at pH 8.3 and 10. First, DLS measurements were performed to investigate the influence on the cloud point (Figure 8). At pH 4, no transition could be detected over the complete investigated temperature range. Due to the high degree of protonation of the PDMAEMA segments ( $pK_a$  around 6), the polymer is highly soluble and shows no  $T_{CP}$  in aqueous solution.<sup>[26]</sup> From pH 5.6 to 8.3, one transition could be identified with an increasing  $T_{CP}$  from 30 °C at pH 8.2 to 40 °C at pH 5.6. This increase of  $T_{CP}$  with decreasing pH value is also based on a higher degree of protonation of PDMAEMA, leading to increased hydrophilicity. Heating above  $T_{CP}$  at pH 10 (around 30 °C) led to precipitation of the polymer, due to the reduced solubility of the PDMAEMA block at basic pH, when nearly all amine groups are deprotonated. The variation of count rate above 30 °C is a result of the sedimentation of these precipitates. Here, also hydrodynamic radii of several  $\mu\text{m}$  are obtained, which is above the reliable measurement range of DLS and, therefore, indicated as  $> 1,000$  nm in Figure 8B.

Self-assembled structures in the range of 20 to 30 nm were observed for samples at pH 5.6 to 8.3 of all temperature above  $T_{CP}$  (until 65 °C), except for pH 5.6 at 40 °C. Here, a  $R_h$  of around 60 nm was obtained. Currently, we assume that this effect is based on the higher degree of protonation of the PDMAEMA segments. Compared to earlier data at pH 4, the charge density is not sufficient to ensure solubility over the whole temperature range but electrostatic repulsion results in the formation of larger, probably less compact, structures. The cloud point can also be observed by measurements of the zeta potential (Figure 9A). As the measured zeta potential depends on the ionic strength of the buffer solution, the ionic strength of all buffers was depicted in Figure 9A. At pH 5.6 and 8.3, one transition can be seen, which is in good agreement with DLS measurements. As the ionic strength in both solutions was quite similar, the absolute difference in zeta potential can be attributed to the lower degree of protonation of the PDMAEMA block at basic pH. At pH 7.2, the zeta potential is close to zero at all temperatures, which is due to the high ionic strength of phosphate buffers (trivalent anion) and the resulting reduction in range of electrostatic contributions, masking possible transitions. A zeta potential close to zero is obtained at pH 10 in a low ionic strength buffer. This is attributed to the deprotonation of PDMAEMA and the slight variation of zeta potential above  $T_{CP}$  has to be considered carefully, as precipitation and sedimentation occur at these temperatures. At pH 4, the zeta potential is nearly constant over the whole temperature range and no transition could be observed, which is in agreement with the offline DLS data.

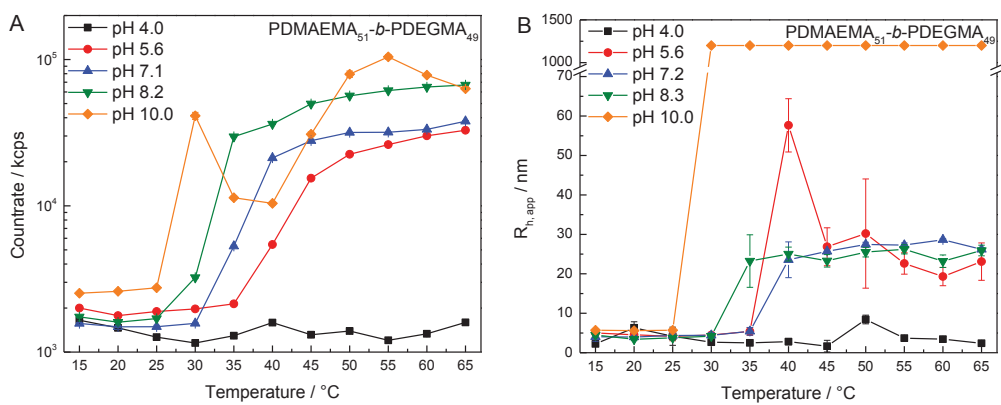


**Figure 8: (A) Count rate and (B) DLS measurements of the apparent hydrodynamic radius of PDMAEMA<sub>51</sub>-b-PDEGMA<sub>49</sub> at varying temperature and pH values.**

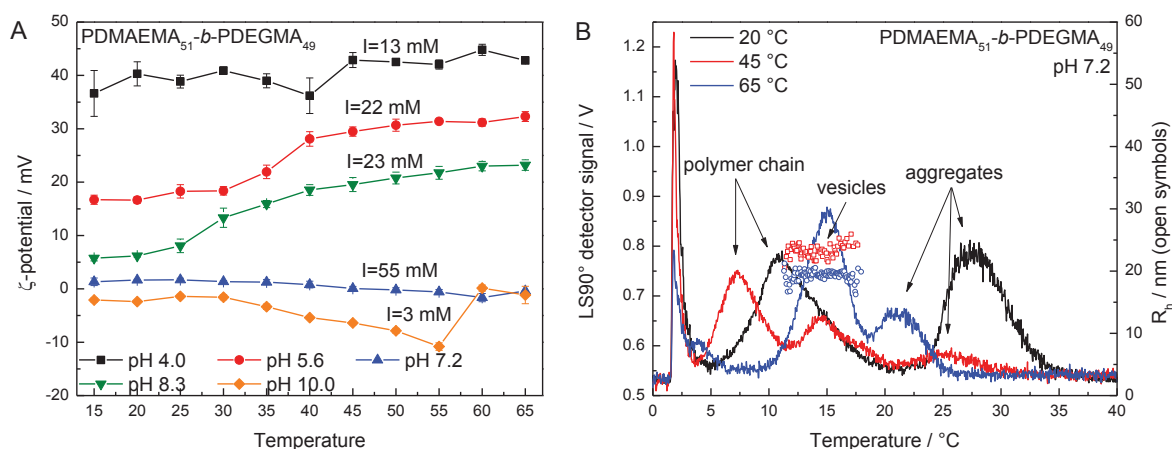


**Figure 9: (A) Zeta potential of PDMAEMA<sub>51</sub>-b-PDEGMA<sub>49</sub> at varying temperatures and pH values. (B) AF4-MALLS-DLS fractograms (light scattering trace at 90°) of PDMAEMA<sub>51</sub>-b-PDEGMA<sub>49</sub> at pH 7.2 and representative temperatures with indicated hydrodynamic radii obtained by online DLS.**

The influence of the pH value on the self-assembly of PDMAEMA-*b*-PDEGMA was also investigated by AF4. At pH 7.2, below 35 °C the free polymer chain was observed at around 11 min (Figure 9B). With increasing temperature, less block copolymer unimers were detected and the peak is shifted to lower elution times due to the increase in diffusion coefficient caused by the higher temperature. Above the T<sub>CP</sub>, a second population with an R<sub>g</sub> and R<sub>h</sub> of 23 nm could be observed, which corresponds to the formed vesicles. Until 65 °C, their size decreases slightly to 19 nm. The obtained AF4 and offline DLS data are in good agreement. Furthermore, in all experiments at pH 7.2, a small fraction of large aggregates was observed, which was found to be due to membrane interactions based on the phosphate buffer. Nevertheless, their amount is rather small as they were not detectable by online DLS or UV. An increase of the pH value enhances these adsorption effects as the block copolymer becomes more hydrophobic. This results in a very low recovery (< 60%) for measurements at pH 8.3 and 10 at 20 °C. At temperatures above the transition temperature, the recovery is reduced to < 30% at pH 8.3, which prevents any meaningful determination of hydrodynamic radii. At pH 10, the formation of large precipitates led to a blockage of the backpressure tubing, which is in good

accordance with DLS measurements, where also large aggregates were observed. At pH 4 and 5.6, recovery rates above 80% were obtained. At all investigated temperatures at pH 4, one peak was observed, whose elution time decreases with temperature and which corresponds to block copolymer unimers, as indicated by MALLS detection. Results at pH 5.6 (elution time and size) were similar to pH 7.2, more specific the observation of block copolymer unimers at 20 °C and vesicular structures ( $R_h$  21 nm) at 65 °C. In contrast to pH 7.2 and offline DLS, no vesicles could be detected at 45 °C. This could be explained with the lower concentration in the AF4 channel as already described above. DLS measurements at dilutions similar to concentrations in the AF4 channel ( $0.04 \text{ mg}\cdot\text{mL}^{-1}$ ) revealed that the cloud point at this concentration and pH value is increased to around 47 °C. These results demonstrate that by variation of the pH value the phase transition of the copolymer can easily be adjusted in a broad temperature range, without changing the particle's size or shape.

## Conclusion

In this study, we present a detailed investigation on the thermo-induced self-assembly of PDMAEMA-*b*-PDEGMA with varying block ratios. By combination of turbidimetry, DLS, LDV, DSC, and AF4-MALLS-DLS up to two structural transitions could be identified in dependence on the block ratio. Thereby, only the first cloud point corresponds to an actual phase transition. To our current knowledge, the second change is associated with a reordering of the internal structure of the formed vesicles, most probably, the formation of unilamellar vesicles out of multilamellar structures. This is due to the collapse of PDMAEMA segments and a migration of more polar PDEGMA groups back to the surface. This is supported by  $^1\text{H}$  NMR and cryo-TEM experiments of a previous study<sup>[20]</sup> as well as zeta potential measurements. For PDMAEMA<sub>51</sub>-*b*-PDEGMA<sub>49</sub>, the influence of ionic strength and pH value was further investigated. It was found that the cloud point can be decreased by an increase in ionic strength or pH value as this reduces the range of electrostatic interactions and the protonation of the PDMAEMA block. This enables an exact control of the phase transition by adjusting the solution parameters over a wide temperature range and, subsequently, the application as soluble polymeric sensors for pH value, temperature and salt concentration.

Furthermore, AF4 could be successfully applied for temperature dependent investigations on thermo-responsive polymers. Thereby, two restricting factor have to be considered. First of all, the eluent used for AF4 should be identical with the solution used for other studies, as the cloud point of materials containing a polyelectrolyte block is highly sensitive against changes in pH value or ionic strength. This might lead to problems during AF4 fractionation, as strong repulsive or attractive interactions can result in (irreversible) adsorption on the membrane or an irregular elution behavior. The second issue is related to the concentration in the AF4 channel, which is usually considerably

lower than the concentrations used for offline techniques. Therefore, the transition temperature detected by temperature dependent AF4 was in the present case higher than by other methods. Also the trend for aggregation might vary with concentration. Nevertheless, AF4 was confirmed to be a powerful tool to obtain detailed insights into the size and shape of colloidal structures. In case of PDMAEMA-*b*-PDEGMA, the self-assembly into vesicular structures for PDMAEMA<sub>51</sub>-*b*-PDEGMA<sub>49</sub> and micelles for PDMAEMA<sub>64</sub>-*b*-PDEGMA<sub>36</sub> could be confirmed by the shape ratio ( $R_g/R_h$ ). For (offline) DLS, where different algorithms and differently weighted datasets are available, which renders interpretation of bi- or multimodal distributions sometimes difficult, coupling to AF4 represents a promising alternative.

## Acknowledgements

This project was funded by the Carl-Zeiss Foundation (Strukturantrag JCSM). Felix Schacher is acknowledged for critical reading of the manuscript.

## References

- [1] H. G. Schild, *Prog. Polym. Sci.* **1992**, *17*, 163-249.
- [2] C. Pietsch, R. Hoogenboom, U. S. Schubert, *Angew. Chem. Int. Ed.* **2009**, *48*, 5653-5656.
- [3] J. M. Hu, S. Y. Liu, *Macromolecules* **2010**, *43*, 8315-8330.
- [4] I. Dimitrov, B. Trzebicka, A. H. E. Müller, A. Dworak, C. B. Tsvetanov, *Prog. Polym. Sci.* **2007**, *32*, 1275-1343.
- [5] J. Z. Du, R. K. O'Reilly, *Soft Matter* **2009**, *5*, 3544-3561.
- [6] S. T. Hemp, A. E. Smith, W. C. Bunyard, M. H. Rubinstein, T. E. Long, *Polymer* **2014**, *55*, 2325-2331.
- [7] J. Hu, G. Zhang, Z. Ge, S. Liu, *Prog. Polym. Sci.* **2014**, *39*, 1096-1143.
- [8] M. H. Li, P. Keller, *Soft Matter* **2009**, *5*, 927-937.
- [9] Y. Li, B. S. Lokitz, C. L. McCormick, *Angew. Chem. Int. Ed.* **2006**, *45*, 5792-5795.
- [10] Y. T. Li, B. S. Lokitz, C. L. McCormick, *Macromolecules* **2006**, *39*, 81-89.
- [11] B. M. Discher, Y. Y. Won, D. S. Ege, J. C. M. Lee, F. S. Bates, D. E. Discher, D. A. Hammer, *Science* **1999**, *284*, 1143-1146.
- [12] D. E. Discher, A. Eisenberg, *Science* **2002**, *297*, 967-973.
- [13] D. Schmaljohann, *Adv. Drug Delivery Rev.* **2006**, *58*, 1655-1670.
- [14] S. H. Qin, Y. Geng, D. E. Discher, S. Yang, *Adv. Mater.* **2006**, *18*, 2905-2909.
- [15] O. Onaca, R. Enea, D. W. Hughes, W. Meier, *Macromol. Biosci.* **2009**, *9*, 129-139.
- [16] J. F. Coelho, P. C. Ferreira, P. Alves, R. Cordeiro, A. C. Fonseca, J. R. Gois, M. H. Gil, *EPMA J.* **2010**, *1*, 164-209.
- [17] E. S. Gil, S. M. Hudson, *Prog. Polym. Sci.* **2004**, *29*, 1173-1222.
- [18] L. Yang, T. Liu, K. Song, S. Wu, X. Fan, *J. Appl. Polym. Sci.* **2013**, *127*, 4280-4287.
- [19] T. Thavanesan, C. Herbert, F. A. Plamper, *Langmuir* **2014**, *30*, 5609-5619.
- [20] C. Pietsch, U. Mansfeld, C. Guerrero-Sanchez, S. Höppener, A. Vollrath, M. Wagner, R. Hoogenboom, S. Saubern, S. H. Thang, C. R. Becer, J. Chiefari, U. S. Schubert, *Macromolecules* **2012**, *45*, 9292-9302.
- [21] F. A. Plamper, A. Schmalz, M. Ballauff, A. H. E. Müller, *J. Am. Chem. Soc.* **2007**, *129*, 14538-14539.

- [22] T. Ishizone, A. Seki, M. Hagiwara, S. Han, H. Yokoyama, A. Oyane, A. Deffieux, S. Carlotti, *Macromolecules* **2008**, *41*, 2963-2967.
- [23] P. van de Wetering, N. J. Zuidam, M. J. van Steenberg, O. A. G. J. van der Houwen, W. J. M. Underberg, W. E. Hennink, *Macromolecules* **1998**, *31*, 8063-8068.
- [24] S. Yamamoto, J. Pietrasik, K. Matyjaszewski, *Macromolecules* **2008**, *41*, 7013-7020.
- [25] R. Paris, I. Quijada-Garrido, *Eur. Polym. J.* **2010**, *46*, 2156-2163.
- [26] F. A. Plamper, M. Ruppel, A. Schmalz, O. Borisov, M. Ballauff, A. H. E. Müller, *Macromolecules* **2007**, *40*, 8361-8366.
- [27] Q. Zhang, J.-D. Hong, R. Hoogenboom, *Polym. Chem.* **2013**, *4*, 4322-4325.
- [28] F. L. Baines, S. P. Armes, N. C. Billingham, Z. Tuzar, *Macromolecules* **1996**, *29*, 8151-8159.
- [29] F. L. Baines, N. C. Billingham, S. P. Armes, *Macromolecules* **1996**, *29*, 3416-3420.
- [30] K. Sui, X. Zhao, Z. Wu, Y. Xia, H. Liang, Y. Li, *Langmuir* **2012**, *28*, 153-160.
- [31] C. M. Schilli, M. F. Zhang, E. Rizzardo, S. H. Thang, Y. K. Chong, K. Edwards, G. Karlsson, A. H. E. Muller, *Macromolecules* **2004**, *37*, 7861-7866.
- [32] X. Han, X. Zhang, H. Zhu, Q. Yin, H. Liu, Y. Hu, *Langmuir* **2013**, *29*, 1024-1034.
- [33] J. Gigault, T. J. Cho, R. I. MacCuspie, V. A. Hackley, *Anal. Bioanal. Chem.* **2013**, *405*, 1191-1202.
- [34] J. Gigault, W. Zhang, G. Lespes, B. Charleux, B. Grassl, *Anal. Chim. Acta* **2014**, *819*, 116-121.
- [35] S. Boye, D. Appelhans, V. Boyko, S. Zschoche, H. Komber, P. Friedel, P. Formanek, A. Janke, B. I. Voit, A. Lederer, *Biomacromolecules* **2012**, *13*, 4222-4235.
- [36] J. R. Silveira, A. G. Hughson, B. Caughey, *Method Enzymol* **2006**, *412*, 21-33.
- [37] M. Wagner, S. Holzschuh, A. Traeger, A. Fahr, U. S. Schubert, *Anal. Chem.* **2014**, *86*, 5201-5210.
- [38] J. C. Giddings, *J. Sep. Sci.* **1966**, *1*, 123-125.
- [39] J. C. Giddings, *Science* **1993**, *260*, 1456-1465.
- [40] K. G. Wahlund, J. C. Giddings, *Anal. Chem.* **1987**, *59*, 1332-1339.
- [41] A. Litzén, K. G. Wahlund, *Anal. Chem.* **1991**, *63*, 1001-1007.
- [42] A. Litzén, *Anal. Chem.* **1993**, *65*, 461-470.
- [43] J. C. Giddings, F. J. Yang, M. N. Myers, *Anal. Chem.* **1976**, *48*, 1126-1132.
- [44] M. Wagner, C. Pietsch, L. Tauhardt, A. Schallon, U. S. Schubert, *J. Chromatogr. A* **2013**, *1325*, 195-203.
- [45] G. Yohannes, J. Shan, M. Jussila, M. Nuopponen, H. Tenhu, M.-L. Riekkola, *J. Sep. Sci.* **2005**, *28*, 435-442.
- [46] A. C. Makan, T. Otte, H. Pasch, *Macromolecules* **2012**, *45*, 5247-5259.
- [47] K. Glinel, C. Vaugelade, G. Muller, C. Bunel, *Int. J. Polym. Anal. Charact.* **2000**, *6*, 89-107.
- [48] K. Knop, A.-F. Mingotaud, N. El-Akra, F. Violleau, J.-P. Souchard, *Photochem. Photobiol. Sci.* **2009**, *8*, 396-404.
- [49] K. Loos, A. Boker, H. Zettl, A. F. Zhang, G. Krausch, A. H. E. Müller, *Macromolecules* **2005**, *38*, 873-879.
- [50] M. Andersson, B. Wittgren, K. G. Wahlund, *Anal. Chem.* **2003**, *75*, 4279-4291.
- [51] A. V. Delgado, F. Gonzalez-Caballero, R. J. Hunter, L. K. Koopal, J. Lyklema, *J. Colloid Interface Sci.* **2007**, *309*, 194-224.
- [52] H. Ohshima, *J. Colloid Interface Sci.* **1994**, *168*, 269-271.
- [53] M. A. Benincasa, C. Delle Fratte, *J. Chromatogr. A* **2004**, *1046*, 175-184.
- [54] A. Ulrich, S. Losert, N. Bendixen, A. Al-Kattan, H. Hagedorfer, B. Nowack, C. Adlhart, J. Ebert, M. Lattuada, K. Hungerbühler, *J. Anal. At. Spectrom.* **2012**, *27*, 1120-1130.
- [55] S. Hupfeld, D. Ausbacher, M. Brandl, *J. Sep. Sci.* **2009**, *32*, 3555-3561.
- [56] M. A. Benincasa, J. C. Giddings, *Anal. Chem.* **1992**, *64*, 790-798.
- [57] G. Yohannes, M. Jussila, K. Hartonen, M.-L. Riekkola, *J. Chromatogr. A* **2011**, *1218*, 4104-4116.
- [58] M. Pontie, *J. Membr. Sci.* **1999**, *154*, 213-220.
- [59] V. S. Joseph, S. Kim, Q. Zhang, R. Hoogenboom, J.-D. Hong, *Polymer* **2013**, *54*, 4894-4901.

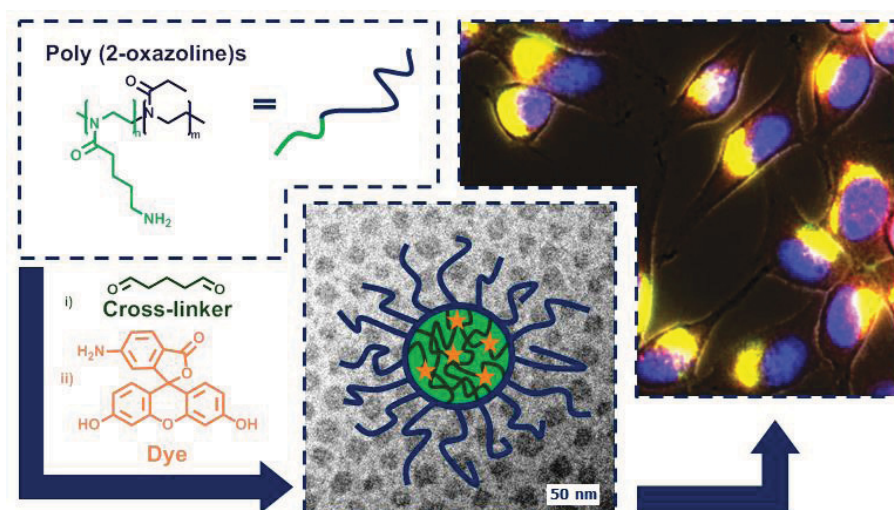
- [60] J. Gao, G. Haidar, X. H. Lu, Z. B. Hu, *Macromolecules* **2001**, *34*, 2242-2247.
- [61] W. Burchard, *Adv. Polym. Sci.* **1999**, *143*, 113-194.
- [62] M. J. Barthel, A. C. Rinckenauer, M. Wagner, U. Mansfeld, S. Hoepfener, J. A. Czaplewska, M. Gottschaldt, A. Traeger, F. H. Schacher, U. S. Schubert, *Biomacromolecules* **2014**, *15*, 2426-2439.

## Publication P4

Core cross-linked micelles and vesicles based on the self-assembly of double hydrophilic poly(2-oxazoline) block copolymers as potential drug carrier

M. Hartlieb, D. Pretzel, M. Wagner, S. Höppener, P. Bellstedt, M. Görlach,  
C. Englert, K. Kempe, U. S. Schubert

*Manuscript submitted.*







# Core cross-linked micelles and vesicles based on the self-assembly of double hydrophilic poly(2-oxazoline) block copolymers as potential drug carriers

*Matthias Hartlieb,<sup>1,2</sup> David Pretzel,<sup>a,b</sup> Michael Wagner,<sup>a,b</sup> Stephanie Hoepfener,<sup>a,b</sup> Peter Bellstedt,<sup>3</sup> Matthias Görlach,<sup>c</sup> Christoph Englert,<sup>a,b</sup> Kristian Kempe,<sup>a,b,†</sup> Ulrich S. Schubert<sup>a,b,\*</sup>*

1 Laboratory of Organic and Macromolecular Chemistry (IOMC), Friedrich Schiller University Jena, Humboldtstrasse 10, 07743, Jena, Germany

2 Jena Center for Soft Matter (JCSM), Friedrich Schiller University Jena, Philosophenweg 7, 07743, Jena, Germany

3 Biomolecular NMR spectroscopy, Leibniz Institute for Age Research – Fritz Lipmann Institute, Beutenbergstr. 11, 07745 Jena, Germany

† Current address: Department of Chemistry, University of Warwick, Gibbet Hill Road, Coventry, CV4 7AL, U.K.

\*Address correspondence to [ulrich.schubert@uni-jena.de](mailto:ulrich.schubert@uni-jena.de)

Keywords: Nanogel, poly(2-oxazoline), micelle, vesicle, self-assembly, nanomedicine;

## Abstract

The synthesis of poly(2-oxazoline)-based block copolymers consisting of a cationic and a hydrophilic segment is described. The self-assembly of these macromolecules in organic solvents results in the formation of micelles and vesicles, respectively, depending on the solvent used. To transfer the systems into water, cross-linking using glutaraldehyde was applied, followed by the consumption of excessive aldehyde functions by either diethylamine or 6-aminofluorescein (6AF). The cross-linked assemblies were analyzed regarding their size and shape by electron microscopy and light scattering methods, as well as for their chemical composition by solid state NMR spectroscopy. 6AF associated samples were examined with respect to their absorption and fluorescence behavior in aqueous environment, revealing a fluorescence even at a pH value of 4, bypassing the intrinsic pH dependency of the fluorescence of fluorescein. The toxicity of the presented nanostructures against mouse fibroblast cell line L929 was examined by XTT assay and was found to be low for concentrations up to  $2.5 \text{ mg mL}^{-1}$ . The efficient concentration and time dependent cellular uptake of micelles and vesicles was investigated by flow cytometry and fluorescence microscopy. Additionally, the internalization and precise intracellular localization of the nanostructures suggests a future potential applicability of the material as drug carrier and fluorescent probe.

## Introduction

Cancer remains one of the most important health problems, still constituting one of the leading causes of death and, thus, representing one of the biggest challenges for modern medicine.<sup>1</sup> Chemotherapy, *i.e.*, the administration of cytostatic drugs such as *cis*-platin or doxorubicin, is frequently accompanied by massive side effects for the patient, mostly rooted in the poor tissue specificity of anti-cancer drugs.<sup>2</sup> A second problem, limiting the applicable dose of some therapeutic agents, is their poor water solubility. This issue creates another significant challenge as approximately 40% of all newly developed drugs are water insoluble.<sup>3</sup>

Nanomedicine constitutes a promising field of research to eventually overcome both issues. It addresses the delivery of small molecules to the site of action using nanoscale objects such as liposomes, nanoparticles, and dendrimers, as well as polymeric micelles which in an ideal case (i) protect the drug against degradation, (ii) deliver it to the tumor site, and (iii) release it in this specific region in a preferably homogeneous manner.<sup>4</sup>

Passive targeting of nano-sized drug delivery systems is attributed to the enhanced permeability and retention (EPR) effect.<sup>5</sup> This principle relies on the leaky architecture and the lack of lymphatic drainage most tumors exhibit due to their rapid growth rate. This may result in an accumulation of nano-scaled objects in cancerous tissue, if their circulation time in the blood is sufficiently long. The size of the carrier plays a key role in this context because objects smaller than 10 nm are cleared from the blood stream by renal filtration within a relatively short time. On the other hand, larger structures (>150 nm) lack the required diffusion behavior to distribute homogeneously over the tumor tissue.<sup>6</sup> Furthermore, the nanocontainer have to be shielded from interaction with blood components or the vascular walls, which is often achieved by endowing the periphery of the carriers with anti-fouling properties.<sup>7</sup>

Stability represents another important issue since the carrier has to remain intact until it reaches the cancerous tissue and, at the same time, has to prevent the drug from being released spontaneously into the blood stream. Polymeric micelles display an excellent basis for the development of cancer specific drug delivery systems. They are formed *via* the self-assembly of block copolymers consisting of hydrophilic and hydrophobic segments in aqueous solution.<sup>8</sup> While the hydrophilic shell protects the system against interaction with non-cancerous tissue and blood components, the hydrophobic core contains and protects the therapeutic molecule.

Lammers and co-workers recently reviewed polymeric micelles as drug carriers and propose three major requirements:<sup>9</sup> (1) Cross-linking to prevent premature disassembly, (2) (reversible) covalent drug attachment to keep the drug within the carrier until delivery, and (3) attachment of active targeting entities, including folate,<sup>10</sup> aptamers,<sup>11</sup> transferrin,<sup>12</sup> sugars,<sup>13</sup> antibodies<sup>14</sup> and peptides.<sup>15</sup>

There are several examples of polymeric micelles based on poly(ethylene glycol) (PEG) with core-forming blocks, such as poly(lactic acid) (PLA),<sup>16</sup> poly(aspartic acid),<sup>17</sup> poly(glutamic acid),<sup>18</sup> and poly(lactic-*co*-glycolic acid),<sup>19</sup> which are already in different phases of clinical trials. Although these systems exhibit significant beneficial properties for the administration of drugs compared to the pure administration, they fulfill none of the above mentioned requirements. The critical micelle concentration (CMC) of polymeric micelles is rather low ( $10^{-6}$  to  $10^{-7}$  mol L<sup>-1</sup>) as compared to surfactant based nanocarriers ( $10^{-3}$  to  $10^{-4}$  mol L<sup>-1</sup>).<sup>3</sup> However, even above their CMC a component exchange or a disassemble is possible. Additionally, the drug is not covalently linked to the structures but immobilized *via* hydrophobic interactions with the core.

Most of the literature on polymeric micelles for drug delivery applications focuses on PEG as hydrophilic component. While PEG has numerous positive properties with respect to the

physiological applicability, there are also drawbacks, such as its non-biodegradability, the induction of hypersensitive reactions or the toxicity of its side products.<sup>20</sup> In addition, PEG suffers from a rather elaborated synthesis set-up and difficulties to introduce functionalities into the structures. Poly(2-oxazoline)s (POx) represents a potential alternative for biomedical applications. Such as PEG, poly(2-methyl oxazoline) (PMeOx) and poly(2-ethyl-2-oxazoline) (PEtOx) are highly water and organo soluble polymers, which exhibit stealth properties.<sup>21</sup> The cationic ring-opening polymerization (CROP) of 2-oxazolines provides access to multifunctional polymers with a wide range of possible structural variations, using different functional initiators, terminating agents and functional monomers.<sup>22, 23</sup> This versatility in combination with the possibility to combine different monomers in distinct architectures, including statistical, gradient or block copolymers, renders the CROP a powerful toolbox for the production of functional polymers for biological applications.<sup>24</sup>

To date, PEtOx and PMeOx have been described as hydrophilic segments in amphiphilic copolymers, which were studied for their self-assembly in aqueous solution, including block copolymers,<sup>25-27</sup> gradient<sup>28</sup>, brush,<sup>29, 30</sup> and star shaped polymers.<sup>31, 32</sup> Moreover, triblock copolymers have been reported, such as ABA,<sup>33-35</sup> and ABC systems.<sup>36, 37</sup> The influence of the substituent in 2-position of the 2-oxazoline on the cellular uptake was investigated in detail by Luxenhofer *et al.* covering a wide range of di- and triblock copolymers.<sup>38</sup>

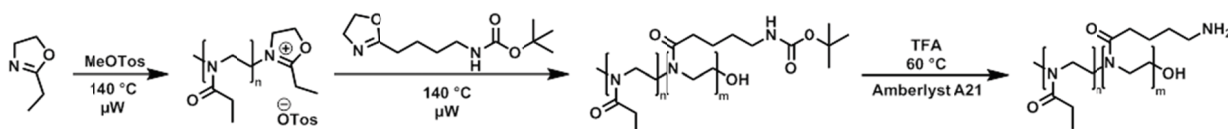
However, up to date, only a limited number of reports described the synthesis and potential of cross-linked POx aggregates. The type of cross-linking reaction is of central interest for designing drug delivery systems with sufficient stability and the ability of the resulting nanocarriers to release their cargo on demand.<sup>39</sup> Covalent cross-linked POx micelles, stabilized by thiol-yne chemistry,<sup>40</sup> UV mediated cross-linking<sup>41, 42</sup> as well as electron beam irradiation<sup>43, 44</sup> are described. However, to best of our knowledge only one systems using a reversible linker (disulfide bridge) is reported.<sup>45</sup>

Here, we describe the synthesis of POx based block copolymers including an amphiphilic (PEtOx) and a hydrophilic cationic (PAmOx) block and their self-assembly in organic solvents. We demonstrate that it is possible to control size, architecture and uniformity by changing the solvent and the ratio between the two segments, respectively. The nano-assemblies were cross-linked by Schiff-base chemistry and covalently loaded with 6-amino fluorescein as model cargo prior to their transfer into aqueous media. The carriers were characterized extensively and their suitability as a drug delivery system was studied *in vitro* showing excellent cellular uptake and low toxicity as well as a pronounced co-localization with acidic lysosomes.

## Results and discussion

### Polymer synthesis

In this study we describe the synthesis of block copoly(2-oxazoline)s and their self-assembly into nano-scaled objects. The block copolymer P(EtOx-*b*-AmOx) consists of a hydrophilic (EtOx) and a hydrophilic/cationic segment (AmOx).<sup>46</sup> While EtOx is known to be biocompatible<sup>47</sup> and soluble in a wide range of solvents, including water, the second block is (after deprotection) cationically charged due to the primary amine groups in the side chain and, therefore, lacks solubility in organic solvents.



**Scheme 1.** Schematic representation of the synthesis of amphiphilic block copolymers (P(EtOx-*b*-AmOx)).

The synthesis of P(EtOx-*b*-AmOx) is depicted in Scheme 1. The polymerization of EtOx, which constitutes the first block, was initiated by methyl tosylate (MeOTos) at 140 °C under

microwave irradiation (see reference<sup>48</sup> for optimized polymerization conditions). After close to full conversion ( $\ln([M]_0/[M]_t) = 4$ ) of the first monomer, the living polymer was chain extended with 2-(4-((*tert*-butoxycarbonyl)amino)butyl)-2-oxazoline (BocOx), the Boc-protected precursor of the cationic AmOx segment, which was deprotected after termination of the polymerization using trifluoroacetic acid (TFA) and Amberlyst A21 solid phase catalyst to remove trifluoroacetate salts. By changing initiator-to-monomer ratios and polymerization times, block copolymers of different compositions were prepared, as summarized in Table 1. To determine the length of the polymer chains, <sup>1</sup>H NMR investigations were conducted directly after polymerization and the integral of the initiator tosylate peaks was compared to the integral of the polymer backbone revealing total degree of polymerization (DP) values of around 100 for all macromolecules. The block ratios were calculated from the <sup>1</sup>H NMR spectra before and after deprotection, respectively (Supporting information. Figure S1 and S2). The difference in the calculated values can be explained by the overlap of peaks originating from the EtOx-CH<sub>3</sub>-group and the Boc signal, which limits the accuracy of the determination. After deprotection, the Boc signal disappears and the peaks of the AmOx side chain, as well as the CH<sub>3</sub> signal are baseline separated. Thus, we refer in the following to the values obtained from the latter calculation. Size exclusion chromatography (SEC) measurements of protected polymers indicated  $M_n$  values around 10,000 g mol<sup>-1</sup>. Low dispersity ( $\mathcal{D}$ ) values prove a narrow molar mass distribution of the synthesized block copolymers. After deprotection, SEC measurements of the block copolymers were performed in *N,N*-dimethyl acetamide (DMAc), a non-selective solvent for both blocks, showing an increase in  $M_n$  and  $\mathcal{D}$ . However, due to the lack of cationic SEC standards a precise determination of  $M_n$  and  $\mathcal{D}$  is hardly possible. The comparison of the SEC derived  $M_n$  and  $\mathcal{D}$  values of the PEtOx homopolymer (which increases when changing

the solvent to DMAc) indicated a similar size and uniformity of the protected and the deprotected polymers.

As a consequence, to gain further information about the size distribution of the cationic P(EtOx-*b*-AmOx) copolymers, asymmetric flow field-flow fractionation (AF4) investigations were performed. The measurements were carried out at a low pH value (3.5) to ensure a neutral or cationic charge of the membrane resulting in an electrostatic repulsion of the cationic samples to reduce adsorption phenomena. The obtained size values fit well with the expected values based on the monomer-to-initiator ratio and the  $M_n$  values derived from the  $^1\text{H}$  NMR experiments. Since the determination of the molar masses was carried out using a multi-angle laser light scattering detector (MALLS) to obtain absolute molar mass values, the AF4 results are more reliable than the data derived from SEC measurements without available cationic calibration standards. Again, small  $\text{Đ}$  values indicate narrow size distributions of the block copolymers. Nevertheless, the molar masses obtained by AF4 might be slightly overestimated as most probably some low molar mass fractions are washed out through the membrane (Nominal cut-off  $10,000 \text{ g mol}^{-1}$ ). This is supported by a recovery rate of around 75 to 85% (Supporting information. Table S1).



**Table 1.** Analytical data and composition of the prepared block copolymers.

Sample	Composition	NMR	SEC (CHCl <sub>3</sub> )		SEC (DMAc)		AF4		Co-monomer [%]
		M <sub>n</sub> [g mol <sup>-1</sup> ]	M <sub>n</sub> [g mol <sup>-1</sup> ]	Đ	M <sub>n</sub> [g mol <sup>-1</sup> ]	Đ	M <sub>n</sub> [g mol <sup>-1</sup> ]	Đ	
1	P(EtOx <sub>104</sub> )	10,300	9,900	1.11	20,600	1.17			0
2	P(EtOx <sub>112</sub> - <i>b</i> -BocOx <sub>6</sub> )	12,600	7,700	1.18					5
3	P(EtOx <sub>92</sub> - <i>b</i> -BocOx <sub>10</sub> )	11,600	7,400	1.16					10
4	P(EtOx <sub>85</sub> - <i>b</i> -BocOx <sub>15</sub> )	12,100	8,900	1.20					15
5	P(EtOx <sub>84</sub> - <i>b</i> -BocOx <sub>20</sub> )	13,200	8,900	1.17					20
6	P(EtOx <sub>70</sub> - <i>b</i> -BocOx <sub>22</sub> )	12,300	7,600	1.18					22
7	P(EtOx <sub>113</sub> - <i>b</i> -AmOx <sub>5</sub> )	12,000			14,500	1.34	11,700	1.10	5
8	P(EtOx <sub>92</sub> - <i>b</i> -BocOx <sub>10</sub> )	10,600			16,800	1.23	9,200	1.14	10
9	P(EtOx <sub>72</sub> - <i>b</i> -BocOx <sub>18</sub> )	9,700			16,100	1.22	13,300	1.10	18
10	P(EtOx <sub>82</sub> - <i>b</i> -BocOx <sub>23</sub> )	11,400			18,100	1.23	13,600	1.09	22
11	P(EtOx <sub>64</sub> - <i>b</i> -BocOx <sub>26</sub> )	10,100			15,600	1.30	12,500	1.26	29

#### *Lower critical solution temperature (LCST) behavior*

In a recent publication we described the formation of cationic hydrogels originating from statistical copolymers P(EtOx-*stat*-AmOx) with comparable compositions, which were formed due to phase separation during the gelation leading to micron-sized hydrogel beads.<sup>49</sup> This behavior was observed under strong basic conditions (5 wt% aqueous NaOH) at elevated temperatures (50 °C). As a consequence, the prepared P(EtOx-*b*-AmOx) block copolymers were investigated regarding their LCST behavior at the conditions described earlier, revealing a similar phase transition (Supporting information, Figure S3). However, also a PEtOx homopolymer was included into the study and showed a lower T<sub>cp</sub> than any of the copolymers. This leads to the conclusion that PEtOx is the segment which phase separates upon heating, which can be explained by a chaotropic influence of the high hydroxyl ion concentrations in solution.<sup>50, 51</sup>

### Self-assembly of block copolymers

To induce the self-assembly of P(EtOx-*b*-AmOx), the diminished solubility of the cationic block in organic solvents was exploited. First, the self-assembling behavior of P(EtOx-*b*-AmOx) (**7-11**) was screened in three organic solvents (MeOH, *i*PrOH and CHCl<sub>3</sub>) using dynamic light scattering (Supporting information. Figure S4). The results of these measurements are summarized in Table 2. As expected, pure PEtOx showed no aggregation in these solvents. All block copolymers however formed structures in the range between 4 and 112 nm depending on the solvent and the composition. Surprisingly, the ratio between the two blocks did not influence the size of the aggregates as much as the polarity of the solvents used. All samples assembled in CHCl<sub>3</sub> formed structures with radii between 4 and 17 nm, which can be addressed to objects with a micellar character. In *i*PrOH, size distributions between 68 and 105 nm were detected, which indicates the formation of vesicular assemblies and MeOH led to structures with even larger radii (77 to 113 nm).

**Table 2.** DLS screening of the self-assembling behavior of the block copolymers in organic solvents (5 mg mL<sup>-1</sup>; size indication in radius; number plot; no size value is specified, if the number weighted plot shows only the polymer precursor).

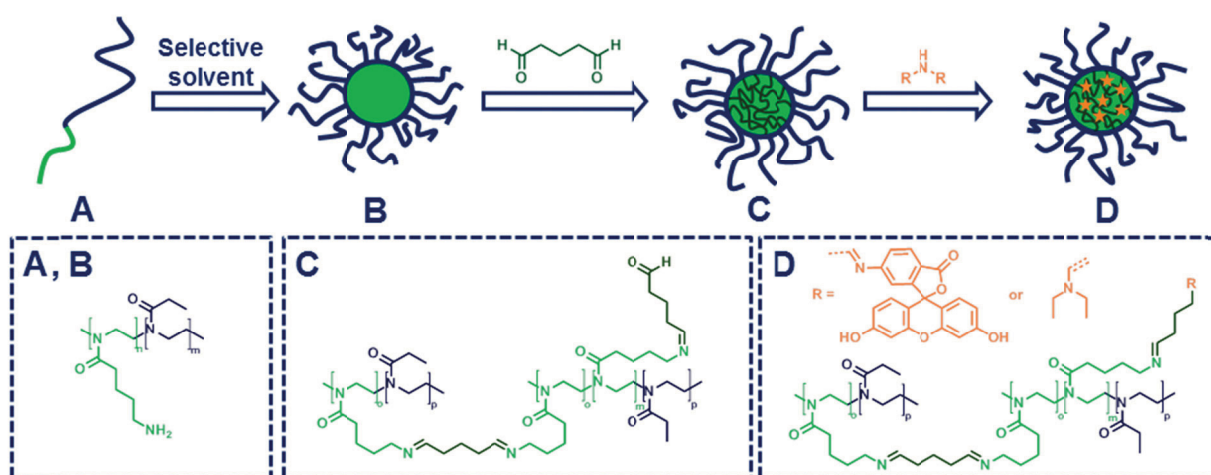
Solvent	0% AmOx ( <b>1</b> )		5% AmOx ( <b>7</b> )		10% AmOx ( <b>8</b> )		18% AmOx ( <b>9</b> )		22% AmOx ( <b>10</b> )		29% AmOx ( <b>11</b> )	
	Size [nm]	PDI	Size [nm]	PDI	Size [nm]	PDI	Size [nm]	PDI	Size [nm]	PDI	Size [nm]	PDI
MeOH	-	-	-	-	-	-	113	0.334	83	0.646	77	0.335
<i>i</i> PrOH	-	-	71	0.550	105	0.714	99	0.561	92	0.509	68	0.111
CHCl <sub>3</sub>	-	-	4	0.360	8	0.217	16	0.256	13	0.376	17	0.048

A possible explanation for this trend is a swelling of the selective block in dependence of the polarity of the solvent. While the amine group has a potentially cationic charge, the side chain and the backbone of the block can be readily solubilized by organic solvents resulting

in a gel-like core instead of a complete collapse of the AmOx segment. When the polarity of the applied solvent increases, swelling should equally increase, resulting in a higher steric demand of the selective block, while the hydrophilic PEtOx block reveals a similar solubilization in all used solvents. Thus, the transition from a micellar to a vesicular structure might be attributed to the change in the ratio between the volume of the two segments.<sup>52</sup>

### *Cross-linking and labelling*

To transfer these structures into aqueous systems, the core of the agglomerates has to be cross-linked since both polymer blocks are readily water soluble. For this purpose, two samples, which showed the most uniform size distribution in organic solvents were chosen (highlighted in Table 2) and cross-linked with glutaraldehyde (GA) (Scheme 2).



**Scheme 2.** Schematic representation of the self-assembly of P(EtOx-*b*-AmOx) followed by cross-linking and quenching/loading.

As a *bis*-aldehyde, GA is able to form imine bonds with the amine groups present in the core and, consequently, lock the structure of the assemblies. However, a direct transfer of the micelles into water yielded only hydrogels, which indicated that even though GA was added

in stoichiometric amounts, a sufficient number of free amine and aldehyde groups remained to cross-link the structures among each other. As demonstrated by Lecommandoux and co-workers, the amount of cross-linked amine groups for such reactions is only about 35%, when aiming for a full conversion.<sup>53</sup> To overcome this drawback, low molar mass amines have to be added in large excess after the cross-linking step to consume the residual aldehydes. This strategy, in turn, does not only enable the stabilization of the self-assembled structure but also allows the simultaneous incorporation of drug molecules or fluorescence labels into the system. Here, diethylamine (DEA) and 6-amino fluorescein (6AF), respectively, were used to quench the cross-linking process. After this treatment the assembled structures could be transferred into aqueous solution.

**Table 3.** Characterization data for cross-linked nanostructures (DLS: 5 mg mL<sup>-1</sup>, size indication in radius). Polymer **11** served as precursor for all assemblies. The content of fluorescein was determined by the absorbance at 470 nm.

Sample	Solvent for self-assembly	Capping agent	DLS in solvent		DLS in water			AF4			Content of capping agent (wt%)
			Size, r [nm]	PDI	Size, r [nm]	PDI	Zeta [mV]	R <sub>g</sub>	R <sub>h</sub>	ρ	
<b>12</b>	CHCl <sub>3</sub>	DEA	17	0.048	17	0.093	+ 7	-	19	< 0.8	n. d.
<b>13</b>		6AF			15	0.199	+ 17	-	20.0	< 0.8	29
<b>14</b>	<i>i</i> PrOH	DEA	68	0.111	59	0.246	+ 17	41	37	1.11	n. d.
<b>15</b>		6AF			50	0.179	+ 23	40	40.0	1.00	29

#### *Characterization of self-assembled structures by light scattering*

To purify the systems from unbound amine or cross-linker molecules, the crude products were precipitated in diethyl ether and dialyzed in a water/methanol mixture (4:1), where methanol acted as a solubility mediator for 6AF, which is barely soluble in water. A first indication of successfully cross-linked structures was provided by DLS experiments, which indicated distributions in the same size range as observed in organic solvents (Table 3, Supporting information, Figure S5). The PDI values of the locked systems increased slightly,

which suggested an agglomeration caused by unconsumed aldehyde groups in the core. However, the values are still in a good range for synthetic nano-sized objects. The zeta potential of all cross-linked assemblies was found to be positive, indicating the presence of free amine groups in the core.

A further investigation of size and uniformity was conducted using asymmetric flow field-flow fractionation (AF4) measurements. Utilizing this technique it is possible to separate the samples by the diffusion coefficient and to determine the hydrodynamic radius ( $R_h$ , by online DLS measurements) and the radius of gyration ( $R_g$ , by multi-angle laser light scattering (MALLS) measurements). The data depicted in Table 3 (Graphs in supporting information: Figure S6) are similar to the values obtained by DLS measurements. For samples originating from *i*PrOH the obtained offline DLS values are significantly smaller than the collected sizes from the AF4-DLS measurements, which can be attributed to the AF4 separation technique. While DLS investigations provide a radius comprising also aggregates, after separation by AF4 single micellar or vesicular structures are examined. An additional information provided by this analysis is a measure of the particle shape by the comparison of both, hydrodynamic radius and radius of gyration, expressed in the ratio  $\rho$  ( $\rho = R_g/R_h$ ). For particles assembled in  $\text{CHCl}_3$ , the  $R_g$  value could not be determined since they were too small for detection with the MALLS detector (limit around 15 nm).<sup>54</sup> This indicates a  $R_g$  below 15 nm and, hence, a  $\rho$  ratio less than 0.8, which is characteristic for hard spheres and, therefore, supports the assumption of a micellar architecture of the assembled particles.<sup>55</sup> Larger ratios (around 1) as obtained for *i*PrOH derived structures indicate less dense and soft or hollow sphere structures, such as vesicles.<sup>55</sup> Considering the block architectures of P(EtOx-*b*-AmOx) and the fact that a fully stretched polymer chain is with roughly 32 nm length (calculated from the bond length; C-C = 154 pm, C-N = 135 pm under consideration of the bond angles) shorter than the radius of the assemblies, a vesicular morphology of these samples is most likely.

### Electron microscopy studies

To visualize the proposed structures, (cryo) transmission electron microscopy (cryoTEM) measurements were performed. Samples in aqueous media (Figure 1C and D) as well as non-cross-linked polymers were investigated (Figure 1A and B). The non-cross-linked systems could be examined only in the dried state as vitrification of the solutions was not successful. However, the remaining polymer shells of collapsed vesicular systems were found in samples derived from MeOH and *i*PrOH (Figure 1A and B).

CryoTEM images of the chloroform assembled and cross-linked micelles show uniform nano-objects, which are arranged in a regular pattern (Figure 1C). The space between the micelles could be interpreted to be the result of a corona which is not visible in the TEM images due to low electron density. However, this interpretation is not consistent with the block ratio of the polymers. Hence, the apparent distance between the micelles discernible in the images could also be explained by electrostatic repulsion due to the cationic charge of the assemblies. For both, micelles and vesicles, the radii of structures visible in the TEM images are in good agreement with the values obtained by DLS and AF4 measurements.

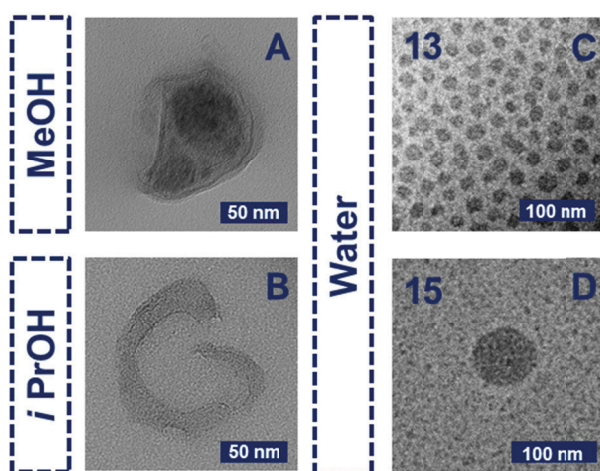


**Figure 1.** TEM images of the dried structures assembled in methanol (A) and *i*PrOH (B), and cryoTEM images of self-assembled as well as cross-linked structures (C, D).

### *Determination of 6AF loading*

For samples which were loaded with 6AF, the amount of covalently bound dye was determined using its absorption and fluorescence properties. The absorption and emission spectra of 6AF-containing samples were measured in water at a pH value of 7 in order to compare the data to pure 6AF, which was measured in the presence of a 100-fold excess of GA to ensure a quantitative conversion to the imine form (Figure 2). While 6AF shows the typical absorption and emission spectra of the lacton derivative at a pH value of 7 (low absorption, maximum at 440 nm), both, micelles as well as vesicles absorb and emit similar to the ring-opened di-anionic carboxy isomer state of the dye (Figure 2A). This behavior seems best explained by the high density of amine groups in the core of the assemblies leading to a locally increased pH value, which, in turn, causes the formation of the di-anionic species characterized by a strong absorption at 490 nm.<sup>56</sup> A closer look at the photochemical behavior of the nano-assemblies shows that even at a pH value of 4 still a significant amount of 6AF emits. A direct comparison with pure 6AF is not possible due to the diminished solubility of the dye in this pH range. However, for the labelling of the nanostructures, this effect is highly advantageous as the micelles or vesicles, respectively, show a high fluorescence intensity even at low pH values as for instance present in the lysosome compartment of cells rendering the system efficient fluorescent probes.

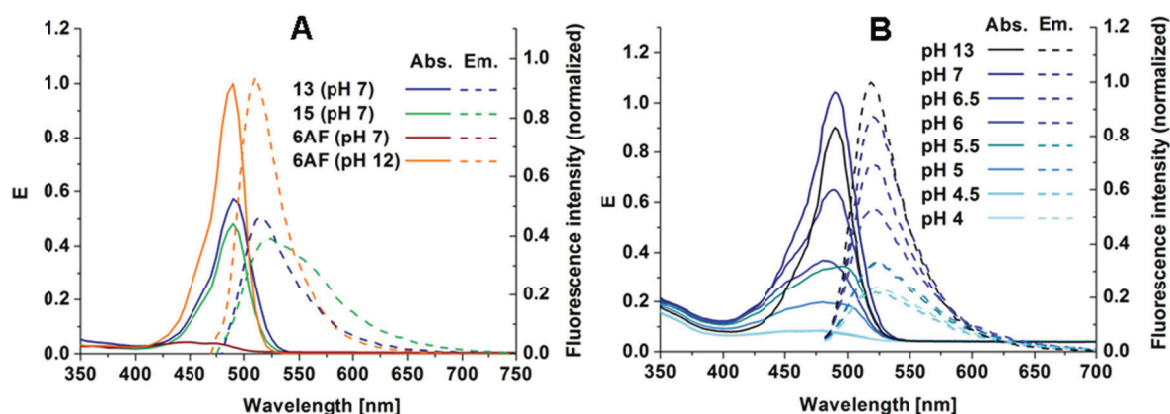


**Figure 2.** A) Absorption and fluorescence spectra of 6AF (pH dependent) and dye quenched nanostructures; B) pH dependent absorbance and fluorescence of compound **15** ( $0.05 \text{ mg mL}^{-1}$ ).

To determine the amount of loaded dye, samples were investigated in aqueous NaOH solution ( $0.1 \text{ mol L}^{-1}$ ) to ensure the quantitative presence of the carboxy-form of fluorescein in the 6AF calibration. For a better comparison with the bound dye, a 100-fold excess of GA was added to the free 6AF generating the imine derivative *in situ* as described before. Both, absorption as well as fluorescence spectra showed equal maxima and shape for the samples as well as calibration. The amount of incorporated 6AF was found to be 29% for the micelles, as well as for the vesicles. This high loading efficiency is equivalent to 12 6AF molecules per polymer chain, which complies with the conversion of amine groups by GA in similar systems ( $\sim 35\%$ ).<sup>53</sup> An equal loading efficiency for both nano-architectures was expected as the chemical composition of both systems should be identical, while only the shape varies.

#### *Liquid and solid state (ss) NMR spectroscopy*

While light scattering and electron microscopy experiments shed light on size and shape of the assemblies, they do not provide insights into their chemical composition. Liquid state and



solid state NMR spectroscopy was employed for a more detailed characterization. Both, micelles and vesicles yield non-turbid solutions in solvents ranging from water to chloroform. In the liquid state  $^1\text{H}$  NMR spectra (Supporting information. Figure S7), solely signals of the PEtOx block are visible, probably as they represent highly mobile groups once they are in contact with the solvent. In contrast, cross-linking of the core is likely to physically link the mobility of individual core components to the overall rotational correlation time of the vesicle/micelle, thereby increasing the relaxation rate of the core components significantly and, hence, leading to an absence of signals attributable to the AmOx side chain, GA and DEA or 6AF, respectively.

To qualitatively assess the cross-linked system, natural abundance CP MAS solid state  $^{13}\text{C}$  NMR spectroscopy was employed (Figure 3). We assigned the prominent signals (1) to the carbonyl function and (3) to the backbone, respectively, and signals (5) and (7) to the side groups of the PEtOx. Furthermore, the resonance (4) detectable at  $\sim 30$  ppm represents the central methylene groups of the AmOx side chain as well as of the GA spacer. The presence of the AmOx part is further supported by a resonance at 60 ppm (2) and the shoulder at 20 ppm (6), both of which are attributed to the outer methylene groups of the AmOx spacer which, in turn, are the least abundant groups. However, a quantitative assessment *via* integration of signals of the individual chemical groups, as typically performed in liquid state NMR, is not reliable due to the non-uniform efficiency of the cross-polarization transfer (CP) step in the ssNMR experiment. The comparably low intensity of signal (2), however, suggested an under-representation of the core, which might be due to a conformational heterogeneity with concomitant line broadening in the cross-linked region.

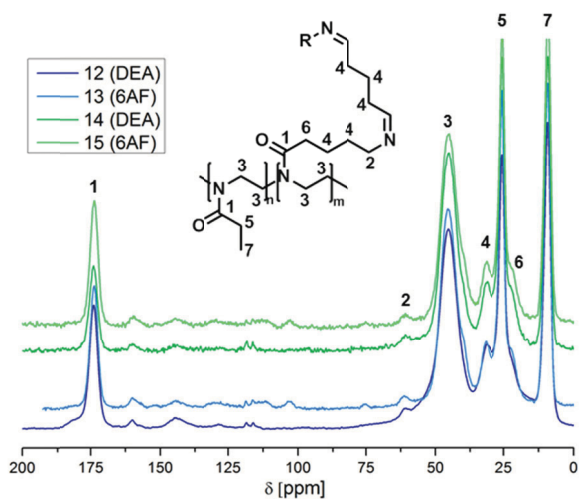


**Figure 3.** Solid state  $^{13}\text{C}$  NMR spectra of cross-linked micelles (samples **12** and **13**) and vesicles (samples **14** and **15**).

Likewise, signals for the 6AF are of an intensity lower than expected from the quantitative fluorescence analysis (Table 3). To assign resonances arising from the 6AF moiety, we compared commercial microcrystalline 6AF with amorphous and with KOH treated, ring-opened 6AF (Supporting information. Figure S8). From this comparison, we concluded that the signals detectable at 155 ppm, at 120 to 100 ppm and a shifted signal at 75 ppm arise from 6AF. Notably, already the conversion of micro crystalline into amorphous 6AF, produced by dissolving in MeOH, flash-freezing and lyophilisation, caused a severe line broadening in the ssNMR spectra of some of the 6AF resonances and other lines become virtually undetectable. This clearly indicates that a certain degree of conformational heterogeneity (‘amorphousness’) of the 6AF moiety causes severe line-broadening or undetectability of some groups in the ssNMR spectra. In summary, we interpret the low intensity signal pattern of the 6AF moiety as resulting from differences in the CP transfer efficiency, severe line broadening and the mainly ring-open form (see fluorescence

experiments) and a residual proportion of amorphous 6AF, the latter giving rise to the signals at 155, 100 to 120 and 80 ppm, respectively.

#### *Cytocompatibility of self-assembled structures*

The evaluation of the biocompatibility is one of the first steps to assess the applicability of the micellar/vesicular structures presented herein for potential biomedical applications. Hence, adverse effects on the cellular metabolism upon incubation with 6AF labeled micelles (sample **13**) and vesicles (sample **15**) were evaluated using the established L929 cell line, which is characterized and documented by its sensitivity towards cytotoxic agents.<sup>57</sup>

The *in vitro* cytotoxicity experiments were performed *via* a XTT assay according to the German standard institution guideline DIN ISO 10993-5 as a reference for biomaterial testing. After 24 h of incubation with different micelle/vesicle concentrations (0.005, 0.05, 0.5, 2.5 and 5 mg mL<sup>-1</sup>) the metabolic activity of the treated cells was found to be at the level of the untreated controls, with the exception that only the highest concentration of micelles (5 mg mL<sup>-1</sup>) led to a significant reduction of cell viability (50%). The reason for this effect at this dosage is not understood by now and requires further investigation. Interestingly, the vesicular structures did not show any cytotoxic potential even at the highest concentration (Figure 4 top). One possible explanation for this behavior could be related to the size of the vesicles. The larger diameter of the structures in comparison to micelles leads to a smaller surface/volume ratio. Furthermore, related to the vesicular architecture, half of the surface faces the inside of the nano-assembly. However, the micelle concentrations which did not show an overt toxicity effect were more than adequate for potential applications.

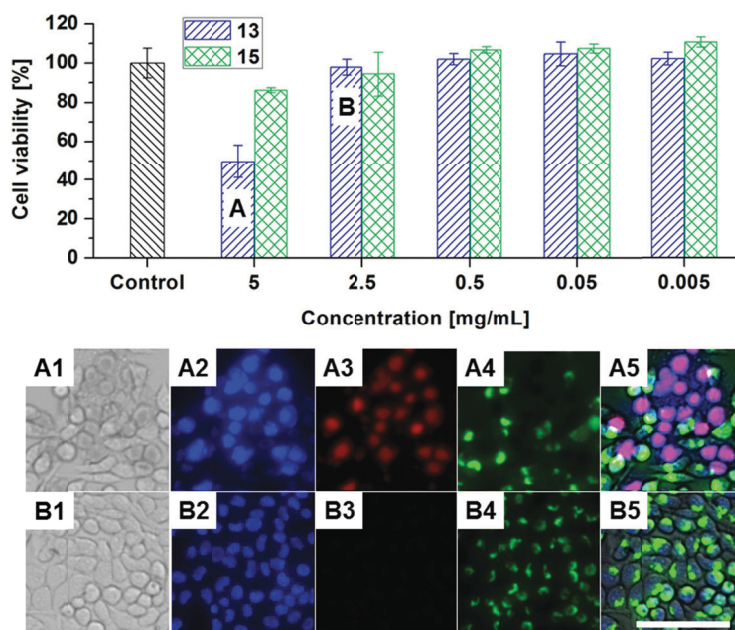


**Figure 4.** Top: Cell viability of L929 mouse fibroblasts after incubation with micelles (13)/vesicles (15) up to  $5 \text{ mg mL}^{-1}$  for 24 hours. Bottom: Representative bright field and fluorescence microscopy images of Hoechst 33342/PI stained L929 mouse fibroblast cells cultured for 24 h in the presence of sample 13 (A1-A5;  $5 \text{ mg mL}^{-1}$ ) and sample 15 (B1-B5;  $0.5 \text{ mg mL}^{-1}$ ). Blue fluorescent Hoechst dye labels nuclei of all cells present (A2 and B2), while red fluorescent PI signals (A3 and B3) indicate nuclei of dead cells. Green fluorescence originates from the dye containing nanostructures (A4 and B4). Additionally, overlay images of all four channels are displayed (A5 and B5). Scale bar  $100 \mu\text{m}$ .

Microscopic assessment of the proportion of live and dead cells confirmed the findings from the XTT assay – the membrane integrity of viable cells was proven by the exclusion of red fluorescent PI from cell nuclei indicating their excellent viability (Figure 4 bottom panel; B3). In addition, the microscopic investigations provided first hints for a cellular internalization of the fluorescein containing micelles (Figure 4, B5). In the case of the highest micelle concentration, images revealed a disintegration of the cell membrane (PI positive cell nuclei) accompanied by a reduced intracellular localization of micelles, which might be

caused by a diffusion of the micelles through the leaky membrane of the dead cells (Figure 4, A3 and A4).

These results confirm the low cytotoxicity generally observed for PEOx-based materials with different molar masses and PEOx-containing block copolymers, which were evaluated before.<sup>58</sup>

#### *Flow cytometric (FC) investigations on time and concentration dependent uptake*

The time and concentration dependent uptake of the fluorescein containing micelles/vesicles was quantified by FC measurements. For this purpose, cells were incubated either with different concentrations (0.05, 0.1, 0.25, and 0.5 mg mL<sup>-1</sup>) of the materials for 24 h at 37 °C or with one concentration (0.5 mg mL<sup>-1</sup>) for different time scales (0.5, 1, 3, 12, and, 24 h; 37 °C). Following the incubation, the excess of micelle/vesicle material was removed by washing with PBS. Subsequently, the cells were trypsinized and subjected to FC analysis.

The fluorescence intensity distributions (histogram plots in Figure 5) clearly display a concentration-dependent right-shift to higher fluorescence intensity for both, the micellar and vesicular structures indicating a concentration-dependent uptake. Interestingly, the increase in fluorescence intensity was more pronounced for the vesicle samples, suggesting an increased cellular accumulation/association as compared to micelles.

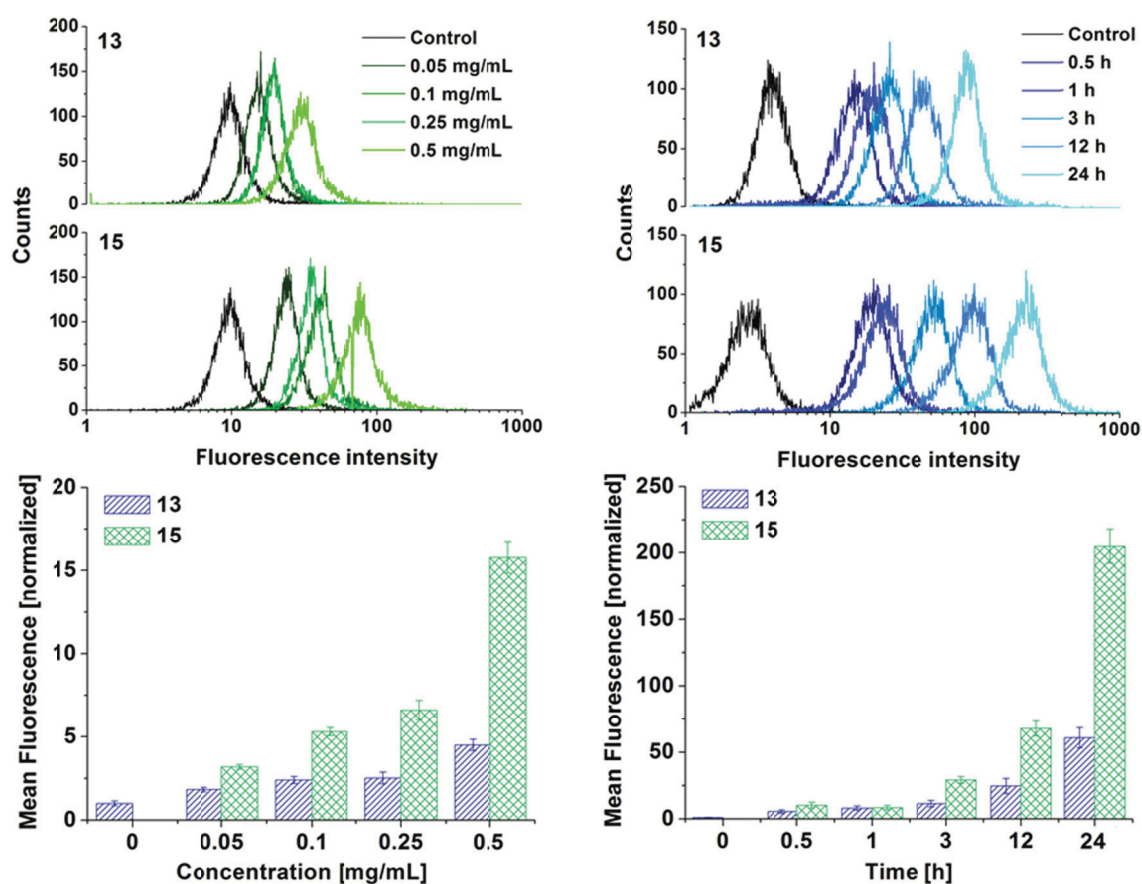


**Figure 5.** Flow cytometry investigation on the time and concentration dependent uptake of 6AF containing micelles/vesicles by L929 mouse fibroblasts at 37 °C. For time dependent uptake cells were incubated between 0.5 and 24 h with micelles (**13**)/vesicles (**15**) with a concentration of 0.5 mg mL<sup>-1</sup>, whereas the concentration dependent uptake was investigated over an incubation time of 24 h using micelle/vesicle concentrations in the range between 0.05 and 0.5 mg mL<sup>-1</sup>. Cells incubated only with culture medium served as control. For histogram plots the fluorescence intensity on the x-axis is plotted against the number of events on the y-axis. A shift of the histogram toward the right side demonstrates an increasing amount of dye containing micelles/vesicles associated to the cells. The bar charts depict the results for the corresponding normalized mean fluorescence intensities, obtained from flow cytometry of the analyzed cell populations. The data are expressed as mean ± SD of triplicates.

This becomes evident in quantitative terms when the mean fluorescence intensities (MFI) of the cell populations are evaluated as depicted in the bar charts (Figure 5). An up to three-fold uptake of the vesicles was obtained as compared to micelles with the same concentration. These results were also confirmed by fluorescence microscopic observations of the treated cell populations (Supporting information. Figure S9). Interestingly, the proportion of “positive cells” having associated micelles or vesicles did not only increase at higher material concentrations but was also higher for vesicular compared to micellar samples, *e.g.* at  $0.05 \text{ mg mL}^{-1}$  83 to 13% and at  $0.5 \text{ mg mL}^{-1}$  98 to 88% (data not shown).

For the time-dependent uptake trends similar to the concentration-dependent internalization were observed. The cellular accumulation of material proceeds over time for both the micelles and vesicles without reaching a plateau after 24 h. Additionally, the cellular uptake of the vesicular formulation exceeds the internalization rate of the micelles by a factor of 3 and, again, supports the interpretation of a higher cellular internalization of the vesicles. It should be noted that the initially conducted fluorescence measurements of the micelle and vesicle suspensions at equivalent concentrations (weight/volume) demonstrated that both show similar fluorescence values (Figure 3). Therefore, the observed increase in cell associated fluorescence can clearly be attributed to an enhanced vesicle uptake.

The different cellular internalization efficiency could be caused by a slower sedimentation rate of the small micelles in comparison to the larger vesicles leading to a delayed contact and interaction of the substances with the cellular plasma membrane and, hence, a later internalization.<sup>59</sup> Additionally, the cellular uptake mechanism could play a critical role in the internalization rate of the substances. It is known that very large particles enter cells by phagocytosis, whereas, in the case of nanoparticles, most internalization occurs *via* various endocytotic pathways, which can be different with regard to the nature of the surface and the structural properties of nanoparticles (*e.g.* clathrin or caveolin dependent pathways).

Depending on the particular pathway and also its energy dependent or independent nature, different internalization rates are achieved<sup>60</sup> – this could also impact the uptake efficiency of the presented micelles and vesicles. To elucidate these phenomena further investigations are required, *e.g.* by assessing or blocking certain uptake pathways using specific inhibitors.

#### *Internalization and co-localization with cellular compartments*

The cellular internalization and intracellular localization of micelles and vesicles in L929 cells was further elucidated by epifluorescence and confocal laser scanning microscopy (CLSM) investigations. For this purpose, the cells were incubated for 24 h with 0.5 mg mL<sup>-1</sup> of the respective substance at 37 °C and, in order to assign the localization of the fluorescent micelles/vesicles to cellular compartments, the living adherent or suspended cells were stained with specific dyes for the cell plasma membrane (Cell Mask Orange), the nuclei (Hoechst 33342 or SytoRed59) or the acidic late endosomes and lysosomes (LysoTracker), respectively.

A representative distribution of fluorescent vesicles in the context of cellular structures in adherent cells is presented in Figure 6. The epifluorescence images suggest an intracellular, cytoplasmatic localization of the vesicles, since no green fluorescent signal (from the 6AF labeled structures) is detectable at the outer cell membrane, which would be the case when vesicles are adsorbed to, but not transported through the membrane (Figure 6: A2, A3, A5). Additionally, no vesicles were observed within the nuclear compartment: They were rather associated with distinct outer nuclear membrane regions (Figure 6: A5). Hypothesizing that internalization of the vesicles/micelles proceeds *via* endocytotic pathways, an appearance of the internalized structures in the late endosomes or lysosomes was very likely. Indeed, co-localization of stained acidic lysosomes and fluorescent vesicles was observed (Figure 6: B2, B3 and B5).



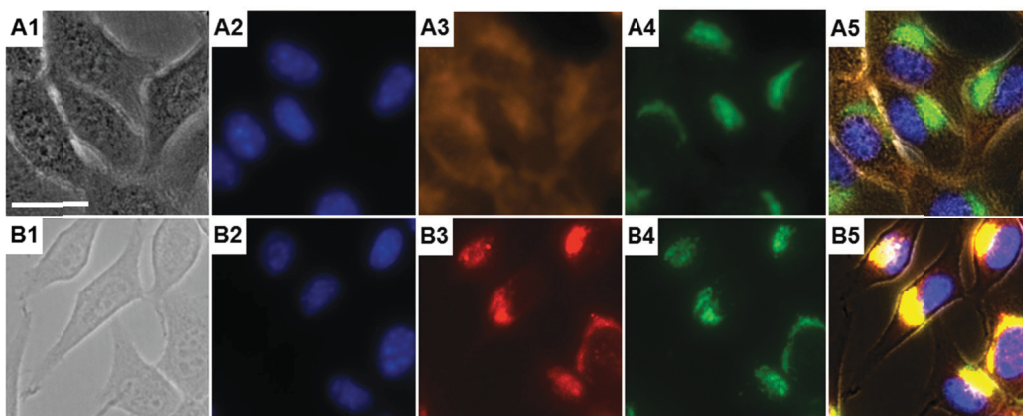


**Figure 6.** Representative bright field (A1 and B1) and epifluorescence images of adherent L929 cells after 24 h incubation at 37 °C with vesicles (**15**) at a concentration of 0.1 mg mL<sup>-1</sup>. Cell nuclei (A2 and B2), cell membranes (A3) or late endosomes/lysosomes (B3) were specifically stained and their fluorescence signal was captured in addition to the fluorescence signal originating from the internalized 6AF labeled vesicles (A4 and B4). Co-localization was examined by overlaying of all four channels (A5 and B5). Identical results were obtained for micelles (Supporting information. Figure S10). The scale bar is 20 μm.

CLSM investigations on cells treated as mentioned above but additionally detached after incubation and subjected to microscopic analysis with precise optical z-sectioning through the cell body confirmed an extra-nuclear presence and the complete internalization of the vesicles into the lysosomal compartment (Figure 7: A1-C3).

Identical results for internalization and lysosomal localization were obtained for the micellar forms suggesting endocytotic uptake and distribution mechanisms for both, vesicles and micelles.

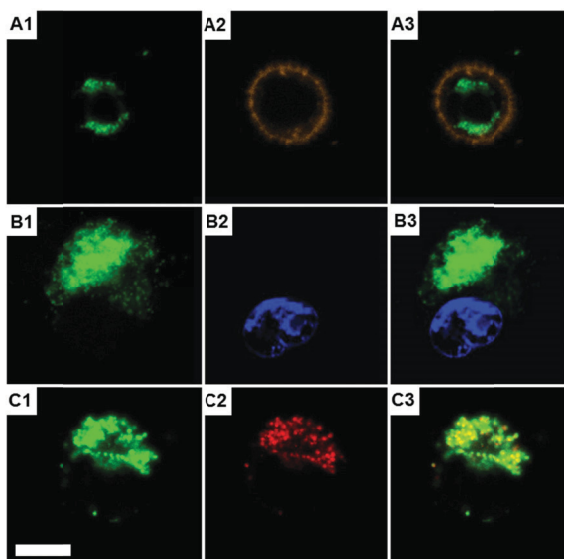


**Figure 7.** Representative CLSM images of detached L929 cells after 24 h incubation at 37 °C with vesicles (**15**) at a concentration of 0.1 mg mL<sup>-1</sup>. Cell membranes (A2), cell nuclei (B2), or late endosomes/lysosomes (C2) were specifically stained and correlated with the fluorescence signal of 6AF labeled vesicles (A1, B1, and C1). Overlay of both channels (A3, B3 and C3) proves an intracellular (A3) but extra-nuclear (B3) localization of the vesicles and their apparent co-localization with lysosomal structures (C3). Identical results were obtained for micelles (Supporting information. Figure 11). The scale bar is 10 μm.

The obtained results are highly promising regarding the proposed applications as drug carrier and/or fluorescence probe. The highly specific accumulation in lysosomes with their pH value of < 5 represents an ideal intracellular location for a release of the cargo or even a disassembly of the structures since imine bonds, necessary for the stabilization of the nanostructures, are known to be acid labile. This behavior, however, cannot be observed with this specific loading since fluorescein after a potential release from the micelles/vesicles immediately faces the low pH value of the surrounding environment and is converted in one of its uncharged isomers. These cannot be detected among the highly fluorescent micelles/vesicles and, additionally, the dye has a much lower solubility in this medium preventing a fast release. Furthermore, electrostatic interactions between the acid

functionality of 6AF and the cationic core components might lower the release rate of the dye. For potential drug delivery applications micelles should be preferred over vesicles since their uptake is less efficient enabling a passive targeting *via* the EPR effect. As fluorescence probes, vesicular structures should be considered, owing to their faster and more efficient uptake and lower toxicity.

## **Conclusion**

We described the microwave-assisted synthesis of block copolymers consisting of hydrophilic EtOx and BocOx, a 2-oxazoline monomer with a Boc-protected amine group in the side chain. Subsequent deprotection led to P(EtOx-*b*-AmOx), a block copolymer with both, a neutral hydrophilic and a cationic hydrophilic segment. The content of the amine containing block was varied from 5 to 29% and AF4 as well as SEC investigations revealed narrow size distributions for all copolymers. The self-assembly behavior of these polymeric precursors was investigated in different organic solvents by dynamic light scattering, revealing structures with radii between 4 and 112 nm depending on the block ratio and the applied solvent. In order to transfer the systems into aqueous solution, cross-linking of selected assemblies was carried out using glutaraldehyde. The remaining aldehyde groups were quenched using diethylamine or 6-aminofluorescein as covalently bound model cargo. Size and uniformity of the nanostructures was investigated using DLS and AF4 measurements, indicating a micellar architecture for samples derived from chloroform and a vesicular structure for systems assembled in *iso*-propanol. Size and shape of the nanostructures were confirmed by electron microscopic methods supporting the assumption of a vesicular architecture of the *iso*-propanol derived samples. The chemical composition was confirmed *via* solid state NMR spectroscopy and 6AF loading was quantified by

measurement of the absorbance and fluorescence of the dye revealing a good fluorescence even at a pH value of 4.

Regarding the behavior of the self-assembled structures in a cellular environment, *in vitro* experiments documented their non-toxicity within a relevant concentration range. This cytocompatibility was not elicited by an inert character as, *e.g.*, shielding from cell contacts: In contrary, they readily interact with the cellular plasma membrane and are subject to an efficient cellular uptake and accumulation within the lysosomal compartment.

The systems presented in this contribution bear several advantages as to potential drug delivery or sensing applications. The architecture of the nanocarriers exposes the biocompatible PEtOx constituent resulting not only in an excellent solubility but also in a low cytotoxicity, while the positive zeta potential generated by remaining amine functions facilitates an efficient cellular uptake. The difference of the internalization efficiency between vesicles and micelles can be used to generate nanomaterials with defined cellular interactions exploiting passive and active targeting effects, respectively. Future studies will show if alterations of the degree of cross-linking can further modulate their uptake characteristics.

An additional advantage is the covalent nature of loading and cross-linking preventing a premature disassembly or a loss of cargo by diffusion. In principle, all drugs bearing an amine group can be attached to the core of such nanostructures rendering them a highly versatile platform. Furthermore, the reversible nature of the cross-linking could lead to an intracellular disassembly, particularly because the micelles/vesicles are exclusively located in the lysosome where they are exposed to an acidic pH value. However, due to the strong pH dependence of the solubility of 6AF, this release cannot be investigated with the present systems. Future studies using different cargo molecules will investigate the drug delivery potential of these nanostructures.

## Supporting information

Materials and instrumentation; NMR and SEC plots of polymers (Figure S1 and S2); cloud-points of P(EtOx-*b*-AmOx) (Figure S3); AF4 data of polymers (Table S1); DLS plots for nanostructures in organic solvent (Figure S4) and water (Figure S5); AF4 plots of cross-linked structures (Figure S6); NMR of assembled structures (Figure S7); solid state NMR of 6AF (Figure S8); epifluorescence pictures of cells for FC analysis (Figure 9); co-localization studies of micelles using epifluorescence (Figure S10) and CLSM (Figure S11).

## Experimental section

*Information about materials and instrumentation can be found in the supporting information.*

*Block copolymers of 2-ethyl-2-oxazoline (EtOx) and 2-(4-((tert-butoxycarbonyl)amino)butyl)-2-oxazoline (BocOx) (P(EtOx-*b*-BocOx)), (2-6)*

In a microwave vial, EtOx (606  $\mu$ L, 6 mmol), MeOTos (12.1  $\mu$ L, 0.08 mmol) and acetonitrile (2.9 mL) were mixed under inert conditions. After heating in the microwave synthesizer at 140  $^{\circ}$ C for 28 min, a solution of BocOx (500  $\mu$ L, 2 mmol) in acetonitrile (1.5 mL) was added through a syringe and the mixture was heated again in the microwave synthesizer (140  $^{\circ}$ C, 22 min). The solution was precipitated in cold ( $-80$   $^{\circ}$ C) diethyl ether. The white precipitate was filtered and dried in high vacuum (994 mg, 92%).

$^1$ H NMR (CDCl<sub>3</sub>, 300 MHz) (**6**):  $\delta$  = 7.67, (d, 8.1 Hz, 0.018 H, tosylate), 7.14 (d, 8.21 Hz, 0.018 H, tosylate), 3.46 (s, 4 H, backbone), 3.10 (s, 0.5 H, CH<sub>2</sub>-CH<sub>2</sub>-NH (BocOx)), 2.50-2.15 (m, 1.96 H, CH<sub>2</sub> (EtOx)/CH<sub>2</sub>-CH<sub>2</sub>-NHBoc), 1.62 (s, 0.46 H, CH<sub>2</sub>-CH<sub>2</sub>-CH<sub>2</sub> (BocOx)), 1.52

(s, 0.46 H, CH<sub>2</sub>-CH<sub>2</sub>-CH<sub>2</sub> (BocOx)), 1.42 (s, 2.1 H, CH<sub>3</sub> (BocOx)), 1.21 (s, 2.1 H, CH<sub>3</sub> (EtOx)) ppm.

Size exclusion chromatography (SEC) (**6**) (eluent: CHCl<sub>3</sub>/*iso*-propanol/NEt<sub>3</sub>, PS-standard): M<sub>n</sub> = 7.600 g mol<sup>-1</sup>, M<sub>w</sub> = 9.000 g mol<sup>-1</sup>, Đ = 1.18.

#### *Deprotection of P(EtOx-stat-BocOx) (P(EtOx-stat-AmOx), (7-11))*

Exemplarily, P(EtOx-*b*-BocOx) (**6**, 500 mg) was dissolved in TFA (5 mL) and heated to 60 °C for 1 h. After stirring for 12 h at room temperature, the mixture was diluted with 10 mL methanol and precipitated in 200 mL of cold (-80 °C) diethyl ether. The precipitate was re-dissolved in methanol (100 mL) and stirred with Amberlyst A21 for 48 h. Subsequently, the solvent was removed, the polymer was dissolved in de-ionized water and freeze dried (-80 °C, 0.003 mbar). The polymer was obtained as white powder (456 mg, 91%).

<sup>1</sup>H NMR (*N,N*-dimethyl formamide (DMF)-D<sub>7</sub>, 300 MHz) (**11**): δ = 5.37 (s, 1.7 H, NH<sub>2</sub>), 3.69 (s, 4 H, backbone), 3.23 (s, 0.55 H, CH<sub>2</sub>-CH<sub>2</sub>-NH<sub>2</sub>), 2.78-2.45 (m, 2.1 H, CH<sub>2</sub> (EtOx)/CH<sub>2</sub>-CH<sub>2</sub>-CO (AmOx)), 2.06-1.72 (m, 1.1 H, CH<sub>2</sub>-CH<sub>2</sub>-CH<sub>2</sub>-CH<sub>2</sub> (AmOx)), 1.2 (s, 2,5 H, CH<sub>3</sub> (EtOx)) ppm.

SEC (**11**) (eluent: DMAc/LiCl, PS-standard): M<sub>n</sub> = 15,600 g mol<sup>-1</sup>, M<sub>w</sub> = 20,300 g mol<sup>-1</sup>, Đ = 1.30.

#### *Determination of cloud point behavior in aqueous sodium hydroxide solution*

To investigate the cloud point behavior P(EtOx-*b*-AmOx) was dissolved in an aqueous solution of sodium hydroxide (5 wt%) in concentrations varying from 2.5 to 20 mg mL<sup>-1</sup>. The turbidity was recorded as a function of the temperature which was modulated between 2 and 98 °C in three cycles (1 °C min<sup>-1</sup>). The cloud point was determined at 50% transmission.

Cloud points were measured in a Crystal 16 from Avantium Technologies connected to a chiller (Julabo FP 40) at a wavelength of 500 nm.

#### *Self-assembly and cross-linking*

To create nanostructures, the block copolymer (**11**, 150 mg, 0.015 mmol, 0.39 mmol of amine) was dissolved in the respective solvent (MeOH, *i*PrOH or CHCl<sub>3</sub>, 5 mg mL<sup>-1</sup>) and stirred for 3 h. Subsequently, glutaraldehyde (19.5 mg, 0.195 mmol, 0.5 eq. per amine) was added and the solution was stirred another 3 h. With proceeding reaction time the color of the solution changed from colorless to yellow. To quench the excess aldehyde function, diethylamine or 6-amino fluorescein was added, respectively, and stirred for 12 h. Subsequently, the amount of solvent was reduced under an argon stream and the residual was precipitated in 100 mL cold diethyl ether (-80 °C). To purify the self-assembled structures from residual amine and cross-linker, dialysis in MeOH/water (1:4) was applied using a membrane with a molar mass cut off of 3,500 g mol<sup>-1</sup> (Roth Zellutrans). After the extraction was finished, the dialysis medium was changed to pure water and the aqueous solution was freeze dried to yield an orange powder (140 mg). The size distribution of all intermediate steps was examined by dynamic light scattering (DLS) measurements.

#### *Determination of dye loading content by absorbance/fluorescence*

The absorbance/fluorescence of nanostructures was investigated under basic conditions (1 mol L<sup>-1</sup> NaOH in water) in diluted solution (0.1, 0.05 and 0.025 mg mL<sup>-1</sup>). The absorbance was determined at a wavelength of 490 nm and compared to a dilution series of 6AF in the same aqueous NaOH solution. To the 6AF stock solution a 100 fold excess of glutaraldehyde was added to ensure that only the imine species of 6AF is present. Emission was detected at an excitation wavelength of 450 nm. Micellar samples, as well as 6AF calibration exhibit an

emission maximum at 510 nm. All measurements were carried out in a 96 well-plate format with 200  $\mu\text{L}$  per well and double determination for each measuring point. The read out was accomplished using a Tecan M200 Pro fluorescence micro plate reader (Crailsheim, Germany). DEA loaded nanostructures served as a reference for all measurements.

#### *Cytotoxicity assay*

For the cytotoxicity screening, the mouse fibroblast cell line L929 was purchased from a commercial cell bank (Cell line service, Eppelheim, Germany). The cells were routinely cultured as follows: Cell culture media Dulbecco's modified eagle's medium (DMEM) was supplemented with 10% fetal calf serum, 100 U  $\text{mL}^{-1}$  penicillin, and 100  $\mu\text{g mL}^{-1}$  streptomycin (all components from Biochrom, Berlin, Germany) at 37 °C in a humidified atmosphere with 5% (v/v)  $\text{CO}_2$ . The cytotoxicity was determined using a XTT assay following the ISO/EN 10993 part 5 protocol: Cells were seeded in 96-well plates at a density of  $1 \times 10^4$  cells/well and grown as monolayer cultures for 24 h. The cells were subsequently incubated separately with different concentrations of the micelles and vesicles (from 0.005 to 5  $\text{mg mL}^{-1}$ ) for 24 h. Control cells were incubated with fresh culture medium. After incubation, the cells were washed once with PBS and a mixture of 100  $\mu\text{L}$  fresh medium and 50  $\mu\text{L}$  of a XTT solution, prepared according to the manufacturer's instructions were added to each well. After 4 h at 37 °C, 100  $\mu\text{L}$  of each solution were transferred to a new micro titer plate and the optical density (OD) was measured photometrically. The control was standardized as 0% of metabolism inhibition and referred as 100% viability. Cell viability below 70% was considered indicative of cytotoxicity. Data are expressed as mean  $\pm$  SD of six determinations.



### *Photometrical and microscopical methods*

For the photometric absorbance measurements, a TECAN Infinite M200 PRO plate reader (TECAN, Crailsheim, Germany) was used to measure the absorption of samples from the XTT cytotoxicity assay (570 nm with a background correction of the optical density (OD) at 690 nm). Each well containing the sample was measured in four different spots each with 25 flashes per scan.

The evaluation of micelles/vesicles uptake was performed by flow cytometry (FC) measured on a Beckmann Coulter Cytomics FC-500 equipped with Uniphase Argon ion laser, 488 nm, 20 mW output and analyzed with the Cytomics CXP software. For time dependent uptake, cells (L929) were incubated between 30 min and 24 h with micelles (**13**)/vesicles (**15**) at a concentration of  $0.5 \text{ mg mL}^{-1}$ , whereas the concentration dependent uptake was investigated over an incubation time of 24 h using micelle/vesicle concentrations in the range between  $0.05$  and  $0.5 \text{ mg mL}^{-1}$ . Cells incubated with culture medium only served as control. Data are expressed as mean  $\pm$  SD of three determinations. To visualize the viability of cells after incubation with the micelles/vesicles as well as for the time/concentration dependent kinetic studies on cellular uptake, the blue/red/green fluorescence signal of cells cultured in a 96 well plate and stained with Hoechst 33342 and propidium iodide (PI) was observed on a Cell Observer Z1 fluorescence microscope (Carl Zeiss, Jena, Germany) equipped with a mercury arc UV lamp and the appropriate filter combinations for excitation and detection of emission. Images of a series were captured with a  $40\times$  objective using identical instrument settings (*e.g.* UV lamp power, integration time, camera gain) and cell-spots in the 96 well plate were addressed using an automated XY table.

For CLSM analysis of uptake and co-localization with cell organelle, the nuclei, late endosomes/lysosomes and cell membranes were either stained with SYTO®Red 59, LysoTracker Red or Cell Mask Orange. CLSM images were acquired using a Zeiss LSM 510

META (Carl Zeiss) with excitation wavelengths/emission filters of 633 nm/LP 650 nm for SYTO®Red and 543 nm/BP 585 to 615 nm for LysoTracker Red and Cell Mask Orange respectively.

Images were captured with a Plan-Apochromat 63 × objective and in multitrack mode, enabling single excitation and emission of fluorescence dyes. Co-localization was visualized in overlay images of the multiple channels.

#### *Microscopic evaluation of cell viability*

In addition to the above described measurement of the metabolic cell activity by the XTT assay, viability of the cells after exposure to the micelles and vesicles was examined microscopically using a propidium iodide (PI)/Hoechst staining assay. After incubation with the test substances, the cells were washed once with PBS, submerged with medium containing PI ( $10 \mu\text{g mL}^{-1}$ ) and Hoechst 33342 ( $10 \mu\text{g mL}^{-1}$ ) and incubated for 10 min at 37 °C. During that time, PI enters into the nuclei of dead cells *via* the leaky cell membrane, whereas the dye is kept outside of viable cells. Hoechst dye is capable of fluorescently labeling nuclei of dead and viable cells and was used to tag the entire cell collective. The blue (Hoechst), red (PI), and green (6AF labeled vesicles and micelles) fluorescence signals of cells were captured on a fluorescence microscope.

#### *Fluorescence microscopy for kinetic studies on cellular uptake of micelles (13)/vesicles (15)*

For kinetic investigations concerning a concentration dependent uptake, the cells, growing as a semiconfluent cell layer in 6 well plates, were incubated separately with different concentrations ( $0.05, 0.1, 0.25$  and  $0.5 \text{ mg mL}^{-1}$ ) of micelles and vesicles for 24 h at 37 °C under 5% CO<sub>2</sub> atmosphere. Control cells were incubated with fresh culture medium. After

incubation, the solutions were aspirated from the wells and any excess materials were removed by washing the cell layer three times with PBS. For flow cytometry, the adherent cells were detached by trypsin treatment and 10.000 cells were analyzed using gates of forward and side scatters to exclude debris and cell aggregates. For microscopic analysis, the adherent cells were additionally stained with Hoechst 33342 ( $10 \mu\text{g mL}^{-1}$ ) and immediately subjected to fluorescence imaging.

For kinetic investigation concerning a time dependent uptake, cells were treated with  $0.5 \text{ mg mL}^{-1}$  of micelles or vesicles for 0.5 h, 1 h, 3 h, 12 h and 24 h at  $37 \text{ }^\circ\text{C}$  under 5%  $\text{CO}_2$  atmosphere. Subsequent analysis was performed as mentioned above.

#### *Co-localization study*

In order to analyze the micelle/vesicle uptake and co-localization with cell organelle, adherent cells were treated with  $0.1 \text{ mg mL}^{-1}$  of micelles/vesicles for 24 h at  $37 \text{ }^\circ\text{C}$  under 5%  $\text{CO}_2$  atmosphere. Subsequently, the nuclei, late endosomes/lysosomes and cell membranes were stained with Hoechst 33342 and LysoTracker Red or Cell Mask Orange according to manufactures instructions (all dyes from Life Technologies, Darmstadt, Germany) and the adherent cell populations were, subsequently, subjected to microscopic investigation immediately using an epifluorescence microscope. In order to prove an effective internalization of the fluorescent micelles (**13**)/vesicles (**15**) and to exclude a false positive fluorescence signal by a simple adsorption on the extracellular leaflet of the cell membrane, CLSM was utilized to perform an optical z-sectioning through the cells. For that purpose, adherent cells were enzymatically detached after the above mentioned incubation with the micelles/vesicles. The nuclei, late endosomes/lysosomes and cell membranes were stained with SYTO®Red 59, LysoTracker Red or Cell Mask Orange according to manufactures instructions and, subsequently, fixed with 4% paraformaldehyde dissolved in PBS. Aliquots

of the cell suspensions were then transferred onto microscopic slides, decorated with coverslips and subjected to CLSM analysis.

### **Acknowledgement**

Cryo-TEM investigations were performed at the cryo-TEM facilities of the Jena Center for Soft Matter (JCSM). TEM facilities were funded by a grant of the DFG (German Research Foundation) and the EFRE (European Fund for Regional Development).

### **References**

1. Steichen, S. D.; Caldorera-Moore, M.; Peppas, N. A. A review of current nanoparticle and targeting moieties for the delivery of cancer therapeutics. *Eur. J. Pharm. Sci.* **2013**, *48*, 416-427.
2. Feng, S.-S.; Chien, S. Chemotherapeutic engineering: Application and further development of chemical engineering principles for chemotherapy of cancer and other diseases. *Chem. Eng. Sci.* **2003**, *58*, 4087-4114.
3. Ding, H.; Wang, X.; Zhang, S.; Liu, X. Applications of polymeric micelles with tumor targeted in chemotherapy. *J. Nanopart. Res.* **2012**, *14*, 1-13.
4. Kiparissides, C.; Kammona, O. Nanoscale carriers for targeted delivery of drugs and therapeutic biomolecules. *Can. J. Chem. Eng.* **2013**, *91*, 638-651.
5. Maeda, H.; Greish, K.; Fang, J. The EPR effect and polymeric drugs: A paradigm shift for cancer chemotherapy in the 21st century. In *Polymer Therapeutics II*, Satchi-Fainaro, R.; Duncan, R., Eds. Springer Berlin Heidelberg: 2006; pp 103-121.
6. Davis, M. E.; Chen, Z.; Shin, D. M. Nanoparticle therapeutics: An emerging treatment modality for cancer. *Nat. Rev. Drug Discov.* **2008**, *7*, 771-782.

7. Deng, C.; Jiang, Y.; Cheng, R.; Meng, F.; Zhong, Z. Biodegradable polymeric micelles for targeted and controlled anticancer drug delivery: Promises, progress and prospects. *Nano Today* **2012**, *7*, 467-480.
8. Xu, W.; Ling, P.; Zhang, T. Polymeric micelles, a promising drug delivery dystem to enhance bioavailability of poorly water-soluble drugs. *J. Drug Deliv.* **2013**, *2013*, 15.
9. Talelli, M.; Rijcken, C. J. F.; Hennink, W. E.; Lammers, T. Polymeric micelles for cancer therapy: 3 C's to enhance efficacy. *Curr. Opin. Solid State Mater. Sci.* **2012**, *16*, 302-309.
10. Sudimack, J.; Lee, R. J. Targeted drug delivery via the folate receptor. *Adv. Drug Deliv. Rev.* **2000**, *41*, 147-162.
11. Gu, F. X.; Karnik, R.; Wang, A. Z.; Alexis, F.; Levy-Nissenbaum, E.; Hong, S.; Langer, R. S.; Farokhzad, O. C. Targeted nanoparticles for cancer therapy. *Nano Today* **2007**, *2*, 14-21.
12. Sahoo, S. K.; Ma, W.; Labhasetwar, V. Efficacy of transferrin-conjugated paclitaxel-loaded nanoparticles in a murine model of prostate cancer. *Int. J. Cancer* **2004**, *112*, 335-340.
13. Liu, C.-C.; Ye, X.-S. Carbohydrate-based cancer vaccines: Target cancer with sugar bullets. *Glycoconjugate J.* **2012**, *29*, 259-271.
14. von Mehren, M.; Adams, G. P.; Weiner, L. M. Monoclonal antibody therapy for cancer. *Annu. Rev. Med.* **2003**, *54*, 343-369.
15. Byrne, J. D.; Betancourt, T.; Brannon-Peppas, L. Active targeting schemes for nanoparticle systems in cancer therapeutics. *Adv. Drug Deliv. Rev.* **2008**, *60*, 1615-1626.
16. Kim, T.-Y.; Kim, D.-W.; Chung, J.-Y.; Shin, S. G.; Kim, S.-C.; Heo, D. S.; Kim, N. K.; Bang, Y.-J. Phase I and pharmacokinetic study of genexol-PM, a cremophor-free, polymeric micelle-formulated paclitaxel, in patients with advanced malignancies. *Clin. Cancer Res.* **2004**, *10*, 3708-3716.
17. Matsumura, Y.; Hamaguchi, T.; Ura, T.; Muro, K.; Yamada, Y.; Shimada, Y.; Shirao, K.; Okusaka, T.; Ueno, H.; Ikeda, M.; Watanabe, N. Phase I clinical trial and pharmacokinetic evaluation of NK911, a micelle-encapsulated doxorubicin. *Br. J. Cancer* **2004**, *91*, 1775-1781.

18. Nishiyama, N.; Okazaki, S.; Cabral, H.; Miyamoto, M.; Kato, Y.; Sugiyama, Y.; Nishio, K.; Matsumura, Y.; Kataoka, K. Novel cisplatin-incorporated polymeric micelles can eradicate solid tumors in mice. *Cancer Res.* **2003**, *63*, 8977-8983.
19. Hrkach, J.; Von Hoff, D.; Ali, M. M.; Andrianova, E.; Auer, J.; Campbell, T.; De Witt, D.; Figa, M.; Figueiredo, M.; Horhota, A.; Low, S.; McDonnell, K.; Peeke, E.; Retnarajan, B.; Sabnis, A.; Schnipper, E.; Song, J. J.; Song, Y. H.; Summa, J.; Tompsett, D.; Troiano, G.; Van Geen Hoven, T.; Wright, J.; LoRusso, P.; Kantoff, P. W.; Bander, N. H.; Sweeney, C.; Farokhzad, O. C.; Langer, R.; Zale, S. Preclinical development and clinical translation of a PSMA-targeted docetaxel nanoparticle with a differentiated pharmacological profile. *Sci. Transl. Med.* **2012**, *4*, 128-139.
20. Knop, K.; Hoogenboom, R.; Fischer, D.; Schubert, U. S. Poly(ethylene glycol) in drug delivery: pros and cons as well as potential alternatives. *Angew. Chem., Int. Ed.* **2010**, *49*, 6288-6308.
21. Adams, N.; Schubert, U. S. Poly(2-oxazolines) in biological and biomedical application contexts. *Adv. Drug Deliv. Rev.* **2007**, *59*, 1504-1520.
22. Kempe, K.; Hoogenboom, R.; Jaeger, M.; Schubert, U. S. Three-fold metal-free efficient ("click") reactions onto a multifunctional poly(2-oxazoline) designer scaffold. *Macromolecules* **2011**, *44*, 6424-6432.
23. Guillerm, B.; Monge, S.; Lapinte, V.; Robin, J.-J. How to modulate the chemical structure of polyoxazolines by appropriate functionalization. *Macromol. Rapid Commun.* **2012**, *33*, 6000-6016.
24. Sedlacek, O.; Monnery, B. D.; Filippov, S. K.; Hoogenboom, R.; Hruby, M. Poly(2-Oxazoline)s – are they more advantageous for biomedical applications than other polymers? *Macromol. Rapid Commun.* **2012**, *33*, 1648-1662.
25. Hoogenboom, R.; Rogers, S.; Can, A.; Becer, C. R.; Guerrero-Sanchez, C.; Wouters, D.; Hoepfener, S.; Schubert, U. S. Self-assembly of double hydrophobic block copolymers in water-ethanol mixtures: from micelles to thermoresponsive micellar gels. *Chem. Commun.* **2009**, 5582-5584.
26. Weberskirch, R.; Preuschen, J.; Spiess, H. W.; Nuyken, O. Design and synthesis of a two compartment micellar system based on the self-association behavior of poly(N-

acylethyleneimine) end-capped with a fluorocarbon and a hydrocarbon chain. *Macromol. Chem. Phys.* **2000**, *201*, 995-1007.

27. Takahashi, R.; Sato, T.; Terao, K.; Qiu, X.-P.; Winnik, F. M. Self-association of a thermosensitive poly(alkyl-2-oxazoline) block copolymer in aqueous solution. *Macromolecules* **2012**, *45*, 6111-6119.

28. Lobert, M.; Hoogenboom, R.; Fustin, C.-A.; Gohy, J.-F.; Schubert, U. S. Amphiphilic gradient copolymers containing fluorinated 2-phenyl-2-oxazolines: Microwave-assisted one-pot synthesis and self-assembly in water. *J. Polym. Sci., Part A: Polym. Chem.* **2008**, *46*, 5859-5868.

29. Weber, C.; Rogers, S.; Vollrath, A.; Hoepfener, S.; Rudolph, T.; Fritz, N.; Hoogenboom, R.; Schubert, U. S. Aqueous solution behavior of comb-shaped poly(2-ethyl-2-oxazoline). *J. Polym. Sci., Part A: Polym. Chem.* **2013**, *51*, 139-148.

30. Weber, C.; Wagner, M.; Baykal, D.; Hoepfener, S.; Paulus, R. M.; Festag, G.; Altuntas, E.; Schacher, F. H.; Schubert, U. S. Easy access to amphiphilic heterografted poly(2-oxazoline) comb copolymers. *Macromolecules* **2013**, *46*, 5107-5116.

31. Knop, K.; Pretzel, D.; Urbanek, A.; Rudolph, T.; Scharf, D. H.; Schallon, A.; Wagner, M.; Schubert, S.; Kiehntopf, M.; Brakhage, A. A.; Schacher, F. H.; Schubert, U. S. Star-shaped drug carriers for doxorubicin with PEOGMA and POEtOxMA brush-like shells: A structural, physical, and biological comparison. *Biomacromolecules* **2013**, *14*, 2536-2548.

32. von der Ehe, C.; Kempe, K.; Bauer, M.; Baumgaertel, A.; Hager, M. D.; Fischer, D.; Schubert, U. S. Star-shaped block copolymers by copper-catalyzed azide-alkyne cycloaddition for potential drug delivery applications. *Macromol. Chem. Phys.* **2012**, *213*, 2146-2156.

33. Han, Y.; He, Z.; Schulz, A.; Bronich, T. K.; Jordan, R.; Luxenhofer, R.; Kabanov, A. V. Synergistic combinations of multiple chemotherapeutic agents in high capacity poly(2-oxazoline) micelles. *Mol. Pharm.* **2012**, *9*, 2302-2313.

34. Schulz, A.; Jaksch, S.; Schubel, R.; Wegener, E.; Di, Z.; Han, Y.; Meister, A.; Kressler, J.; Kabanov, A. V.; Luxenhofer, R.; Papadakis, C. M.; Jordan, R. Drug-induced morphology switch in drug delivery systems based on poly(2-oxazoline)s. *ACS Nano* **2014**, *8*, 2686-2696.

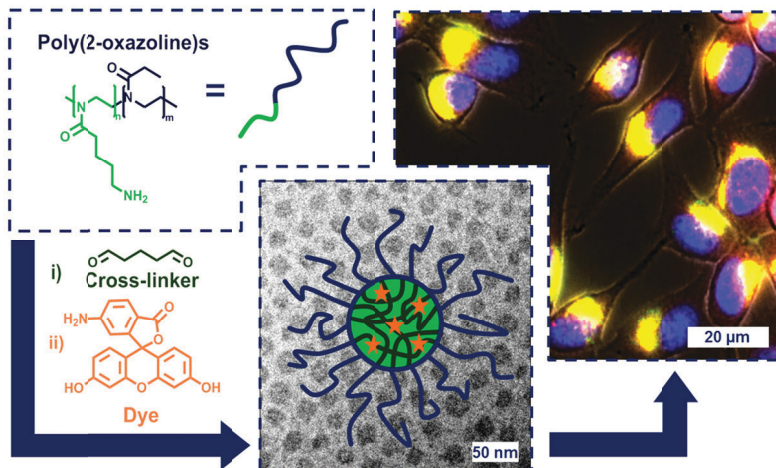
35. Luxenhofer, R.; Schulz, A.; Roques, C.; Li, S.; Bronich, T. K.; Batrakova, E. V.; Jordan, R.; Kabanov, A. V. Doubly amphiphilic poly(2-oxazoline)s as high-capacity delivery systems for hydrophobic drugs. *Biomaterials* **2010**, *31*, 4972-4979.
36. Kempe, K.; Hoogenboom, R.; Hoepfener, S.; Fustin, C.-A.; Gohy, J.-F.; Schubert, U. S. Discovering new block terpolymer micellar morphologies. *Chem. Commun.* **2010**, *46*, 6455-6457.
37. Mansfeld, U.; Hoepfener, S.; Kempe, K.; Schumers, J.-M.; Gohy, J.-F.; Schubert, U. S. Tuning the morphology of triblock terpoly(2-oxazoline)s containing a 2-phenyl-2-oxazoline block with varying fluorine content. *Soft Matter* **2013**, *9*, 5966-5974.
38. Luxenhofer, R.; Sahay, G.; Schulz, A.; Alakhova, D.; Bronich, T. K.; Jordan, R.; Kabanov, A. V. Structure-property relationship in cytotoxicity and cell uptake of poly(2-oxazoline) amphiphiles. *J. Controlled Release* **2011**, *153*, 73-82.
39. O'Reilly, R. K.; Hawker, C. J.; Wooley, K. L. Cross-linked block copolymer micelles: functional nanostructures of great potential and versatility. *Chem. Soc. Rev.* **2006**, *35*, 1068-1083.
40. Brummelhuis, N. t.; Schlaad, H. Stimuli-responsive star polymers through thiol-yne core functionalization/crosslinking of block copolymer micelles. *Polym. Chem.* **2011**, *2*, 1180-1184.
41. Huang, H.; Hoogenboom, R.; Leenen, M. A. M.; Guillet, P.; Jonas, A. M.; Schubert, U. S.; Gohy, J.-F. Solvent-induced morphological transition in core-cross-linked block copolymer micelles. *J. Am. Chem. Soc.* **2006**, *128*, 3784-3788.
42. Liu, Y.; Wang, Y.; Wang, Y.; Lu, J.; Piñón, V.; Weck, M. Shell cross-linked micelle-based nanoreactors for the substrate-selective hydrolytic kinetic resolution of epoxides. *J. Am. Chem. Soc.* **2011**, *133*, 14260-14263.
43. Zschoche, S.; Rueda, J. C.; Binner, M.; Komber, H.; Janke, A.; Arndt, K.-F.; Lehmann, S.; Voit, B. Reversibly switchable pH- and thermoresponsive core-shell nanogels based on poly(NiPAAm)-*graft*-poly(2-carboxyethyl-2-oxazoline)s. *Macromol. Chem. Phys.* **2012**, *213*, 215-226.



44. Zschoche, S.; Rueda, J.; Boyko, V.; Krahl, F.; Arndt, K.-F.; Voit, B. Thermo-responsive nanogels based on poly[NIPAAm-graft-(2-alkyl-2-oxazoline)]s crosslinked in the micellar state. *Macromol. Chem. Phys.* **2010**, *211*, 1035-1042.
45. Legros, C.; De Pauw-Gillet, M.-C.; Tam, K. C.; Lecommandoux, S.; Taton, D. pH and redox responsive hydrogels and nanogels made from poly(2-ethyl-2-oxazoline). *Polym. Chem.* **2013**, *4*, 4801-4808.
46. Hartlieb, M.; Pretzel, D.; Kempe, K.; Fritzsche, C.; Paulus, R. M.; Gottschaldt, M.; Schubert, U. S. Cationic poly(2-oxazoline) hydrogels for reversible DNA binding. *Soft Matter* **2013**, *9*, 4693-4704.
47. Hoogenboom, R.; Schlaad, H. Bioinspired poly(2-oxazoline)s. *Polymers* **2011**, *3*, 467-488.
48. Wiesbrock, F.; Hoogenboom, R.; Abeln, C. H.; Schubert, U. S. Single-mode microwave ovens as new reaction devices: accelerating the living polymerization of 2-ethyl-2-oxazoline. *Macromol. Rapid Commun.* **2004**, *25*, 1895-1899.
49. Hartlieb, M.; Pretzel, D.; Englert, C.; Hentschel, M.; Kempe, K.; Gottschaldt, M.; Schubert, U. S. Matrix supported poly(2-oxazoline)-based hydrogels for DNA catch and release. *Biomacromolecules* **2014**, *15*, 1970-1978.
50. Bloksma, M. M.; Bakker, D. J.; Weber, C.; Hoogenboom, R.; Schubert, U. S. The effect of hofmeister salts on the LCST transition of poly(2-oxazoline)s with varying hydrophilicity. *Macromol. Rapid Commun.* **2010**, *31*, 724-728.
51. Bailey, F. E.; Callard, R. W. Some properties of poly(ethylene oxide) in aqueous solution. *J. Appl. Polym. Sci.* **1959**, *1*, 56-62.
52. Israelachvili, J. N.; Mitchell, D. J.; Ninham, B. W. Theory of self-assembly of hydrocarbon amphiphiles into micelles and bilayers. *J. Chem. Soc., Faraday Trans. 2* **1976**, *72*, 1525-1568.
53. Rodríguez-Hernández, J.; Babin, J.; Zappone, B.; Lecommandoux, S. Preparation of shell cross-linked nano-objects from hybrid-peptide block copolymers. *Biomacromolecules* **2005**, *6*, 2213-2220.

54. Wagner, M.; Holzschuh, S.; Traeger, A.; Fahr, A.; Schubert, U. S. Asymmetric flow field-flow fractionation in the field of nanomedicine. *Anal Chem* **2014**, *86*, 5201-5210.
55. Burchard, W. Solution properties of branched macromolecules. In *Branched Polymers II*, Roovers, J., Ed. Springer Berlin Heidelberg: 1999; pp 113-194.
56. Sjöback, R.; Nygren, J.; Kubista, M. Absorption and fluorescence properties of fluorescein. *Spectrochimica acta part A: Molecular and biomolecular spectroscopy* **1995**, *51*, L7-L21.
57. Tsuchiya, T. Studies on the standardization of cytotoxicity tests and new standard reference materials useful for evaluating the safety of biomaterials. *J. Biomater. Appl.* **1994**, *9*, 138-157.
58. Bauer, M.; Schroeder, S.; Tauhardt, L.; Kempe, K.; Schubert, U. S.; Fischer, D. In vitro hemocompatibility and cytotoxicity study of poly(2-methyl-2-oxazoline) for biomedical applications. *J. Polym. Sci., Part A: Polym. Chem.* **2013**, *51*, 1816-1821.
59. Vollrath, A.; Schallon, A.; Pietsch, C.; Schubert, S.; Nomoto, T.; Matsumoto, Y.; Kataoka, K.; Schubert, U. S. A toolbox of differently sized and labeled PMMA nanoparticles for cellular uptake investigations. *Soft Matter* **2013**, *9*, 99-108.
60. Lerch, S.; Dass, M.; Musyanovych, A.; Landfester, K.; Mailänder, V. Polymeric nanoparticles of different sizes overcome the cell membrane barrier. *Eur. J. Pharm. Biopharm.* **2013**, *84*, 265-274.

## Table of content graphic



# Supporting Information

## Core cross-linked micelles and vesicles based on the self-assembly of double hydrophilic poly(2-oxazoline) block copolymers as potential drug carriers

*Matthias Hartlieb,<sup>a,b</sup> David Pretzel,<sup>a,b</sup> Michael Wagner,<sup>a,b</sup> Stephanie Hoepfener,<sup>a,b</sup> Peter Bellstedt,<sup>c</sup> Matthias Görlach,<sup>c</sup> Christoph Englert,<sup>a,b</sup> Kristian Kempe,<sup>a,b,†</sup> Ulrich S. Schubert<sup>a,b,\*</sup>*

a Laboratory of Organic and Macromolecular Chemistry (IOMC), Friedrich Schiller University Jena, Humboldtstrasse 10, 07743, Jena, Germany

b Jena Center for Soft Matter (JCSM), Friedrich Schiller University Jena, Philosophenweg 7, 07743, Jena, Germany

c Biomolecular NMR spectroscopy, Leibniz Institute for Age Research – Fritz Lipmann Institute, Beutenbergstr. 11, 07745 Jena, Germany

† Current address: Department of Chemistry, University of Warwick, Gibbet Hill Road, Coventry, CV4 7AL, U.K.

\* Address correspondence to [ulrich.schubert@uni-jena.de](mailto:ulrich.schubert@uni-jena.de)

## I Materials and instrumentation

Chemicals and solvents were purchased from Sigma-Aldrich, Merck, Fluka, and Acros. 2-Ethyl-2-oxazoline (EtOx) and methyl tosylate (MeOTos) were distilled to dryness prior to use. EtOx was dried using barium oxide before distillation. 2-(4-((*tert*-Butoxycarbonyl)amino)butyl)-2-oxazoline (BocOx) was synthesized as described in a previous publication.<sup>1</sup>

The Initiator Sixty single-mode microwave synthesizer from Biotage, equipped with a non-invasive IR sensor (accuracy: 2%), was used for polymerizations under microwave irradiation. Microwave vials were heated overnight to 110 °C and allowed to cool to room temperature under argon atmosphere before use. All polymerizations were carried out under temperature control. Size-exclusion chromatography (SEC) of protected polymers was performed on a Shimadzu system equipped with a SCL-10A system controller, a LC-10AD pump, a RID-10A refractive index detector and a PSS SDV column with chloroform/triethylamine (NEt<sub>3</sub>)/*iso*-propanol (94:4:2) as eluent. The column oven was set to 50 °C. SEC of the deprotected statistical copolymers was performed on a Shimadzu system with a LC-10AD pump, a RID-10A refractive index detector, a system controller SCL-10A, a degasser DGU-14A, and a CTO-10A column oven using *N,N*-dimethyl acetamide (DMAc) with 2.1 g L<sup>-1</sup> LiCl as the eluent and the column oven set to 50 °C. Poly(styrene) (PS) samples were used as calibration standards for both solvent systems. Proton NMR spectroscopy (<sup>1</sup>H NMR) measurements were performed at room temperature on a Bruker AC 300 and 400 MHz spectrometer, using CDCl<sub>3</sub> or *N,N* dimethyl formamide (DMF)-D<sub>7</sub> as solvents. The chemical shifts are given in ppm relative to the signal of the residual non-deuterated solvent.

Batch dynamic light scattering (DLS) was performed on a Zetasizer Nano ZS (Malvern Instruments, Herrenberg, Germany). All measurements were performed in folded capillary cells

(DTS1071, Malvern Instruments, Herrenberg, Germany). After an equilibration time of 180 s,  $3 \times 30$  s runs were carried out at 25 °C ( $\lambda = 633$  nm). The counts were detected at an angle of 173°. Each measurement was performed in triplicate. Apparent hydrodynamic radii,  $R_h$ , were calculated according to the Stokes–Einstein equation.

Laser Doppler velocimetry was used to measure the electrokinetic potential, also known as zeta potential. The measurements were performed on a Zetasizer Nano ZS (Malvern Instruments, Herrenberg, Germany) in folded capillary cells (DTS1071). For each measurement, 15 runs were carried out using the fast-field and slow-field reversal mode at 150 V. Each experiment was performed in triplicate at 25 °C. The zeta potential ( $\zeta$ ) was calculated from the electrophoretic mobility ( $\mu$ ) according to the Henry Equation.<sup>2</sup> The Henry coefficient,  $f(ka)$ , was calculated according to Ohshima.<sup>3</sup>

Cryo-TEM investigations were conducted with a FEI Tecnai G<sup>2</sup> 20 at 200 kV acceleration voltage. Specimens were vitrified by a Vitrobot Mark V system on Quantifoil grids (R2/2). The blotting time was 1 s with blotting force offset of 0. The amount of solution was 7  $\mu$ L. Samples were plunge frozen in liquid ethane and stored under liquid nitrogen until transferred to the Gatan cryo-holder and brought into the microscope. Images were acquired with a 4k  $\times$  4k CCD Eagle camera.

#### *Solid state (ss) NMR spectroscopy*

One-dimensional (1D) natural abundance <sup>13</sup>C cross polarization magic angle spinning ssNMR spectroscopy was carried out using a Bruker Avance II spectrometer operating at <sup>1</sup>H (<sup>13</sup>C) frequencies of 500 (125) MHz and using a 3.2 mm triple resonance probe. Sample temperature was 293 K at 20 kHz spinning frequency. Cross polarization contact time was 1.5 ms, and <sup>1</sup>H

decoupling was performed using 90 kHz decoupling field strength. Final spectra were collected with 295006 scans and a 2 s recycle time, processed (exponential window function; line broadening 20 Hz) and evaluated with Bruker Topspin. Referencing was relative to Adamantan setting the methine line to 29.46 ppm relative to neat trimethylsilane.<sup>4</sup>

#### *Asymmetric flow field-flow fractionation (AF4)*

Asymmetric flow field-flow fractionation (AF4) was performed on an AF2000 MT System (Postnova Analytics, Landsberg, Germany) coupled to an UV (PN3211, 260 nm), RI (PN3150), MALLS (PN3070, 633 nm) and DLS (ZetaSizerNano ZS, 633 nm) detector. The eluent is delivered by two different pumps (tip and focus-flow) and the sample is injected by an auto-sampler (PN5300) into the channel. The channel has a trapezoidal geometry and an overall area of 31.6 cm<sup>2</sup>. The nominal height of the spacer was 500  $\mu\text{m}$  and a regenerated cellulose membrane with a molar mass cut-off of 10,000 g mol<sup>-1</sup> was used as accumulation wall. All experiments were carried out at 25 °C. For molar mass determination of the polymers, the eluent was composed of 25 mM acetate buffer at a pH value of 3.5 and 20 mM NaCl. The detector flow rate was set to 0.5 mL min<sup>-1</sup> for all samples and 50  $\mu\text{L}$  (5 mg mL<sup>-1</sup>) were injected with an injection flow rate of 0.2 mL min<sup>-1</sup> for 7 min. For all samples the cross-flow was set to 1.8 mL min<sup>-1</sup>. After the focusing period and a transition time of 1 min, the cross flow was kept constant for 3 min and then decreased under a power function gradient (0.4) to 0 within 15 min. Afterwards, the cross-flow was kept constant at zero for at least 20 min to ensure complete elution. For characterization of the colloidal structures, the eluent was 0.025% NovaChem Surfactant 100 detergents mix. The detector flow rate was set to 0.5 mL min<sup>-1</sup> for all samples and 20  $\mu\text{L}$  (5 mg mL<sup>-1</sup>) were injected with an injection flow rate of 0.2 mL min<sup>-1</sup> for 7 min. For all samples the cross-flow was set to 1.0 mL min<sup>-1</sup>. After the focusing period and a transition time of

1 min, the cross flow was kept constant for 2 min and then decreased under a power function gradient (0.4) to 0 within 18 min. Afterwards, the cross-flow was kept constant at zero for at least 25 min to ensure complete elution. For calculation of the molar mass and the radius of gyration, a Zimm plot was used. All measurements were repeated three times. The refractive index increment ( $dn/dc$ ) of all samples was measured by manual injection of a known concentration directly into the channel without any focusing or cross-flow. The  $dn/dc$  was calculated as the average of at least three injections from the area under the RI curve ( $AUC_{RI}$ ).

## II Analytics of P(EtOx)-*b*-(BocOx) and P(EtOx)-*b*-(AmOx)

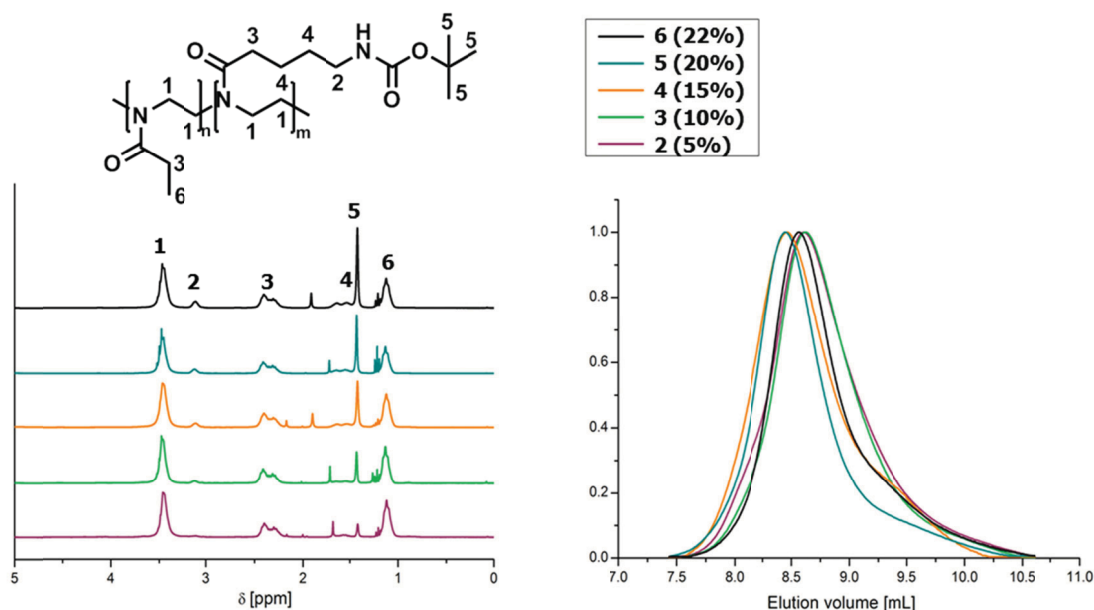


**Figure S1.**  $^1\text{H}$  NMR spectra (300 MHz,  $\text{CDCl}_3$ ) and size exclusion chromatograms (chloroform/ $\text{NEt}_3$ /*iso*-propanol) of the protected block copolymers (P(EtOx)-*b*-BocOx, **2-6**) with BocOx-contents between 5 and 22%.



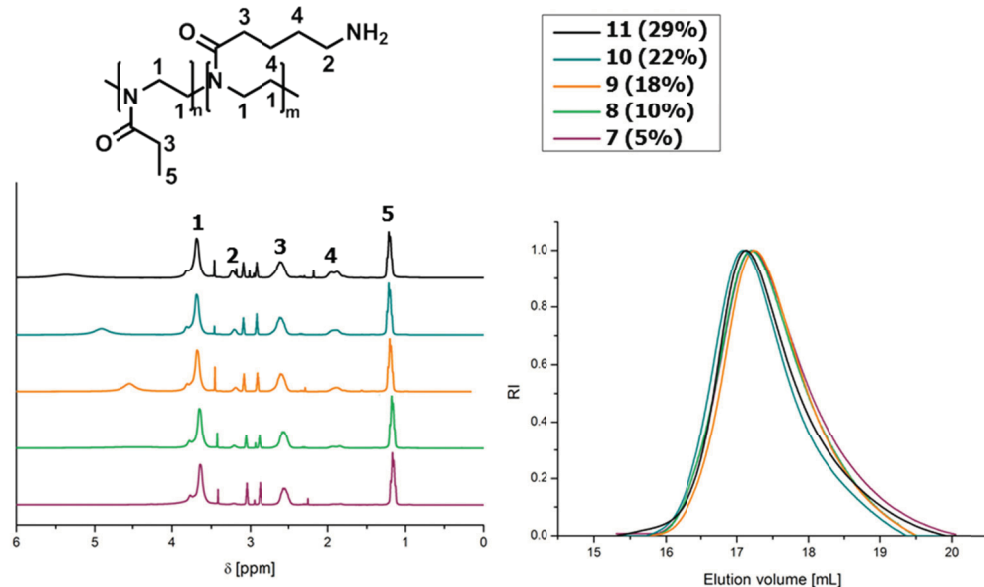


**Figure S2.**  $^1\text{H}$  NMR spectra (300 MHz,  $\text{DMF-D}_7$ ) and size exclusion chromatograms (*N,N*-dimethyl acetamide) of the deprotected block copolymers (P(EtOx-*b*-AmOx, **7-11**) with AmOx-contents between 5 and 29%.

**Table S1.** Asymmetric flow field flow fractionation (AF4) data of the deprotected block copolymers.

Sample	$\frac{dn}{dc}$ [ $\text{mL g}^{-1}$ ]	$M_n$ [ $\text{g mol}^{-1}$ ]	Error [ $\text{g mol}^{-1}$ ]	$M_w$ [ $\text{g mol}^{-1}$ ]	Error [ $\text{g mol}^{-1}$ ]	$M_z$ [ $\text{g mol}^{-1}$ ]	Error [ $\text{g mol}^{-1}$ ]	$\bar{D}$	Error	Rec [%]	Error [%]
<b>7</b>	0.153	11,700	670	12,900	530	14,000	560	1.10	0.024	73.7	0.1
<b>8</b>	0.160	9,200	360	10,500	840	11,300	860	1.14	0.065	74.9	0.9
<b>9</b>	0.153	13,300	340	14,600	270	15,900	260	1.10	0.008	77.6	0.3
<b>10</b>	0.156	13,600	430	14,900	450	16,600	820	1.09	0.003	77.1	0.5
<b>11</b>	0.139	12,500	500	15,700	180	18,100	380	1.26	0.039	75.9	0.9

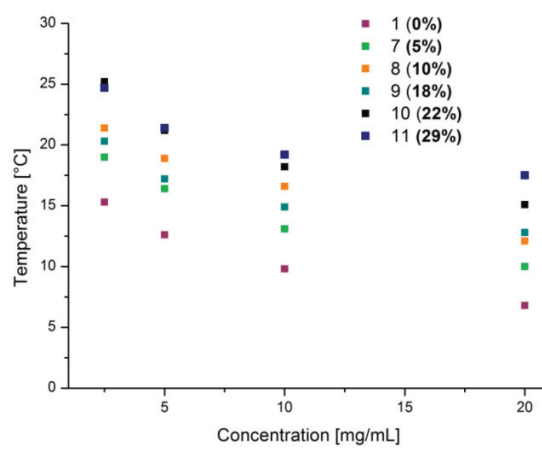


**Figure S3.** Cloud-points of P(EtOx-*b*-AmOx) in dependency of the concentration.

### III Analytics of cross-linked and non-cross-linked self-assembled structures.

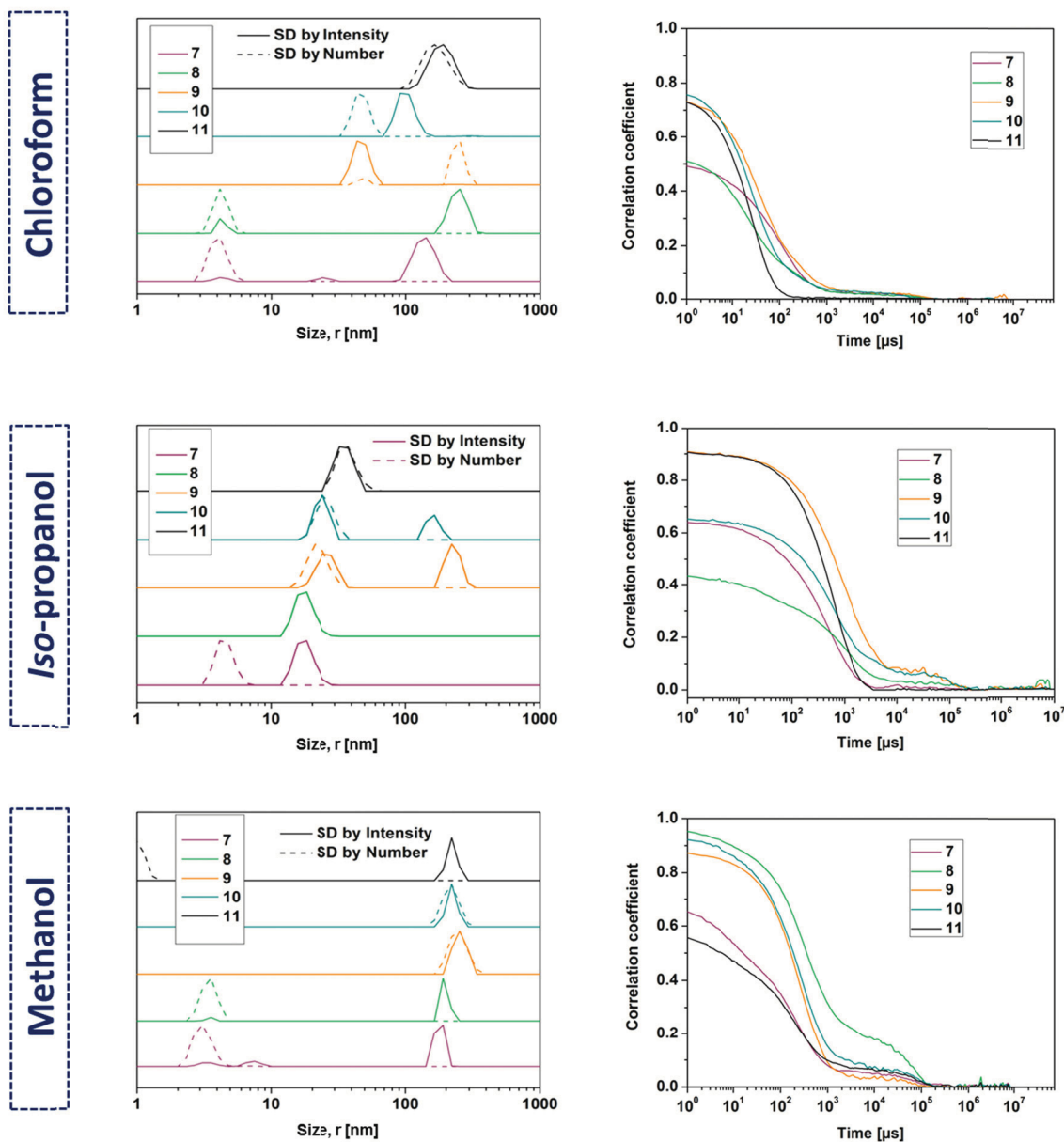


Figure S4. DLS size distributions and correlation functions of P(EtOx-*b*-AmOx) in organic solvents ( $1 \text{ mg mL}^{-1}$ ).

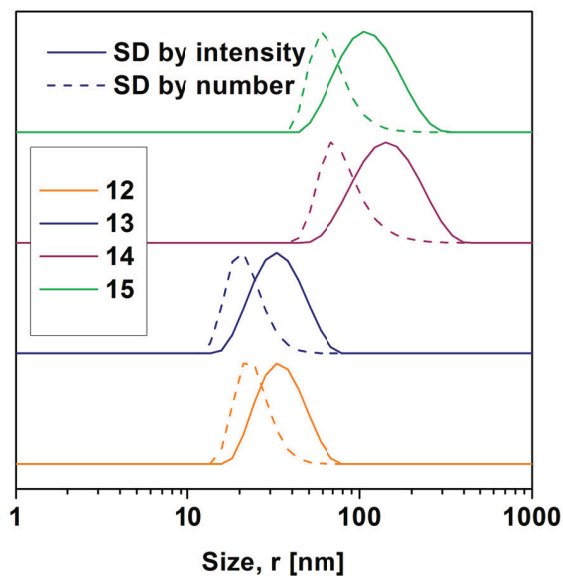
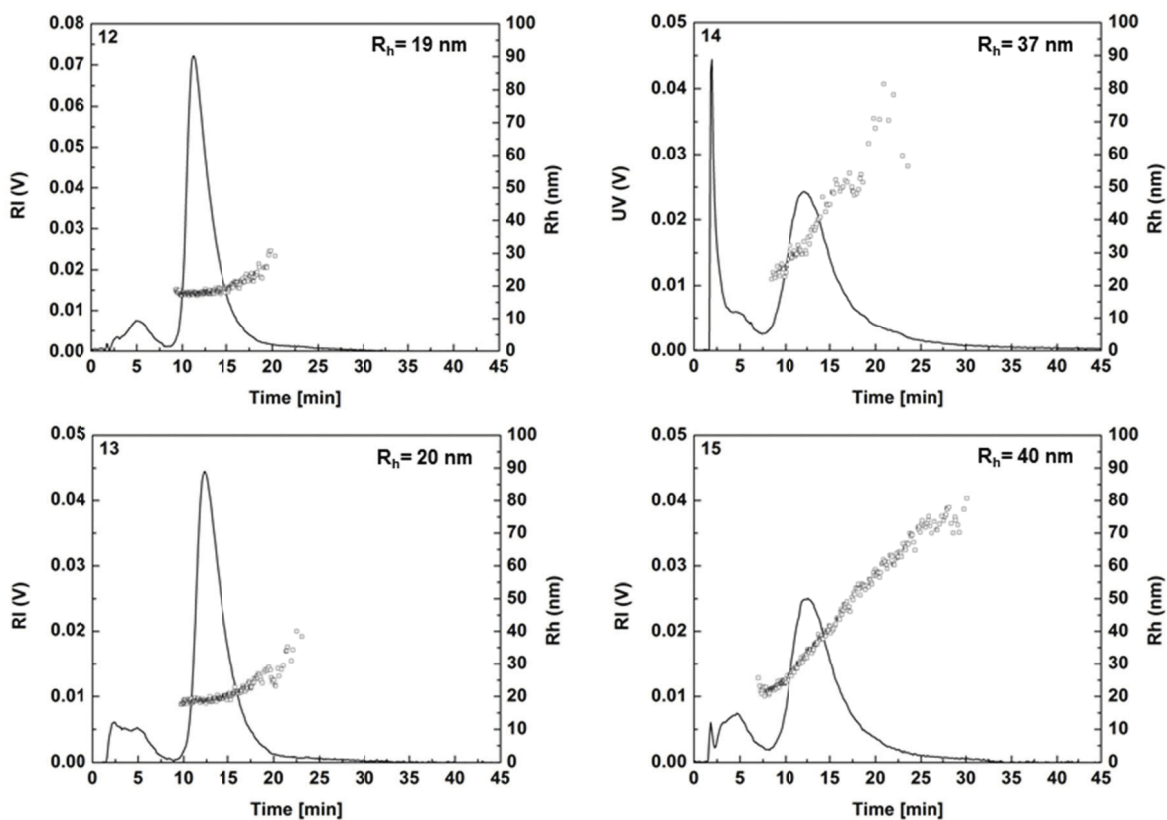
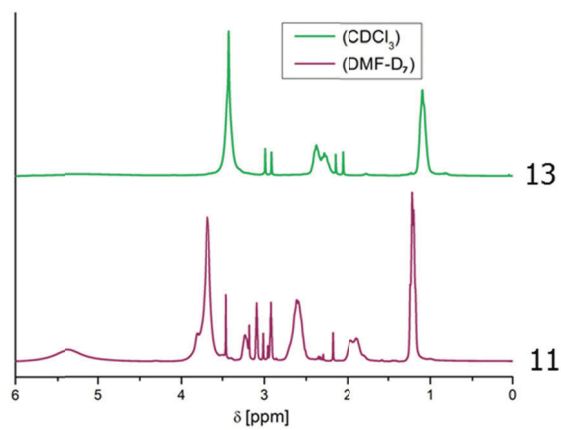


Figure S5. DLS size distributions of cross-linked nanostructures in water.



**Figure S6.** AF4 elugrams of cross-linked nanostructures (in 0.025% NovaChem Surfactant 100 detergents mix).



**Figure S7.** Comparison of the <sup>1</sup>H NMR spectra of polymer **11** in CDCl<sub>3</sub> (self-assembly) and DMF-D<sub>7</sub> (no assembly).

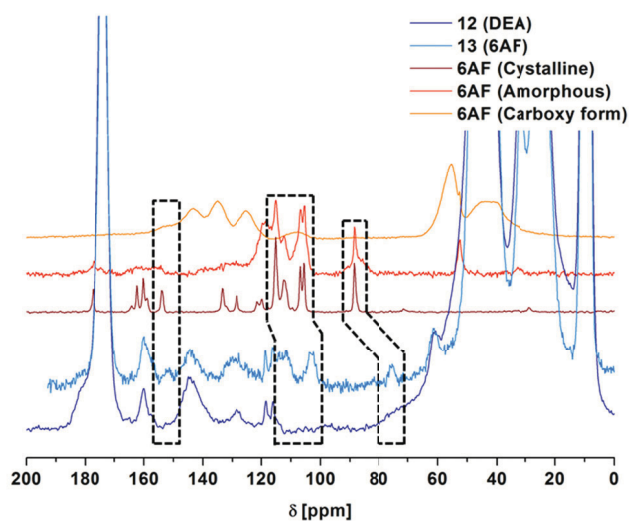


**Figure S8.** Solid state  $^{13}\text{C}$  NMR spectra of different 6AF forms and micelles with (**13**) and without (**12**) 6AF. Commercial, microcrystalline 6AF, amorphous 6AF and KOH-induced ring-opened 6AF were analyzed by natural abundance  $^{13}\text{C}$  CP MAS ssNMR. All MAS ssNMR spectra were acquired at 293 K, with 295006 scans, 2 s recycle time and a CP contact time of 1.5 ms. Microcrystalline 6AF was used as commercially supplied, amorphous 6AF was produced by dissolving commercial 6AF in MeOH, flash-freezing in liquid  $\text{N}_2$  and subsequent lyophilisation; ring-open 6AF was derived from microcrystalline material by dissolving it in 1 M KOH, subsequent flash-freezing and lyophilisation.

IV Cellular uptake and co-localization studies of nano-assemblies.

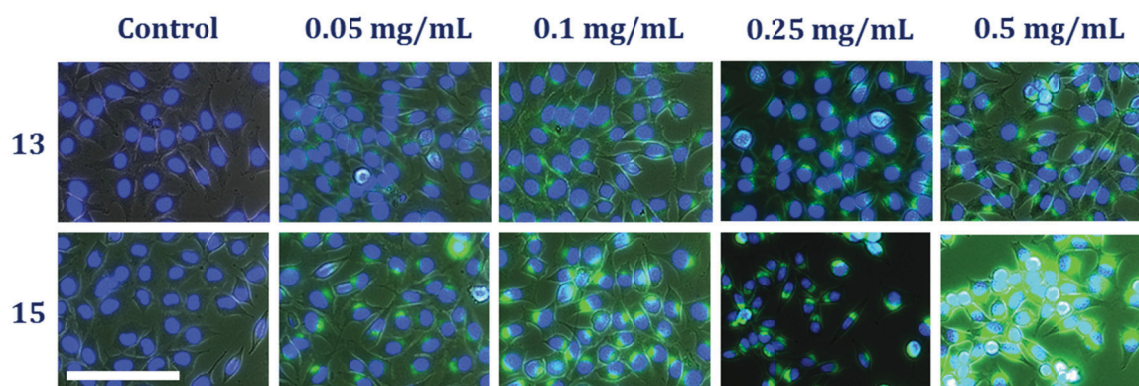


**Figure S9.** Overlay fluorescence microscopy images on the concentration dependent uptake of dye containing micelles (**13**)/vesicles (**15**) by L929 mouse fibroblasts. Cells were incubated over an incubation time of 24 h using micelle/vesicle concentrations in the range between 0.05 and 0.5 mg mL<sup>-1</sup>. Cells incubated only with culture medium served as control. The cell nuclei were additionally stained with blue fluorescent Hoechst 33342. The increasing green fluorescence from the dye containing micelles/vesicles indicates the concentration dependent internalization of both structures with an elevated uptake of vesicles vs. micelles. Scale bar 50  $\mu$ m.

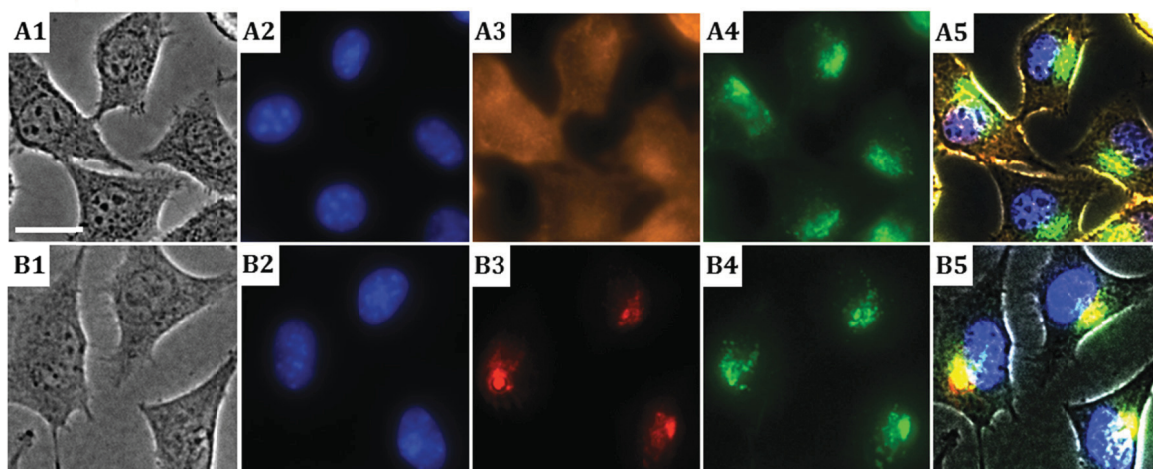


**Figure S10.** Representative bright field (A1 and B1) and epifluorescence images of adherent L929 cells after 24 h incubation at 37 °C with micelles (**13**) at a concentration of 0.1 mg mL<sup>-1</sup>. Cell nuclei (A2 and B2), cell membranes (A3) or late endosomes/lysosomes (B3) were specifically stained and their fluorescence signal was captured in addition to the fluorescence signal originating from the internalized 6AF labeled vesicles (A4 and B4). Overlay of all four channels (A5 and B5). Scale bar 20  $\mu$ m.



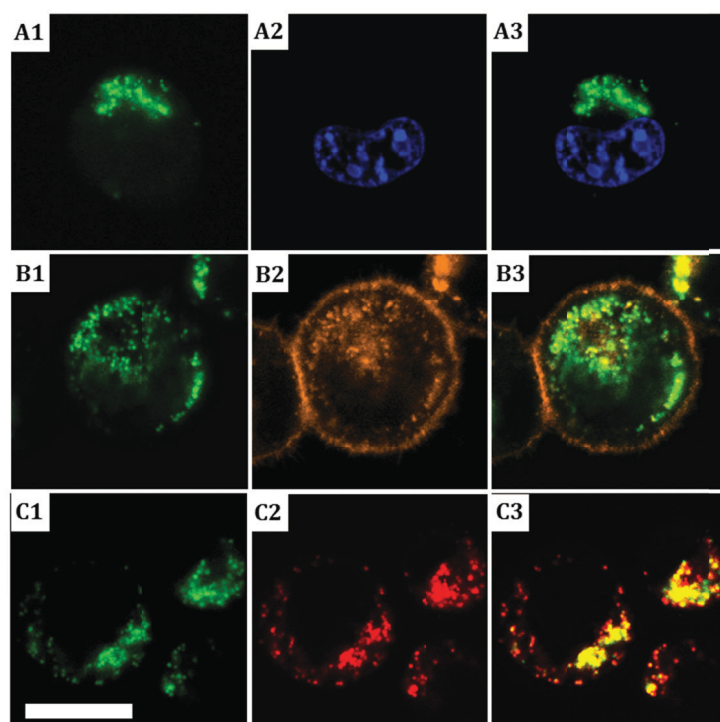


**Figure S11.** Representative CLSM images of detached L929 cells after 24 h incubation at 37 °C with micelles (**13**) at a concentration of 0.1 mg mL<sup>-1</sup>. Cell membranes (A2), cell nuclei (B2), or late endosomes/lysosomes (C2) were specifically stained and correlated with the fluorescence signal of 6AF labeled micelles (A1, B1, and C1). Overlay of both channels (A3, B3 and C3) proves intracellular (A3) but extra-nuclear (B3) localization of the vesicles and their apparent co-localization with lysosomal structures (C3). Scale bar 10 μm.

## References

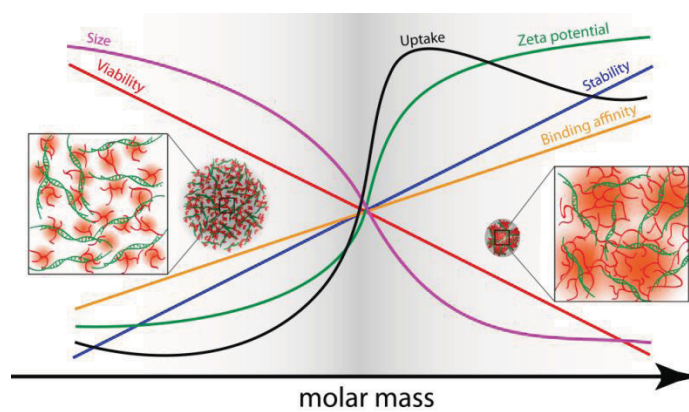
1. Hartlieb, M.; Pretzel, D.; Kempe, K.; Fritzsche, C.; Paulus, R. M.; Gottschaldt, M.; Schubert, U. S. Cationic poly(2-oxazoline) hydrogels for reversible DNA binding. *Soft Matter* **2013**, *9*, 4693-4704.
2. Delgado, A. V.; Gonzalez-Caballero, F.; Hunter, R. J.; Koopal, L. K.; Lyklema, J. Measurement and interpretation of electrokinetic phenomena. *J. Colloid Interface Sci.* **2007**, *309*, 194-224.
3. Ohshima, H. A Simple expression for henry's function for the retardation effect in electrophoresis of spherical colloidal particles. *Journal of Colloid and Interface Science* **1994**, *168*, 269-271.
4. Morcombe, C. R.; Zilm, K. W. Chemical shift referencing in MAS solid state NMR. *J. Magn. Reson.* **2003**, *162*, 479-486.

## Publication P5

Opposites attract: Influence of the molar mass of branched poly(ethylene imine) on biophysical characteristics of siRNA-based polyplexes

M. Wagner, A. C. Rinkenauer, A. Schallon, U. S. Schubert

*RSC Advances* **2013**, 3, 12774-12785.





## PAPER

# Opposites attract: influence of the molar mass of branched poly(ethylene imine) on biophysical characteristics of siRNA-based polyplexes

Cite this: *RSC Advances*, 2013, 3, 12774

Michael Wagner,<sup>ab</sup> Alexandra C. Rinkenauer,<sup>ab</sup> Anja Schallon<sup>ab</sup> and Ulrich S. Schubert<sup>\*ab</sup>

Polymer-based carriers, in particular polycations, represent an interesting alternative to viral vectors, as they form so-called polyplexes with nucleic acids by entropic driven, electrostatic interactions. In this study, we investigate in detail polyplexes based on small interfering RNA (siRNA), the delivery of which into eukaryotic cells represents an attractive route for treating genetic diseases by inhibition of harmful gene expression. Although plasmid DNA (pDNA) based polyplexes are well characterized, we show that not all knowledge can be adopted from pDNA, as siRNA is around 250 times smaller and shows a higher rigidity. The used polymer component is the polycation branched poly(ethylene imine) (B-PEI) of a high range of molar masses (0.6, 1.8, 10, 25 kDa), which are further analyzed by potentiometric titration and cytotoxicity tests. The formation, size, and net-charge of the polyplexes are examined at different ratios of nitrogen of the different polymers and phosphates of the RNA (N/P). Moreover, the stability of siRNA polyplexes against heparin and time was investigated. The obtained physicochemical parameters were then correlated to the cellular internalization of polyplexes. A strong dependency of the molar mass on the polyplex characteristics of the used B-PEI was found. Thereby, high molar mass B-PEI  $\geq 10$  kDa forms smaller polyplexes of around 50 nm radius with zeta potentials  $> 25$  mV, increased long-term stability, and enhanced cellular uptake compared to low molar mass ones. To gain deeper insight into the differences and characteristics of siRNA based polyplexes, the characterization by analytical and preparative ultracentrifugation (AUC, PUC) is applied on siRNA polyplexes for the first time and referred to conventional characterization methods such as DLS. AUC was also used to identify non-complexed PEI in the polyplex solutions. A virtual N/P of 1.3 for siRNA was measured, independent of the used molar masses of B-PEI. Additionally, differences in cellular uptakes of siRNA and pDNA based polyplexes were found. The results of this study will help to understand the properties of siRNA-based polyplexes and could lead to more efficient polymer design.

Received 26th February 2013,  
Accepted 15th May 2013

DOI: 10.1039/c3ra42069h

[www.rsc.org/advances](http://www.rsc.org/advances)

## Introduction

Since the discovery of the RNA interference mechanism by Fire *et al.* in 1998,<sup>1</sup> siRNA delivery represents an attractive route for treating genetic diseases by inhibition of the expression of harmful genes. Compared to the delivery of pDNA, siRNA only needs to be delivered into the cytoplasm of the cells but not into the nucleus, which avoids the need for transport of the delivered molecules across the nuclear membrane. There are, however, two serious limitations of siRNA as a therapeutic agent. One of them is its high negative net-charge, which renders its delivery through the also negatively charged cell

membrane difficult.<sup>2</sup> Beside this, genetic material, in particular siRNA, is not stable under physiological conditions but will be rapidly degraded by RNases.<sup>3</sup> Thus, the half-life time of siRNA in blood serum varies from several minutes to an hour.<sup>4</sup> Both problems make the application of siRNA for *in vitro* and *in vivo* gene delivery challenging. To overcome them, non-viral polymeric carriers, in particular polycations, can be applied for the delivery of the genetic material into the cells and the subsequent expression of foreign genes,<sup>5–7</sup> as has been shown by recent intense research.<sup>8–10</sup> Although the transfection efficiencies of polymeric vectors, the so-called polyplexes, are lower compared to viral vectors, they have substantial advantages,<sup>11,12</sup> as their easy large-scale production, their safety for clinical uses,<sup>13,14</sup> and their potential for chemical modifications.<sup>15–17</sup> Among the polymers applied, the commercially available poly(ethylene imine) (PEI), which is intensively characterized in literature, is the most popular one and is

<sup>a</sup>Laboratory of Organic and Macromolecular Chemistry (IOMC), Friedrich Schiller University Jena, Humboldtstrasse 10, Jena D-07743, Germany.

E-mail: [ulrich.schubert@uni-jena.de](mailto:ulrich.schubert@uni-jena.de)

<sup>b</sup>Jena Center for Soft Matter (JCSM), Friedrich Schiller University Jena, Philosophenweg 7, Jena D-07743, Germany

widely investigated for the delivery of pDNA as well as siRNA.<sup>18–22</sup> Despite the broad interest, the polyplex formation of siRNA and PEI and their characteristics are only partially understood and not yet investigated in detail.

The primary driving force for complexation of nucleic acids by PEI is entropy. The ionic interactions between the negative phosphates in the nucleic acids and the protonated amine groups in the polymer induce a release of counter ions, which leads to an increase of translational entropy.<sup>12,23</sup> The gain of entropy is of course significantly smaller for siRNA than for pDNA, due to its shorter chain length. This results in a weaker binding in the polyplexes. The complexation is influenced also by other factors, like the 3-D structure of the polymers (linear or branched),<sup>24</sup> their molar mass,<sup>25</sup> or further intermolecular forces *e.g.* hydrophobic interactions. While linear PEI (L-PEI) contains mainly secondary amines, branched PEI (B-PEI) consists of primary, secondary, and tertiary amines. The resulting degree of protonation is essential for polyplex formation and for the release of the polyplexes from the endosome according to the postulated proton sponge effect.<sup>5</sup> Non-complexed PEI also influences the transfection efficiencies of polyplexes as well as the toxicity.<sup>26</sup> Besides the polymer itself, also the complexation conditions, *e.g.* buffer components, pH value, or ionic strength play an important role. Added salts can interact with the polyplexes or screen electrostatic forces. It was shown that, *e.g.*, low ionic strength promotes the formation of smaller pDNA polyplexes.<sup>27</sup>

An efficient gene carrier has to combine two features. On the one hand, the complexation has to be sufficiently strong to protect against degradation and to transport the siRNA through the cell membrane. On the other hand, the cellular uptake should be promoted and the release of the genetic material from the polyplex in the cytosol has to be possible. The development of polymers that offer a balance between the two features is an important goal. Above all, of course, the perfect gene carrier should be non-toxic.

For the detailed biophysical and physicochemical characterization of nanoparticles in general, different techniques and methods were established, in the first place light scattering (in particular dynamic light scattering) for measuring the translational diffusion coefficient and the hydrodynamic radius, respectively. Other hydrodynamic methods, *e.g.*, analytical ultracentrifugation (AUC), were up to now not used for analyzing siRNA-based polyplexes. AUC is well-known as a means for the characterization of the molar mass and size of proteins<sup>28–30</sup> but can be also applied for studying nanoparticles and synthetic polymers.<sup>31–33</sup> The efficiency of gene delivery depends on the molar mass of the polymer applied. For B-PEI, the best results for transfection of pDNA were obtained up to now with molar masses of 25 kDa.<sup>34</sup> Beside this, an increase in the molar mass of B-PEI and various other polymers often caused higher cytotoxic effects.<sup>35,36</sup> However, with siRNA 25 kDa B-PEI did not yield an efficient delivery of the nucleic acid, without any obvious reason.<sup>34</sup> This accentuates the importance of a detailed understanding of the polyplex properties.

Herein, the importance of a wide range of molar masses of B-PEI used for siRNA delivery will be presented. Therefore, the influence of the polymer on the formation, stability, size, and net-charge of the polyplexes at different N/P ratios (ratio of nitrogen in the polymer and phosphates in the RNA) will be elucidated in detail. As the knowledge of siRNA polyplexes based on results obtained with pDNA, we also focus on the differences of both genetic materials concerning their stiffness, amount of free PEI, and cellular uptake behavior. In addition, AUC will be applied for the characterization of such polyplexes and the obtained results compared to the revealed data by conventional methods. The potential of this powerful technique for detailed analysis of free and complexed PEI will be demonstrated.

## Experimental

### Materials

B-PEI of molar masses of 0.6, 1.8, and 10 kDa was purchased from Polysciences (Eppelheim, Germany), and 25 kDa B-PEI as well as heparin were purchased from Sigma Aldrich (Steinhausen, Germany). B-PEI was dissolved in sterile 20 mM 4-(2-hydroxyethyl) piperazine-1-ethanesulfonic acid (HEPES) and 5% (w/w) glucose buffer (HBG, pH 7.2) to obtain stock solutions of 0.2 mg mL<sup>-1</sup>. The quality of B-PEI was checked by dynamic light scattering and analytical ultracentrifugation to exclude an influence on the polyplex experiments later on. Control siRNA duplex negative control with 19 bp and Cy3 labeled siRNA was obtained from Eurogentech (Cologne, Germany). Stock solutions of siRNA were prepared by dissolving solid siRNA in sterile RNase free water to yield a concentration of 20 μM. Ethidium bromide solution 1% was purchased from Carl Roth (Karlsruhe, Germany). AlamarBlue and YOYO-1 was obtained from Life Technologies (Darmstadt, Germany). Cell culture materials, cell culture media, and solutions were obtained from PAA (Pasching, Austria). All other chemicals were purchased from Sigma Aldrich and are of analytical grade or better and used without further purification.

### Polyplex preparation

Polyplexes of siRNA and B-PEI were prepared by mixing stock solutions of siRNA and B-PEI at a certain N/P ratio. The indicated amounts of B-PEI were added to a certain volume of 20 μM siRNA solution. Subsequently, the solutions were vortexed for 5 s at 2500 rpm. After incubation at room temperature for 20 min the mixture was diluted with HBG to a total volume of 1 mL and an overall siRNA concentration of 15 μg mL<sup>-1</sup>.

### Potentiometric titration

For potentiometric titration, 6 mg B-PEI were dissolved in 6 mL pure water. Titration experiments were performed using a Metrohm 765 Dosimat (Filderstadt, Germany) and a Greisinger GMH 3530 pH meter (Regenstauf, Germany), using 0.1 M hydrochloric acid or 0.1 M sodium hydroxide as titrant. The titration was started at pH > 11. For this, a defined

amount of 0.1 M sodium hydroxide solution was added. Then, the solution was titrated against 0.1 M hydrochloric acid. The titration was stopped at pH 2. Each experiment was carried out in triplicate at 25 °C as described in the literature.<sup>37</sup>

### Ethidiumbromide quenching assay (EBA)

The polyplex formation of siRNA and B-PEI was detected by quenching of the ethidium bromide (EB) fluorescence as described previously.<sup>38</sup> Briefly, 15  $\mu\text{g mL}^{-1}$  siRNA in a total volume of 100  $\mu\text{L}$  HBG was incubated with EB (0.4  $\mu\text{g mL}^{-1}$ ) for 10 min at room temperature, and then polyplexes with increasing amounts of B-PEI were formed in black 96-well plates (Nunc, Langensfeld, Germany). The samples were equilibrated for 20 min before the fluorescence was measured using a Tecan Genios Pro fluorescence microplate reader (Tecan, Crailsheim, Germany); the excitation and emission wavelength were 525 and 605 nm, respectively. A sample containing only siRNA and EB was used to calibrate the device to 100% fluorescence against a background of 0.4  $\mu\text{g mL}^{-1}$  of EB in HBG solution. The percentage of dye displaced upon polyplex formation was calculated using eqn (1):

$$\text{RFU} = \frac{F_{\text{sample}} - F_0}{F_{\text{siRNA}} - F_0} \quad (1)$$

Here, RFU is the relative fluorescence and  $F_{\text{sample}}$ ,  $F_0$ , and  $F_{\text{siRNA}}$  are the fluorescence intensities of a given sample, the EB in HBG alone, and the EB intercalated into siRNA alone.

### Heparin dissociation assay

To investigate the release of siRNA from polyplexes, the heparin dissociation assay was used.<sup>24</sup> For this purpose, 15  $\mu\text{g mL}^{-1}$  siRNA were incubated for 10 min with EB (0.4  $\mu\text{g mL}^{-1}$ ) in a total volume of 100  $\mu\text{L}$  HBG before polyplexes at N/P 10 were formed. After 15 min the polyplexes were transferred into black 96-well plates and heparin at the indicated concentrations was added. The solution was mixed and incubated for further 30 min at 37 °C. The fluorescence of EB (Ex 525 nm/Em 605 nm) was measured, and the percentage of intercalated EB was calculated as described before (1).

### Dynamic light scattering

Dynamic light scattering (DLS) was performed on an ALV-CGS-3 system (ALV, Langen, Germany) equipped with a He-Ne laser operating at a wavelength of  $\lambda = 633$  nm. The counts were detected at an angle of 90°. All measurements were carried out at 25 °C after an equilibration time of 120 s. For analyzing the autocorrelation function (ACF), the cumulant analysis and the CONTIN algorithm<sup>39</sup> were applied. Apparent hydrodynamic radii were calculated according to the Stokes-Einstein Equation (eqn (2)):

$$R_{\text{H}} = \frac{kT}{6\pi\eta D_0} \quad (2)$$

Here,  $R_{\text{H}}$  is the hydrodynamic radius,  $k$  the Boltzmann constant,  $T$  the absolute temperature,  $\eta$  the viscosity of the sample, and  $D_0$  the translational diffusion coefficient.

### Electrophoretic light scattering

Electrophoretic light scattering was used to measure the electrokinetic potential, also known as zeta potential. The measurements were performed on a Zetasizer Nano ZS (Malvern Instruments, Herrenberg, Germany) by applying laser Doppler velocimetry.<sup>40</sup> For each measurement, 20 runs were carried out using the slow-field reversal and fast-field reversal mode at 150 V. Each experiment was performed in triplicate at 25 °C. The zeta potential ( $\zeta$ ) was calculated from the electrophoretic mobility ( $\mu$ ) according to the Henry Equation (eqn (3)) with  $f(ka) = 1.5$  (Smoluchowski model):

$$\zeta = \frac{3\eta\mu}{2\epsilon f(ka)} \quad (3)$$

Here,  $\eta$  is the viscosity of the solution,  $\epsilon$  the dielectric constant, and  $f(ka)$  the Henry constant.

### Analytical and preparative ultracentrifugation

Analytical ultracentrifugation was performed on a Beckman XL-I analytical ultracentrifuge (Krefeld, Germany). Experiments were carried out in double-sector aluminum centerpieces with optical path length of 12 mm in a four holes rotor setup. Each cell was filled with 0.42 mL of solvent (HBG) and 0.4 mL of sample. A rotor speed between 1000 to 40 000 rpm was used, depending on the sample. The system was equilibrated for 40 min at 25 °C in the centrifuge. Sedimentation data were recorded by absorbance or interference optics, depending on the sample. Data analysis was done by the Sedfit software.<sup>41</sup> For  $c(s)$  analysis of sedimentation data, the partial specific volume of the compound was determined *via* AUC using the “density variation method” as described by Mächtle.<sup>42</sup> The partial specific volume ( $v$ ) of pure siRNA was taken from the literature.<sup>43</sup> For calculating the hydrodynamic radius ( $R_{\text{H}}$ ) and the molar mass ( $M$ ), the Svedberg equation was transformed into eqn (4) and (5), respectively.<sup>44</sup>

$$R_{\text{H}} = \frac{3}{2} (2[s]v)^{1/2} \quad (4)$$

$$M = 9\pi\sqrt{2}N_{\text{A}} \left[ [s] \left( \frac{f}{f_{\text{sph}}} \right) \right]^{3/2} v^{1/2} \quad (5)$$

Here,  $N_{\text{A}}$  is Avogadro's constant,  $[s]$  the intrinsic sedimentation coefficient,  $f$  the frictional coefficient of the solute, and  $f_{\text{sph}}$  that of a hard sphere. Preparative ultracentrifugation (PUC) in combination with photometric detection of PEI by forming a copper complex was used to determine the amount of non complexed PEI. Therefore the polyplex solutions were formed in a volume of 2.5 mL at the stoichiometry of N/P 10 and centrifuged at 20 000 rpm for 2 h on a Beckmann Optima L-XP to remove the polyplexes. Afterwards the supernatant was collected. The concentration of PEI was determined by mixing of 100  $\mu\text{L}$  supernatant and 100  $\mu\text{L}$  copper acetate solution (20 mM) in a clear 96-well plate and determination of the absorbance at 285 nm of the copper-PEI complex.<sup>45</sup> The

concentration was determined from a calibration, which was recorded in the same way as the samples. Each measurement was repeated three times.

### Cytotoxicity

For L929 cells (CCL-1, ATCC), the cytotoxicity assay was performed as described by ISO10993-5. In detail, cells were seeded at 10 000 cells per well in a 96-well plate and incubated for 24 h. No cells were seeded in the outer wells. Afterwards, polymers at the indicated concentrations were added, and the cells were incubated at 37 °C for further 24 h. Subsequently, the medium was replaced by D-PBS and AlamarBlue as recommended by the supplier. After incubation for 4 h, the fluorescence was measured at Ex 570/Em 610 nm, with untreated cells on the same well plate serving as controls.

### Cellular uptake studies

For cellular uptake HEK-293 cells (CRL-1573, ATCC) were seeded at  $10^5$  cells per mL in a 12-well plate with 500  $\mu$ L growth media (RPMI 1640 media, 10% fetal calf serum (FCS), 100  $\mu$ g mL<sup>-1</sup> streptomycin, 100 IU mL<sup>-1</sup> penicillin, and 2 mM L-glutamine). The cells were cultured at 37 °C in a humidified 5% CO<sub>2</sub> atmosphere for 24 h. The media was changed by OptiMEM 1 h before polyplexes were added. Polyplexes containing siRNA were prepared at a final Cy3 labeled siRNA concentration of 15  $\mu$ g mL<sup>-1</sup> in HBG as described before. The labeling of pDNA was realized 1 h before polyplex formation. Therefore, 0.026  $\mu$ L YOYO-1 (1 mM) per 1  $\mu$ g pDNA were mixed in a small amount of pure water. Afterwards, HBG was added to a final concentration of 15  $\mu$ g mL<sup>-1</sup> pDNA. Polymers were added at the indicated N/P ratio, and the polyplex solution was treated as described before and added to the cells. After 4 h of incubation, the cells were harvested and 10% trypan blue was added to quench the outer fluorescence of cells and identify only cells, taken up the genetic material. To determine the relative uptake of NPs, 10 000 cells were quantified by flow cytometry using a Cytomics FC 500 (Beckman Coulter).

### Statistical analysis

Group data are reported as mean  $\pm$  SD. To determine the significance of more than two groups of data, ANOVA was used.

## Results and discussion

### Cytotoxicity of the polymers used

As cationic polymers are known to cause toxic effects, the influence of the B-PEI molar mass on the cytotoxicity was investigated. The current “gold standard” for transfection of pDNA is 25 kDa PEI.<sup>5</sup> Here, the investigated polyplexes were formed with siRNA that is 250 times smaller compared to pDNA; therefore the use of PEIs with molar masses much lower than 25 kDa seemed to be adequate. The toxicity was tested in a worst case scenario, where only the polymers were used instead of the less toxic polyplexes. The polymers were incubated for 24 h and analyzed by AlamarBlue.<sup>46</sup> The relative viability of cells incubated with PEI compared to non-treated cells is shown in Fig. 1, where a strong correlation between

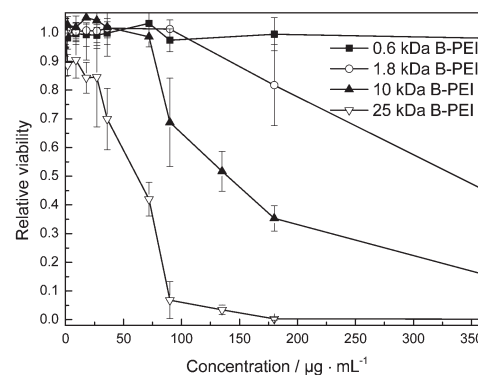


**Fig. 1** Cytotoxicity of B-PEI with different molar masses at increasing concentration. The IC<sub>50</sub> of 1.8, 10 and 25 kDa B-PEI was 335  $\mu$ g mL<sup>-1</sup>, 140  $\mu$ g mL<sup>-1</sup> and 62  $\mu$ g mL<sup>-1</sup>, respectively.

molar mass and toxicity can be seen. The IC<sub>50</sub>-value (the concentration of polymer where only 50% of the cells are viable) distinctly decreases with higher molar mass, meaning a toxic effect at lower compound concentration. Furthermore, the smallest B-PEI (0.6 kDa) shows no significant toxicity up to 360  $\mu$ g mL<sup>-1</sup> (ANOVA). The investigated concentration range of PEI is adequate, keeping in mind that 360  $\mu$ g mL<sup>-1</sup> PEI corresponds to a N/P ratio above 200 (15  $\mu$ g mL<sup>-1</sup> siRNA) and all experiments were carried out below this ratio. It should be noted that all polymers investigated by us are not toxic (>80% viability) at N/P ratios up to 20. Polyplexes of B-PEI with molar masses higher than 25 kDa will not be investigated here, due to their high toxicity which makes them unsuitable for *in vitro* and *in vivo* studies.<sup>47</sup>

### Potentiometric titration of branched PEI

One of the major postulated advantages of PEI as gene carrier is its high buffer capacity, which leads to osmotic swelling under the acidic conditions in the endosome and the release of the polyplexes into the cytosol.<sup>48,49</sup> Beside this, the degree of protonation can also have an impact on the stability and formation of the siRNA polyplexes. To study the influence of molar mass on the pK<sub>a</sub> and the degree of protonation, titration curves of all four B-PEIs, at the same nitrogen (monomer unit) concentration, were measured by potentiometric titration. It must be mentioned that the titration behavior as well as the pK<sub>a</sub> values strongly depend on the ionic strength and the polymer concentration itself, as reported first by Suh *et al.*<sup>37</sup> The data shown in Fig. 2 represents only apparent values, due to the fact that at lower pH value the protonated amines electrostatically suppress further protonation of neighboring amines. The corresponding apparent pK<sub>a</sub> values were listed in Table 1. Values of pK<sub>a</sub><sup>b</sup> correspond mainly to protonation of secondary amines, whereas pK<sub>a</sub><sup>a</sup> is probably based on protonation of tertiary ones.<sup>50</sup> It was found that the titration behavior as well as the pK<sub>a</sub> values of 10 and 25 kDa B-PEI do not differ significantly, whereas the protonation of 0.6 and 1.8 kDa B-PEIs differ (Fig. 2, Table 1). Both pK<sub>a</sub> values decrease with increasing molar mass from 5.7 to 4.8 and 9.8 to 8.3, respectively, which is in good accordance with values reported by others for PEI polymers.<sup>6,18</sup> Even if there are small



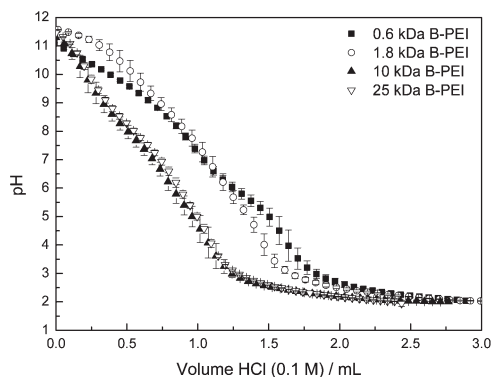


**Fig. 2** Titration curves of  $1 \text{ mg ml}^{-1}$  B-PEI of indicated molar mass in water against HCl.

differences in the  $\text{p}K_{\text{a}}$  values, this probably does not influence polyplex formation. One reason is that these values only represent apparent ionization data as mentioned above. In addition, the buffer capacity at pH 7.2, where the polyplexes were prepared, is very similar for all commercial B-PEIs as well as the ratio of primary, secondary, and tertiary amines as reported in the literature.<sup>47</sup> It is, however, not known which nitrogen atoms of the branched polymer are accessible for siRNA interaction during polyplex formation.

### Polyplex formation and binding affinity

Polyplexes can be formed in different buffer solutions or non-buffered 150 mM NaCl. It was reported that the kind of buffer used has an influence on the polyplex characteristics, *e.g.* size.<sup>51</sup> Therefore, the polyplexes were always prepared in HBG (20 mM HEPES, 5% (w/v) glucose) to circumvent any influence due to changes of the solution conditions, like ionic strength or adsorption of ions. In contrast to saline buffers or physiological NaCl, the ionic strength is relatively low, which minimizes electrolysis during electrophoretic light scattering. The sugar content provides the physiological osmolarity for biological applications. A dependence of the results on the mixing protocol was not observed (data not shown).

To characterize the polyplex formation of siRNA and PEI, the ethidium bromide quenching assay (EBA) was used. The fluorescence intensity of ethidium bromide (EB) increases significantly when it intercalates into the double stranded siRNA.<sup>52</sup> After complexation of the siRNA with polymers like PEI, EB is excluded from the nucleic acid, which leads to a decrease of the fluorescence signal, as seen in Fig. 3. This displacement is probably caused by electrostatic and hydro-

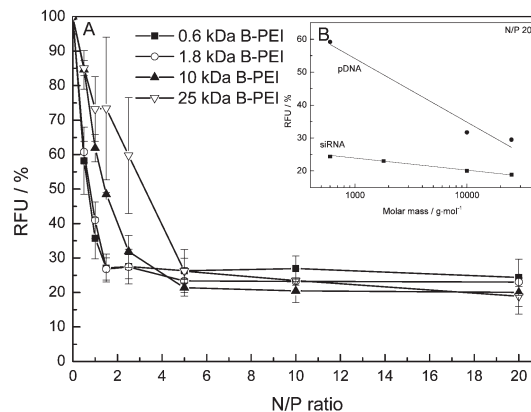


**Fig. 3** Binding affinity of siRNA to B-PEI according to EBA ( $n = 3$ ). A: different molar masses of B-PEI at different N/P ratios. B: binding affinity at N/P 20. The fluorescence of pure siRNA (N/P 0) is normalized to 100%.

phobic interactions of the polymer and the genetic material. Polyplex formation was observed for all B-PEIs, as indicated by RFU (eqn (1)) below 35%. At small N/P ratios ( $<2$ ), 0.6 kDa and 1.8 kDa B-PEI show a higher affinity to siRNA compared to the 10 and 25 kDa analogues. Between N/P ratios of 2 and 5, no significant differences between data for different molar masses of B-PEI could be found. At  $\text{N/P} > 5$ , a constant fluorescence level is reached for all B-PEIs, indicating a complete complexation of the siRNA with the polymers. The fluorescence for higher molar mass B-PEI is slightly lower (Fig. 3B), indicating that the binding affinity increases with increasing molar mass of B-PEI. The dependency of binding affinity on the molar mass of B-PEI is stronger if pDNA was used as genetic material.

From these results, it can be concluded that a N/P ratio of 5 or higher is necessary for a complete complexation of the siRNA. The binding affinity of the polyplexes seems to increase with increasing molar mass of the polymer. A slightly decreased affinity of a 0.8 kDa B-PEI in comparison to the 25 kDa analogue was also reported in the literature;<sup>24,25</sup> this tendency was confirmed here over a wide range of molar masses.

### Surface charge density-electrokinetic potential

As siRNA is negatively charged, it needs to be complexed by cationic polymers to be transported through the negatively charged cell membrane. The electrokinetic potential, also known as zeta potential, can serve as an indicator of the surface charge density of the complexes; it is one of the characteristics measured by electrophoretic light scattering and can be calculated from it by applying the Henry equation. We have used it for measuring the net-charge of the siRNA/B-PEI polyplexes at different N/P ratios. The results are shown in Fig. 4. At N/P ratios  $<1$ , no zeta potential could be measured as there was no detectable Doppler shift during the experiment. Binding between siRNA and B-PEI could, however, be detected even at low N/P ratios by EBA. This could indicate the formation of rather small polyplexes or the formation of a loosely bound network. All polyplexes at small N/P ratios (1 to

**Table 1**  $\text{p}K_{\text{a}}$  values determined by potentiometric titration against HCl

Polymer	$\text{p}K_{\text{a}}^{\text{a}}$	$\text{p}K_{\text{a}}^{\text{b}}$
0.6 kDa	5.7	9.8
1.8 kDa	5.3	9.5
10 kDa	4.9	8.2
25 kDa	4.8	8.3

<sup>a</sup> protonation of tertiary amines. <sup>b</sup> protonation of secondary amines.

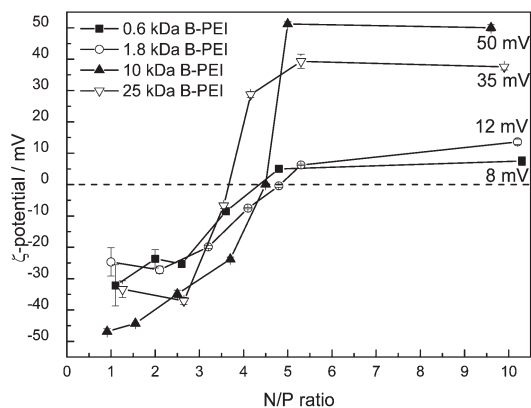


**Fig. 4** Zeta potential of siRNA and B-PEI of different molar masses at different N/P ratios ( $n = 3$ ).

3) show a negative zeta potential, ranging from  $-50$  to  $-25$  mV. At a N/P ratio of around 4, the zeta potential increases and shifts to positive values. At N/P 5, a nearly constant positive value of 35, 50, 12, and 5 mV for 25, 10, 1.8, and 0.6 kDa B-PEI polyplexes is reached, respectively. Obviously, a higher molar mass of the B-PEI leads to a higher zeta potential. A zeta potential of around 25 mV indicates stable polyplexes with positive charge density, whereas at 10 mV the complexes seem to be less stable. Higher values of the zeta potential are, however, difficult to interpret since the Helmholtz–Smoluchowski model is not valid any more.<sup>40</sup> Nevertheless, there is no further significant change in zeta potential at  $N/P > 5$ . These findings are in agreement with the binding affinities, where also a constant plateau is reached at those N/P ratios.

#### Investigation of polyplex size by DLS

It is well-known that the uptake of nanoparticles<sup>53</sup> as well as polyplexes<sup>54</sup> is influenced by their size. The internalization route resulting in successful gene expression therefore depends not only on the cell line but also on the PEI polyplex type.<sup>55</sup> Large polyplexes interact with the membrane, but the uptake is rather inefficient. Because of the importance of polyplex size for biological applications, the hydrodynamic radius of the polyplexes was analyzed in detail by DLS.

The hydrodynamic radii of polyplexes made of siRNA and the four different B-PEIs studied, at different N/P ratios, are presented in Fig. 5. For the calculations, the CONTIN algorithm was used. Radius measurements were unsuccessful for polyplexes at N/P ratios  $< 1$  due to a counting rate too small for application of the CONTIN algorithm, probably caused by the presence of very small polyplexes or of a loosely bound network only (see above). At N/P ratios from 1 to 3, hydrodynamic radii  $< 100$  nm were found: 30 to 50 nm for 0.6, 10, and 25 kDa B-PEI, and 60 up to 90 nm for 1.8 kDa B-PEI polyplexes, respectively. An increase in the B-PEI concentration and, thus, in the N/P ratio causes an increase in the hydrodynamic radius for all B-PEIs used. At N/P ratios of approximately  $4 \pm 0.5$ , maxima were observed: at 350 nm for 0.6 kDa, 600 nm for 1.8 kDa,  $> 1000$  nm for 10 kDa, and

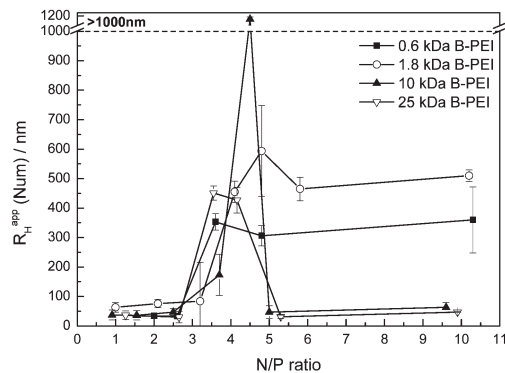


**Fig. 5** Apparent hydrodynamic radius of the main population of polyplexes containing B-PEI of different molar masses at different N/P ratios, as obtained by CONTIN analysis. Radii larger than 1000 nm are presented as “ $> 1000$ ”, due to the fact that the values determined are outside the reliable measuring range ( $n = 3$ ).

450 nm for 25 kDa B-PEI polyplexes. At N/P ratios  $\geq 5$ , again a constant value was reached. For polyplexes of high molar mass B-PEIs (10 and 25 kDa), the hydrodynamic radius decreases to around 40 nm and 50 nm for 25 and 10 kDa B-PEI, respectively. The 0.6 and 1.8 kDa B-PEI formed larger polyplexes, with radii at around 350 nm and 500 nm, respectively. Taking all facts together, smaller polyplexes were formed using high molar mass B-PEI. As the uptake of large polyplexes into cells is less efficient, this could be one reason, why low molar mass B-PEI is less efficient for gene delivery.<sup>56</sup>

Fig. 6A–D shows, analogous to Fig. 5, the distributions of the hydrodynamic radii (linear number weighted) versus N/P. It should be noted that, according to Fig. 6, for all B-PEIs and investigated N/P ratios also some larger aggregates with high polydispersity are present besides the main polyplex population. For polyplexes of 0.6 kDa B-PEI, the amount of aggregates increases at higher N/P ratio (Fig. 6A). In addition, the radius of the aggregates increases from around 100 nm (N/P 2) to above 400 nm at N/P ratio 3. Polyplexes of 1.8 kDa B-PEI (Fig. 6B) show a similar behavior. For polyplexes of 10 kDa (Fig. 6C) and 25 kDa (Fig. 6D) B-PEI, the results are more complex. At  $N/P < 4$ , the behavior is comparable to that described above, which means that the amount of aggregates increases with increasing N/P ratio. At  $N/P 4 \pm 0.5$ , only large aggregates (around 1000 nm for 10 kDa B-PEI, 400 nm for 25 kDa B-PEI) are present, whereas at N/P ratio of  $\geq 5$  also polyplexes with small hydrodynamic radii ( $< 50$  nm) and only a low amount of aggregates with a radius of around 150 nm were observed. This confirms the previous results that  $N/P \geq 5$  is necessary for complete complexation of the siRNA and the formation of compact nanocomplexes. In general, this is in accordance with literature, but it has to be kept in mind that often different buffers, concentrations and N/P ratios were investigated.<sup>25</sup>

Furthermore, the pure B-PEI polymers were also measured by DLS at concentrations between 5 to 20  $\text{mg mL}^{-1}$ . For 25 and 10 kDa B-PEI a hydrodynamic radius of around 4 and 2 nm was found, respectively. For 1.8 and 0.6 kDa B-PEI no DLS measurements could be performed as the molar mass of the

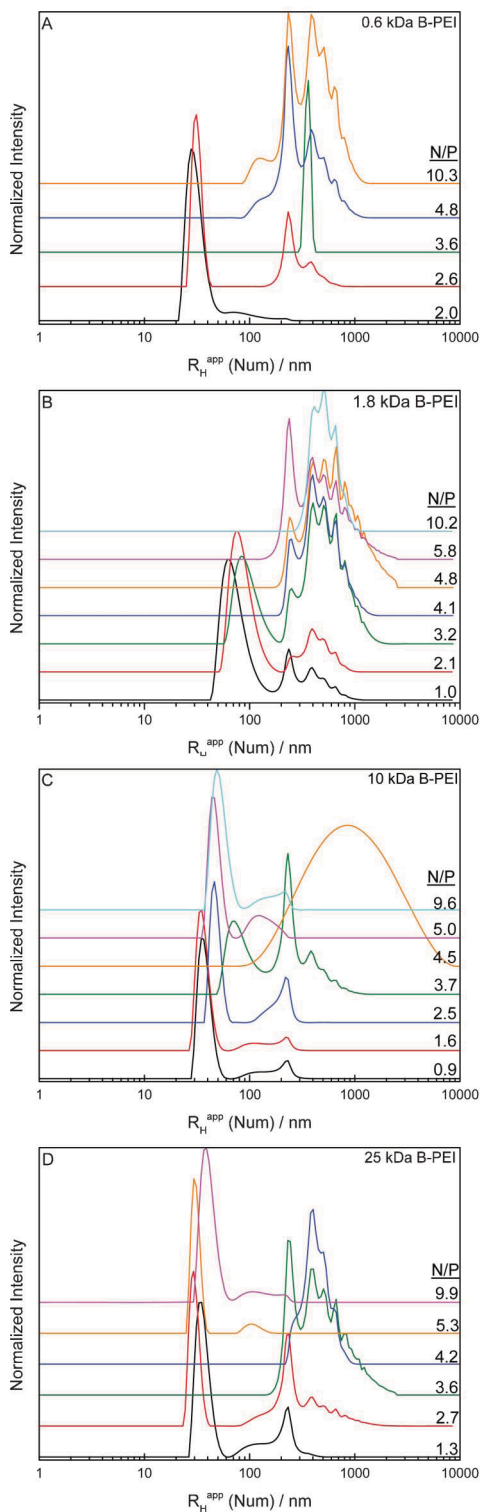
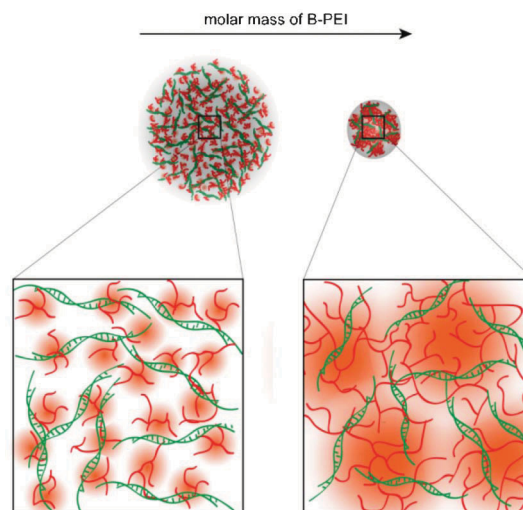


**Fig. 6** Distribution of the hydrodynamic radii of siRNA/B-PEI polyplexes at different N/P ratios. The CONTIN algorithm was used for analyzing the ACF. The B-PEI molar masses were A) 0.6, B) 1.8, C) 10, and D) 25 kDa.

polymer, or to be more precisely, oligomer, is too low to yield any reliable data. At the concentrations, used for formation of polyplexes, no autocorrelation function could be obtained for

all B-PEI samples. Therefore, an influence of the free PEI on the DLS results of the polyplex solutions can be excluded.

A comparison of zeta potential and hydrodynamic radii of the polyplexes reveals a good correlation. At N/P ratios  $<3$ , where the zeta potential is highly negative, small radii for polyplexes of all four tested B-PEIs were observed. Large aggregates occur for all B-PEI polyplexes at N/P ratio of  $4 \pm 0.5$ , where the zeta potential is around 0 mV. At higher N/P ratios, the radius decreases for polyplexes of higher molar mass B-PEI (10, 25 kDa), whereas the zeta potential reaches high positive values ( $>25$  mV). In addition, polyplexes formed of low molar mass B-PEI (0.6, 1.8 kDa) showed only low positive zeta potentials ( $<15$  mV) and a high tendency to form larger aggregates. From the results, it becomes clear that the electrostatic repulsion, indicated by the zeta potential, dominates the polyplex size and stability in solution. High repulsive interactions stabilize the polyplexes which results in small polyplexes with only low amounts of larger aggregates. In contrast, the presence of low or no repulsive interactions leads to fast aggregation and complexes with high hydrodynamic radius. Both, zeta potential and hydrodynamic radius also correlate with the relative fluorescence of the EBA, where a higher affinity for high molar mass B-PEI was found. To sum up, the binding affinity, the zeta potential as well as the hydrodynamic radius reaches a constant value at N/P ratio  $>5$ . With increasing molar mass of B-PEI, smaller, more positively charged polyplexes with a high binding affinity are formed. These are all arguments that the stability of the polyplexes increases with increasing molar mass of the used B-PEI. A schematic visualization of this situation can be seen in Scheme 1. It is assumed that with low molar mass B-PEI (left) a network-like polyplex is formed, where the polymer acts as a kind of linker. The result is a large, fast aggregating polyplex with only a low excess of positive charges, indicated by low zeta potential. In contrast, high molar mass B-PEI (right) forms smaller polyplexes, and the high excess of positive charges stabilizes the polyplexes electrostatically. Moreover, it becomes also clear that not all nitrogen atoms in the polymer are



**Scheme 1** Model of the polyplex formation by PEI of different molar masses.

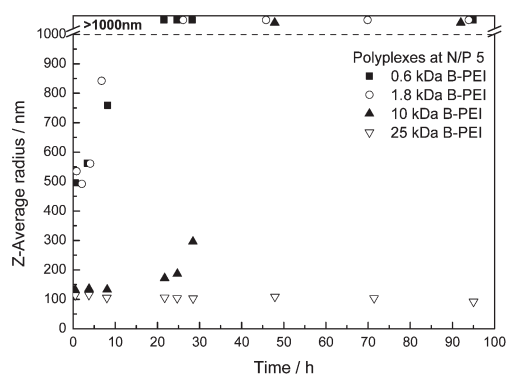


**Fig. 7** Time dependency of the z-average radius, as obtained by cumulant analysis of polyplexes of siRNA and B-PEI of different molar masses at N/P 5. Radii larger than 1000 nm are presented as “>1000” in the upper part of the graphic, due to the fact that they are at the limit of the measurement range.

accessible to siRNA due to its rigidity in comparison with pDNA and the branched structure of PEI.<sup>57</sup> However, this first assumption should be investigated further in future.

### Long-term stability of polyplexes

For the qualitative comparison of the polyplex solutions, the cumulant analysis and the z-average are powerful tools, since the whole system can be described by one single parameter which is sensitive to any changes occurring in the solution. The correct calculation of distributions of the hydrodynamic radius, as shown in Fig. 7, is more difficult. In this case, the analysis of the autocorrelation function (ACF) requires application of a multiple  $\Gamma$  algorithm (*e.g.* CONTIN). The cumulant analysis would reflect the distribution very inaccurately in this case, due to the strong influence of a relatively low amount of aggregates on the obtained z-average and PDI value.

In this study, the cumulant analysis of DLS measurements is used to record the long-term stability of the polyplexes (Fig. 7). It can be seen that the long-term stability of the polyplexes increases with increasing molar mass of the B-PEI used. The polyplexes of 0.6 and 1.8 kDa B-PEI, where already aggregates are present in the solutions, further aggregate within a few hours. Polyplexes of 10 kDa B-PEI are stable for approximately 24 h, whereas 25 kDa polyplexes are stable for more than 4 days. The time-dependent aggregation of the low molar mass B-PEI polyplexes can also be due to their low zeta potential, but this will not explain the aggregation of the 10 kDa B-PEI after one day, since its zeta potential is comparable to that of the 25 kDa B-PEI polyplexes. Even if the stability of all polyplexes is sufficient to carry out the physicochemical experiments, it is questionable, if the stability is high enough for transfections.

### Polyplex dissociation (heparin assay)

A suitable polymer for gene delivery should form stable and small polyplexes but also release its genetic material inside the cell. To investigate the dissociation of the polyplex and the release of siRNA, the well-known heparin dissociation assay was applied.<sup>24</sup> Heparin is a sulfated glycosaminoglycan with high negative charge density that is widely used in medicine as

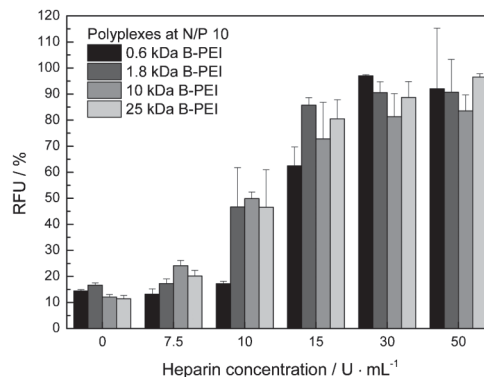


**Fig. 8** Heparin-induced dissociation of polyplexes formed from siRNA and B-PEI of different molar masses, at N/P 10.

anticoagulant. Due to its anionic character, heparin serves as competitor to siRNA and interacts with the cationic polymer.

With increasing amount of heparin, the polyplexes of siRNA and PEI dissolve. To measure the release of siRNA, again EB was used as described before. The polyplexes were prepared at N/P 10, because the polyplex is fully formed at this N/P ratio (compare EBA, zeta potential and size measurements). Fig. 8 clearly shows that it was possible to dissociate all polyplexes studied here. At heparin concentration of  $30 \text{ U mL}^{-1}$  nearly 100% of the siRNA present is free. The low molar mass PEI polyplex shows a higher stability against heparin at  $10 \text{ U mL}^{-1}$  than the other ones. This can be explained by a weaker affinity to anionic substances than the high molar mass ones. So, B-PEI with a weak binding to anionic substances like siRNA, as shown in the EB assay, should also show weaker binding to heparin. Furthermore, no significant difference between B-PEI of higher molar masses on the release of siRNA can be found.

### Analytical and preparative ultracentrifugation experiments

AUC is a powerful technique for characterization of polymers, both biological and synthetic, and of nanoparticles. To the best of our knowledge, AUC has not been applied so far to investigate the solution behavior of siRNA-based polyplexes.

As it is known, that for DLS the intensity of scattered light scales with  $r^6$ , the amount of aggregates is overestimated in the intensity distribution. The calculation of number weighted distributions tries to correct this effect, but the obtained distributions cannot be interpreted quantitatively. Therefore, we apply analytical ultracentrifugation to proof whether the DLS results are precise.

At first, all polyplexes which were analyzed by DLS, were also investigated by AUC to compare both methods. The distribution of hydrodynamic radii of polyplexes formed with 10 kDa B-PEI at different N/P ratios is shown in Fig. 9. The results are in good agreement with those obtained by DLS (Fig. 6C). At N/P ratios below and above  $4 \pm 0.5$ , the polyplex radius is around 30 to 50 nm; some larger aggregates are also present. At N/P 3.7, the radius shifts to higher values of around 150 nm. At N/P 4.5, it was not possible to obtain any reliable sedimentation data. The reason for this is the formation of large aggregates and their extremely fast sedimentation, even

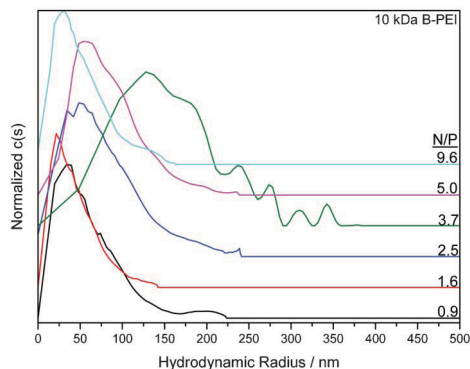


**Fig. 9** Distribution of the hydrodynamic radii calculated from the distribution of sedimentation coefficients (eqn (4)) obtained by AUC of polyplexes of 10 kDa B-PEI and siRNA in HBG at 25 °C.

at a rotor speed of only 1000 rpm. This was also the case for other polyplex solutions and explains why the fraction of larger aggregates cannot be detected by AUC and why no reliable sedimentation data could be obtained for most N/P ratios of 0.6 and 1.8 kDa B-PEI polyplexes.

Typical sedimentation profiles of polyplexes formed of 10 kDa B-PEI at N/P 3.7, together with the corresponding residual plots, are shown in Fig. 10. The large contribution from noise is mainly due to the high sedimentation velocity of the particles. Consequently, the lowest possible rotor speed (1000 rpm) and a high radial step size (for each scan) of 0.1 mm had to be chosen to obtain sufficient data (note: in AUC resolution increases with speed<sup>58</sup>). With polyplex samples containing 10 and 25 kDa B-PEI at N/P > 5, after sedimentation of the polyplexes at 1000 rpm, the supernatants of the solution were centrifuged at 40 000 rpm. This revealed the presence of a second particle population. Its molar mass was calculated according to eqn (5) as 10.9 and 25.6 kDa for 10 kDa B-PEI and 25 kDa B-PEI polyplex solutions, respectively; it thus represents free B-PEI. Free siRNA could not be detected in the polyplex solution, which is in accordance with gel electrophoresis experiments in literature.<sup>16</sup>

As there are hints that free PEI is necessary for cellular uptake<sup>26</sup> the amount was quantified by preparative ultracentrifugation and photometrically determination of the copper chelate complex. In principle the amount of excess PEI can also be determined by AUC, but for the used N/P ratios and

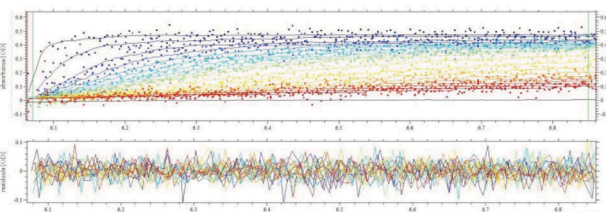


**Fig. 10** Sedimentation velocity data of polyplexes of siRNA and 10 kDa B-PEI at N/P 3.7 in HBG at 25 °C. Rotor speed was 1000 rpm; scans were collected every minute. Top: Sedimentation profiles obtained by absorbance optics at 257 nm. Bottom: Corresponding plot of the residuals.

concentrations, the amount of PEI was too low to give accurate results. Nevertheless, quantification *via* the copper chelate method<sup>45</sup> shows that at N/P 10 around 85% of the PEI is free and not complexed. This corresponds to a virtual N/P ratio of around 1.3 for the polyplexes. Interestingly, this amount depends not on the molar mass of the used polymer. This correlates well to the small differences found in the EB assay and support the theory that only few amine groups of the polymer interact with the polymer whereas the other amines are responsible for the positive surface charge and interaction with other polyplexes.<sup>59</sup> Even if all polyplexes contain the same amount of positive charges, they have different zeta potentials (surface charge densities). This is probably due to their different radii and the different distribution of the charges in the polyplexes (Scheme 1). These results highlight the difference between complexation of siRNA and pDNA, where a value of 2.5 was described.<sup>26</sup> It is also known that polyplexes containing siRNA are slightly larger than pDNA polyplexes.<sup>24,27</sup> Both can be explained by a higher flexibility of pDNA compared to the stiff siRNA. While pDNA consists of more than thousand base pairs, siRNA has only 19 to 23 (~5 nm). With respect to the persistence length of RNA (the length where the chain behaves as a rigid rod) of ~70 nm (260 bp),<sup>57</sup> it becomes obvious that short siRNA cannot condense and behaves as a rigid rod. Fitting of the frictional ratio  $f/f_{\text{sph}}$  from sedimentation velocity data ( $f/f_{\text{sph}} \geq 2$ , data not shown) also indicates a rod-like molecule. For this structure it is more difficult to become fully complexed. This can explain the already mentioned high N/P ratios required for complete complexation and lower virtual NP ratio of siRNA based polyplexes compared to pDNA ones and shows that not all insights gathered from pDNA can be adopted for siRNA.

### Uptake study

The uptake behavior of the used B-PEIs of different molar masses was investigated using a Cy3 labeled siRNA. Therefore, the amount of internalized siRNA was detected with flow cytometry after 4 h, as this time is common for changing the transfection media to growth media during transfection procedure. Here, two N/P ratios were studied, in detail 1.3 and 10, what represent the virtual N/P and fully complexed siRNA (Fig. 3). For the virtual N/P ratio no significant uptake was achieved for B-PEI at all molar masses (Fig. 11). Besides, a significant uptake was detected using higher molar mass (10 and 25 kDa) B-PEI at N/P 10. This shows the potential of B-PEI  $\geq 10$  kDa and the necessity of an excess of polymer for cellular uptake of polyplexes. Taken the previous results into account, the inability of low molar mass PEI could be a consequence of increased polyplex sizes within 4 h, next to less stability indicated by lower zeta potentials, and lower  $pK_a$  values. Furthermore these results draw attention to the importance of size and zeta potential for efficient uptake, next to the potential of polymers to bind and release genetic material. To gain deeper insights into the mechanism of siRNA delivery in contrast to pDNA, the uptake of the latest was investigated using YOYO-1 labeled pDNA (Fig. 11). Again, higher molar masses at N/P 10 lead to a cellular uptake, but in comparison to siRNA, also B-PEI  $\geq 10$  kDa at N/P 1.3 showed internalization. This could be explained by the different molecular ratios

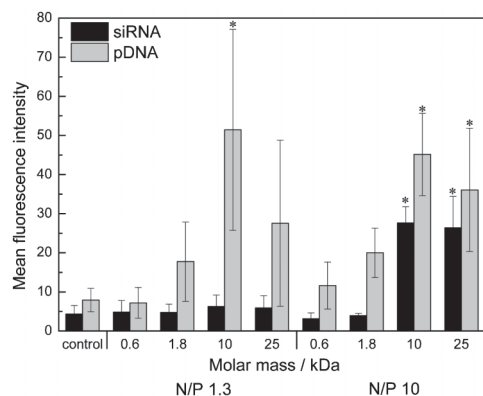


**Fig. 11** Mean fluorescence intensity of HEK cells transfected with Cy3 labeled siRNA and YOYO-1 labeled pDNA after 4 h. Values represent mean  $\pm$  S.D.  $n \geq 3$ ; \* indicate significant difference compared to control.

(polymer/nucleic acid). While around 54 molecules of 10 kDa B-PEI for one pDNA molecule represents N/P 1.3, this ratio is around 0.23 for siRNA (or 4.4 siRNA molecules per polymer) due to its 250 times shorter length. Obvious, the complexation of  $\sim 4$  siRNA molecules by one B-PEI molecule is more difficult.

Additionally the question arises, how far the phosphates of a stiff molecule like siRNA (in contrast to pDNA) are accessible for branched PEI. Here, linear PEI with higher chain flexibility might be more effective. Since, this issue concerning the uptake and length/stiffness of the genetic material still remains to be unclear, it will be part of further investigations. However, using both genetic materials, the molar mass showed a strong impact onto cellular internalization, indicating a critical molar mass for efficient polyplex formation and therefore better cellular uptake.

## Conclusions

In this study, the influence of the molar mass of B-PEI on the stability, formation, and uptake of siRNA-based polyplexes was investigated. We show that the stability of such polyplexes strongly depends on the molar mass of the used B-PEI. Taking the results from EBA, dynamic, and electrophoretic light scattering into account, it becomes clear that complete complexation of siRNA is reached at  $N/P > 5$ . No significant differences in the binding affinity and release of siRNA were observed using different molar masses of B-PEI. A high correlation between net charge (zeta potential) and hydrodynamic radius of the polyplexes was found. At high values of the zeta potential, regardless if negative or positive, small radii occur, whereas at low zeta potential we observe large aggregates. Small hydrodynamic radii and high values of zeta potential were observed at  $N/P < 3$  for all molar masses of B-PEI and at  $N/P \geq 5$  for 10 and 25 kDa B-PEI.

For the first time, we have successfully applied AUC for the characterization of siRNA polyplexes, suitable for polyplexes with radii smaller than 150 nm. Limitations occur due to the

high sedimentation velocity of the polyplexes and the aggregates which requiring low rotor speeds and limited time for data collection only and, thus, leads to low resolution. To assess the problem of accurate size distributions of polyplex systems, containing different species, the establishment of asymmetric flow field-flow fractionation for such samples is currently under investigation.

Nevertheless, AUC represents a powerful technique for characterizing polyplexes in detail, in particular since also free PEI beside the polyplexes can be detected, which is not possible by DLS. By using PUC, a virtual N/P ratio of 1.3 was found. This decreased value compared to pDNA indicates differences of siRNA based polyplexes compared to pDNA based ones due to their shorter length and higher rigidity. Further differences, regarding the genetic material used, were found in cellular uptake. Whereas both, siRNA and pDNA, can be efficiently delivered into cells using B-PEI  $\geq 10$  kDa at N/P 10, no siRNA uptake was detected at N/P 1.3. B-PEI with a molar mass higher 10 kDa seems to be the most promising candidates for siRNA-based polyplexes at  $N/P > 5$ , as the resultant polyplexes show a positive net charge, complete complexation of siRNA, a radius between 20 and 150 nm, necessary for internalization by endocytosis, and a significant cellular uptake.<sup>60,61</sup> Unfortunately, in terms of biological application these two polymers have higher toxicity than the low molar mass ones. Whereas most previous studies used 25 kDa PEI and a single low molar mass PEI ( $< 1$  kDa), our work shows the optimal molar mass is in between these values. *E.g.*, the 10 kDa B-PEI, which was not investigated for gene silencing before, is less toxic compared to the 25 kDa one and forms stable polyplexes with optimal net-charge and size for efficient cellular uptake. Furthermore, the influence of branching can be elucidated in future studies by investigation of linear, branched or star-shaped architectures of PEI. Moreover, statistical copolymers of PEI and poly(2-ethyl-2-oxazoline) might be interesting for gene delivery and polyplex formation, regarding reduced cytotoxicity.

Not all of the insights gathered for pDNA-based polyplexes can be adopted for siRNA, because of a 250 times lower molar mass, a higher rigidity and less flexibility. This study highlights the importance of a detailed analysis of polyplexes in the field of siRNA gene delivery as it not behaves identical as pDNA in all aspects.

## Acknowledgements

This project was funded by the Carl-Zeiss Foundation (Strukturantrag JCSM). Furthermore, the authors would like to thank Dr Stephanie Schubert and Prof. Dr Dieter Schubert for helpful comments and Carolin Fritzsche for performing cytotoxicity assays.

## Notes and references

- 1 A. Fire, S. Q. Xu, M. K. Montgomery, S. A. Kostas, S. E. Driver and C. C. Mello, *Nature*, 1998, **391**, 806–811.
- 2 M. A. Behlke, *Mol. Ther.*, 2006, **13**, 644–670.
- 3 J. J. Turner, S. W. Jones, S. A. Moschos, M. A. Lindsay and M. J. Gait, *Mol. BioSyst.*, 2007, **3**, 43–50.
- 4 D. M. Dykxhoorn, D. Palliser and J. Lieberman, *Gene Ther.*, 2006, **13**, 541–552.
- 5 O. Boussif, F. Lezoualch, M. A. Zanta, M. D. Mergny, D. Scherman, B. Demeneix and J. P. Behr, *Proc. Natl. Acad. Sci. U. S. A.*, 1995, **92**, 7297–7301.
- 6 S. Choosakoonkriang, B. A. Lobo, G. S. Koe, J. G. Koe and C. R. Middaugh, *J. Pharm. Sci.*, 2003, **92**, 1710–1722.
- 7 D. Störkle, S. Duschner, N. Heimann, M. Maskos and M. Schmidt, *Macromolecules*, 2007, **40**, 7998–8006.
- 8 W. J. Kim and S. W. Kim, *Pharm. Res.*, 2009, **26**, 657–666.
- 9 D. W. Pack, A. S. Hoffman, S. Pun and P. S. Stayton, *Nat. Rev. Drug Discovery*, 2005, **4**, 581–593.
- 10 J. B. Lee, J. Hong, D. K. Bonner, Z. Poon and P. T. Hammond, *Nat. Mater.*, 2012, **11**, 316–322.
- 11 K. A. Howard and J. Kjemis, *Expert Opin. Biol. Ther.*, 2007, **7**, 1811–1822.
- 12 K. A. Howard, *Adv. Drug Delivery Rev.*, 2009, **61**, 710–720.
- 13 C. M. Varga, N. C. Tedford, M. Thomas, A. M. Klibanov, L. G. Griffith and D. A. Lauffenburger, *Gene Ther.*, 2005, **12**, 1023–1032.
- 14 F. Y. Xie, M. C. Woodle and P. Y. Lu, *Drug Discovery Today*, 2006, **11**, 67–73.
- 15 Y. Liu, O. Samsonova, B. Sproat, O. Merkel and T. Kissel, *J. Controlled Release*, 2011, **153**, 262–268.
- 16 S. R. Mao, M. Neu, O. Germershaus, O. Merkel, J. Sitterberg, U. Bakowsky and T. Kissel, *Bioconjugate Chem.*, 2006, **17**, 1209–1218.
- 17 M. S. Shim and Y. J. Kwon, *Biomacromolecules*, 2008, **9**, 1355–1355.
- 18 A. von Harpe, H. Petersen, Y. X. Li and T. Kissel, *J. Controlled Release*, 2000, **69**, 309–322.
- 19 Z. Dai and C. Wu, *Macromolecules*, 2012, 120508154954007.
- 20 B. Brissault, A. Kichler, C. Guis, C. Leborgne, O. Danos and H. Cheradame, *Bioconjugate Chem.*, 2003, **14**, 581–587.
- 21 M. Ogris, P. Steinlein, M. Kursa, K. Mechtler, R. Kircheis and E. Wagner, *Gene Ther.*, 1998, **5**, 1425–1433.
- 22 M.-E. Bonnet, P. Erbacher and A.-L. Bolcato-Bellemin, *Pharm. Res.*, 2008, **25**, 2972–2982.
- 23 J. Ziebarth and Y. M. Wang, *Biophys. J.*, 2009, **97**, 1971–1983.
- 24 A. Kwok and S. L. Hart, *Nanomed.: Nanotechnol., Biol. Med.*, 2011, **7**, 210–219.
- 25 A. C. Richards Grayson, A. M. Doody and D. Putnam, *Pharm. Res.*, 2006, **23**, 1868–1876.
- 26 S. Boeckle, K. von Gersdorff, S. van der Piepen, C. Culmsee, E. Wagner and M. Ogris, *J. Gene Med.*, 2004, **6**, 1102–1111.
- 27 D. J. Gary, N. Puri and Y.-Y. Won, *J. Controlled Release*, 2007, **121**, 64–73.
- 28 X. Mao, Z. Y. Ren, G. N. Parker, H. Sondermann, M. A. Pastorello, W. Wang, J. S. McMurray, B. Demeler, J. E. Darnell and X. M. Chen, *Mol. Cell*, 2005, **17**, 761–771.
- 29 P. Schuck, *Anal. Biochem.*, 2003, **320**, 104–124.
- 30 D. G. Myszk, R. W. Sweet, P. Hensley, M. Brigham-Burke, P. D. Kwong, W. A. Hendrickson, R. Wyatt, J. Sodroski and M. L. Doyle, *Proc. Natl. Acad. Sci. U. S. A.*, 2000, **97**, 9026–9031.
- 31 G. M. Pavlov, A. M. Breul, M. D. Hager and U. S. Schubert, *Macromol. Chem. Phys.*, 2012, **213**, 904–916.
- 32 B. Schulze, C. Friebe, S. Hoepfner, G. M. Pavlov, A. Winter, M. D. Hager and U. S. Schubert, *Macromol. Rapid Commun.*, 2012, **33**, 597–602.
- 33 I. Perevyazko, A. Vollrath, S. Hornig, G. M. Pavlov and U. S. Schubert, *J. Polym. Sci., Part A: Polym. Chem.*, 2010, **48**, 3924–3931.
- 34 S. Sundaram, L. K. Lee and C. M. Roth, *Nucleic Acids Res.*, 2007, **35**, 4396–4408.
- 35 E. Wagner, M. Cotten, R. Foisner and M. L. Birnstiel, *Proc. Natl. Acad. Sci. U. S. A.*, 1991, **88**, 4255–4259.
- 36 C. V. Synatschke, A. Schallon, V. Jerome, R. Freitag and A. H. E. Müller, *Biomacromolecules*, 2011, **12**, 4247–4255.
- 37 J. Suh, H. J. Paik and B. K. Hwang, *Bioorg. Chem.*, 1994, **22**, 318–327.
- 38 M. X. Tang and F. C. Szoka, *Gene Ther.*, 1997, **4**, 823–832.
- 39 S. W. Provencher, *Comput. Phys. Commun.*, 1982, **27**, 229–242.
- 40 A. V. Delgado, F. Gonzalez-Caballero, R. J. Hunter, L. K. Koopal and J. Lyklema, *J. Colloid Interface Sci.*, 2007, **309**, 194–224.
- 41 P. Schuck, *Biophys. J.*, 2000, **78**, 1606–1619.
- 42 W. Mächtle, *Makromol. Chem.*, 1984, **185**, 1025–1039.
- 43 G. F. Bonifacio, T. Brown, G. L. Conn and A. N. Lane, *Biophys. J.*, 1997, **73**, 1532–1538.
- 44 G. M. Pavlov, I. Y. Perevyazko, O. V. Okatova and U. S. Schubert, *Methods*, 2011, **54**, 124–135.
- 45 F. Ungaro, G. De Rosa, A. Miro and F. Quaglia, *J. Pharm. Biomed. Anal.*, 2003, **31**, 143–149.
- 46 R. Hamid, Y. Rotshteyn, L. Rabad, R. Parikh and P. Bullock, *Toxicol. in Vitro*, 2004, **18**, 703–710.
- 47 D. Fischer, T. Bieber, Y. X. Li, H. P. Elsasser and T. Kissel, *Pharm. Res.*, 1999, **16**, 1273–1279.
- 48 T. Merdan, K. Kunath, D. Fischer, J. Kopecek and T. Kissel, *Pharm. Res.*, 2002, **19**, 140–146.
- 49 A. Akinc, M. Thomas, A. M. Klibanov and R. Langer, *J. Gene Med.*, 2005, **7**, 657–663.
- 50 M. Borkovec and G. J. M. Koper, *Macromolecules*, 1997, **30**, 2151–2158.
- 51 E. V. B. van Gaal, G. Spierenburg, W. E. Hennink, D. J. A. Crommelin and E. Mastrobattista, *J. Controlled Release*, 2010, **141**, 328–338.
- 52 M. J. Waring, *J. Mol. Biol.*, 1965, **13**, 269–282.
- 53 W. Jiang, B. Y. S. Kim, J. T. Rutka and W. C. W. Chan, *Nat. Nanotechnol.*, 2008, **3**, 145–150.
- 54 J. Rejman, M. Conese and D. Hoekstra, *J. Liposome Res.*, 2006, **16**, 237–247.
- 55 K. von Gersdorff, N. N. Sanders, R. Vandenbroucke, S. C. De Smedt, E. Wagner and M. Ogris, *Mol. Ther.*, 2006, **14**, 745–753.
- 56 O. M. Merkel, D. Librizzi, A. Pfestroff, T. Schurrat, K. Buyens, N. N. Sanders, S. C. De Smedt, M. Béhé and T. Kissel, *J. Controlled Release*, 2009, **138**, 148–159.
- 57 P. Kebbekus, D. E. Draper and P. Hagerman, *Biochemistry*, 1995, **34**, 4354–4357.
- 58 K. L. Planken and H. Cölfen, *Nanoscale*, 2010, **2**, 1849–1869.

- 59 A. Schallon, C. V. Synatschke, D. V. Pergushov, V. Jerome, A. H. E. Müller and R. Freitag, *Langmuir*, 2011, **27**, 12042–12051.
- 60 H. Aoki, M. Satoh, K. Mitsuzuka, A. Ito, S. Saito, T. Funato, M. Endoh, T. Takahashi and Y. Arai, *FEBS Lett.*, 2004, **567**, 203–208.
- 61 H. Gao, W. Shi and L. B. Freund, *Proc. Natl. Acad. Sci. U. S. A.*, 2005, **102**, 9469–9474.

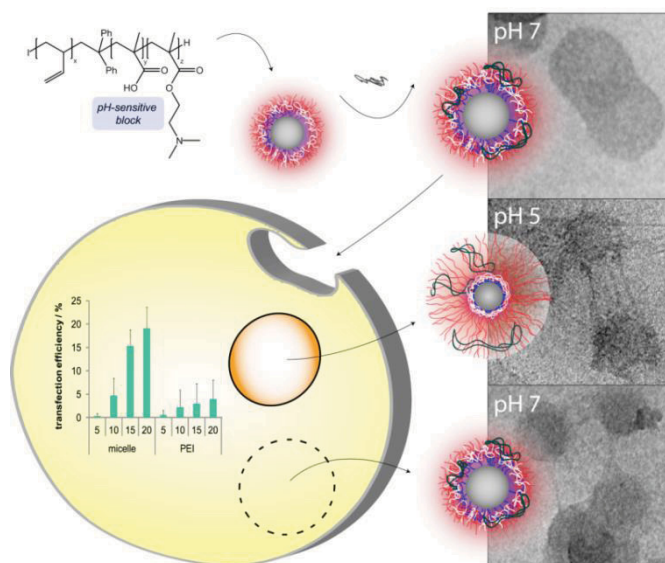


## Publication P6

### A paradigm change: Efficient transfection of human leukemia cells by stimuli-responsive multicompartment micelles

A. C. Rinkenauer, A. Schallon, U. Günther, M. Wagner, E. Betthausen,  
U. S. Schubert, F. H. Schacher

*ACS Nano* **2013**, 7, 9621-9631.



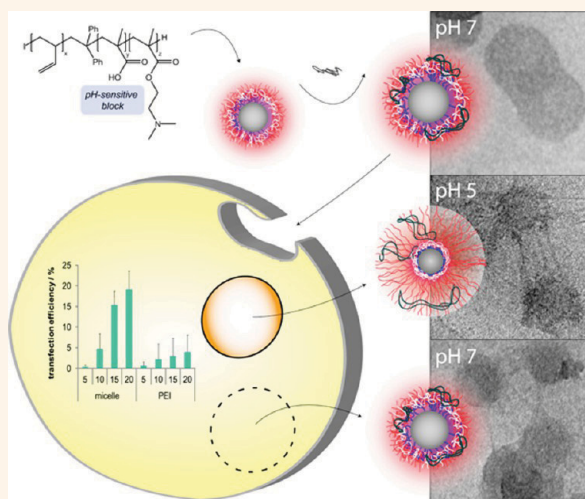


# A Paradigm Change: Efficient Transfection of Human Leukemia Cells by Stimuli-Responsive Multicompartment Micelles

Alexandra C. Rinkenauer,<sup>†,‡</sup> Anja Schallon,<sup>†,‡</sup> Ulrike Günther,<sup>†,‡</sup> Michael Wagner,<sup>†,‡</sup> Eva Betthausen,<sup>§</sup> Ulrich S. Schubert,<sup>†,‡,\*</sup> and Felix H. Schacher<sup>†,‡,\*</sup>

<sup>†</sup>Laboratory of Organic and Macromolecular Chemistry (IOMC), Friedrich Schiller University Jena, Humboldtstrasse 10, 07743, Jena, Germany, <sup>‡</sup>Jena Center for Soft Matter (JCSM), Friedrich Schiller University Jena, Philosophenweg 7, 07743 Jena, Germany, and <sup>§</sup>Macromolecular Chemistry II, Bayreuth Center for Colloids and Interfaces, University Bayreuth, 95440 Bayreuth, Germany

**ABSTRACT** The controlled nonviral delivery of genetic material using cationic polymers into cells has been of interest during the past three decades, yet the ideal delivery agent featuring utmost transfection efficiency and low cytotoxicity still has to be developed. Here, we demonstrate that multicompartment micelles from stimuli-responsive triblock terpolymers, polybutadiene-*block*-poly(methacrylic acid)-*block*-poly(2-(dimethylamino)ethyl methacrylate) (BMAAD), are promising candidates. The structures exhibit a patchy shell, consisting of amphiphilic (interpolyelectrolyte complexes, MAA and D) and cationic patches (excess D), generating a surface reminiscent to those of certain viruses and capable of undergoing pH-dependent changes in charge stoichiometry. After polyplex formation with plasmid DNA, superior transfection efficiencies can be reached for both adherent cells and human leukemia cells. Compared to the gold standard PEI, remarkable improvements and a number of advantages were identified for this system, including increased cellular uptake and an improved release of the genetic material, accompanied by fast and efficient endosomal escape. Furthermore, high sedimentation rates might be beneficial regarding *in vitro* applications.



**KEYWORDS:** multicompartment micelles · interpolyelectrolyte complexes · nonviral gene transfection · polyplexes · human leukemia cells

The controlled delivery of genetic material into eukaryotic cells has been the focus of interdisciplinary scientific activities during the last three decades.<sup>1,2</sup> Within the field of nanomedicine, successful nonviral gene delivery holds great promise for the treatment of a wide variety of diseases, as a suitable transfection agent,<sup>3</sup> once identified, might be used in different approaches. Besides evolutionary qualified and very efficient viral transfection, nonviral delivery is of high interest, reflected in the large number of nonviral transfection agents being proposed. Thereby, among polymeric materials, poly(ethylene imine) (PEI) represents the “gold standard” for *in vitro* applications.<sup>4</sup>

The efficient protection of nucleic acids like plasmid DNA (pDNA) during delivery while maintaining utmost biocompatibility is one of the key requirements for such materials. In general, cationic polyelectrolytes are capable of forming polyplexes with negatively charged pDNA, the main driving forces being electrostatic interactions and a gain in entropy for the whole system.<sup>5,6</sup> Polyplexes with an excess of positive charges support both protection against degradation and uptake *via* the negatively charged cell membrane. Several studies show that the polymer architecture and the overall molar mass have a major influence on the transfection efficiency (TE).<sup>7,8</sup> Nevertheless, it is still

\* Address correspondence to ulrich.schubert@uni-jena.de, felix.schacher@uni-jena.de.

Received for review April 25, 2013 and accepted October 22, 2013.

Published online October 22, 2013 10.1021/nn402072d

© 2013 American Chemical Society

challenging to design systems comprising high TE and low cytotoxicity for gene delivery applications, as in the case of most cationic polymers, like PEI, high TEs are accompanied by increasing cytotoxicity. The use of poly(ethylene glycol) (PEG) as, e.g., biocompatible shell is one straightforward approach to decrease the cytotoxicity but usually leads to lower TE.<sup>9,10</sup>

In addition, up to now most nonviral transfection agents fail in case of suspension cells, e.g., Jurkat T cells, a model cell line for human leukemia cells. This has been attributed to the fact that 3D cultivation decreases the contact probability between cells and polyplexes in general, if compared to the mechanism proposed for the transfection of adherent cells.<sup>11,12</sup> Hence, designing polymers that are capable of efficient gene transfer into suspension cells would allow targeting immune cells for the therapy of immune defects (e.g., HIV), for cancer (e.g., leukemia), or to improve transient transfection in biotechnological approaches.<sup>13</sup> All these issues are further impeded by the fact that the underlying transfection mechanism for pDNA in contrast to siRNA (short interfering RNA) is far from being completely understood, rendering the design of efficient transfection agents for this purpose extraordinarily difficult.<sup>14,15</sup>

Here, we demonstrate for the first time the advantage of pH-responsive multicompartment micelles formed *via* self-assembly of a stimuli-responsive triblock terpolymer, polybutadiene-*block*-poly(methacrylic acid)-*block*-poly(2-(dimethylamino)ethyl methacrylate) (BMAAD, PB<sub>800</sub>-*b*-PMAA<sub>200</sub>-*b*-PDMAEMA<sub>285</sub>; the subscripts denote the degrees of polymerization; the overall molar mass of BMAAD is 105 300 g/mol), as promising transfection agents for pDNA. Multicompartment structures represent a unique class of materials where either core, shell, or corona are further subdivided. Several strategies have been used to induce compartmentalization in block copolymer derived materials, including combinations of highly incompatible segments, kinetic control, or stepwise self-assembly by applying solvent mixtures.<sup>16–18</sup> Although multicompartment architectures have been in the focus for more than two decades, applications have been scarcely demonstrated. One very elegant example, however, was shown by Lodge and co-workers, where the segregated domains within micellar cores could be used to store two different hydrophobic guest molecules.<sup>19</sup> Regarding pH-responsive micellar carriers as gene delivery vehicles, pioneering work was performed by Kataoka and co-workers. For example, they used ABC triblock terpolymers with two cationic segments of different pK<sub>a</sub>, facilitating the disruption of the endosome upon decrease of the pH<sup>20</sup> or, in another example, segments which underwent charge conversion during the uptake process.<sup>21</sup> Also, the use of pH-sensitive linkers between unlike segments of AB diblock copolymers has proven to be advantageous.<sup>22</sup>

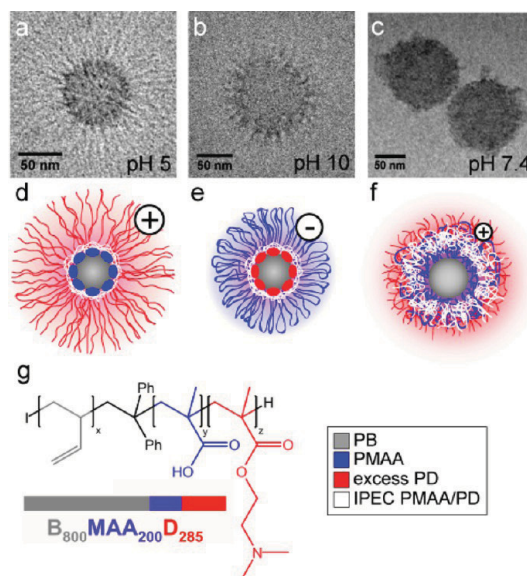


**Figure 1.** Cryo-TEM micrographs and schematic depictions of BMAAD micelles at pH 5 (a, d), pH 10 (b, e), and pH 7.4 (c, f). Structure and block lengths of the used BMAAD triblock terpolymer (g). Cryo-TEM images of pure BMAAD (a, b, c) and schematic illustrations thereof (d, e, f).

The aim of this work was to investigate how the rather heavy and voluminous BMAAD micelles can be used as efficient and pH-responsive nonviral gene transfection agents for adherent cells and human T-lymphocytes. We were interested whether the presence of different surface patches, also known from viral structures (e.g., alpha viruses),<sup>23–25</sup> influences important process bottlenecks such as cytotoxicity or carrier/serum interaction. Further, insights into the underlying mechanism for pDNA transfection (which is far from being completely understood) by using a combination of different analytical techniques including asymmetric flow field-flow fractionation (AF4), cryogenic electron microscopy (cryo-TEM), analytical ultracentrifugation (AUC), and confocal laser scanning microscopy (CLSM) are presented.

## RESULTS AND DISCUSSION

In our case, for BMAAD (PB<sub>800</sub>-*b*-PMAA<sub>200</sub>-*b*-PDMAEMA<sub>285</sub>), the hydrophobic PB forms the micellar core, which, at low pH, is surrounded by a PMAA shell and a PDMAEMA corona (Figure 1). Such micelles are dynamic and show a strong pH-dependence concerning their shape, size, and surface charge.<sup>26</sup> At endosomal pH (~5), PMAA is uncharged, and PDMAEMA forms a cationic corona (Figure 1a and d), whereas at pH 10, PDMAEMA is uncharged and partially collapsed, and merely PMAA now forms a negatively charged corona (Figure 1b and e). Under physiological conditions (pH ~7.4) both blocks are charged, leading to the formation of an intramolecular interpolyelectrolyte complex (*im*-IPEC) shell (Figure 1c and f). Hence, the micellar surface is patchy, featuring both charge neutral (*im*-IPEC) and

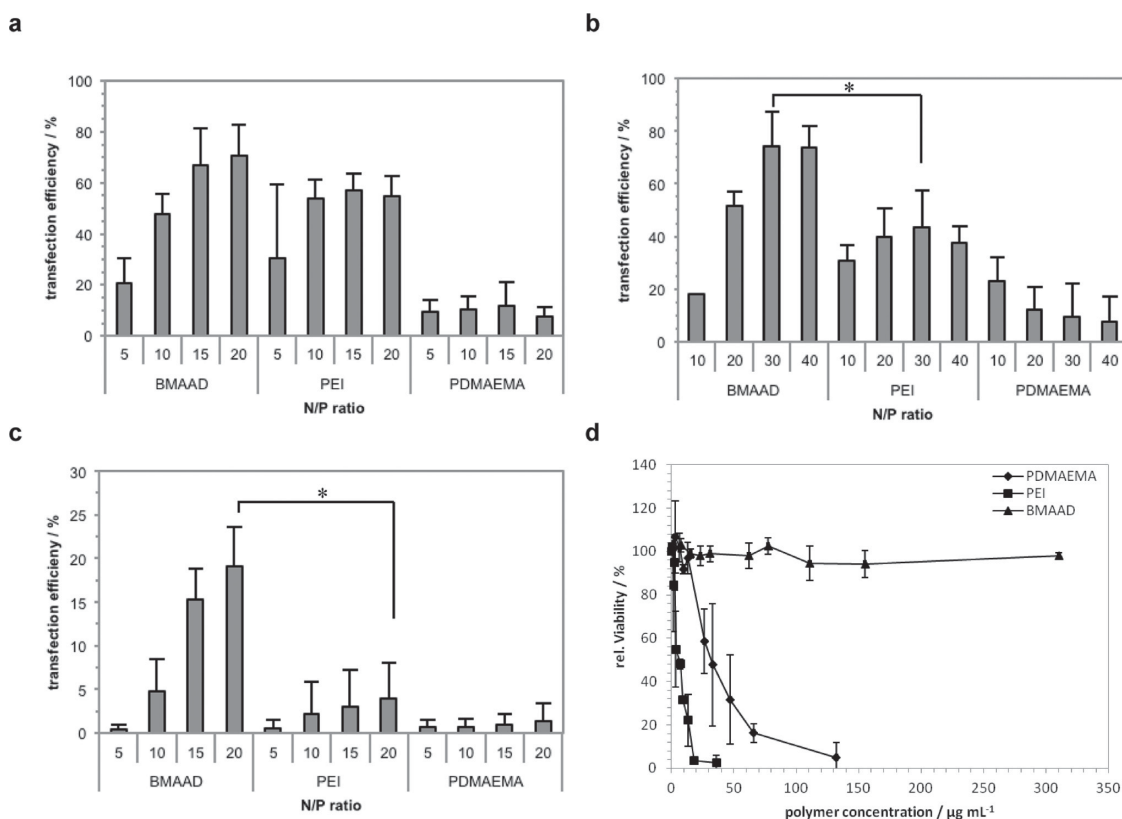


**Figure 2.** Transfection efficiencies of BMAAD, PEI<sub>570</sub>, and PDMAEMA<sub>191</sub> for adherent HEK cells in serum-reduced (a) and serum-containing media (b) and human leukemia cells (c) at different N/P ratios. An EGFP (pEGFP-N1) was used as reporter gene. Cytotoxicity tests using L929 cells (d). Values represent the mean  $\pm$  S.D.; \* represents a significant difference ( $p < 0.01$ ).

cationic domains (the DP of PDMAEMA is higher than for the PMAA segment, resulting in an excess positive net charge). These IPEC patches may lead to an increased polycation density within parts of the corona, and this in turn favors the formation of patchy structures upon further complex formation.<sup>27</sup>

First, transfection studies of BMAAD with pDNA under serum-reduced conditions as well as with media containing 10% serum were performed with adherent HEK293 cells, using linear PEI<sub>570</sub> (25 kDa) and PDMAEMA<sub>191</sub> (30 kDa) as comparison. The BMAAD micelles showed very high TE, even compared to PEI (BMAAD:  $70 \pm 12\%$  at N/P 20; PEI:  $55 \pm 8\%$  at N/P 20) under serum-reduced conditions (Figure 2a and Figure S1, Supporting Information). In contrast, linear PDMAEMA reaches only  $12 \pm 9\%$  at N/P 15. This increased TE for adherent cells by using BMAAD micelles is in agreement with earlier studies on star-shaped PDMAEMA or micelles with a PDMAEMA corona.<sup>28</sup> In the presence of serum even superior results were obtained for BMAAD ( $74 \pm 8\%$  at N/P 30), comparable to Lipofectamine 2000,<sup>29</sup> whereas the TE decreased significantly for PEI ( $43 \pm 7\%$  at N/P 30; Figure 2b). The fact that BMAAD performs even better under serum conditions is remarkable as in general serum leads to unspecific interactions and lower TEs in case of cationic polymers.<sup>28,30</sup>

As the next step, the transfection of Jurkat T suspension cells with pDNA was evaluated. Figure 2c shows a TE of up to  $19 \pm 6\%$  with polyplexes formed from BMAAD and pDNA (N/P 20), whereas both PEI and PDMAEMA show a significantly reduced TE, which is in agreement with literature.<sup>31</sup> The fact that BMAAD micelles reach a 5-fold higher TE compared to PEI highlights the potential of these structures as powerful transfection agents. It should be noted that the presence of PMAA within the *im*-IPEC shell does not decrease the TE. Moreover, transfection experiments under non static conditions (shaking) resulted in similar transfection efficiencies (Figure S8, Supporting Information). We also found no detectable cytotoxicity of BMAAD using sensitive L929 cells (Figure 2d) for concentrations up to  $320 \mu\text{g mL}^{-1}$ , in contrast to PDMAEMA and PEI, which show  $\text{IC}_{50}$  values of 30 and  $6 \mu\text{g mL}^{-1}$ , respectively. Even polyplexes of PEI/pDNA show lower values ( $\text{IC}_{50} \sim 10 \mu\text{g mL}^{-1}$ ).<sup>32</sup> We propose that the PMAA block of BMAAD is responsible for the decreased cytotoxicity, without decreasing the TE in contrast to PEG.<sup>10,33</sup> Hence, the patchy micellar surface featuring cationic domains and neutral *im*-IPECs might serve as leverage to circumvent what is often called the “PEG-dilemma” (decreasing TE in the presence of a shielding PEG corona). The outstanding biocompatibility in combination with high TE values for

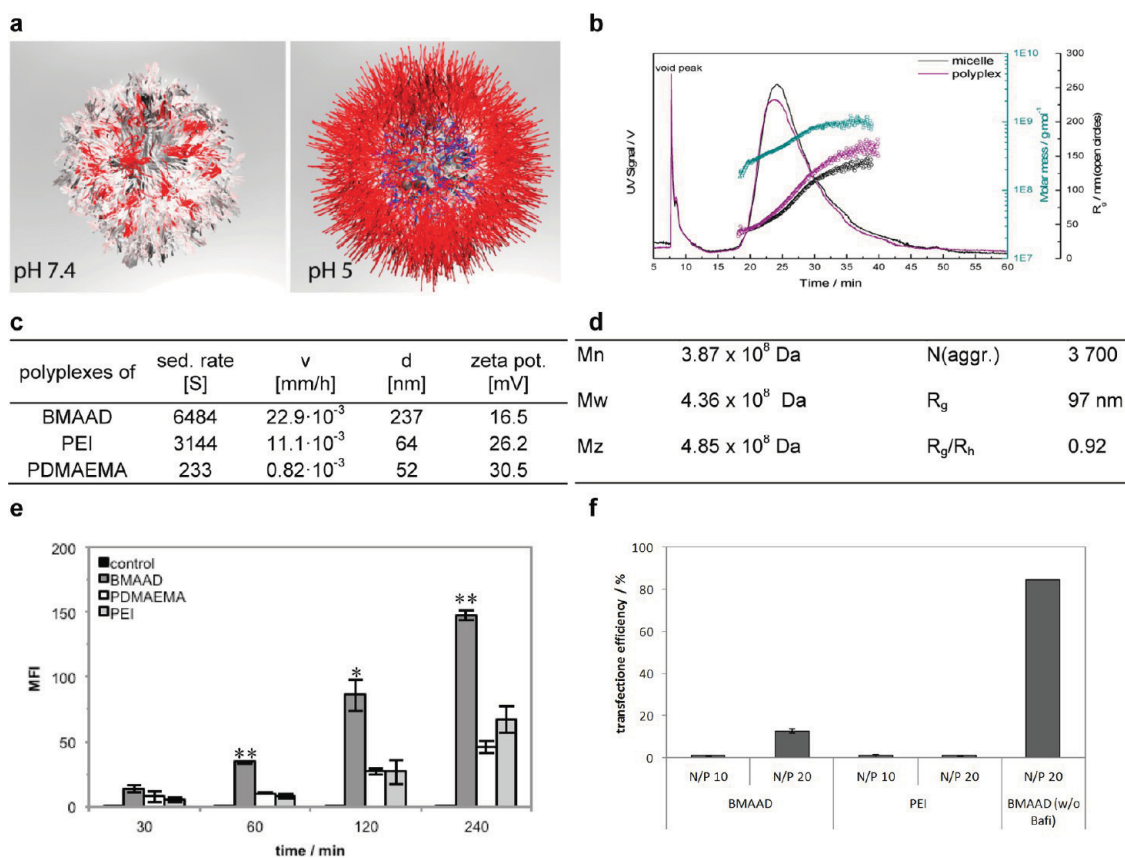


**Figure 3.** Proposed surface characteristics of the BMAAD micelle (color code: red, positive charges/PDMAEMA; blue, negative charges/PMAA; white, neutral *im*-IPEC domains; a). Detailed characteristics of BMAAD micelles obtained by asymmetric flow field flow fractionation (AF4) at pH 7 (b, d). Sedimentation velocity, hydrodynamic diameter, and zeta potential of polyplexes formed at N/P 20 (c). Mean fluorescence intensity (MFI) of cells transfected with YOYO-1 labeled pDNA for indicated time points using BMAAD, PEI<sub>570</sub>, and PDMAEMA<sub>191</sub> (e). Values represent the mean ± S.D.; \* represents a significant difference ( $p < 0.05$ ) to PEI<sub>570</sub> and PDMAEMA<sub>191</sub>; \*\* represents a significant difference ( $p < 0.01$ ) to PEI<sub>570</sub> and PDMAEMA<sub>191</sub>; # represents a significant difference ( $p < 0.01$ ) to PDMAEMA<sub>191</sub>. Transfection efficiencies using EGFP as reporter gene of BMAAD and PEI for adherent HEK cells treated with Bafilomycin (f).

BMAAD is impressive, as generally increases in efficiency are accompanied by higher cytotoxicity for transfection agents.<sup>7,34</sup> Thus, using an amphoteric triblock terpolymer containing both a cationic and an anionic segment allows constructing efficient nonviral gene delivery agents even though the cationic part, PDMAEMA, is usually regarded as being not very efficient.<sup>35</sup>

As such an outstanding performance was not anticipated for BMAAD, we were interested in the underlying mechanism. Therefore, all formed polyplexes were investigated with an ethidium bromide exclusion assay (EBA)<sup>36</sup> and dynamic light scattering (DLS) experiments. Both BMAAD and PDMAEMA show similar binding affinities to pDNA, but the values are lower compared to PEI (Figure S2, Supporting Information). This indicates the successful formation of polyplexes in all cases, as EBA only provides a qualitative assessment.<sup>37</sup> In addition, we performed a DNA gel migration assay, confirming the successful pDNA complexation at N/P 5 as no free pDNA could be detected (Figure S3, Supporting Information).

All polyplexes investigated exhibit a positive net charge at physiological pH, as shown in zeta-potential

measurements (Figure 3c). Hydrodynamic diameters of 64 nm (PEI), 237 nm (BMAAD), and 52 nm (PDMAEMA) can be observed (Figure 3c). For BMAAD, the formed polyplexes are of comparable size as the “bare” micelles (212 nm),<sup>26</sup> which can be explained by a rather tight wrapping of pDNA around the particles.<sup>38</sup> pH-dependent surface characteristics of BMAAD are schematically presented in Figure 3a. At physiological pH (7.4) most of the PDMAEMA forms *im*-IPECs with PMAA (white), whereas a slightly positive surface charge is caused by excess protonated PDMAEMA (DP PDMAEMA > DP PMAA).<sup>26</sup> At endosomal pH (~5), PDMAEMA is highly protonated and stretched, whereas PMAA partially collapses. This is supported by pH-dependent zeta potential measurements. The appearance of neutral *im*-IPECs, cationic patches on the polyplex surface, and strong changes as a response to variations of the pH are also known from clusters of viral particles.<sup>23–25</sup>

The results could also be confirmed by asymmetric flow field-flow fractionation (AF4, Figure 3b), where an R<sub>g</sub> of 97 nm was obtained for BMAAD and 111 nm for the corresponding polyplex; the obtained molar

masses were  $M_n = 3.87 \times 10^8 \text{ g mol}^{-1}$  and  $M_w = 4.36 \times 10^8 \text{ g mol}^{-1}$  for the micelle (Figure 3b and d). From the molar mass of the single triblock terpolymer ( $105\,300 \text{ g mol}^{-1}$ ) the aggregation number can be calculated to roughly 3 700. Combining these results with the DLS data, the general ratio  $R_g/R_h$ , which provides information about the shape and the conformation of the sample, can be calculated. Typical values are 0.775 for a hard sphere, 1.0 for a soft sphere, or 1.78 for a monodisperse linear polymer chain in a good solvent.<sup>39</sup> In this study a value of 0.92 for the micelle and 0.94 for the corresponding polyplex were obtained, which both fit to the expected model of a soft sphere. With decreasing pH, the zeta potential as well as the hydrodynamic diameter increases from 16.5 mV and 237 nm to 30.3 mV and 420 nm (Figures 3c and 5). In addition, the stability of the BMAAD polyplexes in the presence of serum after 4 h was analyzed, and no significant changes could be observed (hydrodynamic diameter 230 nm), suggesting that no protein based aggregation takes place.

To achieve successful transfection in case of human leukemia cells, the binding affinity between polymer and pDNA, size, and zeta potential of the polyplexes is crucial. However, this has to be complemented by an enhanced recognition and uptake by the cells. The uptake is mainly influenced by the charge and a high concentration of polyplexes at the cell surface.<sup>40</sup> The latter can be accessed *via* the sedimentation rate of the polyplexes, as determined by analytical ultracentrifugation (AUC). Presumably, larger particles with higher sedimentation coefficients lead to an increased particle uptake in case of *in vitro* transfection.<sup>41,42</sup> Indeed, the trends observed from DLS studies (Figure 3c) can be confirmed, as polyplexes from BMAAD micelles revealed a higher sedimentation rate (6480 S) compared to PEI (3140 S) and PDMAEMA (230 S), most probably due to the rather dense PB core. This leads to longer and more intensive interactions between the cells and the polyplexes and, hence, an increased internalization.

To investigate the time-dependent cellular uptake of polyplexes, YOYO-1 labeled pDNA was used (Figure 3e and S8, Supporting Information). An enhanced uptake can be clearly achieved with BMAAD micelles compared to PEI or PDMAEMA. Already after 1 h the majority of cells internalized the labeled polyplexes with BMAAD, whereas 4 h are necessary in case of PEI (Figure S8, Supporting Information). Even more impressive, the overall amount of labeled pDNA taken up by all viable cells (mean fluorescence intensity, MFI, Figure 3e) is almost doubled for BMAAD at all indicated time points, demonstrating the enormous potential of these structures.

One previously identified bottleneck during transfection studies is the endosomal escape of polyplexes. For PEI, a rather high buffer capacity is known, causing

the so-called proton sponge effect.<sup>43</sup> In contrast to PEI, PDMAEMA has lower buffer capacities,<sup>26,44</sup> which might explain a lower TE of linear PDMAEMA but not the high TE of BMAAD. Therefore, the behavior of BMAAD at endosomal pH ( $\sim 5$ ) was studied in more detail. Here, a rather stretched PDMAEMA corona and a partially collapsed PMAA shell can be anticipated.<sup>26</sup> The increased amount of positive charges lead to strong interactions with cellular membranes and, potentially, destabilization. This was confirmed both for the polymers and the polyplexes by a hemolysis assay at different pH values (Figure 4a and Figure S7, Supporting Information). While both PEI and PDMAEMA did not exhibit any hemolytic activity (Figure S7, Supporting Information), a strong pH-dependence with up to 30 and 8% at pH 5 was found for the BMAAD micelles and polyplexes, respectively. This supports our assumption that BMAAD destabilizes the endosomal membrane under acidic conditions and that the polyplex is released into the cytoplasm. The fact that this endosomal disruption is pH-dependent demonstrates the unique potential of such structures to react on subtle environmental changes and thereby induce endosomal escape.<sup>45</sup> To confirm the endosomal uptake and the necessity of acidification for an efficient transfection using BMAAD, transfections with bafilomycin were performed. Bafilomycin is known to inhibit the ATPases in the endosomes and therefore prevents acidification. The TEs of BMAAD and PEI are significantly decreased (Figure 3f) to 13 and 1%, respectively. It supports our assumption that endosomal pH facilitates destabilization and destruction of the endosomal membrane by shape/surface charge changes of the proposed BMAAD polyplexes. In addition, transfections were performed at 4 °C (Figure S8, Supporting Information), also significantly reducing the TE. To prove the fast and efficient endosomal escape, the colocalization of transported pDNA was investigated using confocal laser scanning microscopy (CLSM, Figure 4c). Therefore YOYO-1 labeled pDNA (green, Figure 4c) and LysoTracker Red (red, Figure 4c) were used to visualize the polyplexes as well as the late endosomes and lysosomes, respectively. Even after 1 h, a strong correlation of pDNA from PEI and PDMAEMA polyplexes and endosomes could be detected (yellow signal, Figure 4c) in contrast to BMAAD-based polyplexes. To verify the uptake of the BMAAD polyplexes *via* endocytosis, the colocalization of BMAAD polyplexes and early endosomes was demonstrated (Figure S8, Supporting Information).

Once the polyplexes are released into the cytoplasm, their dissociation is of great importance and was investigated using heparin, a negatively charged polysaccharide (Figure 4b). Typically, heparin concentrations of  $10 \text{ U mL}^{-1}$  are necessary to achieve a total release of pDNA from PEI-based polyplexes,<sup>4</sup> whereas  $50 \text{ U mL}^{-1}$  were needed for linear PDMAEMA, which is

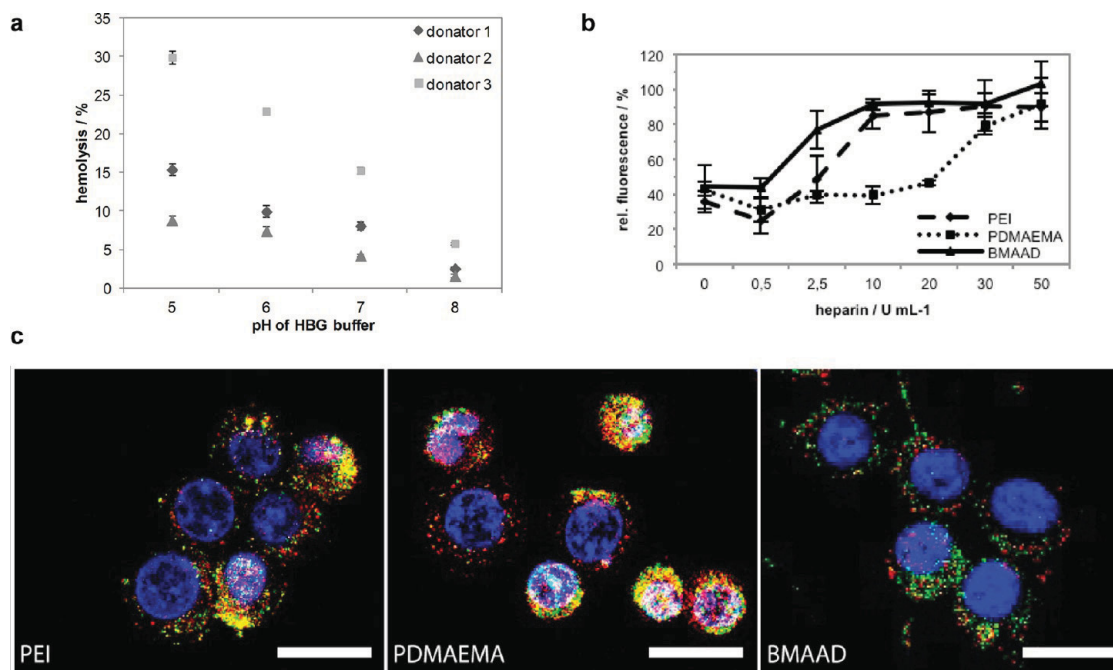


Figure 4. pH-dependent hemolysis assay of BMAAD of three different donors, each  $n = 3$  (a). Dissociation assay of polyplexes formed at N/P 10 with increasing heparin concentrations (b). CLSM images of HEK cells transfected with indicated polymer based polyplexes and YOYO-1 labeled pDNA (green); late endosomes/lysosomes were stained with LysoTracker Red (red), and cell nuclei were stained with Hoechst 33342 (blue); each scale bar represents  $20 \mu\text{m}$ ; colocalization of pDNA and endosomal compartments are depicted in yellow (c).

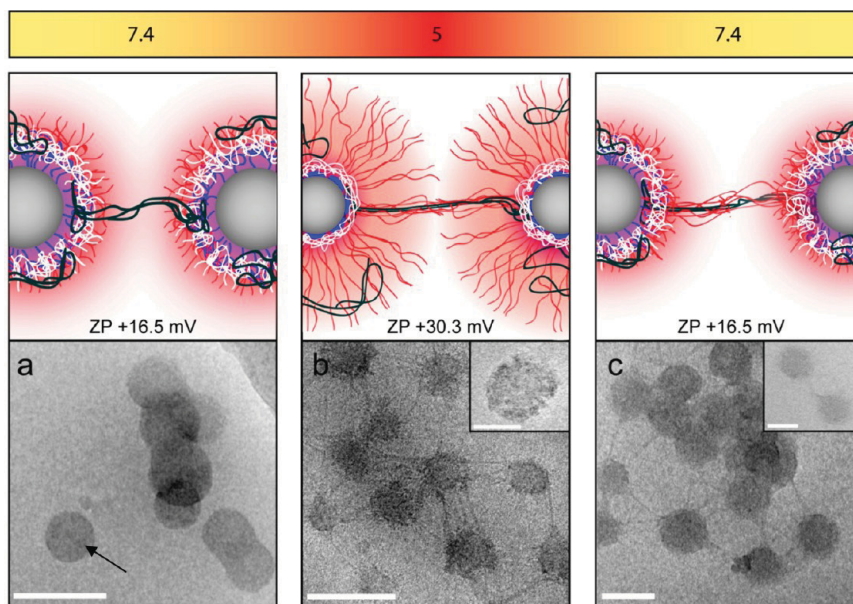


Figure 5. Schematic depiction of the proposed polyplex structure and the corresponding cryo-TEM micrographs at pH 7.4; the black arrow indicates the presence of *im*-IPECs (a), pH 5 (b), and pH 7.4 (c). Zeta potentials (ZP) of BMAAD polyplexes at pH 7.4 (16.5 mV) and pH 5 (30.3 mV). Color code: gray (PB), blue (PMAA), red (PDMAEMA), white (*im*-IPEC), and black (pDNA-polyplex). Scale bars indicate 200 nm and 50 nm in the insets.

a reason for the lower TE. Although BMAAD and PDMAEMA showed comparable binding affinities, the addition of only  $10 \text{ U mL}^{-1}$  of heparin led to an almost complete release of pDNA from BMAAD-based polyplexes. We attribute this to the PMAA block acting as a competing polyanion. In addition, the dissociation assay performed at pH 5 (Figure S5, Supporting

Information) demonstrated a higher binding to pDNA, and thus, no polyplex dissociation in the endosome can be assumed.

The structure of the formed polyplexes was further investigated using cryo-TEM measurements at different pH-values (Figure 5). At pH 7.4, the BMAAD micelles are close to their isoelectric point,<sup>26</sup> and polyplex



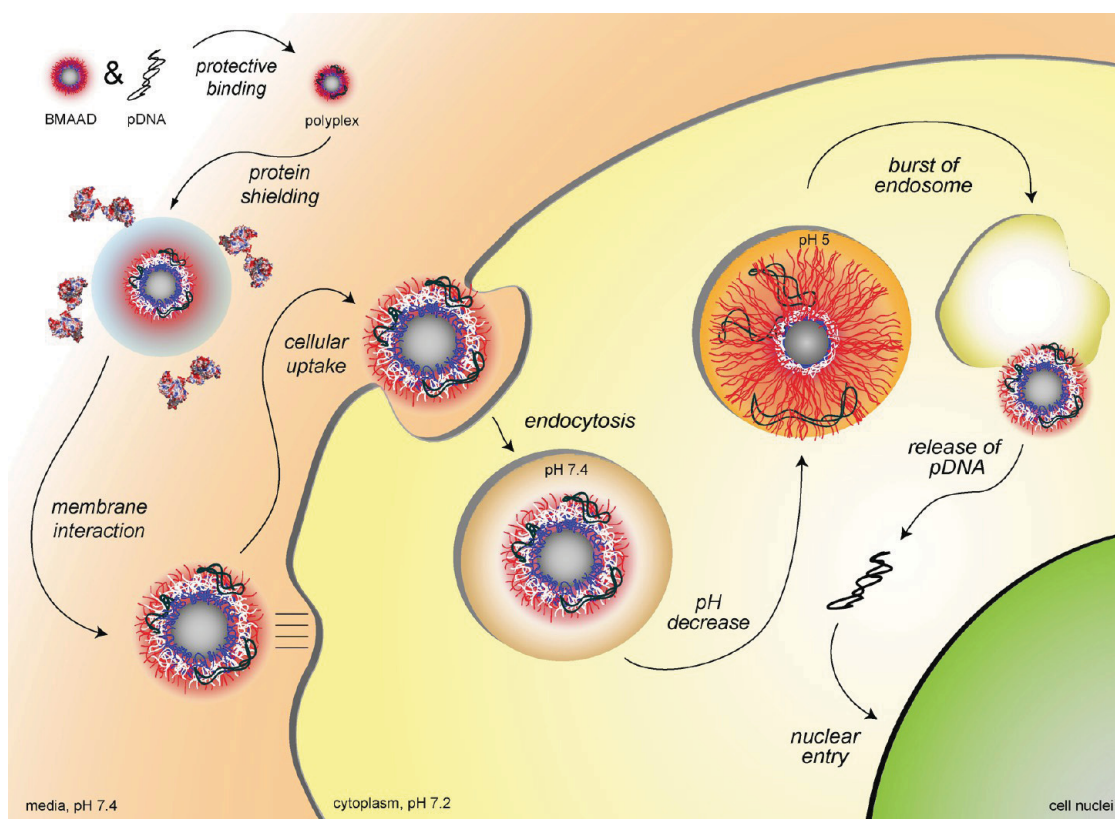


**Figure 6.** Schematic illustration of the proposed transfection mechanism for BMAAD-based polyplexes, with respect to the biological hurdles. The BMAAD micelle protects the genetic material (pDNA), prevents aggregation, and the cationic corona enables a fast and efficient cellular binding and uptake. Inside the endosomes, a decrease in pH leads to a swelling of the cationic corona and to a destabilization of the endosomal membrane. The release of the genetic material inside the cytoplasm is promoted by the middle block, PMAA, acting as a competing polyanion.

formation with pDNA leads to rather homogeneous structures of spherical shape (cryo-TEM, Figure 5a). The observed clustering can be explained by the rather low zeta potential of 16.5 mV. A decrease in pH within the endosome was simulated by the titration with dilute HCl until a pH of 5 was reached. This leads to full protonation and stretching of the PDMAEMA corona ( $pK_a \sim 7.7$ , zeta potential of 30.3 mV). Afterward, severe structural changes occur, as shown in Figure 5b: parts of the micellar core are covered by collapsed PMAA patches (blue), and in addition, the polyplexes formed of PDMAEMA (red) and pDNA (black) appear more dense and rigid, as seen in the protrusions connecting several micellar structures.<sup>26</sup>

These observations support our assumption of an endosomal burst occurring under these conditions and the data provided by hemolysis (Figure 4a). Subsequently, if the polyplex leaves the endosome, the pH within the cytoplasm rises to approximately 7.4, which was simulated for the same polyplex solution (Figure 5c). The cryo-TEM micrograph now shows polyplexes with the combined characteristics of Figure 5a and b: PMAA is resolubilized *via* deprotonation, leading to a more homogeneous overall appearance, and the rather rigid PDMAEMA/pDNA strands are still present, interconnecting several micelles.

The latter can be explained by a closer look at the linear homopolymer of PDMAEMA, showing a rather strong binding between PDMAEMA and pDNA (linear PDMAEMA in Figure 4b). Since the polyplex is formed, neither an increase in pH (4 to 9, data not shown) nor the addition of heparin facilitated an easy release of pDNA. Hence, in the case of the BMAAD the negatively charged PMAA block acts as a competing polyelectrolyte, presumably reduces the binding between PDMAEMA and pDNA, and enables the release of genetic material in the cytoplasm. Comparable structural rearrangements induced by changes in pH have been reported for the Sindbis virus.<sup>25</sup>

So far, the use of BMAAD led to high TE and was accompanied by surprisingly low cytotoxicity and a facilitated release of pDNA. To highlight the advantage of this system, the proposed transfection mechanism with respect to the biological hurdles was schematically illustrated in Figure 6. After polyplex formation with pDNA, the internalization of the resulting structures crucially depends on the interaction with proteins and the cellular membrane. As we observed high transfection efficiency in the presence of serum proteins (Figure 2b) and no protein dependent aggregation, a good shielding behavior can be assumed. On the other hand, extremely fast cellular uptake

(Figure 3e and S8, Supporting Information) is caused by the presence of cationic surface patches, reminiscent to the surface clusters of certain viruses.<sup>46,47</sup> After internalization *via* endocytosis, prompt escape of the polyplexes from the endosome is facilitated by an increase in size and zeta potential due to protonation and swelling of the PDMAEMA segments (Figure 3a and Figure 5), avoiding both digestion and exocytosis (Figure 4c). In the cytoplasm, the release of the genetic material is supported by the presence of the middle block, PMAA, acting as a competing polyanion, resulting in an efficient expression of the reporter gene.

## CONCLUSION

The successful design of powerful gene delivery agents imposes a range of bottlenecks,<sup>15</sup> but research efforts are justified by the potential applications within medicine and biotechnology.<sup>48</sup> Here, we presented a first study on the use of multicompartiment micelles from stimuli-responsive triblock terpolymers as a new class of potential transfection agents. We propose that this might be the first step of a paradigm change for nonviral gene transfection agents as low cytotoxicity can be combined with outstanding TE for both adherent cells and rather hard-to-transfect human leukemia cells. In particular in the latter case, remarkable improvements compared to PEI and linear PDMAEMA were shown.

Detailed investigations of the underlying mechanism revealed a number of advantages for this system: the dense core of the BMAAD micelles leads to higher sedimentation rates and a superior cellular uptake. Furthermore, the interaction of two oppositely

charged weak polyelectrolytes (PMAA and PDMAEMA) leading to *im*-IPECs and charge-neutral patches is to our opinion responsible for the reduced serum aggregation, unaffected viability, enhanced cellular uptake, and an improved pDNA release. In addition, under acidic conditions PDMAEMA provokes an increase in size and zeta potential, responsible for membrane destabilization and the release of the polyplex from the endosome.

Moreover, we believe that our results may aid in a profound understanding of the transfection mechanism of pDNA. Our mechanism was developed based on a combination of hemolysis data, cryo-TEM investigations (which provide structural insight into a model system), and microscopic images. All this is supported by pH-dependent zeta potential and size measurements.

In consequence, these effects render BMAAD a powerful advanced carrier for pDNA transfection studies, outperforming the “gold standard” PEI while maintaining superior biocompatibility. This work shows that by adopting certain design concepts from viruses (defined and responsive surface patches<sup>23–25</sup>) *via* the synthesis of well-defined block copolymers and the corresponding self-assembled aggregates superior control over (mainly) interface-dominated processes can be achieved. Of course, the next step would be to perform electron microscopy under cell culture conditions at different stages of the transfection process. To achieve this, we are currently working on strategies targeting the *in situ* immobilization of cells during different stages of transfection using fast gelation processes in aqueous media.

## METHODS

**Materials.** Linear 25 kDa PEI was purchased from Polysciences (Eppelheim, Germany). Ethidium bromide solution 1% was purchased from Carl Roth (Karlsruhe, Germany). AlamarBlue, cell light early endosomes-RFP, BacMAM and YOYO-1 were obtained from Life Technologies (Darmstadt, Germany). If not stated otherwise, cell culture materials, cell culture media, and solutions were obtained from PAA (Pasching, Austria). Plasmid pEGFP-N1 (4.7 kb, Clontech, USA) was isolated using Qiagen Giga plasmid Kit (Hilden, Germany). All other chemicals were purchased from Sigma Aldrich (Steinhausen, Germany) and are of analytical grade or better and used without further purification. 2-Cyano-2-butyl dithiobenzoate (CBDB) was purchased from Aldrich and used without further purification. Azobis(isobutyronitrile) (AIBN, Aldrich) was recrystallized from methanol. 2-(Dimethylamino)-ethyl methacrylate (DMAEMA) was purchased from Aldrich and passed over a column filled with inhibitor remover prior to usage.

**Synthesis of BMAAD Micelles.** Synthesis and characterization of the BMAAD micelles were described previously.<sup>26</sup> Briefly, linear BTB triblock terpolymers were synthesized *via* sequential living anionic polymerization of the corresponding monomers in THF at low temperatures using *sec*-BuLi as initiator. Prior to the reaction, freshly distilled THF (600 mL) was treated with *sec*-BuLi at  $-20$  °C, followed by stirring overnight at room temperature to produce alkoxides to stabilize the living polybutadienyl chain ends during the polymerization. In a typical reaction, 1,3-butadiene (20.5 mL, 13.3 g, 0.246 mol) was initiated

with *sec*-BuLi (0.2 mL, 0.3 mmol) at  $-70$  °C in THF and polymerized at  $-10$  °C for 8 h. After polymerization of the first block, the living butadienyl chain ends were end-capped with 1,1-diphenylethylene (0.11 mL, 0.11 g, 0.6 mmol) for 1 h at  $-50$  °C to attenuate the nucleophilicity. In this way, transfer reactions upon addition of the second monomer, *t*BMA, could be suppressed. Subsequently, *t*BMA (9.3 mL, 8.2 g, 0.057 mol) was added to the reaction mixture *via* syringe and stirred for 1 h at  $-40$  °C. After polymerization of the second block, DMAEMA (20.2 mL, 18.9 g, 0.12 mol) was added *via* syringe.

**Hydrolysis of the PtBMA Block.** The BTB terpolymers were dissolved in dioxane at a concentration of  $1$  g L<sup>-1</sup>. A spatula of the stabilizer 2,6-di-*tert*-butyl-*p*-cresol (BHT) and a 10-fold excess of hydrochloric acid relative to the ester moieties were added and the reaction mixture was refluxed at 120 °C for 24 h. Afterward, the excess of HCl was removed by dialysis against deionized water. After dialysis, micellar stock solutions in deionized water with concentrations of approximately  $0.5$  g L<sup>-1</sup> were obtained. From these stock solutions changes in pH or salinity were performed by dialyzing against the corresponding buffer solutions.

**Polyplex Preparation.** Polyplexes of pDNA and polymers were prepared by mixing stock solutions of pDNA and polymers at a certain N/P ratio with  $15$   $\mu$ g mL<sup>-1</sup> of pDNA solution in HBG buffer (20 mM 4-(2-hydroxyethyl) piperazine-1-ethanesulfonic acid (HEPES) and 5% (w/v) glucose, pH 7.2). Subsequently, the solutions were vortexed for 10 s at maximal speed and incubated at room temperature for 20 min.

**Transfection of Adherent and Suspension Cells.** HEK-293 cells (CRL-1573, ATCC) and Jurkat (TIB-152, ATCC) cells were maintained in RPMI 1640 culture medium, L929 cells (CCL-1, ATCC) in DMEM culture medium. Both media were supplemented with 10% fetal calf serum (FCS), 100  $\mu\text{g mL}^{-1}$  of streptomycin, 100 IU  $\text{mL}^{-1}$  of penicillin, and 2 mM L-glutamine. Cells were cultivated at 37 °C in a humidified 5%  $\text{CO}_2$  atmosphere.

For transfection of the adherent cell lines, cells were seeded at a density of  $10^5$  cells per well in 12-well plates one day before transfection. One hour prior to transfection, cells were rinsed with PBS and supplemented with 1 mL of OptiMEM (Life Technologies) or fresh serum-containing growth media (without antibiotics). Polyplexes (100  $\mu\text{L}$ ) were added to the cells, and the plates were incubated for 4 h in the incubator. Afterward, the supernatant was replaced by 1 mL of fresh growth medium, and the cells were further incubated for 20 h. For analysis, adherent cells were harvested by trypsinization. In the case of the Bafilomycin experiments, 175 nM Bafilomycin was added briefly before polyplex addition to OptiMEM.

For transfection of suspension cells (Jurkat),  $0.25 \times 10^5$  cells were seeded in 0.25 mL of OptiMEM in 24-well plates, one hour prior to transfection. The polyplex solutions (50  $\mu\text{L}$ ) were added, and the plates were incubated for 4 h in the incubator. Afterward, 0.25 mL of growth medium were added, and the cells were incubated for further 20 h. For determination of the viability during flow cytometry, dead cells were identified *via* counterstaining with propidium iodide. The relative expression of EGFP fluorescence of  $10^4$  cells was quantified *via* flow cytometry using a Cytomics FC 500 (Beckman Coulter). For determination of the transfection efficiency viable cells expressing EGFP were gated. The experiments were performed independently three times. Confocal laser scanning microscopy (CLSM) was performed using as LSM510 (Carl Zeiss).

**Plasmid DNA Labeling.** For labeling of 1  $\mu\text{g}$  pDNA, 0.026  $\mu\text{L}$  of 1 M YOYO-1 solution was mixed with pDNA in 20  $\mu\text{L}$  of pure water. The solution was incubated for 1 h at room temperature protected from light, before HBG was added to the used pDNA concentration described before. Polymers were added at the indicated N/P ratio, and the polyplex solution was treated as described before and added to the cells. After 4 h of incubation, the cells were harvested and 10% trypan blue was added to quench the outer fluorescence of cells and identify only those cells, which have taken up the genetic material. To determine the relative uptake of NPs, 10 000 cells were measured by flow cytometry, and the amount of viable cells showing YOYO-1 signal were gated. For measuring the mean fluorescence intensity, all viable cells were measured.

**Cytotoxicity.** The cytotoxicity was tested with L929 cells, as this sensitive cell line is recommended by ISO10993-5. In detail, cells were seeded at  $10^4$  cells per well in a 96-well plate and incubated for 24 h. No cells were seeded in the outer wells. Afterward, polymers at the indicated concentrations were added, and the cells were incubated at 37 °C for further 24 h. Subsequently, the medium was replaced by D-PBS and Alamar-Blue as recommended by the supplier. After incubation for 4 h, the fluorescence was measured at Ex 570/Em 610 nm, with untreated cells on the same well plate serving as controls. The experiments were performed independently three times.

**Analytical Ultracentrifugation.** Analytical ultracentrifugation (AUC) was performed on a Beckman XL-I analytical ultracentrifuge (Krefeld, Germany). Experiments were carried out in double-sector aluminum centerpieces with an optical path length of 12 mm in a four holes rotor setup. Each cell was filled with 0.42 mL of solvent (HBG) and 0.4 mL of sample. A rotor speed between 1000 to 10 000 rpm was used, depending on the sample. The system was equilibrated for 40 min at 25 °C in the centrifuge. Sedimentation data were recorded by absorbance optics. Data analysis was done by the Sedfit software.<sup>49</sup>

**Asymmetric Flow Field-Flow Fractionation (AF4).** Asymmetric flow field-flow fractionation (AF4) was performed on an AF2000 MT System (Postnova Analytics, Landsberg, Germany) coupled to a UV (PN3211, 260 nm), RI (PN3150), and MALLS (PN3070, 633 nm) detector. The eluent is delivered by three different pumps (tip, focus, cross-flow), and the sample is injected by an autosampler (PN5300) into the channel. The channel has a

trapezoidal geometry and an overall area of 31.6  $\text{cm}^2$ . The nominal height of the spacer was 500  $\mu\text{m}$ , and a regenerated cellulose membrane with a molar mass cutoff of 10 kDa was used as accumulation wall. All experiments were carried out at 25 °C, and the eluent was degassed water containing 0.02%  $\text{NaN}_3$  to avoid bacterial growth. To prevent attractive interactions between the negative surface of the membrane and the positive charges in the corona of the micelle, the membrane surface was saturated by injection of 100  $\mu\text{g}$  of pure PDMAEMA with the same procedure as for the micellar systems described below. Twenty microliters of samples were injected with an injection flow rate of 0.2  $\text{mL min}^{-1}$  and a cross-flow rate of 0.9  $\text{mL min}^{-1}$  for 7 min (detector flow rate was set to 1  $\text{mL min}^{-1}$ ). After a focusing step, the cross-flow rate was reduced under an exponential gradient (0.3) within 15 min to 0.05  $\text{mL min}^{-1}$  and kept constant for 25 min. Afterward the cross-flow rate was reduced to 0  $\text{mL min}^{-1}$  for 15 min to ensure complete elution. The refractive index increment for BMAAD was measured by manual injection of a known concentration directly into the channel without any focusing or cross-flow. Integration of the RI signal gives a  $dn/dc$  of 0.156  $\text{mL g}^{-1}$ . For calculation of the molar mass and the radius of gyration the Berry plot was used.<sup>50</sup> All measurements were repeated 5 times.

**Cryo-TEM Measurements.** For cryo-TEM, 5  $\mu\text{L}$  of the sample solution (in HBG) were applied to copper grids covered with a holey carbon film (Quantifoil R3.5/1 Micro Tools GmbH, Jena, Germany). The excess of the solution was automatically blotted with a filter paper (1 s), and the grid was then plunged rapidly into liquid ethane ( $-180$  °C) in a cryobox (Carl Zeiss NTS GmbH). After removing excess ethane with a filter paper, the samples were transferred with a cryotransfer unit (Gatan 626-DH, Gatan GmbH, Munich, Germany) into the precooled cryoelectron microscope operated at 120 kV (Philips CM 120, Eindhoven, Netherlands) and viewed under low dose conditions with a bottom-mounted 1k CCD camera.

**Conflict of Interest:** The authors declare no competing financial interest.

**Acknowledgment.** We acknowledge funding from the Carl-Zeiss Foundation and the Thuringian Ministry for Education, Science, and Culture (TMBWK; grants #B514-09051, NanoConSens, and #B515-10065, ChaPoNano). E.B. gratefully acknowledges funding by the state of Bavaria through a BayEFG scholarship and support by the Elite Network of Bavaria. F. H. S. is grateful for a fellowship from the Fonds der chemischen Industrie (FCI). Moreover, we thank C. Fritzsche for hemolysis studies and Alamar Blue assays, A. Krieg for the synthesis of PDMAEMA, and A. Press for microscopic investigations. We would further like to thank reviewers #1 and #3 for helpful and critical comments.

**Supporting Information Available:** Additional experimental section. Flow cytometer analysis, ethidium bromide quenching assays, agarose gel migration assays, additional cryo-TEM measurements, heparin dissociation assays, polyplex stability in the presence and absence of serum, pH-dependent hemolysis assays, as well as further data regarding the uptake mechanism of the polyplexes. This material is available free of charge *via* the Internet at <http://pubs.acs.org>.

## REFERENCES AND NOTES

- Miyata, K.; Nishiyama, N.; Kataoka, K. Rational Design of Smart Supramolecular Assemblies for Gene Delivery: Chemical Challenges in the Creation of Artificial Viruses. *Chem. Soc. Rev.* **2012**, *41*, 2562–2574.
- Ringsdorf, H. Hermann Staudinger and the Future of Polymer Research Jubilees—Beloved Occasions for Cultural Piety. *Angew. Chem., Int. Ed.* **2004**, *43*, 1064–1076.
- Itaka, K.; Kataoka, K. Recent Development of Nonviral Gene Delivery Systems with Virus-like Structures and Mechanisms. *Eur. J. Pharm. Biopharm.* **2009**, *71*, 475–483.
- Breunig, M.; Lungwitz, U.; Liebl, R.; Goepferich, A. Breaking up the Correlation Between Efficacy and Toxicity for Nonviral Gene Delivery. *Proc. Natl. Acad. Sci. U. S. A.* **2007**, *104*, 14454–14459.

5. Howard, K. A. Delivery of RNA Interference Therapeutics Using Polycation-Based Nanoparticles. *Adv. Drug Delivery Rev.* **2009**, *61*, 710–720.
6. Pergushov, D. V.; Müller, A. H. E.; Schacher, F. H. Micellar Interpolyelectrolyte Complexes. *Chem. Soc. Rev.* **2012**, *41*, 6888–6901.
7. Synatschke, C. V.; Schallon, A.; Jerome, V.; Freitag, R.; Müller, A. H. E. Influence of Polymer Architecture and Molecular Weight of Poly(2-(dimethylamino)ethyl methacrylate) Polycations on Transfection Efficiency and Cell Viability in Gene Delivery. *Biomacromolecules* **2011**, *12*, 4247–4255.
8. Majewski, A. P.; Schallon, A.; Jerome, V.; Freitag, R.; Müller, A. H. E.; Schmalz, H. Dual-Responsive Magnetic Core-Shell Nanoparticles for Nonviral Gene Delivery and Cell Separation. *Biomacromolecules* **2012**, *13*, 857–866.
9. Nguyen, J.; Xie, X.; Neu, M.; Dumitrascu, R.; Reul, R.; Sitterberg, J.; Bakowsky, U.; Schermuly, R.; Fink, L.; Schmehl, T.; *et al.* Effects of Cell-Penetrating Peptides and Pegylation on Transfection Efficiency of Polyethylenimine in Mouse Lungs. *J. Gene Med.* **2008**, *10*, 1236–1246.
10. Mishra, S.; Webster, P.; Davis, M. E. PEGylation Significantly Affects Cellular Uptake and Intracellular Trafficking of Nonviral Gene Delivery Particles. *Eur. J. Cell Biol.* **2004**, *83*, 97–111.
11. Behr, J. P. Synthetic Gene Transfer Vectors II: Back to the Future. *Acc. Chem. Res.* **2012**, *45*, 980–984.
12. Jordan, M.; Wurm, F. Transfection of Adherent and Suspended Cells by Calcium Phosphate. *Methods* **2004**, *33*, 136–143.
13. Keller, H.; Yunxu, C.; Marit, G.; Pla, M.; Reiffers, J.; Theze, J.; Froussard, P. Transgene Expression, But Not Gene Delivery, Is Improved by Adhesion-Assisted Lipofection of Hematopoietic Cells. *Gene Ther.* **1999**, *6*, 931–938.
14. Gary, D. J.; Puri, N.; Won, Y. Y. Polymer-Based siRNA Delivery: Perspectives on the Fundamental and Phenomenological Distinctions from Polymer-Based DNA Delivery. *J. Controlled Release* **2007**, *121*, 64–73.
15. Whitehead, K. A.; Langer, R.; Anderson, D. G. Knocking Down Barriers: Advances in siRNA Delivery. *Nat. Rev. Drug Discovery* **2009**, *8*, 129–138.
16. Moughton, A. O.; Hillmyer, M. A.; Lodge, T. P. Multicompartment Block Polymer Micelles. *Macromolecules* **2011**, *45*, 2–19.
17. Cui, H.; Chen, Z.; Zhong, S.; Wooley, K. L.; Pochan, D. J. Block Copolymer Assembly via Kinetic Control. *Science* **2007**, *317*, 647–650.
18. Gröschel, A. H.; Schacher, F. H.; Schmalz, H.; Borisov, O. V.; Zhulina, E. B.; Walther, A.; Müller, A. H. E. Precise Hierarchical Self-Assembly of Multicompartment Micelles. *Nat. Commun.* **2012**, *3*, 710.
19. Lodge, T. P.; Rasdal, A.; Li, Z.; Hillmyer, M. A. Simultaneous, Segregated Storage of Two Agents in a Multicompartment Micelle. *J. Am. Chem. Soc.* **2005**, *127*, 17608–17609.
20. Fukushima, S.; Miyata, K.; Nishiyama, N.; Kanayama, N.; Yamasaki, Y.; Kataoka, K. PEGylated Polyplex Micelles from Triblock Cationomers with Spatially Ordered Layering of Condensed pDNA and Buffering Units for Enhanced Intracellular Gene Delivery. *J. Am. Chem. Soc.* **2005**, *127*, 2810–2811.
21. Lee, Y.; Miyata, K.; Oba, M.; Ishii, T.; Fukushima, S.; Han, M.; Koyama, H.; Nishiyama, N.; Kataoka, K. Charge-Conversion Ternary Polyplex with Endosome Disruption Moiety: A Technique for Efficient and Safe Gene Delivery. *Angew. Chem., Int. Ed.* **2008**, *47*, 5163–5166.
22. Oishi, M.; Sasaki, S.; Nagasaki, Y.; Kataoka, K. pH-Responsive Oligodeoxynucleotide (ODN)–Poly(Ethylene Glycol) Conjugate through Acid-Labile  $\beta$ -Thiopropionate Linkage: Preparation and Polyion Complex Micelle Formation. *Biomacromolecules* **2003**, *4*, 1426–1432.
23. Huang, Q.; Sivaramakrishna, R. P.; Ludwig, K.; Korte, T.; Botcher, C.; Herrmann, A. Early Steps of the Conformational Change of Influenza Virus Hemagglutinin to a Fusion Active State: Stability and Energetics of the Hemagglutinin. *Biochim. Biophys. Acta* **2003**, *1614*, 3–13.
24. Dimitrov, D. S. Virus Entry: Molecular Mechanisms and Biomedical Applications. *Nat. Rev. Microbiol.* **2004**, *2*, 109–122.
25. Paredes, A. M.; Ferreira, D.; Horton, M.; Saad, A.; Tsuruta, H.; Johnston, R.; Klimstra, W.; Ryman, K.; Hernandez, R.; Chiu, W.; *et al.* Conformational Changes in Sindbis Virions Resulting from Exposure to Low pH and Interactions with Cells Suggest that Cell Penetration May Occur at the Cell Surface in the Absence of Membrane Fusion. *Virology* **2004**, *324*, 373–386.
26. Betthausen, E.; Drechsler, M.; Förtsch, M.; Schacher, F. H.; Müller, A. H. E. Dual Stimuli-Responsive Multicompartment Micelles from Triblock Terpolymers with Tunable Hydrophilicity. *Soft Matter* **2011**, *7*, 8880–8891.
27. Schacher, F.; Betthausen, E.; Walther, A.; Schmalz, H.; Pergushov, D. V.; Müller, A. H. E. Interpolyelectrolyte Complexes of Dynamic Multicompartment Micelles. *ACS Nano* **2009**, *3*, 2095–2102.
28. Schallon, A.; Synatschke, C. V.; Jerome, V.; Müller, A. H. E.; Freitag, R. Nanoparticulate Nonviral Agent for the Effective Delivery of pDNA and siRNA to Differentiated Cells and Primary Human T Lymphocytes. *Biomacromolecules* **2012**, *13*, 3463–3474.
29. Keeney, M.; Ong, S.-G.; Padilla, A.; Yao, Z.; Goodman, S.; Wu, J. C.; Yang, F. Development of Poly( $\beta$ -amino ester)-Based Biodegradable Nanoparticles for Nonviral Delivery of Minicircle DNA. *ACS Nano* **2013**, *7*, 7241–7250.
30. Fischer, D.; Bieber, T.; Li, Y.; Elsasser, H. P.; Kissel, T.; Novel Non-Viral, A. Vector for DNA Delivery Based on Low Molecular Weight, Branched Polyethylenimine: Effect of Molecular Weight on Transfection Efficiency and Cytotoxicity. *Pharm. Res.* **1999**, *16*, 1273–1279.
31. Wang, D. A.; Narang, A. S.; Kotb, M.; Gaber, A. O.; Miller, D. D.; Kim, S. W.; Mahato, R. I. Novel Branched Poly(ethylenimine)-Cholesterol Water-Soluble Lipopolymers for Gene Delivery. *Biomacromolecules* **2002**, *3*, 1197–1207.
32. Schallon, A.; Jerome, V.; Walther, A.; Synatschke, C. V.; Müller, A. H. E.; Freitag, R. Performance of Three PDMAEMA-Based Polycation Architectures as Gene Delivery Agents in Comparison to Linear and Branched PEI. *React. Funct. Polym.* **2010**, *70*, 1–10.
33. Vollrath, A.; Schallon, A.; Pietsch, C.; Schubert, S.; Nomoto, T.; Matsumoto, Y.; Kataoka, K.; Schubert, U. S. A Toolbox of Differently Sized and Labeled PMMA Nanoparticles for Cellular Uptake Investigations. *Soft Matter* **2013**, *9*, 99–108.
34. Kwok, A.; Hart, S. L. Comparative Structural and Functional Studies of Nanoparticle Formulations for DNA and siRNA Delivery. *Nanomedicine* **2011**, *7*, 210–219.
35. van de Wetering, P.; Moret, E. E.; Schuurmans-Nieuwenbroek, N. M.; van Steenberghe, M. J.; Hennink, W. E. Structure-Activity Relationships of Water-Soluble Cationic Methacrylate/Methacrylamide Polymers for Nonviral Gene Delivery. *Bioconjugate Chem.* **1999**, *10*, 589–597.
36. Waring, M. J. Complex Formation between Ethidium Bromide and Nucleic Acids. *J. Mol. Biol.* **1965**, *13*, 269–282.
37. Schallon, A.; Synatschke, C. V.; Pergushov, D. V.; Jerome, V.; Müller, A. H. E.; Freitag, R. DNA Melting Temperature Assay for Assessing the Stability of DNA Polyplexes Intended for Nonviral Gene Delivery. *Langmuir* **2011**, *27*, 12042–12051.
38. Alhoranta, A. M.; Lehtinen, J. K.; Urtti, A. O.; Butcher, S. J.; Aseyev, V. O.; Tenhu, H. J. Cationic Amphiphilic Star and Linear Block Copolymers: Synthesis, Self-Assembly, and *in Vitro* Gene Transfection. *Biomacromolecules* **2011**, *12*, 3213–3222.
39. Burchard, W. Solution Properties of Branched Macromolecules. *Polym. Sci.* **1999**, *143*, 113–194.
40. Florian, M. W. Production of Recombinant Protein Therapeutics in Cultivated Mammalian Cells. *Nat. Biotechnol.* **2004**, *13*, 1393–1398.
41. Luo, D.; Saltzman, W. M. Enhancement of Transfection by Physical Concentration of DNA at the Cell Surface. *Nat. Biotechnol.* **2000**, *18*, 893–895.
42. Tros de Ilarduya, C.; Sun, Y.; Duzgunes, N. Gene Delivery by Lipoplexes and Polyplexes. *Eur. J. Pharm. Sci.* **2010**, *40*, 159–170.

43. Akinc, A.; Thomas, M.; Klibanov, A. M.; Langer, R. Exploring Polyethylenimine-Mediated DNA Transfection and the Proton Sponge Hypothesis. *J. Gene Med.* **2005**, *7*, 657–663.
44. Cherng, J. Y. Investigation of DNA Spectral Conformational Changes and Polymer Buffering Capacity in Relation to Transfection Efficiency of DNA/Polymer Complexes. *J. Pharm. Pharm. Sci.* **2009**, *12*, 346–356.
45. Lee, Y.; Miyata, K.; Oba, M.; Ishii, T.; Fukushima, S.; Han, M.; Koyama, H.; Nishiyama, N.; Kataoka, K. Charge-Conversion Ternary Polyplex with Endosome Disruption Moiety: a Technique for Efficient and Safe Gene Delivery. *Angew. Chem., Int. Ed.* **2008**, *47*, 5163–5166.
46. Penin, F.; Combet, C.; Germanidis, G.; Frainais, P. O.; Deleage, G.; Pawlotsky, J. M. Conservation of the Conformation and Positive Charges of Hepatitis C Virus E2 Envelope Glycoprotein Hypervariable Region 1 Points to a Role in Cell Attachment. *J. Virol.* **2001**, *75*, 5703–5710.
47. Karlin, S.; Brendel, V. Charge Configurations in Viral Proteins. *Proc. Natl. Acad. Sci. U. S. A.* **1988**, *85*, 9396–9400.
48. Christie, R. J.; Nishiyama, N.; Kataoka, K. Minireview: Delivering the Code: Polyplex Carriers for Deoxyribonucleic Acid and Ribonucleic Acid Interference Therapies. *Endocrinology* **2010**, *151*, 466–473.
49. Schuck, P. Size-Distribution Analysis of Macromolecules by Sedimentation Velocity Ultracentrifugation and Lamm Equation Modeling. *Biophys. J.* **2000**, *78*, 1606–1619.
50. Andersson, M.; Wittgren, B.; Wahlund, K. G. Accuracy in Multiangle Light Scattering Measurements for Molar Mass and Radius Estimations. Model Calculations and Experiments. *Anal. Chem.* **2003**, *75*, 4279–4291.

## Supporting Information:

# A Paradigm Change: Efficient Transfection of Human Leukemia Cells by Stimuli-Responsive Multicompartment Micelles

Alexandra C. Rinkenauer, Anja Schallon, Ulrike Günther, Michael Wagner, Eva Betthausen,

Ulrich S. Schubert\*, Felix H. Schacher\*

*Laboratory of Organic and Macromolecular Chemistry (IOMC), Friedrich-Schiller-University  
Jena, Humboldtstrasse 10, Jena D-07743, Germany*

*Jena Center for Soft Matter (JCSM), Friedrich-Schiller-University Jena, Philosophenweg 7,  
Jena D-07743, Germany*

*E-Mail: [felix.schacher@uni-jena.de](mailto:felix.schacher@uni-jena.de); [ulrich.schubert@uni-jena.de](mailto:ulrich.schubert@uni-jena.de)*

### **Experimental section**

#### **Synthesis of PDMAEMA**

A solution of 1.54 mL DMAEMA (1.43 g, 9.1 mmol), 8.5 mg CBDB (0.03 mmol) and 1 mg AIBN (0.0061 mmol) in 4 mL anisole was prepared in a microwave vial. The reaction vessel was capped, flushed with argon for 30 minutes and placed in an oil bath at 70 °C for 15 hours. Afterwards, the reaction solution was cooled down to ambient temperature and precipitated into 30 mL hexane to receive the final polymer. The dried polymer was characterized by size exclusion chromatography (SEC), providing its molar mass ( $M_n$ ) of 27,600 and a PDI value of 1.28.

#### **Size exclusion chromatography**

SEC was measured on a Shimadzu system equipped with a SCL-10A system controller, a LC-10AD pump, and a RID-10A refractive index detector using a solvent mixture containing chloroform, triethylamine, and isopropanol (94:4:2) at a flow rate of 1 mL min<sup>-1</sup> on a PSS-SDV-linear M 5  $\mu$ m column at 40 °C. The system was calibrated with polystyrene (370 to 67,500 g mol<sup>-1</sup>) and PMMA (2000 to 88,000 g mol<sup>-1</sup>) standards.

### **Ethidium bromide quenching assay**

The polyplex formation of pDNA and polymers was detected by quenching of the ethidium bromide (EB) fluorescence as described previously.<sup>1</sup> Briefly, 15  $\mu\text{g mL}^{-1}$  pDNA in a total volume of 100  $\mu\text{L}$  HBG were incubated with EB (0.4  $\mu\text{g mL}^{-1}$ ) for 10 min at room temperature. Then, polyplexes with increasing amounts of indicated polymers were prepared in black 96-well plates (Nunc, Langensfeld, Germany). The samples were equilibrated for 20 min before the fluorescence was measured using a Tecan Genios Pro fluorescence microplate reader (Tecan, Crailsheim, Germany); the excitation and emission wavelength were 525 and 605 nm, respectively. A sample containing only pDNA and EB was used to calibrate the device to 100% fluorescence against a background of 0.4  $\mu\text{g mL}^{-1}$  of EB in HBG solution. The percentage of dye displaced upon polyplex formation was calculated using equation (1):

$$\text{RFU [\%]} = \frac{F_{\text{sample}} - F_0}{F_{\text{pDNA}} - F_0} \text{RFU [\%]} = \frac{F_{\text{sample}} - F_0}{F_{\text{pDNA}} - F_0} \quad (1)$$

Here, RFU is the relative fluorescence and  $F_{\text{sample}}$ ,  $F_0$ , and  $F_{\text{DNA}}$  are the fluorescence intensities of a given sample, the EB in HBG alone, and the EB intercalated into pDNA alone.

### **Gel migration assay**

The polyplexes were formed as described before in a volume of 50  $\mu\text{L}$  at the indicated N/P ratios and after 15 minutes incubation 5  $\mu\text{L}$  loading buffer (0.25% Bromphenolblue, 40% saccharose) was added. Afterwards the solutions were loaded to an 1% agarose gel, electrophoresis (Bio-Rad, Munich, Germany, Mini-Sub Cell GT System) was carried out with a current of 80 V (PowerPac<sup>TM</sup> Basic as power supply) for 1 h in TBE running buffer solution (107,8 g/L trise-base, 7,4g/L EDTA, 55g/L borate). Subsequently the agarose gel was incubated 30 min in TBE containing ethidium-bromid.

### **Heparin dissociation assay**

To investigate the release of pDNA from polyplexes, the heparin dissociation assay was used. For this purpose, 15  $\mu\text{g mL}^{-1}$  pDNA were incubated for 10 min with EB (0.4  $\mu\text{g mL}^{-1}$ ) in a total volume of 100  $\mu\text{L}$  HBG (pH 7 and 5) before polyplexes at N/P 10 were formed. After 15 min in the dark the polyplexes were transferred into black 96-well plates, and heparin was added at the indicated concentrations. The solution was mixed and incubated for further 30 min at 37 °C in the dark. The fluorescence of EB (Ex 525 nm / Em 605 nm) was measured, and the percentage of intercalated EB was calculated as described before (1).

### **Hemolysis assay**

The membrane damaging properties of the polymers were quantified by analyzing the release of hemoglobin from human erythrocytes. The hemolysis assay was performed as described before.<sup>2</sup> Briefly, blood from sheep was centrifuged at 4.500  $\times$  g for 5 min and the pellet was washed three times with cold DPBS. The stock solutions were diluted in HBG of indicated pH, and polymer solutions were prepared in HBG buffer as well. 100  $\mu\text{L}$  of each solution were mixed and further incubated for 60 min at 37 °C. The release of hemoglobin in the supernatant was determined at 580 nm after centrifugation (2,400 g for 5 min). The absorbance was measured using a plate reader (Genios Pro, Tecan, Germany). For comparison, collected erythrocytes were washed with DPBS and either lysed with 1% Triton X-100 yielding the 100% lysis control value ( $A_{100}$ ) or resuspended in DPBS as reference ( $A_0$ ). The analysis was repeated with blood from at least six independent donors. The hemolytic activity of the polycations was calculated as follow (2):

$$\% \text{ Hemolysis} = 100 * \frac{(A_{\text{sample}} - A_0)}{(A_{100} - A_0)} \quad \% \text{ Hemolysis} = 100 * \frac{(A_{\text{sample}} - A_0)}{(A_{100} - A_0)} \quad (2)$$

Here,  $A_{\text{sample}}$ ,  $A_0$ , and  $A_{100}$  are the absorbance intensities of a given sample, erythrocytes incubated with DPBS, and erythrocytes lysed with Triton X-100.

### **Dynamic and electrophoretic light scattering**

Dynamic light scattering (DLS) was performed on an ALV-CGS-3 system (ALV, Langen, Germany) equipped with a He-Ne laser operating at a wavelength of  $\lambda = 633$  nm. The counts were detected at an angle of 90°. All measurements were carried out at 25 °C after an equilibration time of 120 sec. For analyzing the autocorrelation function (ACF), the CONTIN algorithm<sup>3</sup> was applied. Apparent hydrodynamic radii were calculated according to the Stokes–Einstein equation.

Electrophoretic light scattering was used to measure the electrokinetic potential, also known as zeta potential. The measurements were performed on a Zetasizer Nano ZS (Malvern Instruments, Herrenberg, Germany) by applying laser Doppler velocimetry.<sup>4</sup> For each measurement, 20 runs were carried out using the slow-field reversal and fast-field reversal mode at 150 V. Each experiment was performed in triplicate at 25 °C. The zeta potential ( $\zeta$ ) was calculated from the electrophoretic mobility ( $\mu$ ) according to the Henry Equation. Henry coefficient  $f(\kappa a)$  was calculated according to Oshima.<sup>5</sup>

### ***Serum stability by DLS***

Polyplexes were incubated with serum containing growth media in a micro-cuvette for 4h at 37°C under a CO<sub>2</sub> atmosphere. Afterwards the cuvette was closed and directly transferred to the DLS device (Malvern Zetasizer). Measurements were done at 37 °C, detection at scattering angle of 173° and laser wavelength of 633 nm. Cumulant analysis and a non-negative least-square algorithm were used to obtain distribution of hydrodynamic radius, z-average and PDI.



## Results section

### Flow Cytometer Analysis

The transfection efficiency was determined by measuring the amount of cells that express EGFP (encoded on the transported pDNA). Therefore, non-transfected cells serve as controls and were analyzed by flow cytometry. The histogram of control cells was used to define the amount of EGFP expressing cells (see Figure S1, control). The percentage of cells in the specific area was defined as transfection efficiency in percentage.

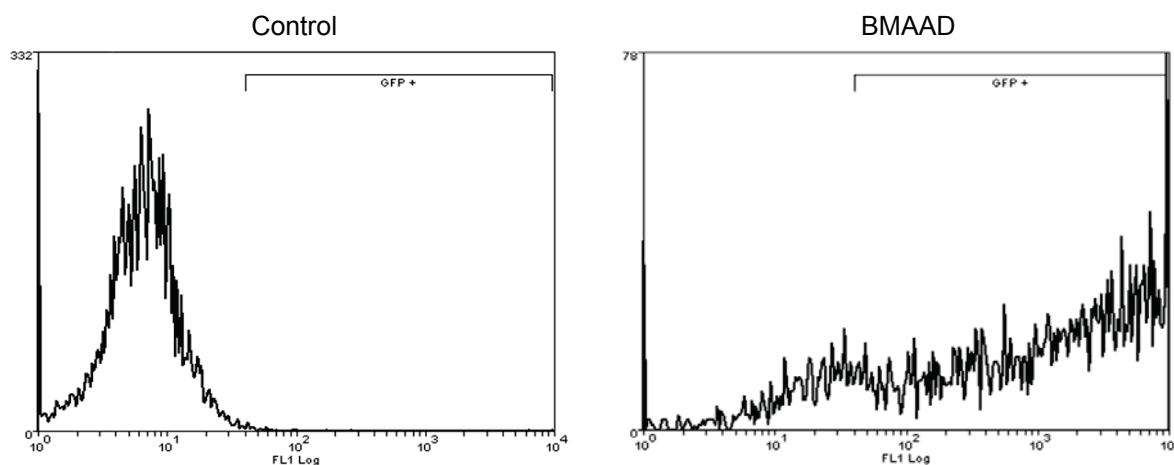


Figure S1. Histograms of non-transfected cells (control) and HEK cell transfected with BMAAD (N/P20). FL1 Log represents green fluorescence by EGFP expression.

### Interaction between used polymers and genetic material

Indicated by the decrease of ethidium bromide fluorescence it is obvious that all polymers lead to a full complexation of the pDNA. Nevertheless, there are differences in the binding affinity. PEI shows a stronger interaction compared to PDMAEMA and BMAAD. The dependence of EBA on the chemical nature of the monomer was previously described.<sup>1</sup>

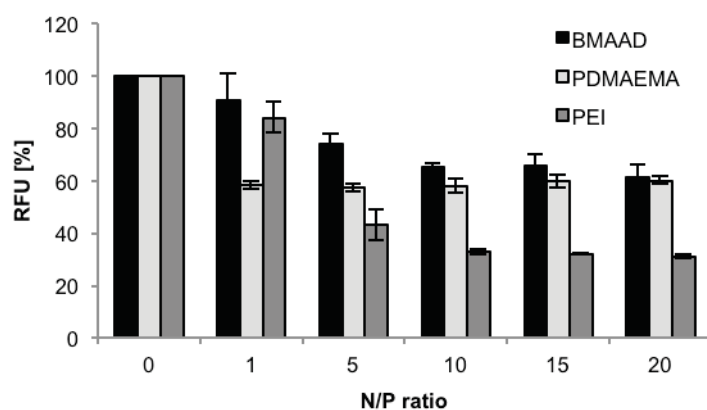


Figure S2. Ethidium bromide quenching assay of pDNA complexed with the indicated polymers. Binding of polymer to the pDNA results in a decrease in fluorescence intensity. The binding affinity was investigated dependent on the N/P ratio.

The agarose gel migration assay was performed with the BMAAD micelle to confirm the full complexation of the pDNA. The results confirm the previous investigations (Figure S2) of the EBA. At an N/P ratio of 5 the pDNA is fully complexed with BMAAD micelles and no free pDNA is detectable.

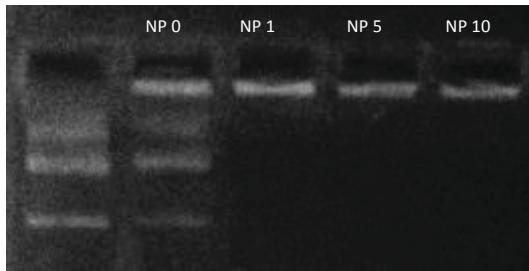


Figure S3. Agarose gel migration assay. Polyplexes were formed at indicated N/P ratio with BMAAD and 15  $\mu$ g pDNA

### ***pDNA release at pH 5***

To investigate the polyplex dissociation and, thus, the pDNA release both cryo-TEM investigations (at pH 5 and 7) and a heparin dissociation assay at pH5 were performed.

### ***Cryo-TEM***

The polyplexes were formed as described at a N/P ratio of 20, after 10 min incubation heparin (10 U/mL) was added and incubated for another 10 min. As can be seen in the micrographs, at pH 5 the polyplex surface remains patchy (Figure S4b), although less protrusions can be observed. For pH 7, in both cases the polyplex surface is rather smooth.

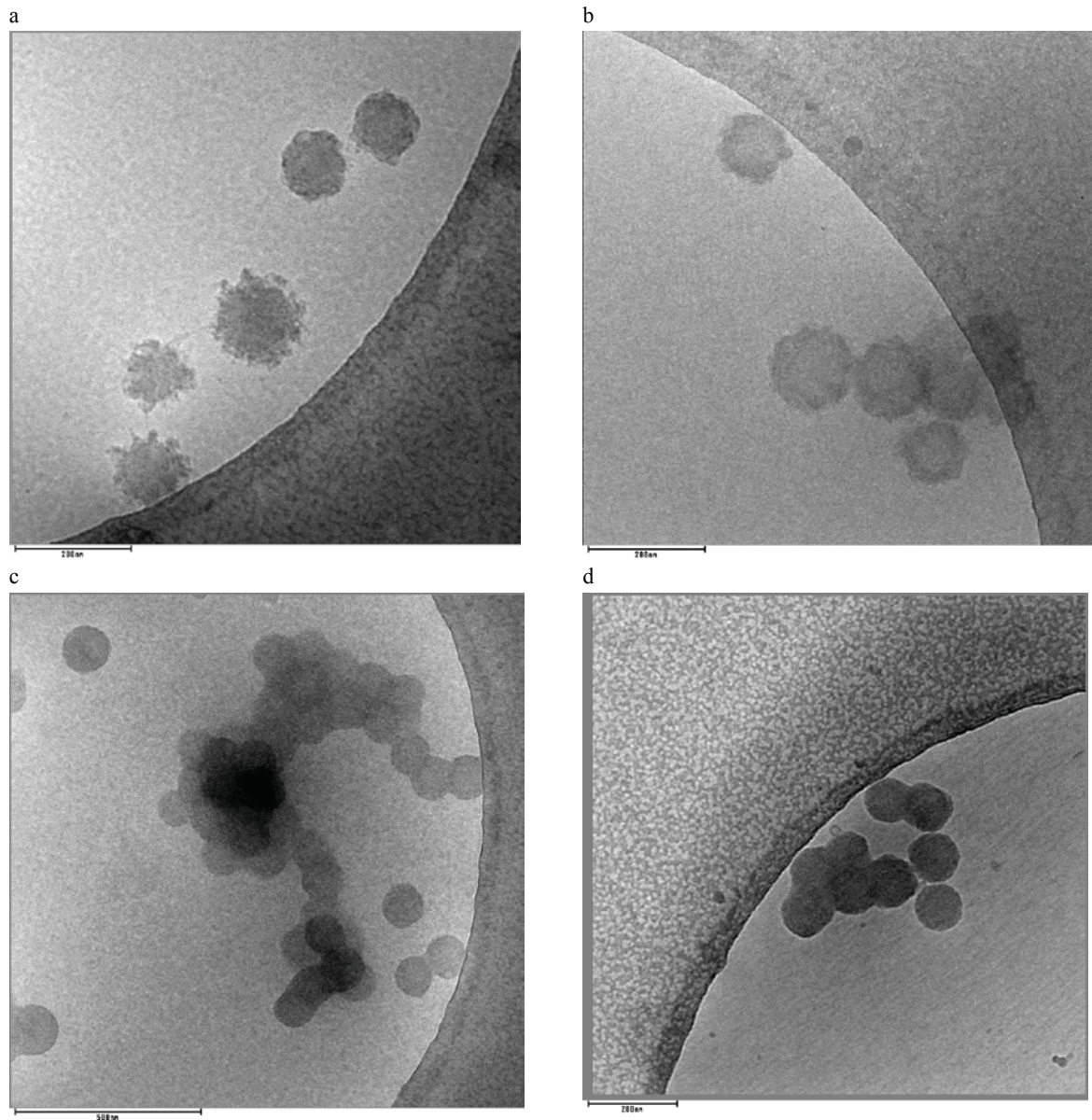


Figure S4. Cryo-TEM micrographs of BMAAD polyplexes incubated without (a, c) and with 10 U/mL heparin (b, d) at pH 5 (a, b) and pH 7 (c, d).

### Heparin dissociation assay

Besides the cryo-TEM investigations a heparin dissociation assay was performed at pH 5. In contrast to the release assay at pH 7 no full decomplexation of the pDNA could be achieved. Moreover at heparin concentration of 2.5 U/mL no fluorescence changes compared to 0.5 U/mL heparin could be detected. Thus, the BMAAD micelles have a much higher binding to the pDNA at pH 5, indicating no polyplex dissociation in the endosome occurring.

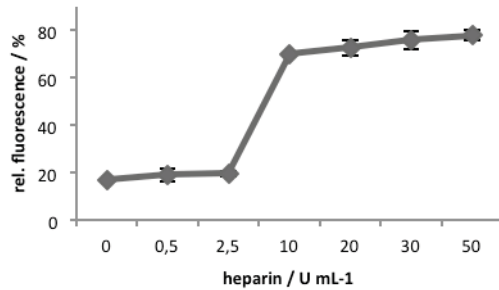


Figure S5: Dissociation assay of polyplexes formed at N/P 10 in pH 5 with increasing heparin concentrations (n=2)

### Polyplex stability in presence and absence of serum

To analyze the aggregation behavior of the BMAAD polyplexes in HBG, their size was investigated over several hours. As obvious no changes in size were detected and thus no aggregation occurred.

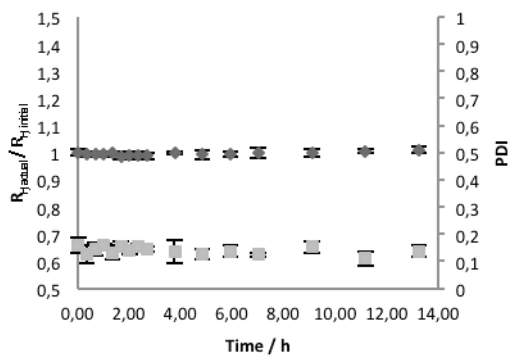


Figure S6: BMAAD polyplex stability in HBG (pH7). The relative diameters are demonstrated over 15 h.

### ***pH dependent hemolysis assay of polyplexes***

The hemolysis assay of the polyplexes confirms the results of the hemolysis assay using the single polymers. The BMAAD polyplexes shows, membrane-perturbing activity at pH 5 (endosomal pH), in contrast to physiological pH. PEI shows no dependency of pH, regarding its hemolysis activity.

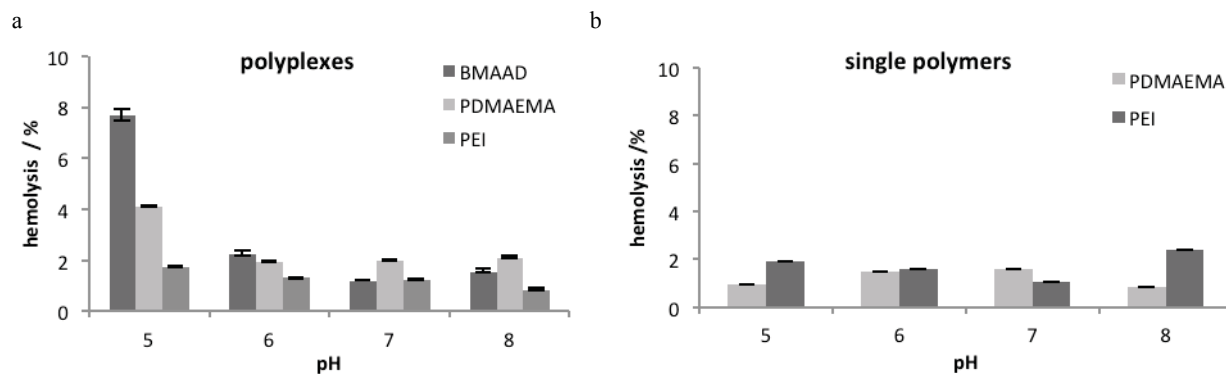


Figure S7. pH-dependent hemolysis assay of polyplexes (a) and single indicated polymers (b). Polyplexes of BMAAD, PDMAEMA, and PEI were formed at N/P ratio 20 and the values represent the mean of three different donors.

## Analysis of polyplex uptake mechanism

To analyze the uptake mechanism of the BMAAD polyplexes in more detail the transfection were performed at 4 °C as endocytosis is energy dependent and should be reduced at this temperature (figure S8b)

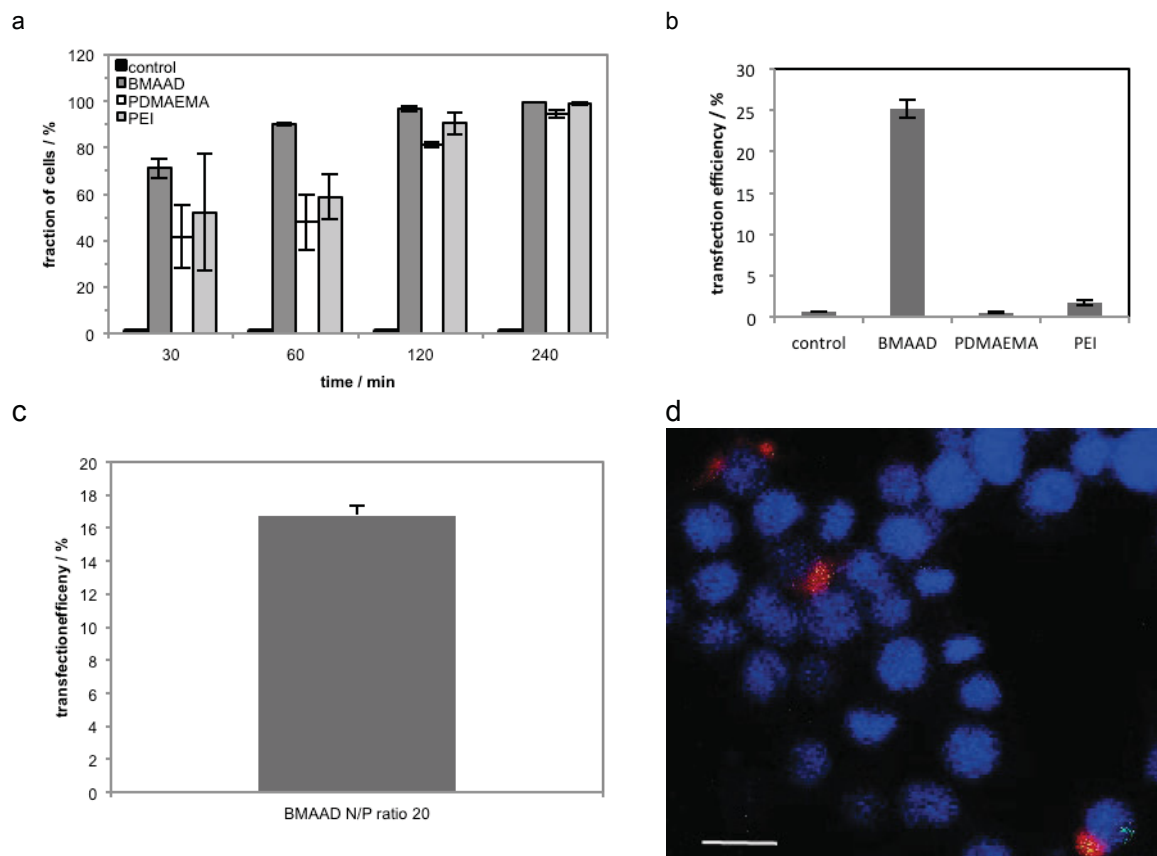


Figure S8: Fraction of cells with Yoyo-1 labeled pDNA for indicated time points using BMAAD, PEI and PDMAEMA (a). Transfection efficiencies with EGFP as reporter gen of BMAAD and PEI for adherent HEK cells performed at 4°C at N/P ratio 20 (b). Transfection efficiencies of Jurkat T cells under non-static conditions (c). CLSM images of HEK cells transfected with indicated BMAAD based polyplexes and YOYO-1 labeled pDNA (green), the early endosomes were stained by cell light early endosome BacMAM2.0 (red), and cell nuclei were stained with Hoechst 33342 (blue). Values represent the mean  $\pm$  S.D; \* represents a significant difference ( $p < 0.01$ ).

The transfection efficiency of BMAAD as well as PEI is significant decreased when incubated for 4 h at 4 C°. This indicates an energy dependent uptake of BMAAD. The remaining TE of 25 % yielded with BMAAD can be explained by a very efficient binding to the cellular membrane.

## References

- Schallon, A.; Synatschke, C. V.; Pergushov, D. V.; Jerome, V.; Müller, A. H. E.; Freitag, R., DNA Melting Temperature Assay for Assessing the Stability of DNA Polyplexes Intended for Nonviral Gene Delivery. *Langmuir* **2011**, *27*, 12042-12051.
- Vollrath, A.; Pretzel, D.; Pietsch, C.; Perevyazko, I.; Schubert, S.; Pavlov, G. M.; Schubert, U. S., Preparation, Cellular Internalization, and Biocompatibility of Highly Fluorescent PMMA Nanoparticles. *Macromol. Rapid Commun.* **2012**, *33*, 1791-1797.
- Provencher, S. W., CONTIN - A General-Purpose Constrained Regularization Program for Inverting Noisy Linear Algebraic and Integral-Equations. *Comput Phys Commun* **1982**, *27*, 229-242.
- Delgado, A. V.; Gonzalez-Caballero, F.; Hunter, R. J.; Koopal, L. K.; Lyklema, J., Measurement and Interpretation of Electrokinetic Phenomena. *J. Colloid Interface Sci.* **2007**, *309*, 194-224.
- Ohshima, H., A Simple Expression for Henrys Function for the Retardation Effect in Electrophoresis of Spherical Colloidal Particles. *J Colloid Interf Sci* **1994**, *168*, 269-271.

## Publication P7

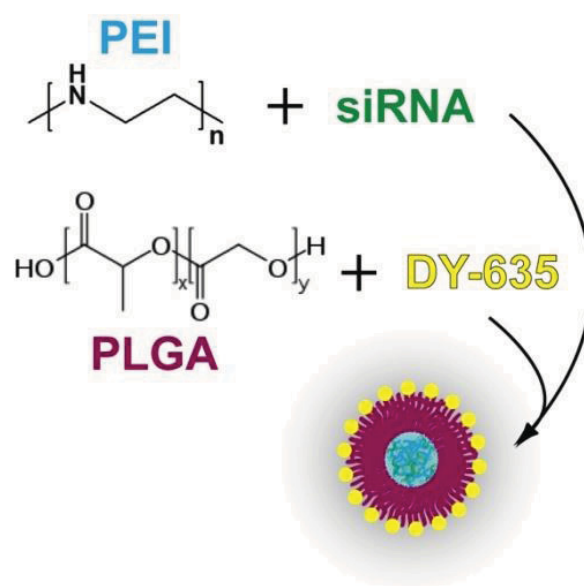
---

### Cell type-specific delivery of short interfering RNAs by dye-functionalized “theranostic” nanoparticles

A. T. Press, A. Träger, C. Pietsch, A. Mosig, M. Wagner, M. G. Clemens, N. Jbeily, N. Koch,  
M. Gottschaldt, N. Bézière, V. Ermolayev, V. Ntziachristos, J. Popp, M. Kessels, B. Qualmann,  
U. S. Schubert, M. Bauer

*Nat. Commun.* **2014**, *accepted*.

---







# Cell type-specific delivery of short interfering RNAs by dye-functionalized theranostic nanoparticles

Adrian T. Press,<sup>1,2\*</sup> Anja Traeger,<sup>2,3\*</sup> Christian Pietsch,<sup>2,3</sup> Alexander Mosig,<sup>4</sup> Michael Wagner,<sup>2,3</sup> Mark G. Clemens<sup>1,5</sup>, Nayla Jbeily,<sup>1</sup> Nicole Koch,<sup>6</sup> Michael Gottschaldt,<sup>2,3</sup> Nicolas Bézière,<sup>7</sup> Volodymyr Ermolayev,<sup>7</sup> Vasilis Ntziachristos,<sup>7</sup> Jürgen Popp,<sup>1,8,9</sup> Michael Kessels,<sup>6</sup> Britta Qualmann,<sup>6</sup> Ulrich S. Schubert,<sup>2,3#</sup> Michael Bauer<sup>1,3,9#</sup>

\*these authors contributed equally; #these authors share the senior authorship

<sup>1</sup> Center for Sepsis Control & Care (CSCC), Jena University Hospital, Erlanger Allee 101, 07747 Jena, Germany

<sup>2</sup> Laboratory of Organic and Macromolecular Chemistry (IOMC), Friedrich-Schiller-University Jena, Humboldtstrasse 10, 07743 Jena, Germany

<sup>3</sup> Jena Center for Soft Matter (JCSM), Friedrich Schiller University Jena, Philosophenweg 7, 07743 Jena, Germany

<sup>4</sup> Molecular Hemostaseology, Jena University Hospital, Bachstraße 18, 07743 Jena, Germany

<sup>5</sup> Department of Biological Sciences and Center for Biomedical Engineering and Science, University of North Carolina at Charlotte, Charlotte NC 28223, USA.

<sup>6</sup> Institute of Biochemistry I, Jena University Hospital, Friedrich-Schiller-University, 07743 Jena, Germany

<sup>7</sup> Chair for Biological and Medical Imaging, Technical University Munich and Helmholtz Zentrum München, Ingolstädter Landstrasse 1, 85764 Neuherberg, Germany

<sup>8</sup> Leibniz Institute for Photonic Technology Jena, Albert-Einstein-Strasse 9, 07745 Jena, Germany

<sup>9</sup> Abbe Center of Photonics, Friedrich-Schiller-University, Max-Wien-Platz 1, 07743 Jena, Germany

## Address for correspondence:

Michael Bauer, MD  
Professor and chief-executive director  
Center for Sepsis Control & Care  
Jena University Hospital  
Erlanger Allee 101  
07743 Jena, Germany  
Tel.: (0049)3641-9323111  
Email: michael.bauer@med.uni-jena.de

## Abstract

Efficient delivery of short interfering RNAs reflects a prerequisite for development of RNA interference therapeutics. Here, we describe highly specific nanoparticles, based on near infrared fluorescent polymethine dye-derived targeting moieties coupled to biodegradable polymers. The fluorescent dye, even when coupled to a nanoparticle, mimics a ligand for hepatic parenchymal uptake transporters resulting in hepatobiliary clearance of approximately 95% of the dye within 45 minutes. Body distribution, hepatocyte uptake and excretion into bile of the dye itself, or dye-coupled nanoparticles can be tracked by intravital microscopy or even non-invasively by multispectral optoacoustic tomography. Efficacy of delivery was demonstrated *in vivo* using 3-hydroxy-3-methyl-glutaryl-CoA reductase siRNA as an active payload resulting in a reduction of plasma cholesterol levels if siRNA was formulated into dye-functionalized nanoparticles. This suggests that organ-selective uptake of a near infrared dye can be efficiently transferred to theranostic nanoparticles allowing novel possibilities for personalized silencing of disease-associated genes.

## Introduction

Drugs based on RNA interference (RNAi) reflect a promising class of therapeutics to interfere with virtually any protein-coding mRNA, thus opening up new treatment strategies for targets that are, at present, deemed not amenable to drug development<sup>1-4</sup>. In contrast to small molecules with a wide range of different physicochemical properties, the chemical similarity of short interfering siRNAs (siRNA) permits the development of platform technologies<sup>5-7</sup>.

The most prominent obstacle in translating RNAi-based approaches into a new class of therapeutics is a specific delivery and release of siRNAs to the targeted cells, tissues and organs, particularly important when off-target effects need to be avoided<sup>8, 9</sup>.

siRNAs are negatively charged, hydrophilic molecules that must overcome the hydrophobic plasma membrane<sup>10, 11</sup> to reach – in a multistep process – the RNA-induced silencing complex as their presumed site of action<sup>12</sup>. Cationic lipids are described as potential carriers to overcome electrostatic repulsion by binding and neutralizing the negative charge of siRNAs simultaneously<sup>13</sup>. In addition, polycationic derivatives can effectively condense nucleic acid cargo for transfer into cells, especially polyethylenimine (PEI) which can be considered a golden standard polymer owing to its high buffering ability for endosomal escape of siRNA to be delivered<sup>14</sup>. Penetrating the cell membrane may be achieved by conjugating siRNAs to small chemical moieties, such as sugar moieties, peptides or lipids<sup>11, 15, 16</sup>. These conjugation approaches enhanced the cellular entry of siRNAs, but confer organ selectivity only to a very limited extent<sup>16</sup>.

To fully exploit the potential of these strategies innovative delivery systems allowing “active targeting” are required, particularly if the systemic delivery of siRNA to internal organs is desired. Approaches previously applied to deliver siRNAs include viruses and non-viral vectors with inherent differing efficiency and toxicity<sup>17, 18</sup>, however these are far from satisfactory<sup>19</sup>. Depending on the application, target tissue, and disease, versatile delivery strategies are of the utmost importance. Ultimately, a theranostic approach<sup>20, 21</sup> is desirable, whereby an upstream diagnostic test could account for any inter-individual variability in carrier and payload uptake such that the type and/or dose of the carrier can be individualized.

Due to its broad metabolic repertoire, the liver, more specifically hepatocytes, constitute particularly important targets for siRNA delivery<sup>22, 23</sup>.

A well-characterized way of delivering siRNA cargos utilizes liposomes that directly release the siRNA into the cytoplasm after fusing with the plasma or endosomal membrane<sup>24</sup>. This allows, albeit with limited cellular selectivity, delivery of siRNA into the liver<sup>25, 26</sup>.

A higher selectivity could potentially be achieved by other uptake mechanisms, such as receptor-mediated endocytosis of polymer-based nanoparticles. Uptake transporters with organ-specific expression pattern are present in epithelial cells, e.g. organic anion transporting polypeptides (OATP)<sup>27, 28</sup> found within the basolateral membrane of hepatocytes. Polymethine dyes, such as indocyanine green, which are ligands for these transporters, have been used for decades to assess hepatic excretory function<sup>29-32</sup>.

Here we report that polymethine dyes, which differ regarding their physicochemical characteristics, are eliminated with high selectivity via the hepato-biliary or renal route. These dyes can be covalently bound to polymers conferring selectivity for organ-specific uptake transporters to subsequently formed siRNA-loaded nanoparticles. As a result, the dye-nanoparticle conjugate (DY-[NP]) reflects an escort system, for which imaging strategies to monitor uptake and clearance can be developed. This could allow the design of a platform-technology for theranostic delivery of RNAi therapeutics to the liver and, potentially, the kidney.

## Results

### NIR fluorescent dyes for functionalization of nanoparticles

We initially screened different polymethine dyes based on benzopyrylium or indolium salts with solubilizing groups, i.e. sulfonic residues. Whereas dyes containing 4 sulfonic residues displayed preferential renal elimination, dyes containing only 1 sulfonic residue were subject to hepatobiliary excretion (Fig. 1 a and Supplementary Tab. 1). Among the studied compounds, DY-780 and DY-635 were excreted preferentially via the bile. While the optical properties of DY-780 proved to be suitable

for imaging by multi-spectral optoacoustic tomography (MSOT), DY-635 revealed superior properties to monitor hepatobiliary clearance by intravital microscopy (Fig. 1 b). Several more hydrophilic dyes, such as DY-704 showed promising pharmacokinetic properties to target renal tubular epithelia (Fig. 1 b).

To develop a theranostic delivery system for liver parenchyma, we selected DY-635 and characterized its affinity to basolateral transporters in a heterologous expression system. While DY-635 exhibited moderate affinity to several important transporters, such as the sodium-taurocholate cotransporting polypeptide NTCP, its affinity to OATP1B1 and OATP1B3 in transfected HEK cells substantially exceeded that of the FDA-proposed ligand for drug development, rifampicin<sup>(33)</sup>, Fig. 1 c). Finally, DY-635 uptake by freshly isolated primary mouse hepatocytes was found to be rapid, temperature sensitive and inhibited dose-dependently by cyclosporine A with an IC<sub>50</sub> of 379 nM (Fig. 1d).

### **Polymer-synthesis and formulation of nanoparticles**

DY-635 was covalently coupled to acid terminated poly-lactide-co-glycolic acid (PLGA) *via* 1-ethyl-3-(3-dimethylaminopropyl)carbodiimid hydrochloride (EDC) chemistry. Covalent coupling of copolymer and dye was confirmed by size exclusion chromatography (SEC) using UV/Vis and RI detectors (Supplementary Fig. 1 a) as well as UV/Vis spectroscopy (Supplementary Fig. 1 b). The calculated labeling efficiency for conjugation was 77%, meaning that every 130<sup>th</sup> (aimed: approximately every 100<sup>th</sup>) polymer chain bears a label. The subsequent nanoparticle formulation was accomplished by nanoprecipitation from pure PLGA (NP), PLGA with coupled dye (DY-635[NP], DY-704[NP]) and PLGA with coupled dye and loaded with additional dyes (DY-635[NP](DY-780), DY-635[NP](NileRed), DY-635[NP](ICG)). For *in vivo* gene silencing, siRNA was complexed with linear PEI of low molar mass (10 kDa; obtained by hydrolysis of poly(2-ethyl-2-oxazoline)). This was then encapsulated by emulsion techniques into a polymeric shell of the respective polymer (Fig. 2 a). Particle surface fluorescence quenching was performed using trypan blue to demonstrate expression of the NIR dye on the particle surface, as this represents an essential feature for specific uptake. The investigations showed a decrease of fluorescence by nearly 75% (Fig. 2 b). This indicates strongly that the dye is exposed to the particle surface and supports the notion that the dye moiety is responsible for targeting properties. The formed NPs were further characterized in detail by different methods to investigate their size, shape and surface charge (Tab. 1). The siRNA was encapsulated achieving an efficiency of  $87.4 \pm 2.5\%$  (Tab. 1) as determined by photometric phosphate quantification. Scanning electron microscopy (SEM) measurements (Fig. 2 c-e) showed no significant differences between [NP], DY-635[NP](-) and DY-635[NP](siRNA). The zeta potentials, representing the surface charges of the nanoparticles, are shown in Figure 2c, indicating negative charge for pure PLGA, DY-635[NP]s and loaded DY-635[NP]s.

DY-635[NP](siRNA) were investigated in further detail using asymmetric flow field-flow fractionation (AF4). A monomodal and nearly monodisperse distribution with low particle polydispersity index (PDI) (1.09) (Supplementary Fig. 1 c), a radius of gyration ( $R_g$ ) of 70 nm and a hydrodynamic radius ( $R_H$ ) of 90 nm, which is in accordance to batch dynamic light scattering (DLS) measurements, could be determined. The shape ratio ( $R_g/R_H$ ) of 0.78 obtained by AF4 measurements (Supplementary Fig. 1 d) corresponds to the theoretical value of a hard sphere (0.775)<sup>34</sup>. To confirm that the siRNA-PEI complexes are encapsulated inside the nanoparticles and not aggregated onto their surface, individualized TEM (Fig. 2 f) as well as cryo-TEM measurements (inset Fig. 2 f) were performed. The PEI core of DY-635[NP](siRNA) was counterstained with  $Cu^{2+}$  ions, demonstrating that the siRNA-PEI complexes were located inside the nanoparticles. Furthermore, bio- and hemocompatibility were studied showing neither hemolysis nor aggregation of erythrocytes (data not shown), supporting the successful encapsulation of the siRNA-PEI complexes. We then tested whether DY-635 conjugated to NPs would retain selective uptake by primary hepatocytes. Similar to what was observed with free dye (Fig 1 d) DY-635[NP](-) was rapidly accumulated in a temperature sensitive manner by primary hepatocytes and dose-dependently inhibited by cyclosporine A with an  $IC_{50}$  similar to that observed for inhibition of uptake of the free dye (209 nM, Fig 2 g).

### **Body-distribution and traceability of D-635[NP]**

Having demonstrated that organ specificity can be transferred to dye-functionalized nanoparticles, body distribution of DY-635[NP], carrying contrast agents as cargo, was analyzed regarding active versus passive targeting properties. Athymic Nude-Foxn1<sup>nu</sup> mice bearing a highly vascularized MDA-MB-231 human breast cancer xenograft were injected with DY-635[PLGA](DY-780) and analyzed after cryoslicing by low-power fluorescence microscopy. While liver, gall bladder, and subsequently the intestinal lumen showed dye signal suggesting uptake by hepatocytes followed by biliary excretion, no dye signal was detected in the tumor (Fig. 3 a). This is indicative of primarily active targeting to liver parenchyma rather than passive targeting even in the presence of a highly vascularized tumor. Subsequently we tested whether the optical properties of DY-780 DY-704 would allow non-invasive imaging of organ distribution using MSOT in anesthetized, healthy CD1 mice. Consistent with the uptake pattern in nude mice, a DY-780-derived signal in liver parenchyma, biliary tree and gut could be detected by MSOT indicating that hepatocytes take up and secrete DY-780 into bile (Fig. 3 b,c). Further experiments were conducted to confirm the need for a hepatoselective dye to target liver parenchyma. MSOT confirmed unspecific uptake of all applied NPs in spleen and to a much lesser extent in the liver (Fig. 4 a). While NPs with DY-635 as targeting moiety were extensively accumulated by the liver, either absence of dye or functionalizing with DY-704, i.e. a dye that is not a substrate for hepatocyte transporters, failed to show active targeting to the liver. Moreover, *in vivo* laser

scanning microscopy indicated that bare NPs carrying Nile red were taken up by the liver and found almost exclusively in sinusoidal lining cells (primarily Kupffer cells). In contrast, DY-635 functionalized NPs were taken up by hepatocytes with the Nile red cargo retained in the cytoplasm and the DY-635 transported into the bile (Fig. 5 a,b). Thus, the nanoparticles maintain their affinity to hepatic uptake transporters and allow tracking of drug delivery by biophotonic strategies.

### **Uptake mechanisms of DY-635 and DY-635[NP](-)**

A microfluidic-assisted organoid that mimics the sinusoidal anatomy enabling us to study uptake kinetics of a human hepatocellular cell line (HepaRG) in the presence of human umbilical vascular endothelial cells (HUVEC) under static or flow conditions was used to assess mechanisms of uptake (Supplementary Fig. 2). As shown in Figures 6 a and 6 b, uptake of DY-635[NP](-) was significantly increased under conditions of flow compared to static culture. In the presence of flow, the pressure gradient in the flow chamber results in efflux of perfusate (including nanoparticles) out of the “vascular” space into the space surrounding the HepaRG cells (analog of space of Disse *in vivo*) at the inflow and back into the vascular space at the outflow. In this way DY-635[NP] are delivered to the HepaRG cells similar to what occurs in the liver *in vivo*. In a co-culture of HepaRG and HUVEC cells we could also demonstrate selectivity of DY-635[NP](-) to hepatocytes and inhibition of nanoparticle uptake by cyclosporine A and Pitstop-2 supporting an OATP-dependent clathrin-mediated endocytosis (Fig. 6 b,c). Basal uptake of NP made from unfunctionalized PLGA and loaded with NileRed for detection was not affected by cyclosporine A (Fig. 6 d).

Since high selectivity for hepatocytes was confirmed for DY-635[NP](-) and because liver parenchyma could secrete free DY-635 into bile<sup>32</sup>, we performed *in vivo* pharmacokinetic measurements of DY-635[NP](-) to assess (1) plasma disappearance, (2) hepatocellular clearance and (3) appearance of the dye in collected bile. After central venous administration of DY-635[NP](-), plasma kinetics in arterial blood revealed a peak at 4 min after administration. Disappearance followed an exponential decay with biliary excretion reaching its maximum at 15 min (Fig. 7 a). Monitoring of parallel urine samples was consistent with almost exclusive secretion of DY-635 from DY-635[NP](-) *via* the hepatobiliary route. When biliary recovery of DY-635 was quantified, the ratio of secreted DY-635 to injected DY-635 bound to DY-635[NP](-) exceeded 90% after 45 minutes (Fig. 7 b). A change in the relative fluorescence intensity decrease in the hepatocyte from an exponential decay (free dye) to an almost linear kinetic after injection of DY-635[NP](-) was observed supporting the assumption that DY-635 and DY-635[NP] are processed differently and that rate limiting intracellular reactions have to occur prior to secretion of the dye (Fig. 7 c). Sublobular distribution of DY-635[NP](-) with liver tissue, as shown in

Figure 7 d, confirmed the highest concentrations around central veins with a steady decrease toward the lobular periphery early upon injection (Figure 7 d, upper and middle panel). The fluorescence signal subsequently displayed a spreading towards the periportal region (Figure 7 d, lower panel).

To assess the potential use of the free dye to predict uptake of DY-635[NP] in a theranostic system, we injected DY-635 and DY-635[NP](-) sequentially. After DY-635 injection an increase in fluorescence intensity was observed followed by an exponential decay. Administration of DY-635[NP](-) 20 min after DY-635 injection resulted in a second peak with a linear decay as shown for the individual compounds (Fig. 7 e), whereas distribution of DY-635 and DY-635[NP] were similar (Fig. 7 f)

### **Cell-type specific RNAi of *hmgcr* using DY-635[NP](siHMGCR)**

Next, we performed functional analysis of DY-635[NP](siRNA) delivery of siRNA in Hepa1-6 cells. In comparison to untreated controls, we observed a decrease in *hmgcr* mRNA-levels of 75% after 16 h and of 60% after 24 h. In contrast, DY-635[NP](siCtrl) loaded with a control siRNA showed some stimulatory effect on HMGCR mRNA at 16 h and 24 h after treatment so that the total (net) inhibitory effect of *hmgcr* RNAi was even more substantial in comparison to DY-635[NP](siCtrl) at both 16 h and 24 h (Fig. 8 a).

As successful RNAi was critical to our therapeutic strategy, we next validated the RNAi effects directly at the protein level. We first demonstrated the knockdown of the catalytic domain of HMGCR fused to GFP and expressed under a CMV-promotor from vectors that additionally drive either specific RNAi or scrambled RNAi in HEK293 cells using quantitative immunoblotting (Fig. 8 b).

Second, we directly assessed the knockdown of endogenous HMGCR by quantitative immunofluorescence analyses in HepG2 cells. Both RNAi constructs led to a significant reduction of anti-HMGCR immunosignals (Fig. 8 c; Supplementary Fig. 3). We then tested whether knockdown with DY-635[NP](siHMGCR) would be effective *in vivo* using a mouse model. After two injections via a venous port, liver tissue was analyzed. An absolute decrease of *hmgcr* mRNA of 70 % versus untreated animals was achieved (Fig. 8 d). This decrease in mRNA was functionally significant, as DY-635[NP](siHMGCR) treatment-mediated decrease of *hmgcr* mRNA resulted in a significant reduction of plasma cholesterol compared to the controls (Fig. 8 e). Again it was observed that treatment with DY-635[NP](siCtrl) lead to an up-regulation of *hmgcr* accompanied by an increase in *hmgcr* mRNA (7d) and plasma-cholesterol levels (Fig. 8 e). This is likely the result of low level activation of lipid metabolic pathways known to be associated with transient penetrations of the cell wall<sup>35</sup>.

## Discussion

In this study, we characterized multifunctional nanoparticles generated by covalent conjugation of a fluorescent dye with known hepatobiliary clearance to a biodegradable polymer (PLGA) as a carrier system for PEI-complexed RNAi therapeutics<sup>36-39</sup>. The highly organ-selective uptake of the NIR dye was maintained after covalent binding to PLGA-NPs. Furthermore, the NIR dye moiety allowed monitoring of distribution, uptake and clearance using biophotonic approaches. Assessing the pharmacokinetics of DY-635[NP](-) confirmed hepatobiliary clearance exceeding 90% in less than one hour. The conjugate thus represents a fundamentally new class of theranostic delivery systems with a highly efficient active-targeted delivery and the option, based on preceding injection of the free dye, to predict the tissues that will eventually take up a nanoformulated drug before it is administered. Since these dyes can be modified with regard to their physicochemical properties (as shown exemplarily for DY-704 which is eliminated primarily via the kidney), a platform technology to deliver dye-functionalized NPs to a variety of cells and tissues expressing these transporter systems seems feasible. We could identify organic anion transporter proteins as the transporters responsible for uptake of DY-635. Their critical role in the active targeting of DY-635[NP](-) to achieve basolateral uptake into hepatocytes is supported by the observation of cyclosporine A-sensitive uptake by HepaRG cells cultured under flow conditions. Our *in vitro* and *vivo* findings suggest a model where the DY-635[NP]s are immobilized at the cell surface of hepatocytes through interaction of DY-635 with OATPs followed by subsequent clathrin-mediated endocytosis. Due to their size (170nm), DY-635[NP](-) cannot be transported directly by the OATPs<sup>40</sup> and endocytosis after immobilization via binding to the uptake transporters on the basolateral membrane is the likely mechanism. Dahlman et al have recently reported siRNA encapsulated in nanoparticles that specifically target vascular endothelial cells.<sup>41</sup> The NP appear to be taken up via receptor mediated endocytosis, but this mechanism is distinct from the dye functionalized nanoparticles that we describe. The vascular endothelium is in direct contact with the intravascular space and exhibits effective but not very specific endocytosis. In contrast, hepatocytes are separated from the vascular space and our technology exploits recognition of transporters that are very specific to the hepatocytes. Thus while the technology of Dahlman et al appears to be very effective for targeting vascular lining cells, it is not likely to be able to target nonvascular cells.

Likewise, DY-635 labeled PLGA cannot be secreted directly into bile due to its molar mass (MW) of 12 kDa (non-modified polymer) and hydrophobicity. Based on the data in figure 5 a, showing hepatocyte uptake and excretion of both, Nile red cargo and DY-635 as functionalizing moiety, degradation by intracellular esterases of PLGA with desorption of DY-635 and subsequent secretion into bile is likely. This is also supported by the observation that the decay of fluorescence followed an exponential function for the free dye, while it was delayed and almost linear for the DY-635[NP](-)-associated signal. It would also be consistent with a multistep processing within the



endosome, with disruption and release of the payload into the cytosol, supported by the cationic polymer PEI<sup>42,43</sup>. Escape of siRNA from the endosome is a critical and rate-limiting step for delivery approaches<sup>44</sup>. Quantification of this delivery for lipid-based nanoparticle (LNP) delivery has been previously determined to be in the range of 1-2% of the applied siRNA<sup>44</sup>. Thus, confirmation of uptake of nanoparticles does not necessarily imply functional delivery of the RNAi therapeutic. While assessment of the intracellular handling of the cargo is beyond the scope of the present study, we demonstrated a significant inhibition of cholesterol biosynthesis with encapsulation of a siRNA directed against *hmgcr* into DY-635[NP]. *Hmgcr* was chosen as an exemplary pathway that reflects a key metabolic function of the liver but also based on the observation that DY-635[NP](-) increased plasma cholesterol while toxicology screening otherwise revealed no unwarranted side effects. The observed increase in *hmgcr* and plasma cholesterol with the empty carrier is a phenomenon likely to be associated with the penetration of the cell membrane NPs leading to an adaptive increase of cholesterol biosynthesis as described for endocytosis<sup>45</sup> or in response to pore-forming toxins<sup>35</sup>. This side effect may confer protection in the acute setting<sup>46</sup> but is of concern if repeated administration seems required. The increase in plasma cholesterol could be blunted if siRNA directed against *hmgcr* was the cargo in non-functionalized NPs, or substantially decreased if the same NPs were functionalized by DY-635 to target hepatocytes as a primary site of cholesterol synthesis.

During degradation of DY-635[NP](siRNA) and the associated release of the siRNA into the cytosol, DY-635 is presumably desorbed from the polymer and secreted into bile. The zonal distribution of the dye during this process with primary uptake in the pericentral region and subsequent cell-to-cell transport to midzonal and periportal regions of the low molar mass dye (potentially also an RNAi therapeutic) is likely to explain the spreading of the fluorescence signal ostensibly through gap junctions<sup>47,48</sup>.

Intravital microscopy also confirmed that uptake of DY-635[NP](-) was almost exclusively associated with hepatocytes, primarily in zone 3 of the acinus. No significant accumulation in non-parenchymal cells, most notably Kupffer cells that are primarily sited in zone 1 of the acinus and that take up significant portions of LNPs<sup>49</sup>, was observed for DY-635[NP](-). This extends the concept of active targeting of the liver (with a high proportion of phagocytic and immunocompetent cells) to an active and highly specific targeting of liver parenchymal cells, i.e. the primary goal for targeted interventions into metabolic pathways.

While fluorescence microscopy is a suitable tool to study these fundamental questions regarding uptake and fate of DY-635[NP](-), the ability to monitor body distribution non-invasively by MSOT provides new opportunities to guide the delivery of RNAi therapeutics. Theranostics, a linguistic blend of diagnostics and therapy, reflects an increasingly important concept in personalizing health care. This aims to explain inter-individual and population-to-population variabilities in health intervention outcomes using diagnostic tests such that either the type or extent of the intervention can be individualized<sup>20</sup>. Our present approach allows this concept to be applied to the

delivery of nano-formulated active drugs, in particular those with significant off-target effects, by predicting the targeted cells and tissues individually before administration of the carrier and cargo.

In summary, the present study demonstrates that uptake receptors can be targeted very efficiently with polymethine dyes. Using DY-635, a dye with known hepatobiliary clearance, we demonstrate that this approach extends the concept of delivery to the liver, e.g. with LNPs to exclusive targeting of hepatic parenchymal cells. In addition to exploring a novel, well-defined uptake route the use of dyes to functionalize the NPs also enables their tracking, even non-invasively by MSOT<sup>50-52</sup>. This suggests that organ-selective uptake of a dye can be transferred to nanoparticles to generate theranostic drug carriers allowing fundamental novel options in personalized health care.

## Methods

### Animals

Animal studies were conducted in accordance with animal welfare legislation under pathogen-free conditions in the animal facility of the Jena University Hospital or the Helmholtz-Center Munich. During all procedures and imaging methods, animals remained under deep general anesthesia using Isoflurane and pain-reflexes were assessed to gauge the depth of anesthesia.

### In vivo pharmacokinetics of various polymethine dyes

Catheters were placed in the jugular vein, carotid artery, bladder and bile duct of male Wistar rats (300-400 g body weight (BW)). After i.v. administration of DY-635 (13 pmol per g BW), DY-630 (13 pmol per g BW), DY-750 (13 pmol per g BW), DY-751 (13 pmol per g BW), DY-731 (13 pmol per g BW), DY-777 (14 pmol per g BW), DY-682 (13 pmol per g BW), DY-704 (17 pmol per g BW), DY-732 (13 pmol per g BW), DY-754 (17 pmol per g BW), DY-678 (14 pmol per g BW), DY-778 (14 pmol per g BW) or 6.5 µg DY625-[NP] per g BW, bile was collected every 5 min and 200 µl arterial blood taken at defined times into heparinized tubes. DY-635 fluorescence in bile and plasma was measured in a spectrofluorometer (FluoStar Optima, BMG Labtech). Results are mean ± SEM of 3 biological replicates.

### Analysis of DY-635 interaction with human hepatic basolateral transporters.

HEK293 cells were transfected with OATP1B1 (*SLCO1B1*, NM\_006446), OATP1B3 (*SLCO1B3*, NM\_019844), OCT1 (*SLC22A1*, NM\_003057.2), OAT2 (*SLC22A7*, NM\_006672), NTCP (*SLC10A1*, NM\_003049), NaDC3 (*SLC13A3*, AF154121) or the empty vector (pcDNA5). Transfected HEK293 cells were seeded at  $2 \times 10^5$  cells per

well and cultured for three days. To determine the interaction of DY-635 with different transporters mock- and transporter-transfected cells were incubated with radio-labeled substrates for OATP1B1 ( $[^3\text{H}]$ estrone-sulfate, 30 nM), OATP1B3 ( $[^3\text{H}]$ sulfobromophthalein, 50 nM), OCT1 ( $[^3\text{H}]$  1-methyl-4-phenylpyridinium iodide, 10  $\mu\text{M}$ ), OAT2 ( $[^3\text{H}]$ cGMP, 10  $\mu\text{M}$ ), NTCP ( $[^3\text{H}]$ estrone-sulfate, 10  $\mu\text{M}$ ) or NaDC3 ( $[^{14}\text{C}]$ succinate, 10  $\mu\text{M}$ ), in the absence and presence of 10  $\mu\text{M}$  DY-635 or an inhibitor for OATP1B1 (rifampicin, 20  $\mu\text{M}$ ), OATP1B3 (rifampicin, 20  $\mu\text{M}$ ), OCT1 (decynium22, 50  $\mu\text{M}$ ), OAT2 (indomethacin, 100  $\mu\text{M}$ ), NTCP (cyclosporine A, 50  $\mu\text{M}$ ) and NaDC3 (succinate, 100  $\mu\text{M}$ )..

### Hepatocyte Isolation

. Male FVB/NRj were sacrificed using cervical dislocation, The abdomen was opened and the portal vein catheterized and perfused briefly with pre-warmed Dulbecco's PBS (DPBS) (Sigma Aldrich) containing 0.5 mM EGTA and 0.1 % Penicillin/Streptomycin at 6.5 ml per min.followed by 4 to 6 min perfusion using pre-warmed DPBS containing 0.5 mg collagen per ml and 1 mM  $\text{CaCl}_2$  (pH7.4). The digested liver was transferred to Leibovitz- Buffer (Gibco, Life Technologies) and hepatocytes separated and centrifuged at 50 x g for 5min at 4 °C. The pellet was rinsed through a 40  $\mu\text{m}$  cell and resuspended with 20 ml ice-cold hepatocyte wash media (Gibco, Life Technologies) containing 0.1 % Penicillin/Streptomycin. This was repeated seven times to yield highly purified hepatocytes. 80,000 hepatocytes per well were seeded using William`s Medium E (10 % FKS, 0.025% Insulin (v/v), 0.1 % Glutamaxx (2mM) (Gibco, Life Technologies), 0.1% Penicillin/Streptomycin). After 6-8 h media was changed to remove non-attached hepatocytes.

### DY-635 and nanoparticle uptake by primary hepatocytes

Murine primary hepatocytes isolated and cultured on collagen-coated 96-well- for 2 to 3 days were used to measure the uptake of DY-635 (amino-terminated), DY-635[NP](NileRed) and [NP](NileRed) in absence and presence of cyclosporine A. Hepatocytes were washed with PBS before a 2x inhibitor solution containing Krebs-Henseleit Buffer (KHB, Biochrome), 2% fetal calf serum and 2x cyclosporine A was added. This was then diluted 1:1 (v/v) with either 400 nM DY-635 (amino-terminated) or 10  $\mu\text{g}$  NP in KHB. After 2 min (DY-635) or 30 min (NP) incubation at 37°C or 4°C media was removed and cells were washed twice with ice-cold PBS containing 50  $\mu\text{M}$  cyclosporine A. Cells were lysed in 5 % Acetonitril and 0.1 % Tween-20. Lysates were analyzed on a Tecan plate reader (Excitation: 488 $\pm$ 09 nm, Emission 530 $\pm$ 20 nm). A NileRed-standard curve allowed calculation of intracellular NileRed-amounts.A correction factor was calculated from serial dilutions of the NP to correct for different NileRed concentration in [NP](NileRed) and DY-635[NP](NileRed). Data were normalized to cellular protein (Bradford).

### Polymer labeling

Conjugation of acid terminated poly-lactide-co-glycolic acid (PLGA, 50:50) and amino-terminated DY-635 or DY-704 was performed *via* EDC chemistry (to label every hundredth polymer chain). 0.95 g -COOH terminated PLGA (Sigma-Aldrich,  $M_w = 7\ 000$  to  $17\ 000\ \text{g mol}^{-1}$ ) and 0.52 mg ( $2.72\ \mu\text{mol}$ ) EDC were reacted in 20 ml dried methylene chloride for 1 h at room temperature. Subsequently, 1 mg ( $1.36\ \mu\text{mol}$ )  $\text{NH}_2$  terminated DY-635 ( $\text{C}_{40}\text{H}_{53}\text{N}_4\text{O}_5\text{SCI}$ , Dyomics GmbH, Jena, Germany), in 1 ml DMF was added and stirred at room temperature for 12 h. The solvent was evaporated under reduced pressure and the solid residue dissolved in acetone. The resulting PLGA-DY-635 or PLGA-DY-704 was precipitated (very fast) in cold water to generate a dispersion and this was further purified by dialysis against water using a Spectra/Por 3 dialysis membrane (Spectrumlabs,  $3,500\ \text{g mol}^{-1}$  cut-off). Finally, the product was filtered and lyophilized. The calculated labeling efficiency for conjugation was 77%. Size-exclusion chromatography (SEC) was performed on a Shimadzu system equipped with a SCL-10A system controller, a LC-10AD pump, a RID-10A refractive index detector, a UVD SPD-10AD UV/Vis detector and a PSS SDV linear S,  $5\ \mu\text{m}$  column ( $8 \times 300\ \text{mm}$ ) with chloroform/triethylamine/2-propanol (94:4:2) as eluent at  $1\ \text{ml min}^{-1}$ , and the column oven was set to  $40\ ^\circ\text{C}$ . A calibration with low polydispersity polystyrene standards (ranging  $M_n$  from 380 to  $128\ 000\ \text{g mol}^{-1}$ ) was used.

#### UV/Vis spectroscopy

UV/Vis absorption spectra were recorded using a UV/Vis spectrometer Specord 250 (Analytik Jena AG) in a  $1 \times 1\ \text{cm}$  quartz sample cell. The labeling efficiency for conjugation was estimated *via* UV/Vis spectroscopy using the molar extinction coefficient of the dyes and calculated via equation (1) :

$$\text{labeling efficiency} = \frac{\text{theoretical labeling degree}}{\text{estimated labeling degree}} \times 100 \quad (1)$$

#### Scanning electron microscopy (SEM)

Nanoparticle suspensions were diluted with deionized water. One droplet was placed on a mica surface and lyophilized for 3 h. Finally, the samples were coated with platinum (5 nm), using a BAL-TEC SCD005 sputtering device (Balzers, Liechtenstein). SEM measurements were performed on a Zeiss (LEO) 1530 Gemini FESEM operating at 8 to 10 kV using the InLens detector.

#### Dynamic light scattering

Batch dynamic light scattering (DLS) was performed on a ZetaSizer Nano ZS (Malvern, Herrenberg, Germany) equipped with a He-Ne laser operating at a

wavelength of 633 nm. Counts were detected at an angle of 173°. All measurements were conducted at 25 °C after an equilibration of 120 sec in triplicate. For analyzing the autocorrelation function (ACF), the cumulative analysis and a NNLS algorithm (non-negative least-squares) were applied. Apparent hydrodynamic radii were calculated using to the Stokes–Einstein Equation (equation 2):

$$R_h = \frac{kT}{6\pi\eta D} \quad (2)$$

where,  $R_h$  = hydrodynamic radius,  $k$  = Boltzmann constant,  $T$  = absolute temperature,  $\eta$  = viscosity of the sample, and  $D$  = apparent translational diffusion coefficient.

### Electrophoretic light scattering

Electrophoretic light scattering (ELS) was used to measure the electrokinetic potential (zeta potential). Measurements were performed on a Zetasizer Nano ZS (Malvern Instruments, Herrenberg, Germany) by applying laser Doppler velocimetry. For each measurement, 10 to 30 runs were carried out using the slow-field reversal and fast-field reversal modes at 150 V. Each experiment was performed in triplicate at 25 °C. The zeta potential ( $\zeta$ ) was calculated from the electrophoretic mobility ( $\mu$ ) according to the Henry Equation (equation 3) with  $f(ka) = 1.5$ :

$$\zeta = \frac{3\eta\mu}{2\varepsilon f(ka)} \quad (3)$$

where  $\varepsilon$  = dielectric constant, and  $f(ka)$  = Henry constant.

### Nanoparticle formulation

siRNA or ICG encapsulated in particles ([NP](siRNA), DY-635[NP](siRNA), [NP](ICG) or DY-635[NP](ICG)) were prepared by the double emulsion water/oil/water (w/o/w) evaporation, as described<sup>53</sup>. siRNA encapsulation polyplexes of linear polyethylenimine (L-PEI) and siRNA (Supplementary Tab. 2) were prepared in pure water. L-PEI with a degree of polymerization of 200 was synthesized as previously described<sup>54</sup>. L-PEI and siRNA were diluted in pure water to a stock concentration of 1 mg·ml<sup>-1</sup>. Polyplexes were formed of 8 µg siRNA and 9.8 µg L-PEI in a total volume of 250 µl, vortexed briefly, and incubated for 20 min at room temperature. A total mass of 100 mg PLGA or PLGA-DY-635 were diluted in 5 ml ethylacetate (20 mg·ml<sup>-1</sup>). The polyplex solution was added and the mixture immediately sonicated for 20 sec (Sonics VibraCell VC505; 500 Watt) with a replaceable 1/8" tapered microtip, and 30% amplitude for 20 sec. An aqueous solution of 3% (w/v) poly(vinyl alcohol) (PVA,  $M_w = 67,000 \text{ g mol}^{-1}$ , 86.7 to 88.7 mol% hydrolyzed, Sigma Aldrich) (5 ml, PVA diluted in ddH<sub>2</sub>O) was then added to the first emulsion and sonicated as for the first emulsion. The double emulsion was added to 45 ml ddH<sub>2</sub>O. Ethylacetate evaporation was performed with stirring overnight. The particles were washed by centrifugation (14,000 g, 10 min) and twice resuspended in ddH<sub>2</sub>O. Particles were lyophilized and stored at – 20 °C until use. For encapsulation of DY-780 or Nile red, the polymer and dye were diluted in acetone to a final polymer concentration of 7.5 mg·ml<sup>-1</sup> with 2 %

(w/w) of each dye. The polymer dye solution was transferred to a syringe and automatically injected (13.02 ml/h) into a 3-fold excess of ultra-pure water. To stabilize the formed nanoparticles and to enable lyophilization 1 µg PVA was added to 100 mg polymer. Finally the nanoparticle solution was lyophilized and stored at – 20 °C until use.

#### Asymmetric flow field-flow fractionation

Asymmetric flow field-flow fractionation (AF4) was performed on an AF2000 MT System (Postnova Analytics, Landsberg, Germany) coupled to an UV (PN3211, 260 nm), RI (PN3150), multi-angle light scattering (MALLS, PN3070, 633 nm) and DLS (ZetaSizer Nano ZS) detector. The eluent was delivered by three different pumps (tip, focus, cross-flow) and the sample injected by autosampler (PN5300) into the channel. The channel has a trapezoidal geometry and an overall area of 31.6 cm<sup>2</sup>. The nominal height of the spacer was 500 µm. A regenerated cellulose membrane with a molar mass cut-off of 10 kDa served as accumulation wall. All experiments were carried out at 25 °C with pure water as eluent. 10 µl of sample (1 mg·ml<sup>-1</sup>) was injected with an injection flow rate of 0.2 ml·min<sup>-1</sup> and a cross-flow rate of 1.2 ml·min<sup>-1</sup> for 7 min (detector flow rate 0.5 ml·min<sup>-1</sup>, focus flow rate 1.5 ml·min<sup>-1</sup>). After the focusing step, the cross-flow rate was reduced under an exponential gradient (0.4) within 10 min to 0 ml·min<sup>-1</sup>. The cross-flow was kept constant at 0 ml·min<sup>-1</sup> for 40 min to ensure complete elution. All measurements were in triplicate.

#### Determination of siRNA content

siRNA content of the nanoparticles was determined by determination of total phosphorus according to Chen *et al*<sup>55</sup>. 10 to 16 mg of freeze-dried nanoparticles and phosphorus standards (0 - 0.195 µmol, KH<sub>2</sub>PO<sub>4</sub>, Sigma-Aldrich) were placed in separate tubes. After adding 0.45 ml of 8.9 N H<sub>2</sub>SO<sub>4</sub>, tubes were heated at 210 °C for 25 min. After cooling to room temperature, 150 µl H<sub>2</sub>O<sub>2</sub> (30 wt. %) were added and samples were reheated at 210°C for 30 min. After cooling 3.9 ml deionized water and 0.5 ml of ammonium molybdate (VI) tetrahydrate solution (2.5 wt. %) were added. After vortexing (20 sec), 0.5 ml of L-ascorbic acid solution (10 wt. %) was added and the tubes vortexed again for 20 sec. Tubes were capped and heated for 7 min at 80°C. Absorbance of solutions was measured at 820 nm on a Specord 250 UV/Vis – spectrometer (Analytik Jena AG, Jena, Germany) in a 1 cm quartz cell. siRNA content was determined based on phosphorous content and number of base pairs in the siRNA.

#### Multispectral Optoacoustic Tomography

Multispectral Optoacoustic Tomography (MSOT) was performed as described<sup>56</sup>. Briefly, a commercial MSOT (iThera medical, Munich, Germany) with an array of 256 cylindrically-focused transducers was disposed around the mouse and simultaneously collected signals from an optical plane.. CD1 or athymic Nude-

Foxn1<sup>nu</sup> mice bearing a MDA-MB-231 human breast cancer xenograft were placed inside the tomograph. Multispectral image stacks were taken from the whole abdomen immediately before and 20 min after injection of 7 µg of either DY635-[NP](DY-780), [NP](ICG), DY-635[NP](ICG) or DY-704[NP](-) per g BW. DY-780 could be only detected by MSOT after release from the nanoparticles. DY-780, DY-704, and ICG signals could be spatially localized upon spectral unmixing of MSOT images and comparison with previously recorded DY-780 spectra. Animals were frozen immediately after the imaging experiment for validation by multispectral epillumination cryoslice imaging<sup>57</sup>.

### Dynamic cell culture

HUVEC and HepaRG cells were co-cultured using a microfluidic-supported chip. (Supplementary Fig. 2). HepaRG cells were cultured as described<sup>58</sup>.  $2.7 \cdot 10^4$  cells per  $\text{cm}^2$  were seeded in William's E medium supplemented with 10% fetal bovine serum,  $100 \text{ U} \cdot \text{ml}^{-1}$  penicillin,  $100 \text{ g} \cdot \text{ml}^{-1}$  streptomycin,  $5 \text{ U} \cdot \text{ml}^{-1}$  insulin, and  $5 \cdot 10^{-5} \text{ M}$  hydrocortisone-hemisuccinate and cultured for two weeks. For HepaRG differentiation, cells were cultured with 2% dimethylsulfoxide (DMSO) for two more weeks. Differentiated HepaRG cells were seeded at 4,000 cells per  $\text{mm}^2$  at the bottom of the chip cavities beneath the membrane. 300,000 HUVEC (4,300 cells per  $\text{mm}^2$ ) were seeded above the membrane and co-cultured with differentiated HepaRG cells in for 24 h before the uptake experiments. Cells were perfused with  $50 \text{ µg} \cdot \text{ml}^{-1}$  nanoparticles in Williams E medium. Three independent experiments to assess DY-635[NP](-) uptake were done for each group (static and dynamic). For each time point three pictures were taken and 200 ROI per picture were analyzed. Images in figure 6 c were corrected by subtracting the mean local background intensity from the mean fluorescence intensity of a neighboring ROI.

### Intravital Microscopy

For intravital microscopy (IVM) the jugular vein of male FVB/NRj mice (25 to 30 g BW) was cannulated and the liver exposed via a right lateral abdominal incision 70 pmol DY-635  $\text{g}^{-1}$  BW (in DMSO (1 M) and diluted to 20 µM in 0.9% NaCl) or 7 µg DY-635[NP], DY-704[NP], DY-630[NP](NileRed) per g BW ( $1 \text{ mg} \cdot \text{ml}^{-1}$  in 5% glucose) were injected i.v.. Intravital microscopy was performed using an inverted epifluorescence microscope (AxioObserverR Z1; Zeiss, Jena, Germany) as described previously<sup>8, 30</sup>. DY-635 or DY-635[NP](-) were visualized at 633 nm (exposure time 40 ms). Co-localization of DY-635 or DY-635(NP) and liver tissue was performed using 8-bit, grey-value tiff-images and ImageJ with a pseudo color scale. For Figure 7 f pictures taken 8 min after injection of DY-635 and after 28 min (8 min after DY-635[NP](-) injection) were overlaid and colocalized pixels counted. This number was then corrected for the amount of colocalized pixel that might persist from the injection of free dye DY-635 using the following formula for DY-635 relative fluorescence decrease:  $\text{FI}(\text{DY-635}) [\%] = 71.6^{-\text{time}/12.3} + 151,9^{-\text{time}/3.7}$  (Fig. 7 c).

### In vivo confocal laser scanning microscopy

For in vivo confocal laser scanning microscopy a tail-vein catheter (30G) was placed in male FVB/NRj mice (25 to 30 g BW). The liver or/ and kidney was exposed and placed on a cover-slip. Images were acquired using a LSM-780 (Zeiss, Jena, Germany) using an air corrected 40x plan-apochromatic objective (NA: 0.95). Lasers and filters used are summarized in Supplementary Table 3 Nanoparticles or free dyes were injected in similar concentration as described above via the tail vein-catheter.

### HMGCR-RNAi validation in vitro

Hepa1-6 cells were cultured in DMEM with 10% FBS and penicillin-streptomycin..  $8 \cdot 10^5$  cells per well were seeded in 12-well plates 24 h prior to transfection. Lyophilized DY-635[NP](siHMGCR) were dissolved in OptiMem (Life technologies) to  $500 \mu\text{g} \cdot \text{ml}^{-1}$ . Cells were washed twice in PBS and incubated with 1 ml DY-635[NP](siHMGCR). After 4 h media were changed to normal growth media for a further 12 or 20 hours and *hmgcr* steady state transcript levels assessed by RT-qPCR (Supplementary Tab. 4). To measure HMGCR-protein knockdown efficacy, HEK293 cells were transfected with pRNAT H1.1 vectors encoding the *hmgcr*-shRNA used for nanoparticle encapsulations (Supplementary Tab. 3) as well as mouse GFP-HMGCR (419-887) instead of GFP (for plasmid and cloning information see Supplementary Figure 3). After 24 h cells were lysed and protein levels analyzed via anti-GFP immunoblotting<sup>59, 60</sup>.

To confirm the heterologous *hmgcr* RNAi results by immunofluorescence analyses of endogenous HMGCR, anti-human HMGCR antibodies (Santa Cruz) were tested for recognition of purified recombinant HMGCR(aa419-887) fusion proteins of overexpressed murine GFP-HMGCR(aa419-887) and of endogenous HMGCR. For RNAi validations in HepG2-cells, cells transfected with GFP-coexpressing RNAi vectors were processed for fluorescence analysis using a Zeiss CellObserver with an apotome. 16 h after transfection Z-stacks were accumulated and integrated intensities of SUM-projections of the anti-HGCR signal were measured in ImageJ. Two independent cellular assays with  $n > 16$  cells were conducted.

The effects of siHMGCR#2 on gene expression were assessed in  $8 \cdot 10^5$  Hepa1-6 cells incubated for 24 h with 2 ml full growth media (DMEM/F12, 10% FCS, 1% penicillin/streptomycin) at 37 °C, 5% CO<sub>2</sub>. Directly before transfection lyophilized DY-635[NP](siHMGCR) or DY-635[NP](siCtrl) were dissolved in OptiMEM (Life Technologies) to a final concentration of 100, 200 or 500  $\mu\text{g}$  NP per ml. Growth Media were removed and the cells washed twice with PBS. 1 ml of the NP-solutions was added to the cells. Four h later the NP was removed and full growth media added. Cells were harvested after an additional 14 or 20 hours for RT-qPCR. See Supplementary Table 2 for primer-pairs. Results of 3 independent experiments with 3 technical replicates were used for *in vitro* gene expression analysis. Data are mean  $\pm$  S.E.M.



### *In vivo RNAi*

A venous access port was placed in male FCB/NRj mice at 5 weeks. The mice were treated with antibiotics for seven days to prevent infection. Fourteen days after the operation lyophilized [NP](siHMGCR), DY-635[NP](siHMGCR) or DY-635[NP](siCtrl) were dissolved in 5% glucose to a concentration of 1 mg NP per ml. 7 µg NP (7µl) per g BW was administered twice i.v. within 24 h. 16 h after the second injection mice were sacrificed by and blood collected into heparinized tubes. Plasma and organs were frozen for subsequent analysis. Metabolites were analyzed from randomized, blinded samples of plasma (Fujifilm DRI-CHEM 3500i). Gene expression was analyzed in randomized tissue homogenates. n =4-9 (individual number are in the legend for Figure 8).

### *Statistics*

Data were tested for normal distribution and analyzed by appropriate ANOVA models as described in figure legends. Post-hoc analysis was performed using Dunnett's test when comparing multiple groups to a single control or Tukey test when performing post hoc pair-wise analysis.



## Acknowledgement

Grant support by the German Federal Ministry of Education and Research (BMBF) within the framework of the PROGRESS consortium (01KI07111) is gratefully acknowledged, as well as the Carl Zeiss Foundation and the Thuringian Ministry for Education, Science and Culture (TMBWK; #B514-09051, NanoConSens). Our research was further supported by Dyomics GmbH, Jena, Germany who kindly provided their dyes for polymer-synthesis and screening. We thank C. Fritzsche for preparation of some of the nanoparticles and performance of cytotoxicological and hemocompatibility studies, S. Hoepfner for performance of cryo-TEM measurements and Steffi Stumpf for assistance in the SEM investigations as well as A. Keib and U. Vetterling for support during animal experiments and sample-preparation. We thank Stephanie Schubert for help in the particle preparation and helpful comments.

## Contributions

**Adrian T. Press:** Planning, performing and analyzing experiments (Figure 1 a-d, 2 b, h, 5, 6, 7, 8 a,d,e), Planning experiments (Figure 3, 4 a, 5, 6), statistical analysis of the data, preparation of graphs and figures; wrote parts of the manuscript.

**Anja Traeger:** Planning and supervising the particle formation and characterization; wrote parts of the manuscript.

**Alexander Mosig:** Planning, performing and analyzing experiments (Figure 5a-d).

**Christian Pietsch:** Planning, performing and analyzing the polymer-synthesis and characterization (Suppl. Figure 1 a, c, Figure 2 d, f)

**Michael Wagner:** Planning and performing the characterization of the nanoparticles and loading efficiency (Figure 2 c, Suppl. Figure 1).

**Mark Clemens:** Planning and analyzing *in vivo* LSM experiments (figure 5 b), planning and analyzing primary hepatocyte experiments (figure 1 d and 2 h), planning statistical analysis, writing portions of the manuscript.

**Nayla Jbeily:** Mainly contributed to the performance of intravital microscopy experiments

**Nicole Koch:** Planning, performing and analyzing experiments for RNAi and anti-HMGCR antibody (Figure 7 b, c, and Suppl. Figure 3).

**Michael Gottschaldt:** Scientific supervision of nanoparticle analysis, supervised and designed nanoparticle characterization

**Volodymyr Ermolayev and Nicolas Bézière:** Performed MSOT experiments

**Vasilis Ntziachristos:** Planned, designed and supervised MSOT analyses

**Jürgen Popp:** Suggested use of MSOT to image nanoparticles; planned and designed biophotonic analyses

**Michael Kessels:** Planning and scientific supervision of *hmgcr* cloning and immunodetections, wrote parts of the manuscript

**Britta Qualmann:** Planning and scientific supervision of *hmgcr* cloning and immunodetections, wrote parts of the manuscript

**Ulrich S. Schubert:** Design of study (chemistry), planning and supervision of nanoparticle design, wrote the manuscript

**Michael Bauer:** Design of study (life sciences), planning of functionalized nanoparticles, wrote the manuscript

### **Competing financial interests**

Anja Traeger, Ulrich S. Schubert and Michael Bauer are co-founders of SmartDyeLivery GmbH, a university spin-off company engaged in the development of a platform for nanoformulated drugs to restore critical cellular signaling functions. The IP based upon the present data will be transformed from the University Hospital Jena and the Friedrich-Schiller University Jena to SmartDyeLivery GmbH.

## Citations

1. de Fougerolles, A., Vornlocher, H.P., Maraganore, J. & Lieberman, J. Interfering with disease: a progress report on siRNA-based therapeutics. *Nat. Rev.* **6**, 443-453 (2007).
2. Kole, R., Krainer, A.R. & Altman, S. RNA therapeutics: beyond RNA interference and antisense oligonucleotides. *Nat. Rev.* **11**, 125-140.
3. Davidson, B.L. & McCray, P.B., Jr. Current prospects for RNA interference-based therapies. *Nat. Rev.* **12**, 329-340.
4. Dudek, H., Wong, D.H., Arvan, R., Shah, A., Wortham, K., Ying, B., Diwanji, R., Zhou, W., Holmes, B., Yang, H., Cyr, W.A., Zhou, Y., Sah, A., Farkiwala, R., Lee, M., Ling, Y., Rettig, G.R., Collingwood, M.A., Basu, S.K. Behlke, M.A., Brown, B.D. Knockdown of  $\beta$ -catenin with Dicer-Substrate siRNA Reduces Liver Tumor BURden In vivo. *Mol. Ther.* **22**, 92-101 (2014)
5. Shim, M.S. & Kwon, Y.J. Efficient and targeted delivery of siRNA in vivo. *FEBS J.* **277**, 4814-4827.
6. Hong, B.J., Chipre, A.J. & Nguyen, S.T. Acid-Degradable Polymer-Caged Lipoplex (PCL) Platform for siRNA Delivery: Facile Cellular Triggered Release of siRNA. *J. Am. Chem. Soc.* **135** 17655–17658 (2013).
7. David, S., Pitard, B., Benoit, J.P. & Passirani, C. Non-viral nanosystems for systemic siRNA delivery. *Pharmacol. Res.* **62**, 100-114.
8. Yu, B. et al. Targeted nanoparticle delivery overcomes off-target immunostimulatory effects of oligonucleotides and improves therapeutic efficacy in chronic lymphocytic leukemia. *Blood* **121**, 136-147.
9. Recknagel, P. et al. Liver dysfunction and phosphatidylinositol-3-kinase signalling in early sepsis: experimental studies in rodent models of peritonitis. *PLoS Med.* **9**, e1001338 (2012).
10. Wang, J., Lu, Z., Wientjes, M.G. & Au, J.L. Delivery of siRNA therapeutics: barriers and carriers. *AAPS J.* **12**, 492-503.
11. Whitehead, K.A., Langer, R. & Anderson, D.G. Knocking down barriers: advances in siRNA delivery. *Nat. Rev.* **8**, 129-138 (2009).
12. Qasim, W. & Thrasher, A.J. RISC control for gene therapy. *Nat. Biotechnol.* **24**, 661-662 (2006).
13. Buyens, K. et al. Liposome based systems for systemic siRNA delivery: stability in blood sets the requirements for optimal carrier design. *J. Control Release* **158**, 362-370.
14. Islam, M.A. et al. Major degradable polycations as carriers for DNA and siRNA. *J. Control Release* (2014).
15. Nishina, K. et al. Efficient in vivo delivery of siRNA to the liver by conjugation of alpha-tocopherol. *Mol. Ther.* **16**, 734-740 (2008).
16. Soutschek, J. et al. Therapeutic silencing of an endogenous gene by systemic administration of modified siRNAs. *Nature* **432**, 173-178 (2004).
17. Mingozzi, F. & High, K.A. Therapeutic in vivo gene transfer for genetic disease using AAV: progress and challenges. *Nat. Rev.* **12**, 341-355 (2011).
18. Wagner, E. Polymers for siRNA Delivery: Inspired by Viruses to be Targeted, Dynamic, and Precise. *Acc. Chem. Res.* **45**, 1005–1013 (2012).
19. Kay, M.A. State-of-the-art gene-based therapies: the road ahead. *Nat. Rev.* **12**, 316-328.
20. Ozdemir, V. et al. Shifting emphasis from pharmacogenomics to theragnostics. *Nat. Biotechnol.* **24**, 942-946 (2006).

21. Pan, D.P.J. Theranostic Nanomedicine with Functional Nanoarchitecture. *Mol. Pharmaceut.* **10**, 781-782 (2013).
22. Quaglia, A. et al. Liver after hepatocyte transplantation for liver-based metabolic disorders in children. *Cell transplantation* **17**, 1403-1414 (2008).
23. Dhawan, A., Mistry, R.R. & Hughes, R.D. Hepatocyte transplantation for liver-based metabolic disorders. *J. Inherit. Metab. Dis.* **29**, 431-435 (2006).
24. Schroit, A.J., Madsen, J. & Nayar, R. Liposome-cell interactions: in vitro discrimination of uptake mechanism and in vivo targeting strategies to mononuclear phagocytes. *Chem. Phys. Lipids* **40**, 373-393 (1986).
25. Sato, A., Takagi, M., Shimamoto, A., Kawakami, S. & Hashida, M. Small interfering RNA delivery to the liver by intravenous administration of galactosylated cationic liposomes in mice. *Biomaterials* **28**, 1434-1442 (2007).
26. Akinc, A. et al. Development of lipidoid-siRNA formulations for systemic delivery to the liver. *Mol. Ther.* **17**, 872-879 (2009).
27. Roth, M., Araya, J.J., Timmermann, B.N. & Hagenbuch, B. Isolation of modulators of the liver-specific organic anion-transporting polypeptides (OATPs) 1B1 and 1B3 from *Rollinia emarginata* Schlecht (Annonaceae). *J. Pharmacol. Exp. Ther.* **339**, 624-632.
28. Stieger, B. The role of the sodium-taurocholate cotransporting polypeptide (NTCP) and of the bile salt export pump (BSEP) in physiology and pathophysiology of bile formation. *Handbook of experimental pharmacology*, 205-259 (2011).
29. Okamoto, E., Kyo, A., Yamanaka, N., Tanaka, N. & Kuwata, K. Prediction of the safe limits of hepatectomy by combined volumetric and functional measurements in patients with impaired hepatic function. *Surgery* **95**, 586-592 (1984).
30. Cherrick, G.R., Stein, S.W., Leevy, C.M. & Davidson, C.S. Indocyanine green: observations on its physical properties, plasma decay, and hepatic extraction. *J. Clin. Invest.* **39**, 592-600 (1960).
31. Leevy, C.M., Mendenhall, C.L., Lesko, W. & Howard, M.M. Estimation of hepatic blood flow with indocyanine green. *J. Clin. Invest* **41**, 1169-1179 (1962).
32. Recknagel, P., Claus, R.A., Neugebauer, U., Bauer, M. & Gonnert, F.A. In vivo imaging of hepatic excretory function in the rat by fluorescence microscopy. *J Biophoton.* **5**, 571-581 (2012).
33. (CDER), U.S.D.o.H.a.H.S.F.a.D.A.C.f.D.E.a.R. Drug Interaction Studies — Study Design, Data Analysis, Implications for Dosing, and Labeling Recommendations. *Clin.Pharmacol.* (2012).
34. Burchard, W. Solution properties of branched macromolecules. *Adv. Polym. Sci.* **143**, 113-194 (1999).
35. Gurcel, L., Abrami, L., Girardin, S., Tschopp, J. & van der Goot, F.G. Caspase-1 activation of lipid metabolic pathways in response to bacterial pore-forming toxins promotes cell survival. *Cell* **126**, 1135-1145 (2006).
36. Chumakova, O.V. et al. Composition of PLGA and PEI/DNA nanoparticles improves ultrasound-mediated gene delivery in solid tumors in vivo. *Cancer letters* **261**, 215-225 (2008).
37. Liang, G.F. et al. PLGA-based gene delivering nanoparticle enhance suppression effect of miRNA in HePG2 cells. *Nanoscale research letters* **6**, 447 (2011).
38. Patil, Y. & Panyam, J. Polymeric nanoparticles for siRNA delivery and gene silencing. *Int. J. Pharm.* **367**, 195-203 (2009).

39. Su, W.P., Cheng, F.Y., Shieh, D.B., Yeh, C.S. & Su, W.C. PLGA nanoparticles codeliver paclitaxel and Stat3 siRNA to overcome cellular resistance in lung cancer cells. *International journal of nanomedicine* **7**, 4269-4283 (2012).
40. Karlgren, M. et al. In vitro and in silico strategies to identify OATP1B1 inhibitors and predict clinical drug-drug interactions. *Pharm. Res.* **29**, 411-426 (2012).
41. Dahlman, J.E., et al. in vivo endothelial siRNA delivery using polymeric nanoparticles with low molecular weight. *Nat. Biotechnol.* **9**, 648-55 (2014)
42. Cartiera, M.S., Johnson, K.M., Rajendran, V., Caplan, M.J. & Saltzman, W.M. The uptake and intracellular fate of PLGA nanoparticles in epithelial cells. *Biomaterials* **30**, 2790-2798 (2009).
43. Panyam, J., Zhou, W.Z., Prabha, S., Sahoo, S.K. & Labhasetwar, V. Rapid endo-lysosomal escape of poly(DL-lactide-co-glycolide) nanoparticles: implications for drug and gene delivery. *FASEB J.* **16**, 1217-1226 (2002).
44. Gilleron, J. et al. Image-based analysis of lipid nanoparticle-mediated siRNA delivery, intracellular trafficking and endosomal escape. *Nat. Biotechnol.* **31**, 638-646 (2013).
45. Puri, V. et al. Cholesterol modulates membrane traffic along the endocytic pathway in sphingolipid-storage diseases. *Nat. Cell Biol.* **1**, 386-388 (1999).
46. Weber, M. et al. Hepatic induction of cholesterol biosynthesis reflects a remote adaptive response to pneumococcal pneumonia. *FASEB J.* **26**, 2424-2436 (2012).
47. Neijssen, J. et al. Cross-presentation by intercellular peptide transfer through gap junctions. *Nature* **434**, 83-88 (2005).
48. De Maio, A., Gingalewski, C., Theodorakis, N.G. & Clemens, M.G. Interruption of hepatic gap junctional communication in the rat during inflammation induced by bacterial lipopolysaccharide. *Shock* **14**, 53-59 (2000).
49. Kamps, J.A., Morselt, H.W., Swart, P.J., Meijer, D.K. & Scherphof, G.L. Massive targeting of liposomes, surface-modified with anionized albumins, to hepatic endothelial cells. *Proc. Natl Acad Sci U S A* **94**, 11681-11685 (1997).
50. Su, R., Ermilov, S.A., Liopo, A.V. & Oraevsky, A.A. Three-dimensional optoacoustic imaging as a new noninvasive technique to study long-term biodistribution of optical contrast agents in small animal models. *J. Biomed. Opt.* **17**, 101506 (2012).
51. Tsyboulski, D.A. et al. Enabling in vivo measurements of nanoparticle concentrations with three-dimensional optoacoustic tomography. *J Biophoton.* **7**, 581-588 (2014).
52. Wang, L.V. & Hu, S. Photoacoustic tomography: in vivo imaging from organelles to organs. *Science (New York, N.Y)* **335**, 1458-1462 (2012).
53. Cohen, J.L., Schubert, S., Hornig, S., Cohen, J.A. & Frechet, J.M.J. Acetal-modified dextran particles for siRNA delivery. *Bioconj. Chem.* **22** (2011).
54. Rinkenauer, A.C. et al. Parallel High-Throughput Screening of Polymer Vectors for Nonviral Gene Delivery: Evaluation of Structure-Property Relationships of Transfection. *Acs. Comb. Sci.* **15**, 475-482 (2013).
55. Chen, P.S., Toribara, T.Y. & Warner, H. Microdetermination of Phosphorus. *Anal. Chem.* **28**, 1756-1758 (1956).
56. Razansky, D., Buehler, A. & Ntziachristos, V. Volumetric real-time multispectral optoacoustic tomography of biomarkers. *Nat. Protoc.* **6**, 1121-1129 (2011).

57. Sarantopoulos, A., Themelis, G. & Ntziachristos, V. Imaging the bio-distribution of fluorescent probes using multispectral epi-illumination cryoslicing imaging. *Mol. Imaging Biol.* **13**, 874-885 (2011).
58. Gripon, P. et al. Infection of a human hepatoma cell line by hepatitis B virus. *Proc Natl Acad Sci U S A* **99**, 15655-15660 (2002).
59. Schwintzer, L. et al. The functions of the actin nucleator Cobl in cellular morphogenesis critically depend on syndapin I. *EMBO J.* **30**, 3147-3159 (2011).
60. Dharmalingam, E. et al. F-BAR proteins of the syndapin family shape the plasma membrane and are crucial for neuromorphogenesis. *J. Neurosci.* **29**, 13315-13327 (2009).



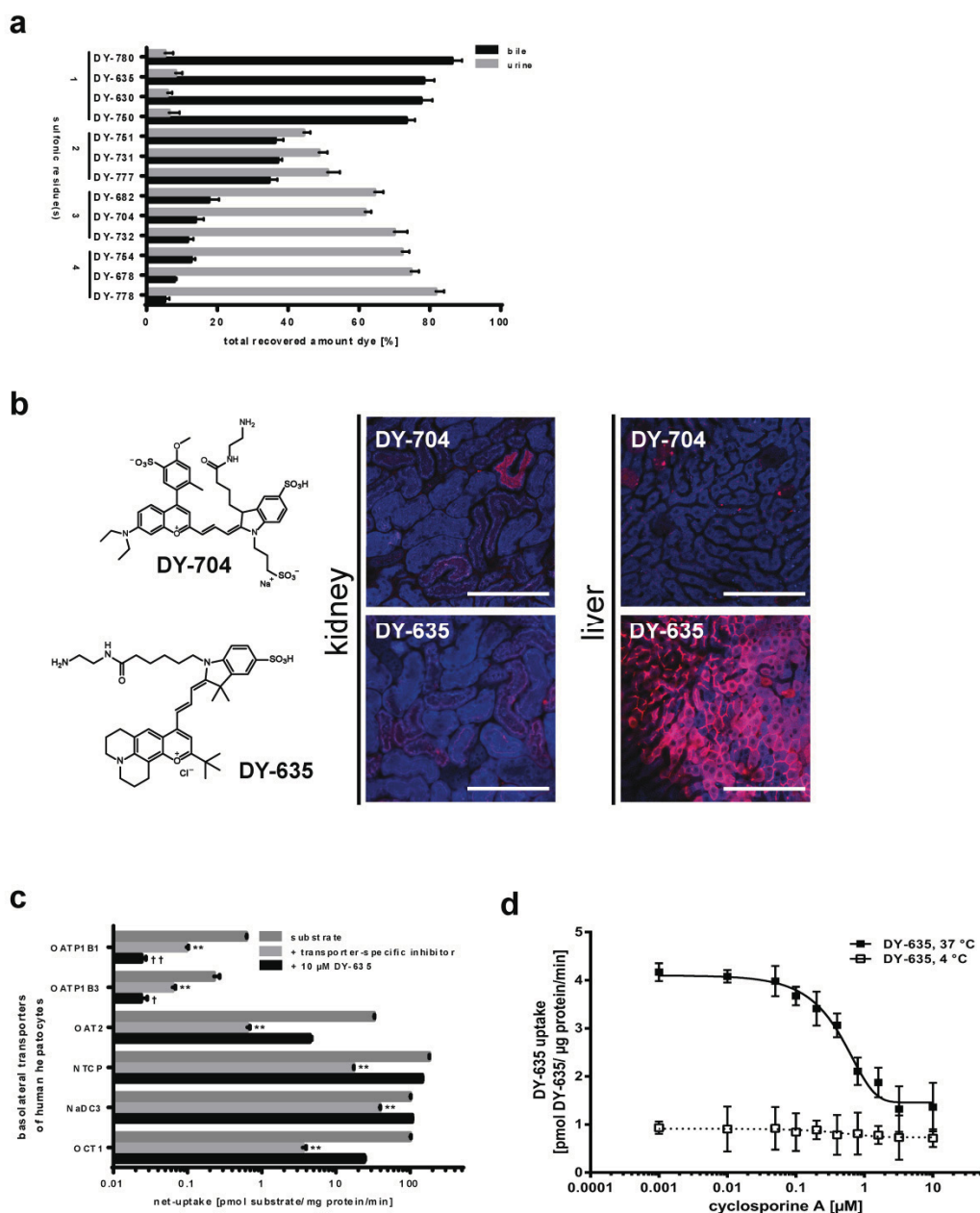


**Figure 1 Selection of polymethine dyes with organ-selective elimination** (a) A variety of polymethine dyes with varying numbers of sulfonic residues were screened in rats regarding net organ-specific clearance by liver and kidneys and their applicability for biophotonic detection, e.g. by intravital microscopy; ( $n = 3$ ; mean  $\pm$  S.E.M.). (b) Structures of DY-635, a dye with preferential hepatobiliary clearance and DY-704 with preferential renal elimination and their cell-specific uptake as visualized by intravital laser scanning confocal microscopy in liver and kidney (scale bars 150  $\mu\text{m}$ ). (c) DY-635 was further characterized regarding its affinity to transporters responsible for uptake of substrates into the liver in a heterologous expression system (HEK cells). While DY-635 exhibited moderate affinity to several transporters, its affinity to OATP1B1 and OATP1B3 exceeded that of rifampicin or cyclosporine A, i.e. the FDA-proposed competitors for drug development purposes. Bars show mean  $\pm$  S.E.M.; significance was tested by one-way ANOVA followed by Tukey's test; \* indicates  $p < 0.05$  \*\* indicates  $p < 0.01$  for uptake of substrate in the presence of DY-635 (hatched bars) or the FDA-proposed competitor (black bars) compared to substrate alone. † and †† indicate  $p < 0.05$  and  $p < 0.01$ , respectively, for the comparison between DY-635 and the FDA-proposed competitor. (d) Uptake of DY-635 by primary murine hepatocytes is temperature sensitive and inhibited by cyclosporine A in a dose dependent manner with an  $\text{IC}_{50}$  of 379 nM.

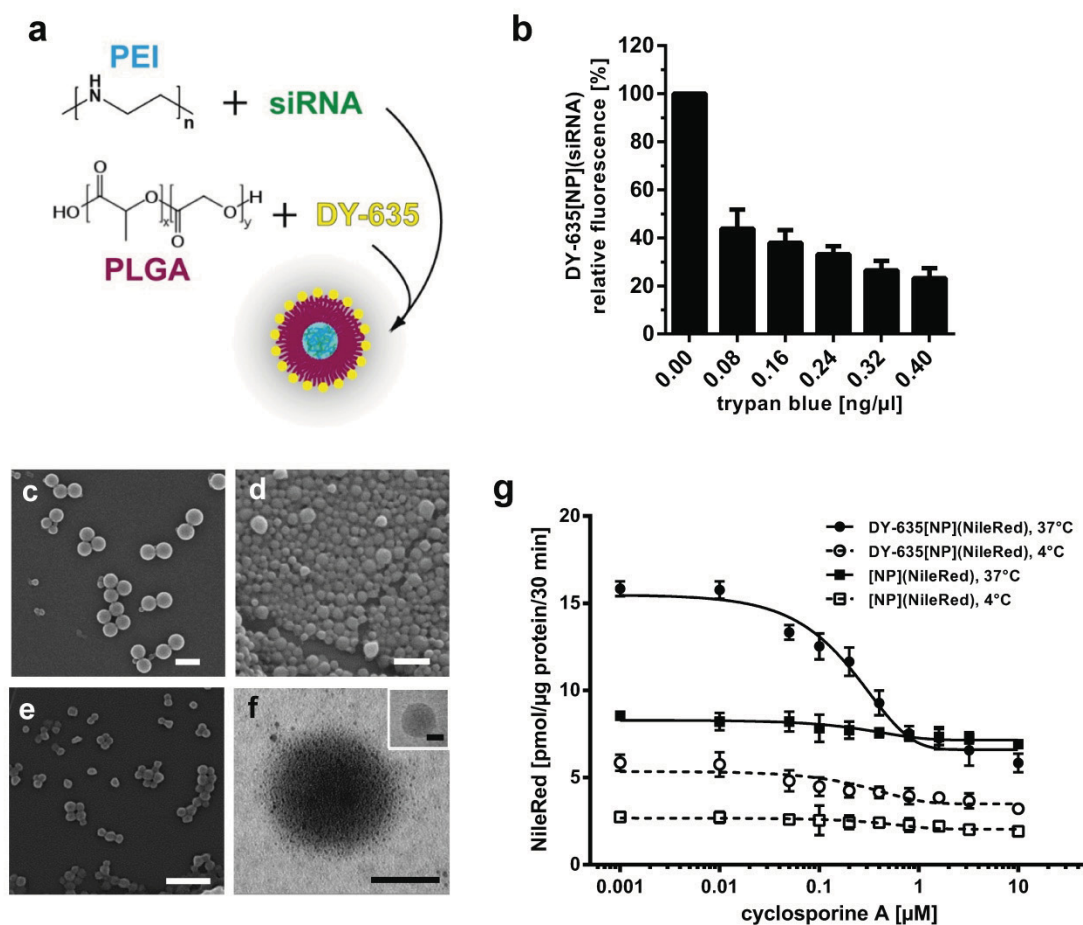


**Figure 2 Formation and characterization of nanoparticles** (a) Dye-functionalization of nanoparticles. PLGA is labelled with DY-635 via EDC coupling, siRNA is complexed with LMW PEI, and nanoparticles are formed by double emulsion procedure. (b) Surface fluorescence quenching of DY-635[NP](-) indicates that DY-635 is exposed at the NP surface (n=3, mean  $\pm$  S.E.M.) (c-e) Electron microscopy of nanoparticles ([NP](-), DY-635[NP](-), DY-635[NP](siRNA)) reveals regular round shape (scale bars 500 nm) (f) Higher power TEM of DY-635[NP](siRNA) after treatment with  $\text{Cu}^{2+}$ -ions (inset shows the corresponding cryo-TEM image) suggests siRNA is encapsulated and not aggregated to the surface. (scale bars 100 nm) (g) Uptake of DY-635 functionalized nanoparticles is enhanced compared to non-functionalized NP and, unlike that of non-functionalized NP is inhibited in a dose-dependent manner by cyclosporine A with an  $\text{IC}_{50}$  of 209 nM, similar to the uptake of free DY-635.

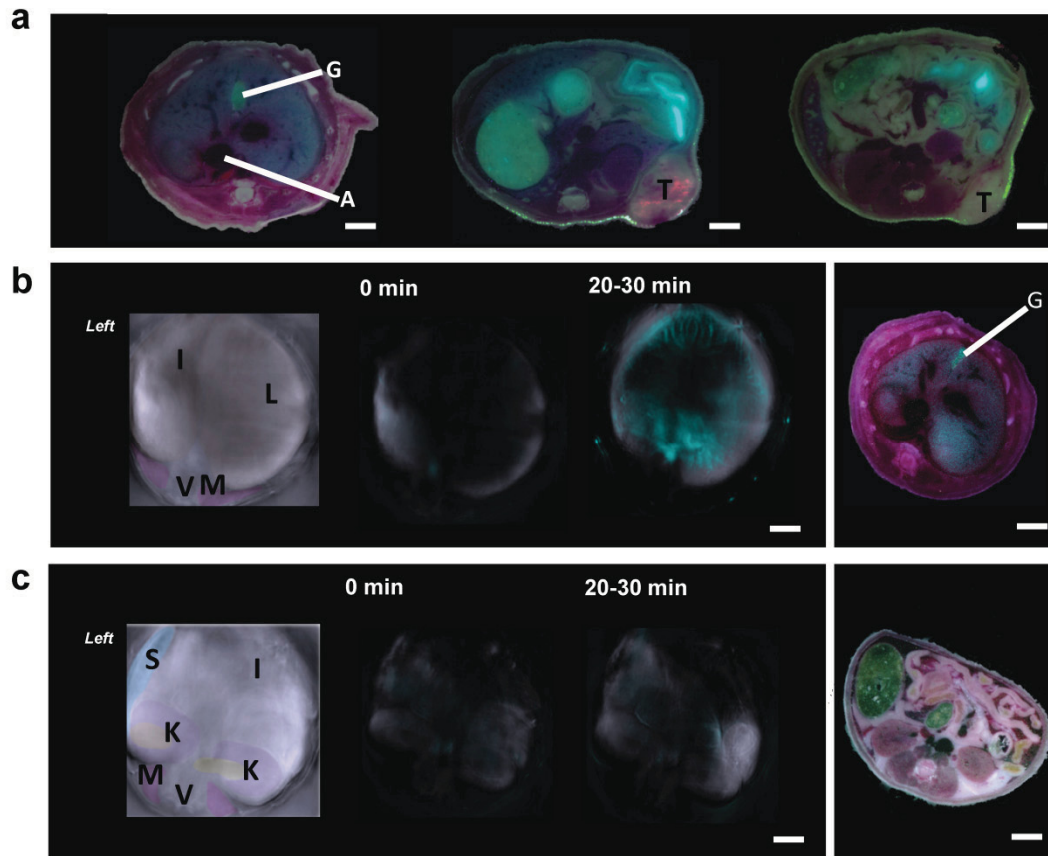


**Figure 3 Biodistribution of nanoparticles** (a) Body distribution of dye-functionalized nanoparticles with an infrared cargo (DY-635[NP](DY-780)) in an athymic Nude-Foxn1<sup>nu</sup> mouse bearing a MDA-MB-231 human breast cancer xenograft (“T”) confirmed selective uptake and excretion via the hepatobiliary route as reflected in accumulation of the dye in the gall bladder (“G”).(b,c) CD1 mice injected with the same nanoparticle and assessed by Multispectral Optoacoustic Tomography acquiring image data from several wavelengths (690 nm, 710 nm, 750 nm, 770 nm, 780 nm, 800 nm, 810 nm, 850 nm, 4 frames/ wavelength, 0.1 mm step size) over an abdominal area of 1.7 cm using a frequency of 54.55 kHz (scale bars 5 mm).(b) Sections through the upper abdomen are single-spectral that elucidate anatomical structures (left panel; “I” intestines, “L” liver, “V” vertebral column, “M” autochthonous back muscles, “A” = aorta) or processed multispectrally to visualize the dye cargo (DY-780) immediately prior to injection (0 min) or during early uptake (20 - 30 min after injection). Far right panel: Corresponding cryosection of the upper abdomen; “G” indicates gall bladder containing the dye. (c) Subsequent sections through the lower abdomen processed for structural information (left panel; in addition the kidneys (“K”) and spleen (“S”) are visible) middle and right panels are processed to visualize the dye cargo. The IR dye is restricted to the upper abdomen and depicts liver and biliary tree.

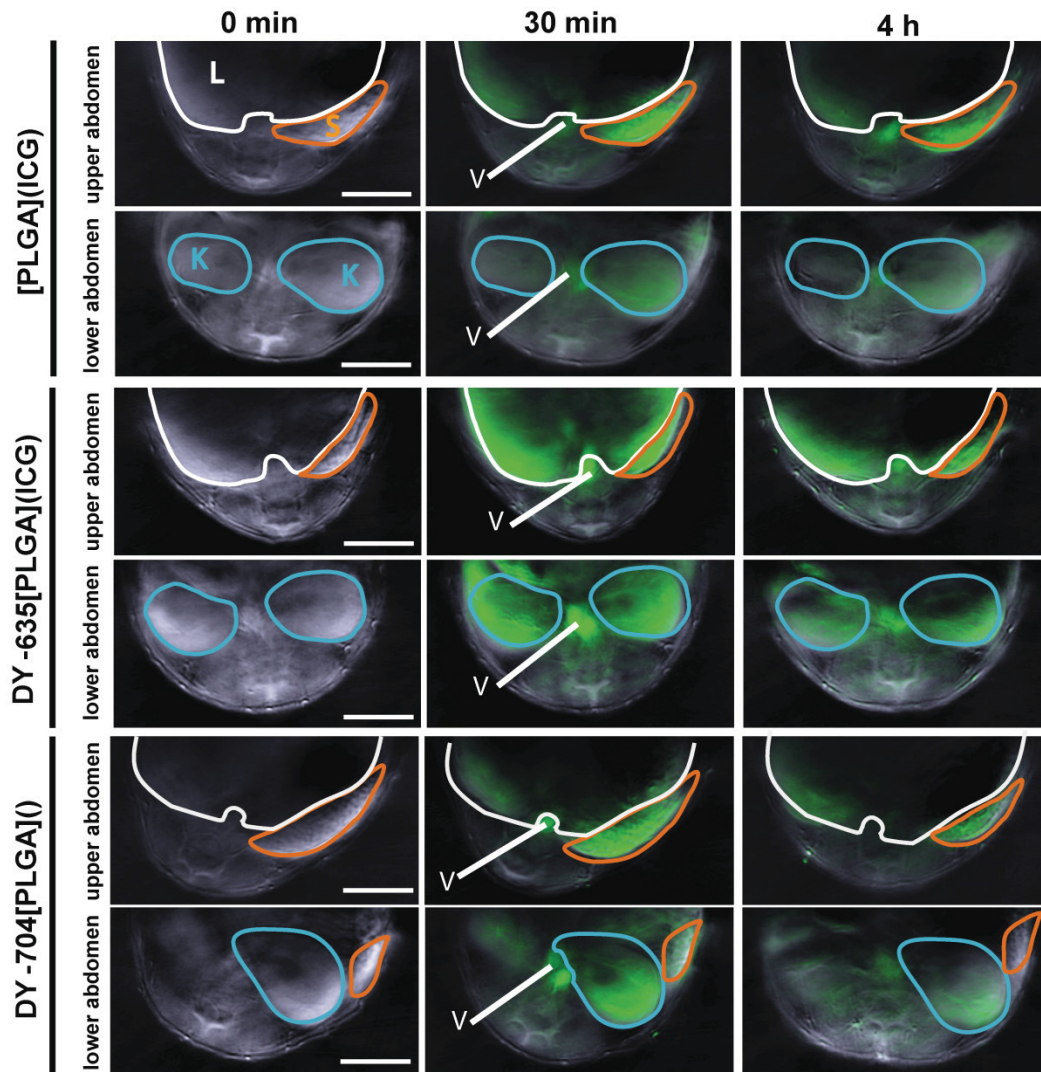


**Figure 4 Organ distribution of dye-functionalized NP** MSOT images of non-functionalized NP or NP functionalized with DY-635 with ICG as cargo or functionalized with DY-704. The dye-moiety (in case of DY-704) or ICG cargo (in the case of DY-635 or non-functionalized NP) were used for imaging by MSOT; NP are shown in green irrespective of the dye moiety. All NP were identified in the circulation (V = retroperitoneal vessels) and showed uptake by spleen (S) indicating phagocytic clearance; however, only DY-635 functionalized NP showed significant uptake by the liver (L), whereas DY-704 functionalized nanoparticle had an increased accumulation in the kidneys (K) (scale bars 5 mm)

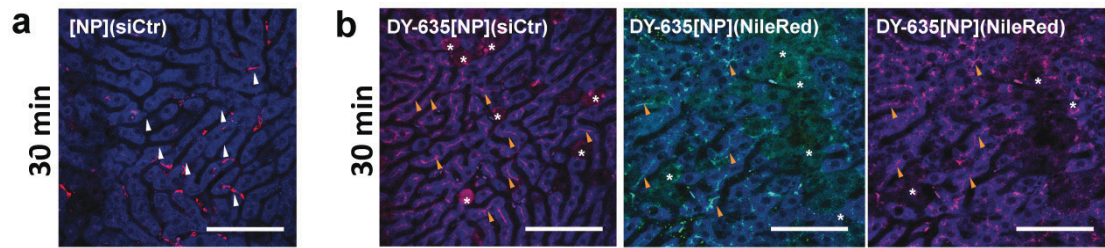


**Figure 5 Cell-type distribution of dye-functionalized NP** (a) *In vivo* laser scanning confocal images of mouse liver (blue) 30 minutes following injection of bare PLGA-nanoparticles containing Nile red (red). These appear almost exclusively in sinusoidal lining cells (Kupffer cells, white arrow; scale bar 100  $\mu\text{m}$ ), (b) NP functionalized with DY-635, in contrast, accumulate in hepatocytes where the Nile red cargo (green) and DY-635 (red) are found either in bile canaliculi (orange arrows) or in hepatocyte cytoplasm (\*) (scale bars 100  $\mu\text{m}$ ).

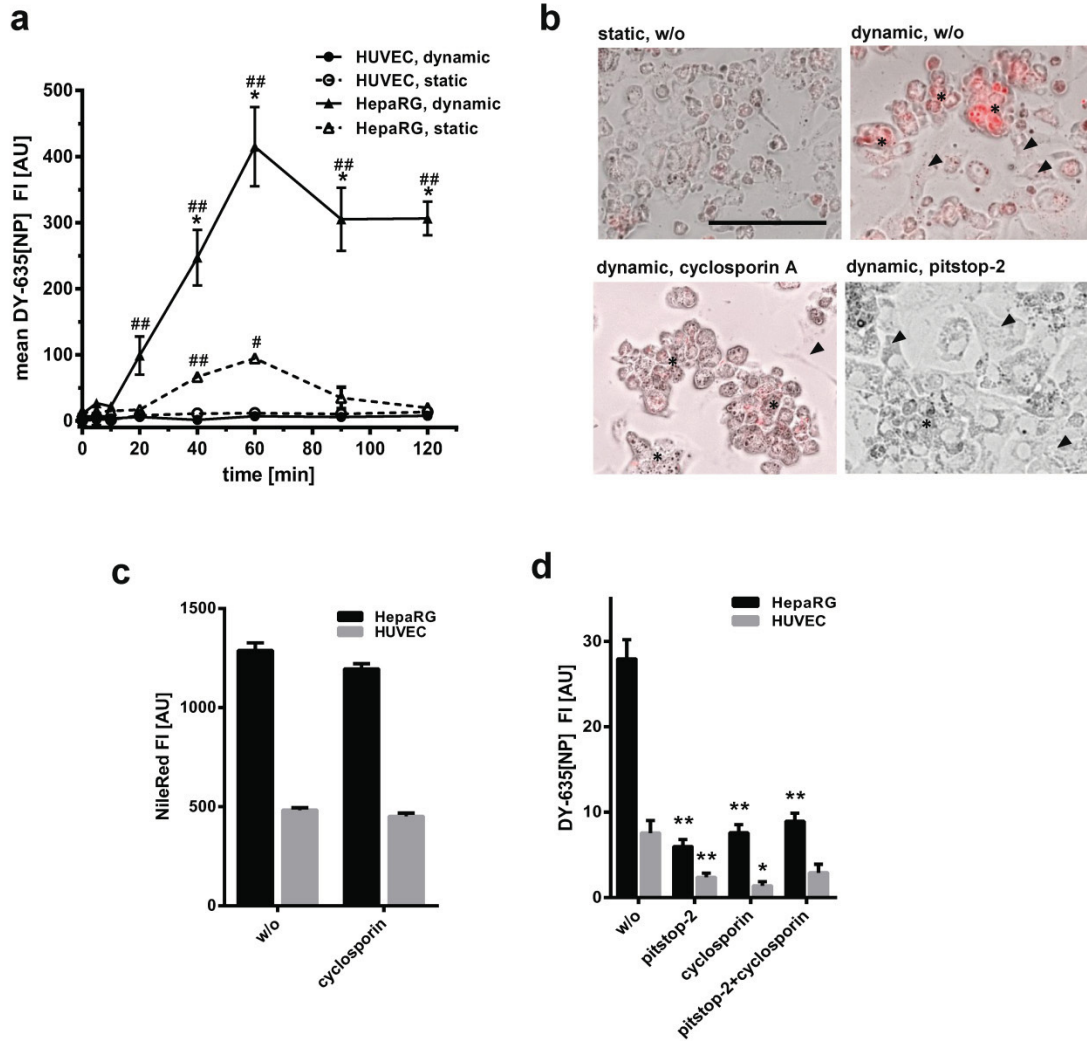


**Figure 6 Uptake of nanoparticles exposing DY-635 on their surface *in vitro*** (a) A microfluidic-assisted ‘organoid’ composed of co-cultured human hepatoma (HepaRG) and human vascular endothelial (HUVEC) cells demonstrates an increased uptake by the hepatocytes preferentially if cells are subjected to flow conditions (“dynamic”). Under flow conditions, this organoid better recapitulates the function of the liver *in vivo* by circulating fluid containing NP through the equivalent of the space of Disse. (b) Representative overlay of brightfield and fluorescence images of HepaRG cells differentiated to hepatocytes (stars) or endothelia like (arrow head) cells cultured under static or dynamic conditions reflect increased uptake of DY-635[NP](-) (red) after 90 min of incubation if cells are subjected to flow. This uptake can be inhibited by cyclosporine A as well as Pitstop-2. DY-635[NP](-) uptake was assessed by epi-fluorescence microscopy (Cy5 channel); (scale bar 100  $\mu$ m). To characterize cell selectivity and uptake mechanisms, further experiments were conducted: (c) Uptake of DY-635[NP](-) is inhibitable by cyclosporine A, a ligand for OATPs and NTCP in HepaRG but not in HUVEC that do not express these transporters; inhibition by Pitstop-2 suggests clathrin-mediated endocytosis as molecular mechanism of cellular uptake. (d) Cyclosporine A failed to affect the overall less pronounced basal uptake of [NP](nile red) that are not exposing DY-635 on their surface. For the statistical analysis a generalized mixed model was applied, taking into account dependent (time, flow condition) and independent (cell type) data. Post hoc analysis was performed using Tukey’s test. In panel (a) \* indicates  $p < 0.05$  comparing respective static vs dynamic conditions; # indicates  $p < 0.05$ , ## indicates  $p < 0.01$  for the comparison between HepaRG and HUVEC. In panel (c)† and †† indicate  $p < 0.01$  and  $p < 0.01$  respectively, for the uptake of DY-635[NP](-) in HepaRG or HUVEC in the absence of a co inhibitor (w/o) compared to the uptake in presence of cyclosporine A or Pitstop-2.

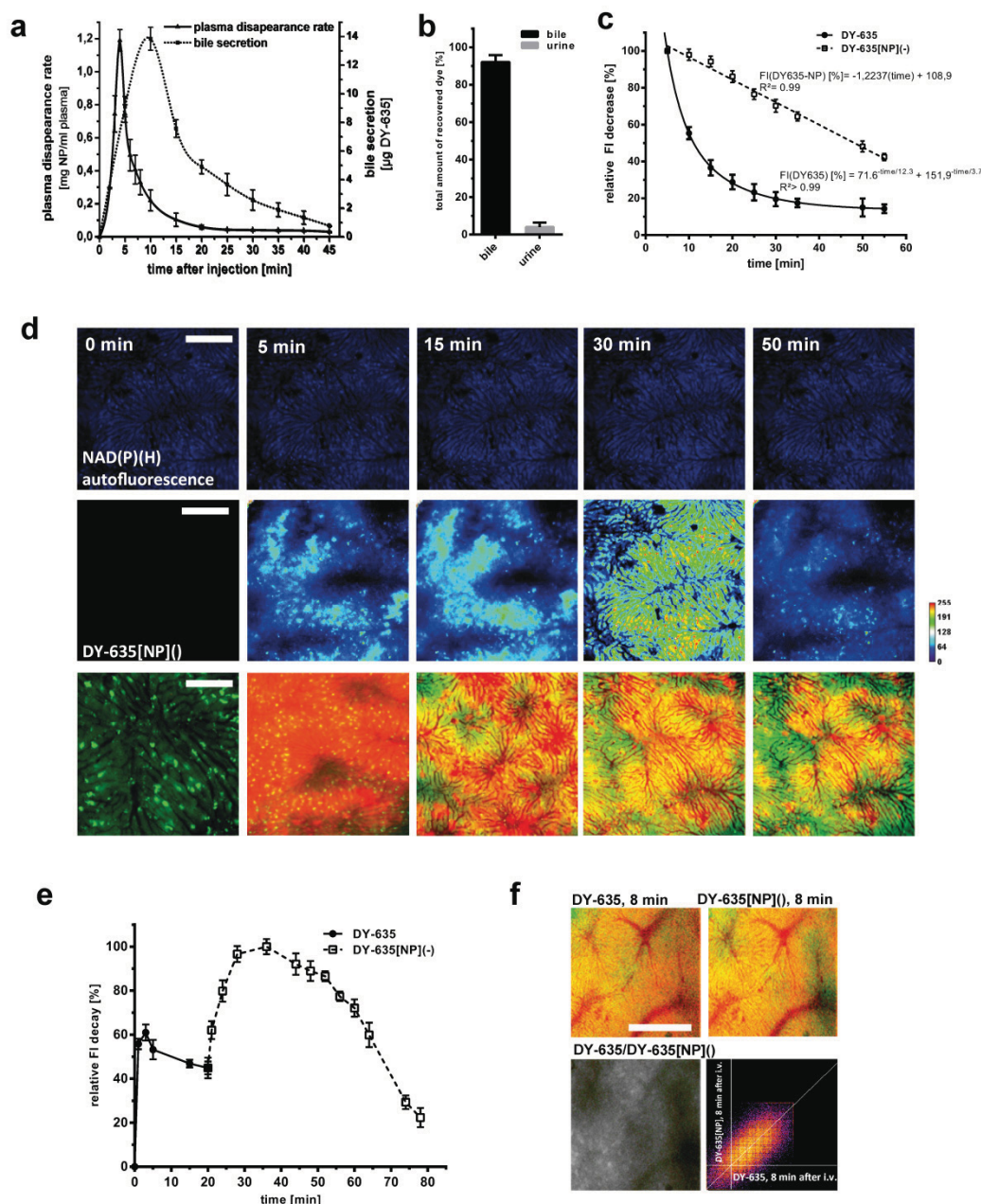


**Figure 7 Pharmacokinetics of DY-635[NP](-)** (a) Time course of arterial plasma concentration after central venous application of DY-635[NP](-) (left ordinate) at time “0” and appearance of the desorbed dye in bile (right ordinate) (n=3, mean ± SE.M.). (b) Percentage of recovered free dye in bile and urine after administration of DY-635[NP](-). (c) Fluorescence decay over liver parenchyma in the Cy5 channel after administration of unbound DY-635 or DY-635[NP](-) revealing exponential decay for the free dye and almost linear decay for DY-635[NP](-)-associated fluorescence (n=3 per 25 ROIs per n; mean ± SE.M.). (d) Intravital epifluorescence microscopy to visualize acinar distribution of DY-635[NP](-). Upper panel background fluorescence of the liver (blue). Middle panel: Heatmap (blue: low intensity, red: high intensity) reflecting signal distribution which is associated with the pericentral region of the liver lobule early upon injection of DY-635[NP](-) and spreads toward midzonal and even periportal region over time. Lower panel: Corresponding false color images of association of DY-635-associated fluorescence (red) with liver parenchyma (green): Fluorescence is restricted to the vascular compartment early upon injection (5 min); Yellow signal indicating colocalization of dye with liver parenchyma is increasingly observed over time. (scale bars 100 µm) (e) Theranostic use of the free dye DY-635 to predict subsequent uptake of DY-635[NP](-). DY-635 was injected at time “0” followed by injection of DY-635[NP](-) at 20 min. (f) Intensity of fluorescence signal over liver parenchyma; right panel: signals obtained upon injection of free dye and dye-functionalized nanoparticles are correlated. (n=2, 20 ROIs per n; mean ± S.E.M.) (scale bar 100 µm).

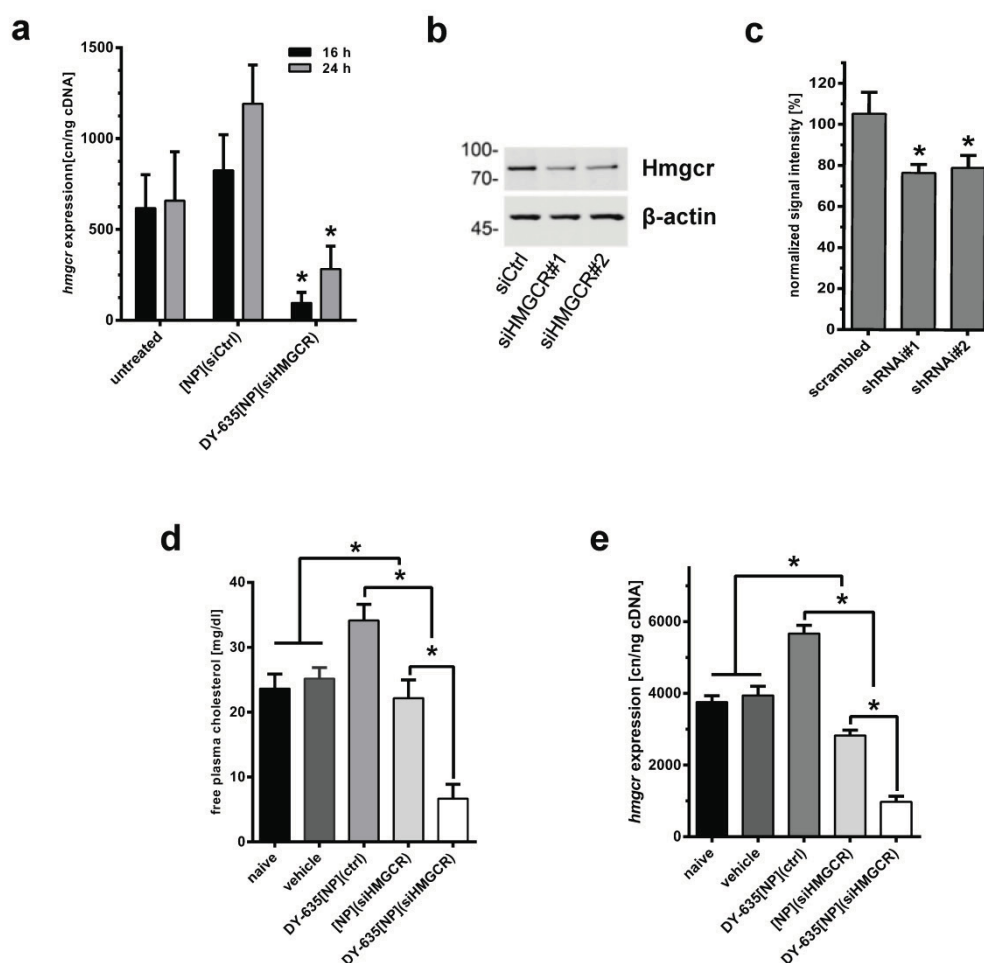


**Figure 8** *hmgcr* RNAi using DY-635[NP] as carrier (a) A significant reduction in *hmgcr* gene-expression was achieved with a maximum at 16 hours after transfection in naive Hepa1-6 cells. In contrast to DY-635[NP](siRNA) an increase in *hmgcr* was observed after application of the carrier (DY-635[NP](siCtrl)). Mean  $\pm$  S.E.M. \*  $p < 0.05$  compared to respective siCtrl by ANOVA and Tukey posthoc. (b,c) To validate siRNAs, the efficacy of two RNAi sequences (shRNA#1, shRNA#2) against *hmgcr* was analyzed in a heterologous expression model using western blot (b), and addressed by determining endogenous HMGCR levels in HepG2 cells using anti-HMGCR immuno-fluorescence analysis (c). A significant reduction in *hmgcr* protein could be achieved with both RNAs; for further RNAi experiments RNAi sequence#2 was selected. Mean  $\pm$  S.E.M. \*  $p < 0.05$  vs. control by ANOVA and Dunnett's test. (d) *In vivo* RNAi results in mice injected with [NP](siHMGR) (n=9) or DY-635[NP] loaded with siHMGR (n=12) or a control RNA (siCtrl) (n=12); animals injected with the vehicle (5 % sterile glucose solution; n=4) served as sham controls. *hmgcr* gene expression was analyzed using relative quantification compared to untreated animals (n=4) in RNA prepared from liver tissue by RT-qPCR. Consistent with the results of the cell culture, DY-635[NP](siCtrl) induced the *hmgcr* gene expression while [NP](siHMGR) blunted this effect but failed to lower the *hmgcr* expression compared to untreated or sham animals. Using similar siHMGR amounts encapsulated in DY-635[NP](siHMGR), *hmgcr* expression was lowered by 75 % compared to untreated animals. Mean  $\pm$  S.E.M. \*  $p < 0.05$  by ANOVA and Tukey test. (e) Altered gene expression of *hmgcr* was reflected in plasma-cholesterol levels of these animals. Mean  $\pm$  S.E.M. by ANOVA and Tukey test.



**Table 1 Characterization of nanoparticles**

	targeting moiety	active payload	size <sup>a</sup> (d in nm)	surface charge <sup>b</sup> (in mV)	further data
[NP](-)	-	-	210 ± 50	-7 ± 2	
[NP](siRNA)	-	siRNA <sup>e</sup>	190 ± 32	+78 ± 5	
[NP](NileRed)	-	NileRed	196 ± 24	-25 ± 18	
[NP](ICG)	-	ICG	145 ± 45	-24 ± 6	
DY-635[NP](-)	+	-	170 ± 5	-13 ± 5	
DY-635[NP](siRNA)	+	siRNA <sup>e</sup>	176 ± 22	-11 ± 6	0.78 <sup>c</sup> , 87.4 ± 2.5% <sup>d</sup>
DY-635[NP](NileRed)	+	ICG	142 ± 18	-19 ± 7	2 wt%f
DY-635[NP](ICG)	+	NileRed	151 ± 32	-63 ± 3	2 wt%f
DY-704[NP](-)	+	-	155 ± 37	-42 ± 6	

<sup>a</sup> determined by DLS

<sup>b</sup> zeta potential

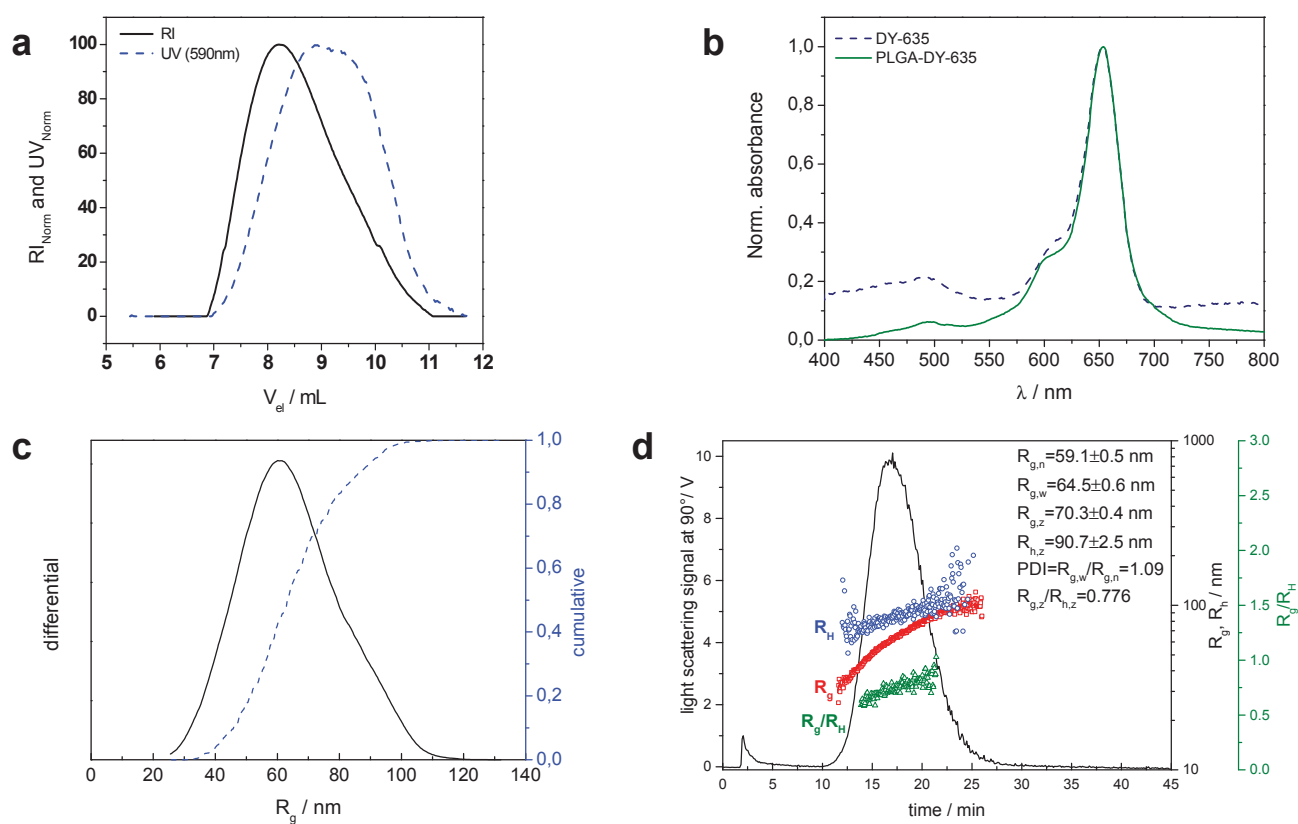
<sup>c</sup> Rg/Rh determined by AF4

<sup>d</sup> encapsulation efficiency

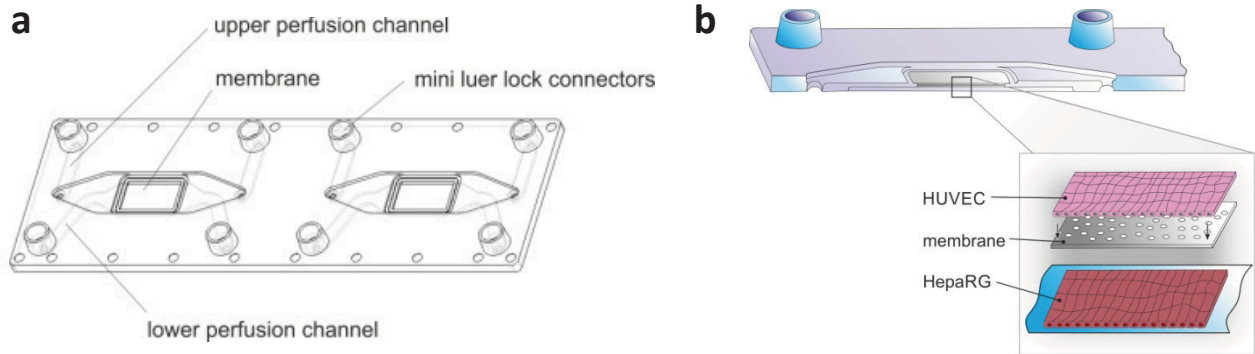
<sup>e</sup> complexed with LMW PEI, N/P10

<sup>f</sup> nanoprecipitation, indicated weight %

## Supporting information

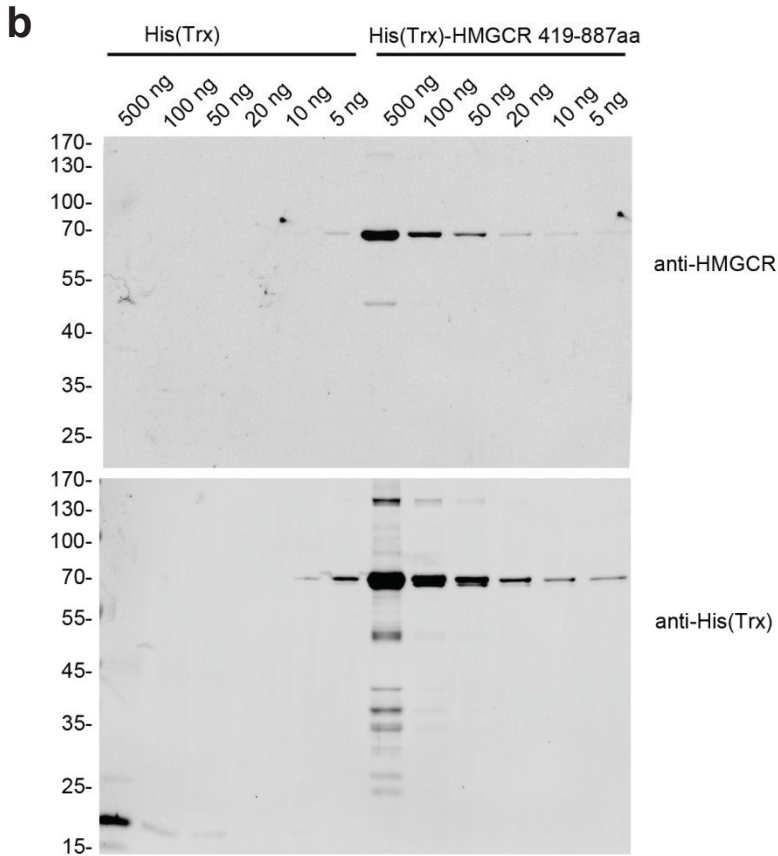
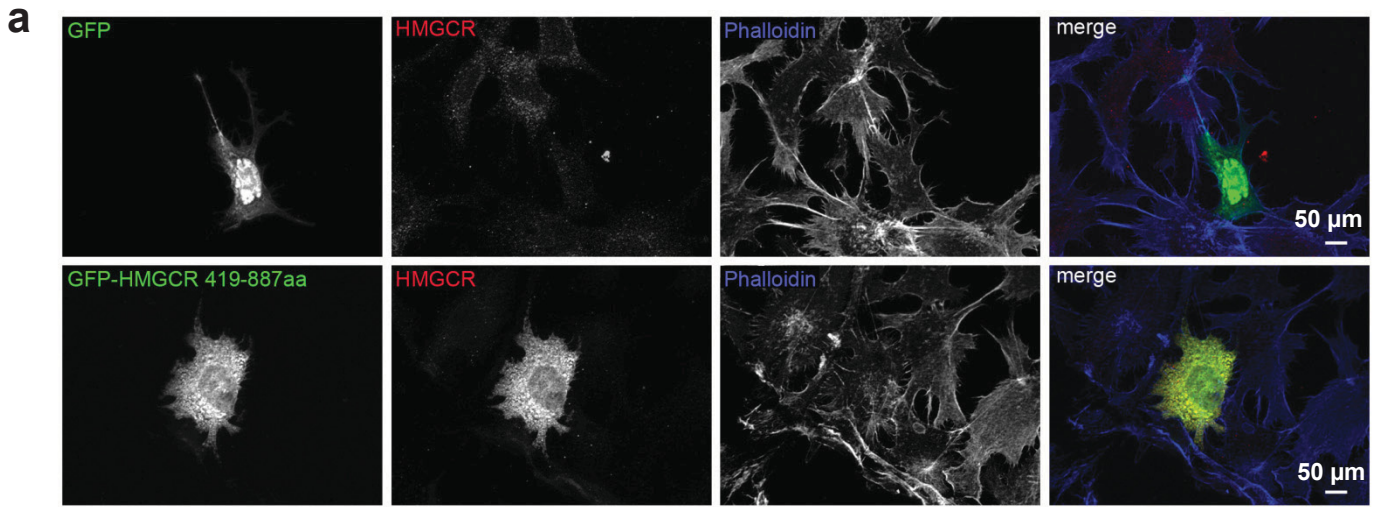


**Supplementary Figure 1: Characterization of polymers and nanoparticles.** (a) PLGA is labeled with DY-635 *via* 1-ethyl-3-(3-dimethylaminopropyl)carbodiimide (EDC) coupling. Successful coupling leads to a strong UV-Vis response in the SEC trace at 590 nm (dotted blue line). (b) UV/Vis spectra of DY-635 and PLGA-DY-635 showing  $\lambda_{\max}$  at 653 nm. (c) The AF4 based  $R_g$  distribution of DY-635[NP](-) show low polydispersity and uniformity of DY-635[NP](-). (d) AF4 measurements show a monomodal distribution (polydispersity index of 1.09) of spheric DY-635[NP](-).  $R_{g,i}$  represent the different averages of the root-mean-square radius. The hydrodynamic radius,  $R_h$ , represents the diffusion based radius. Furthermore, the calculated shape factor ( $R_g/R_h$ ) indicates a spherical geometry of the analyte.



**Supplementary Figure 2: Microfluidics-supported chip for coculture of HepaRG with HUVEC cells under flow conditions (“organoid”).**

**(a)** Structure of a microfluidic-supported chip, **(b)** scheme of the co-culture of HepaRG and HUVEC. Cells are separated by a porous membrane (pore diameter of 100  $\mu\text{m}$ ). NP were perfused exclusively via the upper perfusion channel with direct contact to the HUVEC cells to mimic anatomy of liver sinusoids regarding the architecture of endothelium, Disse space and hepatocytes.



**Supplementary Figure 3:**

**Anti-HMGCRCR characterization.**

**(a)** Antibody validation in HepG2 cells overexpressing GFP-HMGCRCR 419-877 or GFP as control. The anti-HMGCRCR antibody specifically recognizes GFP-HMGCRCR 419-877 and shows a weak endogenous HMGCRCR signal. Cells were additionally stained with Phalloidin to visualize untransfected cells. **(b)** Antibody validation via Western Blot. Distinct, different amounts of recombinant His(Trx) and His(Trx)-HMGCRCR fusion protein were blotted and detected with anti-HMGCRCR and anti-His(Trx) antibodies, respectively. The anti-HMGCRCR antibody detects specific bands within 500 ng to 10 ng HMGCRCR fusion protein.

**Supplementary Table 1** List of dyes and tissue specific combinations

Dye <sup>1</sup>	Sulfonic residues	Suggested polymers <sup>2</sup>	Target tissue	Optical modality <sup>3</sup>
DY-680 amine	1		Hepatocyte	LSM, NIR-Imaging, MSOT, Epi
DY-780 amine	1		Hepatocyte	NIR-Imaging, MSOT, Epi
DY-880 amine	1		Hepatocyte	MSOT
DY-635 amine	1		Hepatocyte	LSM, NIR-Imaging, Epi
DY-735 amine	1		Hepatocyte	LMS, NIR-Imaging, MSOT, Epi
DY-835 amine	1	Poly(D,L-lactide-co-glycolide), acid terminated, 50:50	Hepatocyte	NIR-Imaging, MSOT, Epi
DY-730 amine	1		Hepatocyte	LSM, NIR-Imaging, MSOT, Epi
DY-830 amine	1	(CAS Number 26780-50-7)	Hepatocyte	NIR-Imaging, MSOT, Epi
DY-750 amine	1	Poly(D,L-lactide) , acid terminated, 50:50	Hepatocyte	NIR-Imaging, MSOT, Epi
DY-850 amine	1		Hepatocyte	NIR-Imaging, MSOT, Epi
ICG NHS	2	(CAS Number 26680-10-4)	Hepatocyte	NIR-Imaging, MSOT, Epi
DY-778 amine	4	Polycaprolactone (CAS Number 24980-41-4)	Renal parenchymal cells	NIR-Imaging, MSOT, EPI
DY-878 amine	4		Renal parenchymal cells	NIR-Imaging, MSOT, EPI
DY-704 amine	3		Renal parenchymal cells	MSOT
DY-754 amine	4		Renal parenchymal cells	NIR-Imaging, MSOT, Epi
DY-854 amine	4		Renal parenchymal cells	NIR-Imaging, MSOT, Epi
IRDye800CW NHS	4		Renal parenchymal cells	NIR-Imaging, MSOT, Epi

<sup>1</sup> Amine-terminated dyes are provided by Dyomics GmbH, Germany, IRDye80 CW was purchased from Li-Cor as NHS-ester, ICG-NHS ester from Intrace medical .

<sup>2</sup> Polymers are purchased from Sigma Aldrich.

<sup>3</sup> LSM: (confocal) Laser scanning microscopy (also in vivo), may need a tuneable Ti:sapphire laser to excite NIR-Dyes; NIR-Imaging: devices such as IVIS or Maestro (PerkinElmer), MSOT: Multi-spectral optoacoustic tomograph, e.g. iTheraMedical GmbH, EPI: Epifluorescence Microscope equipped with suitable filter-sets and proper (N)IR-Sensitive detection systems.

**Note that we only can provide a small selection of dye-polymer-pairs since numerous dye-functionalization and polymers are available which can lead to successful coupled functional polymers.**

**Supplementary Table 2** siRNA sequences used for hmgcr-RNAi

Name	Target Ref. Seq	Primer Sequence (5' → 3')	
		sense	antisense
<b>RNA#1</b>	NM_008255.2	acuugcucaauguccau	gcauggacauugagcaagu
<b>RNA#2</b>	NM_008255.2	guaccugccuuacagag	aucucuguaaggcaggua

**Supplementary Table 3** Excitation and emission wavelength used for in vivo confocal scanning microscopy

Confocal laser scanning microscopy	Excitation (nm)	Emission (nm)	Strucutre
<b>NAD(P)H autofluorescence</b>	405±30	410-440	liver architecture
<b>NileRed</b>	488	530-630	payload
<b>DY-635/ DY-704</b>	633	LP 640	targeting moiety

**Supplementary Table 4** Primer sequences used in qPCR

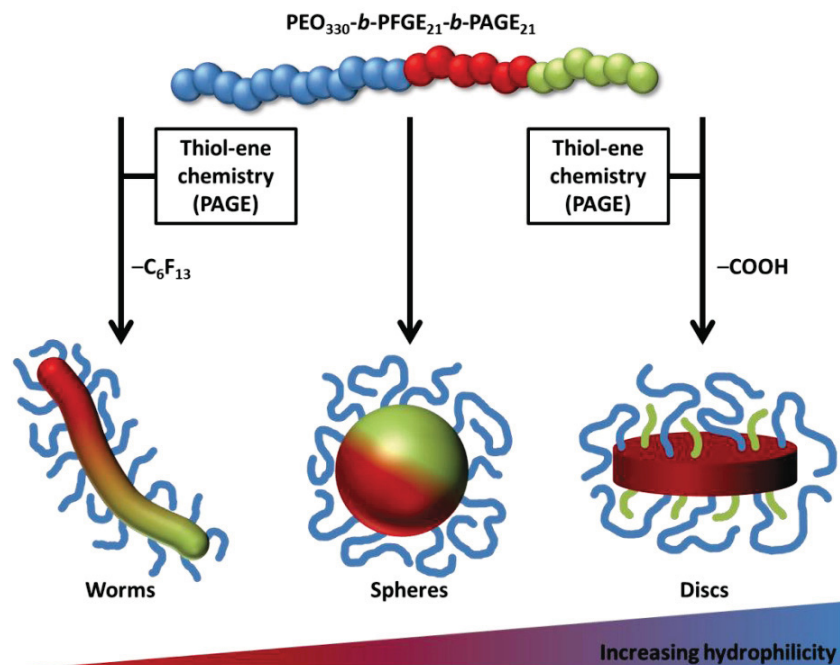
Gene name	Host	Target Ref. Seq	Primer Sequence (5' → 3')	
			forward	reverse
<i>hmgcr</i>	Mouse	NM_008255.2	tgg ttc ttt ccg tgc tgt gt	acc agt ttc cag ctt gtg gt
<i>hprt</i>	Mouse	NM_013556.2	tga cac tgg caa aac aat gca	ggt cct ttt cac cag caa gct

## Publication P8

Solution self-assembly of poly(ethylene oxide)-*block*-poly(furfuryl glycidyl ether)-*block*-poly(allyl glycidyl ether) based triblock terpolymers: A field-flow fractionation study

M. Wagner, M. J. Barthel, R. R. A. Freund, S. Höppener, A. Träger,  
F. H. Schacher, U. S. Schubert

*Polym. Chem.* **2014**, DOI: 10.1039/c4py00863d.









Cite this: DOI: 10.1039/c4py00863d

# Solution self-assembly of poly(ethylene oxide)-*block*-poly(furfuryl glycidyl ether)-*block*-poly(allyl glycidyl ether) based triblock terpolymers: a field-flow fractionation study†

Michael Wagner,<sup>a,b</sup> Markus J. Barthel,<sup>a,b,c</sup> Robert R. A. Freund,<sup>a,b</sup> Stephanie Hoepfner,<sup>a,b</sup> Anja Traeger,<sup>a,b</sup> Felix H. Schacher\*<sup>a,b</sup> and Ulrich S. Schubert\*<sup>a,b,c</sup>

A well-defined ABC triblock terpolymer, poly(ethylene oxide)-*block*-poly(furfuryl glycidyl ether)-*block*-poly(allyl glycidyl ether) (PEO-*b*-PFGE-*b*-PAGE), was synthesized *via* sequential living anionic ring-opening polymerization, and subsequently functionalized by thiol-ene click chemistry. In that way, either a fluorocarbon chain or carboxy groups were introduced into the C segment (PAGE). The self-assembly of the resulting materials in water as selective solvent was studied in detail by asymmetric flow field-flow fractionation (AF4) coupled to multi-angle laser light scattering and dynamic light scattering (DLS). The obtained results were compared with batch DLS and cryogenic transmission electron microscopy (cryo-TEM) results. The influence of the separation conditions on the retention behavior of the triblock terpolymers was evaluated to reveal possible limitations associated with AF4 measurements. The influence of pH value and ionic strength on the solution behavior of the materials, in particular for PEO-*b*-PFGE-*b*-PAGE<sub>COOH</sub>, was investigated as well. Crosslinking of the PAGE<sub>COOH</sub> by chelating metal ions (Fe<sup>3+</sup>) was studied under different conditions. In case of PEO-*b*-PFGE-*b*-PAGE, spherical micelles of approximately 20 nm ( $R_h$ ) were observed, whereas the introduction of a fluorocarbon chain led to an increase in size (30 nm,  $R_h$ ) and the formation of worm-like structures. Carboxy functionalization rendered small (5 nm) disk-like structures. In the latter case, subsequent addition of FeCl<sub>3</sub> resulted in the formation of spherical nanostructures ranging from 10 to 60 nm in size, depending on the pH value and the polymer/metal ion ratio.

Received 20th June 2014,  
Accepted 19th August 2014

DOI: 10.1039/c4py00863d

www.rsc.org/polymers

## Introduction

Micellar structures of different morphology formed *via* self-assembly of amphiphilic linear ABC triblock terpolymers represent an interesting class of nanoparticles and have been intensively studied in the last few years.<sup>1</sup> For drug or gene delivery applications, certain progress could be observed recently, as such systems enable smart delivery and stimuli-responsive behavior based on the combination of different functional groups and properties within a single material.<sup>2</sup> In the case of aqueous systems, poly(ethylene oxide) (PEO) is

mostly used as hydrophilic block (A) to ensure water solubility.<sup>3</sup> PEO is non-toxic, biocompatible, and shows the so-called stealth-effect.<sup>4</sup> Among other examples, poly(glycidyl ether)s like poly(furfuryl glycidyl ether) (PFGE) or poly(allyl glycidyl ether) (PAGE) can be used as hydrophobic (core-forming) blocks.<sup>5</sup> The encapsulation of drugs or dyes for diagnostic or therapeutic issues has already been realized for such systems.<sup>6</sup> The functionalization of PAGE *via* thiol-ene click chemistry using the pendant double bonds in the side chain enables efficient incorporation of different functional groups.<sup>7</sup> In that respect, the hydrophilicity and, hence, solution behavior of such triblock terpolymers can be effectively adjusted. As an example, the attachment of fluorocarbons significantly increases the hydrophobicity and has been shown to lead to additional compartmentalization within the (hydrophobic) core of micellar aggregates.<sup>2c,8</sup> On the other hand, carboxy groups can serve as a model example to increase the hydrophilicity and to implement stimuli-responsive solution behavior based on changes in either pH value or ionic strength.<sup>2b,9</sup>

<sup>a</sup>Laboratory of Organic and Macromolecular Chemistry (IOMC), Friedrich Schiller University Jena, Humboldtstrasse 10, 07743 Jena, Germany

<sup>b</sup>Jena Center for Soft Matter (JCSM), Friedrich Schiller University Jena, Philosophenweg 7, 07743 Jena, Germany

<sup>c</sup>Dutch Polymer Institute (DPI), P.O. Box 902, 5600 AX Eindhoven, the Netherlands. E-mail: ulrich.schubert@uni-jena.de, felix.schacher@uni-jena.de

† Electronic supplementary information (ESI) available. See DOI: 10.1039/c4py00863d

To investigate the variety of morphologies formed by such triblock terpolymers, dynamic (DLS) and static (SLS) light scattering techniques are commonly used, and are often supported by cryogenic transmission electron microscopy (cryo-TEM). Unfortunately, batch light scattering techniques provide only average values (SLS) or are problematic for highly polydisperse or multimodal systems, which require careful data interpretation. Therefore, field-flow fractionation (FFF) as an emerging technique for separation and characterization of a wide range of nanoparticles and polymers can be applied to overcome these problems.<sup>10</sup> The general principle of field-flow fractionation (FFF) was first described by J. Calvin Giddings in 1966 and is discussed in detail elsewhere.<sup>11</sup> Nowadays, asymmetric flow FFF (AF4) with one semipermeable membrane is the most frequently applied method. An important advantage of AF4, in comparison with classic chromatography techniques such as size exclusion chromatography (SEC), is the absence of a stationary phase. This reduces shear forces and undesired interactions of the sample with any column material, and leads to a less tortuous flow. Hence, this technique is ideally suited for the investigation of sensitive samples.<sup>12</sup> After the separation, a multi-angle laser light scattering (MALLS) or DLS detector is commonly used to obtain independent information about molar mass, radius of gyration ( $R_g$ ), hydrodynamic radius ( $R_h$ ), dispersity ( $D$ ), or shape.<sup>13</sup>

In this study, we describe a triblock terpolymer toolbox based on poly(ethylene oxide)-*block*-poly(furfuryl glycidyl ether)-*block*-poly(allyl glycidyl ether) (PEO-*b*-PFGE-*b*-PAGE) synthesized *via* sequential living anionic ring-opening polymerization (AROP). The PAGE block was functionalized using thiol-ene click chemistry to attach either 1*H*,1*H*,2*H*,2*H*-perfluorooctanethiol (PFOT, increasing hydrophobicity) or 3-mercaptopropionic acid (MPA, increasing hydrophilicity and introducing negative charges). The self-assembly of the resulting triblock terpolymers was studied by offline (batch) DLS, laser Doppler velocimetry (LDV), cryo-TEM, and AF4, where the latter was coupled with UV/RI, MALLS and DLS. The fractionation parameters in AF4 were varied to enable an optimization of the separation conditions. This should also reveal potential interactions with the membrane and show how these affect the retention behavior. Micellar structures formed by PEO-*b*-PFGE-*b*-PAGE<sub>COOH</sub> were studied in more detail to gain deeper insight into the influence of ionic strength and pH value. The influence of metal ions as chelating agent (Fe<sup>3+</sup>) was investigated. Thereby, we discuss potential advantages as well as possible limitations of AF4 with regard to block copolymer micelles.

## Experimental

### Materials

Ethylene oxide, furfuryl glycidyl ether (FGE), allyl glycidyl ether (AGE), 3-mercaptopropionic acid, 1*H*,1*H*,2*H*,2*H*-perfluorooctanethiol, calcium hydride, potassium, naphthalene, diphenylmethane, 2,2-dimethoxy-2-phenylacetophenone (DMPA), *N,N*-

dimethylformamide (DMF), tetrahydrofuran (THF), chlorobenzene, ethanol, methanol, ethylacetate, *n*-hexane and diethyl ether were purchased from Aldrich. Sodium chloride, sodium acetate trihydrate, ammonium chloride, iron(III) chloride hexahydrate and tris(hydroxymethyl)aminomethane were purchased from Carl Roth. Acetic acid (100%), hydrochloric acid (37%) and ammonia solution (25%) were purchased from VWR. THF was distilled from sodium/benzophenone. Ethylene oxide was distilled from sodium. Furfuryl glycidyl ether was purified by column chromatography (eluent: ethylacetate-*n*-hexane 5/1) and dried under vacuum before use. Allyl glycidyl ether was dried over calcium hydride and distilled under reduced pressure. Diphenylmethyl potassium (DPMK) was synthesized using the standard literature procedure.<sup>14</sup> The PEO precursor ( $M_n = 14\,500\text{ g mol}^{-1}$ ) was synthesized *via* living anionic ring-opening polymerization of ethylene oxide with DPMK in THF in a BüchiGlasUster PicoClave. If not specified otherwise, the chemicals were used as received.

### Sample preparation

The following procedure was used for the preparation of aqueous stock solutions of all micelles with a concentration of  $10\text{ g L}^{-1}$ . 20 mg of the corresponding triblock terpolymer were dissolved in 0.5 mL THF. Then 2 mL of pure water (type 1) were added slowly *via* syringe and the THF was allowed to evaporate by stirring overnight. Afterwards the solution was transferred to a 2 mL volumetric flask and the solution was filled up again to a volume of 2 mL. Different formulations of the nanostructures were obtained by mixing the aqueous polymer solutions with stock solutions of different salts or buffers and subsequent vortexing for 15 s. The pH-value of stock solutions containing buffer salts was adjusted by mixing the different sodium salts or free acids/bases, respectively. The ionic strength of all buffers and NaCl solutions was calculated considering the dissociation constants of the individual ion species. For pH dependent investigations with different buffer salts, a buffer concentration of 20 mM was used and the ionic strength of the buffer solutions was fixed at  $I = 20\text{ mM}$  by adding the respective amounts of NaCl.

### <sup>1</sup>H NMR

<sup>1</sup>H NMR spectra were recorded on a Bruker AC 300 MHz or on a Bruker AC 250 MHz spectrometer in deuterated chloroform or DMSO.

### Size exclusion chromatography (SEC)

Size exclusion chromatography (SEC) of PEO-*b*-PFGE-*b*-PAGE and PEO-*b*-PFGE-*b*-PAGE<sub>PFOT</sub> was performed on a Shimadzu SCL-10A system (with a LC-10AD pump, a RID-10A refractive index detector, and a PL gel 5  $\mu\text{m}$  mixed-D column at RT), the eluent was a mixture of chloroform-triethylamine-*iso*-propanol (94:4:2) with a flow rate of  $1\text{ mL min}^{-1}$ . The system was calibrated with poly(ethylene oxide) standards from PSS ( $M_n = 1470\text{ g mol}^{-1}$  to  $42\,000\text{ g mol}^{-1}$ ). In case of PEO-*b*-PFGE-*b*-PAGE<sub>COOH</sub> an Agilent Technologies 1200 Series size-exclusion chromatography system equipped with a G1329A autosampler,

a G131A isocratic pump, a G1362A refractive index detector, and both a PSS Gram 30 and a PSS Gram 1000 column placed in series was used. As eluent a 0.21% LiCl solution in *N,N*-dimethylacetamide (DMAc) was used at a 1 mL min<sup>-1</sup> flow rate and a column oven temperature of 40 °C. The system was calibrated with poly(ethylene oxide) standards from PSS ( $M_n = 1470 \text{ g mol}^{-1}$  to  $42\,000 \text{ g mol}^{-1}$ ).

### MALDI-ToF mass spectrometry

MALDI-ToF mass spectra were obtained using an Ultraflex III ToF/ToF mass spectrometer (Bruker Daltonics) with *trans*-2-[3-(4-*tert*-butylphenyl)-2-methyl-2-propenylidene] malononitrile (DCTB) or 2,5-dihydroxybenzoic acid (DHB) as the matrix in reflector as well as in linear mode. The instrument was calibrated prior to each measurement with an external PMMA standard from PSS Polymer Standards Services GmbH.

### Dynamic light scattering (DLS)

Batch dynamic light scattering was performed on a Zetasizer Nano ZS (Malvern Instruments, Herrenberg, Germany). All measurements were performed in folded capillary cells (DTS1071, Malvern Instruments, Herrenberg, Germany). After an equilibration time of 180 s, 3 × 30 s runs were carried out at 25 °C ( $\lambda = 633 \text{ nm}$ ). The counts were detected at an angle of 173°. Each measurement was performed in triplicate. Apparent hydrodynamic radii,  $R_h$ , were calculated according to the Stokes–Einstein equation.

### Laser Doppler velocimetry (LDV)

Laser Doppler velocimetry was used to measure the electrokinetic potential, also known as the zeta potential. The measurements were performed on a Zetasizer Nano ZS (Malvern Instruments, Herrenberg, Germany) in folded capillary cells (DTS1071). For each measurement, 15 runs were carried out using the fast-field reversal mode at 100 V. Each experiment was performed in triplicate at 25 °C. The zeta potential ( $\zeta$ ) was calculated from the electrophoretic mobility ( $\mu$ ) according to the Henry equation.<sup>15</sup> For each sample, the Henry coefficient,  $f(\text{ka})$ , was calculated separately according to Ohshima.<sup>16</sup>

### Asymmetric flow field-flow fractionation (AF4)

Asymmetric flow field-flow fractionation (AF4) was performed on an AF2000 MT System (Postnova Analytics, Landsberg, Germany) coupled to an UV (PN3211, 260 nm), RI (PN3150), MALLS (PN3070, 633 nm) and DLS (ZetaSizer Nano ZS, 633 nm) detector. The eluent is delivered by two different pumps (tip and focus-flow) and the sample is injected by an autosampler (PN5300) into the channel. The channel has a trapezoidal geometry and an overall area of 31.6 cm<sup>2</sup>. The nominal height of the spacer was 500  $\mu\text{m}$  and a regenerated cellulose membrane with a molar mass cut-off of 10 000 g mol<sup>-1</sup> was used as the accumulation wall. All experiments were carried out at 25 °C and the eluent was 5 mM NaCl, if not stated otherwise. The detector flow rate was set to 0.5 mL min<sup>-1</sup> for all samples and 50  $\mu\text{L}$  (2 mg mL<sup>-1</sup>) were injected with an injection flow rate of 0.2 mL min<sup>-1</sup> for 7 min, if not

stated otherwise. For all samples the cross-flow was set to 1 mL min<sup>-1</sup>. After the focusing period and a transition time of 1 min, the cross flow was kept constant for 5 min and then decreased under a power function gradient (0.4) to 0 within 25 min. Afterwards the cross-flow was kept constant at zero for at least 35 min to ensure complete elution. For calculation of the molar mass and the radius of gyration, a Zimm plot or a random coil fit (for large aggregates) was used, respectively. All measurements were repeated three times. The refractive index increment ( $dn/dc$ ) of all samples under different conditions (e.g. ionic strength, pH) was measured by manual injection of a known concentration directly into the channel without any focusing or cross-flow. The  $dn/dc$  was calculated as the average of at least three injections from the area under the RI curve ( $AUC_{RI}$ ).

### Transmission electron microscopy (cryo-TEM)

Cryo-TEM images were acquired with a 200 kV FEI Tecnai G<sup>2</sup> 20 equipped with a 4k × 4k Eagle HS CCD and an Olympus MegaView camera for overview images. Sample preparation was performed by plunge-freezing with a Vitrobot Mark IV system. 7  $\mu\text{L}$  of the aqueous solutions were blotted (blot force 0; blotting time 0.5 s) on Quantifoils (R2/2) and were vitrified in liquid ethane. The grids were rendered hydrophilic by Ar-plasma cleaning for 30 s (Diener Electronics). Samples were stored in liquid nitrogen until transfer to the microscope was performed with a Gatan cryo stage.

### Synthesis of the PEO-*b*-PFGE-*b*-PAGE triblock terpolymer

3.45 g (0.24 mmol) of the PEO precursor was dried under vacuum at 80 °C for 2 h, cooled to RT and dissolved in 30 mL THF. The polymer was activated under an argon atmosphere by the dropwise addition of DPMK until a stable, slightly red colorization could be observed. Subsequently, 0.66 mL (0.74 g, 4.8 mmol) FGE were added to the reaction mixture and stirred for 22 h at 45 °C. For the formation of the third block, 0.85 mL (0.82 g, 7.2 mmol) AGE was introduced into the reaction vessel and the mixture was allowed to stir for further 22 h. The reaction was terminated by the addition of 1 mL methanol, the product was precipitated in cold diethyl ether, filtered and dried under vacuum. The product was obtained as a white solid.

SEC (CHCl<sub>3</sub>-iPrOH-Et<sub>3</sub>N, 94 : 2 : 4; PEO-standard):  $M_n = 17\,800 \text{ g mol}^{-1}$ ;  $M_w = 18\,900 \text{ g mol}^{-1}$ ;  $D = 1.06$ .

MALDI-ToF MS:  $M_{\text{peak maximum}} = 19\,600 \text{ g mol}^{-1}$ .

<sup>1</sup>H NMR (300 MHz, DMSO-d<sub>6</sub>,  $\delta$  [ppm]): 7.54 (s, 1H, C=C(H)O, furfuryl), 7.21–7.09 (m, 10H, Ph), 6.35 (s, 2H, C=C(H)-(H)C=C, furfuryl), 5.82 (m, 1H, C=C(H)-C, allyl), 5.16 (m, 2H, H<sub>2</sub>C=C, allyl), 4.35 (s, 2H, CH<sub>2</sub>, furfuryl), 3.91 (t, 2H, CH<sub>2</sub>CH<sub>2</sub>O), 3.77 (t, 1H, <sup>3</sup>J<sub>H,H</sub> = 7.9 Hz, Ph<sub>2</sub>CH), 3.6–3.1 (br s, PEO-backbone).

### Functionalization of PEO<sub>330</sub>-*b*-PFGE<sub>21</sub>-*b*-PAGE<sub>21</sub> with 3-mercaptopropionic acid

250 mg of the triblock terpolymer (corresponding to 0.26 mmol allyl groups), 0.12 mL 3-mercaptopropionic acid

(149 mg, 1.40 mmol, 5.4 eq.) and 36 mg DMPA (0.14 mmol, 0.5 eq.) were dissolved in 3 mL of a mixture of DMF and ethanol (3 : 1) and irradiated with UV-light (365 nm) for 24 h. The crude product was purified by size-exclusion chromatography (Biobeads SX-1, THF) and the final product was dried under vacuum. PEO-*b*-PFGE-*b*-PAGE<sub>COOH</sub> was obtained as yellowish, highly viscous oil (272 mg). The degree of functionalization was determined by <sup>1</sup>H NMR spectroscopy.

<sup>1</sup>H NMR (250 MHz, DMSO-d<sub>6</sub>, δ [ppm]): 7.54 (s, 1H, C=C(H)O, furfuryl), 7.21–7.09 (m, 10H, Ph), 6.35 (s, 2H, C=C(H)-(H)C=C, furfuryl), 4.36 (s, 2H, CH<sub>2</sub>, furfuryl), 4.06 (t, 1H, <sup>3</sup>J<sub>H,H</sub> = 7.9 Hz, Ph<sub>2</sub>CH), 3.6–3.2 (br s, PEO-backbone), 3.10–2.59 (m, 4H, CH<sub>2</sub>CH<sub>2</sub>CO<sub>2</sub>H), 2.58–2.40 (m, 2H, DMSO + SCH<sub>2</sub>CH<sub>2</sub>O), 1.98–1.62 (m, 2H, SCH<sub>2</sub>CH<sub>2</sub>O).

Degree of functionalization (*f*): 97%.

#### Functionalization of PEO<sub>330</sub>-*b*-PFGE<sub>21</sub>-*b*-PAGE<sub>21</sub> with 1H,1H,2H,2H-perfluorooctanethiol

200 mg of the triblock terpolymer (corresponding to 0.21 mmol allyl groups), 0.26 mL 1H,1H,2H,2H-perfluorooctanethiol (396 mg, 1.04 mmol, 5.0 eq.) and 11 mg DMPA (0.04 mmol, 0.2 eq.) were dissolved in 1.5 mL chlorobenzene and irradiated with UV-light (365 nm) for 72 h. The crude product was purified by size-exclusion chromatography (Biobeads SX-1, THF) and the final product was dried under vacuum. PEO-*b*-PFGE-*b*-PAGE<sub>PFO</sub> was obtained as a yellowish, highly viscous oil (267 mg). The degree of functionalization was determined by <sup>1</sup>H NMR spectroscopy.

SEC (CHCl<sub>3</sub>-iPrOH-Et<sub>3</sub>N, 94 : 2 : 4; PEO-standard): *M*<sub>n</sub> = 18 100 g mol<sup>-1</sup>; *M*<sub>w</sub> = 20 500 g mol<sup>-1</sup>; *D* = 1.13.

<sup>1</sup>H NMR (250 MHz, CDCl<sub>3</sub>, δ [ppm]): 7.35 (s, 1H, C=C(H)O, furfuryl), 7.23 (s, 10H, Ph), 6.37–6.15 (m, 2H, C=C(H)-(H)C=C, furfuryl), 4.40 (s, 2H, CH<sub>2</sub>, furfuryl), 4.10 (t, 1H, <sup>3</sup>J<sub>H,H</sub> = 7.7 Hz, Ph<sub>2</sub>CH), 3.81–3.22 (br, PEO-backbone), 2.78–2.65 (m, 2H, CH<sub>2</sub>CH<sub>2</sub>CF<sub>2</sub>), 2.61 (t, 2H, <sup>3</sup>J<sub>H,H</sub> = 7.0 Hz, SCH<sub>2</sub>CH<sub>2</sub>O), 2.47–2.17 (m, 2H, CH<sub>2</sub>CH<sub>2</sub>CF<sub>2</sub>), 1.93–1.70 (m, 2H, SCH<sub>2</sub>CH<sub>2</sub>O).

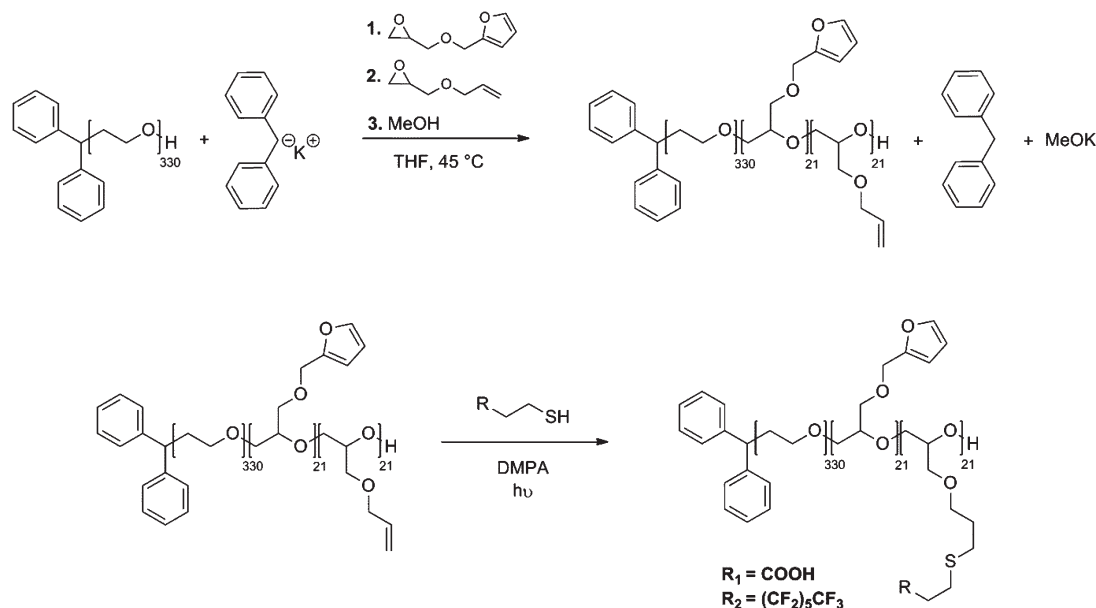
Degree of functionalization (*f*): 96%.

## Results & discussion

### Synthesis and post-polymerization functionalization of PEO-*b*-PFGE-*b*-PAGE

As shown in former studies, incorporation of functional poly-(glycidyl ether)s as building blocks in polyether-based block copolymers leads to a broad range of possible applications for these materials.<sup>5b,17</sup> Furthermore, modification of the reactive groups in the side chain (e.g., allyl or furfuryl) by post-polymerization functionalization represents a facile methodology to tune the material characteristics.<sup>6b,18</sup> Here, one possibility is the attachment of different moieties to influence hydrophilicity/hydrophobicity and, hence, self-assembly behavior in water as the selective solvent.<sup>5d</sup>

In the present work, we targeted the synthesis and modification of an amphiphilic triblock terpolymer. For this purpose, a pre-synthesized PEO precursor was re-activated by titration with diphenylmethyl potassium (DPMK). Subsequently, PEO-*b*-PFGE-*b*-PAGE was synthesized by sequential addition of furfuryl glycidyl ether and allyl glycidyl ether (Scheme 1, Table 1). As shown by size exclusion chromatography (SEC, Fig. S1†), a well-defined triblock terpolymer with a narrow molar mass distribution could be obtained. Further-



**Scheme 1** Schematic representation of the synthesis of a poly(ethylene oxide)-*block*-poly(furfuryl glycidyl ether)-*block*-poly(allyl glycidyl ether) (PEO-*b*-PFGE-*b*-PAGE) triblock terpolymer by sequential living anionic ring-opening polymerization (AROP) as well as subsequent post-polymerization functionalization using thiol-ene chemistry.

**Table 1** Characterization data of the synthesized triblock terpolymers

Sample <sup>a</sup>	$M_n^b$ [g mol <sup>-1</sup> ]	$M_w^b$ [g mol <sup>-1</sup> ]	$D^b$	$f^a$ [%]
PEO <sub>330</sub>	14 800	15 500	1.05	—
PEO <sub>330</sub> - <i>b</i> -PFGE <sub>21</sub>	17 400	18 100	1.04	—
PEO <sub>330</sub> - <i>b</i> -PFGE <sub>21</sub> - <i>b</i> -PAGE <sub>21</sub>	17 800	18 900	1.06	—
PEO <sub>330</sub> - <i>b</i> -PFGE <sub>21</sub> - <i>b</i> -PAGE <sub>21,COOH</sub>	—	—	—	97
PEO <sub>330</sub> - <i>b</i> -PFGE <sub>21</sub> - <i>b</i> -PAGE <sub>21,PFOT</sub>	18 100	20 500	1.13	96

<sup>a</sup> Degree of polymerization (subscripts) and functionalization was determined by <sup>1</sup>H NMR spectroscopy. <sup>b</sup> Determined by size-exclusion chromatography (CHCl<sub>3</sub>-iPrOH-Et<sub>3</sub>N, 94 : 2 : 4; PEO-calibration).

more, the characteristic signals of the functional groups (furfuryl and allyl) could be detected by <sup>1</sup>H NMR spectroscopy (Fig. S2†). In contrast to the PFGE middle block, the conversion of PAGE did not reach 100%, confirming our earlier studies.<sup>6c</sup>

To alter the hydrophilic/hydrophobic balance of the material and to investigate the resulting micellar morphologies formed *via* self-assembly in aqueous media, we used post-polymerization functionalization reactions. Therefore, the PAGE segment was modified by the attachment of either 3-mercaptopropionic acid or 1*H*,1*H*,2*H*,2*H*-perfluorooctanethiol. The functionalization with 3-mercaptopropionic acid (-COOH) was performed as reported before in a 3 : 1 DMF-EtOH mixture.<sup>17</sup> The reaction progress was monitored by SEC and <sup>1</sup>H NMR measurements. As shown in Fig. S3,† functionalization with -COOH leads to a strong shift to higher molar masses. Due to strong interactions of the carboxy groups with the column material the polymer elutes in the non-calibrated area. Therefore, the obtained values are not displayed in Table 1. Nevertheless, a monomodal distribution could be detected, indicating a successful reaction. The degree of functionalization (*f*) was determined by <sup>1</sup>H NMR (Fig. S4†). Here the decreasing signal of the furan ring (*f* ~ 97%). The functionalization with 1*H*,1*H*,2*H*,2*H*-perfluorooctanethiol was carried out as reported in the literature in a minimum amount of chlorobenzene, since for other solvent mixtures (*e.g.*, DMF, THF or MeOH)

solubility problems were encountered.<sup>19</sup> Again, the reaction process was monitored by SEC (Fig. S5†) and <sup>1</sup>H NMR measurements (Fig. S6†). A monomodal shift to higher molar masses was detected and <sup>1</sup>H NMR spectra indicated a *f* value of 96%.

In the next section, a detailed study concerning the self-assembly of the triblock terpolymers and the influence of the functionalization of the PAGE segment on the solution properties is provided. We assume at this point that PFGE and PAGE build up the core of micellar structures in aqueous media and PEO forms the corresponding corona. Increasing the hydrophilicity of the PAGE segment can, in principle, lead to a mixed or phase-separated PAGE<sub>COOH</sub>/PEO corona.<sup>20</sup> In contrast, introduction of a fluorocarbon chain might even lead to phase separation of both hydrophobic blocks.

### Dynamic light scattering and laser Doppler velocimetry

Prior to detailed investigations by AF4, batch (offline) DLS and LDV were carried out. Self-assembly was induced by the solvent displacement method: a certain amount of the respective triblock terpolymer was dissolved in THF as a non-selective solvent. Subsequently, water was added (2 mL) (selective for the PEO block or, in case of PEO<sub>330</sub>-*b*-PFGE<sub>21</sub>-*b*-PAGE<sub>21,COOH</sub>, for PEO and PAGE<sub>COOH</sub>) and THF was allowed to evaporate. According to DLS, all samples show rather broad hydrodynamic radii distributions (intensity weighted) and a rather high dispersity in the range of 0.5 to 0.8 as obtained by cumulant analysis (Fig. 1A). Considering number weighted distributions, a dominating population with  $R_h = 19$  nm for PEO-*b*-PFGE-*b*-PAGE, 23 nm for PEO-*b*-PFGE-*b*-PAGE<sub>PFOT</sub>, and 7 nm for PEO-*b*-PFGE-*b*-PAGE<sub>COOH</sub> could be identified. The high PDI value in all cases might be a hint for the presence of larger aggregates. Nevertheless, batch DLS results and cumulant analysis in these cases have to be interpreted with care. To access the corresponding zeta potentials, LDV was applied at varying ionic strengths (different concentrations of NaCl). In water, a zeta potential of around -12 mV was obtained for PEO-*b*-PFGE-*b*-PAGE (Fig. 1B). Introduction of a hydrophobic side chain, which contains highly electronegative fluorine, leads to

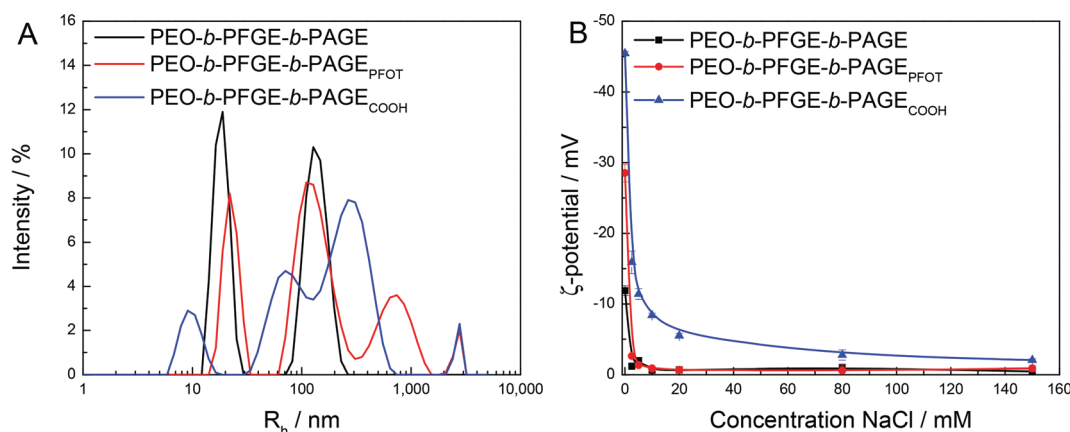


**Fig. 1** (A) DLS based  $R_h$  distributions of aqueous solutions of PEO-*b*-PFGE-*b*-PAGE, PEO-*b*-PFGE-*b*-PAGE<sub>PFOT</sub> and PEO-*b*-PFGE-*b*-PAGE<sub>COOH</sub>. (B) Zeta potentials of PEO-*b*-PFGE-*b*-PAGE, PEO-*b*-PFGE-*b*-PAGE<sub>PFOT</sub> and PEO-*b*-PFGE-*b*-PAGE<sub>COOH</sub> at varying ionic strengths.

an increase of the absolute value of zeta potential to around  $-29$  mV for PEO-*b*-PFGE-*b*-PAGE<sub>PFOT</sub>. Finally, for PEO-*b*-PFGE-*b*-PAGE<sub>COOH</sub>, containing (partially) deprotonated carboxy groups, a zeta potential of around  $-45$  mV was found. In all cases, the zeta potentials decrease exponentially with increasing ionic strength according to the Stern model and, except for PEO-*b*-PFGE-*b*-PAGE<sub>COOH</sub>, 5 mM NaCl are sufficient to reduce the zeta potential to 0 mV.

### Influence of separation parameters in asymmetric flow field-flow fractionation

Before a sample can be fully characterized by AF4-MALLS-DLS, the separation conditions have to be optimized and a suitable method has to be found to ensure a representative fractionation. Therefore, we started with the investigation of self-assembled structures of PEO-*b*-PFGE-*b*-PAGE and systematically investigated the influence of the cross-flow (and its programming), the focusing time, and the membrane type, as well as the eluent composition on the retention behavior. Two different membranes, regenerated cellulose (RC) and poly(ether sulfone) (PES) membranes with a molar mass cut-off of  $10\,000\text{ g mol}^{-1}$ , were used. In principle, both membranes were suitable, but the RC membrane yielded higher recovery rates and was therefore chosen for all further experiments. To investigate the influence of cross- and focusing flow, the outlet/detector flow was fixed at  $0.5\text{ mL min}^{-1}$  and water containing 5 mM NaCl was used as the eluent. After optimization, a method consisting of a constant (5 min) cross-flow followed by a power decay gradient (exponent 0.4) to 0 within 25 min was found to be best. After the cross-flow reaches 0, the flow was continued for 35 min to ensure complete elution. The result of the variation of the starting point of the cross-flow is shown in Fig. 2A. It can be observed that with increasing cross-flow the obtained peak is shifted to higher elution times, the peak height is increased and the void peak is reduced. The shift in elution time is based on larger forces resulting from higher cross-flow, dragging the sample closer to the membrane, which is in accordance to the AF4 theory.<sup>21</sup> The recovery rates, shown in the inlay of Fig. 2A, indicate that a cross-flow higher than  $0.75\text{ mL min}^{-1}$  provides the best fractionation. As a consequence, a value of  $1\text{ mL min}^{-1}$  was chosen for investigation of the influence of the focusing time (Fig. 2B). An appropriate duration of the focusing step is important for an adequate concentration of the sample and to reduce band broadening. Otherwise, a very long focusing period leads to increased interactions between the sample and the membrane as well as sample species. In the present case, it can be seen that the void peak is reduced with higher focusing time and that the peak height as well as the recovery rate (inlay, Fig. 2B) increases until an optimum is reached at around 7 to 9 min. For higher focusing times, the recovery rate decreases, probably due to increasing interactions, as mentioned above. Therefore, a time of 7 min was used for the following fractionation experiments. Finally, the ionic strength of the eluent was varied by addition of different amounts of NaCl to tune the electrostatic interactions between sample and membrane (Fig. 2C). In pure water, an irregular elution with a broad

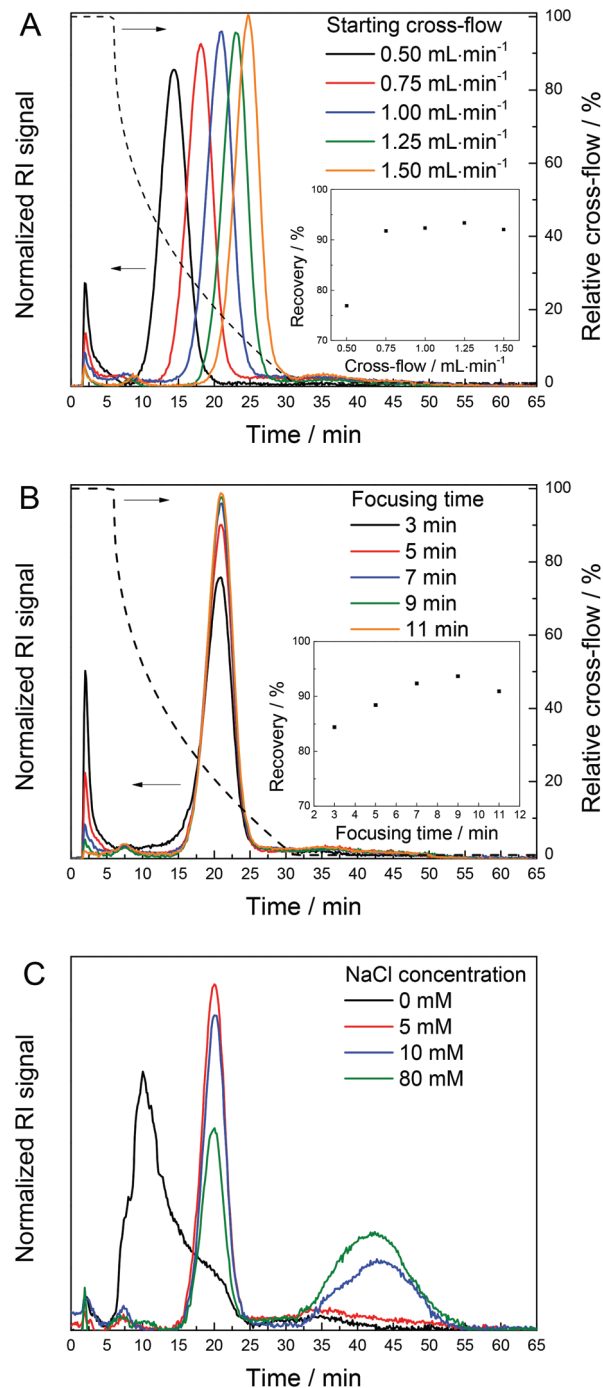


**Fig. 2** Variation of cross-flow (A), focusing time (B) and ionic strength (NaCl concentration) of the eluent (C) for separation of PEO-*b*-PFGE-*b*-PAGE via AF4. The inlays show the recovery rate of each separation as determined by RI detection.

peak can be observed, while for all eluents containing at least 5 mM NaCl a constant elution time and a nearly symmetric peak shape were obtained. We attribute this to repulsive electrostatic interactions between the negatively charged RC membrane and the sample (with a negative zeta potential) and between the micellar aggregates themselves.<sup>22</sup> In particular, during the focusing step, when the sample is concentrated

**Table 2** Properties of self-assembled structures in aqueous solution

	PEO- <i>b</i> -PFGE- <i>b</i> -PAGE	PEO- <i>b</i> -PFGE- <i>b</i> -PAGE <sub>PFOT</sub>	PEO- <i>b</i> -PFGE- <i>b</i> -PAGE <sub>COOH</sub>
$dn/dc$ [mL g <sup>-1</sup> ]	0.139 ± 0.001	0.09 ± 0.0004	0.158 ± 0.0008
$M_n$ [kg mol <sup>-1</sup> ]	705 ± 5.9	1684 ± 35	82.0 ± 2.5 <sup>c</sup>
$M_w$ [kg mol <sup>-1</sup> ]	723 ± 1.3	1921 ± 14	101.5 ± 2.1 <sup>c</sup>
$D_M$ ( $M_w/M_n$ )	1.03 ± 0.01	1.14 ± 0.02	1.24 ± 0.02
$N_{agg}$ <sup>a</sup>	35 ± 0.3	56 ± 1.2	3.7 ± 0.1
$R_g$ (peak 1) [nm]	14 ± 0.9	20 ± 2	—
$R_h$ (peak 1) [nm]	21 ± 0.3	29.5 ± 1.2	4.6 ± 0.7
$R_g/R_h$ (peak 1)	0.67 ± 0.04	0.68 ± 0.05	—
$R_{h, batch DLS}$ [nm]	18.5 ± 1	23.3 ± 3.8	7 ± 3
$R_g$ (peak 2) [nm]	—	42.5 ± 9 <sup>b</sup>	—
$R_h$ (peak 2) [nm]	—	146 ± 14	—
$R_g/R_h$ (peak 2)	—	2.92 ± 0.22	—
Recovery [%]	92.3 ± 1.4	85.1 ± 1.3	85.3 ± 0.3

<sup>a</sup> Based on  $M_n$  and polymer molar masses obtained by <sup>1</sup>H NMR. <sup>b</sup> Based on the random coil scattering factor. <sup>c</sup> For calculation the single chain fraction was excluded.

within a small area, increased interparticle interactions can cause the observed phenomena. While these interactions are long-ranged in nearly electrolyte free water, this is significantly reduced upon addition of NaCl. Already 5 mM NaCl are sufficient to obtain a defined peak and an appropriate elution behavior. This is also in accordance with LDV measurements of

PEO-*b*-PFGE-*b*-PAGE as mentioned above, where a zeta potential close to zero for 5 mM NaCl was found. Additionally, it can be seen that if the ionic strength is further increased, the peak height decreases and small amounts of aggregates are formed during the separation, probably due to increased attractive membrane interactions as repulsive electrostatic contributions are screened. Thus, 5 mM NaCl were found to be an optimum and used for all further AF4 experiments. Nevertheless, we assume at this point that different separation conditions as well as eluent compositions containing NaCl do not influence micellar characteristics, as no difference in size and molar mass could be observed (MALLS/DLS detection).

### Self-assembly in water

Using the above established conditions all triblock terpolymer micelles could be fractionated and characterized by AF4-MALLS-DLS (Table 2). For all samples, a recovery rate above 85% was achieved, which indicates that the AF4 fractograms are representative and suitable to describe both size and molar mass distribution. For PEO-*b*-PFGE-*b*-PAGE, two fractions can be detected: one main fraction of smaller particles and some larger aggregates as minority fractions (as indicated by the low RI and large LS 90° signal, Fig. 3A). The molar mass of the main fraction was around 705 kg mol<sup>-1</sup> ( $M_n$ ) with a dispersity

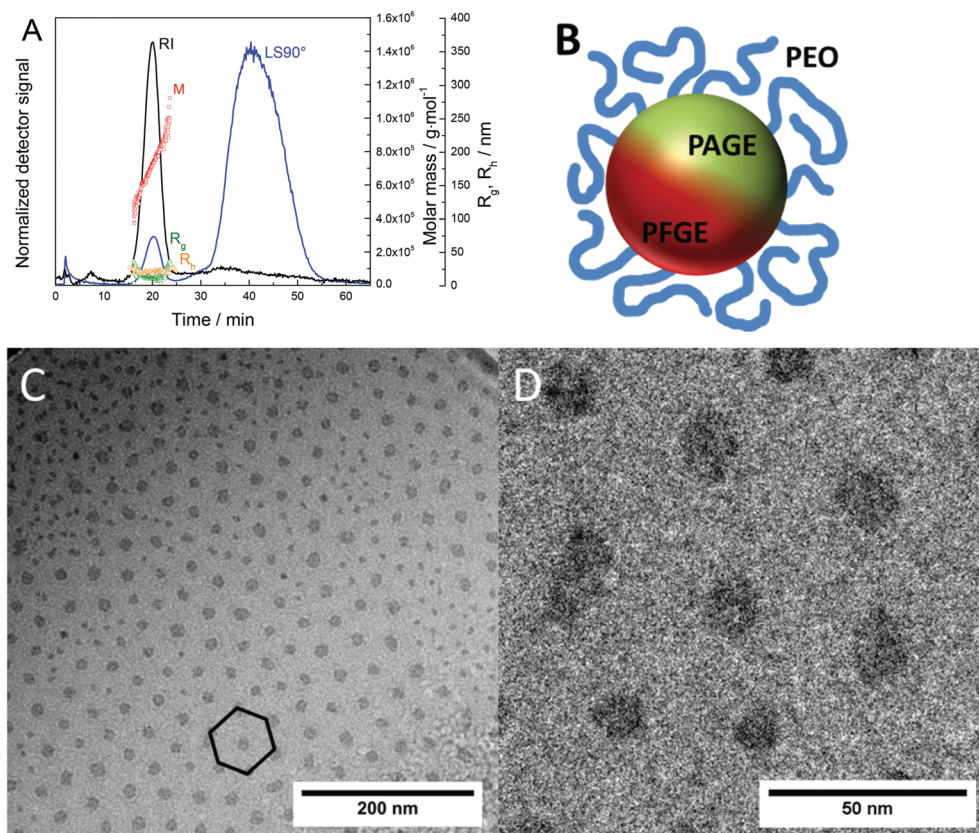


**Fig. 3** (A) AF4-MALLS-DLS fractogram of PEO-*b*-PFGE-*b*-PAGE and (B) schematic representation of the proposed micellar structure for PEO-*b*-PFGE-*b*-PAGE. The different colors of PFGE/PAGE indicate a possible phase separation but we do not assume the formation of a Janus core. (C) Cryo-TEM micrograph of PEO-*b*-PFGE-*b*-PAGE. (D) Cryo-TEM micrograph showing representative hexagonal ordering of the micelles (the contrast was slightly increased using the ImageJ software).

of 1.03 (MALLS detector). Considering the molar mass of a single triblock terpolymer chain ( $20\,100\text{ g mol}^{-1}$ ), this results in an aggregation number  $N_{\text{agg}}$  of around 35 chains per particle. The radius of gyration  $R_g$  (z-average root-mean-square radius) was around 14 nm and online DLS reveals a hydrodynamic radius  $R_h$  of around 21 nm, which is in agreement with the offline batch DLS ( $R_{h, \text{batch}}$  around 19 nm). Calculation of the shape ratio  $\rho$  ( $R_g/R_h$ ) provides a value of around 0.67, which is slightly below the expected value for a hard sphere (0.775).<sup>23</sup> Interpretation of this shape ratio should be done carefully, as  $R_g$  is close to the lower detection limit of around 10 nm. Nevertheless, the obtained shape ratio as well as the radii indicate the presence of compact spherical micelles.<sup>23b</sup> To support the results obtained by AF4, cryo-TEM was applied (Fig. 3C). Here, again spherical micelles with an average core-to-core distance of around 40 nm were found. We assume that the core-to-core distance is defined by the PEO corona and, hence, half this distance (around 20 nm) can be attributed to the hydrodynamic radius, which is in excellent agreement with the  $R_h$  value obtained by AF4 as well as by offline DLS. According to cryo-TEM, the inner core has a radius of around 7 nm and shows slight differences in contrast. We attribute this to

both PFGE and PAGE being located in the micellar core. According to differences in electron density, phase separation can be the reason for the presence of brighter (PAGE) and darker areas (PFGE, Fig. 3D). Also, it can be seen that the micellar cores are not perfectly spherical in shape. Considering the dimension of the core, the PEO corona has a thickness of around 13 nm. Based on eqn (1) and (2), the hydrodynamic radius of a PEO chain in a good solvent can be calculated, where  $a$  is the segment length (0.36 for PEO) and  $N$  the degree of polymerization.<sup>24</sup> The factor of 1.78 is based on the assumption of a random coil for a monodisperse linear chain in a good solvent.<sup>23b</sup> In the present case, a theoretical radius of 6.6 nm was calculated (diameter 13.2 nm), which is in excellent agreement with the experimental values from cryo-TEM and in accordance with the proposed structure (Fig. 3B).

$$R_g = aN^{3/5} \quad (1)$$

$$R_h = \frac{R_g}{1.78} \quad (2)$$

In contrast to PEO-*b*-PFGE-*b*-PAGE, the fractogram of PEO-*b*-PFGE-*b*-PAGE<sub>PFOT</sub> shows a bimodal distribution (Fig. 4A). For

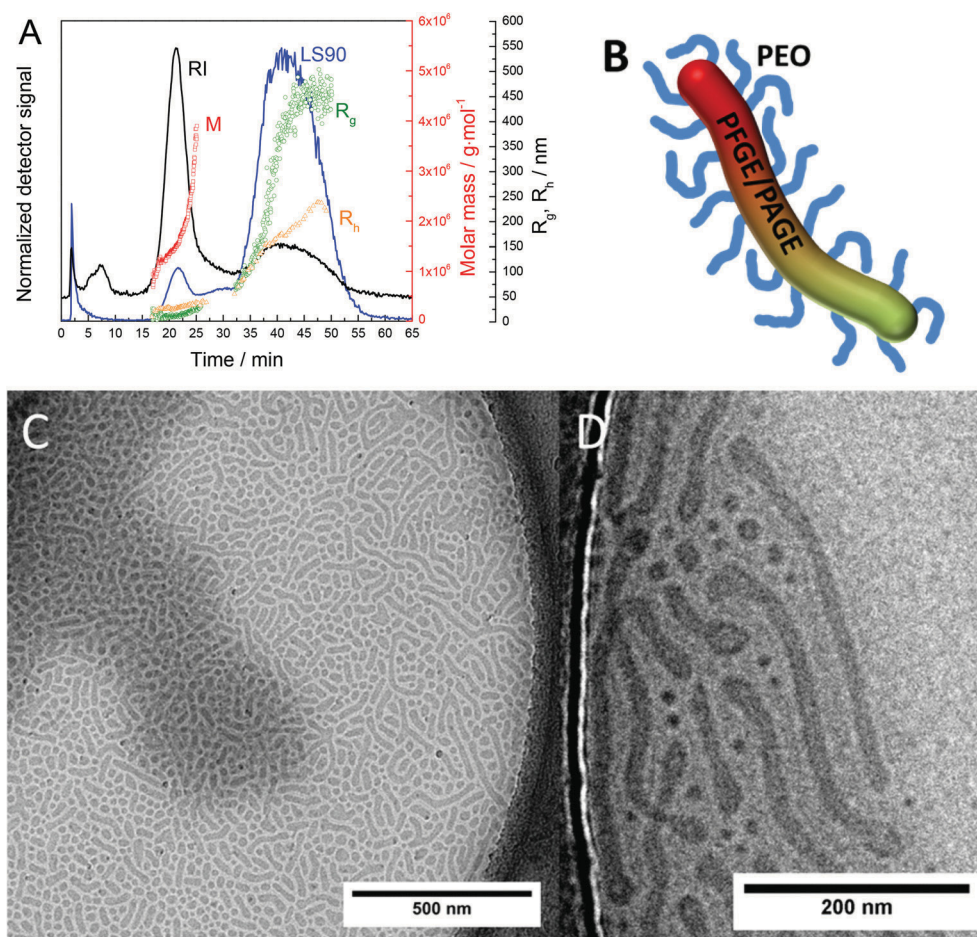


**Fig. 4** (A) AF4-MALLS-DLS fractogram of PEO-*b*-PFGE-*b*-PAGE<sub>PFOT</sub> and (B) schematic representation of the worm-like structures of PEO-*b*-PFGE-*b*-PAGE<sub>PFOT</sub>. (C) Cryo-TEM micrograph of PEO-*b*-PFGE-*b*-PAGE<sub>PFOT</sub> (representative for the entire sample). (D) Cryo-TEM micrograph of PEO-*b*-PFGE-*b*-PAGE<sub>PFOT</sub> showing worm-like structures with spherical endcaps.



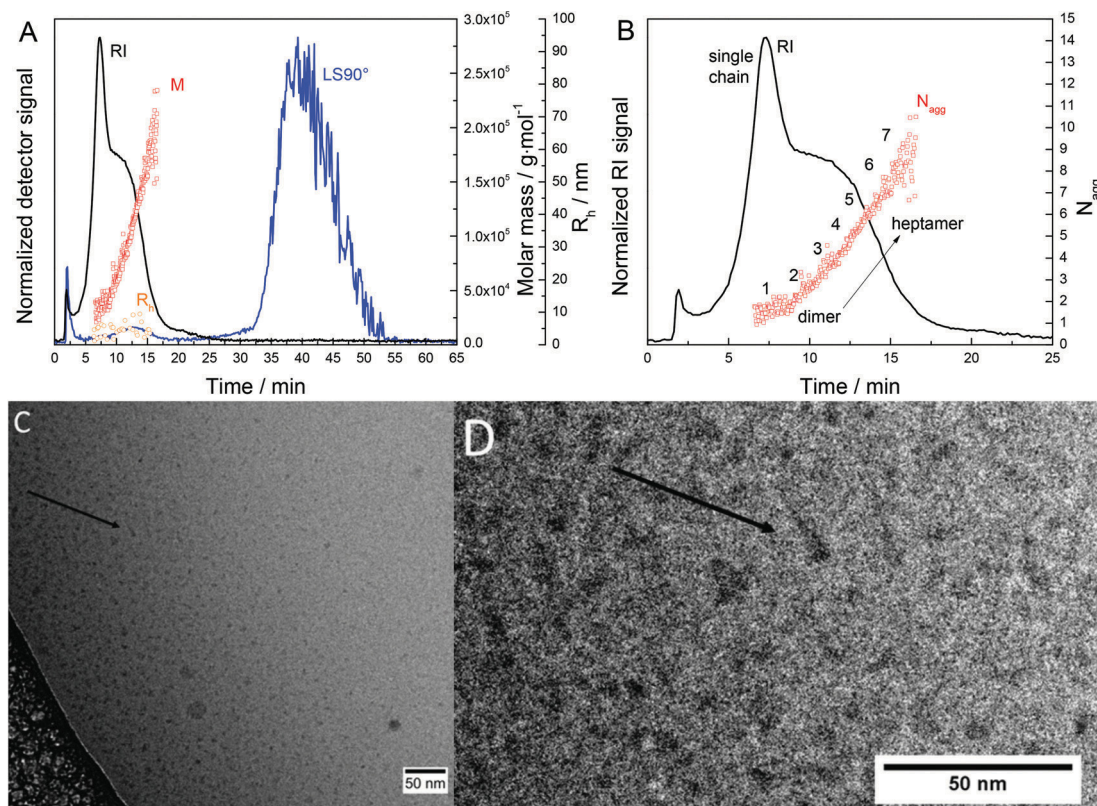


**Fig. 5** (A) AF4-MALLS-DLS fractogram of PEO-*b*-PFGE-*b*-PAGE<sub>COOH</sub> and (B) aggregation number  $N_{agg}$  of the different species on the basis of the molar mass obtained by MALLS. (C) Cryo-TEM micrograph of PEO-*b*-PFGE-*b*-PAGE<sub>COOH</sub>. (D) Enlarged image of the disc-like structures (the contrast has been slightly increased using the ImageJ software).

the first peak, a molar mass of around  $1700 \text{ kg mol}^{-1}$  was obtained, corresponding to a higher aggregation number  $N_{agg} = 56$ . The radius of gyration is around 20 nm and  $R_h$  was found to be 30 nm (online DLS). The resulting shape ratio  $\rho$  of 0.68 is similar to PEO-*b*-PFGE-*b*-PAGE. The second population, as observed in AF4, represents the minority fraction according to the RI signal and, here, an average  $R_g$  of 425 nm and an  $R_h$  of 146 nm are obtained *via* light scattering. This large difference results in a high average shape ratio  $\rho$  of around 2.92, hinting towards the presence of elongated or worm-like structures.<sup>25</sup> The fact that the shape ratio increases during the elution from a value of around 1 at the beginning of the peak until 2 to 3 at the end strongly indicates that the second population is of high dispersity in terms of “length”. These results were also confirmed by cryo-TEM (Fig. 4C), where both small spherical objects and worm-like micelles could be observed. The attachment of fluorocarbon chains to the PAGE block increases the overall hydrophobicity and leads to the formation of worm-like micelles (Fig. 4B). The width of these structures is within the same range as the diameter of the spherical micelles. This indicates a similar block arrangement with PFGE and PAGE<sub>PFOT</sub> forming the core, while PEO forms the corona. Furthermore, it can be seen that in most cases spherical endcaps are present (cryo-TEM of worm-like structures Fig. 4D), which can be an additional indication for fusion/fission processes of spherical particles as origin of this morphology.<sup>26</sup> In contrast

to PEO-*b*-PFGE-*b*-PAGE, no phase separation within the hydrophobic core of the cylinders can be directly observed. Although this has been reported for lipophilic and fluorophilic domains, in our case this might be prevented by the relatively low degrees of polymerization of the PFGE and PAGE<sub>PFOT</sub> segments.<sup>8,27</sup> Nevertheless, in some cases brighter (PAGE) and darker domains (PFGE) can be seen within the cores of spherical micelles present in the sample (see Fig. 4D).

The introduction of carboxy groups renders the PAGE segment hydrophilic, depending on the solution pH value. According to the AF4-fractogram, one main population at lower elution time and a negligible amount of larger aggregates (compare RI and LS 90° trace) are present (Fig. 5A). In

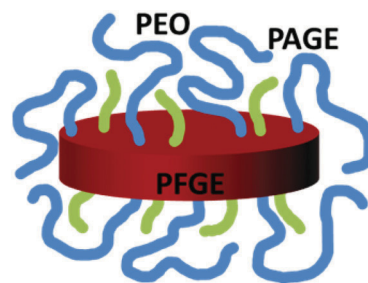


**Fig. 6** Schematic representation of the disc-like structures of PEO-*b*-PFGE-*b*-PAGE<sub>COOH</sub>.

agreement with the elution time, online DLS shows rather small micelles with an average  $R_h$  of around 4 to 5 nm. The radius of gyration could not be obtained as the particles reveal isotropic scattering and, therefore, are below the size limit of the MALLS detector. A closer look at the obtained peak and its molar mass distribution reveals that the peak maximum corresponds to one single polymer chain, while the observed shoulder represents different assemblies ranging from a dimer to a heptamer (Fig. 5B). The average molar mass ( $M_n$ ) of the self-assembled fraction (excluding the single chain fraction) is around  $82 \text{ kg mol}^{-1}$ , which corresponds to an average aggregation number  $N_{\text{agg}}$  of 3.7 and clearly shows that these particles are composed of only a few terpolymer chains. A full separation of the single chain and the aggregates by AF4 was not possible. The sample was also studied by cryo-TEM (Fig. 5C) and, again, small objects of just a few nanometers in size could be observed. Furthermore, a careful evaluation of the data reveals the presence of short lines in the micrographs (Fig. 5D). Combination of both observations indicates a disc-like shape for the larger assemblies of PEO-*b*-PFGE-*b*-PAGE<sub>COOH</sub>, where the lines represent discs which are oriented perpendicular to the observation plane. This morphology might be explained by a parallel ordering of the involved terpolymer chains, with the PFGE segment forming the core and both PEO and PAGE<sub>COOH</sub> acting as the corona (schematic visualization Fig. 6). However, we are aware that this interpretation has to be treated with caution as the size of these micelles approaches the limits of AF4 as well as cryo-TEM. In the latter case only a weak contrast is generated by such small polymeric aggregates, which complicates the interpretation.

#### Influence of pH and ionic strength on micelles formed by PEO-*b*-PFGE-*b*-PAGE<sub>COOH</sub>

The introduction of charges to the material can, in principle, lead to stimuli-responsive behavior with regard to solution pH or ionic strength. While the solution pH regulates the total number of charges by (de)protonation of the carboxy groups, the ionic strength controls the range of electrostatic inter-

actions. Therefore, AF4 was applied to investigate PEO-*b*-PFGE-*b*-PAGE<sub>COOH</sub> at varying pH values and ionic strengths. Fig. 7A shows the AF4 fractograms at different concentrations of NaCl, which was used to adjust the ionic strength of the sample solutions as well as the eluent. It can be seen that for all experiments containing NaCl the typical peak shape is obtained. In case of pure water, no appropriate separation could be obtained, which is due to long-ranged repulsive electrostatic interactions between the negatively charged membrane and the negatively charged sample ( $\zeta = -45 \text{ mV}$ ). This strong repulsion dominates the retention behavior, resulting in fast elution and inhibiting separation from the void peak. Addition of NaCl leads to screening of these repulsive interactions. Subsequently, with increasing ionic strength a shift to higher elution times can be observed until a concentration of around 80 mM NaCl is reached. This shift in elution time is directly correlated to the zeta potential (Fig. 7B) and can therefore solely be attributed to the reduction of the range of electrostatic interactions being involved.<sup>12b</sup> Additionally, with increasing ionic strength a reduction of the peak height was also observed, which can be explained by an increasing influence of attractive forces like van der Waals interactions and, hence, membrane adsorption. Nevertheless, no influence on the molar mass or size of the sample could be observed at all investigated concentrations of NaCl. Also, offline DLS did not show changes in the hydrodynamic radius either. Furthermore, it can be seen in the fractogram that the percentage of disc-like assemblies increases in comparison with the amount of single chains, which is probably due to a favorable stabilization of the nanostructures, also based on the increase of ionic strength and the resulting shielding of electrostatic repulsion between the carboxy groups of the PAGE<sub>COOH</sub> blocks. On the other hand, preferential adsorption of single terpolymer chains during AF4 measurements cannot be fully excluded.

To further investigate the influence of the pH value on the self-assembly behavior of PEO-*b*-PFGE-*b*-PAGE<sub>COOH</sub>, different buffer systems (acetate, tris(hydroxymethyl)-aminomethane

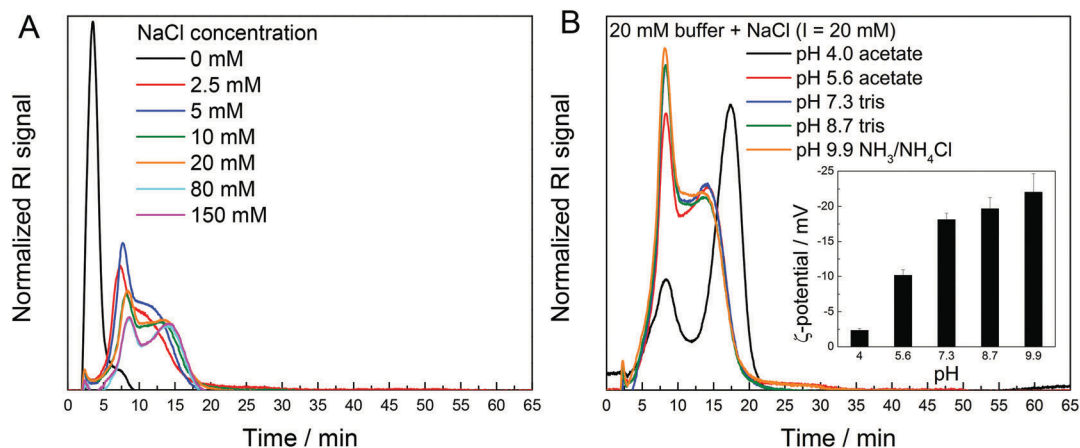
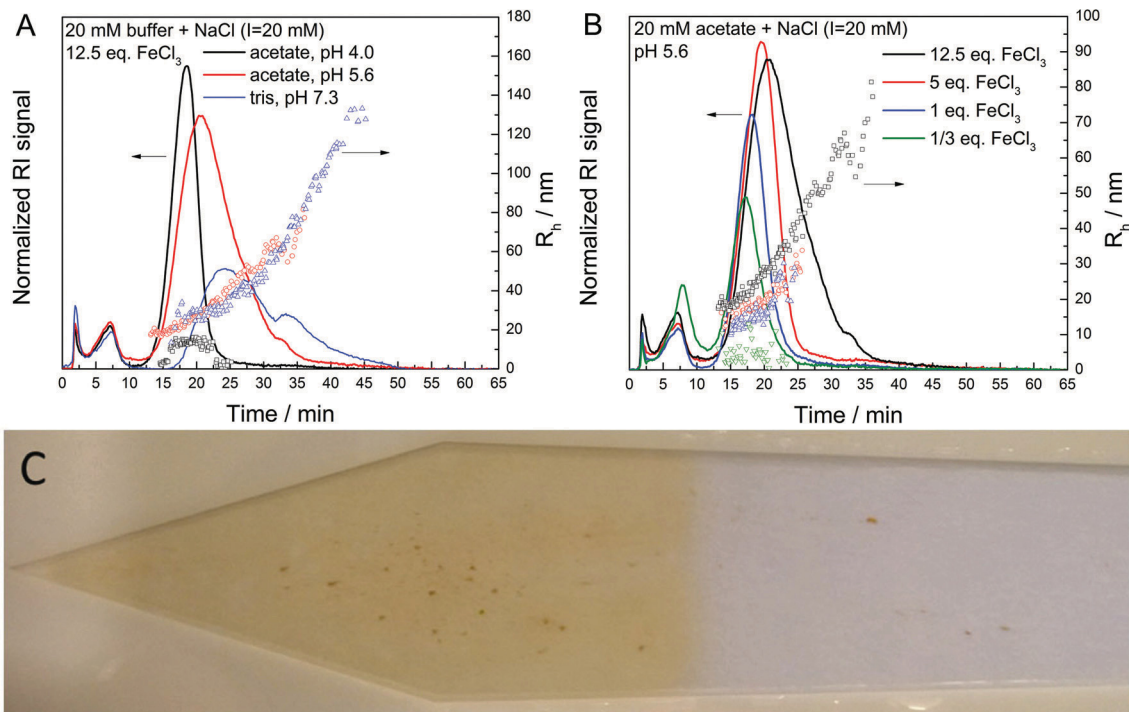


Fig. 7 (A) AF4 fractograms of PEO-*b*-PFGE-*b*-PAGE<sub>COOH</sub> at varying ionic strengths. (B) AF4 fractograms of PEO-*b*-PFGE-*b*-PAGE<sub>COOH</sub> at varying pH values. The inset shows the corresponding zeta potentials of the sample.



**Fig. 8** AF4 fractograms of PEO-*b*-PFGE-*b*-PAGE<sub>COOH</sub> (A) with 12.5 eq. of FeCl<sub>3</sub> (compared to carboxy groups) at different pH values and (B) at pH 5.6 with different equivalents of FeCl<sub>3</sub>. (C) Photograph of the AF4 membrane after Fe(OH)<sub>3</sub> precipitation at pH 8.7 (20 mM tris buffer, 12.5 eq.).

(tris), and ammonia/ammonium chloride) were prepared at a concentration of 20 mM each. To rule out any influence of varying ionic strength, the latter was fixed at 20 mM by adding a corresponding amount of NaCl. The results obtained by AF4-MALLS-DLS can be seen in Fig. 7B. At all pH values except for pH 4, similar elution times, molar masses, and  $R_h$  values as described above were found. This can be understood as the constant ionic strength of 20 mM reduces the range of electrostatic interactions to 2.2 nm according to the Debye-Hückel theory. The consistency in mass and size is probably due to an efficient shielding of the micelles by the long PEO corona chains, even if the electrostatic repulsion between the carboxy groups of the PAGE<sub>COOH</sub> block increases with the pH value (inlay Fig. 7B). At pH 4, where nearly all carboxy groups are protonated, the fraction of micelles is considerably increased, and the sample shows a marginally increased  $R_h$  of around 7 nm. This might be explained based on the absence of electrostatic repulsion between the PAGE<sub>COOH</sub> chains. Offline (batch) DLS reveals no difference in size at varying pH values. The lower recovery rate of around 60% at pH 4 is probably due to increased membrane adsorption as the isoelectric point of the used membrane is close to pH 4 and therefore almost no electrostatic repulsion between membrane and sample occurs.<sup>22</sup>

#### Complexation of metal ions by PEO-*b*-PFGE-*b*-PAGE<sub>COOH</sub>

Another possible way to influence the solution structures of amphiphilic block copolymers is the addition of multivalent metal ions to induce crosslinking by chelation or complexation. For the carboxy groups of PEO-*b*-PFGE-*b*-PAGE<sub>COOH</sub>,

we used Fe<sup>3+</sup> as trivalent counter ion and added different amounts of FeCl<sub>3</sub> to aqueous solutions of PEO-*b*-PFGE-*b*-PAGE<sub>COOH</sub>. Moreover, as also a strong influence of the pH value on the overall charge of the carboxy groups and the stability of the complexes can be anticipated, the experiments were performed at varying pH values using the buffer systems mentioned above. First, an excess of 12.5 equivalents FeCl<sub>3</sub> (compared to the total number of carboxy groups) was added and the pH value was varied from 4 to 9. To rule out a complexation by PEO, Fe<sup>3+</sup> was also added to PEO-*b*-PFGE-*b*-PAGE, where no changes in elution time, peak shape, and size could be observed in the AF4 fractogram (data not shown). The results obtained for PEO-*b*-PFGE-*b*-PAGE<sub>COOH</sub> by AF4-MALLS-DLS are shown in Fig. 8A. At all pH values, a shift to higher elution times and an increase in size could be observed. Thereby, the radius depends on the pH value of the eluent. While smaller particles with an average  $R_h$  of 12 nm are obtained at pH 4.0, the hydrodynamic radius increases to 30 or 61 nm at pH 5.6 or 7.3, respectively (Table 3). The radius of gyration also increases

**Table 3** AF4-MALLS-DLS results of PEO-PFGE-PAGE<sub>COOH</sub> with varying amounts of FeCl<sub>3</sub> and at different pH values

pH	Fe <sup>3+</sup> eq.	$R_g$ [nm]	$R_h$ [nm]	$R_g/R_h$
4.0	12.5	10.2	12.2	0.84
5.6	12.5	25.1	30.0	0.84
5.6	5	16.4	21	0.78
5.6	1	12.8	15	0.85
5.6	1/3	—	4.9	—
7.3	12.5	50.9	61.3	0.83

from around 10 nm at pH 4 to 25 nm at pH 5.6 and 50.9 nm at pH 7.3. At pH 8.7, Fe(OH)<sub>3</sub> precipitates and is massively adsorbed onto the membrane (Fig. 8C). Therefore, no reliable results could be obtained at higher pH values. Besides, calculation of the shape ratio  $R_g/R_h$  provides a value of around 0.84 for all measurable pH values, which indicates soft spherical particles as this is in between the value of a hard (0.775) and a Gaussian sphere (1.0). For pH 4, interpretation of  $R_g/R_h$  has to be performed carefully as  $R_g$  is close to the instrument's limit. Moreover, all particles show a positive zeta potential (around 5 mV). As the increase of size correlates with the pH value, we assume that the chelation is strongly influenced by an increasing amount of charges being present. With increasing pH, more Fe<sup>3+</sup> can enter the corona, which leads to reduced hydrophilicity and, subsequently, to aggregation.

To investigate the influence of the iron(III) content, the pH value was kept constant (acetate buffer 5.6) and the amount of added FeCl<sub>3</sub> was varied (Fig. 8B). It can be seen that the particle size increases with the amount of iron(III) (Table 3). While the addition of 1/3 eq. has almost no effect on  $R_h$ , a value of 15 nm is obtained for 1 eq. and 21 nm for 5 eq., respectively. The radius of gyration is 16.4 nm and 12.8 nm for 5 or 1 equivalents iron(III), respectively, but could not be determined for 1/3 eq. As already described, the low  $R_g$  values as well as the resulting shape ratio have to be interpreted with care. In general, values ranging from 0.78 to 0.85 were obtained, indicating the presence of spherical particles. Comparison of the AF4 fractograms at pH 5.6 without FeCl<sub>3</sub> and with 1/3 eq. showed that the addition of iron(III) leads to a shift in elution time, even if there is no significant change in  $R_h$ . This leads us to the assumption that Fe<sup>3+</sup> is complexed by the carboxy groups of a single particle, leading to a positive zeta potential (5 to 10 mV depending on the polymer:Fe<sup>3+</sup> ratio, -5 mV for 1/3 eq.), increased attractive interactions with the negatively charged membrane, and higher retention times. With increasing amounts of iron(III), more carboxy groups are complexed, which leads to larger particles as more of the small nanostructures can be crosslinked by complexation. These first investigations of the chelation by Fe<sup>3+</sup> demonstrate that pH value and metal ion concentration can be used to control the size of such micelles. In that respect, further studies concerning *e.g.* the type of metal ion will follow.

## Conclusion

In this study, we presented a toolbox of triblock terpolymers based on PEO<sub>330</sub>-*b*-PFGE<sub>21</sub>-*b*-PAGE<sub>21</sub>. Post-polymerization functionalization *via* thiol-ene chemistry of the PAGE segment allowed the efficient introduction of side chains of different functionality and/or solubility. 1H,1H,2H,2H-Perfluorooctanethiol was used to increase the hydrophobicity of the PAGE segment and 3-mercaptopropionic intro-

duces carboxy groups into the PAGE segment. The self-assembly of the obtained materials in water as selective solvent was studied using AF4 coupled to MALLS and DLS as well as offline DLS and cryo-TEM. Thereby, depending on the material investigated, spherical (PEO-*b*-PFGE-*b*-PAGE) and worm-like (PAGE<sub>PFO</sub>) micellar structures (PAGE<sub>COOH</sub>) were found. Cryo-TEM of PEO-*b*-PFGE-*b*-PAGE<sub>COOH</sub> indicated the formation of disc-shaped structures although AF4-MALLS-DLS was not able to support these findings, as the objects were too small to obtain reliable information on  $R_g$  or  $R_h$ . Furthermore, AF4 was shown to represent an outstanding technique for in-depth characterization of micellar aggregates concerning an efficient determination of molar mass, size, and shape of the particles. Moreover, the effects of different separation conditions on the elution behavior were investigated and, in particular in case of PEO-*b*-PFGE-*b*-PAGE<sub>COOH</sub>, the behavior at varying ionic strengths and pH was analyzed. No significant influence on the formed structures was observed by AF4, except for pH 4, where a slight increase in  $R_h$  could be detected. Finally, the addition of Fe<sup>3+</sup> to micelles from PEO-*b*-PFGE-*b*-PAGE<sub>COOH</sub> induced corona crosslinking and the formation of particles, whose size can be adjusted by the amount of Fe<sup>3+</sup> and the solution pH value. All results obtained by AF4 were supported by cryo-TEM measurements, where also additional information about shape and, in one case, potential phase separation within the micellar core was observed. Our study clearly shows that at least two independent techniques are necessary to evaluate and interpret micelles formed by such materials.

## Acknowledgements

This project was funded by the Carl-Zeiss Foundation (Strukturantrag JCSM). The work of M. J. Barthel forms part of the research program of the Dutch Polymer Institute (DPI), project #690 (technology area HTE). The cryo-TEM facilities of the Jena Center for Soft Matter (JCSM) were established with a grant from the German Research Council (DFG) and the European Fonds for Regional Development (EFRE). U. S. S. and F. H. S. are grateful to the Thuringian Ministry for Education, Science, and Culture (TMBWK, grants #B514-09051, NanoConSens and #B515-10065, ChaPoNano) for financial support.

## References

- (a) A. L. Brocas, M. Gervais, S. Carlotti and S. Pispas, *Polym. Chem.*, 2012, **3**, 2148–2155; (b) A. L. Brocas, C. Mantzaridis, D. Tunc and S. Carlotti, *Prog. Polym. Sci.*, 2013, **38**, 845–873; (c) C. Auschra and R. Stadler, *Macromolecules*, 1993, **26**, 6364–6377; (d) A. H. Gröschel, A. Walther, T. I. Löbbling, F. H. Schacher, H. Schmalz and A. H. E. Müller, *Nature*, 2013, **503**, 247–251.

- 2 (a) B. Obermeier, F. Wurm, C. Mangold and H. Frey, *Angew. Chem., Int. Ed.*, 2011, **50**, 7988–7997; (b) A. C. Rinkenauer, A. Schallon, U. Günther, M. Wagner, E. Betthausen, U. S. Schubert and F. H. Schacher, *ACS Nano*, 2013, **7**, 9621–9631; (c) T. P. Lodge, A. Rasdal, Z. B. Li and M. A. Hillmyer, *J. Am. Chem. Soc.*, 2005, **127**, 17608–17609; (d) P. Lundberg, N. A. Lynd, Y. N. Zhang, X. H. Zeng, D. V. Krogstad, T. Paffen, M. Malkoch, A. M. Nystrom and C. J. Hawker, *Soft Matter*, 2013, **9**, 82–89.
- 3 (a) X. Y. Huang, S. Chen and J. L. Huang, *J. Polym. Sci., Part A: Polym. Chem.*, 1999, **37**, 825–833; (b) R. K. Jing, G. W. Wang, Y. N. Zhang and J. L. Huang, *Macromolecules*, 2011, **44**, 805–810; (c) M. Hrubby, C. Konak and K. Ulbrich, *J. Controlled Release*, 2005, **103**, 137–148.
- 4 (a) K. Knop, R. Hoogenboom, D. Fischer and U. S. Schubert, *Angew. Chem., Int. Ed.*, 2010, **49**, 6288–6308; (b) M. J. Barthel, F. H. Schacher and U. S. Schubert, *Polym. Chem.*, 2014, **5**, 2647–2662.
- 5 (a) S. L. Lin, W. J. Zhu, X. H. He, Y. H. Xing, L. Y. Liang, T. Chen and J. P. Lin, *J. Phys. Chem. B*, 2013, **117**, 2586–2593; (b) M. J. Barthel, U. Mansfeld, S. Hoepfener, J. A. Czaplewska, F. H. Schacher and U. S. Schubert, *Soft Matter*, 2013, **9**, 3509–3520; (c) M. Libera, B. Trzebicka, A. Kowalczyk, W. Walach and A. Dworak, *Polymer*, 2011, **52**, 250–257; (d) M. J. Barthel, K. Babiuch, T. Rudolph, J. Vitz, S. Hoepfener, M. Gottschaldt, M. D. Hager, F. H. Schacher and U. S. Schubert, *J. Polym. Sci., Part A: Polym. Chem.*, 2012, **50**, 2914–2923.
- 6 (a) K. Kataoka, A. Harada and Y. Nagasaki, *Adv. Drug Delivery Rev.*, 2001, **47**, 113–131; (b) B. Obermeier and H. Frey, *Bioconjugate Chem.*, 2011, **22**, 436–444; (c) M. Hrubby, C. Konak and K. Ulbrich, *J. Appl. Polym. Sci.*, 2005, **95**, 201–211.
- 7 (a) M. J. Robb, L. A. Connal, B. F. Lee, N. A. Lynd and C. J. Hawker, *Polym. Chem.*, 2012, **3**, 1618–1628; (b) S. Tamesue, M. Ohtani, K. Yamada, Y. Ishida, J. M. Spruell, N. A. Lynd, C. J. Hawker and T. Aida, *J. Am. Chem. Soc.*, 2013, **135**, 15650–15655; (c) K. L. Killops, N. Gupta, M. D. Dimitriou, N. A. Lynd, H. Jung, H. Tran, J. Bang and L. M. Campos, *ACS Macro Lett.*, 2012, **1**, 758–763.
- 8 J.-N. I. Marsat, M. Heydenreich, E. Kleinpeter, H. v. Berlepsch, C. Böttcher and A. Laschewsky, *Macromolecules*, 2011, **44**, 2092–2105.
- 9 (a) P. J. Sun, Y. Zhang, L. Q. Shi and Z. H. Gan, *Macromol. Biosci.*, 2010, **10**, 621–631; (b) K. Van Butsele, S. Cajot, S. Van Vlierberghe, P. Dubruel, C. Passirani, J. P. Benoit, R. Jerome and C. Jerome, *Adv. Funct. Mater.*, 2009, **19**, 1416–1425.
- 10 (a) J. Gigault, T. J. Cho, R. I. MacCuspie and V. A. Hackley, *Anal. Bioanal. Chem.*, 2013, **405**, 1191–1202; (b) J. Gigault, W. Zhang, G. Lespes, B. Charleux and B. Grassl, *Anal. Chim. Acta*, 2014, **819**, 116–121;
- (c) S. Boye, D. Appelhans, V. Boyko, S. Zschoche, H. Komber, P. Friedel, P. Formanek, A. Janke, B. I. Voit and A. Lederer, *Biomacromolecules*, 2012, **13**, 4222–4235; (d) J. R. Silveira, A. G. Hughson and B. Caughy, *Methods Enzymol.*, 2006, **412**, 21–33.
- 11 (a) J. C. Giddings, *J. Sep. Sci.*, 1966, **1**, 123–125; (b) J. C. Giddings, *Science*, 1993, **260**, 1456–1465; (c) K. G. Wahlund and J. C. Giddings, *Anal. Chem.*, 1987, **59**, 1332–1339; (d) A. Litzén and K. G. Wahlund, *Anal. Chem.*, 1991, **63**, 1001–1007; (e) A. Litzén, *Anal. Chem.*, 1993, **65**, 461–470; (f) J. C. Giddings, F. J. Yang and M. N. Myers, *Anal. Chem.*, 1976, **48**, 1126–1132.
- 12 (a) H. Cölfen and M. Antonietti, *Adv. Polym. Sci.*, 2000, **150**, 67–187; (b) M. Wagner, S. Holzschuh, A. Traeger, A. Fahr and U. S. Schubert, *Anal. Chem.*, 2014, **86**, 5201–5210.
- 13 (a) P. D. Petrov, M. Drechsler and A. H. E. Müller, *J. Phys. Chem. B*, 2009, **113**, 4218–4225; (b) K. Knop, A.-F. Mingotaud, N. El-Akra, F. Violleau and J.-P. Souchard, *Photochem. Photobiol. Sci.*, 2009, **8**, 396–404; (c) K. Loos, A. Boker, H. Zettl, A. F. Zhang, G. Krausch and A. H. E. Müller, *Macromolecules*, 2005, **38**, 873–879; (d) M. Andersson, B. Wittgren and K. G. Wahlund, *Anal. Chem.*, 2003, **75**, 4279–4291.
- 14 H. Normant and B. Angelo, *Bull. Soc. Chim. Fr.*, 1960, 354–359.
- 15 A. V. Delgado, F. Gonzalez-Caballero, R. J. Hunter, L. K. Koopal and J. Lyklema, *J. Colloid Interface Sci.*, 2007, **309**, 194–224.
- 16 H. Ohshima, *J. Colloid Interface Sci.*, 1994, **168**, 269–271.
- 17 M. J. Barthel, A. C. Rinkenauer, M. Wagner, U. Mansfeld, S. Hoepfener, J. A. Czaplewska, M. Gottschaldt, A. Traeger, F. H. Schacher and U. S. Schubert, *Biomacromolecules*, 2014, **15**, 2426–2439.
- 18 (a) Y. Koyama, M. Umehara, A. Mizuno, M. Itaba, T. Yasukouchi, K. Natsume, A. Suginaka and K. Watanabe, *Bioconjugate Chem.*, 1996, **7**, 298–301; (b) J. N. Hunt, K. E. Feldman, N. A. Lynd, J. Deek, L. M. Campos, J. M. Spruell, B. M. Hernandez, E. J. Kramer and C. J. Hawker, *Adv. Mater.*, 2011, **23**, 2327–2331; (c) M. J. Barthel, T. Rudolph, S. Crotty, F. H. Schacher and U. S. Schubert, *J. Polym. Sci., Part A: Polym. Chem.*, 2012, **50**, 4958–4965.
- 19 M. D. Dimitriou, Z. L. Zhou, H. S. Yoo, K. L. Killops, J. A. Finlay, G. Cone, H. S. Sundaram, N. A. Lynd, K. P. Barteau, L. M. Campos, D. A. Fischer, M. E. Callow, J. A. Callow, C. K. Ober, C. J. Hawker and E. J. Kramer, *Langmuir*, 2011, **27**, 13762–13772.
- 20 A. Walther, X. Andre, M. Drechsler, V. Abetz and A. H. E. Müller, *J. Am. Chem. Soc.*, 2007, **129**, 6187–6198.
- 21 F. A. Messaud, R. D. Sanderson, J. R. Runyon, T. Otte, H. Pasch and S. K. R. Williams, *Prog. Polym. Sci.*, 2009, **34**, 351–368.
- 22 M. Pontie, *J. Membr. Sci.*, 1999, **154**, 213–220.

- 23 (a) A. Rolland-Sabate, P. Colonna, M. G. Mendez-Montealvo and V. Planchot, *Biomacromolecules*, 2007, **8**, 2520–2532; (b) W. Burchard, *Adv. Polym. Sci.*, 1999, **143**, 113–194.
- 24 A. Besheer, J. Vogel, D. Glanz, J. Kressler, T. Groth and K. Mäder, *Mol. Pharm.*, 2009, **6**, 407–415.
- 25 J. R. Silveira, G. J. Raymond, A. G. Hughson, R. E. Race, V. L. Sim, S. F. Hayes and B. Caughey, *Nature*, 2005, **437**, 257–261.
- 26 E. Betthausen, C. Hanske, M. Müller, A. Fery, F. H. Schacher, A. H. E. Müller and D. J. Pochan, *Macromolecules*, 2014, **47**, 1672–1683.
- 27 (a) S. Kubowicz, J. F. Baussard, J. F. Lutz, A. F. Thunemann, H. von Berlepsch and A. Laschewsky, *Angew. Chem., Int Ed.*, 2005, **44**, 5262–5265; (b) Z. B. Li, E. Kesselman, Y. Talmon, M. A. Hillmyer and T. P. Lodge, *Science*, 2004, **306**, 98–101.

Supporting Information for:

## Solution self-assembly of poly(ethylene oxide)-*block*-poly(furfuryl glycidyl ether)-*block*-poly(allyl glycidyl ether) based triblock terpolymers: A field-flow fractionation study

Michael Wagner,<sup>1,2</sup> Markus J. Barthel,<sup>1,2,3</sup> Robert R. A. Freund,<sup>1,2</sup> Stephanie Höppener,<sup>1,2</sup> Anja Traeger,<sup>1,2</sup> Felix H. Schacher<sup>1,2\*</sup>, Ulrich. S. Schubert<sup>1,2,3\*</sup>

1 - Laboratory of Organic and Macromolecular Chemistry (IOMC), Friedrich Schiller University Jena, Humboldtstrasse 10, 07743 Jena, Germany

2 - Jena Center for Soft Matter (JCSM), Friedrich Schiller University Jena, Philosophenweg 7, 07743 Jena, Germany

3 - Dutch Polymer Institute (DPI), P.O. Box 902, 5600 AX Eindhoven, the Netherlands

[ulrich.schubert@uni-jena.de](mailto:ulrich.schubert@uni-jena.de), [felix.schacher@uni-jena.de](mailto:felix.schacher@uni-jena.de)

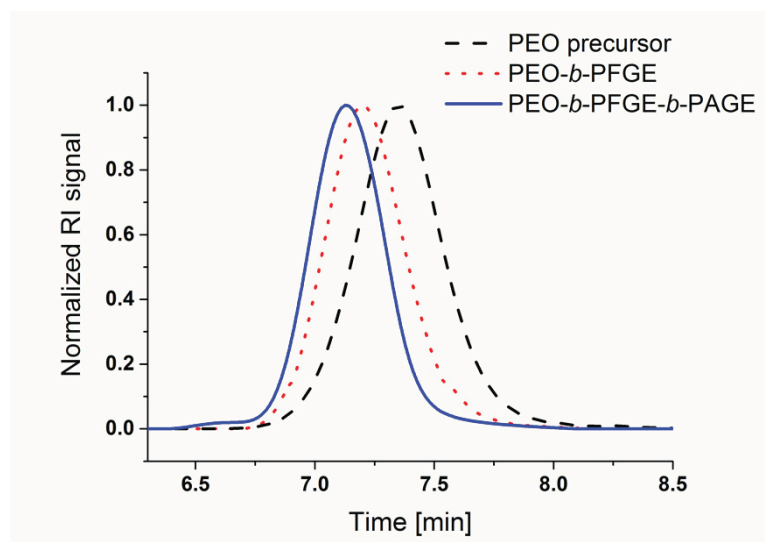


**Figure S1:** SEC traces of PEO (black dashed line), PEO-*b*-PFGE (red pointed line), and PEO-*b*-PFGE-*b*-PAGE (blue line, solvent: CHCl<sub>3</sub>/*i*PrOH/Et<sub>3</sub>N).

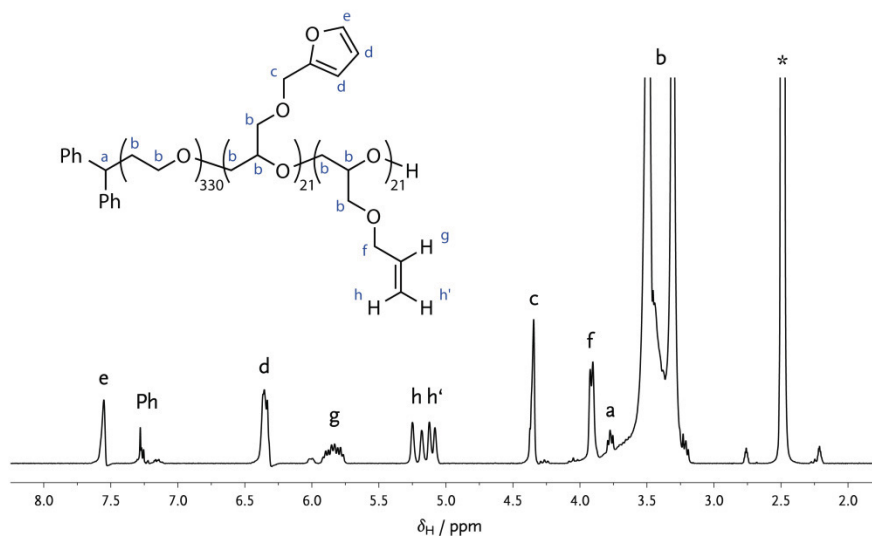


**Figure S2:**  $^1\text{H-NMR}$  spectrum (300 MHz,  $\text{DMSO-}d_6$ ) of  $\text{PEO-}b\text{-PFGE-}b\text{-PAGE}$ .

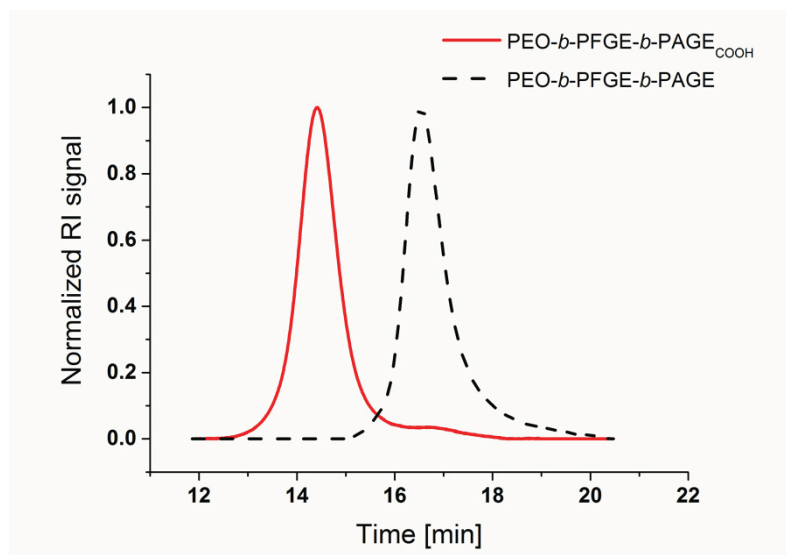


**Figure S3:** SEC traces of  $\text{PEO-}b\text{-PFGE-}b\text{-PAGE}$  and  $\text{PEO-}b\text{-PFGE-}b\text{-PAGE}_{\text{COOH}}$  (solvent: DMAc).



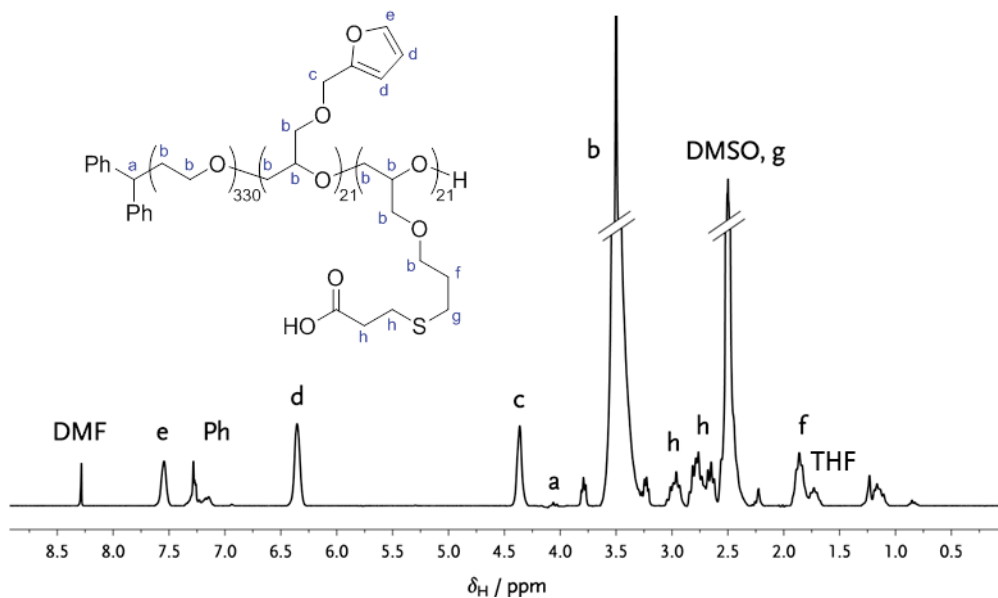


**Figure S4:**  $^1\text{H-NMR}$  spectrum (250 MHz,  $\text{DMSO-}d_6$ ) of  $\text{PEO-}b\text{-PFGE-}b\text{-PAGE}_{\text{COOH}}$ . The signal at 1.75 ppm corresponds to residual amounts of THF from the BioBeads column. Signals in the range of 0.8 to 1.6 ppm are most probably caused by impurities from vacuum grease.

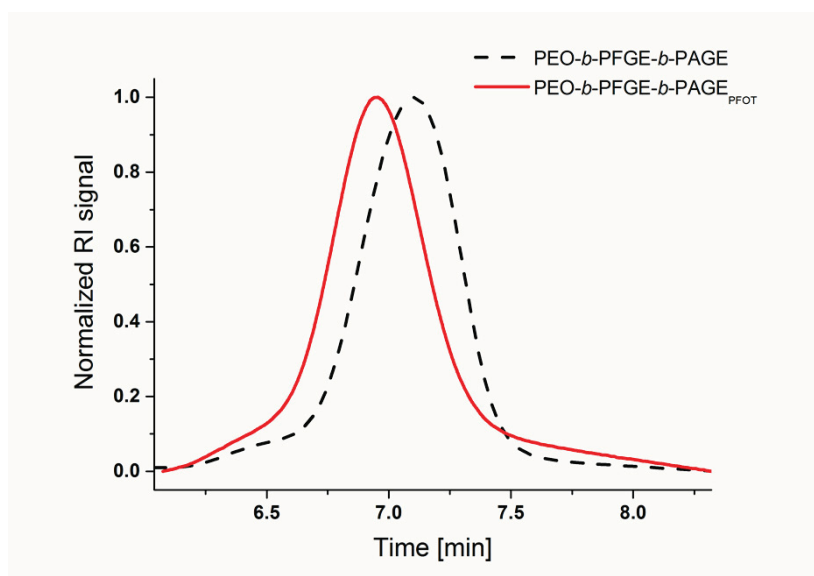


**Figure S5:** SEC traces of  $\text{PEO-}b\text{-PFGE-}b\text{-PAGE}$  and  $\text{PEO-}b\text{-PFGE-}b\text{-PAGE}_{\text{PFOT}}$  (solvent:  $\text{CHCl}_3/i\text{PrOH}/\text{Et}_3\text{N}$ ).

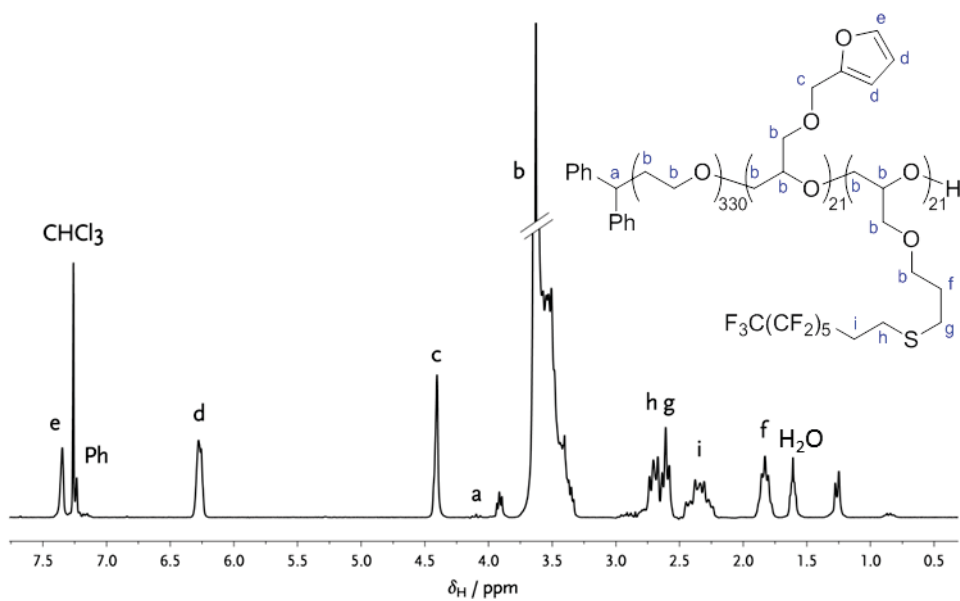


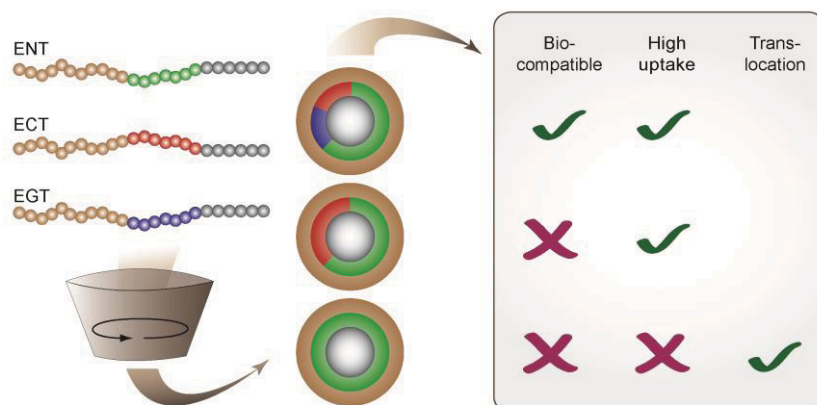
**Figure S6:** <sup>1</sup>H-NMR spectrum (250 MHz, CDCl<sub>3</sub>) of PEO-*b*-PFGE-*b*-PAGE<sub>PFOT</sub>. Signals in the range of 0.8 to 1.6 ppm are most probably caused by impurities from vacuum grease. The signal at 1.6 ppm represents residual amounts of water.

## Publication P9

Small but powerful: Co-assembly of polyether-based triblock terpolymers into sub-30 nm micelles and synergistic effects on cellular interactions

M. J. Barthel, A. C. Rinkenauer, M. Wagner, U. Mansfeld, S. Höppener, J. A. Czaplewska,  
M. Gottschaldt, A. Träger, F. H. Schacher, U. S. Schubert

*Biomacromolecules* **2014**, *15*, 2426-2439.





# Small but Powerful: Co-Assembly of Polyether-Based Triblock Terpolymers into Sub-30 nm Micelles and Synergistic Effects on Cellular Interactions

Markus J. Barthel,<sup>†,‡,§,||</sup> Alexandra C. Rinkenauer,<sup>†,‡,§</sup> Michael Wagner,<sup>‡,§</sup> Ulrich Mansfeld,<sup>‡,§</sup> Stephanie Hoepfener,<sup>‡,§</sup> Justyna A. Czaplewska,<sup>‡,§</sup> Michael Gottschaldt,<sup>‡,§</sup> Anja Träger,<sup>‡,§</sup> Felix H. Schacher,<sup>\*,‡,§</sup> and Ulrich S. Schubert<sup>\*,‡,§,||</sup>

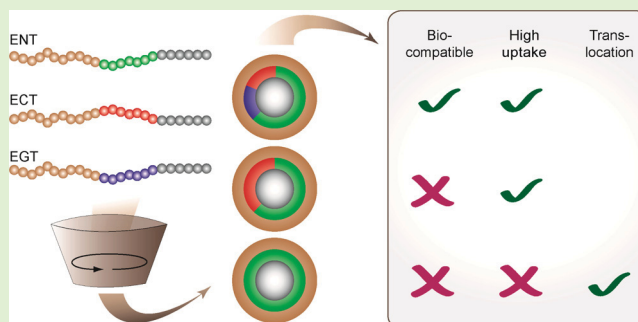
<sup>†</sup>Laboratory of Organic and Macromolecular Chemistry (IOMC), Friedrich Schiller University Jena, Humboldtstrasse 10, 07743 Jena, Germany

<sup>§</sup>Jena Center for Soft Matter (JCSM), Friedrich Schiller University Jena, Philosophenweg 7, 07743 Jena, Germany

<sup>||</sup>Dutch Polymer Institute (DPI), P.O. Box 902, 5600 AX Eindhoven, The Netherlands

## S Supporting Information

**ABSTRACT:** We introduce a versatile ABC triblock terpolymer platform based on poly(ethylene oxide)-*block*-poly(allyl glycidyl ether)-*block*-poly(*tert*-butyl glycidyl ether) (PEO-*b*-PAGE-*b*-PtBGE) and subsequent functionalization of the PAGE segment with thiogalactose (hydroxyl), cysteamine (amino), and 2-mercaptopropionic acid (carboxy) by thiol-ene chemistry. These materials are used to prepare core-shell-corona micelles with a PtBGE core, a PAGE shell, and a PEO corona and sizes below 30 nm in aqueous media. We investigate the influence of different functional groups on micelle formation and cellular uptake. Moreover, co-assembly of differently functionalized materials allows to create micelles with a mixed shell and adjustable charge and, in that way, important characteristics such as cell uptake or cytotoxicity can be controlled. Furthermore, we demonstrate that even the uptake mechanism depends on the substitution pattern of the underlying triblock terpolymer.



## INTRODUCTION

The synthesis and self-assembly of amphiphilic block copolymers into micellar structures of defined size, shape, and composition represents a very active field of research and such nanostructures show high potential for their use in potential biomedical and pharmaceutical applications.<sup>1,2</sup> The introduction of further functionalities or stimuli-responsive segments as well as the morphological variety being accessible benefit from the introduction of a third segment (C) resulting in ABC triblock terpolymers.<sup>3</sup> Since first attempts in the 1980s and the pioneering work of Stadler and co-workers later in the 1990s, increasing research efforts have been devoted to the preparation and application of such materials.<sup>4–7</sup> One intriguing aspect of ternary materials is that multicompartment micelles can be realized, structures which are further subdivided in core, shell, or corona. As a consequence of their architecture, multicompartment micelles can be used to simultaneously store two different payloads within one micellar core or to implement several responsive segments.<sup>8–11</sup> In this context, we recently reported that multicompartment micelles with pH-dependent charge and morphology bear enormous potential as nonviral

gene transfection agents, enabling high delivery efficiency in combination with low cytotoxicities.<sup>12,13</sup>

Typically, each segment of ABC triblock terpolymers is attributed a specific “task” in solution: One block (e.g., A) ensures solubility in the desired environment. In water, often poly(ethylene oxide) (PEO) is used as this material is water-soluble, nontoxic, and prevents unspecific protein interactions (“stealth” effect).<sup>14–17</sup> Another segment (B) can be used to introduce functional groups or the possibility to carry out postpolymerization functionalization reactions (e.g., allyl glycidyl ether) to further fine-tune the material properties or to attach targeting moieties.<sup>18–21</sup> The third block (C) often is utilized as solvophobic block, resulting in amphiphilic triblock terpolymers in the case of hydrophobic segments. Related to this, we recently reported that hydrophobic glycidyl ethers, for example, *tert*-butyl glycidyl ether or furfuryl glycidyl ether, can be used as core forming segments in micellar aggregates.<sup>18,19,22,23</sup> These micellar cores can be applied, for example,

Received: February 24, 2014

Revised: May 27, 2014

Published: May 29, 2014

to encapsulate hydrophobic guest compounds such as drugs or dyes.<sup>24</sup> If suitable building blocks are realized, the response of block copolymer nanostructures toward changes in temperature or pH value can be easily realized.<sup>25,26</sup> This often induces quite drastic changes of the material properties and can be used to trigger the controlled release of encapsulated cargo or to enable endosomal release after cell internalization.<sup>12,27,28</sup> Nevertheless, to date, the number of solution applications involving ABC triblock terpolymers is rather low, probably due to high synthetic efforts that often involve the combination of different polymerization techniques, modification sequences, or stepwise assembly procedures.

An alternative approach for the design of complex block copolymer micelles is the simple mixing of block copolymers. For instance, AB and AC diblock copolymers, where A represents identical hydrophobic blocks, which are mixed in nonselective solvents and then transferred to a solvent or solvent mixture selective for B and C. It is generally believed that comparable degrees of polymerization (DP) for block A are beneficial. This could be shown, for example, for PEO-*b*-PLA and PNIPAM-*b*-PLA diblock copolymers. Co-assembly in aqueous solution leads to the formation of micelles with a PLA core and a mixed PEO/PNIPAM shell. These materials showed potential as smart carriers in drug delivery processes.<sup>29–32</sup> In this context, Kabanov and co-workers have demonstrated that micelles prepared from mixtures of amphiphilic and cationic copolymers based on Pluronic can be applied for an efficient delivery of oligonucleotide sequences.<sup>33</sup> Such concepts have also been employed for the preparation of multicompartment micelles.<sup>34,35</sup>

Besides efforts to design structures of increased complexity for drug delivery applications, Kataoka et al. demonstrated that size does indeed matter and showed that micelles with diameters below 100 nm are highly interesting candidates in such approaches.<sup>36</sup> Commonly, nanostructures with diameters between 50 to 200 nm are used because endocytosis as predominant internalization process can be assumed, the interaction with the immune system is reduced, and renal clearance can be avoided.<sup>37,38</sup> In contrast, polymeric micelles with sizes far below 100 nm are scarce in literature and, up to now, rarely studied with regard to interactions with biological matter.<sup>37</sup> In this context, spherical core–shell micellar structures of approximately 30 nm were found to effectively penetrate poorly permeable tumor membranes.<sup>36</sup> Besides size, also charge significantly influences cell interactions of polymeric micelles, as well as their cytotoxicity and hemocompatibility. In general, the presence of cationic charges leads to increased interactions with the negatively charged cell membrane. Although this is advantageous for uptake, it also favors membrane destabilization and increases cytotoxicity. These side effects can be circumvented by using PEO as corona, but often at the cost of decreased cell interaction.<sup>39,40</sup> As an alternative, the presence of negatively charged segments allows to decrease both the cytotoxicity and nonspecific interactions with serum proteins.<sup>41</sup> Hence, direct control over the charge balance in (block co-) polymer nanostructures seems to be a promising strategy to balance cellular interactions, efficient uptake, and simultaneously suppress nonspecific interactions and lower cytotoxicity. This can be achieved, e.g., via the combination of positively and negatively charged blocks in block copolymers and has been recently demonstrated for multicompartment micelles from polybutadiene-*block*-poly(methacrylic acid)-*block*-poly(2-dimethylaminoethyl methacry-

late) (BMAAD) triblock terpolymers. These structures comprise a polybutadiene core, a patchy shell consisting of *intra*-micellar interpolyelectrolyte complexes (*im*-IPEC) between PMAA and PDMAEMA, and a cationic corona of excess PDMAEMA.<sup>12</sup> We could demonstrate that the presence of the *im*-IPECs and the inherent pH-dependent dynamics of the system favor cellular uptake, while the PMAA middle segment acts as competing polyelectrolyte during delivery of pDNA and, at the same time, reduces cytotoxicity and facilitates release of the genetic material. Nevertheless, this approach suffers from a severe drawback: Preparation conditions, micellar size, and pH-dependent characteristics depend strongly on the terpolymer composition and, thus, have to be investigated and optimized for each new material being synthesized. This motivated us to probe a different, more versatile and general approach: Co-assembly of a small library of structurally similar ABC triblock terpolymers with different functional groups being present within the segment B.

We therefore introduce a triblock terpolymer platform based on poly(ethylene oxide)-*block*-poly(allyl glycidyl ether)-*block*-poly(*tert*-butyl glycidyl ether) (PEO-*b*-PAGE-*b*-PtBGE), synthesized by sequential living anionic ring-opening polymerization (AROP), as versatile carriers for hydrophobic compounds. The pendant double bonds of the PAGE block were functionalized by thiol–ene chemistry to introduce model ligands (thiogalactose), amine groups to provide positive charges (cysteamine), as well as carboxylic groups to generate negative charges (3-mercapto propionic acid). The obtained triblock terpolymers are subsequently used for the co-assembly into well-defined spherical core-shell-corona micelles with diameters below 30 nm and precisely adjustable charge and composition. Depending on the latter, we found synergistic effects regarding cellular uptake and cytotoxicity. In addition, the internalization efficiency (and pathway) was analyzed under serum-reduced and serum-containing conditions, showing an effective shielding by the PEO corona and providing first insights into the underlying uptake mechanism.

## ■ EXPERIMENTAL SECTION

**Instruments and Methods.** <sup>1</sup>H NMR spectra were recorded on a Bruker AC 300 MHz spectrometer in deuterated chloroform.

**Size Exclusion Chromatography (SEC).** Size exclusion chromatography (SEC) was performed on a Shimadzu SCL-10A system (with a LC-10AD pump, a RID-10A refractive index detector, and a PL gel 5 μm mixed-D column at RT), the eluent was a mixture of chloroform/triethylamine/isopropanol (94:4:2) with a flow rate of 1 mL/min. The system was calibrated with poly(ethylene glycol) standards from PSS ( $M_n = 1470$  to 42000 g/mol).

**Matrix Assisted Laser Desorption Ionization - Time of Flight Mass Spectrometry (MALDI-ToF).** MALDI-ToF mass spectra were obtained using an Ultraflex III ToF/ToF mass spectrometer (Bruker Daltonics) with *trans*-2-[3-(4-*tert*-butylphenyl)-2-methyl-2-propenylidene] malononitrile (DCTB) or 2,5-dihydroxybenzoic acid (DHB) as matrix in reflector as well as in linear mode. The instrument was calibrated prior to each measurement with an external PMMA standard from PSS Polymer Standards Services GmbH.

**Dynamic Light Scattering (DLS).** Dynamic light scattering (DLS) was performed at a scattering angle of 90° on an ALV CGS-3 instrument and a He–Ne laser operating at a wavelength of  $\lambda = 633$  nm at 25 °C. The CONTIN algorithm was applied to analyze the obtained correlation functions. Apparent hydrodynamic radii were calculated according to the Stokes–Einstein equation. All CONTIN plots are number-weighted.

**Cryogenic Transmission Electron Microscopy (cryo-TEM).** Cryo-TEM measurements were carried out at 120 kV using a Philips-CM

120 equipped with a  $1k \times 1k$  CCD camera. Sample preparation was performed on Quantifoil grids (holey carbon R2/2) after plasma cleaning. Vitrification of the samples was carried out in a home-built system with a temperature control unit. A drop of the polymer solution (5  $\mu$ L) was placed on the grid, which was blotted and subsequently plunged into a cryogen reservoir containing liquid ethane. The samples were afterward stored in liquid nitrogen and were transferred to the TEM keeping the temperature below  $-176$  °C to avoid the formation of crystalline ice layers.

**Asymmetric Flow Field-Flow Fractionation (AF4).** Asymmetric flow field-flow fractionation (AF4) was performed on an AF2000 MT System (Postnova Analytics, Landsberg, Germany) coupled to an UV (PN3211, 260 nm), RI (PN3150), MALLS (PN3070, 633 nm), and DLS (ZetaSizer Nano ZS) detector. The eluent is delivered by three different pumps (tip, focus, cross-flow) and the sample is injected by an autosampler (PNS300) into the channel. The channel has a trapezoidal geometry and an overall area of 31.6 cm<sup>2</sup>. The nominal height of the spacer was 500  $\mu$ m and a regenerated cellulose membrane with a molar mass cutoff of 10 kg/mol was used as accumulation wall. All experiments were carried out at 25 °C and the eluent was degassed water containing 20 mM NaCl. The detector flow rate was set to 0.5 mL/min for all samples and 20  $\mu$ L (5 mg/mL) were injected with an injection flow rate of 0.2 mL/min for 7 min. For EAT the cross-flow was set to 2 mL/min and decreased under an exponential gradient (0.5) to 0 within 20 min. For EGT the cross-flow was set to 2 mL/min and decreased under a linear gradient to 0 within 20 min. For ECT the cross-flow was set to 2 mL/min and decreased under an exponential gradient (0.5) to 0 within 25 min. For ENT the cross-flow was set to 1.3 mL/min and decreased under an exponential gradient (0.7) to 0 within 25 min. For (ENT/ECT)<sup>1:2.6</sup> the cross-flow was set to 2 mL/min and decreased under a linear gradient to 0 within 35 min. For (ENT/ECT)<sup>1:2.1</sup>, the cross-flow was set to 2 mL/min and decreased under a linear gradient to 0 within 30 min. For (ENT/ECT)<sup>3.5:1</sup>, (ENT/ECT/EGT)<sup>3.5:1:0.5</sup>, and (ENT/ECT/EGT)<sup>3.4:1:2.3</sup>, the cross-flow was set to 1.3 mL/min and decreased under an exponential gradient (0.7) to 0 within 25 min. After the cross-flow reaches zero, for all samples, the cross-flow was kept constant at zero for at least 30 min to ensure complete elution. For calculation of the molar mass and the radius of gyration a Berry plot was used.<sup>42</sup> All measurements were repeated three times. The refractive index increment ( $dn/dc$ ) of all samples was measured by manual injection of a known concentration directly into the channel without any focusing or cross-flow. The  $dn/dc$  was calculated as the average of at least three injections from the area under the RI curve ( $AUC_{RI}$ ).

**Electrophoretic Light Scattering (ELS).** Electrophoretic light scattering was used to measure the electrokinetic potential, also known as zeta potential. The measurements were performed on a Zetasizer Nano ZS (Malvern Instruments, Herrenberg, Germany) by applying laser Doppler velocimetry.<sup>43</sup> For each measurement, 20 runs were carried out using the slow-field reversal and fast-field reversal mode at 150 V. Each experiment was performed in triplicate at 25 °C. The zeta potential ( $\zeta$ ) was calculated from the electrophoretic mobility ( $\mu$ ) according to the Henry equation. Henry coefficient  $f(ka)$  was calculated according to Ohshima.<sup>44</sup>

**Gel Migration Assay.** The micelles (40  $\mu$ g) were incubated with 5  $\mu$ L loading buffer (0.25% bromphenolblue, 40% saccharose). Afterward, the solutions were loaded on a 1% agarose gel, electrophoresed (Bio-Rad, Munich, Germany, Mini-Sub Cell GT System) was carried out with a current of 80 V (PowerPac Basic as power supply) for 30 min in TBE running buffer solution (107.8 g/L tris-base, 7.4 g/L EDTA, 55 g/L borate). Subsequently, the agarose gel was irradiated with an UV-lamp to induce fluorescence of the bands.

HEK-293 cells (CRL-1573, ATCC) were maintained in RPMI 1640 culture medium, L929 cells (CCL-1, ATCC) in DMEM culture medium, and HepG2 (HB-8065, ATCC) in DMEM-F12 culture medium. Both media were supplemented with 10% fetal calf serum (FCS), 100  $\mu$ g/mL streptomycin, 100 IU/mL penicillin, and 2 mM L-glutamine. Cells were cultivated at 37 °C in a humidified 5% CO<sub>2</sub> atmosphere.

**Cytotoxicity.** For L929 cells, the cytotoxicity assay was performed as described by ISO10993-5. In detail, cells were seeded at  $1 \times 10^4$  cells per well in a 96-well plate and incubated for 24 h. No cells were seeded in the outer wells. Afterward, polymers at the indicated concentrations were added, and the cells were incubated at 37 °C for further 24 h. Subsequently, the medium was replaced by fresh media and AlamarBlue, as recommended by the supplier. After incubation for 4 h, the fluorescence was measured at Ex 570/Em 610 nm, with untreated cells on the same well plate serving as controls.

**Hemolysis Assay.** The membrane damaging properties of the polymers were quantified by analyzing the release of hemoglobin from human erythrocytes. The erythrocyte-containing blood was centrifuged at 700 g for 10 min. The obtained pellet was washed three times with D-PBS pH 7.4 by centrifugation at 700 g for 10 min and resuspended in HBG buffer of pH 7. Polymer solutions were added to the erythrocytes (100  $\mu$ L) and incubated for 60 min under constant shaking at 37 °C. After centrifugation (700 g, 10 min), the supernatant was analyzed for released hemoglobin at 580 nm. The absorbance was measured using a plate reader (Genios Pro, Tecan, Germany). For comparison, collected erythrocytes were washed with DPBS and either lysed with 0.2% Triton X-100, yielding the 100% lysis control value ( $A_{100}$ ) or resuspended in DPBS as reference ( $A_0$ ). The analysis was repeated with blood from at least six independent donors. The hemolytic activity of the polycations was calculated as follow:

$$\% \text{hemolysis} = 100 \times (A_{\text{sample}} - A_0) / (A_{100} - A_0) \quad (1)$$

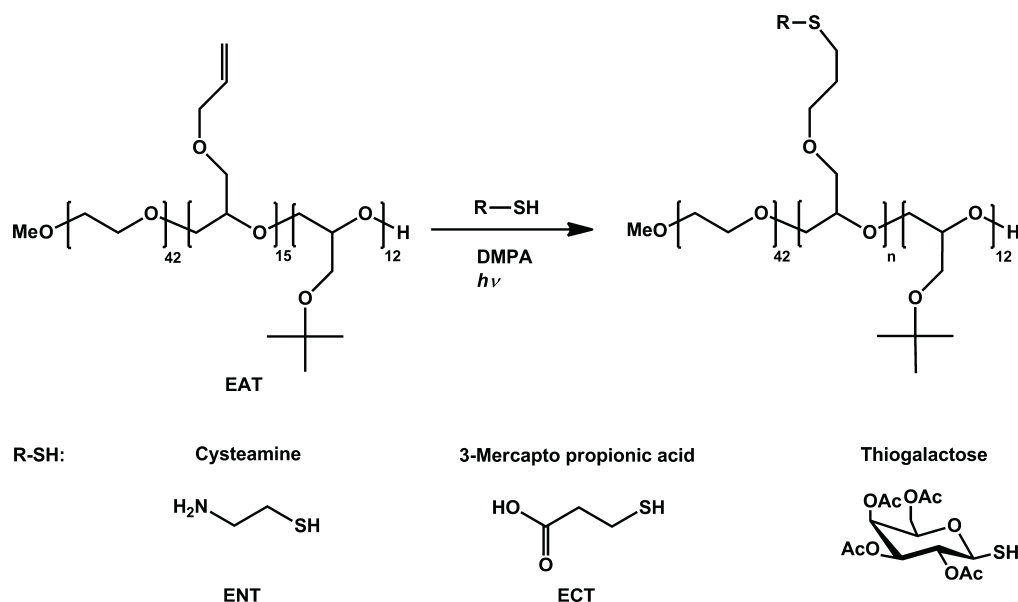
Here,  $A_{\text{sample}}$ ,  $A_0$ , and  $A_{100}$  are the absorbance intensities of a given sample, erythrocytes incubated with D-PBS, and erythrocytes lysed with Triton X-100.

**Uptake Studies.** For uptake of the adherent cell lines, cells were seeded at a density of  $10^5$  cells per well in 12-well plates 1 day before internalization experiment. A total of 1 h prior to addition of micelles, cells were rinsed with PBS and supplemented with 1 mL OptiMEM (Life Technologies) or fresh serum containing growth media. Micelles were added at indicated end concentration to the cells and the plates were incubated for 24 h in the incubator. For analysis, the cells were harvested by trypsinization and 10% trypan blue was added. Subsequently, the cells were analyzed via flow cytometry using a Cytomics FC 500 (Beckman Coulter). For determination of the viability during flow cytometry, dead cells were identified in the SSC/FSC dot plot. The relative uptake of encapsulated Nile red fluorescence of  $10^4$  cells was quantified. For determination of the uptake efficiency, viable cells containing Nile red were gated. The experiments were performed at least independently three times.

**Materials.** The triblock terpolymer precursor PEO<sub>42</sub>-*b*-PAGE<sub>15</sub>-*b*-PtBGE<sub>12</sub> (SEC:  $M_n = 3350$  g/mol;  $M_w = 3500$  g/mol;  $D = 1.05$ ; obtained with PEO calibration; NMR:  $M_n = 5122$  g/mol) as well as 2,3,4,6-tetra-*O*-acetyl-1-thio- $\beta$ -D-galactopyranose (acetylated thio galactose) were synthesized as reported previously.<sup>19,45,46</sup> 2,2-Dimethoxy-2-phenylacetophenone (DMPA), cysteamine, 3-mercapto propionic acid, sodium methanolate (0.5 M in methanol), Nile red, DOWEX SOWX8-200, methanol, *N,N*-dimethylformamide (DMF), tetrahydrofuran (THF), and ethanol were purchased from Aldrich and used as received. AlamarBlue was obtained from Life Technologies (Darmstadt, Germany). If not stated otherwise, cell culture materials, cell culture media, and solutions were obtained from PAA (Pasching, Austria). All other chemicals were purchased from Sigma-Aldrich (Steinhausen, Germany) and are of analytical grade or better and were used without further purification.

**Cysteamine Functionalization of PEO<sub>42</sub>-*b*-PAGE<sub>15</sub>-*b*-PtBGE<sub>12</sub>.** A total of 300 mg (0.059 mmol, corresponding to 0.88 mmol of PAGE) of the triblock terpolymer were dissolved in 5 mL of a mixture of DMF, EtOH, and MeOH (ratio 1:0.3:1). Aliquots of 45 mg (0.18 mmol, 0.2 equiv) DMPA and 339 mg cysteamine (4.39 mmol, 5 equiv) were added to the mixture. The reaction mixture was degassed and stirred under UV irradiation (366 nm, 6 W) for 24 h. The increase of the molar mass ( $M_n$ ) and the decrease of the signal intensity of the peaks of the double bond were monitored by SEC and <sup>1</sup>H NMR, respectively. The reaction mixture was purified by dialysis against

**Scheme 1. Schematic Representation of the Thiol–Ene Modification of PEO<sub>42</sub>-*b*-PAGE<sub>15</sub>-*b*-PtBGE<sub>12</sub> Using Cysteamine (N), 3-Mercapto Propionic Acid (C), and Acetylated Thiogalactose<sup>a</sup>**



<sup>a</sup>The abbreviations (EAT, ENT, ECT) will be used later on for the nomenclature of the micelles generated via self-assembly of the modified triblock terpolymers.

water, a THF/water mixture (1:1) and pure THF. The solvent was removed by distillation under reduced pressure and the product dried under vacuum. Yield: 250 mg.

<sup>1</sup>H NMR (300 MHz, CDCl<sub>3</sub>-*d*<sub>6</sub>,  $\delta$  in ppm): 6.00–5.75 (m, 1H), 5.34–5.07 (m, 2H), 4.04–3.9 (m, 2H), 3.9–3.2 (m, PEO backbone), 2.74–1.94 (br, 4H, CH<sub>2</sub>-CH<sub>2</sub>-S), 2.74–1.93 (br, 2H, S-CH<sub>2</sub>), 1.3–0.97 (s, 9H). *f* = 53%. SEC: *M*<sub>n</sub> = 3500 g/mol, *M*<sub>w</sub> = 3600 g/mol, *D* = 1.06.

**3-Mercapto Propionic Acid Functionalization of PEO<sub>42</sub>-*b*-PAGE<sub>15</sub>-*b*-PtBGE<sub>12</sub>.** A total of 450 mg (0.088 mmol, corresponding to 1.32 mmol of PAGE) of the triblock terpolymer was dissolved in 5 mL of a mixture of DMF/EtOH (ratio 3:1). Subsequently, 68 mg (0.27 mmol, 0.2 equiv) DMPA and 0.23 mL of 3-mercapto propionic acid (2.64 mmol, 2 equiv) were added. The reaction mixture was degassed and stirred under UV irradiation (366 nm, 6 W) for 24 h. The increase of the molar mass (*M*<sub>n</sub>) and the decrease of the signal intensity of the peaks of the double bond were monitored by SEC and <sup>1</sup>H NMR, respectively. The reaction mixture was purified by dialysis against a THF/water mixture (5:1) and pure THF. The solvent was removed by distillation under reduced pressure and the product dried under vacuum. Yield: 600 mg.

<sup>1</sup>H NMR (300 MHz, CDCl<sub>3</sub>-*d*<sub>6</sub>,  $\delta$  in ppm): 3.94–3.24 (m, PEO backbone), 2.87–2.72 (m, 4H, CH<sub>2</sub> linker), 1.92–1.76 (m, 2H), 1.24–1.09 (s, 9H). Degree of functionalization: *f* = 100%. SEC: *M*<sub>n</sub> = 3550 g/mol, *M*<sub>w</sub> = 3700 g/mol, *D* = 1.05.

**Thiogalactose Functionalization of PEO<sub>42</sub>-*b*-PAGE<sub>15</sub>-*b*-PtBGE<sub>12</sub>.** A total of 450 mg (0.088 mmol, corresponding to 1.32 mmol of PAGE) of the triblock terpolymer were dissolved in 5 mL of a mixture of DMF/EtOH (ratio 3:1). To the mixture, 68 mg (0.27 mmol, 0.2 equiv) DMPA and 963 mg acetylated thiogalactose (2.64 mmol, 2 equiv) were added. The reaction mixture was degassed and stirred under UV irradiation (366 nm, 6 W) for 72 h. The increase of the molar mass (*M*<sub>n</sub>) and the decrease of the signal intensity of the peaks of the double bond were monitored by SEC and <sup>1</sup>H NMR, respectively. The reaction mixture was purified by size exclusion chromatography (Biobeads SX-1) and the product was dried under vacuum. Yield: 600 mg.

<sup>1</sup>H NMR (300 MHz, CDCl<sub>3</sub>-*d*<sub>6</sub>,  $\delta$  in ppm): 6.00–5.76 (m, 1H), 5.7–4.9 (m, 3H, Gal), 4.56–4.43 (m, 1H, Gal), 4.40–4.21 (m, 3H, Gal), 4.20–3.03 (m, PEO backbone), 2.86–2.62 (m, 2H), 2.57–1.47

(m, 12H-Ac), 1.28–1.04 (s, 9H). Degree of functionalization: *f* = 70%. SEC: *M*<sub>n</sub> = 4200 g/mol, *M*<sub>w</sub> = 4350 g/mol, *D* = 1.04.

**Deprotection of PEO<sub>42</sub>-*b*-(PAGE<sub>5</sub>-*co*-PAGE<sub>10,Gal</sub>)-*b*-PtBGE<sub>12</sub>.** A total of 600 mg (0.066 mmol, corresponding to 2.64 mmol of acetyl groups) of the triblock terpolymer was dissolved in 15 mL of dry methanol. To the mixture, 7 mL (3.5 mmol, 1.3 equiv) of a 0.5 M sodium methanolate solution was added and the mixture was allowed to stir for 1 h. Afterward, a DOWEX 50WX8–200 ion-exchange resin was added and stirred for 15 min to neutralize the reaction mixture. The resin was filtered off, and the crude product was dialyzed against a water/THF mixture (5:1), pure water, and pure THF. The solvent was removed by distillation under reduced pressure and product was dried under vacuum. Yield: 250 mg.

<sup>1</sup>H NMR (300 MHz, CDCl<sub>3</sub>-*d*<sub>6</sub>,  $\delta$  in ppm): 6.0–5.76 (m, 1H), 5.5–4.84 (m, 3H-Gal), 4.10–2.80 (m, PEO backbone), 1.26–1.01 (s, 9H). SEC: *M*<sub>n</sub> = 10400 g/mol, *M*<sub>w</sub> = 11500 g/mol, *D* = 1.10.

**Preparation of Triblock Terpolymer Micelles.** The following procedures with the respective stoichiometry were used for the preparation of all micellar nanostructures with a concentration of 10 g/L in aqueous solution.

A total of 100 mg of the corresponding triblock terpolymer was dissolved in 5 mL of THF, and 4 mg of Nile red was added to the solution. To the mixture was then added slowly 10 mL of Milli-Q water via syringe, and the THF was allowed to evaporate by stirring overnight. Non-encapsulated dye was filtered off by a 0.45  $\mu$ m nylon syringe filter. In case of evaporation of water, the solution was filled up again to a volume of 10 mL. After filtration, a clear pink solution could be obtained.

**Binary Co-micelles.** Here, the preparation of a 1.2:1 mixture of PEO<sub>42</sub>-*b*-(PAGE<sub>8,NH2</sub>-*co*-PAGE<sub>7</sub>)-*b*-PtBGE<sub>12</sub> and PEO<sub>42</sub>-*b*-PAGE<sub>15,COOH</sub>-*b*-PtBGE<sub>12</sub> is reported. Due to the different degrees of functionalization, a 2:1 ratio regarding the masses was used.

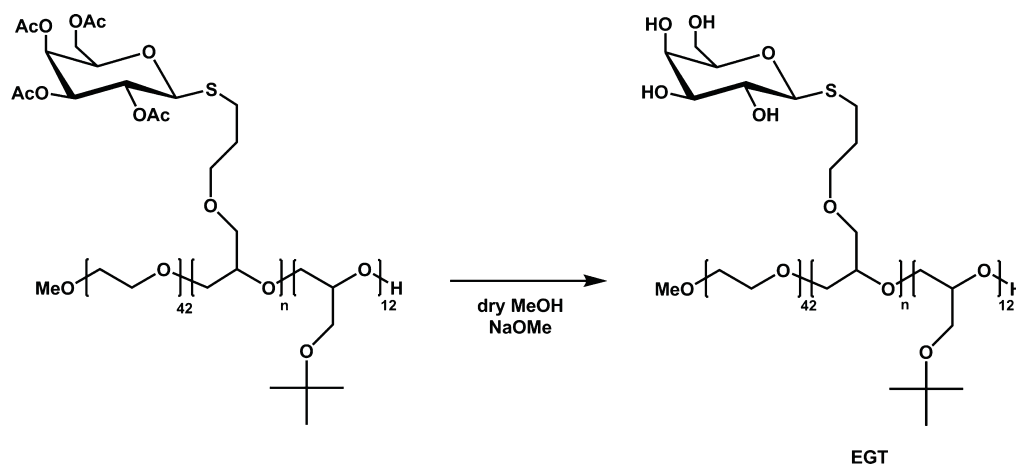
A total of 6.6 mg of PEO<sub>42</sub>-*b*-(PAGE<sub>8,NH2</sub>-*co*-PAGE<sub>7</sub>)-*b*-PtBGE<sub>12</sub> and 3.3 mg of PEO<sub>42</sub>-*b*-PAGE<sub>15,COOH</sub>-*b*-PtBGE<sub>12</sub> were dissolved in 0.3 mL of THF, and approximately 2 mg of Nile red was added to the solution. The solution was then slowly added to 1 mL of Milli-Q water and the THF was allowed to evaporate by stirring overnight. Nonencapsulated dye remained as precipitate in the solution and was filtered off by a 0.45  $\mu$ m nylon syringe filter. In case of evaporation of water, the solution was filled up again to a volume of 1 mL. After filtration, a clear pink solution could be obtained.



Table 1. Characterization Data of the Synthesized Triblock Terpolymers<sup>a</sup>

sample	abbreviation	SEC			<sup>1</sup> H NMR	
		<i>M<sub>n</sub></i> (g/mol)	<i>M<sub>w</sub></i> (g/mol)	<i>D</i>	<i>M<sub>n</sub></i> (g/mol)	<i>f</i> (%)
PEO <sub>42</sub> - <i>b</i> -PAGE <sub>15</sub> - <i>b</i> -PtBGE <sub>12</sub>	EAT	3350	3500	1.05	5100	
PEO <sub>42</sub> - <i>b</i> -(PAGE <sub>8,NH<sub>2</sub></sub> - <i>co</i> -PAGE <sub>7</sub> )- <i>b</i> -PtBGE <sub>12</sub>	ENT	3500	3600	1.06	5750	53
PEO <sub>42</sub> - <i>b</i> -PAGE <sub>15,COOH</sub> - <i>b</i> -PtBGE <sub>12</sub>	ECT	3550	3700	1.05	6700	100
PEO <sub>42</sub> - <i>b</i> -(PAGE <sub>10,AcGal</sub> - <i>co</i> -PAGE <sub>5</sub> )- <i>b</i> -PtBGE <sub>12</sub>		4200	4350	1.04	8800	70
PEO <sub>42</sub> - <i>b</i> -(PAGE <sub>10,Gal</sub> - <i>co</i> -PAGE <sub>5</sub> )- <i>b</i> -PtBGE <sub>12</sub>	EGT	10400	11500	1.10	7100	70

<sup>a</sup>The subscripts represent the degree of polymerization. The shown abbreviations are used later on when describing self-assembled structures of the materials.

Scheme 2. Schematic Representation of the Deprotection of Acetylated Thiogalactose (G) Attached to a PEO-*b*-PAGE-*b*-PtBGE Triblock Terpolymer<sup>a</sup>

<sup>a</sup>The abbreviation EGT will be used later on for the nomenclature of micelles generated via self-assembly of the modified triblock terpolymer.

**Ternary Comicelles.** Here, the preparation of a 3.4:1:2.3 mixture of PEO<sub>42</sub>-*b*-(PAGE<sub>8,NH<sub>2</sub></sub>-*co*-PAGE<sub>7</sub>)-*b*-PtBGE<sub>12</sub>, PEO<sub>42</sub>-*b*-PAGE<sub>15,COOH</sub>-*b*-PtBGE<sub>12</sub>, and PEO<sub>42</sub>-*b*-(PAGE<sub>10,AcGal</sub>-*co*-PAGE<sub>5</sub>)-*b*-PtBGE<sub>12</sub> is reported. Due to the different degrees of functionalization, a 6:1:3.5 ratio regarding the stoichiometry of the amino and carboxy functionalized triblock terpolymers was used.

A total of 12 mg of PEO<sub>42</sub>-*b*-(PAGE<sub>8,NH<sub>2</sub></sub>-*co*-PAGE<sub>7</sub>)-*b*-PtBGE<sub>12</sub>, 2 mg of PEO<sub>42</sub>-*b*-PAGE<sub>15,COOH</sub>-*b*-PtBGE<sub>12</sub>, and 7 mg PEO<sub>42</sub>-*b*-(PAGE<sub>10,AcGal</sub>-*co*-PAGE<sub>5</sub>)-*b*-PtBGE<sub>12</sub> were dissolved in 0.4 mL of THF, and approximately 3 mg of Nile red was added to the solution. The solution was then slowly added to 2.1 mL of Milli-Q water, and the THF was allowed to evaporate by stirring overnight. Non-encapsulated dye remained as precipitate in the solution and was filtered off by a 0.45 μm nylon syringe filter. In the case of evaporation of water, the solution was filled up again to a volume of 2.1 mL. After filtration, a clear pink solution could be obtained.

## RESULTS AND DISCUSSION

**Synthesis and Postpolymerization Functionalization of PEO<sub>42</sub>-*b*-PAGE<sub>15</sub>-*b*-PtBGE<sub>12</sub>.** Based on earlier studies regarding the synthesis and functionalization, we used a polyether-based triblock terpolymer, poly(ethylene oxide)-*block*-poly(allyl glycidyl ether)-*block*-poly(*tert*-butyl glycidyl ether) (PEO-*b*-PAGE-*b*-PtBGE), as starting material for the synthesis of triblock terpolymers with identical A and C segments but different functionalities present in the B block.<sup>18,19</sup> The synthesis of PEO<sub>42</sub>-*b*-PAGE<sub>15</sub>-*b*-PtBGE<sub>12</sub> by AROP has been described previously (the subscripts denote the degrees of polymerization of the respective segment).<sup>19</sup> To generate differently functionalized examples for co-assembly, PEO<sub>42</sub>-*b*-PAGE<sub>15</sub>-*b*-PtBGE<sub>12</sub> was modified by thiol-ene chemistry: Cysteamine (2-aminoethanethiol) was used to

introduce NH<sub>2</sub> groups and the possibility to form cationic charges in aqueous media, 3-mercaptopropionic acid enables the introduction of carboxylic acid moieties and, hence, negative charges, and thiogalactose represents a model targeting moiety to ensure selective cellular uptake in hepatocytes.<sup>47,48</sup> In the latter case, acetyl-protected thiogalactose was used initially (Scheme 1).

The reactions were performed in mixtures of DMF/EtOH for tetraacetyl thiogalactose and 3-mercaptopropionic acid, whereas a mixture of DMF/EtOH/MeOH was used for cysteamine due to the rather low solubility of this compound. The reaction progress was monitored by size exclusion chromatography (SEC, shift to lower elution volumes in all cases) and <sup>1</sup>H NMR spectroscopy (Figures S1–S3). The degree of functionalization was determined by <sup>1</sup>H NMR spectroscopy through the decrease in intensity of the characteristic signals for the pendant double bonds of PAGE at 5.85 and 5.20 ppm compared to the *t*-butyl group of the PtBGE block at 1.15 ppm (Table 1). For the functionalization with 3-mercaptopropionic acid, full conversion could be reached after 24 h of irradiation. In contrast, only 53% functionalization could be obtained for cysteamine despite probing longer reaction times, higher irradiation intensity, or different triblock terpolymer/thiol ratios. We attribute this to the lower solubility observed for cysteamine. Similarly, in case of the acetylated thiogalactose only 70% functionalization could be reached, presumably also due to solubility issues of either the starting material or the triblock terpolymer after modification. Therefore, PEO<sub>42</sub>-*b*-(PAGE<sub>8,NH<sub>2</sub></sub>-*co*-PAGE<sub>7</sub>)-*b*-PtBGE<sub>12</sub> (ENT), PEO<sub>42</sub>-*b*-PAGE<sub>15,COOH</sub>-*b*-PtBGE<sub>12</sub> (ECT),

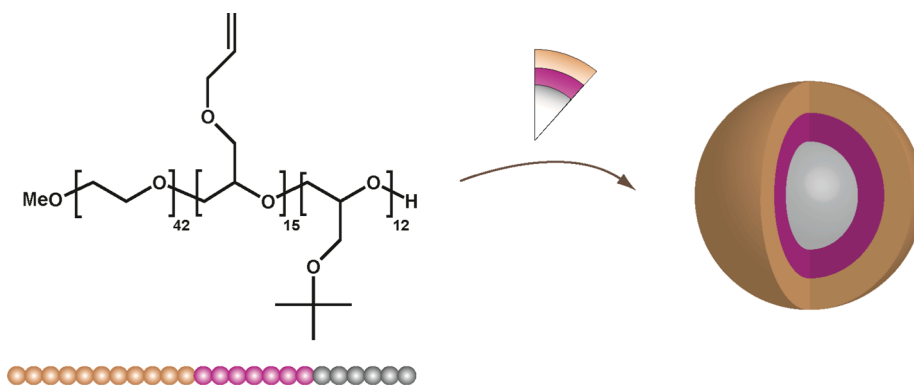


**Figure 1.** Schematic representation of a core–shell–corona micelle formed by PEO<sub>42</sub>-*b*-PAGE<sub>15</sub>-*b*-PtBGE<sub>12</sub> in aqueous media with a PtBGE core (gray), a PAGE shell (purple), and a PEO corona (brown).

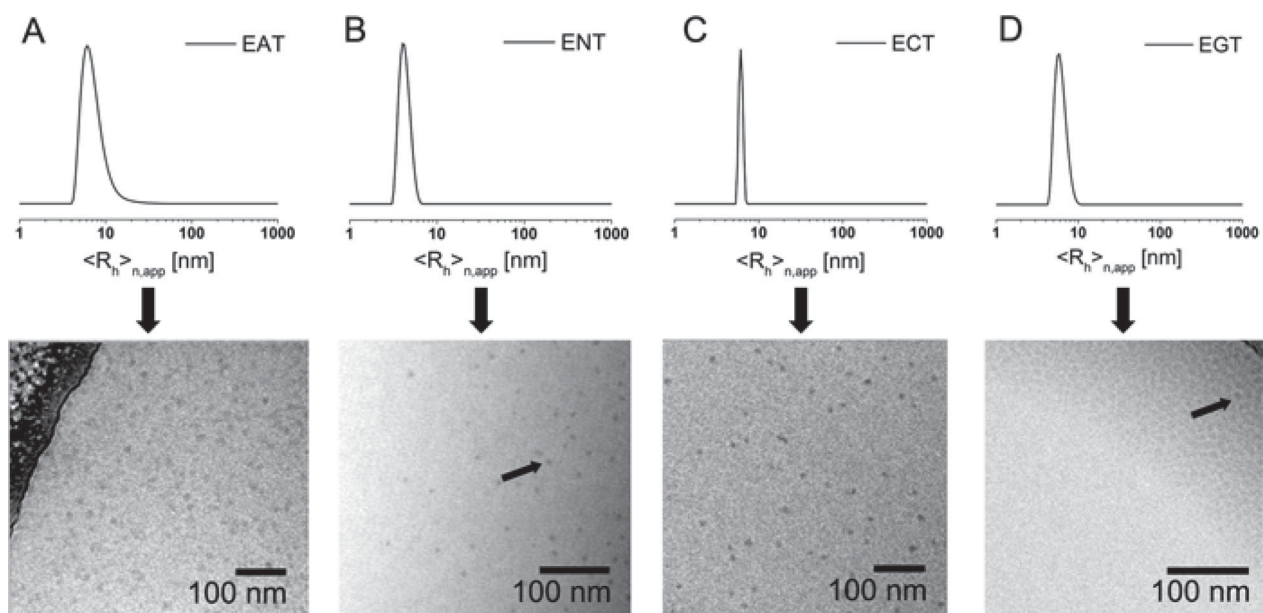


**Figure 2.** Number-weighted DLS CONTIN plots (upper section) for EAT (A,  $\langle R_h \rangle_{n,app} = 7$  nm), ENT (B,  $\langle R_h \rangle_{n,app} = 4$  nm), ECT (C,  $\langle R_h \rangle_{n,app} = 6$  nm), and EGT (D,  $\langle R_h \rangle_{n,app} = 6$  nm), as well as the corresponding cryo-TEM images (lower section) of the prepared micelles. Due to the rather low contrast an arrow highlights representative ENT (B) and EGT (D) micellar cores. All cryo-TEM images are displayed as recorded.

**Table 2.** DLS and AF4 Data for the Investigated Triblock Terpolymer Micelles and Co-Micelles<sup>a</sup>

sample	$M_n \times 10^{-5}$ (g/mol)	$\langle R_h \rangle_{n,app}^b$ (nm)	$N_{agg}$	$\langle R_g \rangle$ (nm)	$\langle R_h \rangle^c$ (nm)	$\langle R_g/R_h \rangle^d$	$\langle R_h \rangle^e$ (nm)
EAT	11.48 ± 0.078	7.0	225 ± 2	10.1 ± 0.6	13.0 ± 0.4	0.777 ± 0.021	11.8 ± 0.1
ENT	18.58 ± 0.314	4.2	323 ± 56	15.8 ± 1.1	17.4 ± 1.8	0.916 ± 0.148	9.5 ± 0.3
ECT	10.45 ± 0.007	6.1	156 ± 1	12.2 ± 0.8	14.4 ± 0.1	0.844 ± 0.054	13.5 ± 0.3
EGT	2.224 ± 0.070	6.0	31 ± 1	5.4 ± 0.6	5.3 ± 0.3	1.018 ± 0.136	7.1 ± 0.3
(ENT/ECT) <sup>3.5:1</sup>	11.97 ± 0.366	6.3	204 ± 6	12.3 ± 0.4	15.2 ± 0.5	0.810 ± 0.042	
(ENT/ECT) <sup>1.2:1</sup>	7.323 ± 0.127	4.3	121 ± 2	8.9 ± 0.8	10.6 ± 1.5	0.844 ± 0.051	10.5 ± 0.2
(ENT/ECT) <sup>1:2.6</sup>	6.192 ± 0.039	4.9	99 ± 1	9.0 ± 1.6	10.4 ± 0.5	0.875 ± 0.196	10.5 ± 0.1
(ENT/ECT/EGT) <sup>3.5:1:0.5</sup>	11.34 ± 0.714	8.2	190 ± 12	13.6 ± 1.2	15.9 ± 0.1	0.856 ± 0.084	12.3 ± 0.5
(ENT/ECT/EGT) <sup>3.4:1:2.3</sup>	9.654 ± 0.482	6.7	155 ± 8	13.5 ± 1.2	15.1 ± 0.1	0.899 ± 0.076	11.5 ± 0.5

<sup>a</sup>AF4 was performed using aqueous 20 mM NaCl solution. <sup>b</sup>Batch DLS in pure water. <sup>c</sup>Online DLS (AF4-DLS) in 20 mM NaCl. <sup>d</sup> $R_h$  from AF4-DLS. <sup>e</sup>Batch DLS in 20 mM NaCl.

and PEO<sub>42</sub>-*b*-(PAGE<sub>10,AcGal</sub><sup>-</sup>*co*-PAGE<sub>5</sub>)-*b*-PtBGE<sub>12</sub> (EGT after deprotection) could be successfully prepared using thiol–ene chemistry.

In a second step, the acetylated galactose was deprotected by treatment with sodium methanolate (Scheme 2). For this purpose, the polymer was dissolved in dry methanol, an excess

of sodium methanolate was added, and the solution was stirred for 1 h. The crude product was purified by dialysis and the complete deprotection was confirmed by <sup>1</sup>H NMR measurements (Figure S3, Table 1). As shown in Figure S3, an increase of the molar mass was detected, contrary to what would be expected. We assume that the deprotection and, therefore,

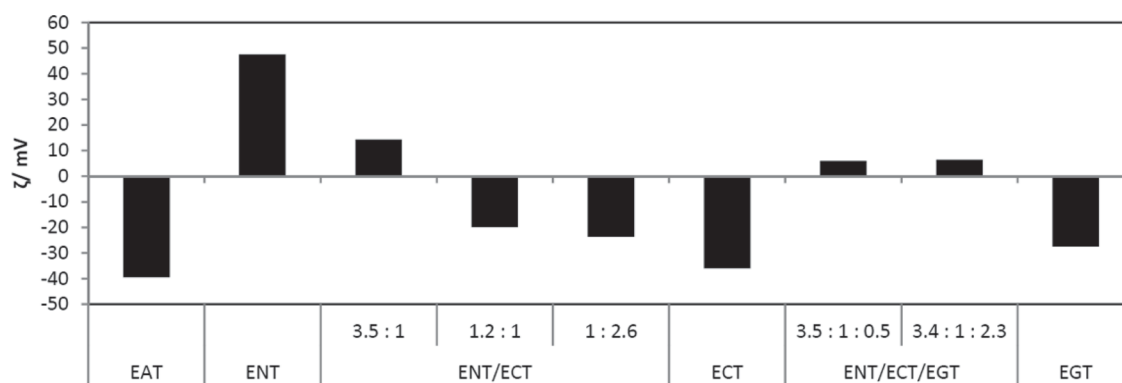


**Figure 3.** Zeta-potential measurements of different triblock terpolymer micelles and comicelles in water.

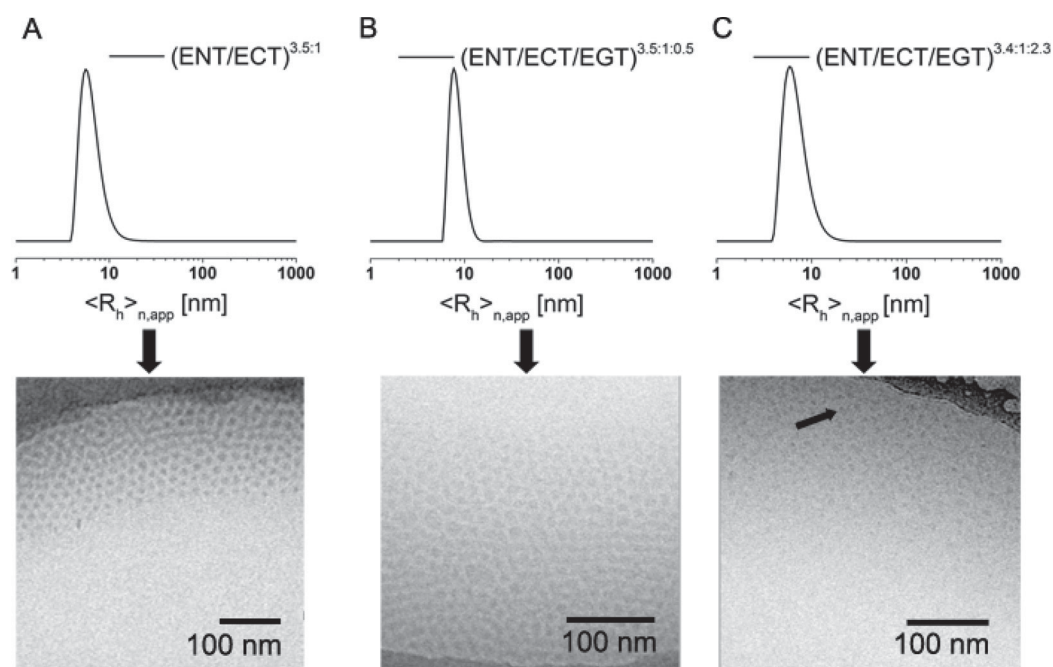


**Figure 4.** Number-weighted DLS CONTIN plots (upper row), for  $(\text{ENT}/\text{ECT})^{3.5:1}$  (A,  $\langle R_h \rangle_{n,\text{app}} = 6$  nm),  $(\text{ENT}/\text{ECT}/\text{EGT})^{3.5:1:0.5}$  (B,  $\langle R_h \rangle_{n,\text{app}} = 8$  nm), and  $(\text{ENT}/\text{ECT}/\text{EGT})^{3.4:1:2.3}$  (C,  $\langle R_h \rangle_{n,\text{app}} = 7$  nm), as well as the corresponding cryo-TEM images (lower row) of the prepared comicelles. Due to the low contrast, one micellar core is highlighted with an arrow for  $(\text{ENT}/\text{ECT}/\text{EGT})^{3.4:1:2.3}$  (C). All cryo-TEM images are displayed as recorded.

changes in solubility significantly influence the hydrodynamic radius, resulting in a shift to lower elution volume. This behavior has also been reported in earlier studies.<sup>49</sup>

For simplicity, the nomenclature ENT, ECT, and EGT will be used for micellar structures generated by self-assembly or co-assembly of these compounds.

**Micelle Formation in Aqueous Media.** We have shown earlier that PEO-*b*-PAGE-*b*-PtBGE triblock terpolymers as well as their thiogalactose-functionalized counterparts undergo self-assembly in aqueous media into micelles with a PtBGE core, a PAGE shell, and a PEO corona (Figure 1).<sup>19</sup> Prior to co-assembly studies, micelles separately formed by EAT (before thiol-ene modification), ENT, ECT, and EGT in aqueous solution were investigated.

Micellar solutions with a concentration of 10 g/L were prepared by the addition of THF solutions of the respective triblock terpolymer to water, followed by evaporation of the organic co-solvent. Subsequently, the solutions were analyzed by dynamic light scattering (DLS) and cryogenic transmission

electron microscopy (cryo-TEM). In Figure 2, the number weighted hydrodynamic radii from DLS are depicted. For all samples, radii ( $R_h$ ) in the range of 4 to 7 nm were detected in ultrapure water (pH = 7), and the results are summarized in Table 2. The corresponding intensity weighted DLS CONTIN plots of all samples are shown in Figure S7.

In addition to DLS experiments, also cryo-TEM measurements were performed. In that way, block copolymer nanostructures in aqueous solution can be visualized without drying artifacts.<sup>50–52</sup> As shown in Figure 2, spherical micelles were found for all samples discussed here. For micelles formed by ENT (Figure 2B) and EGT (Figure 2D) black arrows were added to highlight a representative micellar core. In some cases, a small distribution of worm-like structures was also found in cryo-TEM, presumably due to aggregation of spherical micelles (Figure S4). This phenomenon was also observed in our previous studies.<sup>18,19</sup> In general, for all samples micelles with a particle diameter ranging from 10 to 15 nm could be detected, confirming the results from DLS studies. To ensure the stability

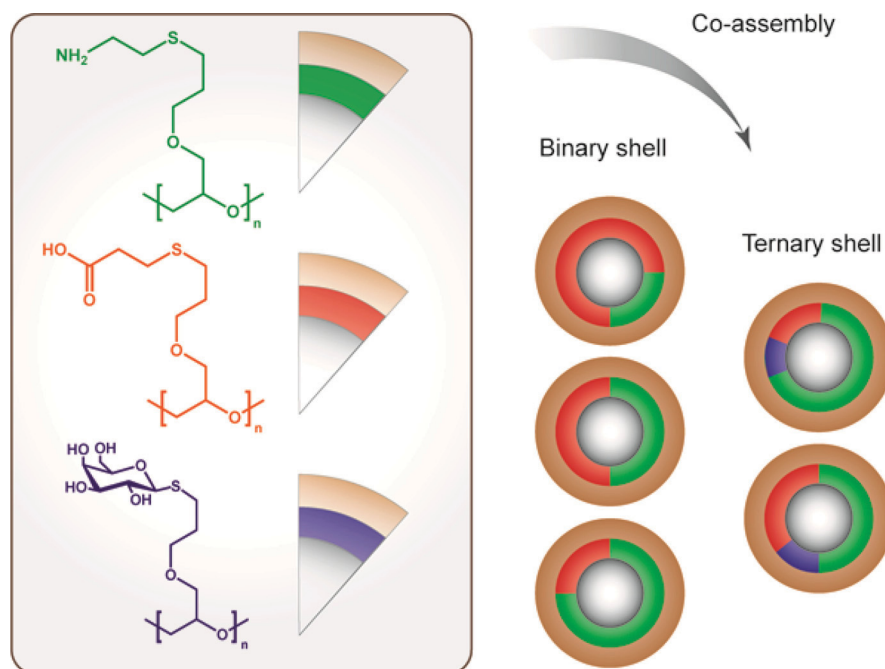


**Figure 5.** Schematic representation of the co-assembly of functionalized triblock terpolymers into binary and ternary core-shell-corona micelles with a mixed shell. The fractions of the modified PAGE shell (color code: green = cysteamine functionalized, red = 3-mercapto propionic acid functionalized, blue = thiogalactose functionalized) represent the mixing ratio during co-assembly.

of the prepared nanoparticles even at low concentrations, in particular for the later shown internalization tests, DLS measurements with diluted solutions of ECT were performed (Figure S5). For this purpose, a sample of 2.06 g/L was diluted stepwise up to a concentration of 0.005 g/L. Even at this concentration, micelles could be detected using DLS experiments. The sample was chosen, as this polymer showed the highest degree of functionalization and, therefore, also the highest hydrophilicity.

**Mixed Micelles Formed via Co-Assembly of Triblock Terpolymers.** We have recently shown that a combination of positively and negatively charged segments within triblock terpolymers (i.e., amphoteric materials) and the resulting multicompartment micelles in aqueous media led to pH-dependent interaction with cells, enhanced cellular uptake, and superior transfection efficiencies for pDNA.<sup>12,28</sup> However, in this particular case, one single material has been used, and it can be anticipated that the charge ratio (cationic/anionic) plays an important role. We were, therefore, interested in the co-assembly of different triblock terpolymers as an alternative strategy to control charge and functionality within such micelles.<sup>29,30</sup> In this context, the above-described triblock terpolymers (ENT, ECT, EGT) represent a versatile and highly flexible tool box. Co-assembly should again lead to the formation of core-shell-corona micelles, featuring a PEO corona and a hydrophobic P $\beta$ BGE core formed by identical segments A and C. The shell (B segment), however, should now be composed of different functional groups, depending on which material combinations are used. As a first example, micelles with different charge ratios (NH<sub>2</sub>/COOH) were prepared by co-assembly of ENT and ECT. For this purpose, mixtures of both triblock terpolymers were dissolved in THF and slowly added into water. Binary comicelles with an excess of positive charges (ENT/ECT)<sup>3.5:1</sup>, a slight excess of positive charges (ENT/ECT)<sup>1.2:1</sup>, and an excess of negative charges (ENT/ECT)<sup>1:2.6</sup> were assembled using this pathway. In all

cases, the superscripts represent the mixing ratio regarding the functional groups of the involved triblock terpolymers. The micellar solutions were afterward analyzed by DLS and cryo-TEM (Figure 4, the DLS CONTIN plots for (ENT/ECT)<sup>1.2:1</sup> and (ENT/ECT)<sup>1:2.6</sup> can be found in Figure S6). A schematic representation of the co-assembly and the formation of comicelles is presented in Figure 5.

Again, spherical micelles with hydrodynamic radii of 4 to 6 nm were obtained by DLS and these results were confirmed by cryo-TEM measurements (diameters of 12–14 nm were observed). As both middle blocks of ENT (NH<sub>2</sub>) and ECT (COOH) are weak polyelectrolytes, we anticipated that the pH value might have an influence during the assembly process. Therefore, the co-assembly was carried out under acidic (pH ~ 4) as well as basic conditions (pH ~ 12), and the results were compared to the data obtained under neutral conditions (pH ~ 7). Additionally, also, the preparation pathway was changed, that is, addition of water to THF solutions instead of vice versa. In all cases, no significant influence on the micellar size and the dispersity was observed (Table S1) and, therefore, all subsequent co-assembly procedures were carried out at pH 7 and via the addition of the THF solution containing the triblock terpolymers into water.

Subsequently, a detailed characterization of the micelles and comicelles regarding charge was carried out using zeta-potential measurements. As structures of rather small size were obtained, it is at the same time highly demanding and crucial to investigate if, for example, comicelles of ENT and ECT or if two separate populations are formed. This is difficult to estimate using only DLS and cryo-TEM. For the zeta-potential measurements and, also, later, for AF4 measurements, gel electrophoresis, and cell uptake studies, Nile red, a hydrophobic red fluorescent dye, was encapsulated into the hydrophobic P $\beta$ BGE core. Nile red is poorly soluble in water and exhibits a strong fluorescence in hydrophobic environment.<sup>53</sup> Therefore, the respective triblock terpolymer (or mixtures) and a small

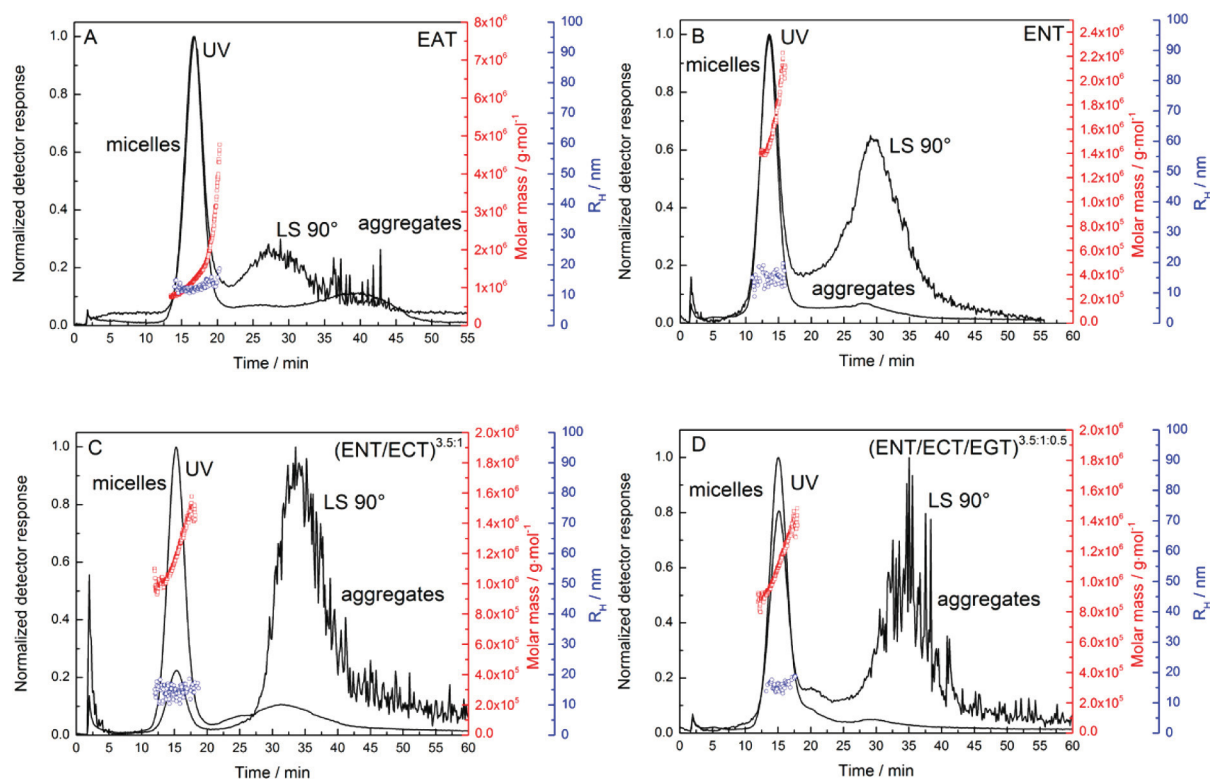


**Figure 6.** AF4 fractograms of triblock terpolymer micelles from EAT (A), ENT (B), (ENT/ECT)<sup>3.5:1</sup> (C), and (ENT/ECT/EGT)<sup>3.5:1:0.5</sup> (D) in 20 mM NaCl solution.

amount of the dye were dissolved in THF and slowly added into a defined amount of water (identical preparation pathway as has been described earlier). Afterward, the organic solvent was evaporated and the excess of non-encapsulated dye was filtered off.

In a first approach, the zeta potential of different micellar populations at a pH value of 7 was analyzed, and the results are depicted in Figure 3. As expected, a negative value is found for ECT (−36 mV) whereas the zeta potential for ENT is positive (47.5 mV). Both EAT and EGT revealed negative values (−39.5 and −27 mV), which can be attributed to the complexation of ions within the PEO corona or charge–dipole and dipole–dipole interactions, which are both known to influence the zeta potential.<sup>43,54</sup>

For binary comicelles (ENT/ECT), a clear dependence of the zeta potential on the mixing ratio can be observed, as with increasing amount of ENT the zeta potential increases (from −23.6 mV for (ENT/ECT)<sup>1:2.6</sup> to 14.2 mV for (ENT/ECT)<sup>3.5:1</sup>). Thus, zeta potential measurements indicate that comicelles are formed. If the co-assembly in the case of, for example, (ENT/ECT)<sup>3.5:1</sup> would lead to two separate populations of ENT and ECT, aggregation of oppositely charged micelles due to electrostatic interactions might be expected. In this case, an increase of the aggregates size and, presumably, precipitation might occur. As an attempt to clarify this, mixtures of ENT and ECT micelles after self-assembly via the above-described protocol were prepared at comparable charge ratios and were investigated using time-dependent DLS measurements (Figure S10A), revealing an increase of the  $R_h$  from 4 to 10 nm within 2 h and partial precipitation of the material after 12 h (Figure S10B). As the comicelles proved to be stable over several weeks, as confirmed by zeta-potential measurements and the presence of a monomodal size

distribution (DLS), an efficient preparation of comicelles by our protocol can be assumed.

Besides charge control in binary systems, also ternary systems were targeted where NH<sub>2</sub> groups (ENT), COOH moieties (ECT), and galactose as model targeting ligand (EGT) are combined. Galactose was chosen to enable selective cellular uptake into hepatocytes, which has been already demonstrated.<sup>47,48</sup> For the ternary systems, two ratios were prepared via co-assembly: (ENT/ECT/EGT)<sup>3.5:1:0.5</sup> and (ENT/ECT/EGT)<sup>3.4:1:2.3</sup>, featuring almost identical charge ratios and mainly differing in the amount of incorporated galactose. The as-prepared micellar solutions were characterized by DLS and cryo-TEM, and the results are depicted in Figure 4B,C and Table 2. In both cases, spherical micelles with  $R_h = 8$  nm for (ENT/ECT/EGT)<sup>3.5:1:0.5</sup> and 7 nm in the case of (ENT/ECT/EGT)<sup>3.4:1:2.3</sup> were found in DLS experiments. In cryo-TEM, again spherical micelles with diameters of 10 to 16 nm could be detected. A decreased contrast was observed for higher amounts of incorporated sugar moieties.

In all cases, evaluation by DLS and cryo-TEM led to comparable results regarding size and shape of both binary and ternary comicelles. Moreover, the ternary comicelles exhibit a decreased zeta potential if compared to the binary (ENT/ECT)<sup>3.5:1</sup> structures with 6 mV for (ENT/ECT/EGT)<sup>3.5:1:0.5</sup> and 6.5 mV for (ENT/ECT/EGT)<sup>3.4:1:2.3</sup>, thus, indicating the presence of EGT within the structures (Figure 3). Also, in this case, the zeta potential measurements indicate that comicelles are formed.

**Asymmetric Flow Field–Flow Fractionation of Triblock Terpolymer Micelles.** To obtain further insights into size, shape, and aggregation number of micelles formed by different triblock terpolymers (and combinations), asymmetric flow field-flow fractionation (AF4) coupled online to multi-

angle light scattering (MALS) and DLS was applied. Here, a 10000 g/mol membrane of regenerated cellulose and an aqueous eluent containing 20 mM NaCl was used for all systems investigated. Fractograms are shown in Figures 6 and S8. For all samples, the main peak represents spherical micelles and, in addition, a small second aggregate population could be detected after the cross-flow reaches zero (labeled “aggregates” in Figure 6). We attribute this to the presence of a small fraction of worm-like structures in accordance with earlier observations and the cryo-TEM experiments.<sup>18</sup> In the case of EGT and (ENT/ECT/EGT)<sup>3.4:1:2.3</sup>, also a small fraction of triblock terpolymer unimers could be identified. Number weighted molar masses  $M_n$  of the micelles and aggregation numbers  $N_{agg}$ , as well as the different radii ( $R_g$ ,  $R_h$ ) and the shape ratio ( $R_g/R_h$ ) derived from AF4 measurements are listed in Table 2. Thereby, the ratio  $R_g/R_h$  provides information about the shape of a macromolecule or colloid. Typical values are 0.778 for a hard sphere, 1.0 for a soft sphere, or 1.78 for a monodisperse linear polymer chain in a good solvent.<sup>55</sup> Additional characteristics ( $dn/dc$  values,  $M_w$ ,  $M_z$ , and  $\bar{D}$ ) can be found in Table S2. Aggregation numbers  $N_{agg}$  were calculated by dividing the molar mass ( $M_n$ ) of the micelles by the molar mass ( $M_n$ , <sup>1</sup>H NMR) of the single triblock terpolymer chain. The hydrodynamic radii measured by AF4-MALS-DLS were significantly higher (around 10–15 nm) in contrast to batch DLS experiments for all samples. We attribute this to the different medium (20 mM NaCl) and, indeed, DLS measurements under these conditions could confirm the results from AF4. The increase in size in the presence of salt might originate from the complexation of sodium ions by the PEO corona or, in case of micelles prepared via co-assembly of ENT and ECT, an increase in ionic strength, and the screening of attractive electrostatic forces between differently charged side chains (COO<sup>-</sup> for ECT; NH<sub>3</sub><sup>+</sup> for ENT) within the shell.<sup>56</sup> Nevertheless, in all cases the ratio  $R_g/R_h$  scales between 0.775 (hard sphere) and 1.0 (soft sphere), indicating a spherical shape.<sup>55,57</sup>

By AF4 experiments, also the absolute molar mass of the micelles could be detected: Comparable values ( $M_n$ ) of 1000 to 2000 kg/mol were obtained for EAT, ENT, and ECT micelles, whereas only 220 kg/mol were found in the case of EGT. This corresponds to  $N_{agg} = 30$  (EGT), 225 (EAT), 323 (ENT), and 156 (ECT), respectively. At this point, we attribute the lower values observed for EGT to the steric demand of the thiogalactose side chains within the PAGE shell, preventing a more compact assembly. This is also in good accordance with the observation of a small fraction of triblock terpolymer unimers in the AF4 fractograms (Figure S8B). The aggregation numbers  $N_{agg}$  of binary and ternary comicelles were calculated by consideration of the different molar masses of the terpolymers and under the assumption that the ratios of polymer chains in the micelles are the same as the mixing ratios of the triblock terpolymers.

Molar masses of binary and ternary comicelles are in between 620 kg/mol [(ENT/ECT)<sup>1:2.6</sup>,  $N_{agg} = 99$ ] and 1200 kg/mol [(ENT/ECT)<sup>3.5:1</sup>,  $N_{agg} = 204$ ]. This indicates the formation of more compact structures with increasing amounts of ENT for the investigated range of charge ratios.

**Gel Electrophoresis.** In addition to zeta potential measurements, another powerful method for the separation of charged macromolecules (e.g., DNA) is gel electrophoresis. Here, the samples are placed in an agarose gel and an electrical field is applied. The electrical field induces movement within the gel

toward the positive or negative pole, depending on the charge of the sample investigated.

A small amount of labeled micelles and comicelles was placed in an agarose gel and an electric field was applied. We anticipated that comicelles should feature only one band, as additional confirmation of the zeta-potential measurements. As shown in Figure 7, micelles formed by ENT reveal the highest

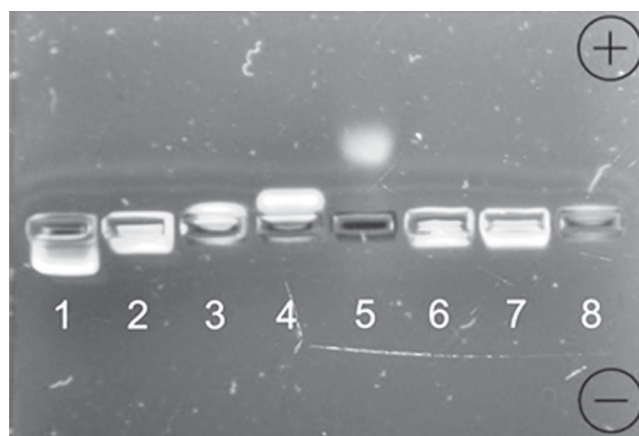


**Figure 7.** Gel electrophoresis using 1% agarose gel and TBE buffer (1 = ENT, 2 = (ENT/ECT)<sup>3.5:1</sup>, 3 = (ENT/ECT)<sup>1.2:1</sup>, 4 = (ENT/ECT)<sup>1:2.6</sup>, 5 = ECT, 6 = (ENT/ECT/EGT)<sup>3.5:1:0.5</sup>, 7 = (ENT/ECT/EGT)<sup>3.4:1:2.3</sup>, 8 = EGT).

shift to the negative pole, whereas ECT moved toward the positive pole. The bands observed for ENT/ECT comicelles of different mixing ratios are, in accordance with their zeta-potential, in between. If two separate populations of ENT and ECT would be formed, two separate bands in gel electrophoresis toward opposite poles might be expected. As only one band is visible for all samples, we regard this as another indication for an efficient co-assembly. In addition, ternary ENT/ECT/EGT exhibited movement toward the negative pole, again confirming the results from zeta-potential measurements. EGT did not show any movement in gel electrophoresis. Contrary to the negative zeta potential of  $-39.5$  mV, EAT micelles exhibited a clear shift to the negative pole (Figure S9). Up to now, we have no conclusive explanation for this behavior as also zeta potential measurements in comparable buffer solutions (the exact composition is given in the experimental part) yielded negative values.

**Cellular Interactions. Cytotoxicity and Hemolysis of Triblock Terpolymer Micelles.** Aiming for a later use of such triblock terpolymer micelles in targeting and/or delivery applications, their cytotoxicity was investigated using an Alamar blue assay. At first, triblock terpolymer micelles formed via the self-assembly of one single material were investigated. Micelles formed of EAT, ECT, or EGT did not show any cytotoxic effects for concentrations up to 0.5 mg/mL (cell viability was above 70%), only in case of ENT the situation was different (Figure 8A). Regarding EAT, ECT, and EGT, these results are in accordance with literature, as all structures exhibited negative zeta potentials.<sup>39,58</sup> For micelles based on ENT, the IC<sub>50</sub> of 300  $\mu$ g/mL can be explained by the presence of cationic charges within the shell (zeta potential of  $+47.5$  mV), which could lead to stronger interactions with or even disruption of the cell membrane. These results can be taken as further proof that the functionalization of the middle block (PAGE) significantly influences interactions of such micelles with biological matter,

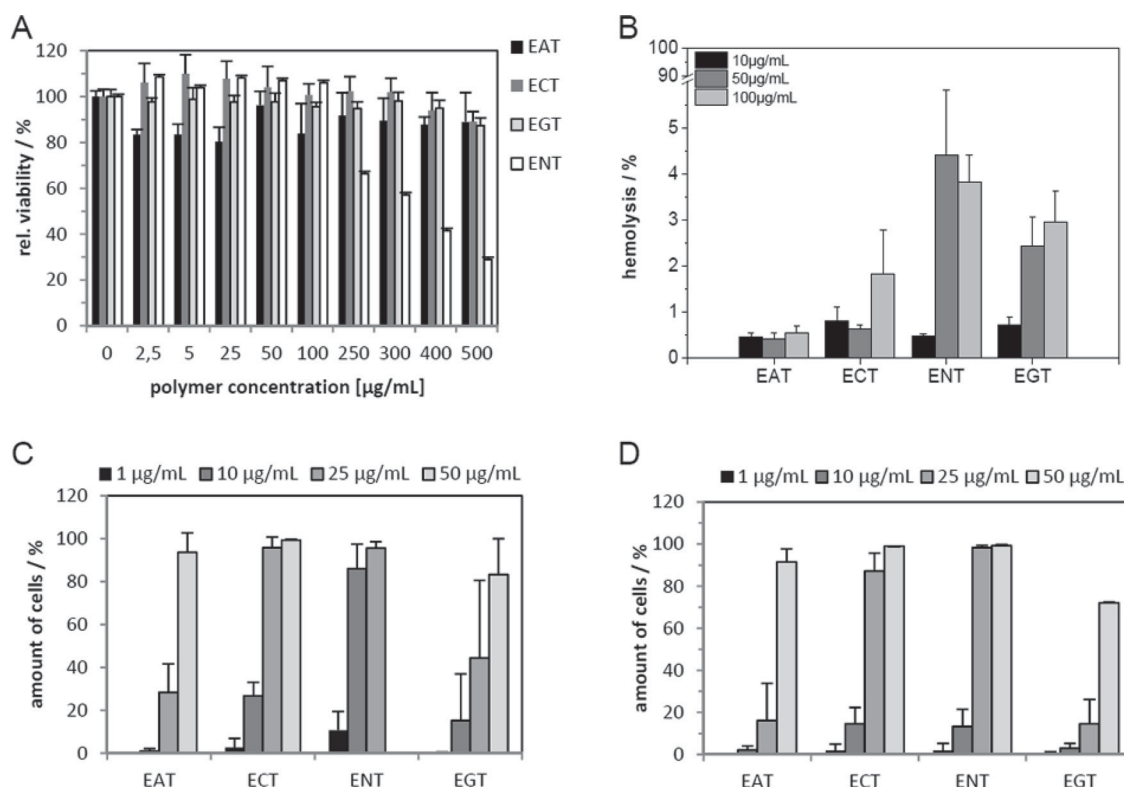


**Figure 8.** Cytotoxicity test of triblock terpolymer micelles using L929 cells (A) and hemolysis assay using three different donors (B). Cellular uptake under serum reduced (C) and serum containing conditions (D) in HEK cells. Values represent the mean  $\pm$  SD.

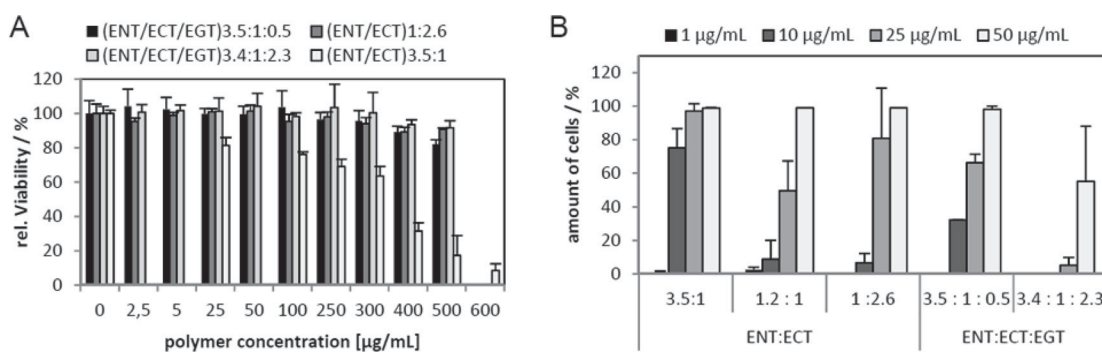


**Figure 9.** Cytotoxicity test of binary and ternary comicelles using L929 cells (A) and cellular uptake in HEK cells (B). Values represent the mean  $\pm$  SD;  $n = 3$ .

even though all structures feature a rather long PEO corona (compared to the degrees of polymerization for PAGE and PtBGE).<sup>59</sup>

A hemolysis assay was performed to gain deeper insight into the interaction of EAT, ENT, ECT, and EGT micelles with negatively charged cell membranes: Here, ENT exhibited slight hemolytic activity at concentrations of 50  $\mu\text{g/mL}$  ( $3.8 \pm 0.6\%$  hemolysis, Figure 8B). No hemolytic activity was found for both EAT and ECT. In contrast,  $2.9 \pm 0.6\%$  hemolysis was observed for EGT micelles. We attribute this to hydrophobic interactions with the cell membrane, possibly even incorporation of EGT into the latter.

**Internalization of Triblock Terpolymer Micelles.** Furthermore, the internalization efficiency of micelles from EAT, ENT, ECT, and EGT into human embryonic kidney (HEK) cells, a model cell line for unspecific uptake studies, was analyzed under serum-reduced and serum-containing conditions. As Nile red was encapsulated in the micelles, the internalization was

analyzed by flow cytometry, at which untreated cells were applied as control (Figure S12). Under serum-reduced conditions the critical concentration, that is, the concentration where EAT shows nearly no uptake ( $1 \pm 1.1\%$ ), was determined to be 10  $\mu\text{g/mL}$  (Figure 8C). From this data set, it becomes obvious that ENT revealed the best uptake into  $79.7 \pm 4.5\%$  (at 10  $\mu\text{g/mL}$ ) of the cells. This can be attributed to the presence of positive charges in the shell and an increased interaction with the cell membrane, also confirmed by the earlier discussed hemolysis assay. Higher concentrations of 50  $\mu\text{g/mL}$  could not be analyzed as the cell viability was too low under serum reduced condition. Compared to ENT, the decreased uptake of ECT and EGT at a concentration of 10  $\mu\text{g/mL}$  with  $26.8 \pm 6.3\%$  and  $15.3 \pm 21.7\%$ , respectively, can be explained by the negative zeta potential of these particles, resulting in decreased interactions with cells. Nevertheless, even ECT and EGT show significantly increased cellular uptake induced either by the introduction of charges (COOH) or

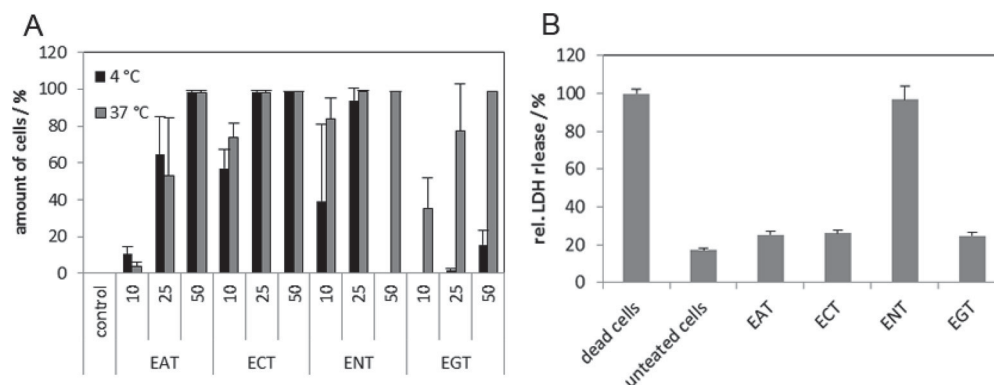


**Figure 10.** Cellular uptake of triblock terpolymer micelles at 4 and 37 °C in HEK cells after 4 h (A) and lactate dehydrogenase assay with HEK cells and 25 μg/mL of the micelles (B). Values represent the mean ± S.D.;  $n = 3$ .

targeting units (thiogalactose) if compared to EAT at 10 μg/mL ( $1 \pm 1.11\%$ ). As the presence of a PEO corona has been shown in many examples to prevent unspecific protein adsorption (“stealth effect”),<sup>17</sup> the uptake was also analyzed in the presence of serum (Figure 8D). Here, only the uptake of ENT decreased significantly from  $86 \pm 11\%$  to  $13 \pm 0.6\%$  at 10 μg/mL ( $p < 0.005$ ), presumably due to stronger interactions with negatively charged serum proteins.<sup>60,61</sup> Nevertheless, the uptake of both ENT and ECT is significantly higher compared to EAT with  $2 \pm 0.5\%$  ( $p < 0.05$ ). The internalization of EGT is similar to EAT at 10 μg/mL, thus, also reduced from 15 to 2.9% in the presence of serum proteins. As the functionalization with thiogalactose is supposed to result in specific uptake into liver cells, we also incubated the EGT micelles with HepG2 cells.<sup>47</sup> Unfortunately, no increased uptake at low concentrations ( $3.9 \pm 5\%$  at 10 μg/mL) could be detected, which would hint toward a targeted internalization process (Figure S11). One explanation might be that the galactose side chains are not sufficiently exposed at the surface and, thus, the interaction with the asialoglycoprotein receptor, specific for galactose in HepG2 cells, is hampered. Further, the PEO corona might form hydrogen bonds with the galactose residues,<sup>62</sup> additionally reducing their accessibility.

**Cytotoxicity and Internalization of Comicelles.** As the up to now used triblock terpolymer micelles (EAT, ENT, ECT, and EGT) already showed significant differences regarding cellular uptake and cytotoxicity, the influence of the composition in binary and ternary comicelles on the cytotoxicity was studied (Figure 9A). (ENT/ECT)<sup>3.5:1</sup> exhibited a positive zeta potential and a similar cytotoxicity ( $IC_{50}$  of 350 μg/mL), if compared to ENT (Figure 8A). In the case of (ENT/ECT)<sup>1.2:1</sup> and (ENT/ECT)<sup>1:2.6</sup>, no cytotoxicity was observed, in accordance with the negative zeta potential.

Interestingly, both the ternary comicelles, (ENT/ECT/EGT)<sup>3.5:1:0.5</sup> and (ENT/ECT/EGT)<sup>3.4:1:2.3</sup>, which feature the same charge ratio as (ENT/ECT)<sup>3.5:1</sup> and exhibited positive zeta potentials, did not show any cytotoxicity at all tested concentrations. This is indeed remarkable, and we propose that this originates from the presence of EGT terpolymer chains in these structures. All prepared comicelles were further investigated regarding their internalization behavior. In this case, (ENT/ECT)<sup>3.5:1</sup> demonstrated outstanding uptake compared to all other samples as already at 10 μg/mL under serum-containing conditions  $75 \pm 11.5\%$  of the cells showed internalization (Figure 9B). These results are comparable to ENT micelles under serum-reduced conditions, thus, indicating

decreased nonspecific interactions of (ENT/ECT)<sup>3.5:1</sup> with serum proteins. For both (ENT/ECT)<sup>1.2:1</sup> and (ENT/ECT)<sup>1:2.6</sup>, reduced uptake with  $8.9 \pm 11\%$  and  $6.7 \pm 5.5\%$  (compared to (ENT/ECT)<sup>3.5:1</sup>) was found. In the case of ternary comicelles, (ENT/ECT/EGT)<sup>3.5:1:0.5</sup> exhibited decreased uptake compared to (ENT/ECT)<sup>3.5:1</sup>, presumably due to the presence of EGT (Figure 9B). A further increase of the galactose content leads to even lower values, which is in accordance with lower uptake of EGT compared to ECT and ENT. Nevertheless, it should be noted that, in contrast to (ENT/ECT)<sup>3.5:1</sup>, both (ENT/ECT/EGT)<sup>3.5:1:0.5</sup> and (ENT/ECT/EGT)<sup>3.4:1:2.3</sup> did not show any cytotoxicity. In summary, by adjusting the micellar composition via co-assembly of ENT, ECT, and EGT, both cellular uptake and cytotoxicity can be controlled and optimized (according to our results).

**Further Investigations Regarding the Pathway for Cellular Uptake.** We were also interested in a more detailed analysis of the internalization process. The size of the core–shell–corona micelles used in the present study is below 30 nm in diameter, a size where studies on the internalization process are rarely found, as normally nanostructures between 50 to 200 nm are used in drug delivery applications. Here, internalization via endocytosis is under debate, as this process is usually observed for structures with sizes between 50 to 500 nm.<sup>63–65</sup> As endocytosis is energy dependent, the uptake efficiencies were investigated at 4 °C, conditions which are known to inhibit energy-dependent mechanisms (Figure 10A).<sup>66</sup> Interestingly, no significant changes under these conditions were found for EAT, ECT, and ENT if compared to 37 °C. In contrast, the internalization efficiency for EGT decreased significantly to  $15 \pm 7.8\%$  (at 50 μg/mL), indicating an energy-dependent mechanism.

Besides, ENT micelles are already cytotoxic at a concentration of 50 μg/mL at 4 °C, in contrast to 37 °C. The increased cytotoxicity at 4 °C might originate from the reduced fluidity of the cell membrane at low temperatures. Therefore, it might occur that cationically charged micelles lead to destabilization and local disruption of the membrane.<sup>67</sup> As the size of the micelles is rather small, these perforations can be easily closed at 37 °C at normal membrane fluidity. At 4 °C, however, this process is significantly slowed down, leading to cell leakage. It has been described in the literature that structures of a few nanometers in size can lead to pore formation and translocation through the cell membrane.<sup>68,69</sup> To evaluate if cell leakage is caused in our case, a lactate dehydrogenase (LDH) assay was performed,<sup>70</sup> which was used



to detect the release of cytosolic LDH into the surrounding media through membrane perforations. For ECT and EAT micelles, no significant LDH release could be observed in contrast to ENT (Figure 10B). This provides a first hint and supports our assumption that EAT and ECT micelles cross the cellular membrane by the formation of reversible membrane pores or penetrate the cell membrane via diffusion. ENT seems to cause larger pores, resulting in LDH release. These first investigations of the internalization process demonstrate that differences in shell composition and functionality of triblock terpolymer micelles influence not only cytotoxicity and uptake efficiency, but also alter the overall internalization process. In that respect, the herein presented toolbox of triblock terpolymers represents an ideal starting point for the purposeful variation of micellar composition and charge and more detailed investigations of the uptake mechanism will follow.

## CONCLUSION

Multifunctional and well-defined triblock terpolymers represent very promising materials for the preparation of efficient drug delivery vehicles. Here, we introduce a concept for the co-assembly of ABC triblock terpolymers with identical A and C segments but different functionalities in the middle block (B) into core-shell-corona micelles with a mixed shell. In that way, sub-30 nm particles with superior control over charge and the location of targeting ligands with the micellar shell were formed. The materials employed are poly(ethylene oxide)-*block*-poly(allyl glycidyl ether)-*block*-poly(*tert*-butyl glycidyl ether) (PEO-*b*-PAGE-*b*-PtBGE) triblock terpolymers where the PAGE segments has been subsequently modified using thiol-ene chemistry to introduce  $-NH_2$  (cysteamine, ENT),  $-COOH$  (3-mercaptopropionic acid, ECT), and thiolgalactose residues (EGT). Depending on whether binary (ENT/ECT) or ternary comicelles (ENT/ECT/EGT) were prepared, charge and, directly linked to that, cytotoxicity of the resulting nanoparticle could be adjusted. In the case of ENT/ECT/EGT comicelles, efficient cellular uptake (even in the presence of serum proteins) could be combined with low cytotoxicity. Different characterization methods, including dynamic light scattering (DLS), asymmetric flow field-flow fractionation (AF4), zeta potential measurements, and cryo-TEM indicate that indeed co-micellization occurs. Moreover, first insights into the internalization process of these sub-30 nm micelles could be provided and our results hint toward uptake via direct penetration through the cell membrane and not via endocytosis, offering interesting possibilities for further detailed studies.

## ASSOCIATED CONTENT

### Supporting Information

Size-exclusion chromatograms and  $^1H$  NMR spectra for the synthesized materials. Further DLS CONTIN plots, TEM images, and information regarding the cellular uptake, as well as detailed data of the AF4 measurements. This material is available free of charge via the Internet at <http://pubs.acs.org>.

## AUTHOR INFORMATION

### Corresponding Authors

\*E-mail: [felix.schacher@uni-jena.de](mailto:felix.schacher@uni-jena.de).

\*E-mail: [ulrich.schubert@uni-jena.de](mailto:ulrich.schubert@uni-jena.de).

## Author Contributions

<sup>†</sup>Both authors contributed equally to this work (M.J.B. and A.C.R.).

## Notes

The authors declare no competing financial interest.

## ACKNOWLEDGMENTS

The authors want to acknowledge C. Fritzsche for hemolysis studies and Alamar Blue assay. The work of M.J.B. forms part of the research programme of the Dutch Polymer Institute (DPI), Project #690. A.C.R., A.S., and M.W. thank the Carl Zeiss Foundation for financial support. F.H.S. is grateful for a fellowship from the Fonds der Chemischen Industrie (FCI). Furthermore, the authors want to acknowledge the Thuringian Ministry for Education, Science and Culture (TMBWK; #B515-10065, ChaPoNano; #B514-09051, NanoConSens).

## REFERENCES

- (1) Mai, Y. Y.; Eisenberg, A. *Chem. Soc. Rev.* **2012**, *41*, 5969–5985.
- (2) Schacher, F. H.; Rupar, P. A.; Manners, I. *Angew. Chem., Int. Ed.* **2012**, *51*, 7898–7921.
- (3) Barthel, M. J.; Schacher, F. H.; Schubert, U. S. *Polym. Chem.* **2014**, *5*, 2647–2662.
- (4) Price, C.; Lally, T. P.; Stubbers, R. *Polymer* **1974**, *15*, 541–543.
- (5) Arai, K.; Kotaka, T.; Kitano, Y.; Yoshimura, K. *Macromolecules* **1980**, *13*, 455–457.
- (6) Mogi, Y.; Kotsuji, H.; Kaneko, Y.; Mori, K.; Matsushita, Y.; Noda, I. *Macromolecules* **1992**, *25*, 5408–5411.
- (7) Auschra, C.; Stadler, R. *Macromolecules* **1993**, *26*, 2171–2174.
- (8) Lodge, T. P.; Rasdal, A.; Li, Z. B.; Hillmyer, M. A. *J. Am. Chem. Soc.* **2005**, *127*, 17608–17609.
- (9) Betthausen, E.; Drechsler, M.; Fortsch, M.; Schacher, F. H.; Müller, A. H. E. *Soft Matter* **2011**, *7*, 8880–8891.
- (10) Gröschel, A. H.; Schacher, F. H.; Schmalz, H.; Borisov, O. V.; Zhulina, E. B.; Walther, A.; Müller, A. H. E. *Nat. Commun.* **2012**, *3*, 710.
- (11) Gröschel, A. H.; Walther, A.; Löbbling, T. I.; Schacher, F. H.; Schmalz, H.; Müller, A. H. E. *Nature* **2013**, *503*, 247–251.
- (12) Rinkenauer, A. C.; Schallon, A.; Günther, U.; Wagner, M.; Betthausen, E.; Schubert, U. S.; Schacher, F. H. *ACS Nano* **2013**, *7*, 9621–9631.
- (13) Schallon, A.; Synatschke, C. V.; Jerome, V.; Müller, A. H. E.; Freitag, R. *Biomacromolecules* **2012**, *13*, 3463–3474.
- (14) Huang, X. Y.; Chen, S.; Huang, J. L. *J. Polym. Sci., Part A: Polym. Chem.* **1999**, *37*, 825–833.
- (15) Arnal, M. L.; Balsamo, V.; Lopez-Carrasquero, F.; Contreras, J.; Carrillo, M.; Schmalz, H.; Abetz, V.; Laredo, E.; Müller, A. J. *Macromolecules* **2001**, *34*, 7973–7982.
- (16) Jing, R. K.; Wang, G. W.; Zhang, Y. N.; Huang, J. L. *Macromolecules* **2011**, *44*, 805–810.
- (17) Knop, K.; Hoogenboom, R.; Fischer, D.; Schubert, U. S. *Angew. Chem., Int. Ed.* **2010**, *49*, 6288–6308.
- (18) Barthel, M. J.; Babiuch, K.; Rudolph, T.; Vitz, J.; Hoepfener, S.; Gottschaldt, M.; Hager, M. D.; Schacher, F. H.; Schubert, U. S. *J. Polym. Sci., Part A: Polym. Chem.* **2012**, *50*, 2914–2923.
- (19) Barthel, M. J.; Mansfeld, U.; Hoepfener, S.; Czaplewski, J. A.; Schacher, F. H.; Schubert, U. S. *Soft Matter* **2013**, *9*, 3509–3520.
- (20) Obermeier, B.; Frey, H. *Bioconjugate Chem.* **2011**, *22*, 436–444.
- (21) Hruby, M.; Konak, C.; Ulbrich, K. *J. Controlled Release* **2005**, *103*, 137–148.
- (22) Lin, S. L.; Zhu, W. J.; He, X. H.; Xing, Y. H.; Liang, L. Y.; Chen, T.; Lin, J. P. *J. Phys. Chem. B* **2013**, *117*, 2586–2593.
- (23) Libera, M.; Trzebicka, B.; Kowalczyk, A.; Walach, W.; Dworak, A. *Polymer* **2011**, *52*, 250–257.
- (24) Kataoka, K.; Harada, A.; Nagasaki, Y. *Adv. Drug Delivery Rev.* **2001**, *47*, 113–131.

- (25) Sun, P. J.; Zhang, Y.; Shi, L. Q.; Gan, Z. H. *Macromol. Biosci.* **2010**, *10*, 621–631.
- (26) Van Butsele, K.; Cajot, S.; Van Vlierberghe, S.; Dubruel, P.; Passirani, C.; Benoit, J. P.; Jerome, R.; Jerome, C. *Adv. Funct. Mater.* **2009**, *19*, 1416–1425.
- (27) Fukushima, S.; Miyata, K.; Nishiyama, N.; Kanayama, N.; Yamasaki, Y.; Kataoka, K. *J. Am. Chem. Soc.* **2005**, *127*, 2810–2811.
- (28) Lee, Y.; Miyata, K.; Oba, M.; Ishii, T.; Fukushima, S.; Han, M.; Koyama, H.; Nishiyama, N.; Kataoka, K. *Angew. Chem., Int. Ed.* **2008**, *47*, 5163–5166.
- (29) Wu, C. L.; Ma, R. J.; He, H.; Zhao, L. Z.; Gao, H. J.; An, Y. L.; Shi, L. Q. *Macromol. Biosci.* **2009**, *9*, 1185–1193.
- (30) Attia, A. B. E.; Ong, Z. Y.; Hedrick, J. L.; Lee, P. P.; Ee, P. L. R.; Hammond, P. T.; Yang, Y. Y. *Curr. Opin. Colloid Interface Sci.* **2011**, *16*, 182–194.
- (31) Liu, X.; Liu, Y.; Zhang, Z. K.; Huang, F.; Tao, Q.; Ma, R. J.; An, Y. L.; Shi, L. Q. *Chem. Eur. J.* **2013**, *19*, 7437–7442.
- (32) Lin, J. P.; Zhu, J. Q.; Chen, T.; Lin, S. L.; Cai, C. H.; Zhang, L. S.; Zhuang, Y.; Wang, X. S. *Biomaterials* **2009**, *30*, 108–117.
- (33) Vinogradov, S. V.; Batrakova, E. V.; Li, S.; Kabanov, A. V. *J. Drug Targeting* **2004**, *12*, 517–526.
- (34) Zheng, R.; Liu, G.; Yan, X. *J. Am. Chem. Soc.* **2005**, *127*, 15358–15359.
- (35) Li, Z.; Hillmyer, M. A.; Lodge, T. P. *Macromolecules* **2006**, *39*, 765–771.
- (36) Cabral, H.; Matsumoto, Y.; Mizuno, K.; Chen, Q.; Murakami, M.; Kimura, M.; Terada, Y.; Kano, M. R.; Miyazono, K.; Uesaka, M.; Nishiyama, N.; Kataoka, K. *Nat. Nanotechnol.* **2011**, *6*, 815–823.
- (37) Dong, H.; Dube, N.; Shu, J. Y.; Seo, J. W.; Mahakian, L. M.; Ferrara, K. W.; Xu, T. *ACS Nano* **2012**, *6*, 5320–5329.
- (38) Alexis, F.; Pridgen, E.; Molnar, L. K.; Farokhzad, O. C. *Mol. Pharmaceutics* **2008**, *5*, 505–515.
- (39) Nguyen, J.; Xie, X.; Neu, M.; Dumitrascu, R.; Reul, R.; Sitterberg, J.; Bakowsky, U.; Schermuly, R.; Fink, L.; Schmehl, T.; Gessler, T.; Seeger, W.; Kissel, T. *J. Gene Med.* **2008**, *10*, 1236–1246.
- (40) Mishra, S.; Webster, P.; Davis, M. E. *Eur. J. Cell. Biol.* **2004**, *83*, 97–111.
- (41) Sun, J.; Zeng, F.; Jian, H.; Wu, S. *Biomacromolecules* **2013**, *14*, 728–736.
- (42) Andersson, M.; Wittgren, B.; Wahlund, K. G. *Anal. Chem.* **2003**, *75*, 4279–4291.
- (43) Delgado, A. V.; Gonzalez-Caballero, F.; Hunter, R. J.; Koopal, L. K.; Lyklema, J. *J. Colloid Interface Sci.* **2007**, *309*, 194–224.
- (44) Ohshima, H. *J. Colloid Interface Sci.* **1994**, *168*, 269–271.
- (45) Gottschaldt, M.; Koth, D.; Müller, D.; Klette, I.; Rau, S.; Görls, H.; Schafer, B.; Baum, R. P.; Yano, S. *Chem. Eur. J.* **2007**, *13*, 10273–10280.
- (46) Ibatullin, F. M.; Shabalin, K. A.; Janis, J. V.; Shavva, A. G. *Tetrahedron Lett.* **2003**, *44*, 7961–7964.
- (47) Babiuch, K.; Pretzel, D.; Tolstik, T.; Vollrath, A.; Stanca, S.; Foertsch, F.; Becer, C. R.; Gottschaldt, M.; Biskup, C.; Schubert, U. S. *Macromol. Biosci.* **2012**, *12*, 1190–1199.
- (48) Yang, R.; Meng, F. H.; Ma, S. B.; Huang, F. S.; Liu, H. Y.; Zhong, Z. Y. *Biomacromolecules* **2011**, *12*, 3047–3055.
- (49) Babiuch, K.; Becer, C. R.; Gottschaldt, M.; Delaney, J. T.; Weisser, J.; Beer, B.; Wyrwa, R.; Schnabelrauch, M.; Schubert, U. S. *Macromol. Biosci.* **2011**, *11*, 535–548.
- (50) Cui, H.; Hodgdon, T. K.; Kaler, E. W.; Abezgauz, L.; Danino, D.; Lubovsky, M.; Talmon, Y.; Pochan, D. J. *Soft Matter* **2007**, *3*, 945–955.
- (51) Holder, S. J.; Sommerdijk, N. A. J. M. *Polym. Chem.* **2011**, *2*, 1018–1028.
- (52) Zhong, S.; Pochan, D. J. *Polym. Rev.* **2010**, *50*, 287–320.
- (53) Greenspan, P.; Mayer, E. P.; Fowler, S. D. *J. Cell. Biol.* **1985**, *100*, 965–973.
- (54) Wagner, M.; Reiche, K.; Blume, A.; Garidel, P. *Colloids Surf., A* **2012**, *415*, 421–430.
- (55) Burchard, W. *Adv. Polym. Sci.* **1999**, *143*, 113–194.
- (56) Benincasa, M. A.; Caldwell, K. D. *J. Chromatogr., A* **2001**, *925*, 159–169.
- (57) Glantz, M.; Hakansson, A.; Mansson, H. L.; Paulsson, M.; Nilsson, L. *Langmuir* **2010**, *26*, 12585–12591.
- (58) Vollrath, A.; Pretzel, D.; Pietsch, C.; Perevyazko, I.; Schubert, S.; Pavlov, G. M.; Schubert, U. S. *Macromol. Rapid Commun.* **2012**, *33*, 1791–1797.
- (59) Verbaan, F. J.; Oussoren, C.; Snel, C. J.; Crommelin, D. J. A.; Hennink, W. E.; Storm, G. *J. Gene Med.* **2004**, *6*, 64–75.
- (60) Ogris, M.; Brunner, S.; Schuller, S.; Kircheis, R.; Wagner, E. *Gene Ther.* **1999**, *6*, 595–605.
- (61) Cherg, J. Y.; vandeWetering, P.; Talsma, H.; Crommelin, D. J. A.; Hennink, W. E. *Pharm. Res.* **1996**, *13*, 1038–1042.
- (62) Belbekhouche, S.; Dulong, V.; Picton, L.; Le Cerf, D. *Colloids Surf., A* **2013**, *428*, 25–31.
- (63) Albanese, A.; Tang, P. S.; Chan, W. C. *Annu. Rev. Biomed. Eng.* **2012**, *14*, 1–16.
- (64) Rejman, J.; Oberle, V.; Zuhorn, I. S.; Hoekstra, D. *Biochem. J.* **2004**, *377*, 159–169.
- (65) Lai, S. K.; Hida, K.; Man, S. T.; Chen, C.; Machamer, C.; Schroer, T. A.; Hanes, J. *Biomaterials* **2007**, *28*, 2876–2884.
- (66) Steinman, R. M.; Mellman, I. S.; Muller, W. A.; Cohn, Z. A. *J. Cell Biol.* **1983**, *96*, 1–27.
- (67) Leroueil, P. R.; Hong, S. Y.; Mecke, A.; Baker, J. R.; Orr, B. G.; Holl, M. M. B. *Acc. Chem. Res.* **2007**, *40*, 335–342.
- (68) Ting, C. L.; Wang, Z. G. *Soft Matter* **2012**, *8*, 12066–12071.
- (69) Ding, H. M.; Tian, W. D.; Ma, Y. Q. *ACS Nano* **2012**, *6*, 1230–1238.
- (70) Choksakulnimitr, S.; Masuda, S.; Tokuda, H.; Takakura, Y.; Hashida, M. *J. Controlled Release* **1995**, *34*, 233–241.

## Supporting information for

### “Small but powerful: Co-assembly of polyether-based triblock terpolymers into sub-30nm micelles and synergistic effects on cellular interactions”

Markus J. Barthel<sup>#, 1,2,3</sup> Alexandra C. Rinke<sup>#, 1,2</sup> Michael Wagner,<sup>1,2</sup> Ulrich Mansfeld,<sup>1,2</sup> Stephanie Hoepfner,<sup>1,2</sup> Justyna A. Czaplewska,<sup>1,2</sup> Michael Gottschald,<sup>1,2</sup> Anja Träger,<sup>1,2</sup> Felix H. Schacher,<sup>\*1,2</sup> Ulrich S. Schubert<sup>\*1,2,3</sup>

<sup>#</sup>Both authors contributed equally to this work.

<sup>1</sup> Laboratory of Organic and Macromolecular Chemistry (IOMC), Friedrich Schiller University Jena, Humboldtstrasse 10, 07743 Jena, Germany.

<sup>2</sup> Jena Center for Soft Matter (JCSM), Friedrich Schiller University Jena, Philosophenweg 7, 07743 Jena, Germany.

<sup>3</sup> Dutch Polymer Institute (DPI), P.O. Box 902, 5600 AX Eindhoven, the Netherlands.

Email: [ulrich.schubert@uni-jena.de](mailto:ulrich.schubert@uni-jena.de); [felix.schacher@uni-jena.de](mailto:felix.schacher@uni-jena.de)

**Table S1:** Influence of the pH value of the solution on the self-assembly process.

Sample	$\langle R_h \rangle_{n,app}$ [nm]
(ENT/ECT) <sup>3.5:1</sup> pH = 7	6
(ENT/ECT) <sup>3.5:1</sup> pH = 3	7
(ENT/ECT) <sup>3.5:1</sup> pH = 11	7

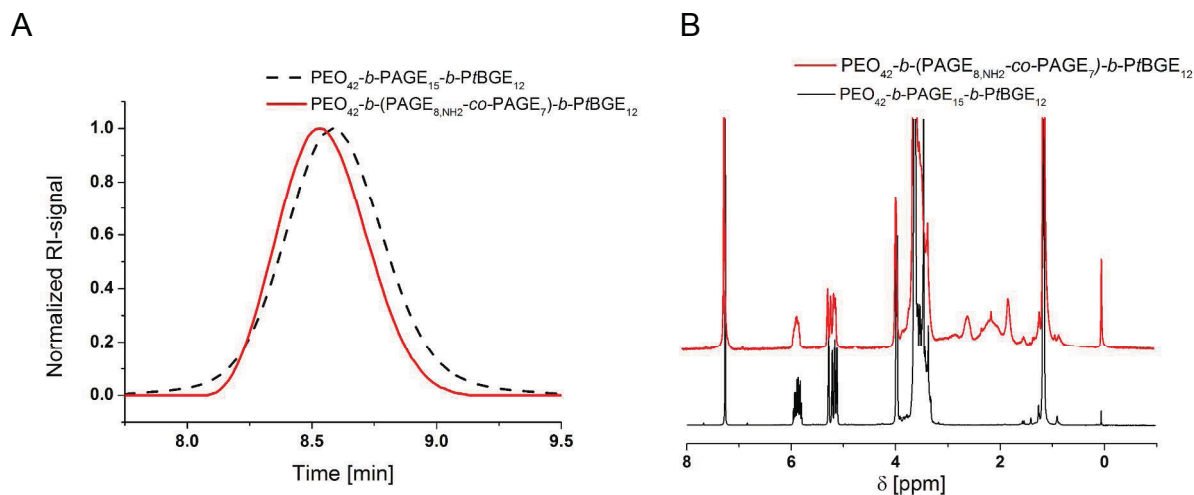


**Figure S1:** SEC traces (A) and  $^1\text{H}$  NMR spectrum (B) of the  $\text{PEO}_{42}\text{-}b\text{-PAGE}_{15}\text{-}b\text{-PtBGE}_{12}$  precursor as well as the cysteamine functionalized triblock terpolymer.

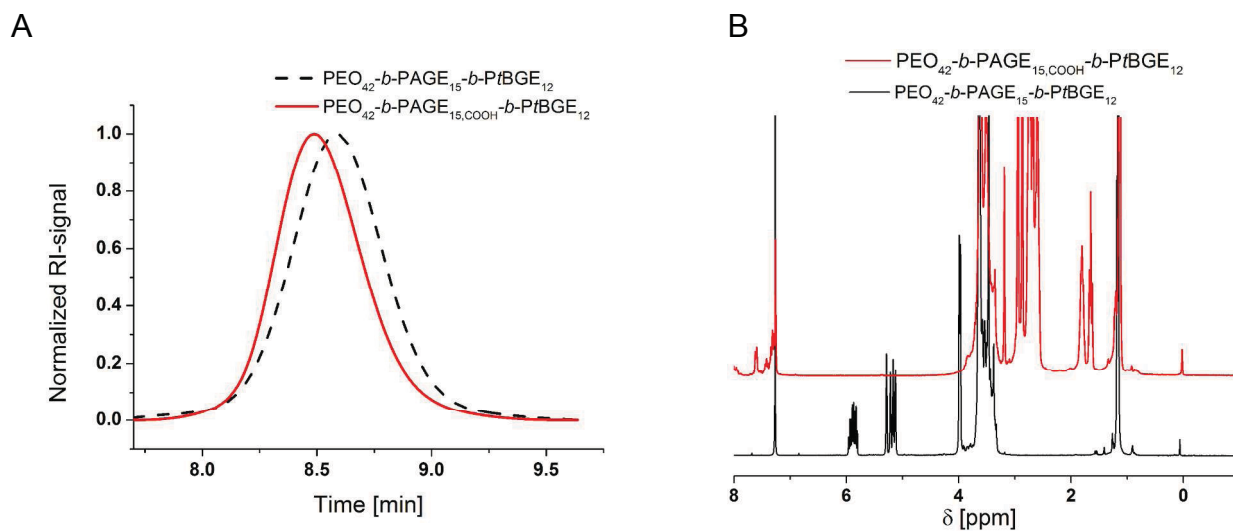


**Figure S2:** SEC traces (A) and  $^1\text{H}$  NMR spectrum (B) of the  $\text{PEO}_{42}\text{-}b\text{-PAGE}_{15}\text{-}b\text{-PtBGE}_{12}$  precursor as well as the 3-mercaptopropionic acid functionalized triblock terpolymer.

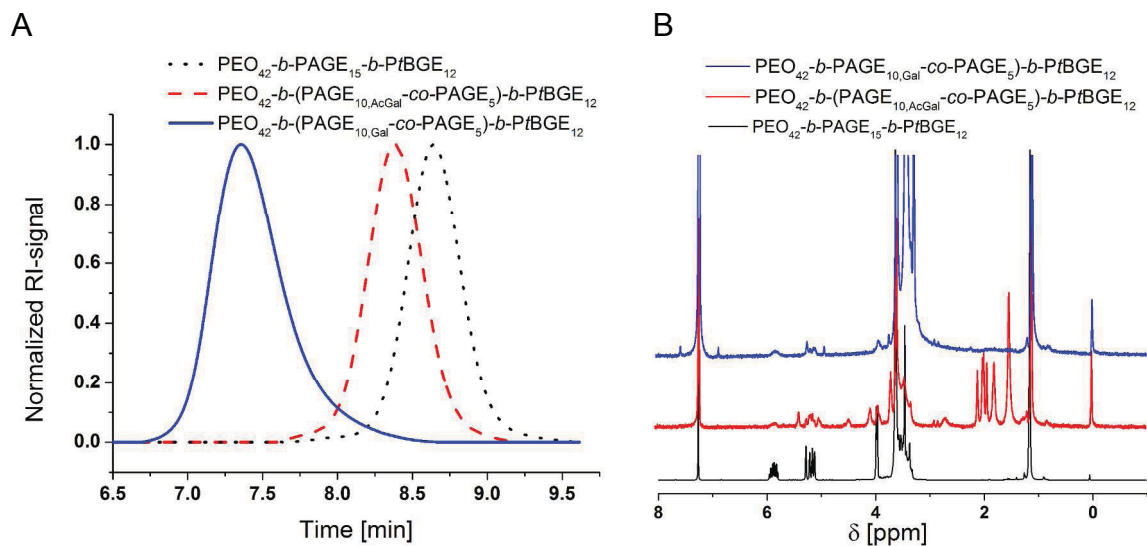


**Figure S3:** SEC traces (A) and  $^1H$  NMR spectrum (B) of the  $PEO_{42}-b-PAGE_{15}-b-PtBGE_{12}$  precursor, the acetylated thiogalactose functionalized triblock terpolymer as well as the deprotected product.

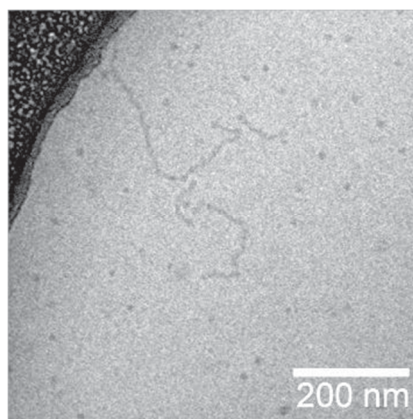


**Figure S4:** Cryo-TEM image of  $PEO_{42}-b-PAGE_{15,COOH}-b-PtBGE_{12}$  (ECT) as example displaying the minor distribution of worm-like structures.

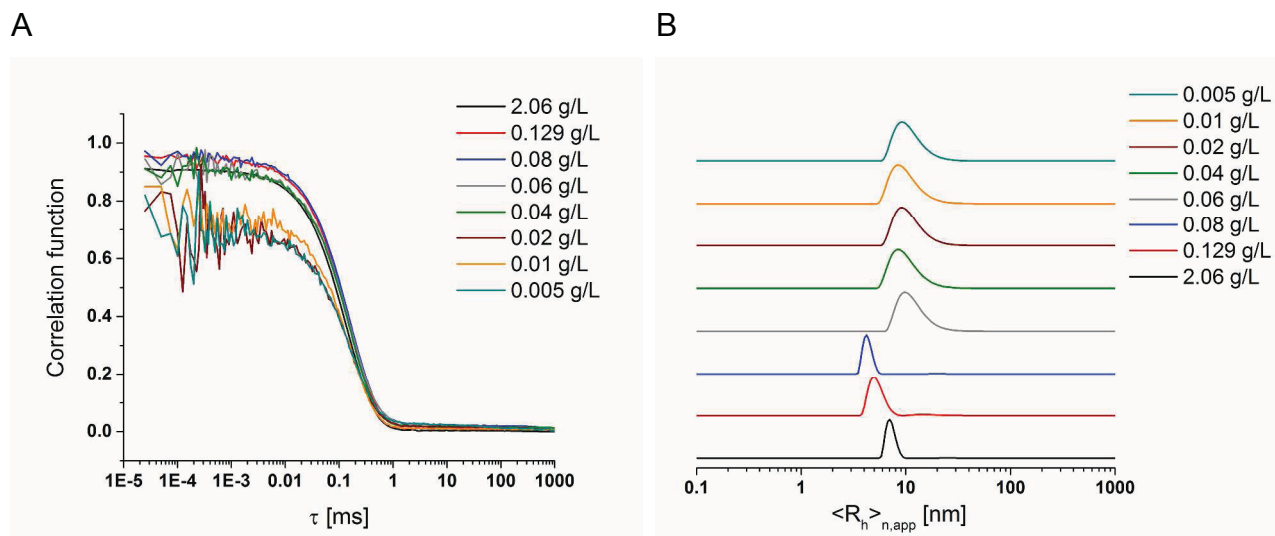


**Figure S5:** Correlation functions of the DLS measurements of the ECT sample at different concentrations (A) as well as the related number weighted CONTIN plots (B).

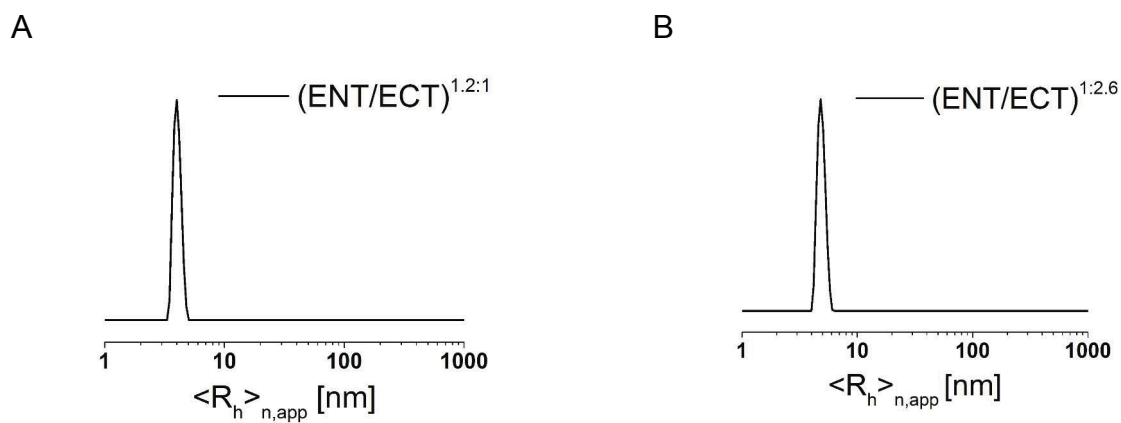


**Figure S6:** Number-weighted DLS CONTIN plots for the 1.2:1 (A) and 1:2.6 (B) mixture of  $PEO_{42}$ -*b*-( $PAGE_{8,NH_2}$ -*co*- $PAGE_7$ )-*b*- $PtBGE_{12}$  /  $PEO_{42}$ -*b*- $PAGE_{15,COOH}$ -*b*- $PtBGE_{12}$  (ENT/ECT).

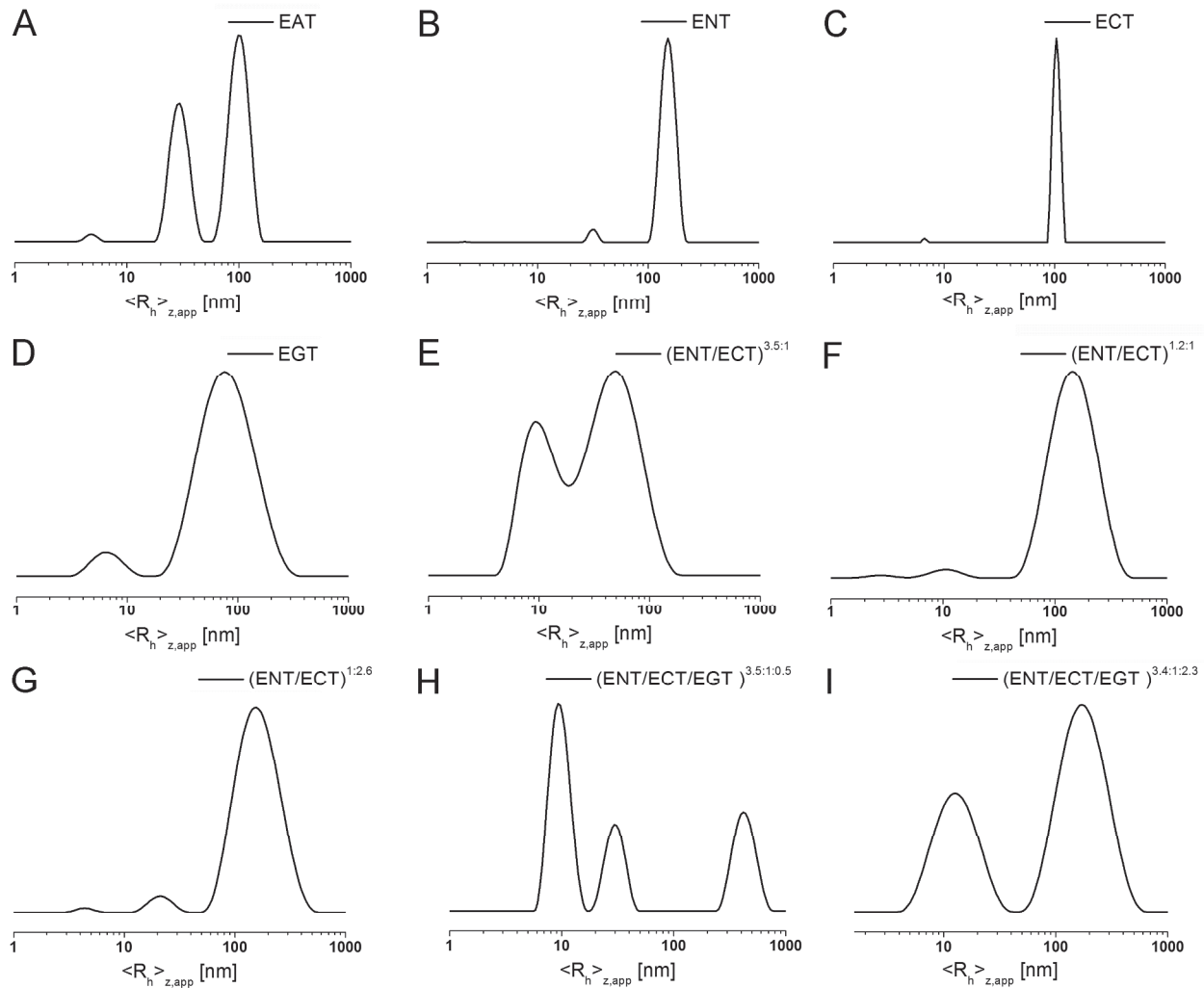


**Figure S7:** Intensity-weighted DLS CONTIN plots for PEO<sub>42</sub>-*b*-PAGE<sub>15</sub>-*b*-PtBGE<sub>12</sub> (EAT, A), PEO<sub>42</sub>-*b*-(PAGE<sub>8,NH2</sub>-*co*-PAGE<sub>7</sub>)-*b*-PtBGE<sub>12</sub> (ENT, B), PEO<sub>42</sub>-*b*-PAGE<sub>15,COOH</sub>-*b*-PtBGE<sub>12</sub> (ECT, C), PEO<sub>42</sub>-*b*-(PAGE<sub>10,Gal</sub>-*co*-PAGE<sub>5</sub>)-*b*-PtBGE<sub>12</sub> (EGT, D), PEO<sub>42</sub>-*b*-(PAGE<sub>8,NH2</sub>-*co*-PAGE<sub>7</sub>)-*b*-PtBGE<sub>12</sub> / PEO<sub>42</sub>-*b*-PAGE<sub>15,COOH</sub>-*b*-PtBGE<sub>12</sub> ((ENT/ECT)<sup>3.5:1</sup>, E), PEO<sub>42</sub>-*b*-(PAGE<sub>8,NH2</sub>-*co*-PAGE<sub>7</sub>)-*b*-PtBGE<sub>12</sub> / PEO<sub>42</sub>-*b*-PAGE<sub>15,COOH</sub>-*b*-PtBGE<sub>12</sub> ((ENT/ECT)<sup>1.2:1</sup>, F), PEO<sub>42</sub>-*b*-(PAGE<sub>8,NH2</sub>-*co*-PAGE<sub>7</sub>)-*b*-PtBGE<sub>12</sub> / PEO<sub>42</sub>-*b*-PAGE<sub>15,COOH</sub>-*b*-PtBGE<sub>12</sub> ((ENT/ECT)<sup>1:2.6</sup>, G), PEO<sub>42</sub>-*b*-(PAGE<sub>8,NH2</sub>-*co*-PAGE<sub>7</sub>)-*b*-PtBGE<sub>12</sub> / PEO<sub>42</sub>-*b*-PAGE<sub>15,COOH</sub>-*b*-PtBGE<sub>12</sub> / PEO<sub>42</sub>-*b*-(PAGE<sub>10,Gal</sub>-*co*-PAGE<sub>5</sub>)-*b*-PtBGE<sub>12</sub> ((ENT/ECT/EGT)<sup>3.5:1:0.5</sup>, H) and PEO<sub>42</sub>-*b*-(PAGE<sub>8,NH2</sub>-*co*-PAGE<sub>7</sub>)-*b*-PtBGE<sub>12</sub> / PEO<sub>42</sub>-*b*-PAGE<sub>15,COOH</sub>-*b*-PtBGE<sub>12</sub> / PEO<sub>42</sub>-*b*-(PAGE<sub>10,Gal</sub>-*co*-PAGE<sub>5</sub>)-*b*-PtBGE<sub>12</sub> ((ENT/ECT/EGT)<sup>3.4:1:2.3</sup>, I).

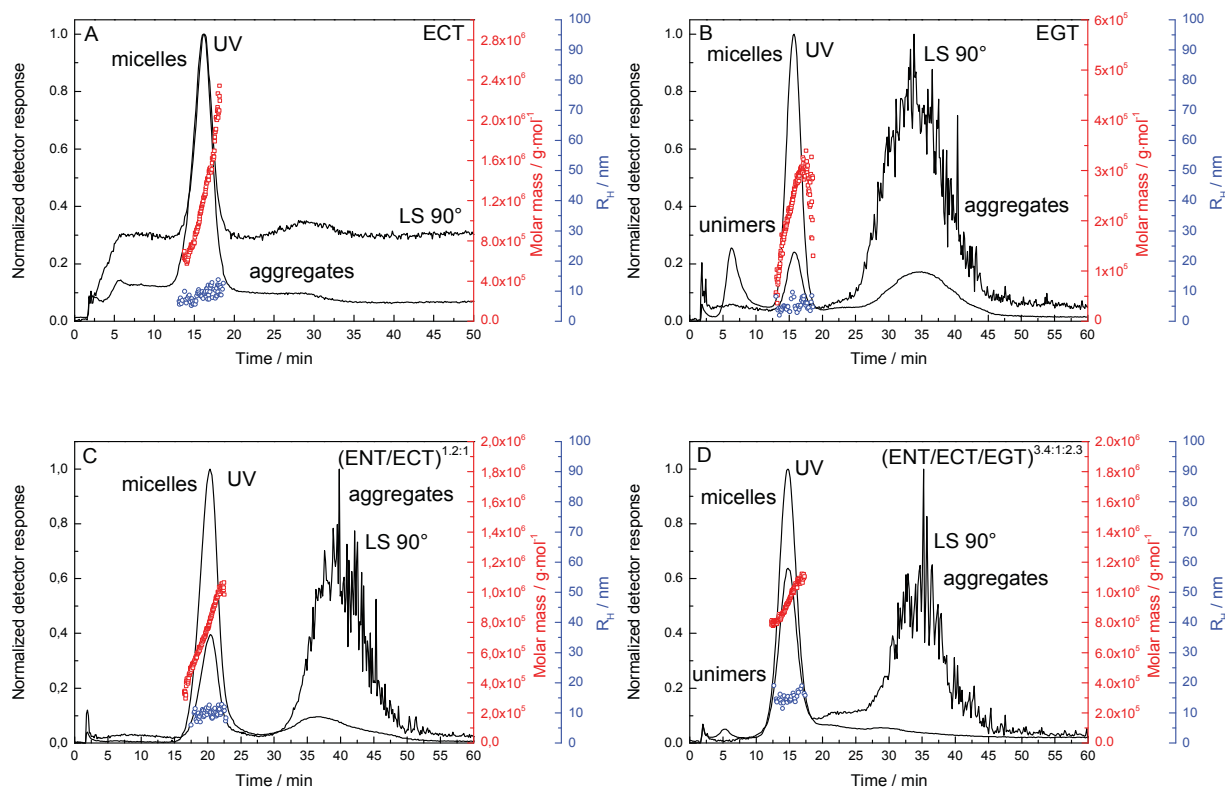


**Figure S8:** AF4 fractograms of self-assembled structures of PEO<sub>42</sub>-*b*-PAGE<sub>15,COOH</sub>-*b*-PtBGE<sub>12</sub> (ECT, A), PEO<sub>42</sub>-*b*-(PAGE<sub>10,Gal-co</sub>-PAGE<sub>5</sub>)-*b*-PtBGE<sub>12</sub> (EGT, B), PEO<sub>42</sub>-*b*-(PAGE<sub>8,NH2-co</sub>-PAGE<sub>7</sub>)-*b*-PtBGE<sub>12</sub> / PEO<sub>42</sub>-*b*-PAGE<sub>15,COOH</sub>-*b*-PtBGE<sub>12</sub> ((ENT/ECT)<sup>1.2:1</sup>, C), PEO<sub>42</sub>-*b*-(PAGE<sub>8,NH2-co</sub>-PAGE<sub>7</sub>)-*b*-PtBGE<sub>12</sub> / PEO<sub>42</sub>-*b*-PAGE<sub>15,COOH</sub>-*b*-PtBGE<sub>12</sub> ((ENT/ECT)<sup>1.2:6</sup>, D) and PEO<sub>42</sub>-*b*-(PAGE<sub>8,NH2-co</sub>-PAGE<sub>7</sub>)-*b*-PtBGE<sub>12</sub> / PEO<sub>42</sub>-*b*-PAGE<sub>15,COOH</sub>-*b*-PtBGE<sub>12</sub> / PEO<sub>42</sub>-*b*-(PAGE<sub>10,Gal-co</sub>-PAGE<sub>5</sub>)-*b*-PtBGE<sub>12</sub> ((ENT/ECT/EGT)<sup>3.4:1:2.3</sup>, C) in 20 mM NaCl.

**Table S2:** Experimental dn/dc values of the different polymer systems in 20 mM NaCl.

Sample	dn/dc (mL/g)	M <sub>w</sub> (g/mol)	M <sub>z</sub> (g/mol)	D
EAT	0.111±0.001	1.226E6±7,371	1.353E6±14,572	1.07±0.001
ENT	0.092±0.008	1.888E6±37,165	1.926E6±36,501	1.02±0.003
ECT	0.128±0.002	1.140E6±8,485	1.239E6±11,314	1.09±0.001
EGT	0.144±0.001	2.428E5±4,327	2.551E5±5,667	1.09±0.037
(ENT/ECT)3.5:1	0.116±0.001	1.213E6±36,638	1.230E6±36,638	1.01±0.001
(ENT/ECT)1.2:1	0.096±0.004	7.665E5±11,067	7.981E5±10,152	1.05±0.003
(ENT/ECT)1:2.6	0.114±0.001	6.386E5±2,113	6.569E5±2,223	1.03±0.004
(ENT/ECT/EGT)3.5:1:0.5	0.101±0.001	1.154E6±74,661	1.175E6±79,952	1.02±0.002
(ENT/ECT/EGT)3.4:1:2.3	0.113±0.002	9.743E5±48,431	9.820E5±46,701	1.01±0.001



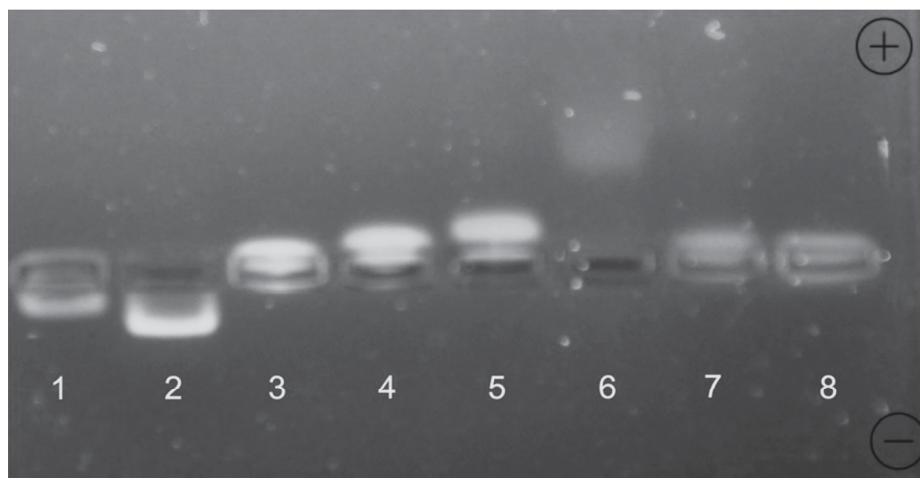


**Figure S9:** Gel-electrophoresis study of the as synthesized material EAT (1), ENT (2), mixtures of ENT and ECT in ratios of 3:1 (3), 1:1 (4), 1:3 (5), ECT (6), a mixture of ECT and EGT in a ratio of 1:1 (7) and EGT(8).

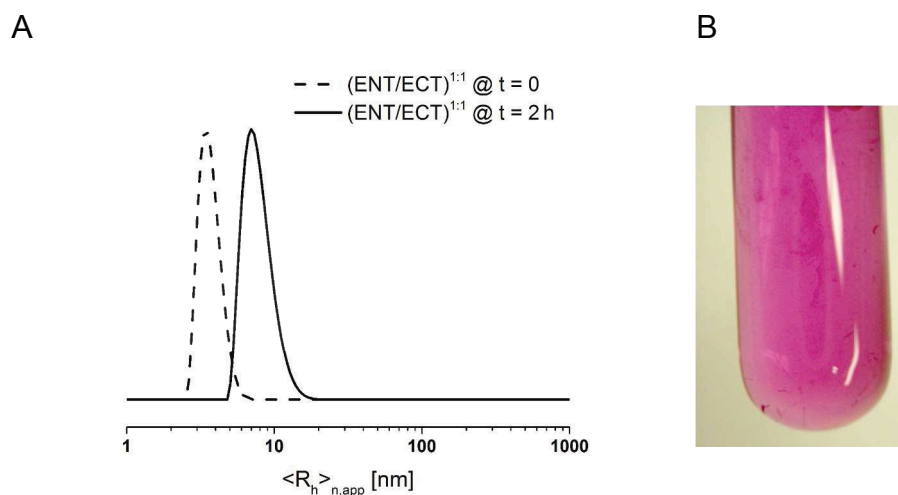


**Figure S10:** Number-weighted DLS CONTIN plots of a 1:1 mixture of PEO<sub>42</sub>-*b*-(PAGE<sub>8,NH2</sub>-*co*-PAGE<sub>7</sub>)-*b*-PtBGE<sub>12</sub> (ENT) micelles with PEO<sub>42</sub>-*b*-PAGE<sub>15,COOH</sub>-*b*-PtBGE<sub>12</sub> (ENT/ECT) directly after mixing and 2 h (ENT/ECT) (A) and a photograph of the solution after 12 h showing precipitated material (B).

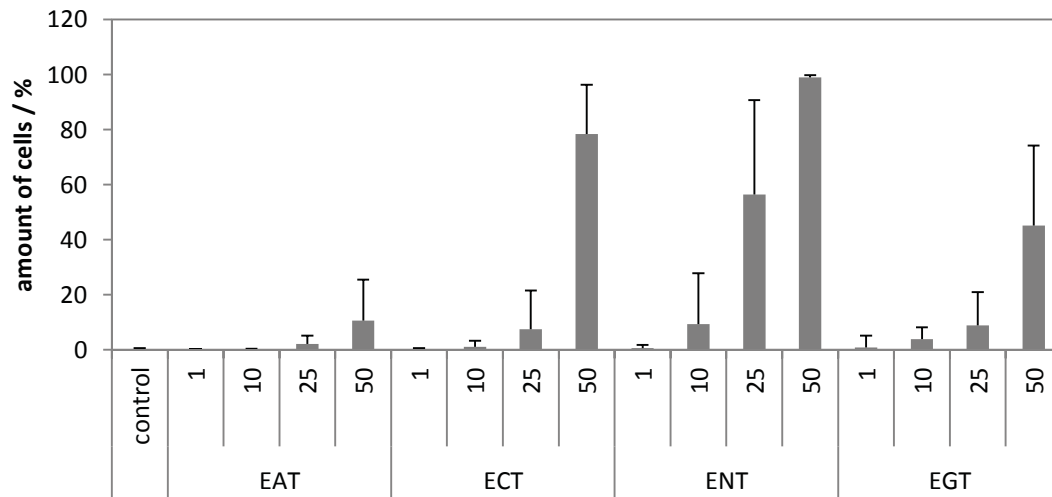


**Figure S11:** Internalization efficiency of triblock terpolymer micelles in HepG2 cells.

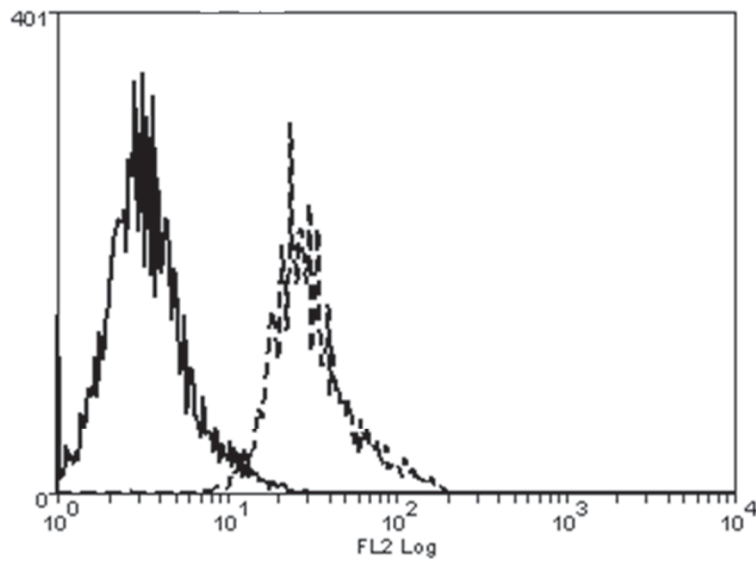


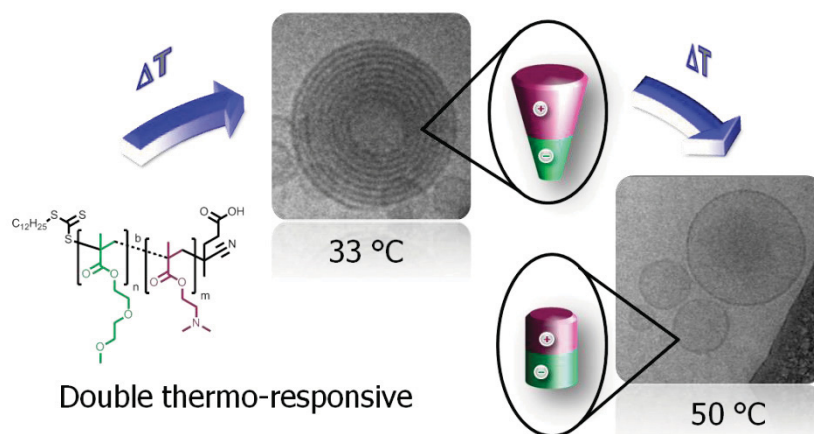
**Figure S12:** Flow cytometer histogram of control cells (continues line) and cell treated with (ENT/ECT)<sup>3.5:1</sup> micelles (dashed line).

## Publication P10

Thermo-induced self-assembly of responsive poly(DMAEMA-*b*-DEGMA) block copolymers into multi- and unilamellar vesicles

C. Pietsch, U. Mansfeld, C. Guerrero-Sanchez, S. Höppener, A. Vollrath, M. Wagner, R. Hoogenboom, S. Saubern, S. H. Thang, C. R. Becer, J. Chiefari, U. S. Schubert

*Macromolecules* **2012**, *45*, 9292-9302.





# Thermo-Induced Self-Assembly of Responsive Poly(DMAEMA-*b*-DEGMA) Block Copolymers into Multi- and Unilamellar Vesicles

Christian Pietsch,<sup>†,‡,§</sup> Ulrich Mansfeld,<sup>†,‡,§</sup> Carlos Guerrero-Sanchez,<sup>||</sup> Stephanie Hoepfener,<sup>†,‡,§</sup> Antje Vollrath,<sup>†,‡</sup> Michael Wagner,<sup>†,‡</sup> Richard Hoogenboom,<sup>⊥</sup> Simon Saubern,<sup>||</sup> San H. Thang,<sup>||</sup> C. Remzi Becer,<sup>#</sup> John Chiefari,<sup>||</sup> and Ulrich S. Schubert<sup>\*,†,‡,§</sup>

<sup>†</sup> Laboratory of Organic and Macromolecular Chemistry (IOMC) Friedrich-Schiller-University Jena, Humboldtstrasse 10, 07743 Jena, Germany

<sup>‡</sup> Jena Center for Soft Matter (JCSM), Humboldtstrasse 10, 07743 Jena, Germany

<sup>§</sup> Dutch Polymer Institute (DPI), John F. Kennedylaan 2, 5612 AB Eindhoven, The Netherlands

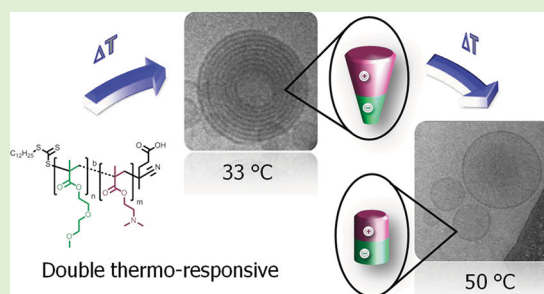
<sup>||</sup> CSIRO, Materials Science and Engineering, Bag 10, Clayton South, 3169 Victoria, Australia

<sup>⊥</sup> Supramolecular Chemistry Group, Department of Organic Chemistry, Ghent University, Krijgslaan 281 S4, 9000 Ghent, Belgium

<sup>#</sup> Department of Chemistry, University of Warwick, CV4 7AL Coventry, United Kingdom

## Supporting Information

**ABSTRACT:** A series of thermoresponsive diblock copolymers of poly[2-(dimethylamino)ethyl methacrylate-*block*-di(ethyleneglycol) methyl ether methacrylate], poly(DMAEMA-*b*-DEGMA), were synthesized by reversible addition–fragmentation chain transfer (RAFT) polymerizations. The series consist of diblock and quasi diblock copolymers. Sequential monomer addition was used for the quasi diblock copolymer synthesis and the macro-chain transfer approach was utilized for the block copolymer synthesis. The focus of this contribution is the controlled variation of the ratios of DMAEMA to DEGMA in the copolymer composition, resulting in a systematic polymer library. One of the investigated block copolymer systems showed double lower critical solution temperature (LCST) behavior in water and was further investigated. The phase transitions of this block copolymer were studied in aqueous solutions by turbidimetry, dynamic light scattering (DLS), variable temperature proton nuclear magnetic resonance (<sup>1</sup>H NMR) spectroscopy, zeta potential, and cryo transmission electron microscopy (cryo-TEM). The block copolymer undergoes a two-step thermo-induced self-assembly, which results in the formation of multilamellar vesicles after the first LCST temperature and to unilamellar vesicles above the second LCST transition. An interplay of ionic interactions as well as the change of the corresponding volume fraction during the LCST transitions were identified as the driving force for the double responsive behavior.



## INTRODUCTION

Stimuli-responsive polymers, which undergo phase transitions in response to an external stimulus, have gained the interest of many researchers in the past decade.<sup>1–5</sup> Such “smart” materials can act with a property change in response to changes in temperature, pH value, electric potential, light, or magnetic field.<sup>6–10</sup> The area of stimuli-responsive polymers represents nowadays a strongly growing field in polymer research, in particular the investigation regarding lower critical solution temperature behavior has attracted significant interest. Particular attention in this context has been paid to the thermosensitive self-organization of amphiphilic block copolymers, especially on the formation of micelles or vesicular structures in aqueous solution. Numerous reports on the micellization of diblock copolymers containing thermosensitive block segments are described.<sup>4,6,7,11–13</sup> The formed vesicles or

polymersomes are usually spherical shell structures with a hydrophobic core-layer and a hydrophilic internal and external corona made from amphiphilic block copolymers.<sup>14–16</sup> Polymer vesicles, which respond to external stimuli such as a change in temperature or the pH value, represent attractive candidates for applications in encapsulation or drug delivery systems.<sup>3,17,18</sup>

LCST polymers are soluble below a certain temperature because of the formation of hydrogen bonds between water molecules of the hydration shell and the polymer chains. By passing the cloud point temperature ( $T_{CP}$ ), the polymer starts to precipitate due to the breaking of hydrogen bonds and due to hydrophobic polymer–polymer interactions because the

Received: September 7, 2012

Revised: November 2, 2012

Published: November 19, 2012

**Table 1.** Overview of the Selected Reaction Conditions Used for the Polymerizations of DMAEMA and DEGMA Using an Automated Parallel Synthesizer

sample	structure	ratio 1st polym DMAEMA/CTA <sup>a</sup>	ratio 2nd polym DEGMA/macroCTA <sup>a</sup>	concn [mol/L]	polym time [h]
H1	homo	90:1		3.0	10.0
B1	quasi		10:1	2.0	6.0
H2	homo	80:1		3.0	10.0
B2	quasi		20:1	2.0	6.0
H5	homo	45:1		3.0	10.0
B5	quasi		55:1	2.0	6.0

<sup>a</sup>Molar ratios of the reaction solution.

entropy term becomes dominant in the Gibbs equation. Besides the gold standard poly(*N*-isopropylacrylamide) (poly(NIPAM)) with a LCST of 32 °C,<sup>1</sup> a number of poly(ethylene glycol) functionalized (meth)acrylates have been reported to exhibit LCST behavior.<sup>19–21</sup> In particular, different oligo(ethylene glycol) methyl ether methacrylate (OEGMA)-based polymers received significant attention as temperature sensitive materials. The large interest is fueled by the easy preparation of well-defined OEGMA-based copolymers by reversible deactivation radical polymerization (RDRP) techniques such as reversible addition–fragmentation chain transfer (RAFT) polymerizations.<sup>22–24</sup> By variation of the side chain length, the  $T_{CP}$  of these copolymers can be tuned, which makes them very attractive systems.<sup>19,25,26</sup> The homopolymer of di(ethylene glycol) methyl ether methacrylate (DEGMA) (two repeating units of ethylene glycol) has a  $T_{CP}$  around 27 °C, which can be increased by copolymerizing with a more hydrophilic monomer.<sup>19,20,26,27</sup> 2-(Dimethylamino)ethyl methacrylate (DMAEMA) has been used as such a comonomer, resulting in a pH- and temperature-responsive copolymer.<sup>28</sup> Poly(DMAEMA) is used in various applications, e.g., in gene delivery systems of transfection agents.<sup>29–31</sup> Various  $T_{CP}$ 's of poly(DMAEMA) have been reported in literature ranging from 20 to 80 °C, which is an indication that the LCST strongly depends on the used molar masses.<sup>28,32–38</sup> Furthermore, the  $T_{CP}$  strongly depends on variations in the pH value due to partial (de)protonation of the basic nitrogen atoms of DMAEMA.<sup>28,35–39</sup>

Block copolymers can be responsive to two different stimuli at the same time, such as temperature and the pH value, as demonstrated for block copolymers of (poly(NIPAM-*b*-AA))<sup>40</sup> and poly(DMAEMA-*b*-MMA).<sup>41</sup> Furthermore, different copolymer brushes of DMAEMA with DEGMA and *tert*-butyl methacrylate (*t*BMA), investigated by Matyjaszewski et al., showed dual responsive properties.<sup>38</sup> The pH and temperature responsive properties were also investigated for different poly(DMAEMA-*co*-DEGMA) hydrogels.<sup>37</sup> Poly(DMAEMA-*b*-DEGMA) block copolymers were recently used to control the self-assembly of virus particles.<sup>42</sup>

The thermoresponsive self-organization of amphiphilic block copolymers in aqueous solution has been described in the literature for several systems.<sup>6,7,11–13,43–47</sup> For example, the self-assembly of double thermoresponsive block copolymers of poly(*N*-*n*-propylacrylamide-*b*-*N*-ethylacrylamide) was reported.<sup>48</sup> Furthermore, the thermo-induced micellization transition of the block copolymer solution of poly(tri(ethylene glycol) methyl ether acrylate)-*b*-poly(4-vinylbenzyl methoxytris(oxyethylene) ether) was described.<sup>49</sup> The formation of double hydrophilic diblock copolymers to vesicle and micelle structures have been studied in detail by Lecomman-

doux and co-workers using poly((dimethylamino)ethyl methacrylate-*b*-glutamic acid).<sup>50</sup> However, the thermo-induced self-assembly of poly(DMAEMA-*b*-DEGMA) is, to the best of our knowledge, not yet reported.

In this contribution, a series of thermoresponsive diblock copolymers of poly(DMAEMA-*b*-DEGMA) was synthesized by RAFT polymerization ranging from pure block to gradient block copolymer (quasi diblock) structures. The macro-chain transfer approach was used for the preparation of these block copolymers. The ratios of DMAEMA to DEGMA were systematically varied, while the degree of polymerization was kept constant. The self-assembly behavior as well as the LCST of the responsive polymers were measured by turbidimetry. Within this series of block copolymers, a double-responsive behavior was observed for one particular composition and the self-assembly characteristic was further investigated by dynamic light scattering, temperature-dependent <sup>1</sup>H NMR spectroscopy, zeta potential analysis, and cryogenic transmission electron microscopy. The formation of spherical structures, like multilamellar and unilamellar vesicles at elevated temperatures, was observed and a model for the formation of these structures was developed.

## ■ EXPERIMENTAL SECTION

**Materials.** Di(ethylene glycol) methyl ether methacrylate (DEGMA) and 2-(dimethylamino)ethyl methacrylate (DMAEMA) were purchased from Sigma-Aldrich and purified by stirring in the presence of inhibitor-remover for hydroquinone or hydroquinone monomethyl ether (Aldrich) for 30 min prior to use. The initiator, 1,1'-azobis(cyclohexane carbonitrile) (VAZO-88), was obtained from DuPont. 4-Cyano-4-[(dodecylsulfanylthiocarbonyl)sulfanyl]pentanoic acid (DTTCP) chain transfer agent (CTA) was prepared according to a literature procedure.<sup>23,51</sup> All analytical grade solvents were purchased from Sigma-Aldrich or Merck KGaA.

**Polymerization in an Automated Parallel Synthesizer.** The quasi block copolymerizations were performed in a Chemspeed Accelerator SLT automated synthesizer using the sequential monomer addition and following similar experimental procedures as reported elsewhere.<sup>52–54</sup> In a typical polymerization experiment, 864 mg of DMAEMA monomer ( $5.5 \times 10^{-3}$  mol), 0.73 mg of VAZO-88 initiator ( $3.0 \times 10^{-6}$  mol), 24.1 mg of DTTCP (used as a CTA) RAFT agent ( $6.00 \times 10^{-5}$  mol), and *N,N*-dimethylformamide (DMF) were mixed together in a 13 mL glass reactor of an automated parallel synthesizer as follows: DMAEMA monomer, DMF solvent reservoir, and individual stock solutions of VAZO-88 (initiator) and DTTCP (CTA) dissolved in DMF were degassed by sparging nitrogen for at least 15 min prior to use. All these reagents were added and combined into one of the reactors of the parallel synthesizer using its automated liquid handling system in order to reach the aforementioned amounts and a monomer concentration of 3.0 M; the ratio of RAFT agent to initiator was 1:0.05. Trioxane dissolved in the DMAEMA monomer was utilized, at a concentration of 5 mg mL<sup>-1</sup> of total reaction mixture, as internal standard to determine the monomer conversion by <sup>1</sup>H

NMR measurements in deuterated chloroform ( $\text{CDCl}_3$ ). Once in the reactor, the reaction mixture was subjected to three freeze–pump–thaw cycles between  $-70$  and  $-10$  °C (5 mbar vacuum for 2 min each cycle) in the parallel synthesizer.<sup>53</sup> Thereafter, the reaction mixtures were heated up to 90 °C and vortexed at 600 rpm for 10 h; the coldfinger reflux condensers were set to 7 °C during the reaction. After the polymerization, samples of 75  $\mu\text{L}$  were withdrawn with the liquid handling system of the apparatus and transferred into NMR tubes and size exclusion chromatography (SEC) vials, which were filled with their corresponding solvent for analysis. The first polymerization step proceeded up to a certain conversion, which resulted in a poly(DMAEMA) macro-chain transfer agents (macro-CTAs). Thereafter, the polymers were chain extended with DEGMA using similar conditions as described above. The DEGMA concentration was kept at 2.0 mol  $\text{L}^{-1}$  for each polymerization experiment. Table 1 summarizes the utilized reaction conditions and  $[\text{M}]/[\text{CTA}]$  ratios. After completion of the polymerization, dichloromethane ( $\text{CH}_2\text{Cl}_2$ ) was added to the final mixtures and the polymers were then manually precipitated into *n*-hexane (with adding  $\text{CH}_2\text{Cl}_2$ , DMF is soluble in *n*-hexane). Afterward, the copolymers were dried in a vacuum oven at 40 °C.

**Polymerization via Classical Conditions.** Block copolymers were also synthesized using the macro-CTA approach with a precipitation step in between to obtain pure block segments. The desired amounts of the monomer (e.g., 2.36 g, 15.0 mmol of DMAEMA) were transferred into Schlenk type reactors and were diluted with DMF. Thereafter, the calculated volumes of stock solutions of CTA (DTTCP, 0.15 mmol, 60.55 mg) as well as the initiator (VAZO-88, 0.008 mmol, 1.83 mg) were added. The ratio between [CTA] and [VAZO-88] was 1:0.05. The prepared solutions were degassed using four freeze–pump–thaw cycles. Subsequently, the reaction was performed in an oil bath at 90 °C for 10 h. After the polymerization,  $\text{CH}_2\text{Cl}_2$  was added to the final mixtures and the polymers were then manually precipitated into *n*-hexane (with adding  $\text{CH}_2\text{Cl}_2$ , DMF is soluble in *n*-hexane). Afterward, the polymers were dried in a vacuum oven at 40 °C. The final poly(DMAEMA)s were used as a macro-CTA and chain extended with DEGMA using similar conditions as described above. The utilized reaction conditions and  $[\text{M}]/[\text{CTA}]$  ratios are summarized in Table 2. All monomer conversions were measured by  $^1\text{H}$  NMR spectroscopy using trioxane as internal standard. The molar masses of the obtained polymers were measured by SEC.

**Instrumentation.** Size-exclusion chromatography (SEC) was performed on a system comprising a Waters 590 HPLC pump and a Waters 410 refractive index detector equipped with three Waters Styragel columns (HT2, HT3, HT4, each 300 mm  $\times$  7.8 mm, providing an effective molar mass range of 100–600000  $\text{g mol}^{-1}$ ). The

**Table 2. Overview of the Selected Reaction Conditions Used for the Polymerizations of DMAEMA and DEGMA via the Schlenk Technique**

sample	structure	ratio feed 1st polym monomer/CTA <sup>a</sup>	ratio feed 2nd polym monomer/macroCTA <sup>a</sup>	concn [mol/L]	polym time [h]
H3	homo	(DMAEMA) 100:1		2.0	10.0
B3	block		(DEGMA) 100:1	1.0	7.5
H4	homo	(DMAEMA) 100:1		3.0	8.0
B4	block		(DEGMA) 100:1	1.0	6.0
H6	homo	(DEGMA) 100:1		2.0	8.0
B6	block		(DMAEMA) 50:1	1.0	6.0

<sup>a</sup>Molar ratios of the reaction solution.

eluent was DMF (containing 0.45% w/v LiBr) at 80 °C with a flow rate of 1 mL  $\text{min}^{-1}$ . Number ( $M_n$ ) and weight-average ( $M_w$ ) molar masses were evaluated using Waters Millennium software. A polynomial was used to fit the log  $M$  vs time calibration curve, which was linear across the molar mass ranges. The SEC columns were calibrated with low polydispersity polystyrene standards (Polymer Laboratories) ranging from  $M_n$  3100 to 650000  $\text{g mol}^{-1}$ . Further SEC experiments were performed on a Shimadzu system equipped with a SCL-10A system controller, a LC-10AD pump, a RID-10A refractive index detector, and a PSS SDV linear S, 5  $\mu\text{m}$  column (8 mm  $\times$  300 mm) with chloroform/triethylamine/2-propanol (94:4:2) as eluent, and the column oven was set to 40 °C. A calibration with low polydispersity polystyrene standards (ranging  $M_n$  from 376 to 128000  $\text{g mol}^{-1}$ ) was used. In addition, further SEC experiments were carried out using an Agilent1200 series system, a G1310A pump, a G1362A refractive index detector, and both a PSS Gram30 and a PSS Gram1000 column in series, whereby *N,N*-dimethylacetamide (DMAc) with 5 mmol lithium chloride was used as an eluent at 1 mL  $\text{min}^{-1}$  flow rate, and the column oven was set to 40 °C. The system was calibrated with polystyrene ( $M_n$  from 374  $\text{g mol}^{-1}$  to 1040000  $\text{g mol}^{-1}$ ) standards. Proton nuclear magnetic resonance ( $^1\text{H}$  NMR) spectra were recorded on a Bruker AC 300 (300 MHz) and 400 (400 MHz) spectrometer at 298 K. The chemical shifts are reported in parts per million (ppm,  $\delta$  scale) relative to the signals from the NMR solvents. The temperature variable  $^1\text{H}$  NMR spectroscopy was recorded on a Bruker AC 400 (400 MHz) spectrometer in deuterium oxide ( $\text{D}_2\text{O}$ ) at a polymer concentration of 5.0 mg  $\text{mL}^{-1}$ . At each temperature step (5 °C) from 25 to 65 °C, the polymer solution was equilibrated for 3 min. Conversions were calculated from  $^1\text{H}$  NMR spectra using 1,3,5-trioxane as an internal standard. The cloud point measurements for the identification of the LCST behavior were performed by heating the polymer (1.0, 2.5, 5.0, and 10.0 mg  $\text{mL}^{-1}$ , respectively) in deionized water from 0 to 105 °C with a heating rate of 1.0 °C  $\text{min}^{-1}$  followed by cooling to 0 °C at a cooling rate of 1.0 °C  $\text{min}^{-1}$  after keeping it 10 min at 105 °C. This cycle was repeated three times. During these controlled cycles, the transmission through the solutions was monitored in a Crystal16 from Avantium Technologies. The cloud points are reported as the 50% transmittance temperature in the second heating run.

High-throughput dynamic light scattering (HT-DLS) measurements were performed on the DynaPro Plate Reader Plus (Wyatt Technology Corporation, Santa Barbara, CA) equipped with a 60 mV linearly polarized gallium arsenide (GaAs) laser of  $\lambda = 832.5$  nm and operating at an angle of 156°. The samples were heated from 25 to 65 °C in a 96-well plate using 10 °C heating steps, and after 5 min equilibration time, each well was measured collecting five acquisitions. The data were analyzed with the Dynamics software version 6.20 by the method of cumulants.<sup>55</sup> The percent of polydispersity is given by  $\%Pd = 100(\mu_2)/\mu_1^2$ , where  $\mu_1$  and  $\mu_2$  are the first- and the second-order cumulant, respectively. The level of homogeneity is considered high when the percent polydispersity is less than 15%. If the level of homogeneity is low (percent polydispersity larger than 30%), the particle population can be considered as being polydisperse. DLS measurements were also carried out on a Zetasizer Nano ZS (Malvern Instruments, Malvern, UK) operating with a laser beam at 633 nm and a scattering angle of 173°. The sample was heated in a quartz cuvette from 25 up to 65 °C in 1 °C steps. At each temperature step, the sample was equilibrated for 120 s and then measured three times including three runs for 30 s. The intensity and the volume distribution of the particle size were calculated applying the NNLS mode.

Electrophoretic light scattering was used to measure the electrokinetic potential, also known as zeta potential. The measurements were performed using a Zetasizer Nano ZS (Malvern Instruments) by applying laser Doppler velocimetry. For each measurement, 20 runs were carried out using the slow-field reversal and fast-field reversal mode at 150 V. Each experiment was performed in triplicate from 25 to 65 °C in 5 °C steps. The zeta potential ( $\zeta$ ) was calculated from the electrophoretic mobility ( $\mu$ ) according to the Henry equation. The Henry coefficient  $f(ka)$  was calculated according to Oshima.<sup>56</sup>

**Scheme 1. Schematic Representation of the Poly(DMAEMA-*b*-DEGMA) Formation Using RAFT Polymerization with the CTA DTTCP and the Radical Initiator VAZO-88**

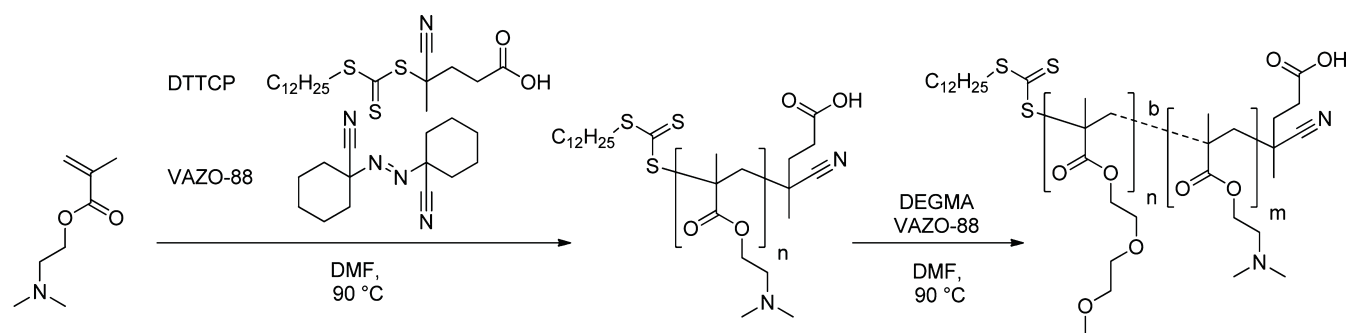


**Table 3. Composition of the Block Copolymers of Poly(DMAEMA-*b*-DEGMA) from SEC and <sup>1</sup>H NMR Spectroscopy with Increasing Ratio of DEGMA Starting from DMAEMA Homopolymer**

sample <sup>a</sup>	SEC (DMF) <sup>b</sup>		SEC (DMAc) <sup>c</sup>		SEC (CHCl <sub>3</sub> ) <sup>d</sup>		conv. <sup>e</sup> [%]	M <sub>n,theo</sub> <sup>f</sup> [g/mol]	ratio [%]	<sup>1</sup> H NMR <sup>g</sup> DMAEMA/DEGMA
	M <sub>n</sub> [g/mol]	PDI	M <sub>n</sub> [g/mol]	PDI	M <sub>n</sub> [g/mol]	PDI				
H1 (h)	18600	1.16					81 <sup>(M1)</sup>	10200	100:0	
H2 (h)	15200	1.17					62 <sup>(M1)</sup>	6200	100:0	
H3 (h)	17600	1.22					80 <sup>(M1)</sup>	13000	100:0	
H4 (h)	15200	1.21	13500	1.43	28700	1.22	83 <sup>(M1)</sup>	13300	100:0	
H5 (h)	8800	1.16					75 <sup>(M1)</sup>	5400	100:0	
B1 (q)	20800	1.29	24700	1.44	29700	1.36	39 <sup>(M2)</sup>	12600	94:6	
B2 (q)	21800	1.25	24100	1.41	30200	1.34	70 <sup>(M2)</sup>	10900	87:13	
B3 (b)	26900	1.27	27400	1.52	<i>h</i>	<i>h</i>	65 <sup>(M2)</sup>	25400	66:34	
B4 (b)	35100	1.54	36600	1.48	<i>h</i>	<i>h</i>	53 <sup>(M2)</sup>	23300	64:36	
B5 (q)	39700	1.35	24000	1.70	<i>h</i>	<i>h</i>	85 <sup>(M2)</sup>	15300	51:49	
B6 (b)	26600	1.32	27100	1.33	33500	1.24	40 <sup>(M1)</sup>	20800	20:80	
H6 (h)	23600	1.23	23700	1.29	27800	1.20	76 <sup>(M2)</sup>	14500	0:100	

<sup>a</sup>Copolymer structure: h = homopolymer, q = quasi diblock copolymer, b = diblock copolymer. <sup>b</sup>Calculated from SEC (DMF) using PS calibration. <sup>c</sup>Calculated from SEC (DMAc) using PS calibration. <sup>d</sup>Calculated from SEC (CHCl<sub>3</sub>/triethylamine/2-propanol = 94/4/2) using PS calibration. <sup>e</sup>Calculated from vinyl integrals of <sup>1</sup>H NMR spectra using trioxane as internal standard, M1 = DMAEMA and M2 = DEGMA. <sup>f</sup>Calculated according to formula ( $M_{n,theo} = ([M]/[CTA] \times conv \times M_{monomer}) + M_{CTA}$ ), besides for block copolymers where  $M_{CTA}$  is  $M_{macroCTA}$ . <sup>g</sup>Calculated from integrated areas of DMAEMA signals ((CH<sub>3</sub>)<sub>2</sub>N-) and the DEGMA (CH<sub>2</sub>-O-) side-group signals. <sup>h</sup>Block copolymer reached the exclusion limit of the SEC.

Cryogenic transmission electron microscopy (cryo-TEM) measurements were performed on a Philips CM120 operating at an acceleration voltage of 120 kV. Images were recorded with a bottom mounted 1 k × 1 k CCD camera. The samples for TEM investigations were prepared and stored at room temperature prior to the investigation (5 mg mL<sup>-1</sup>). For the temperature-dependent investigation, the samples were preheated under frequent agitation for at least 30 min in a water bath at 35 and 50 °C, respectively. A drop of the polymer solution (5 μL) was rapidly placed with a preheated microliter pipet on a perforated carbon grid (Quantifoil R2/2) within an in-house-built controlled environment vitrification system (CEVS) with a saturated water atmosphere. The temperature within the CEVS was adjusted to 38 and 55 °C to ensure that the sample is investigated above the corresponding cloud point temperatures. Prior to the blotting, the liquid was allowed to equilibrate on the grids for at least 2 min to avoid preparation artifacts. The controlled saturated humidity and defined temperature minimizes temperature alterations of the sample due to evaporation effects. The samples were rapidly blotted and plunged into a cryogen reservoir containing liquid ethane. After preparation, the samples were stored and measured at a temperature below -176 °C to avoid the formation of crystalline ice layers. To avoid further preparation artifacts, similar blotting times were used at different temperatures.

## RESULTS AND DISCUSSION

**Synthesis of the Poly(DMAEMA-*b*-DEGMA) Library.** A library of double thermoresponsive poly(DMAEMA-*b*-

DEGMA) diblock copolymers was synthesized using the RAFT polymerization technique in a sequential monomer addition approach. Within this series, the ratios of DMAEMA and DEGMA were varied ranging from 100% DMAEMA to 100% DEGMA with composition changes in 20% steps. Two possibilities of the macro-chain transfer approach were explored, namely with and without a precipitation step after the first polymerization. Using a parallel robot platform, the second DEGMA monomer was added before the full conversion of DMAEMA was reached, resulting in quasi diblock structures. The polymerizations were carried out using 4-cyano-4-[(dodecylsulfanylthiocarbonyl) sulfanyl]pentanoic acid (DTTCP) as CTA and VAZO-88 as radical initiator (see Scheme 1), applying similar conditions as previously described for the MMA polymerization,<sup>57</sup> namely 90 °C with a ratio of DTTCP to VAZO-88 of 20:1.

The quasi diblock copolymers were synthesized in a Chemspeed Accelerator SLT106 automated platform and the diblock copolymers under classical conditions (Schlenk technique) using the same polymerization conditions. The first block segment was polymerized in DMF at a concentration of 3.0 mol L<sup>-1</sup>, followed by the polymerization of DEGMA with a monomer concentration of 2.0 mol L<sup>-1</sup>. For B6, this order was reversed, meaning that first DEGMA was polymerized and



Table 4. Cloud Point Temperatures from Turbidimetry Measurement of the Homo and Block Copolymers

sample DMAEMA/DEGMA [%]	cloud points by turbidimetry (2nd heating run) in °C <sup>a</sup>							
	H4	B1	B2	B3	B4	B5 <sup>c</sup>	B6	H6
100:0	100:0	94:6	87:13	66:34	64:36	51:49	20:80	0:100
10 mg mL <sup>-1</sup>	45.4	43.6	40.7	m <sup>b</sup>	m <sup>b</sup>	32.5:48.0	29.4	25.1
5.0 mg mL <sup>-1</sup>	46.7	44.5	41.7	m <sup>b</sup>	m <sup>b</sup>	33:~49 32:~48 <sup>d</sup>	30.0	25.9
2.5 mg mL <sup>-1</sup>	49.0	46.0	43.2	m <sup>b</sup>	m <sup>b</sup>	34:~46	30.5	28.0
1.0 mg mL <sup>-1</sup>	57.4	48.2	45.3	m <sup>b</sup>	m <sup>b</sup>	~41	31.5	36.4

<sup>a</sup>Estimated in deionized water at 50% transmission for the second heating run. <sup>b</sup>No clear phase separation transition. <sup>c</sup>Estimated at the local maximum at the half %value of transmission. <sup>d</sup>Estimated in D<sub>2</sub>O.

then the corresponding DMAEMA block. In Table 3, the molar masses and polydispersity indices (PDI) measured by SEC are summarized, demonstrating good control over the first blocks (PDI < 1.23) and relatively good control for most block copolymers (PDI < 1.35, except B4). The obtained diblock copolymers were characterized by SEC in DMF, DMAc, and chloroform as eluent, using a refractive index detector (see Supporting Information (SI)). The hydrodynamic volume of poly(DMAEMA) depends strongly on the solvent and, additionally, it is known that interactions with the column material<sup>58</sup> occur due to the basic nitrogen atoms, therefore, different SEC systems were used to characterize the block copolymers. Nevertheless, the obtained values should be handled with care because of both the calibration with polystyrene and the possibility of column interactions.<sup>59</sup>

The monomer conversions of DMAEMA and DEGMA were estimated by <sup>1</sup>H NMR spectroscopy. The conversion of DMAEMA was around 70–80% after 10 h of polymerization. Then the polymerization was stopped to retain high RAFT end-group functionality. A clear molar mass shift could be observed for the block copolymers in the SEC analysis. For the final copolymers, the ratio between both block segments were determined by <sup>1</sup>H NMR spectroscopy using the integrated areas of DMAEMA signals ((CH<sub>3</sub>)<sub>2</sub>N– at 2.26 ppm) and the DEGMA (CH<sub>2</sub>–O– at 3.54–3.66 ppm) ethylene glycol side-group signals (Figure S6, SI). The observed ratios are in a good agreement with the monomer feed ratio.

**Thermoresponsive Properties of Poly(DMAEMA-*b*-DEGMA).** Heating solutions of the polymers in deionized water induces a LCST transition, i.e., the solutions become turbid above the characteristic  $T_{CP}$ , indicating the collapse of the polymer chains (two-phase system). The  $T_{CP}$ 's of the homo- and block copolymers were determined by turbidimetry measurements in deionized water at four different concentrations (1.0, 2.5, 5.0, and 10.0 mg mL<sup>-1</sup>) and are listed in Table 4. All thermo-induced transitions of the copolymers were found to be fully reversible (SI, Figure S7).

The  $T_{CP}$  of the homopolymer poly(DEGMA), H6, is 25.9 °C at 5.0 mg mL<sup>-1</sup>, which correspond well with the literature value of 27 °C.<sup>19,20,27</sup> With increasing amount of DMAEMA, the observed demixing points increase and the highest  $T_{CP}$  is observed for the homopolymer of poly(DMAEMA), H4, namely 46.7 °C at 5.0 mg mL<sup>-1</sup> (see also Figure 1). This observed effect is due to the increased hydrophilicity of the “end-group” by the incorporation of the PDMAEMA block. In some cases, namely for B3 and B4, the solutions showed only weak transitions, presumably due to the formation of mainly smaller aggregates. All  $T_{CP}$  transitions from the turbidimetry measurement of the block copolymers are plotted in Figure 1 against the molar ratio of PDMAEMA to provide a better

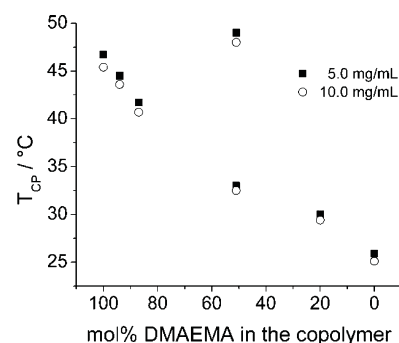
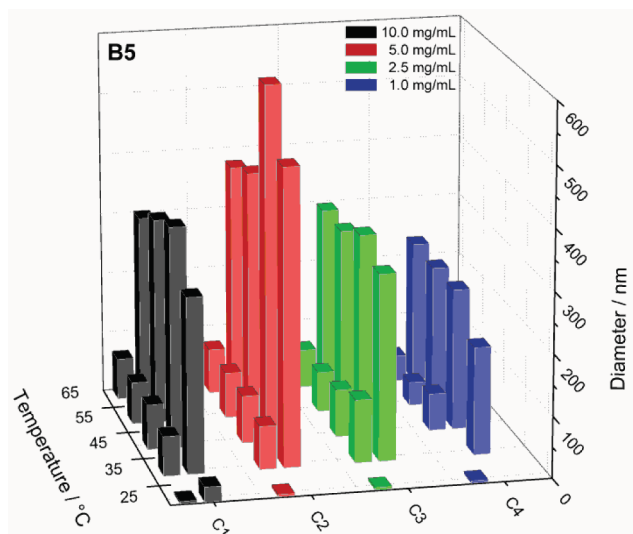


Figure 1. Cloud points ( $T_{CP}$ ) of the studied block copolymers of poly(DMAEMA-*b*-DEGMA) at 5.0 and 10.0 mg mL<sup>-1</sup>.

overview. A roughly linear behavior of the  $T_{CP}$  transitions with increasing amount of mol% DMAEMA in the block copolymers could be observed. Differences between the pure and the quasi diblock copolymer were not observed in the turbidimetry measurements; apparently the gradient is too small to have an influence. For all samples, a lower  $T_{CP}$  is observed with higher concentration due to the statistical influence during the aggregation behavior. Two  $T_{CP}$  values were observed for B5 (see Table 4 and Figure 1), indicating the double thermo-responsive behavior in aqueous solution. The turbidimetry curve of this copolymer shows a weak transition at 33 °C followed by a rearrangement and, therefore, a second transition at 49 °C (see also Figure S8 SI).

Due to its double-responsive behavior, the B5 block copolymer was selected for detailed structural analysis, as it shows the most interesting thermoresponsive behavior of the tested copolymers.

The LCST transition was further investigated in detail by DLS measurements as function of temperature for B5. To efficiently characterize different concentrations of this block copolymer, a high-throughput DLS plate reader setup was used. The demixing values were estimated by this DLS setup in deionized water at four different concentrations (1.0, 2.5, 5.0, and 10.0 mg mL<sup>-1</sup>) starting from 25 °C and heating up to 65 °C in 10 °C steps. The temperature induced collapse of the quasi diblock copolymer B5 (~50% of each block segment) resulted in the appearance of two size distributions (Figure 2), one with a diameter of 40 nm and a second of around 300 nm. The size of the agglomerates of B5 is nearly constant also by further increasing the temperature. In addition, the polymer concentration has no significant influence on the size of the self-assembled structures of the block copolymer. The self-assembled structures might be micelles (ca. 40 nm) and larger vesicular structures (300–400 nm), although no conclusive assignment can be made based on the DLS results alone. To



**Figure 2.** Hydrodynamic diameters of the copolymer coils and globules of **B5** (showing two distribution) at different concentration as function of temperature.

evaluate the aggregation behavior of the chosen copolymer, **B5** was investigated in further detail using a DLS Zetasizer (Malvern).

The experiment was performed in deionized water at a concentration of  $1.0 \text{ mg mL}^{-1}$ , and the temperature run was set up between 25 and 50 °C, with heating in 1 °C steps to have a closer look at the phase transitions. A repeated temperature run ranging from 25 to 65 °C is plotted in the SI (Figure S10), showing a similar size distribution of the observed self-assembled aggregates. No changes in the size above 50 °C are observed. The distribution of the block copolymer assemblies at temperatures below and above the phase

transition is illustrated in Figure 3 (volume distribution; intensity distribution is plotted in the SI, Figure S10). Below the cloud point at 25 °C, the polymer chains are fully soluble and, therefore, a hydrodynamic diameter smaller than 10 nm was obtained, corresponding most probably to individual hydrated polymer chains, taking into account also the molecular dimensions of the block copolymers. An increase in temperature results in an increase in the diameter of the polymer aggregates to  $\sim 100 \text{ nm}$ , indicating the temperature-induced aggregation of the polymer chains. The first transition of the polymer solution is observed at a temperature of 31 °C, i.e., when the collapse of the PDEGMA takes place.

The hydrodynamic diameter of these aggregates is around 100 nm as displayed in Figure 3. By further increasing the temperature, a rearrangement is observed, which is reflected in the appearance of a second distribution. Above 36 °C, two distributions are formed with a hydrodynamic diameter of 65 and 240 nm, respectively. The formed structures appear to be thermodynamically stable in solution, as the aggregate size remains constant even at further increased temperatures.

The temperature induced phase transition of the selected block copolymer **B5** was further investigated by temperature dependent  $^1\text{H}$  NMR spectroscopy to obtain a deeper insight into the aggregation behavior. The phase transition was investigated in  $\text{D}_2\text{O}$  at a concentration of  $5.0 \text{ mg mL}^{-1}$ . At each temperature step (5 °C), the polymer solution was equilibrated for 3 min (it should be noted here that the time scale of the temperature induced formation of micellar structures and larger aggregates is faster than the typical acquisition times required by the NMR spectrometer). The  $^1\text{H}$  NMR spectrum of the block copolymer at 25 °C shows the characteristic signals of poly(DMAEMA-*b*-DEGMA); the corresponding temperature series is plotted in Figure 4. In the  $^1\text{H}$  NMR spectra, the signals at 3.3–3.9 ppm represent the ethylene glycol and  $-\text{OCH}_3$  groups (EG) of poly(DEGMA)

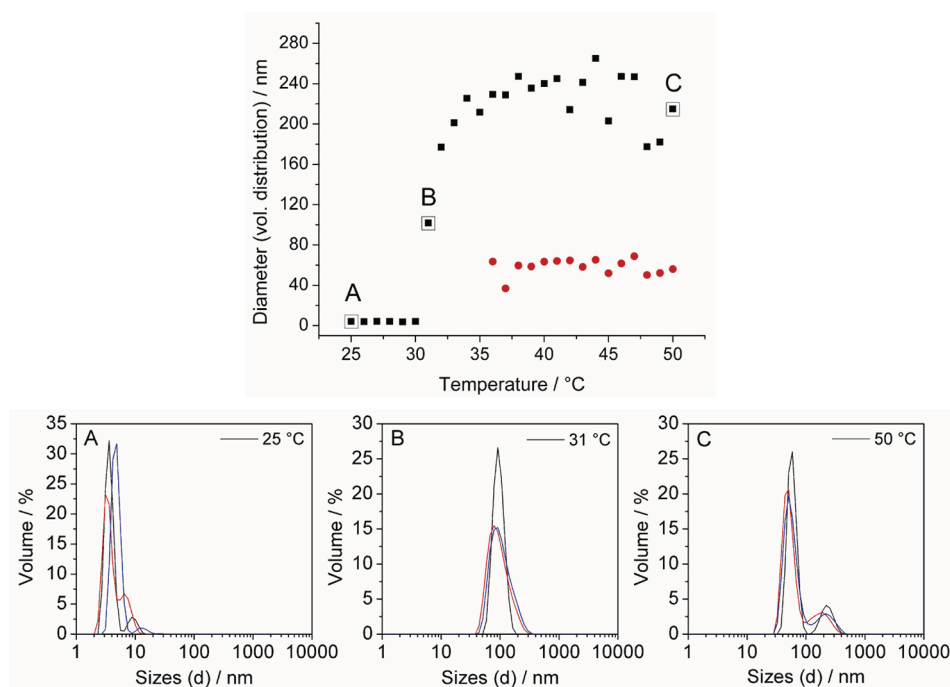


**Figure 3.** The hydrodynamic diameter (volume distribution, average value of three estimations) of the block copolymer chains and globules of **B5** at  $1.0 \text{ mg mL}^{-1}$  is plotted as a function of temperature. (A–C) Hydrodynamic size distribution (three measurements) at the respective temperature.

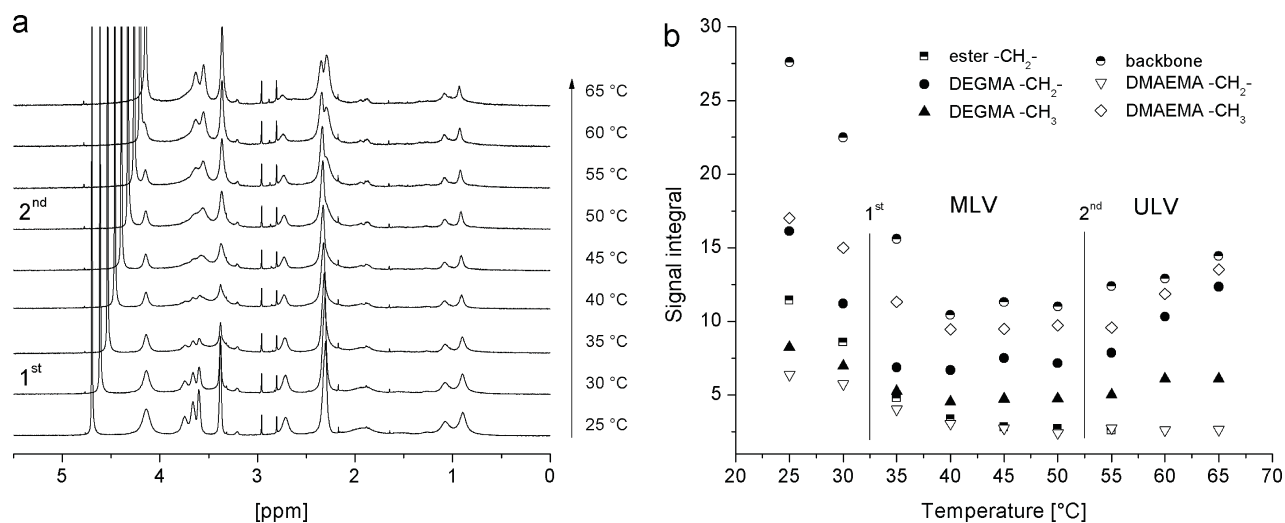


**Figure 4.** Temperature dependent <sup>1</sup>H NMR spectra (a) in D<sub>2</sub>O of B5 (5 mg mL<sup>-1</sup>) showing the evolution of the -CH<sub>2</sub>- and CH<sub>3</sub>- signals of poly(DEGMA) block at 3.3 ppm and 3.5–3.9 ppm, and the -CH<sub>2</sub>- and CH<sub>3</sub>-resonance of the poly(DMAEMA) block segment at 2.7 and 2.3 ppm as well as the polymer backbone in a temperature range from 25 to 65 °C. On the right side (b), the integrals of the block copolymer signals are plotted against the temperature (MLV = multilamellar vesicles and ULV = unilamellar vesicles, see also Figures 5 and 6).

and the signals at 2.3 ppm (CH<sub>3</sub>-N-) represent the poly(DMAEMA) block. The position of the small DMF signals, which are left after the precipitation and drying processes, were used as reference signal (adjustment of changes due to the temperature increase, whereby the DMF is unaffected) and all spectra were normalized in intensity to the D<sub>2</sub>O signal. It is observable (Figure 4) that the DEGMA signals at 3.5–3.9 ppm decrease significantly, denoting the collapse of the DEGMA block which is induced by the temperature increase from 25 to 40 °C. Also, all other signals (backbone at 0.8–1.5 ppm and DMAEMA at 2.3 and 2.8 ppm) decrease by increasing temperature, leading to broad signals due to the reduced flexibility of the polymer chains (see Figure 4). The PDMAEMA block is still visible at 45 °C (CH<sub>3</sub>-N- at 2.2 ppm) as it is supposed that it forms a kind of corona around the hydrophobic PDEGMA aggregates.

Unexpectedly, further increasing the temperature from 50 to 65 °C is accompanied by an increase for some signals corresponding to DMAEMA and to DEGMA (Figure 4b), respectively. These signals are visible for the DMAEMA group (CH<sub>3</sub>-N-) at 2.2 ppm, for the EG groups of DEGMA at 3.6 and 3.7 ppm as well as for the -OCH<sub>3</sub> group at 3.3 ppm. The shifted signals indicate a different microenvironment of (at least parts of) the DMAEMA and DEGMA groups and are supposed to correlate to the corresponding rearrangement of the block copolymer. This second assembly might be induced by the collapse of the DMAEMA block (at 49 °C vs the homopolymer of poly(DMAEMA) at 47 °C as listed in Table 4 for a concentration of 5.0 mg mL<sup>-1</sup>), which appears to be at these temperatures more hydrophobic than in the previous configuration (hydrophilic corona), thus resulting in a structural change. The transformation of the PDMAEMA block is indicated by the high-field shift of the DMAEMA signal, which provides a higher electron density at the methyl groups (CH<sub>3</sub>-N-) caused by the breaking of the H-bonds.

There might also be a migration of the more polar DEGMA groups (higher amount of oxygen atoms in the structure) to the surface of the collapsed structures to stabilize them in aqueous solution. This migration could lead then to a partial hydration of the DEGMA chains, which causes the reappearance of the

corresponding signals in the NMR spectra (Figure 4a at 3.6–3.7 ppm).

**Self-Assembly of Poly(DMAEMA-*b*-DEGMA).** The double responsive behavior of poly(DMAEMA-*b*-DEGMA) motivated the utilization of cryo-TEM to visualize the associated structures. The sample preparation was performed at different temperatures, and the samples were instantaneously vitrified after an equilibration time of ~2 min to preserve the aggregate structure at the blotting temperature. The cryo-TEM images of solutions which were vitrified at a blotting temperature of approximately 33 °C are depicted in Figure 5.

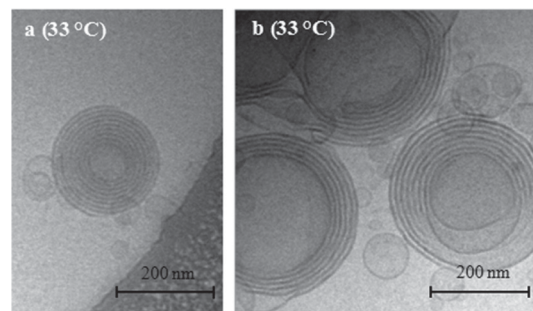


**Figure 5.** Cryo-TEM images (a,b) of B5 block copolymer solution at ~33 °C in H<sub>2</sub>O (preheated, 5.0 mg mL<sup>-1</sup>) showing the formation of multilamellar vesicles and additionally unilamellar vesicles.

At this temperature, which is above the *T*<sub>CP</sub> of PDEGMA and below the *T*<sub>CP</sub> of PDMAEMA, the presence of large multilamellar vesicles (MLV) with a diameter of approximately 200 nm and unilamellar vesicles (ULV), which are observed to be significantly smaller (40 to 90 nm), is observed. The cryo-TEM micrograph shows that the MLVs have a layered structure with comparable distance between the individual lamellae and represent an onion-like form. In this case, a molecular arrangement of the copolymer can be assumed that resembles the structure depicted in Figure 5 (PDEGMA dark; PDMAEMA light).

The formation of MLV is based on one hand on the hydrophilic–hydrophobic character of the block copolymers

and on the other hand on the volume fractions of the individual blocks, respectively. The self-assembly of amphiphiles into well-defined structures, such as vesicles, derives from the hydrophobic attraction at the hydrocarbon–water interface, which induces the molecules to associate, and the hydrophilic part that remain in contact with water.<sup>60</sup> For thermosensitive block copolymers, the individual blocks shows a selective, thermally driven solubility and, therefore, the overall hydrophilic–hydrophobic character can be changed by temperature. At 33 °C, the PDEGMA block is collapsed and therefore hydrophobic, while the PDMAEMA block is hydrophilic and is still in solution due to the fact that the blotting temperature remains below the  $T_{CP}$  of PDMAEMA.

The formation of micelles or vesicle structures depends for block copolymers on their ratio between both hydrophobic and hydrophilic segments.<sup>6,7,45,60</sup> Classically, the “critical packing parameter” is used to define the morphology of the resultant self-assembled structure. The ratio of DMAEMA to DEGMA in the block copolymer **B5** is 51% to 49%. With this composition, the formation of micelles or vesicles can be expected.<sup>6,45</sup> In the present case, the block copolymers revealed a tendency for the formation of multilamellar vesicles. The number of shells in these MLVs is up to nine layers for the block copolymer with a significant size distribution of the formed MLVs. The measured size of the different vesicles is between 225 nm (Figure 5a) and 325 nm (Figure 5b), which is in the same size range as obtained by the DLS measurements (approximately 220 nm). The shell thickness of the MLV of PDMAEMA block (Figure 5a) is approximately 5–8 nm. This value is significantly smaller and can be correlated to the polymer chain length (DMAEMA block has DP of ~45, which equals the length of 11.5 nm when completely stretched) to an interdigitated, very compact arrangement of the PDMAEMA chains.<sup>60</sup> This observation is also supported by the NMR investigations, which show reduced signals of the PDMAEMA block at this temperature. The precipitated PDEGMA core is approximately 6 nm in thickness, which suggests very densely packed chains, which is also supported by the strong dark contrast which is found in the cryo-TEM images.

The polymer was subsequently heated to a temperature above the  $T_{CP}$  of DMEAEEMA, and the resulting structures were investigated by means of cryo-TEM in the same fashion as described above. In contrast to the sample which was investigated at 33 °C, the formation of preferentially unilamellar, large vesicles is observed. MLVs with a large number of shells are not observed anymore. In Figure 6, the cryo-TEM images of **B5** block copolymer solution acquired at ~50 °C (a,b) showed the formation of large unilamellar vesicles in aqueous solution.

The thermoresponsive behavior of the selected block copolymer **B5** was further investigated by temperature variable zeta potential (also known as electrokinetic potential) measurements to gain a deeper insight in the polyelectrolyte nature of the block copolymer during the polymer phase transitions (Figure 7). The phase transition was investigated in water at a concentration of 2.5 mg mL<sup>-1</sup> in the temperature range from 25 to 65 °C during both heating and cooling with temperature steps of 5 °C. The conductivity (red cycles, Figure 7) of the copolymer solution was also measured, indicating a small increase of charge carrier mobility or concentration with increasing temperature, i.e., caused by the increased autodissociation of water. After the cooling cycle, the conductivity of the solution reaches nearly the starting value at 25 °C. The zeta

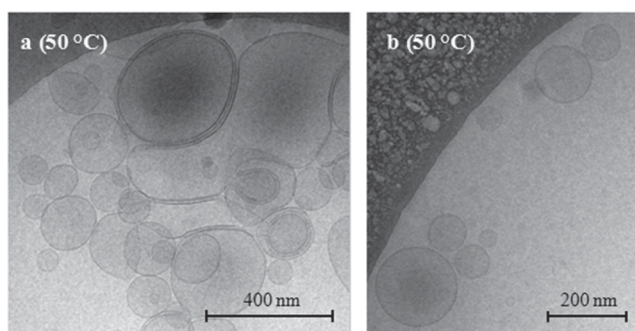


**Figure 6.** Cryo-TEM image (a,b) of **B5** block copolymer solution at ~50 °C in H<sub>2</sub>O (preheated, 5.0 mg mL<sup>-1</sup>) showing the formation of large unilamellar vesicles.

potential measurements show that two reversible thermo-induced transitions are present without showing any hysteresis behavior in the graph (Figure 7, black squares). The first transition takes place at around 30 °C and the second transition around 55–60 °C, whereby a strong decrease in the zeta potential is observed. Over the measured temperature range from 25 to 65 °C, a positive potential was measured due to the cationically charged protonated DMAEMA groups. The high value of the zeta potential indicates stable aggregates (usually a potential >25 mV indicates a stable system), which cannot further assemble together due to repulsion forces. In contrast, the pure PDEGMA homopolymer **H6** revealed a negative potential (partially negative charges due to oxygen atoms and carboxylic acid end groups) over the complete temperature range (see SI, Figure S11). On the basis of these results, it can be assumed that the collapse of the PDEGMA block at 30 °C is associated with an enhancement of the negative charges on the surface of the collapsed aggregates (SI, Figure S11), which support the formation of MLVs. The assembly is promoted by electrostatic interactions between the positive charged PDMAEMA block (corona) and the negatively charged collapsed PDEGMA block. This layer-by-layer assembly above the first transition temperature lowers the overall zeta potential of the aggregates. The charge compensation by the layer-by-layer assembly in MLV structures represents an important thermodynamic contribution to the stability of the self-assembled structures. If the temperature is raised above 50 °C, the DMAEMA block starts to collapse. During this collapse, a migration of the DMAEMA chains to the hydrophobic surface of the PDEGMA layer might occur as observed by <sup>1</sup>H NMR. This effect changes the electrostatic balance of the MLV structures, i.e., the charge compensation, and ultimately leads to the preferential formation of ULV structures. This change of the charge balance is reflected in the corresponding zeta potential values (Figure 7).

On the basis of these experimental observations, a model for the aggregation of the double responsive transition of the block copolymer structures at different temperatures was developed, which is schematically illustrated in Figure 8. In this configuration, the PDEGMA block (negatively charged) becomes insoluble at the first LCST transition temperature and is collapsed in the lamellar structure. The still-soluble PDMAEMA block (positively charged) stabilizes the individual shells by a layer-by-layer assembly and promotes the preferential formation of multilamellar onion-like vesicles. With further increasing temperature also the solubility of the PDMAEMA decreases. As a result, the volume of the

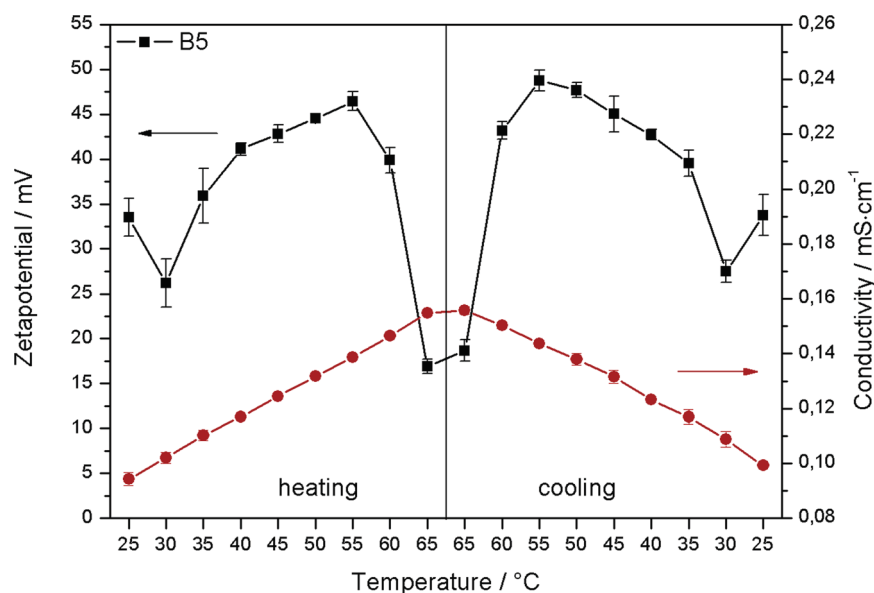


**Figure 7.** Temperature variable zeta potential measurements (black squares, average value of five estimations) of block copolymer **B5** solution at 2.5 mg mL<sup>-1</sup> showing two reversible temperature-induced transitions. Also the conductivity (red cycles) of the copolymer solution was measured.

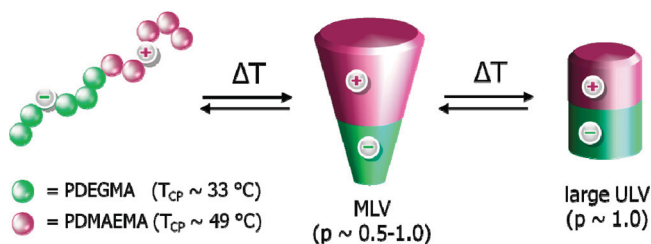


**Figure 8.** Proposed model for the aggregation of the double responsive transition of the block copolymer. In the figure, represent red cycles DEGMA and green cycles DMAEMA units.

hydrophobic part of the copolymer increases and the interbilayer energy changes. Simultaneously, the decreasing size of the hydrophilic corona block is seen as an additional driving force for the modified aggregation behavior due to altered volume fraction and space requirements.

This effect was, e.g., observed for PS-*b*-PAA aggregates,<sup>61</sup> where shorter corona fractions generally resulted in the formation of larger structures.<sup>62</sup> Additionally, the altered charge balance within the structures favors the formation of larger and unilamellar vesicles.

This structural transitions explain also the <sup>1</sup>H NMR observations showing that after the first transition the respective poly(DEGMA) signals disappeared. This could be a direct consequence of the narrow environment, which is formed in the multilamellar vesicle system. As observed from the cryo-TEM images, it can be assumed that above 50 °C a structural transition toward unilamellar vesicles takes place. In this configuration, the packing density of the macromolecules becomes less pronounced, which could be a possible explanation of the reappearance of the poly(DMAEMA) signal in the <sup>1</sup>H NMR spectrum.

## CONCLUSION

The RAFT polymerization method was used for the preparation of a library of double thermoresponsive diblock copolymers, namely poly(DMAEMA-*b*-DEGMA). A series of poly(DMAEMA-*b*-DEGMA) copolymers have been prepared,

with compositions ranging from PDMAEMA to PDEGMA in steps of 20 mol%. The phase transitions of these block copolymers in aqueous solutions were studied in detail by turbidimetry. Higher cloud points of the poly(DMAEMA-*b*-DEGMA) with increasing amount of mol% DMAEMA in the block copolymer were observed. Within this series of block copolymers, a block ratio of 50:50 resulted in a double-responsive LCST behavior. This block copolymer was further investigated to elucidate the self-assembly behavior in detail. Variable temperature <sup>1</sup>H NMR spectroscopy, zeta potential, and cryo-TEM investigations revealed the temperature induced formation of multilamellar vesicular structures at elevated temperature which convert into unilamellar vesicles at higher temperatures. On the basis of the measurements, an illustrative model for the reversible temperature-induced self-assembly is given based on the initial formation of multilamellar vesicular (MLV) aggregates that further assemble into unilamellar vesicle (ULV) structures. This transition could be assigned to the changes of the volume ratios as well as to the ionic interplay between the block copolymers at different temperatures. In particular, the ionic contributions of the negatively charged PDEGMA block and the positively charged PDMAEMA block are supposed to support the layer-by-layer assembly at 33 °C, which favors the formation of multilamellar vesicles (MLV). Further increase of the temperature changes again the volume ratio between the blocks as the solubility of the second block occurs, furthermore the second LCST transition is associated with a changed electrostatic balance between the blocks. This results in the preferential transition of MLVs to ULVs. The present study assumes a facile interplay of the volume ratio and the changes of the ionic interactions. However, both contributions cannot be separated by the investigation of only one polymer. In further studies, the formation of self-assembled structures of different block copolymers and at different pH values will be investigated to gain a deeper understanding of the aggregation process.

The design and self-assembly of such thermoresponsive migrating block copolymers will provide new possibilities for delivery vehicles (for therapies), e.g., temperature-controlled

release of drugs, and will provide important deeper insights into the LCST transition and the formation of MLVs.

## ■ ASSOCIATED CONTENT

### Supporting Information

SEC curves of poly(DMAEMA-*b*-DEGMA), turbidity curves and zeta potential measurements. This material is available free of charge via the Internet at <http://pubs.acs.org>.

## ■ AUTHOR INFORMATION

### Corresponding Author

\*E-mail: [ulrich.schubert@uni-jena.de](mailto:ulrich.schubert@uni-jena.de).

### Notes

The authors declare no competing financial interest.

## ■ ACKNOWLEDGMENTS

We thank W. Günther and G. Sentis for the temperature dependent NMR measurements. Financial support of the Dutch Polymer Institute (DPI, technology area HTE) and the Carl-Zeiss-Foundation (Strukturantrag JCSM) is gratefully acknowledged. C.P. acknowledges also financial support by CSIRO.

## ■ REFERENCES

- (1) Schild, H. G. *Prog. Polym. Sci.* **1992**, *17* (2), 163–249.
- (2) Gil, E. S.; Hudson, S. M. *Prog. Polym. Sci.* **2004**, *29* (12), 1173–1222.
- (3) Schmaljohann, D. *Adv. Drug Delivery Rev.* **2006**, *58* (15), 1655–1670.
- (4) Dimitrov, I.; Trzebicka, B.; Müller, A. H. E.; Dworak, A.; Tsvetanov, C. B. *Prog. Polym. Sci.* **2007**, *32* (11), 1275–1343.
- (5) Weber, C.; Hoogenboom, R.; Schubert, U. S. *Prog. Polym. Sci.* **2012**, *37* (5), 686–714.
- (6) Du, J.; O'Reilly, R. K. *Soft Matter* **2009**, *5* (19), 3544–3561.
- (7) Li, M.-H.; Keller, P. *Soft Matter* **2009**, *5* (5), 927–937.
- (8) Hu, J.; Liu, S. *Macromolecules* **2010**, *43* (20), 8315–8330.
- (9) Pietsch, C.; Schubert, U. S.; Hoogenboom, R. *Chem. Commun.* **2011**, *47* (31), 8750–8765.
- (10) Pietsch, C.; Hoogenboom, R.; Schubert, U. S. *Angew. Chem., Int. Ed.* **2009**, *48* (31), 5653–5656.
- (11) Qin, S.; Geng, Y.; Discher, D. E.; Yang, S. *Adv. Mater.* **2006**, *18* (21), 2905–2909.
- (12) Li, Y.; Lokitz, B. S.; McCormick, C. L. *Angew. Chem., Int. Ed.* **2006**, *45* (35), 5792–5795.
- (13) Hoogenboom, R.; Rogers, S.; Can, A.; Becer, C. R.; Guerrero-Sanchez, C.; Wouters, D.; Hoepfener, S.; Schubert, U. S. *Chem. Commun.* **2009**, *37*, 5582–5584.
- (14) Discher, B. M.; Won, Y.-Y.; Ege, D. S.; Lee, J. C.-M.; Bates, F. S.; Discher, D. E.; Hammer, D. A. *Science* **1999**, *284* (5417), 1143–1146.
- (15) Discher, D. E.; Eisenberg, A. *Science* **2002**, *297* (5583), 967–973.
- (16) Antonietti, M.; Förster, S. *Adv. Mater.* **2003**, *15* (16), 1323–1333.
- (17) Coelho, J.; Ferreira, P.; Alves, P.; Cordeiro, R.; Fonseca, A.; Góis, J.; Gil, M. *EPMA J.* **2010**, *1* (1), 164–209.
- (18) Onaca, O.; Enea, R.; Hughes, D. W.; Meier, W. *Macromol. Biosci.* **2009**, *9* (2), 129–139.
- (19) Han, S.; Hagiwara, M.; Ishizone, T. *Macromolecules* **2003**, *36* (22), 8312–8319.
- (20) Lutz, J.-F.; Hoth, A. *Macromolecules* **2005**, *39* (2), 893–896.
- (21) Lutz, J.-F. *J. Polym. Sci., Part A: Polym. Chem.* **2008**, *46* (11), 3459–3470.
- (22) Moad, G.; Rizzardo, E.; Thang, S. H. *Aust. J. Chem.* **2009**, *62* (11), 1402–1472.
- (23) Keddie, D. J.; Moad, G.; Rizzardo, E.; Thang, S. H. *Macromolecules* **2012**, *45* (13), 5321–5342.
- (24) Pietsch, C.; Fijten, M. W. M.; Lambermont-Thijs, H. M. L.; Hoogenboom, R.; Schubert, U. S. *J. Polym. Sci., Part A: Polym. Chem.* **2009**, *47* (11), 2811–2820.
- (25) Lutz, J.-F.; Akdemir, Ö.; Hoth, A. *J. Am. Chem. Soc.* **2006**, *128* (40), 13046–13047.
- (26) Becer, C. R.; Hahn, S.; Fijten, M. W. M.; Thijs, H. M. L.; Hoogenboom, R.; Schubert, U. S. *J. Polym. Sci., Part A: Polym. Chem.* **2008**, *46* (21), 7138–7147.
- (27) Ishizone, T.; Seki, A.; Hagiwara, M.; Han, S.; Yokoyama, H.; Oyane, A.; Deffieux, A.; Carlotti, S. *Macromolecules* **2008**, *41* (8), 2963–2967.
- (28) Fournier, D.; Hoogenboom, R.; Thijs, H. M. L.; Paulus, R. M.; Schubert, U. S. *Macromolecules* **2007**, *40* (4), 915–920.
- (29) Üzgiin, S.; Akdemir, Ö.; Hasenpusch, G.; Maucksch, C.; Golas, M. M.; Sander, B.; Stark, H.; Imker, R.; Lutz, J.-F.; Rudolph, C. *Biomacromolecules* **2009**, *11* (1), 39–50.
- (30) Cai, J.; Yue, Y.; Rui, D.; Zhang, Y.; Liu, S.; Wu, C. *Macromolecules* **2011**, *44* (7), 2050–2057.
- (31) Hinton, T. M.; Guerrero-Sanchez, C.; Graham, J. E.; Le, T.; Muir, B. W.; Shi, S.; Tizard, M. L. V.; Gunatillake, P. A.; McLean, K. M.; Thang, S. H. *Biomaterials* **2012**, *33* (30), 7631–7642.
- (32) Cho, S. H.; Jhon, M. S.; Yuk, S. H.; Lee, H. B. *J. Polym. Sci., Part B: Polym. Phys.* **1997**, *35* (4), 595–598.
- (33) Büttin, V.; Armes, S. P.; Billingham, N. C. *Polymer* **2001**, *42* (14), 5993–6008.
- (34) Liu, Q.; Yu, Z.; Ni, P. *Colloid Polym. Sci.* **2004**, *282* (4), 387–393.
- (35) Plamper, F. A.; Ruppel, M.; Schmalz, A.; Borisov, O.; Ballauff, M.; Müller, A. H. E. *Macromolecules* **2007**, *40* (23), 8361–8366.
- (36) Plamper, F. A.; Schmalz, A.; Müller, A. H. E. *J. Am. Chem. Soc.* **2007**, *129* (47), 14538–14539.
- (37) Paris, R.; Quijada-Garrido, I. *Eur. Polym. J.* **2010**, *46* (11), 2156–2163.
- (38) Yamamoto, S.-i.; Pietrasik, J.; Matyjaszewski, K. *Macromolecules* **2008**, *41* (19), 7013–7020.
- (39) van de Wetering, P.; Zuidam, N. J.; van Steenberg, M. J.; van der Houwen, O. A. G. J.; Underberg, W. J. M.; Hennink, W. E. *Macromolecules* **1998**, *31* (23), 8063–8068.
- (40) Schilli, C. M.; Zhang, M.; Rizzardo, E.; Thang, S. H.; Chong, Y. K.; Edwards, K.; Karlsson, G.; Müller, A. H. E. *Macromolecules* **2004**, *37* (21), 7861–7866.
- (41) Baines, F. L.; Billingham, N. C.; Armes, S. P. *Macromolecules* **1996**, *29* (10), 3416–3420.
- (42) Kostianen, M. A.; Pietsch, C.; Hoogenboom, R.; Nolte, R. J. M.; Cornelissen, J. J. L. M. *Adv. Funct. Mater.* **2011**, *21* (11), 2012–2019.
- (43) Arotçaréna, M.; Heise, B.; Ishaya, S.; Laschewsky, A. *J. Am. Chem. Soc.* **2002**, *124* (14), 3787–3793.
- (44) Kotsuchibashi, Y.; Ebara, M.; Yamamoto, K.; Aoyagi, T. *Polym. Chem.* **2011**, *2* (6), 1362–1367.
- (45) Blanazs, A.; Armes, S. P.; Ryan, A. J. *Macromol. Rapid Commun.* **2009**, *30* (4–5), 267–277.
- (46) Liu, S.; Armes, S. P. *J. Am. Chem. Soc.* **2001**, *123* (40), 9910–9911.
- (47) Xu, J.; Luo, S.; Shi, W.; Liu, S. *Langmuir* **2005**, *22* (3), 989–997.
- (48) Weiss, J.; Bottcher, C.; Laschewsky, A. *Soft Matter* **2011**, *7* (2), 483–492.
- (49) Hua, F.; Jiang, X.; Zhao, B. *Macromolecules* **2006**, *39* (10), 3476–3479.
- (50) Agut, W.; Brulet, A.; Schatz, C.; Taton, D.; Lecommandoux, S. *Langmuir* **2010**, *26* (13), 10546–10554.
- (51) Farnham, W. B., PCT Int. Appl. WO 2005113493, A1 20051201, 2005.
- (52) Keddie, D. J.; Guerrero-Sanchez, C.; Moad, G.; Rizzardo, E.; Thang, S. H. *Macromolecules* **2011**, *44* (17), 6738–6745.
- (53) Guerrero-Sanchez, C.; Keddie, D. J.; Saubern, S.; Chiefari, J. *ACS Comb. Sci.* **2012**, *14* (7), 389–394.
- (54) Keddie, D. J.; Guerrero-Sanchez, C.; Moad, G.; Mulder, R. J.; Rizzardo, E.; Thang, S. H. *Macromolecules* **2012**, *45* (10), 4205–4215.
- (55) Koppel, D. E. *J. Chem. Phys.* **1972**, *57* (11), 4814–4820.

- (56) Ohshima, H. *J. Colloid Interface Sci.* **1994**, *168* (1), 269–271.
- (57) Moad, G.; Chong, Y. K.; Postma, A.; Rizzardo, E.; Thang, S. H. *Polymer* **2005**, *46* (19), 8458–8468.
- (58) Sahnoun, M.; Charreyre, M.-T.; Veron, L.; Delair, T.; D'Agosto, F. *J. Polym. Sci., Part A: Polym. Chem.* **2005**, *43* (16), 3551–3565.
- (59) Guillaneuf, Y.; Castignolles, P. *J. Polym. Sci., Part A: Polym. Chem.* **2008**, *46* (3), 897–911.
- (60) Israelachvili, J. N., *Intermolecular and Surface Forces*. 3rd ed.; Elsevier, Academic Press: Amsterdam, 2011.
- (61) Zhang, L.; Eisenberg, A. *J. Am. Chem. Soc.* **1996**, *118* (13), 3168–3181.
- (62) Holder, S. J.; Sommerdijk, N. A. J. M.; Williams, S. J.; Nolte, R. J. M.; Hiorns, R. C.; Jones, R. G. *Chem. Commun.* **1998**, *14*, 1445–1446.

Supporting information for:

# Thermo-induced self-assembly of responsive poly(DMAEMA-*b*-DEGMA) block copolymers to multi lamellar vesicles

*Christian Pietsch,<sup>1,2,3</sup> Ulrich Mansfeld,<sup>1,2,3</sup> Carlos Guerrero-Sanchez,<sup>4</sup> Stephanie Hoepfener,<sup>1,2,3</sup> Antje Vollrath,<sup>1,2</sup> Michael Wagner,<sup>1,2</sup> Richard Hoogenboom,<sup>5</sup> Simon Saubern,<sup>4</sup> San H. Thang,<sup>4</sup> C. Remzi Becer,<sup>6</sup> John Chieffari<sup>4</sup> and Ulrich S. Schubert<sup>1,2,3\*</sup>*

<sup>1</sup> Laboratory of Organic and Macromolecular Chemistry (IOMC) Friedrich-Schiller-University Jena,  
Humboldtstr. 10, 07743 Jena, Germany.

<sup>2</sup> Jena Center for Soft Matter (JCSM), Humboldtstr. 10, 07743 Jena, Germany

<sup>3</sup> Dutch Polymer Institute (DPI), John F. Kennedylaan 2, 5612 AB Eindhoven, The Netherlands.

<sup>4</sup> CSIRO, Materials Science and Engineering, Bag 10, Clayton South, 3169 Victoria, Australia.

<sup>5</sup> Supramolecular Chemistry Group, Department of Organic Chemistry, Ghent University,  
Krijgslaan 281 S4, 9000 Ghent, Belgium.

<sup>6</sup> Department of Chemistry, University of Warwick, CV4 7AL, Coventry, United Kingdom.

E-mail corresponding author: [ulrich.schubert@uni-jena.de](mailto:ulrich.schubert@uni-jena.de)



## SEC curves of poly(DMAEMA-*b*-DEGMA)

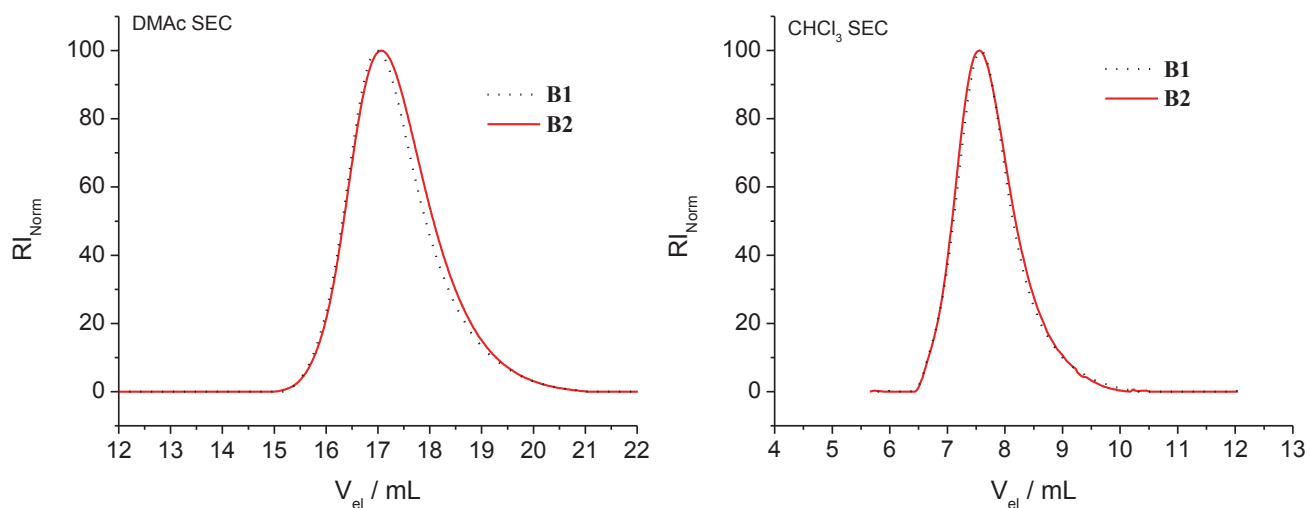


Figure S1. SEC traces (left in DMAc and right in CHCl<sub>3</sub>) of the blockcopolymers **B1** and **B2**.

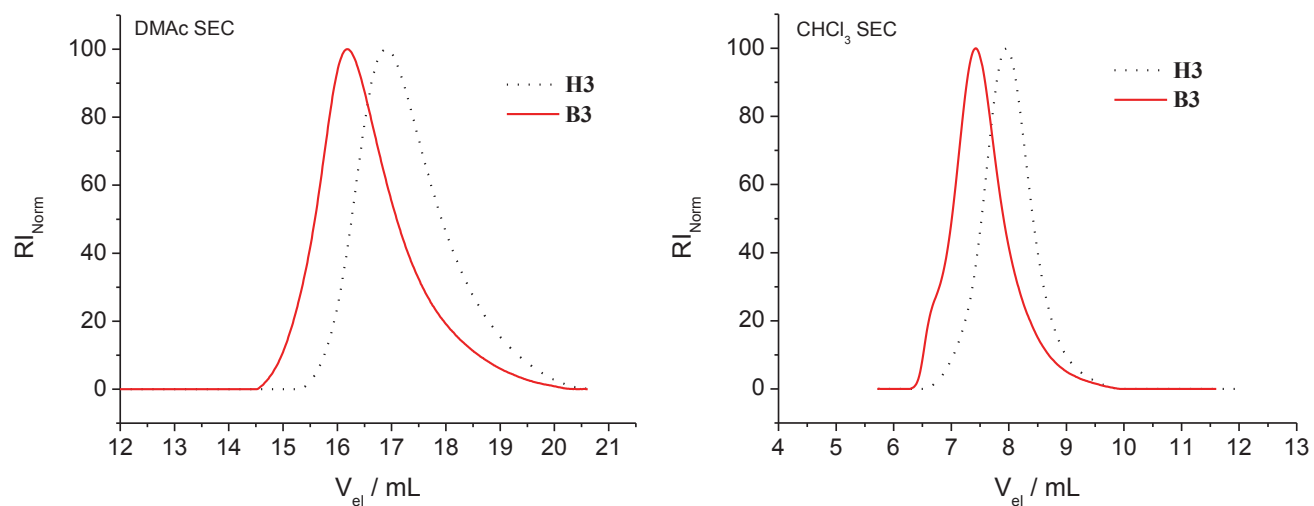


Figure S2. SEC traces (left in DMAc and right in CHCl<sub>3</sub>) of the copolymers **H3** and **B3** (**B3** reaches the exclusion limit of the CHCl<sub>3</sub> SEC).

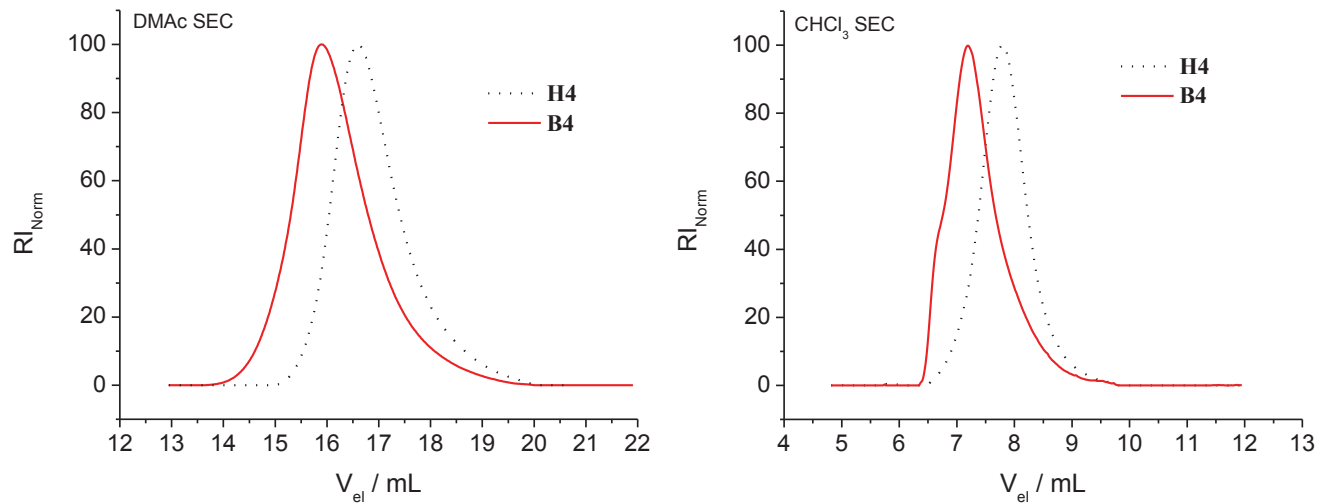


Figure S3. SEC traces (left in DMAc and right in CHCl<sub>3</sub>) of the copolymers **H4** and **B4** (**B4** reaches the exclusion limit of the CHCl<sub>3</sub> SEC).

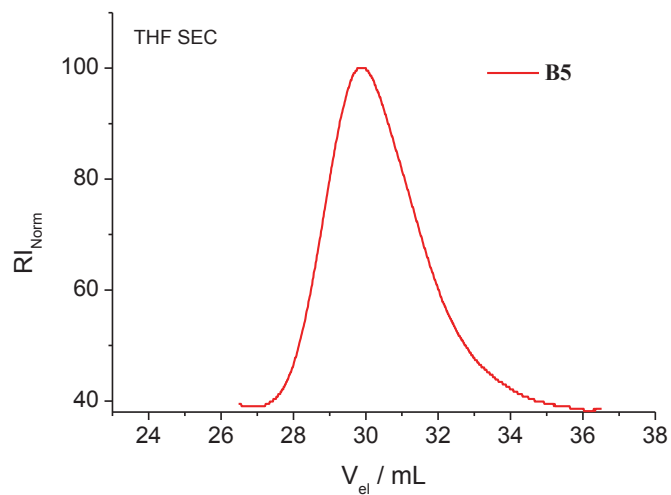


Figure S4. THF SEC traces of block copolymer **B5**.

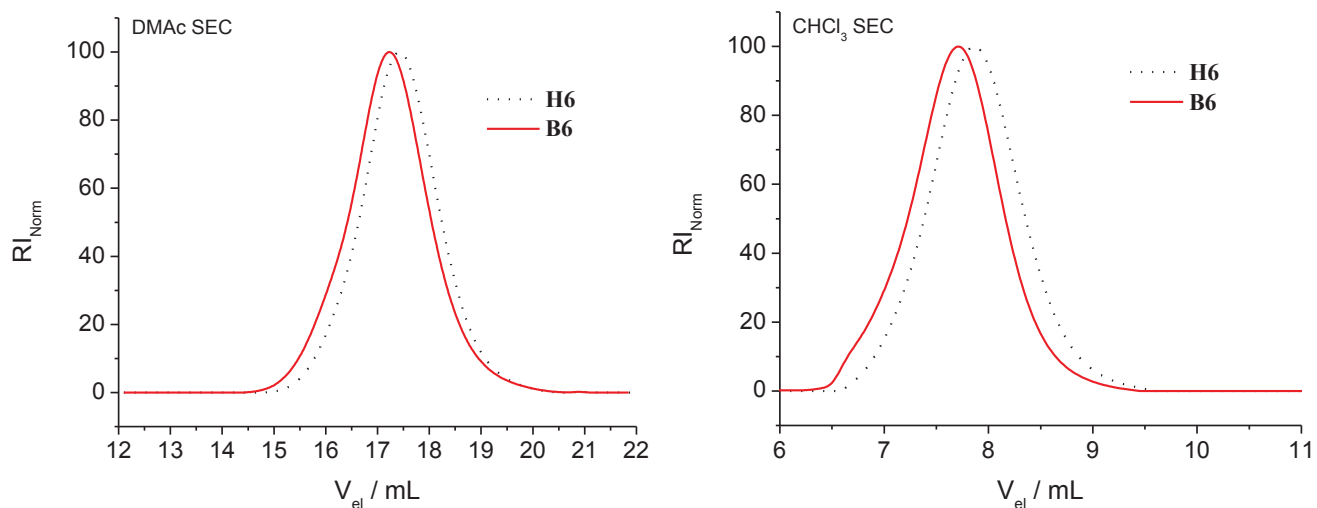


Figure S5. SEC traces (left in DMAc and right in  $CHCl_3$ ) of the copolymers **H6** and **B6**.

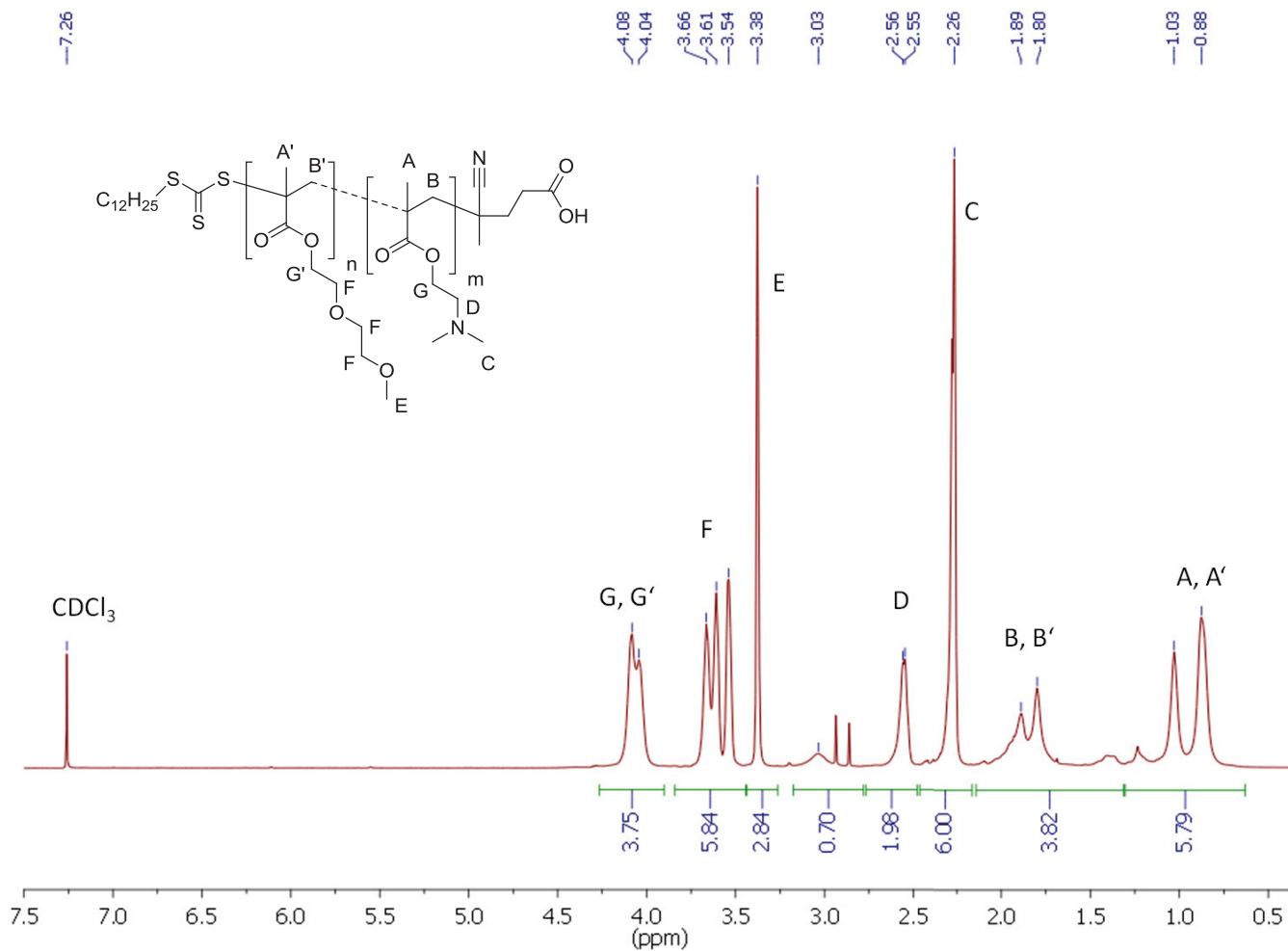


Figure S6.  $^1H$  NMR spectra (400 MHz,  $CDCl_3$ ) of poly(DMAEMA-*b*-DEGMA) **H5** with the corresponding schematic representation of the polymer structure.

## Turbidity curves

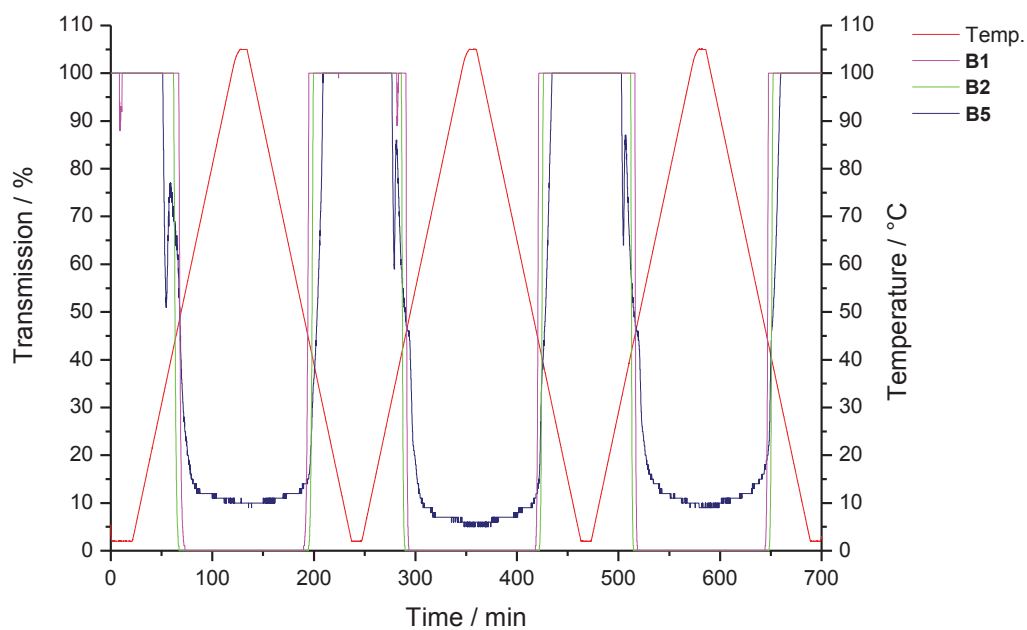


Figure S7. Cloud point measurements ( $5.0 \text{ mg mL}^{-1}$ ) for the identification of the LCST behavior of the copolymer **B1**, **B2** and **B5**.

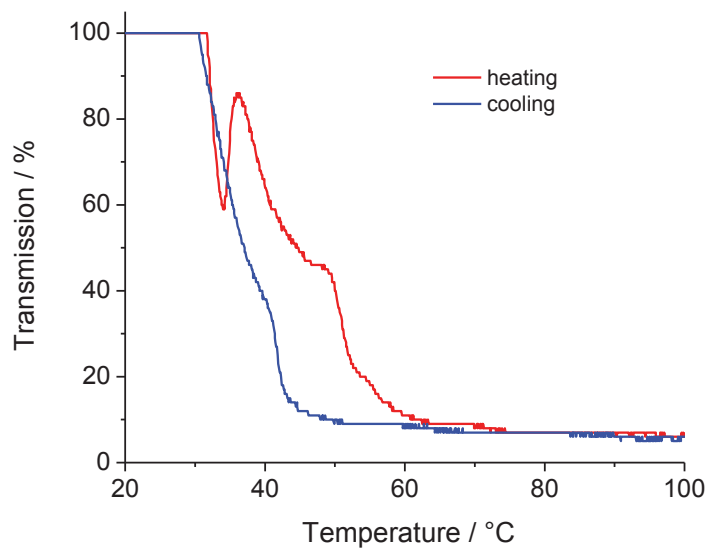


Figure S8. Turbidity measurements of block copolymer **B5** showing two cloud points.

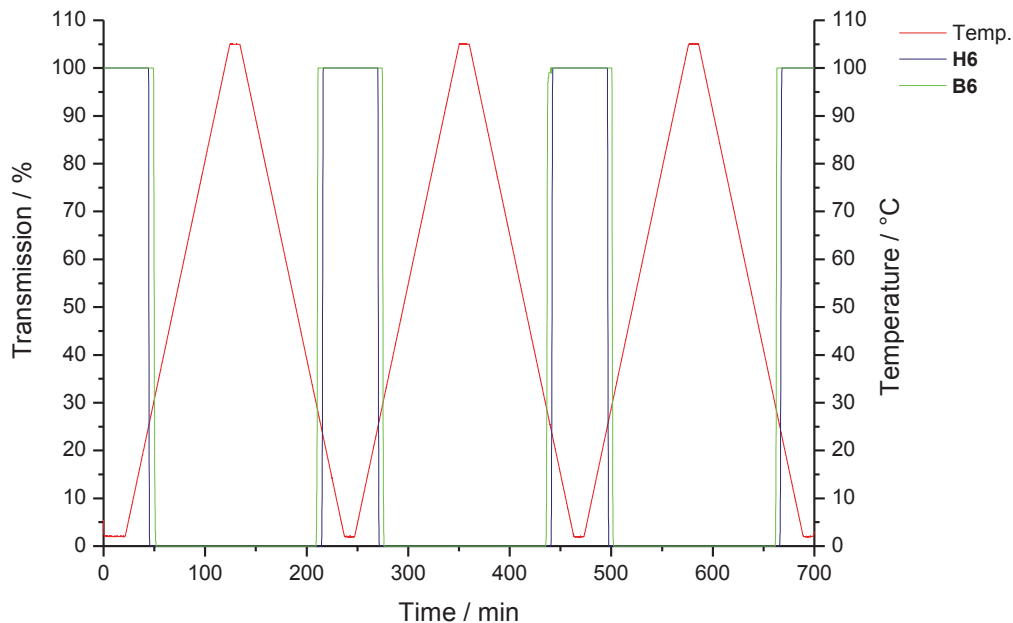


Figure S9. Cloud point measurements ( $5.0 \text{ mg mL}^{-1}$ ) for the identification of the LCST behavior of copolymer **H6** and **B6**.

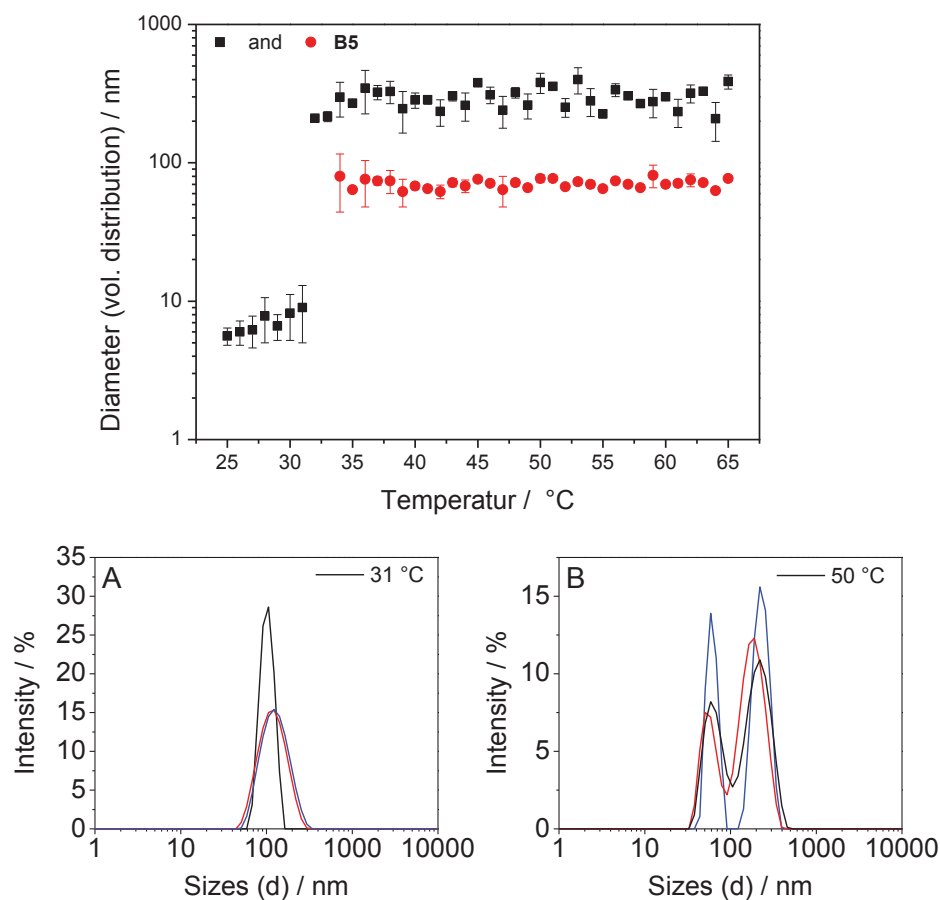


Figure S10. The hydrodynamic diameter (volume distribution, average value of three estimations) of the block copolymer **B5** at  $1.0 \text{ mg mL}^{-1}$  is plotted as a function of temperature. A and B represent the hydrodynamic size distribution (three measurements, intensity distribution) of the block copolymer of **H5** at  $1.0 \text{ mg mL}^{-1}$  at the respective temperature point.

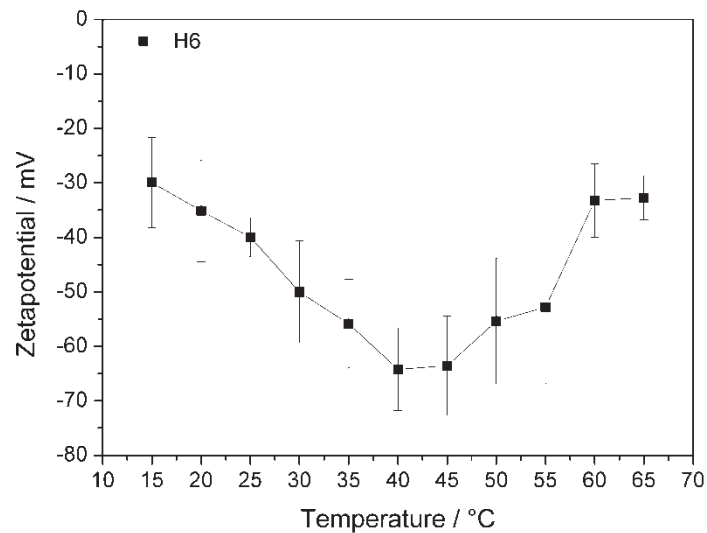


Figure S11. Temperature variable zeta potential measurements (black squares) of homo polymer **H6** ( $2.5 \text{ mg mL}^{-1}$ ) during two cycles of heating and cooling (average value of 5 measurement). The larger error bar of the zeta potential values are due to the large size of the particles ( $R_H \sim 500 \text{ nm}$ ), causing in a reduced mobility and to multiple scattering effects.